Development of a Contemporary Ligand-Field Program for 3d Transition-Metal Complexes

George Nunn

PhD

University of York
Chemistry

September 2023

Abstract

Ligand-field theory (LFT) is a quantum-mechanical model which calculates the physical properties associated with the presence of an incomplete d shell. In this work, the development of a contemporary ligand-field program for $3d^n$ transition-metal complexes is reported. The program, Kestrel is designed to be easy-to-use and performs real time calculations of the d-d transition energies, EPR g-factors, paramagnetic susceptibilities, and single-ion molecular magnetic (SiMM) behaviour of a complex using its real molecular geometry. Kestrel also features the prediction of UV-Vis, circular dichroism (CD), and magnetic circular dichroism (MCD) spectra in non-centrosymmetric systems. The ligand-field model uses metal-ligand bonding parameters to parameterise the ligand field and Racah parameters are used to simulate the effects of interelectronic repulsion. The multiconfigurational effects arising from spin-orbit coupling are also treated. Spectroscopic intensities arising from the electronic dipole mechanism are simulated using transition dipole moment parameters calculated for each ligand using metal-ligand polarisation parameters. Herein, the application of Kestrel to three contemporaneous case studies demonstrates the practical use of the software. First, the program is used to analyse how the SiMM behaviour of three homoleptic cobalt(II) complexes changes with variation in the molecular geometry and metal-ligand bonding. The study outlines suggestions for future synthetic work to enhance the SiMM behaviour of these systems. The second case study focuses on the reproduction of the variable-temperature MCD spectrum of a characterised intermediate-spin (S=1) iron(IV) oxo complex. The analysis shows that Kestrel's assignment of the d-d bands, which differs from that in the literature, can reproduce the reported experimental data. Lastly, the program is used to analyse the full reported experimental characterisation of the resting state and substrate bound *lytic polysaccharide monooxygenase* (LPMO) enzyme LsAA9. The analysis was able to characterise the electronic structure of the copper(II) ion in this enzyme.

List of contents

Abstract 2
List of contents 3
List of figures 12
List of tables 21
List of accompanying material 24
Acknowledgements 25
Author's declaration 27
1 Introduction 28
1.1 Why ligand-field theory? 28
1.2 The ligand field 30
1.2.1 Ligand-field theory is *not* molecular orbital theory: the primogenic effect in $3d^n$ transition-metal ions. 30
1.2.2 The paradigm of ligand-field theory 31
1.2.3 Metal-ligand bonding 32
1.2.4 *Ab initio* ligand-field theory 34
1.3 Available ligand-field programs 35
1.4 This work 37
2 Theory 39
2.1 Effective Hamiltonians 39
2.2 Angular momentum & tensor operators 42
2.2.1 Angular momentum coupling 42
2.2.2 Wigner symbols 44
2.2.3 Rotations of angular momenta and tensor operators 45
2.2.4 Evaluation of the operators of the effective Hamiltonian 47
2.2.4.1 The Wigner Eckart theorem 48
2.2.4.2 The ligand-field potential 49

2.2.4.3 Interelectronic repulsion 49
2.2.4.4 Spin-orbit coupling 51
2.2.4.5 Zeeman interaction 51
2.3 The ligand-field model 52
2.3.1 The multipole expansion 53
2.3.2 The one-electron ligand-field matrix 54
2.3.3 Angular overlap model 55
2.3.3.1 Spherical polar coordinates 56
2.3.3.2 Diagonal perturbations 57
2.3.3.3 Misdirected valence 60
2.3.3.4 4s-3d mixing 61
2.3.4 A theoretical guide to the parameterisation of metal-ligand bonding 62
2.3.4.1 Bonding interactions of ligands 62
2.3.4.1.1 Saturated donors 64
2.3.4.1.2 Cylindrical π bonding 65
2.3.4.1.3 sp^2 hybridised ligands 65
2.3.4.1.4 Phase-coupled ligators 66
2.3.4.1.5 Cyclopentadienyl ligands. 68
2.3.4.1.6 Olefin ligands 68
2.3.4.2 Choosing ligands 69
2.4 Post-diagonalisation methods 70
2.4.1 Projection methods 70
2.4.1.1 Spin projection 70
2.4.1.2 Configuration projection 71
2.4.2 Magnetism 72
2.4.2.1 EPR g-factors 72
2.4.2.2 Paramagnetic susceptibilities 73
2.4.2.3 Mapping eigenvectors on to the magnetic moment operators 73
2.4.3 Spectroscopic intensities 74

2.4.3.1 Electric dipole moment operator 75
2.4.3.2 The transition dipole moment parameters 76
2.4.3.3 Absorption spectroscopy 78
2.4.3.4 Circular dichroism 78
2.4.3.5 Magnetic circular dichroism 79
3 The Kestrel program 81
3.1 KestrelPy 82
3.1.1 Framework of the package 83
3.1.2 The Molecule class. 84
3.1.3 Running calculations 84
3.1.3.1 Construction of the basis set 86
3.1.3.2 Evaluating matrix elements and solving the effective Hamiltonian 87
3.1.4 Calculation of UV-Vis, CD, and MCD 88
3.1.4.1 Calculation of electric transition dipole moment integrals 88
3.1.4.2 Spectrum object 88
3.1.4.3 Calculation of UV-Vis and CD spectra 88
3.1.4.4 Calculations of MCD spectra 89
3.2 Graphical user interface 91
3.2.1 Saving, loading, and starting new files 92
3.2.2 Setting up a molecule in Kestrel 92
3.2.2.1 Import an xyz file 93
3.2.2.2 Selecting the central metal ion 96
3.2.2.3 Defining the ligands 96
3.2.3 Molecular visualiser and display options. 101
3.2.4 Parameters 102
3.2.4.1 Initialising starting “guess” parameters 103
3.2.4.2 Linking parameters together 104
3.2.4.3 Scanning parameters 105
3.2.5 The ligand-field splitting 106

3.2.6 Relative energies of many-electron states 107
3.2.7 EPR g-factors 110
3.2.8 Paramagnetic susceptibilities 111
3.2.9 Plotting the principal and isotropic χT curves 112
3.2.10 Simulations of UV-Vis, CD, and MCD spectra 114
3.2.11 Optimisation 115
3.2.11.1 Getting started 116
3.2.11.2 Varying the parameters 117
3.2.11.3 Choosing to fit a 5×5 ligand-field matrix 120
3.2.11.4 Selecting the optimisation method 122
3.2.11.5 Running the calculation 122
3.2.12 Parameter-space search 123
3.2.12.1 Getting started 124
3.2.12.2 Varying parameters 125
3.2.12.3 Choosing to fit two data sets simultaneously: the EPR g-factors and transition energies 126
3.2.12.3.1 EPR g-factors 127
3.2.12.3.2 d-d transition energies 128
3.2.12.4 Running the calculation 129
3.2.12.5 Visualising the results 129
4 Ligand-field analysis 133
4.1 The rational design of single-ion molecular magnets 133
4.1.1 Introduction 133
4.1.1.1 Use of ligand-field calculations from Kestrel to calculate U_{eff} 135
4.1.2 Methodology 137
4.1.2.1 Ligand-field calculations 137
4.1.2.1.1 Complex 1 137
4.1.2.1.2 Complex 2 139
4.1.2.1.3 Complex 3 139

4.1.2.2 Quantum-chemical calculations 140
4.1.2.3 Calculation of τ_{QTM} and U_{eff} 140
4.1.3 Complex 1 142
4.1.3.1 Electronic structure from experiment, Kestrel analysis 143
4.1.3.2 Origins of the non-Aufbau ground state 148
4.1.3.3 Low-symmetry components of a linear complex 152
4.1.3.4 Enhancing the single-ion molecular magnetic properties, using Kestrel in a predictive sense 154
4.1.3.4.1 The single-ion molecular magnetic properties of complex 1 155
4.1.3.4.2 The single-ion molecular magnetic properties of complex 1 as a function of φ 156
4.1.3.4.3 Future design considerations for enhancing the single-ion molecular magnetic properties of linear complexes 158
4.1.4 Complex 2 159
4.1.4.1 Electronic structure from experiment, Kestrel analysis 159
4.1.4.1.1 Fitting the reported experimental data 159
4.1.4.1.2 Analysis of the ligand-field splitting 161
4.1.4.1.3 Analysis of the d-d transition energies 162
4.1.4.2 Enhancing the single-ion molecular magnetic properties 165
4.1.4.2.1 The single-ion molecular magnetic properties of complex 2 166
4.1.4.2.2 The single-ion molecular magnetic properties of complex 2 as a function of φ 166
4.1.4.2.3 The single-ion molecular magnetic properties of the eclipsed structure of complex 2 as a function of θ 169
4.1.4.2.4 The single-ion molecular magnetic properties of the eclipsed structure of complex 2 as a function of $d\theta$ 171
4.1.4.2.5 The effect of metal-ligand bonding on the axiality of the ground state Kramer's doublet 172
4.1.4.2.6 Future design considerations for trigonal D_3 complexes 174
4.1.5 Complex 3 175
4.1.5.1 Electronic structure from experiment, Kestrel analysis 175

4.1.5.1.1 Fitting of the reported magnetic data 175
4.1.5.1.2 Analysis of the ligand-field splitting 176
4.1.5.1.3 Analysis of the d-d transition energies 177
4.1.5.2 Enhancing the single-ion molecular magnetic properties 180
4.1.5.2.1 The single-ion molecular magnetic properties of complex 3 181
4.1.5.2.2 The single-ion molecular magnetic properties of complex 3 as a function of θ 182
4.1.5.2.3 The single-ion molecular magnetic properties of complex 3 as a function of φ 184
4.1.5.2.4 The single-ion molecular magnetic properties of complex 3 as a function of ψ and $e_{\pi\sigma x}$ 186
4.1.5.2.5 The relationship between metal-ligand bonding and bite angle θ..... 188
4.1.5.2.6 Future design considerations for tetrahedral complexes 191
4.1.6 Conclusion 192
4.2 Ligand fields of nonheme S=1 iron(IV)-oxo complexes 194
4.2.1 Introduction 194
4.2.1.1 Electronic spectroscopy of S=1 Fe(IV) complexes of C_{4v} symmetry 196
4.2.1.2 Spectroscopy of $[Fe(O)(TMC)(NCCH_3)]^{2+}$ 199
4.2.1.3 Computational modelling of ligand-field transitions in iron(IV) oxo systems. 200
4.2.1.3.1 Electronic structure analysis of $[Fe(O)(TMC)(NCCH_3)]^{2+}$ 201
4.2.1.3.2 Electronic structure of other iron(IV) oxo complexes 202
4.2.1.4 Ligand-field analysis of $[Fe(O)(TMC)(NCCH_3)]^{2+}$ 203
4.2.1.5 This work 204
4.2.2 Methodology 205
4.2.2.1 Quantum-chemical calculations 205
4.2.2.2 Ligand-field calculations 205
4.2.2.3 Fitting results of *ab initio* calculations with the ligand-field model 206
4.2.2.4 Fitting experimental band energies with the ligand-field model 207

4.2.2.5 Fitting the experimental UV-Vis and VT-MCD spectra with the ligand-field model 207
4.2.3 Quantum-chemical calculations 208
4.2.3.1 Geometry optimisation 208
4.2.3.2 Minimal active space CASSCF(4, 5) 209
4.2.3.3 Expanded active space CASSCF(12, 9)/NEVPT2 211
4.2.3.3.1 Excited-state spectroscopy 214
4.2.3.4 Covalency of the $[Fe–O]^{2+}$ subunit 216
4.2.4 Ligand-field calculations 217
4.2.4.1 Analysis of the AILFT results 217
4.2.4.2 Analysis of the CASSCF(12, 9)/NEVPT2 transition energies 218
4.2.4.3 Idealised model 220
4.2.4.3.1 Energies of many-electron states 220
4.2.4.3.2 UV-Vis spectroscopy 222
4.2.4.4 Ligand-field analysis of the experiment 225
4.2.4.5 Comparison with experimental data 228
4.2.4.6 Electronic structure 232
4.2.5 Discussion 235
4.2.5.1 The best fit ligand-field, interelectronic repulsion, and spin-orbit coupling parameters 235
4.2.5.2 The best fit transition dipole moment parameters 236
4.2.5.3 The spin-forbidden triplet to quintet $d_{xy} \rightarrow d_{z^2}$ assignment 238
4.2.5.4 Limits of ligand-field theory in Fe(IV)-oxo complexes? 238
4.2.6 Conclusion 239
4.3 Electronic structure investigations of lytic polysaccharide monooxygenases 241
4.3.1 Introduction 241
4.3.1.1 The histidine brace 242
4.3.1.2 The catalytic action of LPMOs 243
4.3.1.2.1 LPMO activity 243
4.3.1.2.2 Substrate binding 244

4.3.1.2.3 The suggested reactive intermediate 245
4.3.1.2.4 The proposed catalytic cycle 247
4.3.1.3 Spectroscopic characterisation and electronic structure 248
4.3.1.4 The aim of this work 249
4.3.2 Methodology 250
4.3.2.1 Ligand-field calculations 250
4.3.2.2 Fitting d-d transition energies and EPR g-factors 252
4.3.2.3 Fitting the experimental UV-Vis, CD, and MCD with the ligand-field model 253
4.3.3 Results 254
4.3.3.1 Transition energies & EPR 254
4.3.3.2 Ligand field of the histidine brace 258
4.3.3.2.1 The effect of the histidine brace dihedral angle on the d-orbital manifold 262
4.3.3.3 The d-d transitions and configurational mixing 263
4.3.3.4 UV-Vis, CD, and MCD spectra 264
4.3.3.4.1 Spectra simulation 264
4.3.3.4.2 The transition dipole moment parameters 271
4.3.4 Discussion 272
4.3.4.1 The ligand field of *Ls*AA9. 272
4.3.4.2 The nature of the exogenous ligand in *Ls*AA9_C6_H_2O 275
4.3.4.3 The d-orbital ordering 277
4.3.4.4 Electrodynamic “torque” 278
4.3.4.5 Catalytic activity 281
4.3.5 Conclusion 282
5 Conclusion and future work 284
6 Appendices 288
6.1 Tables of metal-ligand bonding parameters reported for ligand-field analyses of experimental and computational data 289
6.2 Tabulation of all unique orbital occupations for each d^n electronic configuration 295

6.3 Electrostatic origin of the low-symmetry components of $Co(C(SiMe_2ONaph)_3)_2$ .. 299

6.4 The 5×5 one-electron ligand-field matrix from a converged CASSCF(7, 5)/NEVPT2 calculation on $Co(C(SiMe_2ONaph)_3)_2$..... 301

6.5 The S=1 BP86, ma-def2-tzvp(-f) geometry optimised coordinates of $[Fe(O)(TMC)(NCCH_3)]^{2+}$ in acetonitrile..... 303

6.6 Calculation of the ligand-field traces for V(IV)-oxo systems..... 305

7 List of abbreviations..... 306

8 References..... 307

List of figures

Figure 1.1. An illustrative example of multiconfigurational descriptions of a fictitious d^7 system. 28
Figure 1.2. The interaction symmetries of the e_σ and e_π interactions 32
Figure 2.1 The sampling of eigenstates via an effective Hamiltonian, which represent a "window" of states in the full Hamiltonian. 40
Figure 2.2. The stepwise rotation of a coordinate scheme X (green), Y (blue), and Z (red) by Euler angles in the z-y-z convention 46
Figure 2.3 The mixing of the angular Y(l,m) (l=2, m=2, 1, 0) spherical harmonics in one coordinate frame (XYZ) to reconstruct the spherical harmonics in a rotated coordinate frame (X'Y'Z'). 55
Figure 2.4. The angular geometry of a ligand and the definitions of its spherical polar coordinates. 56
Figure 2.5 The electrodynamic contribution arising from a metal-ligand bonding orbital with the d orbitals (left) and the corresponding pseudo-symmetry representation within LFT from the minimal basis set of d orbitals (right). 58
Figure 2.6 The formation of metal-ligand bonding and antibonding orbitals between a ligand σ function and a combination of the metal 4s/4p functions and its perturbation on the d orbitals (A); the competing π-acceptance and π-donation from both donor/accepting capabilities of a metal-ligand bonding and anti-bonding π function (B). 59
Figure 2.7 Illustrative representation of a destabilising misdirected bond projected into the negative XZ quadrant of the local ligand frame resulting in a positive misdirected parameter value. 60
Figure 2.8. The key types of bonding interactions for different classes of molecules. The subscripts 'x' refer to a direction parallel to the intra-ligand bonds shown and 'y' refers to the direction perpendicular to that. The * next to an e_λ assigns that interaction as an acceptor interaction. 64
Figure 2.9. The out-of-phase χ-type and in-phase ψ-type interactions with the d_{yz} and d_{xz} orbitals for the Orgel effect of phase-coupled ligation. The red and blue arrow represent the molecular Z and Y axes respectively. 66
Figure 2.10. The parameterisation scheme of a phase-coupled ligator ligand from the "Orgel effect" 67

Figure 2.11. The x-ray crystal structure of $(C_6F_5)_3$trenVCN^{t}Bu (left, CSD: WAFGOD) and the representative molecular drawing with the three functional groups coloured in blue, red, and pink (right).[77] 69
Figure 2.12 The reconstruction of a metal-ligand σ bonding function Ψ_σ using a linear combination of metal-centred spherical harmonics of s, p, and f character and the result polarisation effect on the d_{z^2} orbital. 77
Figure 2.13 The A_1, B_0, and C_0 origins of MCD intensity as given by the perturbative expansion. 80
Figure 3.1. Schematic representation of the molecule class object orientated hierarchy and the important class attributes. 84
Figure 3.2. The KestrelPy workflow of calculating the eigenfunctions of the effective Hamiltonian 85
Figure 3.3. The computational workflow for computing the orientationally averaged MCD intensities (left) and an example of a molecular rotation with the full angular grid with a grid size of 15×15 (right) 89
Figure 3.4 An example of the Kestrel window with its molecular visualiser and some of the available dock widgets. 91
Figure 3.5. The procedure for importing the coordinates of an xyz file. 93
Figure 3.6. The process of importing a molecular geometry stored in an xyz file (CSD: WAFGOD) into Kestrel's GUI.[77] 94
Figure 3.7. The ligand-field parameterisation setup window. 95
Figure 3.8. Selecting a central metal ion as part of setting up the molecule using Kestrel's GUI. 96
Figure 3.9. The ligand-field parameterisation setup window after successfully selecting a central metal ion in Kestrel's GUI. 97
Figure 3.10. The process of adding a ligand by assigning the ligand a label. 98
Figure 3.11. The process of assigning a coordinating atom to a ligand. 98
Figure 3.12. Orientating the amide ligand x direction via Kestrel's GUI. 99
Figure 3.13. The final ligand-field parameterisation setup for the example molecule $(C_6F_5)_3$trenVCN^{t}Bu. 100
Figure 3.14. The process of opening the display options for the molecular rendering in Kestrel's GUI. 101
Figure 3.15. The process of opening the parameter dock window in Kestrel's GUI. 102
Figure 3.16. The process of generating illustrative starting parameters via Kestrel's GUI.. 103
Figure 3.17. The process of linking two ligand e_λ parameters together via Kestrel's GUI... 104
Figure 3.18. The process of scanning a parameter via Kestrel's GUI. 105

Figure 3.19. The output of a ligand e_σ parameter scan in Kestrel's GUI (left) and the corresponding plot of the d-orbital energies (right). 105
Figure 3.20. The process of opening the ligand-field dock window. 106
Figure 3.21. The process of opening the transition energies dock widget. 108
Figure 3.22. The definition of the elements of the configuration projection output (A) and the corresponding 22111 electronic occupation in terms of the five d orbitals in ascending order of energy (B). 109
Figure 3.23. The process of opening the EPR results dock window. 110
Figure 3.24. The process of opening the paramagnetic susceptibility results window. 111
Figure 3.25. The process of opening the principal paramagnetic susceptibilities variation with temperature graph in Kestrel. 112
Figure 3.26. The calculated isotropic paramagnetic susceptibility variation with temperature (black) overlaid with comparison data (red). 113
Figure 3.27. The steps to open the ligand-field spectra via Kestrel's GUI. 114
Figure 3.28. The molecular rendering of $[Fe(O)(TMC)(NCCH_3)]^{2+}$ in Kestrel's GUI. 115
Figure 3.29. The steps to open the optimisation dialog via Kestrel's GUI. 116
Figure 3.30. Setting the bounds for the e_σ of the oxo ligand in $[Fe(O)(TMC)(NCCH_3)]^{2+}$ using Kestrel's GUI. 118
Figure 3.31. The format of setting the optimisation bounds of the oxo's e_σ parameter in $[Fe(O)(TMC)(NCCH_3)]^{2+}$ using Kestrel's GUI. 119
Figure 3.32. Enabling the calculation of a 5×5 ligand-field matrix for use in an optimisation calculation via Kestrel's GUI. 120
Figure 3.33. Selecting an ORCA output file to extract the 5×5 ligand-field matrix in Kestrel's GUI. 121
Figure 3.34. The "Solver" tab of the optimisation window. 122
Figure 3.35. The molecular rendering of *Ls*AA9 in Kestrel's GUI. 123
Figure 3.36. The steps to open the parameter-space dialog via Kestrel's GUI. 124
Figure 3.37. Varying the e_σ of the histidine ligands in *Ls*AA9 using Kestrel's GUI. 125
Figure 3.38. The parameter-space range for *Ls*AA9 in Kestrel's GUI. 126
Figure 3.39. Defining the experimental EPR g-factors for *Ls*AA9 to compare to, via Kestrel's GUI. 127
Figure 3.40. Defining the experimental transition energies for *Ls*AA9 to compare to, via Kestrel's GUI. 128
Figure 3.41. The parameter-space "mapping" window in the "Search" tab of the central widget of Kestrel. 129
Figure 3.42. The layout and options of the parameter-space "mapping" window. 130
Figure 3.43. The plotting options of the parameter-space output. 131

Figure 3.44. Examples of the “smoothing” and “Outline Value” plotting options in the parameter-space output window. 132
Figure 4.1. The energy barrier (U) to the reversal of magnetisation at zero external magnetic field of a fictitious J = $^{7}/_{2}$ system. Black bars represent electronic states with the corresponding M_J projection. Red dotted arrows represent QTM transitions between $\pm M_J$ states. Green arrows represent relaxation via a two-step phonon relaxation process known as the Orbach process. Finally, the orange dotted arrow represents the Raman relaxation pathway. 134
Figure 4.2. Structures of complexes 1, 2, and 3 (see text) with the reported energetic splitting between ground and first excited state Kramer’s doublets.[122–124] 136
Figure 4.3. The metal-ligand e_λ bonding interactions used to parameterise the ligand field in complexes 1, 2, and 3. 137
Figure 4.4. The UV-Vis diffuse reflectance spectrum of complex 1 reported by P. C. Bunting, M. Atanasov, E. Damgaard-Møller, M. Perfetti, I. Crassee, M. Orlita, J. Overgaard, J. van Slageren, F. Neese and J. R. Long, *Science*, 2018, 362, eaat7319. Reprinted with permission from AAAS. 143
Figure 4.5. Regions of best fit for complex 1 in the reproduction of the two high energy quartet ligand-field transitions at 12000 and 15000 cm^{-1} with fixed values of e_π. Colour bars are the RMS fit (cm^{-1}) values to the two high energy quartet bands. 145
Figure 4.6. The variation in the computed zero-field splitting energy between the ground state and first excited state Kramer’s doublet and the five lowest lying Kramer’s doublets for the corresponding best fit e_σ and Racah B parameters, as a function of e_π, for complex 1. Zero-field splitting was calculated using a spin-orbit coupling constant of 515 cm^{-1}. 146
Figure 4.7. The Kestrel calculated (black) χT variation as a function of temperature for the corresponding best fit e_σ and Racah B parameters, as a function of e_π, for complex 1. The simulations were performed using a spin-orbit coupling constant of 515 cm^{-1}. The 0.1 T reported experimental data (red) was supplied by the authors.[122] 147
Figure 4.8. The ligand-field splitting as computed by *Bunting et al*. and this work, along with multipole expansion of the x-ray structure (right) for the average best fit parameters in the text.[122] 148
Figure 4.9. The change in relative energies of the complete quartet manifold as a function of the interelectronic repulsion parameter, Racah B. The grey dotted line signifies the interelectronic repulsion strength in which a change in the ground state character occurs. 149
Figure 4.10. The effect that metal-ligand bonding parameters have on the relative energies of the quartet manifold. Variation of e_σ (left) and e_π (right). Grey dotted lines mark a formal change in the ground state electronic configuration. 152
Figure 4.11. The geometric distortion between the two trigonal arms of the ligands in complex 1 154

Figure 4.12. The variation of U_{eff} with temperature as a function of the trigonal distortion, φ. The percentage contribution of the five lowest energy $S=^3/_2$ Kramer's Doublets are also plotted. Calculations are performed using the low symmetry parameterisation of 1, $\zeta = 475$ cm^{-1}, and $k_{iso} = 0.99$. 157
Figure 4.13. The Kestrel calculated isotropic χT variation with temperature for the best fit parameters of complex 2. 161
Figure 4.14. The Kestrel calculated ligand-field splitting diagram and Kestrel rendered orbitals for complex 2. 162
Figure 4.15. The geometric distortions φ, θ, and *d*θ of complex 2. 165
Figure 4.16. The variation the calculated effective barrier of magnetisation against temperature at select angles of φ for complex 2. 168
Figure 4.17. The variation the calculated effective barrier of magnetisation against temperature at select angles of θ for the eclipsed structure of complex 2 (φ = 0°). 170
Figure 4.18. The logarithm of the time taken for quantum tunnelling of magnetisation in complex 2 for the eclipsed structure (φ = 0°). 171
Figure 4.19. The effect that the $e_{\pi y}$ parameter has on the EPR g-factors and the energy of the first three Kramer's doublets calculated using the x-ray crystal structure (anti-prismatic). The dotted line is given for $e_{\pi y} = -160$ cm^{-1} and corresponds to II. The right of the figure shows the configurational interactions under the effect of spin-orbit coupling (ζ = 440 cm^{-1}) for each region. 172
Figure 4.20. The Kestrel calculated isotropic χT variation with temperature for the best fit parameters of complex 3. The reported experimental data (red) supplied by the authors.[124] 176
Figure 4.21. The Kestrel calculated ligand-field splitting and orbital projections rendered using Kestrel of complex 3. 177
Figure 4.22. The geometric distortions θ, φ, and ψ of complex 3. 180
Figure 4.23. Theoretical predictions of U_{eff} and its contributions from the four lowest-lying KDs as a function of temperature for complex 3 calculated using Kestrel. 182
Figure 4.24. The variation in the calculated effective barrier of magnetisation (U_{eff}) of the angle defining the axial elongation in complex 3. 183
Figure 4.25. The energies of the one-electron orbitals as a function of the torsional distortion φ for complex 3, calculated using Kestrel. The axial distortion was set to the optimal angle of θ = 38° 185
Figure 4.26. The local x-frames superimposed on the coordinating atom for 3 against the coordinate axes (A). A schematic depiction of the misdirected valence arising from the geometric distortion about the coordinating atom (B). The variation in the d-orbital energies with ψ, where $e_{\pi\sigma x} = 0$ cm^{-1} (C). The variation in the d-orbital energies with values of $e_{\pi\sigma x}$ for ψ

= 0° (D). All other ligand-field parameters are their best fit values, and the ideal molecular geometry was used with an angle θ = 38° and φ = 90° (see methodology and text)..... 187
Figure 4.27. The variation in the one-electron d-orbital energies of the 3 as a function of the angle θ. The value of e_σ was held constant at 6410 cm^{-1}. The ideal angles φ = 90° and ψ = 0° were used. 189
Figure 4.28. The variation in the magnitude of zero-field splitting for changes in the angle θ and $e_{\pi y}/e_\sigma$ for 3. Calculations were carried out using the ideal model system. 190
Figure 4.29. Illustrative cubic S=1 and trigonal S=2 Fe=O complexes.[151–156] 194
Figure 4.30. (A) The charge transfer processes involved during hydrogen atom abstraction of the CH bond of the $[FeO]^{2+}$ core. (B) the crystal structure (CSDC: WUSJOJ) of $[Fe(O)(TMC)(NCCH_3)]^{2+}$.[151] 195
Figure 4.31. The spin-allowed one-electron d-d excitations in an S=1 tetragonal iron(IV) oxo complex. The d orbitals are generated and rendered using Kestrel and serve as illustrative depictions of their shapes and orientation. 197
Figure 4.32. The zero-field splitting of the $^3A_2$ ground state under C_{4v} symmetry from spin-orbit coupling (top); and the relative MCD intensity of ligand-field bands from the application of directional magnetic fields as a function of temperature (bottom). 198
Figure 4.33. The experimental electronic absorption (A) and VT-MCD (B) spectra of $[Fe(O)(TMC)(NCCH_3)]^{2+}$. Selection rules of electronic transition polarisation (C) and ΔSCF/BP86 computed transition energies and assignments (D). Reprinted with permission from A. Decker, J.-U. Rohde, L. Que, and E. I. Solomon, J. Am. Chem. Soc., 2004, 126, 5378–5379. Copyright 2004, American chemical Society. 200
Figure 4.34. The metal-ligand bonding parameterisation for $[Fe(O)(TMC)(X)]^{2+}$, where X = acetonitrile. 206
Figure 4.35. The optimised geometric structure of $[Fe(O)(TMC)(NCCH_3)]^{2+}$ in acetonitrile overlaid with the chosen molecular axes used for ligand field and *ab initio* calculations. ... 209
Figure 4.36. The CASSCF(12, 9) optimised active space orbitals plotted with a contour value of 0.05. 212
Figure 4.37. The CASSCF(12, 9)/NEVPT2 calculated (red) and reported experimental (black) normalised electronic absorption spectra of $[Fe(O)(TMC)(NCCH_3)]^{2+}$ (top) and the calculated CASSCF(12, 9)/NEVPT2 MCD spectra at 7T (bottom). Spectra are simulated using a FWHM = 2000 cm^{-1}.[165] The experimental UV-Vis is adapted with permission from A. Decker, J.-U. Rohde, L. Que, and E. I. Solomon, J. Am. Chem. Soc., 2004, 126, 5378–5379. Copyright 2004 American Chemical Society. 215
Figure 4.38. Comparison of the CASSCF(12, 9)/NEVPT2 and Kestrel computed transition energies up to 19000 cm^{-1}. Red dotted lines are comparisons between ^3E bands and green dotted lines are comparisons between the components of the $^3\Gamma$ ($d_{xy} \rightarrow d_{x^2-y^2}$) bands..... 218

Figure 4.39. The relative absorption bands of the idealised C_{4v} model for $[Fe(O)(TMC)(NCCH_3)]^{2+}$ using only P and F parameters on the oxo ligands. Simulations performed using a FWHM = 2500 cm^{-1}. Calculations performed in the absence of spin-orbit coupling but with B = 500 cm^{-1} and C = 2000 cm^{-1}. 224
Figure 4.40. The simulated (red) and experimental (black) UV-Vis and 7 T VT-MCD for the parameter sets in Table 4.19. Simulations were performed using a FWHM = 2500 cm^{-1} for each transition. MCD simulations were performed with a 30 × 30 angular grid for θ and φ. The experimental UV-Vis is adapted with permission from A. Decker, J.-U. Rohde, L. Que, and E. I. Solomon, J. Am. Chem. Soc., 2004, 126, 5378–5379. Copyright 2004 American Chemical Society. 229
Figure 4.41. The saturation plots generated using Kestrel for the MCD intensity of the bands of $[Fe(O)(TMC)(NCCH_3)]^{2+}$ at 10400 cm^{-1}, 12900 cm^{-1}, and 17600 cm^{-1} at 7 T using the best fit parameters (see text). 231
Figure 4.42. The Kestrel rendered ligand-field orbitals for the best fit parameter set (see text) of $[Fe(O)(TMC)(NCCH_3)]^{2+}$. 232
Figure 4.43. The effect of polarisation of P and F functions (left) into the d_{xz}/d_{yz} (top) and d_{z^2} (bottom). The degree of polarisation is exaggerated for clarity. The converged CASSCF(12, 9) anti-bonding active space orbitals (right) for the d_{xz}/d_{yz} and d_{z^2}. 237
Figure 4.44. The crystallographic structure of the LPMO enzyme, *Ls*AA9 (PDB: 5ACH) rendered using CCP4MG. 241
Figure 4.45. A representative drawing of the first coordination sphere of the copper(II) active site in *Ls*AA9 (A); and the definition of the dihedral “twist” ψ, between the two planes of the histidine rings (B). 243
Figure 4.46. C1 or C4 oxidation products of cellulose by the action of an LPMO enzyme. 244
Figure 4.47. The oxidised active site of *Ls*AA9 with cellotriose (PDB: 5ACF) with the chloride anion occupying the exogeneous site. Green, blue, and red cylinders represent carbon, nitrogen, and oxygen atoms, respectively. The copper(II) and chloride ions are represented by the orange and yellow spheres, respectively. 245
Figure 4.48. A representative Lewis structure for a metal-oxyl and metal-oxo bond (top) and the destabilisation of a formal metal-oxygen π bond resulting in the oxo all (bottom). 246
Figure 4.49. The proposed catalytic pathways for peroxygenation (left cycle) and oxidation (right cycle) of substrate (labelled as R). 247
Figure 4.50. The truncated structure of the first coordination sphere of *Ls*AA9 (A), *Ls*AA9_C6_H_2O (B), *Ls*AA9_C6_Cl (C), and *Ls*AA9_C6_Br (D) models with hydrogens and the substrate (for B, C, and D) omitted for clarity. The xyz structures are the DFT optimised structures computed by *A. Paradisi*.[220] 249

Figure 4.51. The global x (red), y (green), z (blue) coordinate schemes for *Ls*AA9 (A), *Ls*AA9_C6_H_2O (B), *Ls*AA9_C6_Cl (C), and *Ls*AA9_C6_Br (D). 250
Figure 4.52. The pseudo-symmetries of the local metal-ligand bonding parameters represented by spherical harmonics for the sigma-bonding framework (A); the asymmetric pi-bonding network (B); and the cylindrical pi-bonding network (C); where X = H_2O, Cl, Br. Note the phase information of the spherical harmonics is meaningless in the potential based method. 251
Figure 4.53. The contour maps of best RMS fit (cm^{-1}) values to the transition energies (A) and EPR g-factors (B) of the *Ls*AA9 resting state. The two g-factor orientations given by the two regions of fit to the EPR g-factors (C). 256
Figure 4.54. The absolute one-electron orbital energies from the diagonalisation of the 5×5 one-electron ligand-field matrix for each of the four LsAA9 systems. 260
Figure 4.55. The final d-orbital orientations in *Ls*AA9 resting state (top) and in *Ls*AA9_C6_Cl (bottom) generated using Kestrel. The orbitals are ordered left to right from lowest to highest energy, representing the predominantly $d_{yz} < d_{xy} < d_{xz} < d_{z^2} < d_{x^2-y^2}$. 261
Figure 4.56. The multipole expansions of LsAA9 (A), LsAA9_C6_H_2O (B), LsAA9_C6_Cl (C), and LsAA9_C6_Br (D), rendered using Kestrel. 262
Figure 4.57. The variation in the second (bottom) and third (top) lowest energy d orbitals as a function of the dihedral angle of the histidine brace twist. Green, blue, and red arrows are the x, y, and z axes of the coordinate scheme, respectively. 263
Figure 4.58. The experimental (black) and Kestrel simulated (red) MCD spectra at 7T and 5K (top); Kestrel calculated variable-temperature MCD at 7T (middle); and variation-field MCD at 5K (bottom), for the *Ls*AA9 models. The spectra were simulated using the parameters in Table 4.22. The spectra were simulated using an angular resolution of 30 steps per θ and φ angles. The experimental MCD spectra were recorded and reported by *A. Paradisi*.[220] 267
Figure 4.59. The experimental (black) and Kestrel simulated (red) CD spectra at 300 K for the *Ls*AA9 models. The experimental CD spectra were recorded by *A. Paradisi* at room temperature.[220] 269
Figure 4.60. The experimental (black) and simulated (red) UV-Vis spectrum at 300 K for *Ls*AA9 models, scaled to experiment using a FWHM of 3000 cm^{-1}. The experimental UV-Vis spectra were recorded by *A. Paradisi* at room temperature.[220] 270
Figure 4.61. Schematic representation of the *cis* influence operating through the e_σ parameter in the *Ls*AA9 active site equatorial coordination sphere. 273
Figure 4.62. The definition of the angle of coordination of a water molecule to the copper ion (top) and an illustration of the resulting orbital orientations from the coordination angles in *Ls*AA9 and *Ls*AA9_C6_H_2O (bottom). 276

Figure 4.63. The d-orbital splitting from a D_{4h} square planar system using e_σ only (left) and a combination of e_σ and e_π (right). 277
Figure 4.64. The difference in the equatorial coordination sphere in *Ls*AA9 resting state and *Ls*AA9_C6_Cl where the Cl-Cu-NH_2 vector has rotated about the cartesian x-axis. Truncated forms of the DFT optimised geometries are taken from the work of *A. Paradisi*.[220] Hydrogens attached to carbon atoms have been omitted for clarity. 279
Figure 4.65. Kestrel rendering of the ligand field. The strain results in an electrodynamic torque generated by the twist in the dihedral angle between the two histidine π bonding networks, which drives a rotation about the His2–Cu–His1 axis of the copper d electrons. 280
Figure 4.66. The putative copper-oxygen reactive intermediate *p* orbital alignment with the d_{yz} and d_{xy} orbitals on the copper. 281
Figure 6.1. The truncated xyz structure of the coordinating alkyl ligand and closest second-sphere coordination shell. Asterisks indicate atoms where a point charge is placed. O = red, Si = turquoise, C = grey, and Co = blue. 299
Figure 6.2. The V(IV)-oxo systems (1-3) analysed using a ligand-field model by *Stappen et al*.[188] 305

List of tables

Table 1.1. Summary of available features of the major available ligand-field programs. 37
Table 2.1. General e_λ parameterisation schemes for classes of ligands. (L.P.) = lone pair interaction. 63
Table 3.1. The list of free-ion Russell-Saunders ^{2S+1}L terms used to specify the basis set. The subscript value is not the conventional J value, but a separate index used to distinguish between sets of terms. 86
Table 4.1. The relative energies (cm^{-1}) and electronic occupations of the d orbitals using the representative best fit ligand-field parameters, e_σ = 1950 cm^{-1}, e_π = 375 cm^{-1}, C/B = 4.0, and ζ = 0.0 cm^{-1}. 151
Table 4.2. The Kestrel calculated energies (cm^{-1}) and g-factors of the five lowest lying Kramer's doublets using the low-symmetry parameterisation of 1 with the x-ray structure. Calculations performed using ζ = 475 cm^{-1} and k_{iso} = 0.99..... 155
Table 4.3. The Kestrel calculated g-factors and time taken for quantum tunnelling of the magnetisation in the ground state Kramer's doublet (KD_1) of complex 1 as a function of φ. 156
Table 4.4. Reported experimental and Kestrel calculated non-relativistic transition energies (cm^{-1}).[126,127] The largest configurational contributions are included which together account for 99% of the configurational character of the electronic band. The configurational nomenclature 22111 = $(d_{z^2})^2(d_{x^2-y^2})^2(d_{xy})^1(d_{xz})^1(d_{yz})^1$..... 164
Table 4.5. The Kestrel calculated energies (cm^{-1}), g-factors, and time taken for quantum tunnelling of the magnetisation to occur for the four lowest lying Kramer's doublets of complex 2..... 166
Table 4.6. The Kestrel calculated g-factors and time taken for quantum tunnelling of the magnetisation to occur in the ground state Kramer's doublet (KD_1) of complex 2 as a function of the angle φ. 167
Table 4.7. The energies (cm^{-1}) of the many-electron eigenstates using the best fit ligand-field parameters of *Rechkemmer et al*. to the experimental MCD spectrum in the absence of spin-orbit coupling.[124]..... 178
Table 4.8. The Kestrel calculated energies (cm^{-1}), g-factors, and τ_{QTM} of the four lowest lying Kramer's doublets of complex 3 using the best fit parameters reported by *Rechkemmer et al*. and a k_{iso} = 0.82.[124] 181

Table 4.9. The experimental d-d transition energies of $[Fe(O)(TMC)(NCCH_3)]^{2+}$ with their irreducible representations, transition assignments, and polarisation behaviour reported by *Decker et al.*[165] 199
Table 4.10. Comparison of the reported experimental (CSD: WUSJOJ) and calculated bond lengths (Å) of $[Fe(O)(TMC)(NCCH_3)]^{2+}$.[151] 208
Table 4.11. The CASSCF(4, 5) and NEVPT2 calculated non-relativistic d-d transition energies (cm^{-1}) normalised by the energy of the $^3A_2$ state for $[Fe(O)(TMC)(NCCH_3)]^{2+}$ 210
Table 4.12. The energies (cm^{-1}) and eigenvectors of the 5×5 one-electron ligand-field matrices from the AILFT analysis of the CASSCF(4, 5) and NEVPT2 calculations. 211
Table 4.13. The calculated non-relativistic energies (cm^{-1}) normalised by the energy of the $^3A_2$ state, of the CASSCF(12, 9) and dynamical correlation corrections (NEVPT2) calculations with 12 triplet roots and 1 quintet root. 213
Table 4.14. The percentage contributions of the Fe(IV) d orbitals and the oxo p orbitals to the active space anti-bonding d orbitals for CASSCF(4, 5) and CASSCF(12, 9). 216
Table 4.15. Comparison of the key d-d transition energies (cm^{-1}) computed from the best fit parameters in Kestrel (see text) and CASSCF(12, 9)/NEVPT2 calculations. 219
Table 4.16. The Kestrel calculated relative energies of important triplet and quintet excited states and their configuration projection. For the metal-ligand bonding parameters, see the text. 221
Table 4.17. Possible electronic assignments of the reported experimental band energies (cm^{-1}) of $[Fe(O)(TMC)(NCCH_3)]^{2+}$ to fit in Kestrel. For the electronic assignments, ^3E has labels (1) = $d_{xy} \rightarrow d_{xz}, d_{yz}$, (2) = $d_{xz}, d_{yz} \rightarrow d_{x^2-y^2}$, and (3) = $d_{xz}, d_{yz} \rightarrow d_{z^2}$. 225
Table 4.18. The best fit parameters (±) for fitting the different d-d band assignments (see text) for $[Fe(O)(TMC)(NCCH_3)]^{2+}$. 226
Table 4.19. The best fit ligand-field parameter sets for the reproduction of experimental data. The labels P1 to P5 are alternative fits which offer good reproduction of the available experimental data. 227
Table 4.20. The non-relativistic energies (cm^{-1}), assignments, and configurational projection of the key electronic states for the best fit parameter set. Configurational projections of the $^3\Gamma$ bands are omitted for clarity. 234
Table 4.21. The average d-d transition energies (cm^{-1}) and band assignments taken from the Gaussian deconvolution performed by *A. Paradisi* of the experimental UV, CD, and MCD spectra of the *Ls*AA9 structures.[220] Note that the band numbering in *Ls*AA9_C6_Cl is different from the ordering derived from the transition assignments by *A. Paradisi* (see text). 252
Table 4.22. The best fit ligand-field parameters: bonding parameters (cm^{-1}), isotropic reduction factors, and intensity polarisation parameters (normalised to 100) that provide the best

reproduction of the intensity distributions and EPR g-factors. X refers to the nature of the exogeneous ligand (X = H_2O, Cl, Br). The e_π P_π, and F_π values represent πx interactions for *Ls*AA9_C6_H_2O. 254
Table 4.23. The experimental and Kestrel calculated principal EPR g-factors using the best fit parameters. The experimental EPR g-factors are taken from the simulations of *A. Paradisi*.[220] 258
Table 4.24. The Kestrel calculated relative energies (cm^{-1}) and eigenvectors of the eigenfunctions of the 5 × 5 one-electron ligand-field matrix for *Ls*AA9 and its substrate bound models. 259
Table 4.25. The Kestrel calculated relative energies (cm^{-1}) of the five many-electron energy levels and the mixing of the d^9 configurations (a label 12222 would represent a configuration of $(d_{yz})^1(d_{xy})^2(d_{xz})^2(d_{z^2})^2(d_{x^2-y^2})^2$), where the labelled d orbital denotes the singly occupied d-orbital character of that configuration. 264
Table 6.1. Metal-ligand bonding parameters for transition-metal complexes with a coordination number of 2..... 290
Table 6.2. Metal-ligand bonding parameters for transition-metal complexes with a coordination number of 4..... 291
Table 6.3. Metal-ligand bonding parameters for transition-metal complexes with a coordination number of 6..... 292
Table 6.4.The unique orbital occupations of the *n* electrons for d^n configurations (n = 1 through to 5) 295
Table 6.5. The xyz cartesian coordinates of the DFT optimised structure of $[Fe(O)(TMC)(NCCH_3)]^{2+}$ 303

List of accompanying material

- Kestrel program executable (Windows 10).
- Kestrel graphical user interface codebase.
- KestrelPy codebase.
- Folder of python files used for the studied complexes.

Acknowledgements

Before I begin thanking the many people who have made this journey possible, I would like to briefly reflect on these three years of my life. Research is hard. There is no other way around it. The process was admittedly not helped by the Covid-19 pandemic which started four months into my PhD. However, research is very rewarding, and it has been a great privilege to have devoted three years of my life to it. I was fascinated by electrons even back in secondary school when my chemistry teacher Claire Sibley showed me the probability distribution of a *p* orbital. From there I learnt of this thing called Quantum Mechanics and that it required lots of complicated looking mathematics to work. I had no idea how it worked or what it meant but I found it fascinating. It was from way back then that this journey started, and that journey would not have been possible without the many people who were involved along the way.

I would first like to thank my supervisors, Dr. Martin Bates, Dr. Martin Cockett, and Professor Paul Walton who provided me with this fantastic opportunity. You have been excellent mentors in developing my scientific skills whilst also giving me free-reign to take this project in my own direction. You have taught me so much, provided invaluable feedback, and were very patient with me through a few follies and tangents along the way. I do hope those same follies provided you some amusement too. I would like to especially thank Martin Bates who ignited within me a passion for programming and mathematical modelling that I did not know that I had. I also would like to give special thanks to Paul; you really made sure that I knew my stuff (mostly by questioning everything) but I really appreciated how you treated all my ideas, suggestions, and opinions seriously and with respect, even if they were misguided at times. However, making me read the entirety of *Magnetism and ligand-field analysis* in my final undergraduate year was cruel. That said, I do now own my own copy so you can hopefully pass yours to another unsuspecting undergrad.

I would also like to extend a special thank you to Professor Frank Neese, Professor Mihail Atanasov, and the rest of the Molecular Theory and Spectroscopy department at the Max-Planck-Institut für Kohlenforschung for having me! It was an unforgettable experience in which I learnt so much in such a short space of time. It was a privilege to have had the opportunity to work with some amazingly talented and knowledgeable people. I would like to give a special mention and thanks to Shashank who not only mentored me but reignited my love for chess. Thank you also to Spencer, Tim, Han, and Pauline for welcoming me and for teaching me what a bierturm is. I will always cherish that visit to Germany.

I would like to extend a massive thank you to all the members of the Walton research group, past and present. Not only were the coffee mornings and group meetings a lot of fun, but every trip to Garden of India was truly a blessing. Before I move on, I must give an extra special thank you to Martin and Pete. You guys are the best and I will always cherish the many great times and memories we share together.

I would also like to thank my parents, Meryl and Malcolm, and my grandparents, Ken and Joan for their constant support and for encouraging me to take this opportunity. I wish to also extend my thanks to Sarah and Colin, who have been very supportive, curious, and invested in my research. Finally, I would like to end by thanking Ellie for being my rock. You have been there with me every step of the way throughout this difficult journey, and I can't thank you enough. You have seen me through all the highs and lows of this PhD and continued to encourage me. I could not have emerged out the other side relatively unscathed without you.

Thank you all so much!

Author’s declaration

I declare that this thesis is a presentation of original work unless stated otherwise in the text and that I am the sole author. This work has not previously been presented for a degree or other qualification at this University or elsewhere. All sources are acknowledged as references.

1 Introduction

1.1 Why ligand-field theory?

Quantum chemistry provides chemists the means to predict and understand the physical properties of their molecules. The results of these calculations, when correlated with experimental data, inform chemical design by linking aspects of electronic structure with the molecule's or substance's physical properties.[1]

Understanding the electronic structures of $3d^n$ transition-metal complexes can aid the rational design of biomimetic catalysts, single-ion molecular magnets, and quantum qubits.[2–5] However, the electronic structures of such complexes are complicated by the presence of unpaired electrons occupying the 3d orbitals on the metal ion. These electrons exhibit complicated behaviour as they quantum-mechanically entangle under the effects of interelectronic repulsion and spin-orbit coupling. The culmination of these effects means that simple one-electron, single-determinant theories in quantum chemistry are not often sufficient to accurately calculate the physical properties of a transition-metal complex, since electron-correlation is handled following orbital construction and cannot accommodate the mixing of low-lying excited states. As such, a multiconfigurational approach is required, Figure 1.1.[6]

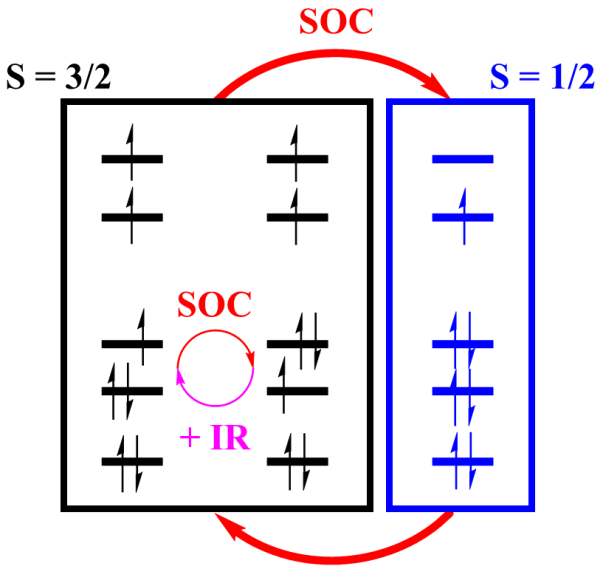

Figure 1.1. An illustrative example of multiconfigurational descriptions of a fictitious d^7 system.

In the literature it is common to see the use of either density-functional theory (DFT) or *ab initio* methods for predicting the physical properties of $3d^n$ transition-metal complexes. The issues of using DFT to describe electronic structures are well known. For instance, DFT is usually a single-Slater determinant method, meaning it considers only one configurational arrangement. Moreover, the method suffers from the so-called self-interaction error, which leads to several artefacts, most notably delocalisation error and the overestimation of covalency.[7–9] In response to such issues, multiconfigurational *ab initio* methods have gained popularity and wider use in the literature. Specifically, complete active space self-consistent field (CASSCF) and N-electron valence perturbation theory (NEVPT2) have been successfully applied to a range of $3d^n$ transition-metal complexes.[10,11] However, despite quantitatively good results, the underlying electronic structure is not easily linked to the spectroscopy/physical properties. Put another way, *ab initio* methods alone do not easily provide chemical insight into the system.

LFT, as originally defined, is multiconfigurational. Indeed, the importance and application of configuration interaction in LFT has been observed as far back as the 1940s when Van Vleck analysed the spin-forbidden excited states of chrome alum.[12] Since then, LFT has been successfully applied to a range of $3d^n$ transition-metal complexes, reproducing and explaining their electronic spectroscopy and magnetism.[13] It is now a standard tool for analysing the results of *ab initio* calculations.[10] Despite being a parameterised semi-empirical method, its continued success and relevance is attributed to the grounding of the model in *ab initio* theory. Hence, through parameterising the electronic structure and comparing the predicted physical properties to experimental data, the link between spectroscopy can be made back to the electronic structure. Provided that the parameters are chemically intuitive and meaningful, multiconfigurational space can also be translated into “chemical language”, such as sigma-donor and pi-acceptor properties of ligands.

In addition to the multiconfigurational basis of LFT, the small d-orbital basis set (upon which the theory is based) offers the possibility for real-time calculations of ligand-field properties. This would provide direct feedback to the chemist as to how changes in the chemical environment of the transition-metal complex affect the spectroscopic and magnetic properties of their system. Through this, one can understand how augmenting σ/π bonding can tune desired properties of their system and how this mixes electronic configurations together.

It is in this context that the work reported in this thesis is founded. The advantages of the ligand-field model offer to fulfil a quantum-chemical niche that can be made accessible

and available to the practicing (bio)inorganic chemist interested in 3d transition-metal systems. Not only does a simple model hold such potential, but it can also be used to calculate a wide range of physical properties, probing both the ground state and excited state electronic structures. The ligand-field model presented herein can compute d-d transition energies, EPR g-factors, paramagnetic susceptibilities, and transition dipole moments.

1.2 The ligand field

It is well known that the predecessor of LFT was crystal-field theory. The development of an electrostatic crystal-field theory can be traced back to Hans Bethe who, in 1929, published a paper describing the splitting of an atom's spectroscopic term symbols by an electric field of a given symmetry.[14] Further development was made by most notably J. H. Van Vleck, William G. Penney, Robert Schlapp, and others in connection to the magnetic properties of transition-metal ion crystals.[15,16] The electrostatic crystal field was unable to rationalise the trend in the magnitude of d-orbital splitting that has now come to be recognised by the spectrochemical series.

It was not until 1935 that the concept of a "ligand" field, rather than an electrostatic crystal field, was introduced when Van Vleck sought to reconcile the hybridisation models of Linus Pauling and Mulliken's molecular orbitals to rationalise the strengths of the crystal-field splitting.[17] Since then, reviews have sought to compare, contrast, and discuss the physical implications of a crystal field versus a ligand field.[18,19] The literature has for a long time considered these two approaches as wholly distinct. It should be stressed that when discussing differences of "crystal" and "ligand" field theories, it is generally meant that the theoretical picture of the underlying bonding or metal-ligand interactions differ. In practice, as has been highlighted recently, LFT is, mathematically speaking, a freely-parameterised form of crystal-field theory.[20] It would not be correct to say LFT "incorporates" aspects of, or is, molecular orbital theory, as no extension of the d-orbital basis set is carried out, nor are molecular orbitals constructed.

1.2.1 Ligand-field theory is *not* molecular orbital theory: the primogenic effect in $3d^n$ transition-metal ions.

When calculating the excited states of $3d^n$ transition-metal complexes, Carl Ballhausen said that "*neither the valence bond method nor the molecular orbital theory can hope to do as well*

[as ligand field theory] within an order of magnitude."[21] This was because the 3d electrons primarily reside in the 3d orbitals on the metal where the effects of interelectronic repulsion are handled by the parameterisation of the free-ion interelectronic repulsion. Sources in the literature wrongly describe LFT as a hybridisation of crystal-field theory and molecular orbital theory.[22,23] Ligand-field calculations do not construct or use molecular orbitals. Instead, the d orbitals are subjected to an effective electrostatic and electrodynamic potential created by the ligands. The empirical success of the restricted basis set and the ability to achieve it using the free-ion interelectronic repulsion and spin-orbit coupling integrals implies that contamination of ligand functions into the 3d orbitals is minimal.[24]

The pseudo non-bonding behaviour of 3d electrons is due to the primogenic effect of the 3d orbitals.[25] As the 3d orbitals are the first atomic orbitals of their *l* quantum number they are nodeless and radially contracted, exhibiting unique physical properties. An article by *Professor Martin Kaupp* details the primogenic effect in 3d transition-metal complexes and their consequences for metal-ligand bonding.[26] The radially contracted nature of the 3d orbitals results in relatively long metal-ligand bonds lengths and poor metal 3d and ligand valence orbital overlap due to greater Pauli repulsions between the metal core and the ligand. Indeed, this effect has been cited as the primary cause as to why 3d transition-metal chromophores do not engage in photoinduced electron transfer chemistry, unlike their 4d and 5d counterparts.[27]

1.2.2 The paradigm of ligand-field theory

The evidence of 'uncoupled' 3d electrons from other functions in a transition-metal complex requires special treatment in a quantum mechanical context. Having reviewed the unique physical properties of this class of complex, attention is turned to the ligand-field treatment of transition-metal complexes. Although LFT is an old model, it was not until the 1980s when *R. G. Woolley*, *J. H. Harding*, and *M. Gerloch* presented a formal development of LFT from quantum chemistry.[13,24,28] Their work established the formal connection between aspects of quantum chemistry and the parameters used in ligand-field analysis. The behaviour of parameters was also derived within this framework. This work separated LFT from the usual criticisms of other semi-empirical theories, the parameters of which are ill-defined and their underlying physical interpretations are unclear.

LFT recognises the unique situation of the 3d orbitals and treats them specifically. *Woolley*, *Harding*, and *Gerloch* showed that all other functions (both metal and ligand) need not be defined explicitly and the effects that these functions have on the d orbitals can be

treated as a perturbation. These perturbations define the radial changes of the d orbitals upon interaction with their surroundings but leave the free-ion angular properties (l = 2) unchanged. Put another way, perturbations from the d orbital surroundings alter the values of the ligand-field parameters.

It is this explicit neglect of all other metal and ligand functions which makes LFT an appropriate model for 3d, rather than 4d or 5d, transition-metal complexes, as discussed in section 1.2.1. The successful application of this model to a range of 3d transition-metal complexes corroborates this observation and justifies the use of a free ion angular basis.[29]

1.2.3 Metal-ligand bonding

In LFT, it is possible to parameterise the ligand field using metal-ligand bonding parameters by so-called "e-values". These e-values are labelled as e_λ, where $\lambda = \sigma, \pi$, and δ. The symmetries of the e_σ and e_π parameters are shown in Figure 1.2. In practice, one can associate a set of e_λ values at the coordinating atom position of a ligand and fit the strength of its bonding with the metal by a numerical quantity (typically given in units of cm^{-1}). The signs of the parameters also reflect the chemical concept of donor/acceptor properties of a given ligand. A positive e_λ parameter is associated with a λ-donor interaction, destabilising the interacting d orbitals. In contrast, a negative e_λ parameter is associated with a λ-acceptor interaction, stabilising the interacting d orbitals. One can easily appreciate the chemical transparency in this parameterisation scheme.

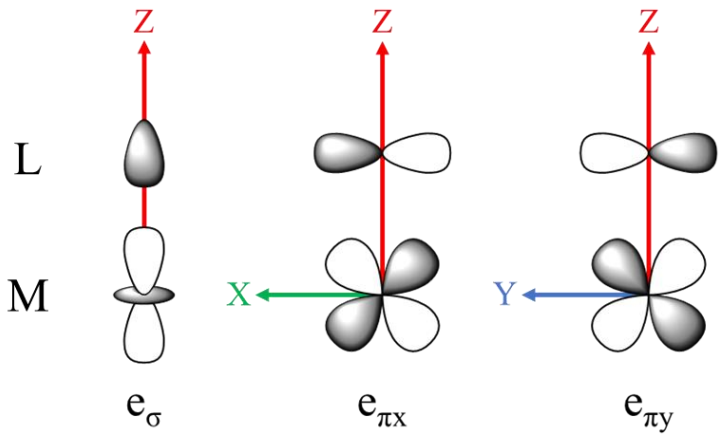

Figure 1.2. The interaction symmetries of the e_σ and e_π interactions

If one were to assign a unique e_σ, $e_{\pi x}$, $e_{\pi y}$, $e_{\delta xy}$, and $e_{\delta x^2-y^2}$ for each ligand, the number of freely adjustable parameters quickly surpasses the amount of data points to fit to; the parameterisation will likely not be unique. Fortunately, there are some chemically sensible assumptions that can be made to reduce the number of adjustable parameters. The first and most obvious is that similar ligands likely share similar metal-ligand bonding parameters and can be approximated to engage in equivalent bonding with the central metal ion. The second assumption is the neglect of the e_δ parameters by setting them to 0 cm^{-1}, on the justification that ligands rarely have functions of δ-symmetry to interact with. Instead, the remaining e_σ and e_π parameters should be read as being normalised by e_δ, such that $e_\lambda = e_\lambda' - e_\delta'$.

Application of this model, and its assumptions, has led to the successful ligand-field analysis of experimental/computational data using metal-ligand bonding parameters. Tables of compiled e_λ values taken from experimental and computational analysis in the literature are given in Table 6.1 (Appendix). In general, an e_σ parameter is typically > 0 cm^{-1} and has a magnitude in the 1000s cm^{-1}. The e_π parameters are typically in the range of –2000 to 2000 cm^{-1} and near 0 cm^{-1} for formally non π bonding interactions. There are, of course, exceptions to this rule of thumb. The types of exceptions, when they arise, and how to treat them are found in chapter 2.3.4, which details the theoretical aspects of parameterising the metal-ligand bonding of a range of ligands. Despite this, the values in Table 6.1 typically conform to chemically intuitive ideas of metal-ligand bonding in 3d transition-metal complexes.

This model of parameterising the ligand field is known in the chemical literature as the angular overlap model (AOM) or the cellular ligand-field model. They are, at their core, mathematically identical. However, their assumptions of the parameter magnitudes and the chemical interpretation of the parameterisation are different. The AOM was formulated by C. E. Schäffer and C. K. Jørgensen who sought to reformulate the original incarnation of the AOM (*vide infra*) to be a ligand-field procedure, involving explicitly the d orbitals only acting as a first order perturbation on the d-orbital manifold. However, care has been made in this work to distinguish the general metal-ligand bonding situation described above from the AOM model as the latter was borne out of the so-called Wolfsberg-Helmholz model.[30] The Wolfsberg-Helmholz model is an explicit semi-empirical molecular orbital model which required evaluation of the direct overlap of ligand functions and metal d orbitals. The model relied on an assumption that the energy of the antibonding d orbital is directly proportional to the square of the overlap integrals. The model featured other assumptions, such as an added ill-defined F_λ factor which took an approximate value of 2.00, which ultimately led to its decline in the chemical literature. It should be stressed that the metal-ligand bonding parameterisation used in this work is not a molecular orbital model, nor is it the Wolfsberg-Helmholz model.

There are extensions to the parameterisation to include effects of misdirected valence $e_{\sigma\pi}$, stabilisation effects of d-s and d-p mixing e_{ds}, e_{dp}, and differential π contributions from bidentate ligands with conjugated π networks using e_{ψ} and e_{χ}. The primary downside with the general metal-ligand bonding framework in LFT is the degree of parameterisation. The number of e_{λ} parameters can quickly become large unless certain assumptions are made or the range of experimental data to be fitted expands. However, notwithstanding the potential issues of over parameterisation, the e_{λ} parameters enable a chemist to simply see how changing the bonding of a given ligand at a given geometry can affect the physical properties. This seemingly trivial point is not so easily accomplished using other quantum chemical methods. It is not always straightforward to change a ligand in a molecular model without first editing the structure by hand inside of a molecular editor, which often requires a geometry optimisation before a sophisticated calculation of the electronic structure is ever performed. With this model, that problem is circumvented; the insight is achieved by simply changing the magnitude and/or sign of the parameter. The change in the e_{λ} parameter is also clear and unambiguous. It is not always clear from the results of an *ab initio* calculation to evaluate how the bonding in the molecule has changed. Many of the issues of over parameterisation can be circumvented with the advent of *ab initio* LFT.

1.2.4 *Ab initio* ligand-field theory

LFT, despite being an old model, continues to enjoy a healthy resurgence in the chemical literature. An important work, published in 2011, compared the performance of LFT to state of the art *ab initio* calculations using CASSCF wavefunctions with NEVPT2 improved energies.[31] The authors developed the *ab initio* ligand-field theory (AILFT) method which allowed an unambiguous determination of ligand-field parameters from the results of correlated multireference wavefunctions. The procedure allows one to extract interelectronic repulsion B and C, and spin-orbit coupling ζ - if relativistic effects are included in the calculations. The ligand field is extracted in the form of the symmetric 5×5 one-electron ligand-field potential (V_{LFT}) matrix. One can directly fit the V_{LFT} matrix by generating a corresponding matrix using e_{λ} parameters and a molecular geometry. AILFT is restricted to wavefunctions produced from a minimal active space of n electrons in five d orbitals. Hence, the AILFT analysis is limited by the quality of the minimal active space wavefunctions and energies. Nevertheless, the method extracted e_{λ} values which reproduced the chemical trends in e_{λ} values extracted from experiment. Hence, LFT is validated theoretically by *ab initio* theory and the former is now a common tool for analysing the results of CASSCF/NEVPT2 calculations. The results of

CASSCF/NEVPT2 calculations are not easily interpretable on their own, whereas the ligand-field parameters are more chemically transparent.

The AILFT has been successful in analysing the metal-ligand bonding trends for a range of 3d transition-metal complexes.[10] Collections of e_λ parameters found in the literature are reported in the tables of appendix 6.1, some of which are extracted from AILFT. In comparison with experimentally extracted e_λ, B, and C parameters the Racah parameters reported by AILFT are nearly always overestimated, due to not correctly balancing the contributions of static and dynamical correlation effects. Interestingly, comparing the parameters from *ab initio* results with ligand-field parameters extracted from well resolved experimental data has provided validation of the *ab initio* calculations and further development of multiconfigurational correlated wavefunctions methods, not the other way around. However, there are still limitations to this approach and the NEVPT2 level of correction to the dynamical correlation is constrained by not allowing the CASSCF states to mix under dynamical correlation. This effect, which can be carried out using DCD-CAS(2) and HQD-NEVPT2 methods, allow better agreement between AILFT and calculated *ab initio* results.[32] Despite this, LFT has emerged as a general tool for use in conjunction with state of the art quantum chemical calculations where it converts those results into chemical language.

1.3 Available ligand-field programs

Constructing expressions for ligand-field electronic states for each case or symmetry is inconvenient and difficult. Ligand-field calculations are generally performed using a computer program. There are several programs for transition-metal complexes that are used in the literature. They have different features and uses. In this section, the programs AOMX, CAMMAG, LIGFIELD, and the orca_lft module are reviewed and compared. These programs represent the most widely used ligand-field programs in the literature. A summary of their features is presented in Table 1.1.

CAMMAG (which stands for “CAM”bridge “MAG”netism) was developed for analysing the magnetic properties of single-crystal samples of d^n transition-metal complexes.[33,34] The program developed as far as CAMMAG5 which featured: calculation of d-d transition energies with their irreducible representation and spin-projections; calculation of EPR g-factors for Kramers systems and molecular/crystal paramagnetic susceptibility tensors; and d-d intensities of electronic absorption and CD spectroscopies. The ligand-field was parameterised using the cellular ligand-field model. The program has been extensively used to characterise a range of systems from their optical and magnetic properties.[29] A recently

developed program BonnMag with similar features and syntax to CAMMAG was designed to compute the spectroscopic properties of *f* complexes.[35]

AOMX was developed by Heribert Adamsky and uses the AOM parameterisation.[36] The program uses an alternative approach to CAMMAG and constructs the final Hamiltonian in the basis of Slater determinants. This means that the n-electron configurational occupations of the final d orbitals can be extracted from the eigenfunctions. The program does not compute magnetic properties but does feature direct fitting to transition energies (with symmetry labels) and anisotropic interelectronic repulsion and spin-orbit coupling. The program is used consistently in the analysis of AILFT results.

LIGFIELD was developed by Jesper Bendix in the 1980s and computes the ligand-field Hamiltonian for all possible p^n, d^n, and some f^n configurations.[37] To the author's knowledge, this ligand-field program is the only example that features a graphical user interface. It shares similarities in its features with AOMX and has been used to analyse the optical spectroscopy and zero-field splitting spin Hamiltonian parameters extracted from experiment for a range of systems.[38–40]

The "orca_lft" program is a module of the larger ORCA program introduced with the recent version 5.0 release.[41,42] The program is a script based command line tool. Its intended use is to submit the ligand-field results of an AILFT analysis of a previous calculation into this module and start varying ligand-field parameters. Unlike the previous programs, orca_lft does not use metal-ligand bonding parameters but instead uses a direct parameterisation of the 15 unique elements of the symmetric 5×5 one-electron ligand-field matrix. To extract e_λ parameters, a different program must be used, such as AOMX. The module also uses B, C, and ζ. The module can also simulate ligand-field spectra of essentially any type using the available basis sets in ORCA.

Each program has their advantages and disadvantages, and they each contribute a set of useful features, which makes them distinct and useful in their own respect. Except for LIGFIELD, each program is command line based, which introduces a barrier to entry for the non-specialist user. On the other hand, LIGFIELD does not compute d-d intensities. This shows that there is a need for a new contemporaneous program that provides these features along with a user-friendly interface to explore ligand-field analysis.

Table 1.1. Summary of available features of the major available ligand-field programs.

Features	AOMX	CAMMAG	LIGFIELD	orca_lft (5.0.3)
e_λ parameters	Yes	Yes	Yes	No
Magnetic field	Yes	No	Yes	Yes
Anisotropic interelectronic repulsion	Yes	No	No	No
Anisotropic spin-orbit coupling	Yes	No	No	No
Calculates Energies	Yes	Yes	Yes	Yes
Calculates Magnetism	No	Yes	Yes	Yes
Calculates Intensities	No	Yes	No	Yes
Configuration Projection	Yes	No	Yes	No
Symmetry Projection	Yes	Yes	No	No
Optimisation	Yes	No	Yes	Planned
Mapping	No	Yes	No	No
Parameter variation	Yes	Yes	Yes	Yes
Graphical user interface	No	No	Yes	No
p configs	No	No	Yes	No
f configs	No	No	Yes	No
Crystal frames	No	Yes	No	No

1.4 This work

Thus far, a brief overview of LFT and its place in the contemporary chemical literature has been outlined. Historically, LFT was focussed on reproducing experimental data; however, the model is often used nowadays to analyse the results of *ab initio* calculations. The reason for

this shift in focus stems from a lack of user-friendly software that was freely available and made multiconfigurational language accessible to synthetic chemists. There is also a perception that LFT is not a sophisticated model and therefore second to *ab initio* models. However, the success of LFT, spanning nearly a century, means one should not be so quick to disregard the model.

The increased computational power available to chemists along with the renewed interest in LFT has given fertile ground for a new contemporary ligand-field program. The software developed in this thesis, called Kestrel, is designed to address the link between spectroscopy and electronic structure first. That means the program is ultimately intended to be applied to experimental data where available. Kestrel aims to compute d-d transition energies, EPR g-factors, paramagnetic susceptibilities, and UV, CD, and MCD intensities. The program has been designed to feature an integrated graphical user interface that runs 'out of the box' with minimal setup.

This thesis presents the development of Kestrel and its application to three case studies. Chapter 2 describes in more detail the theoretical background of the ligand-field model and provides a more thorough description of the chemical interpretation of the ligand field. Chapter 3 reviews the features of Kestrel and serves as a guide to using the program. Finally, Chapter 4 provides three applications of the program. The first of these is an application of the program to facilitate rational chemical design of some cobalt(II) single-ion molecular magnets, to enhance the axiality of their electronic structure. The second study is a reanalysis of a non-heme iron(IV) oxo complex, where an attempt to falsify a reassignment made using an experimental version of the program was instead able to simulate the experimental data. Finally, the program is applied to the fully spectroscopic characterisation of a copper(II) lytic polysaccharide monooxygenase (LPMO) enzyme.

2 Theory

LFT concerns itself with the evaluation of an effective Hamiltonian, described by states constructed from the free-ion angular d-orbital basis. There are four main sources of energetic contribution that must be accounted for: interelectronic repulsion; spin-orbit coupling; Zeeman splitting; and the ligand field. The effective Hamiltonian operator (described formally in section 2.1) is written as

$$H^{eff} = H_{IR} + V_{LF} + H_{SOC} + H_{Zee}. \tag{2.1}$$

For 1st row d^n transition-metal ions, the contribution from the ligand field typically dominates, with contributions in the order $V_{LF} > H_{IR} > H_{SOC} \gg H_{Zee}$. For 2nd and 3rd row transition metals the spin-orbit coupling can be large enough to no longer be considered as a relatively small perturbation.

This chapter begins by reviewing the mathematical formalism and origin of the effective Hamiltonian and discusses its application and limitations. Following this, the mathematics of angular momentum coupling are reviewed along with the final expression for the evaluation of the operators in (2.1) in an angular momentum basis. Next, the methods and definitions that are used to parameterise the ligand-field interactions are reviewed and a more in-depth look is taken into the different types of metal-ligand interactions. Finally, the different post-diagonalisation operations for calculating the configuration projection, magnetism, and spectroscopic intensities are discussed.

2.1 Effective Hamiltonians

In electronic structure theory, effective Hamiltonians (Figure 2.1) are constructed to model a region of eigenstates of a more complete "eigenspectrum".[43] LFT is concerned with eigenstates that are solutions of an effective Hamiltonian acting within a restricted basis of metal d orbitals. These states are connected primarily with the unique spectroscopic properties of d^n transition-metal ion complexes.

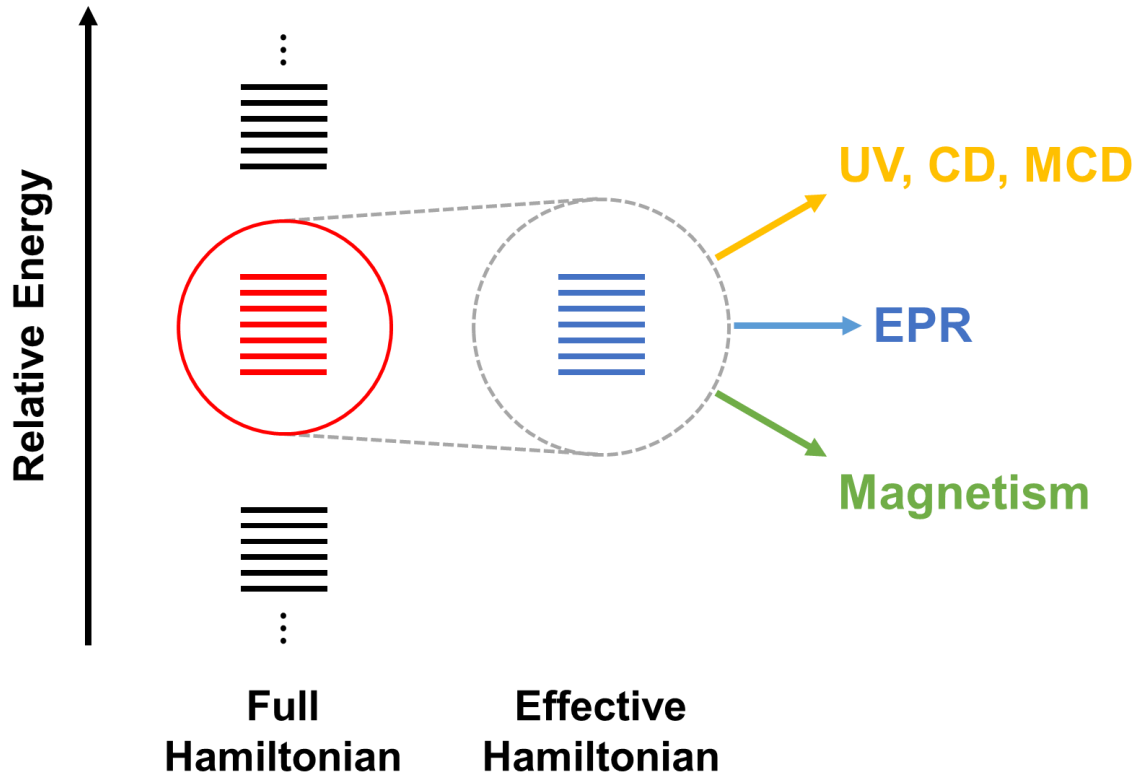

Figure 2.1 The sampling of eigenstates via an effective Hamiltonian, which represent a "window" of states in the full Hamiltonian.

The effective ligand-field Hamiltonian can be constructed by the partitioning of the full eigen spectrum of the molecule into two subspaces: *a* and *b*.[44] The former is the model space, which includes many-electron states arising from pure angular d-orbital states and their configurational occupations. The latter is the outer space, which represents the eigenstates arising from all other functions in the molecule and is typically much larger than the model space. The partition begins with the full many-electron Schrödinger equation,

$$\hat{H}\Psi = E\Psi \tag{2.2}$$

where it is assumed that the eigenfunctions can be constructed from a linear combination of a complete and orthonormal set of basis functions, such that

$$\Psi = \sum_i c_i \varphi_i \,. \tag{2.3}$$

It is convenient to rewrite the original Schrödinger equation in its matrix representation as

$$\mathbf{Hc} = E\mathbf{c}\,. \tag{2.4}$$

The full many-electron Schrödinger equation describes all electronic states. From Löwdin, it

is possible to partition the Hamiltonian into the two subspaces defined prior.[45] In doing so, the eigenvalue equation of (2.4) then turns into a partitioned eigenvalue problem

$$\begin{pmatrix} \mathbf{H}^{aa} & \mathbf{H}^{ab} \\ \mathbf{H}^{ba} & \mathbf{H}^{bb} \end{pmatrix} \begin{pmatrix} \mathbf{c}^{a} \\ \mathbf{c}^{b} \end{pmatrix} = E \begin{pmatrix} \mathbf{c}^{a} \\ \mathbf{c}^{b} \end{pmatrix} \tag{2.5}$$

where the outer space coefficients can be solved for explicitly

$$\mathbf{c}^{b} = \left(E \cdot \mathbf{1}^{bb} - \mathbf{H}^{bb} \right)^{-1} \mathbf{H}^{ba} \mathbf{c}^{a} . \tag{2.6}$$

The outer space coefficients can be substituted back into (2.5) to yield

$$E\mathbf{c}^{a} = \mathbf{H}^{aa}\mathbf{c}^{a} + \mathbf{H}^{ab}(E \cdot \mathbf{1}^{bb} - \mathbf{H}^{bb})^{-1}\mathbf{H}^{ba}\mathbf{c}^{a} \tag{2.7}$$

where the original Schrödinger equation can now be rewritten as

$$\mathbf{H}^{eff}\left(E\right)\mathbf{c}^{a} = E\mathbf{c}^{a} . \tag{2.8}$$

The result is an exact reformulation of the original Schrödinger equation where the solutions of the model space can be modelled. Impressively, no approximations have been made in this derivation. However, within this effective Hamiltonian is an energy dependent term $(E \cdot \mathbf{1}^{bb} - \mathbf{H}^{bb})^{-1}$, which encapsulates the influence of the outer space on the model space. Providing that this term is small, the effective Hamiltonian is a good one. In other words, providing that the solutions of the outer space do not cross into the model space then this term remains *relatively* small. Assuming that the full many-electron Hamiltonian can be divided into a 0th and 1st order perturbation operator results in

$$H\Psi = \left(H^{(0)} + H^{(1)} \right)\Psi = E\Psi . \tag{2.9}$$

By also assuming that the solutions of (2.8) are good, then the Hamiltonian can be replaced with the outer space eigenvalues, E^{bb}. Doing so, it is possible to rewrite $\mathbf{H}^{eff}$ as

$$\mathbf{H}^{eff} = \mathbf{H}^{aa} - \mathbf{H}^{ab}\left(E^{bb} - \mathbf{1} \cdot E \right)^{-1} \mathbf{H}^{ba} \tag{2.10}$$

whose matrix elements can be expanded as

$$\left(\mathbf{H}^{eff}\right)_{ij} = \delta_{ij} E_{i}^{(0)} + \left\langle \Psi_{i}^{(0)} \middle| H^{(1)} \middle| \Psi_{j}^{(0)} \right\rangle - \sum_{k \in b} \frac{\left\langle \Psi_{i}^{(0)} \middle| H^{(1)} \middle| \Psi_{k}^{(0)} \right\rangle \left\langle \Psi_{k}^{(0)} \middle| H^{(1)} \middle| \Psi_{j}^{(0)} \right\rangle}{E_{k}^{(0)} - E_{a}} \tag{2.11}$$

Where the full form of the effective Hamiltonian has been derived. From (2.11) the 1st order perturbation constitutes two parts, as given by (2.10). There is a perturbation that encapsulates the interaction of the functions within the a space. The second-order term describes the influence of the b space on the a space. The zeroth order contribution, $\delta_{ij} E_{i}^{(0)}$ represents the unperturbed energies.

On this basis, 3d transition-metals make good candidates for the effective Hamiltonian of LFT.[43] From equation (2.5) there is a clear division to be made between ligand-field states (a space) and other electronic states (e.g. charge transfer), the former being primarily related to the spectroscopic properties of those systems. Also, the primogenic nature of the 3d orbitals, as discussed in section 1.2.1, means that the d orbitals are sufficiently decoupled from all other functions in Werner-type complexes. Hence, the crossover of the b space functions with the ligand-field space functions should be small, resulting in a small $(E \cdot \mathbf{1}^{bb} - \mathbf{H}^{bb})^{-1}$ term.

2.2 Angular momentum & tensor operators

LFT is concerned with the calculation of matrix elements between a basis set of angular momentum quantum numbers. The evaluation is carried out by a series of operators represented as tensor operators. This section deals with spherical tensor operators within a spherical basis. However, this section does not intend to cover the full scope of tensor operator methods (which are detailed elsewhere) but covers the equations and mathematics used to compute the integrals appearing in the effective Hamiltonian, equation (2.1).[46]

2.2.1 Angular momentum coupling

For first row transition-metal complexes where spin-orbit coupling is a small perturbation when compared to the size of the ligand field, Russell-Saunders coupling is used. We define a quantum number, j and a z-projection m written as a ket $|jm\rangle$. A state with two quantum numbers uncoupled from one another is written as

$$|j_1 j_2 m_1 m_2\rangle = |j_1 m_1\rangle |j_2 m_2\rangle . \tag{2.12}$$

Upon coupling, the new state is defined with a total angular momentum, $j = j_1 + j_2$ and the resulting ket is written as $|j_1 j_2 jm\rangle$. These coupled functions are eigenvectors of the operators $\mathbf{J}^2$ and J_Z, representing the total angular momentum squared, and the z-projection, defined by[34]

$$\mathbf{J}^2 = \left(\mathbf{J}_1 + \mathbf{J}_2\right)^2$$
$$J_z = J_{1z} + J_{2z} \tag{2.13}$$

where the uncoupled set of angular momentum numbers are eigenfunctions of their respective $\mathbf{J}_i$ and J_{iz} operators. The eigenvalues of the operators in (2.13) are

$$\mathbf{J}^2 = j\left(j+1\right)\left|j_1 j_2 jm\right\rangle$$
$$J_z = m\left|j_1 j_2 jm\right\rangle \quad . \tag{2.14}$$

In the Russell-Saunders coupling scheme, the coupling of total orbital angular momentum, L and total spin angular momentum, S form a total angular momentum set spanning[47]

$$J = \left\{L+S, L+S-1, \ldots, \left|L-S\right|\right\}. \tag{2.15}$$

Likewise, the coupling of the z-projections of both the orbital and spin angular momentum (M_L and M_S respectively) combine to form a total projection $M_J = M_L + M_S$, as defined in (2.13) . The result is that the M_J spans the set

$$M_J = \left\{J, J-1, \ldots, -J\right\}. \tag{2.16}$$

Hence, we can write the uncoupled basis as $\left|LSM_L M_S\right\rangle = \left|LM_L\right\rangle\left|SM_S\right\rangle$ and the coupled basis as $\left|LSJM_J\right\rangle$.

However, there are often different sets of quantum numbers that can couple to give the same resulting ket. For example, both the uncoupled bases $\left|2,1\right\rangle\left|½,-½\right\rangle$ and $\left|2,0\right\rangle\left|½,½\right\rangle$ result in the coupled ket $\left|2,½,⅝,½\right\rangle$. The coupled set of angular momentum quantum numbers are built from a linear combination of the uncoupled set of quantum numbers. Writing generally, the relation between a coupled basis and an uncoupled basis is given by

$$\left|j_1 j_2 jm\right\rangle = \sum_{m_2=-j_1}^{j_2} \sum_{m_2=-j_2}^{j_2} \left|j_1 m_1 j_2 m_2\right\rangle\left\langle j_1 m_1 j_2 m_2 \middle| j_1 j_2 jm\right\rangle \tag{2.17}$$

where the unit dyadic has been used $\left|j_1 m_1 j_2 m_2\right\rangle\left\langle j_1 m_1 j_2 m_2\right| = \mathbf{1}$. The scalar product $\left\langle j_1 m_1 j_2 m_2 \middle| j_1 j_2 jm\right\rangle$ is the Clebsch-Gordan coefficient (also denoted $C^{j_1 j_2 j}_{m_1 m_2 m}$) which is an expansion coefficient of a coupled basis in terms of its uncoupled basis. Note that equation (2.17) is simply the transformation from one basis to another. It is equally possible to write the uncoupled basis in terms of coupled functions

$$\left|j_1 j_2 m_1 m_2\right\rangle = \sum_{jm} \left|j_1 j_2 jm\right\rangle\left\langle j_1 j_2 jm \middle| j_1 j_2 m_1 m_2\right\rangle. \tag{2.18}$$

In principle, there is no right or wrong choice in choosing a coupled or an uncoupled basis, both are related by a unitary transformation.

There are relationships that can be deduced to determine whether the Clebsch-Gordan coefficient will be zero or not. From (2.15), if j lies outside the bounds of $j_1 + j_2 \geq j \geq |j_1 - j_2|$ then the $C^{j_1 j_2 j}_{m_1 m_2 m} = 0$. Also, from (2.13) and (2.16), if the z projections do not sum to zero, then $C^{j_1 j_2 j}_{m_1 m_2 m} = 0$. This means that upon coupling, the z projections of the uncoupled basis are not conserved and instead are replaced by a total z-component.

An expression is quoted for the evaluation of the Clebsch-Gordan coefficient that was given by Racah[48]

$$\begin{aligned}\langle j_1 j_2 m_1 m_2 \,|\, jm\rangle &= \delta_{m_1+m_2,m}\Delta(j_1 j_2 j_3) \\ &\times \left[(2j+1)(j_1+m_1)!(j_1-m_1)!(j_2+m_2)!(j_2-m_2)!(j+m)!(j-m)!\right]^{1/2} \\ &\times \sum_z (-1)^z \left[(j_1-m_1-z)!(j-j_2+m_1+z)!(j_2+m_2-z)!(j-j_1-m_2+z)!\right. \\ &\times \left. z!(j_1+j_2-j-z)!\right]^{-1} \end{aligned} \tag{2.19}$$

where z in (2.19) sums over integer values which lead to non-negative factorials. The $\Delta(j_1 j_2 j)$ function is given by

$$\Delta(j_1 j_2 j) = \left[\frac{(j_1+j_2-j)!(j_1-j_2+j)!(-j_1+j_2+j)!}{(j_1+j_2+j+1)!}\right]^{1/2}. \tag{2.20}$$

The Clebsch-Gordan coefficient possesses strange symmetry relations. Because of this, it is convenient to work with Wigner symbols, which are related to the Clebsch-Gordan coefficient but feature convenient symmetry properties.

2.2.2 Wigner symbols

To evaluate the coefficients of angular momentum coupling, Wigner 3j and 6j symbols are used. These Wigner symbols are required for the evaluation of the ligand field, spin-orbit coupling, and magnetic moment operator matrix elements. The 3j symbol, which couples two sets of angular momenta together, is related to the Clebsch-Gordan coefficient, given by[49]

$$\begin{pmatrix} j_1 & j_2 & j_3 \\ m_1 & m_2 & m_3 \end{pmatrix} = (-1)^{j_1 - j_2 - m_3} (2j_3+1)^{-1/2} \langle j_1 j_2 m_1 m_2 \,|\, j_3 - m_3\rangle \tag{2.21}$$

where the Clebsch-Gordan coefficient is to be evaluated using equations (2.19) and (2.20).

The Wigner 6j symbol represents the coupling between three sets of angular momenta and is written with curly brackets. The expression for calculating Wigner 6j symbols is given by[50]

$$\begin{Bmatrix} a & b & c \\ d & e & f \end{Bmatrix} = (-1)^{a+b+c+d} W(a\,b\,c\,d;e\,f) \tag{2.22}$$

in which the symbol is related to the Racah W-coefficient[48]

$$\begin{aligned} W(a\,b\,c\,d;e\,f) &= \Delta(abc)\Delta(acf)\Delta(bdf)\Delta(cde) \\ &\times \sum_z (-1)^z (a+b+c+d+1-z)!\big[z!(e+f-a-d+z) \\ &\times (e+f-b-c+z)!(a+b-e-z)!(c+d-e-z)! \\ &\times (a+c-f-z)!(b+d-f-z)!\big]^{-1} \end{aligned} \tag{2.23}$$

where the Δ function is defined in equation (2.20).

2.2.3 Rotations of angular momenta and tensor operators

The rotation of angular momenta states is of the upmost importance. Computing physical observables, represented by operators, requires an understanding of how an operator acts under a given coordinate scheme. Two observers, with different frames of reference (which are related by a unitary transformation) must still observe the same magnitude of the physical observable. The orientation of the physical observable will be described differently, however, for a different (but still) complete basis set.

We define an operator, $\hat{T}$ represented by an irreducible spherical tensor $\mathbf{T}^k$ of order k with $2k+1$ operators, which share similar properties to angular momentum numbers. For example, the operator spans projections $q = \{k, k-1, \ldots, -k\}$ and is given by[34]

$$\mathbf{T}^k = \sum_{q=k}^{-k} T_q^k \,. \tag{2.24}$$

The physical observable must be invariant under rotation, which can be written as a unitary transformation:

$$\hat{T} = U^\dagger \hat{T} U = U \hat{T} U^\dagger \,. \tag{2.25}$$

Now, the rotation of an angular momentum eigenstate, $|jm\rangle$ under a rotation operator, $\hat{D}$ can be written as a linear combination of the $(2j+1)$ states,

$$\hat{D}\left|jm\right\rangle = \sum_{m'=-j}^{j} D^{j}_{m'm}\left|jm'\right\rangle \tag{2.26}$$

where the expansion coefficients $D^{j}_{m'm}$ are matrix elements of the Wigner rotation matrix.[46] Likewise, a tensor operator of rank k and projection q also transform under rotation by

$$\hat{D}T^{k}_{q} = DT^{k}_{q}D^{\dagger} = \sum_{q'=-k}^{k} D^{k}_{q'q}T^{k}_{q'}\,. \tag{2.27}$$

This means that under a general rotation, a tensor operator transforms as a linear combination of the $2k+1$ elements of the irreducible tensor operator of rank k. For our purposes, the explicit form of the Wigner rotation matrices, defined for a complex basis, are only required for the evaluation of spectroscopic intensities in section 2.4.3.1. However, rotation matrices defined for the real basis are also required for evaluating the ligand-field potential matrix in the one-electron basis (section 2.3.2).

Thus far, no mention of the definitions of the rotations have been made. For rotations in three dimensions, it is convenient to work in Euler angles (α,β,γ) using a z-y-z convention, as shown in Figure 2.2. Note that the Euler angles are directly related to the spherical polar coordinates in the ISO convention with an extra spherical angle ψ, such that $(\alpha,\beta,\gamma)=(\phi,\theta,\psi)$.

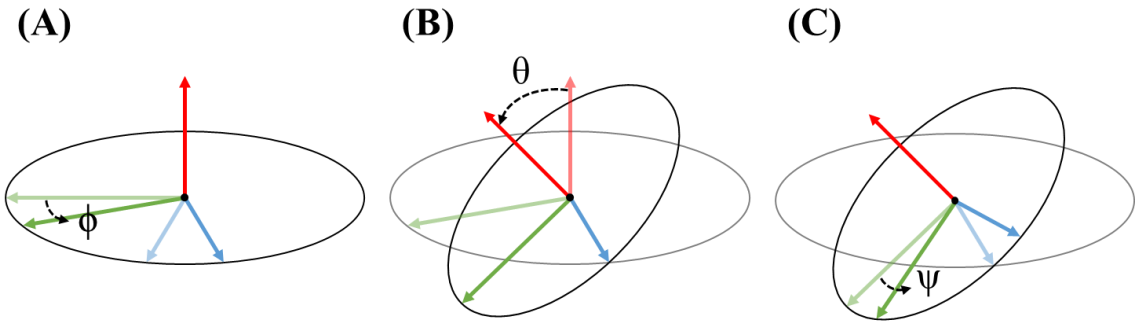

Figure 2.2. The stepwise rotation of a coordinate scheme X (green), Y (blue), and Z (red) by Euler angles in the z-y-z convention

The full transformation from an initial coordinate scheme (X,Y,Z) to a final coordinate scheme (X''',Y''',Z''') is given by the product of three separate rotation operators

$$\hat{R}(\phi\theta\psi) = \hat{R}_{Z''}(\psi)\hat{R}_{Y'}(\theta)\hat{R}_{Z}(\phi) \tag{2.28}$$

where the primes indicate the transformed axes after the primed operation. The transformation proceeds as thus:

1. A rotation about Z by an angle ϕ (α) to give the coordinate scheme (X',Y',Z').
2. A rotation about Y' by an angle θ (β) to give the coordinate scheme (X'',Y'',Z'').
3. A rotation about Z'' by an angle ψ (γ) to give the coordinate scheme (X''',Y''',Z''').

Note that a positive rotation about an axis is defined as a clockwise rotation when looking down the axis from the origin. Similarly, we define an inverse rotation as,

$$\hat{R}(\phi\theta\psi)^{-1} = \hat{R}_{Z}(-\phi)\hat{R}_{Y'}(-\theta)\hat{R}_{Z''}(-\psi) \tag{2.29}$$

where,

$$\hat{R}\hat{R}^{-1} = \mathbf{1}. \tag{2.30}$$

The form of the rotation operator is given by

$$\hat{R}_{n}(\omega) = e^{i\omega l_n} \tag{2.31}$$

where n is the axis (x,y,z), ω is the angle in radians, $i = \sqrt{-1}$, and l_n is the orbital angular momentum operator for axis n. Equations for the evaluation of these terms in the complex and real bases are given by Wigner and Schaffer respectively.[50,51]

2.2.4 Evaluation of the operators of the effective Hamiltonian

To evaluate the effective Hamiltonian, an expression for the matrix elements of each perturbation acting within a basis of angular momentum quantum numbers is required. Each matrix element is then multiplied by a radial coefficient and summed to form the matrix representation of the effective Hamiltonian. From equation (2.1), the final effective Hamiltonian matrix equation is given by

$$\mathbf{H}^{eff} = \sum_{k=0,2,4} F^{k}(B,C)\mathbf{H}_{IR}^{k} + \sum_{k,q} c_{kq}\mathbf{V}_{LF}^{kq} + \zeta\mathbf{H}_{SOC} + \sum_{\alpha=x,y,z} B_{\alpha}\mathbf{H}_{Zee}^{\alpha} \tag{2.32}$$

where $F^{k}(B,C)$ is the Condon-Shortley radial integral calculated from Racah B and C parameters, c_{kq} is the global multipole expansion coefficient of order k and projection q, ζ is the spin-orbit coupling constant, and B_{α} is the magnetic field strength in the cartesian direction α. Note that with exception of the multipole expansion coefficients of the ligand-field perturbation (see section 2.3), all other coefficients are parameters that are directly inputted.

Operators belonging to a Hamiltonian must themselves be scalar quantities. We have seen in section 2.2.3 how an operator can be represented by a tensor of arbitrary rank in any coordinate scheme (which is related to another via a rotation) by a linear combination of tensor operators in the starting frame. This is used directly for the evaluation of the ligand-field potential, $\mathbf{V}_{LF}$. However, both the coulombic operator of the interelectronic repulsion and the spin-orbit coupling operator are assumed to be spherical and are therefore invariant under a rotation of the coordinate scheme.

The evaluation of the matrix elements between a coupled angular momentum basis set for the ligand field, interelectronic repulsion, spin-orbit coupling, and magnetic moment operators are solved and have been adapted from the work of *Gerloch et al*.[33] The final expressions are standalone and can be used without prior knowledge of their formulation.

2.2.4.1 The Wigner Eckart theorem

For the largest case of d^5 with a basis size of 252 and up to 24 operators in total including 18 ligand field, 2 interelectronic repulsion, 1 spin-orbit coupling, and 3 magnetic field, the calculation would require the evaluation of 1,524,096 matrix elements, which would then need to be stored. The operators, represented as either scalars, vectors, or tensors, must conserve angular momentum. This conservation of angular momentum, that is implicit within the Wigner 3j and 6j symbols, allows for the symmetry of the SO(3) rotation group to be fully exploited and reduces the number of matrix elements that require evaluation and storage.

The Wigner Eckart theorem states that a matrix element of a tensor operator of arbitrary rank k is proportional to the Clebsch-Gordan coefficient. The theorem is written as[52–54]

$$\left\langle j\,m\left|T_q^k\right|j'm'\right\rangle = \left\langle j\,m\,k\,q\,\middle|\,j'm'\right\rangle \left\langle j\left\|T_q^k\right\|j'\right\rangle \tag{2.33}$$

where the general matrix element is related to a “reduced” matrix element (denoted by the double bar) and the Clebsch-Gordan coefficient. The Clebsch-Gordan coefficient is related to the Wigner 3j-symbol, given by equation (2.21). Hence, we write

$$\left\langle j\,m\left|T_q^k\right|j'm'\right\rangle = (-1)^{j-m}\begin{pmatrix} j & k & j' \\ -m & q & m' \end{pmatrix}\left\langle j\left\|T_q^k\right\|j'\right\rangle . \tag{2.34}$$

The evaluation of these reduced matrix elements in the suitable quantisation has been tabulated by Nielson & Koster for each of the required reduced operators (U^k, F^k, and V^{11}; *vide infra*) between Russell-Saunders terms of the form ${}^{2S+1}L$.[55] Since the number of Russell-

Saunders terms are much smaller than the full basis size (spanning the full J, M_J space), these reduced matrix elements only require evaluation once. Use of the rules of the Wigner 3j symbol can determine, just by examining the quantum numbers involved and the rank of the operator, whether the matrix element is zero or not, avoiding needless computation.

2.2.4.2 The ligand-field potential

As will be detailed in section 2.3, the ligand-field perturbation is represented by a multipole expansion. This expansion requires evaluation of the basis function under spherical harmonic operators, of the form Y_q^k. This means that the effective ligand-field potential operator, $\mathbf{V}_{LF}$ in the many electron basis is constructed using the expression[33]

$$\left\langle L\,S\,J\,M_J\left|\hat{V}_{LF}\right|L'\,S\,J'M_J'\right\rangle = \sum_k \sum_{q=-k}^{k} c_{kq}\left\langle L\,S\,J\,M_J\left|Y_q^k\right|L'\,S\,J'M_J'\right\rangle \tag{2.35}$$

where c_{kq} is the global radial multipole expansion coefficient of rank and order k and q (see section 2.3 for detail of their construction) and unlike the other radial parameters is not directly inputted. Application of the Wigner-Eckart theorem and expansion of the reduced matrix elements gives the final expression[33]

$$\begin{aligned}\left\langle L\,S\,J\,M_J\left|Y_q^k\right|L'\,S\,J'M_J'\right\rangle = \\ (-1)^{J+J'+L+S-M_J+k+l}\sqrt{(2J+1)(2J'+1)}(2l+1)\sqrt{\frac{2k+1}{4\pi}} \\ \times\begin{pmatrix} J & k & J' \\ -M_J & q & M_J\end{pmatrix}\begin{pmatrix} l & k & l \\ 0 & 0 & 0\end{pmatrix}\begin{Bmatrix} L & J & S \\ J' & L' & k\end{Bmatrix}\left\langle LS\left\|\mathbf{U}^k\right\|L'S\right\rangle.\end{aligned} \tag{2.36}$$

2.2.4.3 Interelectronic repulsion

The interelectronic repulsion involves the two electron coulombic repulsion operator, which is a function of the inverse of the distance between any two electrons written as $1/r_{ij}$ in atomic units.[34] It is possible to expand the angular part of the operator of $1/r_{ij}$ into a linear combination of Legendre polynomials:[34]

$$\frac{1}{r_{ij}} = \sum_k \frac{r_<^k}{r_>^{k+1}} P_k(\cos\omega) \tag{2.37}$$

where the Legendre polynomial can be expressed as the scalar product of two spherical tensor operators, $\mathbf{C}^k(1)\cdot\mathbf{C}^k(2) = P_k(\cos\omega)$, resulting in the coulombic repulsion operator given by

$$\frac{1}{r_{ij}} = \sum_k \frac{r_<^k}{r_>^{k+1}} \left(\mathbf{C}^k(i) \cdot \mathbf{C}^k(j) \right). \tag{2.38}$$

The angular integral of $\mathbf{C}^k(1) \cdot \mathbf{C}^k(2)$ between a bra and ket of angular momentum quantum numbers is given by:[34]

$$\left\langle LSJM \left| \mathbf{C}^k(1) \cdot \mathbf{C}^k(2) \right| L'S'J'M' \right\rangle = \delta_{JJ'} \delta_{MM'} (-1)^{L'+S'+J} \begin{Bmatrix} L & S & J \\ L' & S' & k \end{Bmatrix} \left\langle L \left\| \mathbf{C}^k(1) \right\| L' \right\rangle \left\langle S \left\| \mathbf{C}^k(2) \right\| S' \right\rangle. \tag{2.39}$$

The operator can be expressed by a tensor of order k (like with the spherical harmonic operators of the ligand field in section 2.2.4.2, are truncated at k = 0, 2, and 4). The radial parameter given in (2.32), the F^k parameters, are Slater-Condon parameters. These F^k parameters are parameterised expressions of the double integral[56]:

$$F^k = e^2 \int_0^\infty \int_0^\infty \frac{r_<^k}{r_>^{k+1}} R^2(r_1) R^2(r_2) dr_1 dr_2 \tag{2.40}$$

where < and > denote the lesser and greater of the distances r_1 and r_2 and R^2 is the radial part of the electron orbital. These parameters are related to F_k which are normalised versions of the F^k parameters, given by the relation:

$$\begin{pmatrix} F_0 \\ F_2 \\ F_4 \end{pmatrix} = \begin{pmatrix} F^0 \\ \frac{1}{49} F^2 \\ \frac{1}{441} F^4 \end{pmatrix} \tag{2.41}$$

An alternative parameterisation scheme to the Slater integrals are the Racah parameters A, B, and C. The Racah parameters are related to the Slater-Condon parameters and a transformation can be written as[48]

$$\begin{pmatrix} A \\ B \\ C \end{pmatrix} = \begin{pmatrix} 1 & 0 & -49 \\ 0 & 1 & -5 \\ 0 & 0 & 35 \end{pmatrix} \begin{pmatrix} F^0 \\ \frac{1}{49} F^2 \\ \frac{1}{441} F^4 \end{pmatrix} \tag{2.42}$$

where simple algebra allows us to find the transformations,

$$\begin{aligned} F^0 &= A + \tfrac{7}{5} C \\ F^2 &= 49B - 7C \\ F^4 &= \tfrac{63}{5} C \end{aligned} \quad . \tag{2.43}$$

By combining both equations (2.40) and (2.39), the final form of the matrix element is given by:[33]

$$\left\langle LSJM_J \left| \sum_{i<j} \frac{1}{r_{ij}} \right| L'S'J'M_J' \right\rangle = \sum_k \left\langle LSJM_J \left\| \mathbf{F^k} \right\| L'S'J'M_J' \right\rangle F^k \delta_{LL'} \delta_{SS'} \delta_{JJ'} \delta_{M_J M_J'} \tag{2.44}$$

2.2.4.4 Spin-orbit coupling

The spin of an electron has associated with it a magnetic dipole, as does the orbital motion of the charge. In a one-electron system, the interaction of the two magnetic dipoles is given by the operator $\zeta \mathbf{l} \cdot \mathbf{s}$, where ζ is the radial parameter given in (2.32). The effective mean radial parameter is given by the expression[56]

$$\zeta_{nl} = \hbar^2 \int_0^\infty R_{nl}^2 \xi(r)\, dr \tag{2.45}$$

where

$$\xi(r) = \frac{1}{2\mu^2 c^2}\left(\frac{1}{r}\frac{dU}{dr}\right). \tag{2.46}$$

By using a coulombic potential, $U = -Ze^2/r$ and the hydrogenic radial wavefunction, equation (2.46) becomes:

$$\zeta_{nl} = \frac{e^2\hbar}{2\mu^2 c^2 a_0{}^3}\frac{Z^4}{n^3 l\left(l+\tfrac{1}{2}\right)(l+1)}. \tag{2.47}$$

The radial parameter is proportional to Z^4 and inversely proportional to n^3. Hence, the parameter is larger for elements down a group and across a period. For the many electron case, the spin-orbit coupling operator is written as:

$$\hat{H}_{SOC} = \sum_i \mathbf{l}_i \cdot \mathbf{s}_i \tag{2.48}$$

which is a compound scalar operator and so can be expressed using equation (2.39). The final angular matrix element is given by[33]

$$\left\langle LSJM_J \left| \sum_i \mathbf{l}_i \cdot \mathbf{s}_i \right| L'S'J'M_J{}' \right\rangle =$$
$$\delta_{JJ'}\delta_{M_J M_J'}(-1)^{L'+S+J}\sqrt{l\left[(l+1)(2l+1)\right]}\begin{Bmatrix} L & S & J \\ S' & L' & 1 \end{Bmatrix}\left\langle LS \left\| \mathbf{V^{11}} \right\| L'S' \right\rangle \tag{2.49}$$

where a factor of $\sqrt{3/2}$ is subsumed into the reduced matrix element; the factor has to be used explicitly when computing spin-orbit coupled matrix elements for d^1 or d^9 using (2.49).

2.2.4.5 Zeeman interaction

The Zeeman interaction involves the use of the magnetic moment operator and represents the interaction of the basis functions with an external magnetic field. The magnetic moment

operator is used to compute magnetic properties (2.4.2), magnetic dipole transition intensities, and CD spectra (2.4.3.4). the Zeeman interaction is used to compute MCD intensities (2.4.3.5).

The magnetic moment operator itself is the sum of the orbital and spin angular momentum operators, $\mu = kL + g_e S$, given by[33]

$$\begin{aligned}
\langle LSJ\,|L|\,LSJ'\rangle &= (-1)^{L+S+J'+1}\sqrt{(2J+1)(2J'+1)}\sqrt{L(L+1)(2L+1)}\begin{Bmatrix} J & 1 & J' \\ L & S & L \end{Bmatrix} \\
\langle LSJ\,|S|\,LSJ'\rangle &= (-1)^{L+S+J+1}\sqrt{(2J+1)(2J'+1)}\sqrt{S(S+1)(2S+1)}\begin{Bmatrix} J & 1 & J' \\ S & L & S \end{Bmatrix}
\end{aligned} \qquad (2.50)$$

where $g_e = 2.0023$ is the Landé g-factor and k is the orbital reduction factor. The spherical basis is used throughout so a conversion to cartesian directions proceeds via the relations $\mu_x = \left(1/\sqrt{2}\right)(\mu_{-1} - \mu_{+1})$, $\mu_y = \left(i/\sqrt{2}\right)(\mu_{-1} + \mu_{+1})$, and $\mu_z = \mu_0$ to yield:

$$\begin{aligned}
\langle LSJM_J\,|\mu_z|\,LSJ'M_J\rangle &= \mu(-1)^{J-M_J}\begin{pmatrix} J & 1 & J' \\ -M_J & 0 & M_J \end{pmatrix} \\
\langle LSJM_J\,|\mu_x|\,LSJ'M_J'\rangle &= \mu\frac{1}{\sqrt{2}}(-1)^{J-M_J}\left[\begin{pmatrix} J & 1 & J' \\ -M_J & -1 & M_J' \end{pmatrix} - \begin{pmatrix} J & 1 & J' \\ -M_J & 1 & M_J' \end{pmatrix}\right] \\
\langle LSJM_J\,|\mu_y|\,LSJ'M_J'\rangle &= \mu\frac{i}{\sqrt{2}}(-1)^{J-M_J}\left[\begin{pmatrix} J & 1 & J' \\ -M_J & -1 & M_J' \end{pmatrix} + \begin{pmatrix} J & 1 & J' \\ -M_J & 1 & M_J' \end{pmatrix}\right].
\end{aligned} \qquad (2.51)$$

One can simply apply the Zeeman splitting by the multiplication of the magnetic field in the cartesian directions:

$$\frac{\boldsymbol{\mu}\cdot\mathbf{B}}{\mu_B} = \mu_x B_x + \mu_y B_y + \mu_z B_z\,. \qquad (2.52)$$

where μ_B is the Bohr magneton in units of $cm^{-1}\ T^{-1}$.

2.3 The ligand-field model

The expression for the ligand-field contribution in equation (2.36) describes the angular matrix element for a series of spherical harmonic operators. The radial contribution is given by multipole expansion coefficients. The details and physical significance of this are presented in the proceeding chapter. The “ligand field” refers to a potential field generated by the ligands which are bound to the central metal ion. The ligand field is physically distinct when compared to the more typical forms of bonding from molecular orbital theory, or valence bond theory.

In the case of representing a π-bond in ethylene with molecular orbital theory, for example, we require explicit descriptions of the two p_z orbitals that overlap to form a bonding orbital occupied by *bonding* electrons. Hence, the description of those electrons requires a Hamiltonian that describes the overlap of *two* p_z orbitals on different atomic sites. This type of description is unnecessary for Werner-type complexes, where only the angular description of the free-ion d orbitals is required. The d electrons and their configurations belong wholly, or primarily, to the central metal-ion. Their unique properties result from the fact that they do not often pair with electrons on other atomic centres.

To formulate this theory fully in a predictive way, one must know the radial forms of the d orbitals, the ligand orbitals, and the rest of the metal orbitals. The radial forms are not known *a priori*; the angular integrals, as given by equation (2.36), are known and complete. Hence, the parameterisation of the radial part of the ligand field serves to circumvent the difficult and relatively computationally expensive approach of optimisation, aiming to extract that information from experiment itself.

2.3.1 The multipole expansion

In LFT, the field generated around the central metal ion at the origin is given by a distribution of potentials, or charges. This type of distribution can be represented by a multipole expansion that is built from a linear combination of spherical harmonics[34]

$$V(r,\theta,\varphi)=\sum_{k}^{\infty}\sum_{q=-k}^{k}c_q^k(r)Y_q^k(\theta,\varphi) \tag{2.53}$$

where V is a scalar effective potential and c_q^k are the local expansion coefficients that subsume the radial integrals.

Now, the ligand-field potential must act within a basis of d orbitals. This can be represented by a potential, approximated by the multipole expansion, acting on the one-electron d-orbital spherical harmonics. Using a d-orbital one electron basis that spans the $|lm\rangle$ space, where $m=\{-2,-1,\ 0,\ 1,\ 2\}$, the potential can be written as

$$\langle lm|V(r,\theta,\varphi)|lm'\rangle=\sum_{k=0}^{4}\sum_{q=-k}^{k}\langle lm|c_q^k(r)|lm'\rangle\langle lm|Y_q^k(\theta,\varphi)|lm'\rangle\,. \tag{2.54}$$

Observing that the matrix element $\langle lm|Y_q^k(\theta,\varphi)|lm'\rangle$ contains the Wigner 3j symbol $\begin{pmatrix} l & k & l \\ 0 & 0 & 0 \end{pmatrix}$ which is only non-zero for $k=0,2,4$ when l is even, means that the summation

over k can be truncated. *McMeeking et al*. have written the relationship between the expansion coefficients c_q^k and the general matrix elements of the potential $\langle lm|V|lm'\rangle$.[33]

2.3.2 The one-electron ligand-field matrix

Having established that the global multipole expansion coefficients can be computed from matrix elements of the ligand-field potential between the one-electron d orbitals, the question of how to construct the matrix and its elements immediately follows. In general, the method of parameterisation of the 5 × 5 one-electron ligand-field matrix, V_{LFT} is what separates the global methods of crystal-field theory (with parameters of Dq, Ds, Dt, etc) and other models such as the AOM. *McMeeking et al*. have tabulated the inversion of the multipole expansion, which expresses the expansion coefficients of (2.54) in terms of the matrix elements of the one-electron ligand-field matrix.[33] It is this general conversion from a potential V in a one-electron basis, to the potential acting on a many-electron basis, that allows for the evaluation of the ligand-field potential in (2.32) and (2.36).

It is useful to compute the real form of V_{LFT} explicitly. Computing the matrix explicitly with the ligand-field model means that comparisons can be made with the same matrix computed from AILFT to extract e_λ values from the results of *ab initio* calculations.[10,31] The second reason is that the eigenvalue solutions of the one electron V_{LFT} matrix furnish the energies of the five mixed one-electron d orbitals and their eigenvectors in the real d-orbital basis.

The energies are invariant under the rotation of the coordinate scheme. However, the eigenvector coefficients change. This means that the interpretation of the d-orbital character is sensitive to the choice of cartesian axes. To illustrate this with a simple example, we can imagine a d_{z^2} orbital in the conventional scheme, aligned along the Z axis in a cartesian orientation (XYZ). If we were to rotate about the Y axis by 45°, it is possible to construct the new orientated d_{z^2}' (the prime indicates the new rotated scheme X'Y'Z') in terms of the d orbitals in the original XYZ scheme. In Figure 2.3, the linear combination of the d_{z^2}, d_{xz} and $d_{x^2-y^2}$ in XYZ can reproduce the shape and orientation of the new d_{z^2}' orbital. However, visualising spherical harmonic mixing is not easy and hence a suitable coordinate scheme should be chosen to make chemical sense of the resulting ligand-field splitting.

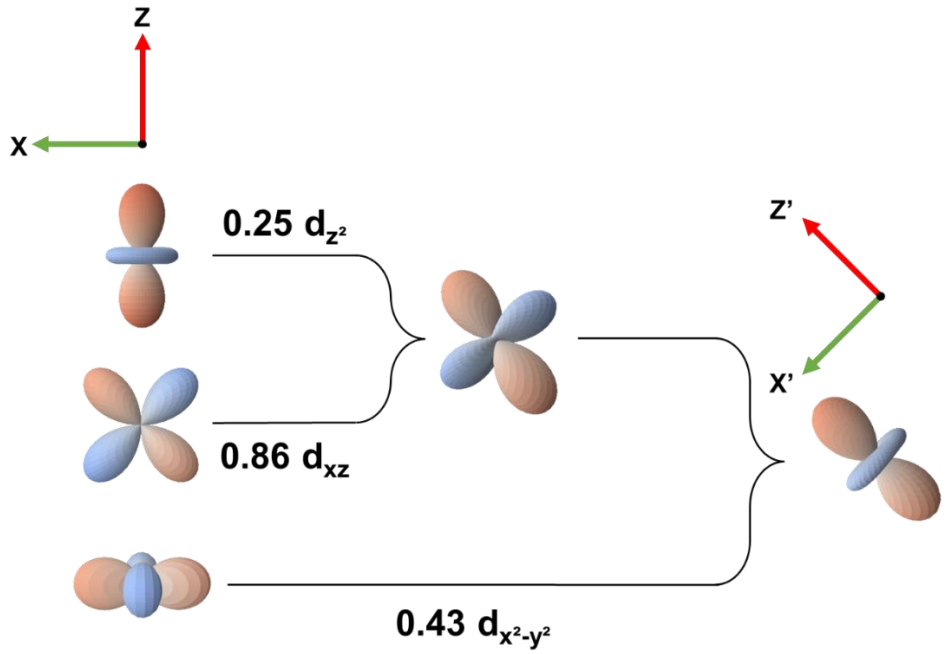

Figure 2.3 The mixing of the angular Y(l,m) (l=2, m=2, 1, 0) spherical harmonics in one coordinate frame (XYZ) to reconstruct the spherical harmonics in a rotated coordinate frame (X'Y'Z').

We are now concerned with the parameterisation of the 15 unique matrix elements of the one-electron ligand-field potential matrix in terms of e_λ parameter, which have a tangible and physical (chemical) meaning attached to their parameter values and can be applied to any molecular geometry.

2.3.3 Angular overlap model

The AOM is one possible method of parameterising the V_{LFT} matrix. The parameterisation requires only two parameter sets: the angular geometry $\{\theta,\phi,\psi\}$, which is known from either x-ray crystallography or from a calculated structure; and the individual metal-ligand bonding parameters $\{e_\lambda\}$ for each ligand.[57]

The AOM aims to reproduce the energetic perturbations experienced by a d electron on the metal via an electrostatic potential over the entire metal, which is constructed from the sum of a series of local electronic perturbations. This is simply the consequence of using a multipole expansion in (2.53). Technically speaking, it is possible to decompose this global

field into an infinite number of spatial regions. It is the task of the user to choose a sensible decomposition. Hence, assuming some sort of interaction between the central metal ion and a “coordinating” atom exists, a potential must arise from that spatial region that the ligand occupies. Explicit equations for the extraction of the angular geometry are presented and an overview of the various metal-ligand bonding e-parameters are given.

2.3.3.1 Spherical polar coordinates

The model requires angular, rather than cartesian, coordinates. There exists simple expression relating the spherical polar coordinates θ and ϕ to the cartesian coordinates of a given coordinating atom:

$$\theta = \cos^{-1}\left(\frac{z}{\sqrt{x^2+y^2+z^2}}\right) = \cos^{-1}\left(\frac{z}{r}\right)$$

$$\phi = \tan^{-1}\left(\frac{y}{x}\right). \qquad . \qquad (2.55)$$

There also exists a simple relationship between the spherical polar coordinates and the Euler angles in the z-y-z convention as described in section 2.2.3: $\alpha = \phi$ and $\beta = \theta$.

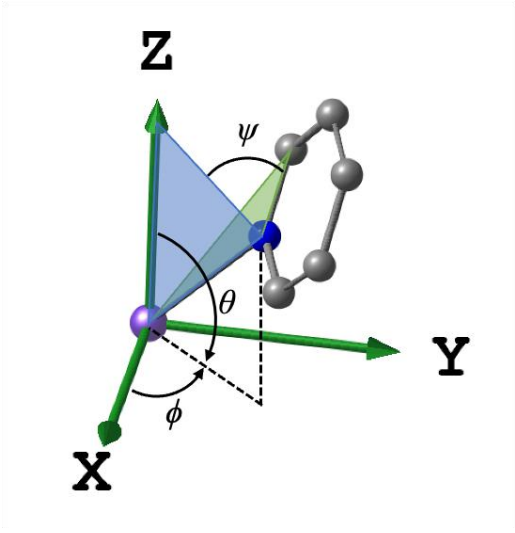

Figure 2.4. The angular geometry of a ligand and the definitions of its spherical polar coordinates.

This description of the angular geometry is complete for any ligand that engages in linear π bonding, or is void of π bonding, but incomplete for ligands which asymmetrically π bond (e.g., pyridine). In doing so, we must align one of the local frames (x or y) with another plane. This angle is given by the final Euler angle γ. The definition is simply defined as the dihedral between the plane formed by the unit z-coordinate axis (Z), the central metal-ion (M), and the coordinating atom (L), and the plane formed by the central metal-ion, the coordinating atom, and the final coordinate that defines the local x-direction (O). In other words, the final Euler angle is given by the dihedral Z-M-L-O. The final complete angular description of the geometry of a metal-ligand bond is illustrated in Figure 2.4.

2.3.3.2 Diagonal perturbations

Considering the diagonal frame, centred on some point, one can define a series of local matrix elements[34]

$$\begin{aligned} e_{\sigma} &= \left\langle d_{z^2} \middle| v \middle| d_{z^2} \right\rangle \\ e_{\pi x} &= \left\langle d_{xz} \middle| v \middle| d_{xz} \right\rangle \\ e_{\pi y} &= \left\langle d_{yz} \middle| v \middle| d_{yz} \right\rangle \\ e_{\delta xy} &= \left\langle d_{xy} \middle| v \middle| d_{xy} \right\rangle \\ e_{\delta x^2-y^2} &= \left\langle d_{x^2-y^2} \middle| v \middle| d_{x^2-y^2} \right\rangle \end{aligned} \tag{2.56}$$

where the operator v is the local potential in the frame of the angular coordinate. These perturbative potentials are symmetric about the metal-ligand axis and as a result the pseudo-symmetry of these interactions can represent the metal-ligand bonding modes of the ligand. These diagonal perturbations are then rotated by means of a Schaffer rotation matrix $\mathbf{R}(\theta,\phi,\psi)$, transforming the local perturbation matrix elements to the global perturbation frame[51]

$$\left\langle I,m \middle| V_{LFT} \middle| I,m' \right\rangle = \sum_{i=1}^{N} \mathbf{R}\left(\theta_i,\varphi_i,\psi_i\right) \mathbf{v} \mathbf{R}^{T}\left(\theta_i,\varphi_i,\psi_i\right) \tag{2.57}$$

where the sum is over all ligands. The additivity to the global ligand field of all ligands is a key assumption of the model.

It must be remembered that no explicit overlap has occurred between metal d orbitals and ligand functions. There of course will be *some* overlap but it is generally small. The explicit first principles derivation of the magnitude of the e_{λ} is quoted as[31]

$$e_\lambda = \langle d_\lambda | v | d_\lambda \rangle + \sum_\alpha \frac{\left| \langle d_\lambda | v | \varphi_\alpha \rangle \right|^2}{E_d - E_\alpha} \tag{2.58}$$

where the parameter features a first order and second order term. The first order term is referred to as the electrostatic contribution and the second order term is referred to as the electrodynamic contribution. These two physical effects have fundamentally different origins. The electrostatic contribution is more akin to a “crystal-field” like perturbation; it is the static electric field generated by all the other electrons in the molecule perturbing the d electrons. The electrodynamic contribution arises from the correlation energy that occurs when the d electrons instantaneously approach electrons in a metal-ligand (anti)bonding orbital, illustrated in Figure 2.5.

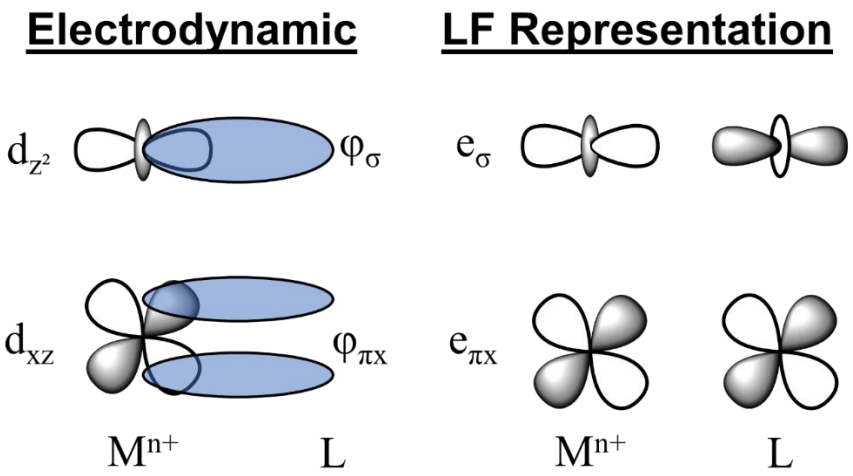

Figure 2.5 The electrodynamic contribution arising from a metal-ligand bonding orbital with the d orbitals (left) and the corresponding pseudo-symmetry representation within LFT from the minimal basis set of d orbitals (right).

The chemical notion of bonding arises from the electrodynamic contribution. It is the interaction between the metal d orbitals and the electrons contained in metal-ligand bonds (formed from a combination of ligand and other metal functions). For electrons to instantaneously approach in a dynamic electric field they must spatially overlap (occupy the same volumes). The denominator term in equation (2.58) determines the sign of the interaction. If the bond orbital is of a *higher* energy than the mean d-orbital energy, this contribution is negative, and vice versa if the bond orbital is of a *lower* energy. Hence, a strong and stable σ bond would be expected to be lower in energy than the d orbitals and hence be a positive contribution ($e_\lambda > 0$). A π anti-bonding orbital has electron density in an orbital which

is higher in energy and would result in a negative contribution ($e_\lambda < 0$). This is in line with the notional donor and acceptor behaviour of ligands. An illustration of this concept is shown in Figure 2.6.

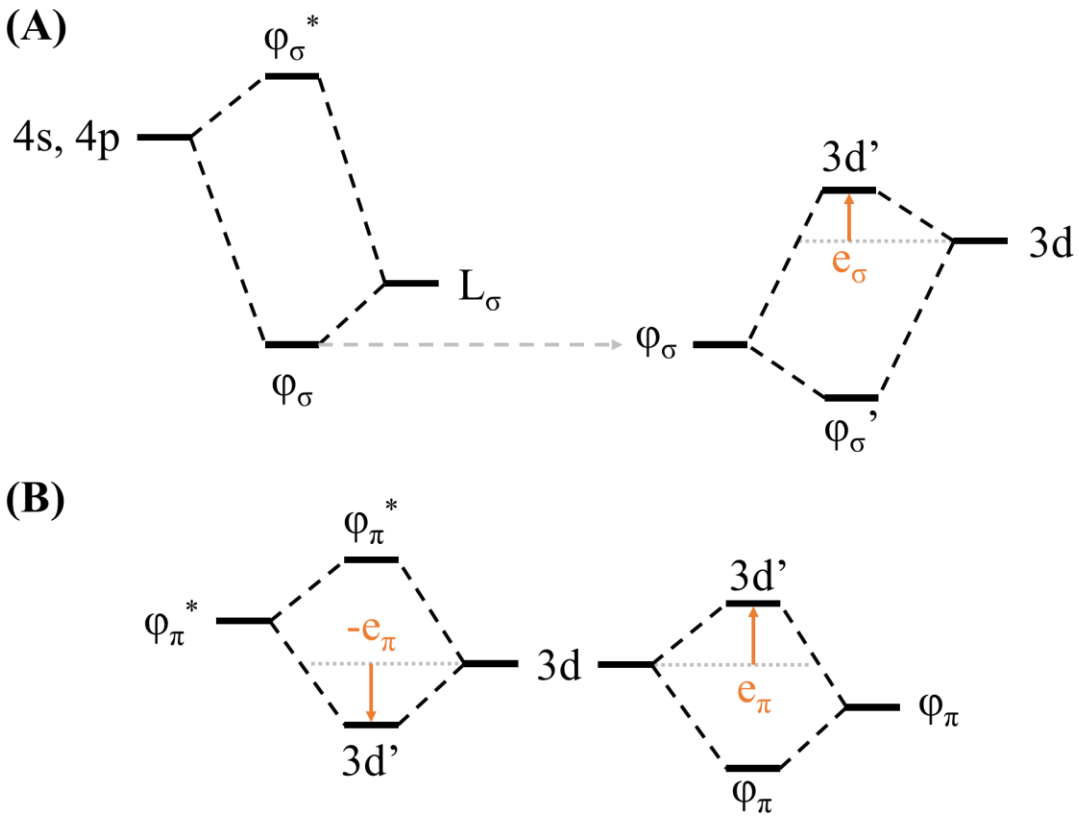

Figure 2.6 The formation of metal-ligand bonding and antibonding orbitals between a ligand σ function and a combination of the metal 4s/4p functions and its perturbation on the d orbitals (A); the competing π-acceptance and π-donation from both donor/accepting capabilities of a metal-ligand bonding and anti-bonding π function (B).

It is not trivial untangling the electrostatic and electrodynamic contributions from one another. *Gerloch* and *Wooley* have argued that the electrostatic part is probably sizeable in the e_σ parameter but negligible in the e_π parameter.[24] However, *Singh et al*. have argued that the electrostatic part (which they associate as belonging to calculated CASSCF energies and electrodynamic contributions being attributed to the NEVPT2 contribution) is a much larger contribution to the e_λ parameter.[31]

2.3.3.3 Misdirected valence

There is also the notion of a “misdirected” bond where a local perturbation does not sit symmetrically about a metal-ligand axis. Examples of this are lone non-bonding electron pairs, or geometric constraints that physically misdirect a σ or π function on the ligand. These perturbations are represented by the local matrix element $\left\langle d_{z^2} \middle| v \middle| d_{xz} \right\rangle = \left\langle d_{xz} \middle| v \middle| d_{z^2} \right\rangle = e_{\pi\sigma x}$ and $\left\langle d_{z^2} \middle| v \middle| d_{yz} \right\rangle = \left\langle d_{yz} \middle| v \middle| d_{z^2} \right\rangle = e_{\pi\sigma y}$.

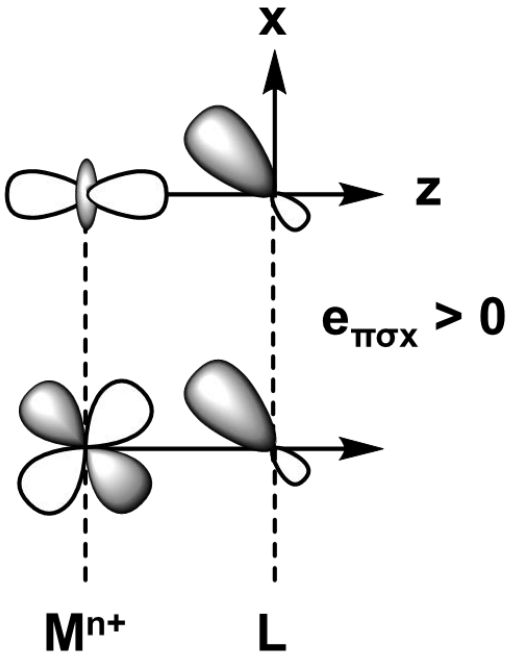

Figure 2.7 Illustrative representation of a destabilising misdirected bond projected into the negative XZ quadrant of the local ligand frame resulting in a positive misdirected parameter value.

Unlike with the diagonal perturbations (*vide supra*), a simple relationship does not exist between the sign of the parameter and its notional donor/acceptor behaviour. Rather it is a function of both the donor/acceptor behaviour *and* the directed quadrant that the misdirected interaction is placed. The electrodynamic contribution to the $e_{\pi\sigma}$ parameter can be derived by equation (2.58) and is written as[58]

$$e_{\pi\sigma x}(\text{dynamic}) = \sum_{\alpha} \frac{\langle d_{xz} | v | \varphi_{\alpha} \rangle \langle \varphi_{\alpha} | v | d_{z^2} \rangle}{E_d - E_{\alpha}} \tag{2.59}$$

where the numerator is not necessarily always positive since the d_{z^2} and d_{xz} in this case may, or may not, be in-phase. Imagine a ligand function projected into the positive local x direction (Figure 2.7) and its perturbation represented by the $e_{\pi\sigma x}$ parameter. Assuming (as would often be the case) the function is a destabilising interaction, the denominator in (2.59) contribution is defined as positive. In these instances, the $e_{\pi\sigma x}$ parameter would also be positive. However, If the destabilising interaction is projected into the negative local x direction instead, the parameter will be negative.

2.3.3.4 4s-3d mixing

Early evidence of 4s mixing with the $3d_{z^2}$ orbital, in effective square planar complexes, was presented by spin Hamilton analysis of EPR spectroscopy. In those works, the analysis of the Fermi term suggested that there was 4s mixing into the $3d_{z^2}$ orbital.[59,60] The implications that this mixing would have for ligand-field analysis was later demonstrated by *Hitchman* and *Cassidy* who were able to unambiguously assign the d-orbital energy sequence of square planar $CuCl_4^{2-}$ as $d_{x^2-y^2} >> d_{xy} > d_{xz} > d_{yz} > d_{z^2}$.[61] They showed that the AOM model, which assigned an e_{σ} and e_{π} to each chloride ligand, could not account for the relatively low energy of the d_{z^2} orbital. Since then, the stabilisation of the d_{z^2} orbital in axially weak ligand fields has been well documented.[62] Within the ligand-field literature, two methods have been developed to deal with this phenomenon.

The first method was to use a so-called “coordination void”, where a potential (e_{σ}) is placed at the distant ligand, or in a region absent of any ligation, above and below the equatorial plane.[62] The stabilisation is accounted for by a negative e_{σ} parameter at the coordination void. There have been recent suggestions that a negative e_{π} value should also be attributed to these coordination voids.[63] The primary issue with this method is that it is not always straightforward to decide where the coordination void should be placed.

The alternative approach of accounting for this stabilisation is to evaluate the angular matrix elements of the 3d-4s interaction and parameterise this. Practically, this would involve placing a shared e_{ds} parameter on each ligand. The interaction perturbation is written as:[64]

$$\langle l, m | V_{4s} | l, m' \rangle = \sum_{n} F_m^n F_{m'}^n e_{ds}^n \tag{2.60}$$

where the elements of the angular overlap, F_m are:

$$
\begin{aligned}
F_{xy} &= \sqrt{3/2}\sin^2(\theta)\sin(2\phi) \\
F_{yz} &= \sqrt{3}\cos(\theta)\sin(\theta)\sin(\phi) \\
F_{z^2} &= 1/2\left(3\cos^2(\theta)-1\right) \\
F_{xz} &= \sqrt{3}\cos(\theta)\sin(\theta)\cos(\phi) \\
F_{x^2-y^2} &= \sqrt{3/2}\sin^2(\theta)\cos(2\phi) \quad .
\end{aligned} \tag{2.61}
$$

The 4s perturbation is a stabilising effect on the overall ligand-field matrix. Thus, the matrix elements of the V_{4s} operator are subtracted from the matrix elements belonging to the 5×5 global ligand-field potential V_{LFT} operator, given by equation (2.57), to yield:

$$
\langle I,m|V_{\text{total}}|I,m'\rangle = \langle I,m|V_{LFT}|I,m'\rangle - \langle I,m|V_{4s}|I,m'\rangle \tag{2.62}
$$

2.3.4 A theoretical guide to the parameterisation of metal-ligand bonding

The preceding sections detail the theoretical groundwork for the metal-ligand bonding framework. However, the choice of the types of (or how many) interactions to assign to the ligand-field parameterisation is not always obvious. This section collates the main bonding interactions for a wide range of metal-ligand bonds and offers a rationale for how one might choose to define the bonding in those metal-ligand interactions. Finally, a short example is given, which shows how a ligand-field parameterisation scheme might be configured for a real molecule.

2.3.4.1 Bonding interactions of ligands

Common to every ligand-field analysis, except those carried out on isolated free-ions, is the assignment of bonding interactions to ligands. Inorganic chemistry features a diverse range of ligands with different bonding modes. Although it is impossible to cover every possible ligand, the most common ligand classes from inorganic and organometallic chemistry are considered here as a useful reference and guide. The aim is to not only allow a user to check a parameterisation scheme for a type of ligand but to also see the rationalisation, so that one can determine what bonding parameters and likely interaction types (donor or acceptor) can arise for similar or different classes of ligands. The general e_λ parameterisation scheme for a range of ligands is given in Table 2.1. The table is not meant to cover every scenario or to be used without context. Some interactions might not be included depending on the chemical or

parametric context (reducing the number of free adjustable parameters in the latter case, for example).

Table 2.1. General e_λ parameterisation schemes for classes of ligands. (L.P.) = lone pair interaction.

Ligand	e_σ	e_π	$e_{\pi x}$, $e_{\pi y}$	$e_{\sigma\pi}$ (L.P)	e_δ
Saturated amines (NR_3)	Donor	0	0	0	0
H_2O	Donor	0	Donor or 0	Donor or 0	0
OH^-	Donor	0	Donor	Donor or 0	0
F^-, Cl^-, Br^-, I^-	Donor	Donor	0	0	0
CN, CO, SCN^-	Donor	Donor or acceptor (linear)	Donor or acceptor (bent bonding)	0	0
Phosphines	Donor	Acceptor	0	0	0
Thiolates[65] (bent)	Donor	0	Donor	Donor	0
Oxo (M=O)	Donor	Donor	0	0	0
Heterocyclic ligands	Donor	0	Donor or acceptor	0	0
Carbenes	Donor	0	Donor or acceptor	0	0
Conjugated bidentate ligands	Donor	0	Donor or acceptor	Donor or 0	Donor or acceptor
η^5-Cp	Donor	Donor	0	0	Acceptor
η^2-Olefin	Donor	0	Acceptor	0	0

A visual summary of the key interactions for different ligand types are given in Figure 2.8. The following subsections discuss the different classes of ligands in more detail. In general, one can often get a sense for the types of interactions and their respective donor/acceptor properties by considering the frontier valence orbitals.

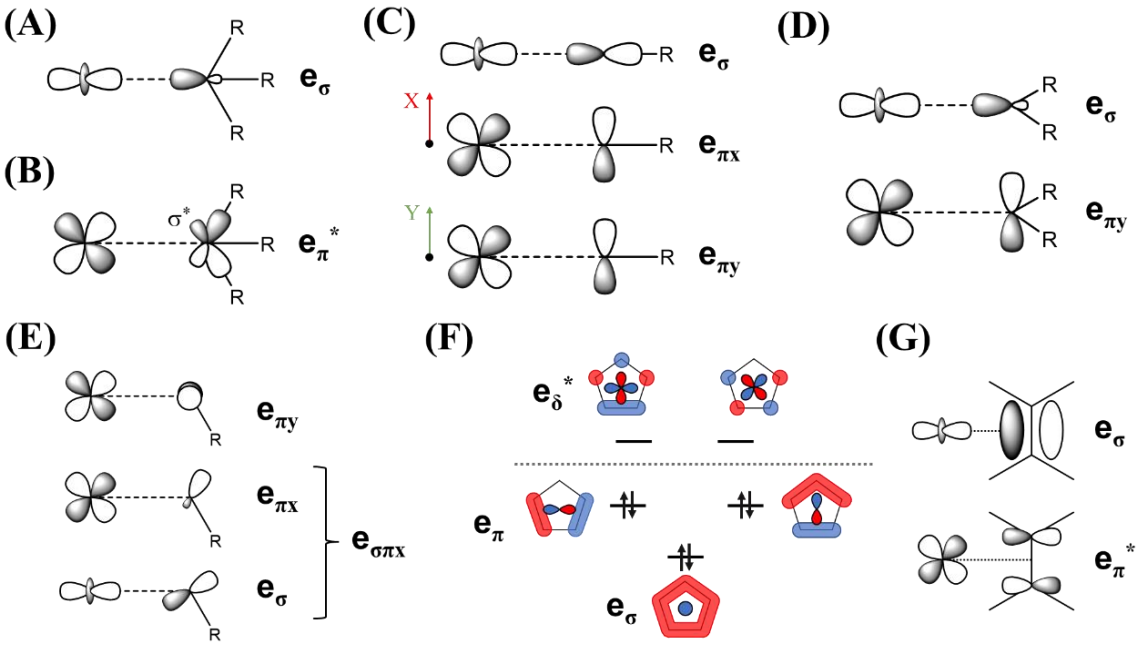

Figure 2.8. The key types of bonding interactions for different classes of molecules. The subscripts 'x' refer to a direction parallel to the intra-ligand bonds shown and 'y' refers to the direction perpendicular to that. The * next to an e_λ assigns that interaction as an acceptor interaction.

2.3.4.1.1 Saturated donors

Saturated donors contain ligands that are often presumed to be σ-donor only ligands. Examples include ammonia, primary amines, secondary amines, tertiary amines, and alkyl ligands. This class of ligand is the simplest requiring only one variable parameter e_σ, illustrated by Figure 2.8 (A).

There are cases where an e_π parameter *might* arise from this class of donor. The first relates to the possibility of large electrostatic contributions to the metal-ligand bond. The size of this perturbation is a matter of current debate.[66] A ligand-field analysis of the experimental data of a linear dialkyl cobalt(II) complex later in this thesis provides evidence for a small electrostatic contribution to the e_π value. The second possibility comes from apparently

saturated ligands that do engage in π-bonding (e.g., phosphines as shown in Figure 2.8 (B)). The third possibility is in the formation of a partial double metal-ligand bond from an agnostic effect that has been described in M–C–H (M = metal) bonds.[67]

It is also possible for these ligands to have an $e_{\sigma\pi}$ parameter due to misdirected valence of the σ bonding orbital. There are multiple uses of this reported in the literature.[58,68–71] In these instances, the misdirected valence will be a destabilising interaction.

2.3.4.1.2 Cylindrical π bonding

Cylindrical π interactions are equal π perturbations about a metal-ligand axis (i.e. $e_{\pi x} = e_{\pi y}$), illustrated in Figure 2.8 (C). This is common for ligands with a single atomic centre (e.g. the halides) or for linear ligands coordinating in a linear fashion (CO, $^{-}$CN, acetonitrile, etc). Other examples include ligands with local C_{3v} symmetry, such as the π-acceptance of phosphines. Even in ligands with a lower local symmetry it can be useful to approximate the ligand as engaging in cylindrical π bonding to lower the number of free parameters.

The relative donor or acceptor capability of some ligands is well known: halides, for example, are π donors; phosphines are π acceptors. However, for some ligands (e.g. cyanide, acetonitrile, and azide), the e_{π} parameter measures the *net* donor/acceptor capability.[72] It is possible to have a value that is small or near 0 cm^{-1} and indicates either a lack of π-bonding, or more likely, that the donor and acceptor functions cancel each other out. It is impossible with the ligand-field model to separate out the separate donor and acceptor interactions.

2.3.4.1.3 sp^2 hybridised ligands

Ligands whose coordinating atoms are essentially sp^2 hybridised engage in asymmetric π-bonding, the example bonding diagram is given in Figure 2.8 (D). These ligands require definitions of their local x direction which is aligned with one of the atoms bonded to the coordinating atom. Examples of this type of ligand are imines, pyridines, pyrroles, thiolates, and hydroxides. Typically, the $e_{\pi x}$ parameter is set to 0 cm^{-1} as it is often associated with occupied sp^2 orbitals engaged in σ-bonding with the ligand framework. Sometimes one of the sp^2 orbitals is not engaged in σ-bonding and instead houses a lone pair. This is common for ligands such as thiolates, or phenolates, where the coordinating atom features one intra-ligand bond. That lone pair will have associated with it an in-plane lone pair e_{π} and, if parameterisation will allow, a misdirected $e_{\pi\sigma}$ parameter, as illustrated in Figure 2.8 (E).

Typically, these ligands are often found to be π-donors, particularly if they are anionic or possess occupied π-orbitals. However, some ligands might have functions of π-symmetry which are unoccupied or are depleted via electron-withdrawing groups, such as that found in some carbenes. Again, in those systems the $e_{\pi y}$ parameter measures the net donor or acceptor properties of the ligand as discussed in 2.3.3.2.

2.3.4.1.4 Phase-coupled ligators

The class of phase-coupled ligators are thought to engage in differential π bonding. Although there have been attempts to explain the spectroscopic properties of these complexes using misdirected valence[58,68], this parameterisation was not able to account for the spectroscopic properties of $Cr(acac)_3$, where acac = acetylacetone.[67] Instead, the ligand-field parameterisation of the acac ligands was extended to consider the phase coupling of the delocalised π bonding networks. This phase coupling – referred to as the "Orgel effect"[73] – has been successfully applied within the ligand-field model to the reproduction the physical properties of $Cu(acac)_2$.[74]

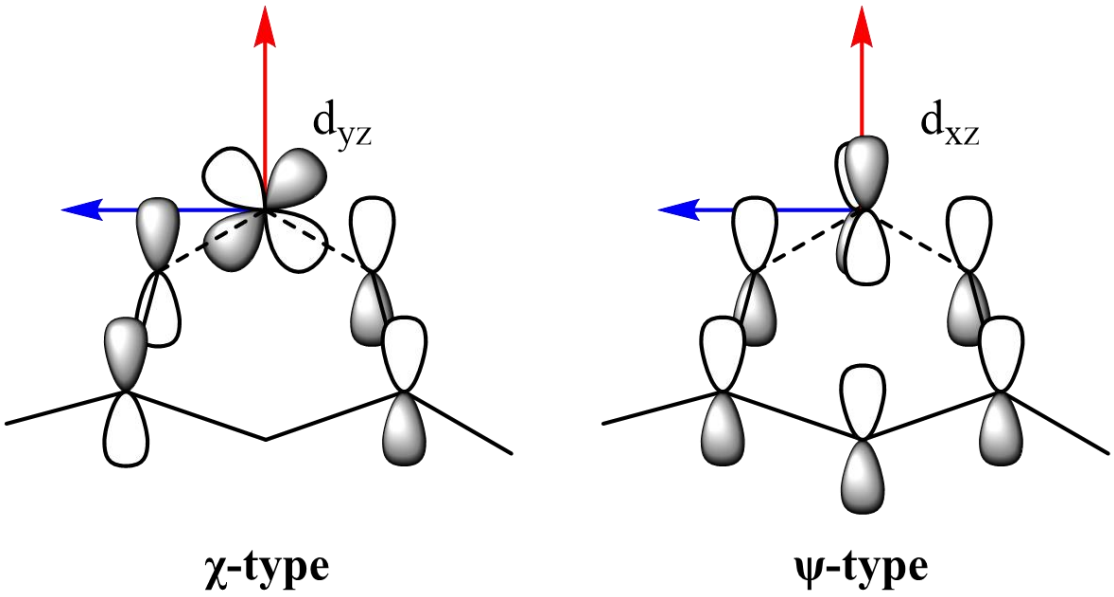

Figure 2.9. The out-of-phase χ-type and in-phase ψ-type interactions with the d_{yz} and d_{xz} orbitals for the Orgel effect of phase-coupled ligation. The red and blue arrow represent the molecular Z and Y axes respectively.

An illustration of the Orgel effect is presented in Figure 2.9. The π bonding of the conjugated π networks produce two sets of π interactions: an out-of-phase interaction (χ-type, Figure 2.9 left); and an in-phase interaction (ψ-type, Figure 2.9 right). These two phases differentially interact with the d_{xz} and d_{yz} orbitals of local π symmetry and given that the in-phase and out-of-phase π networks would be of different energies, the individual perturbations will be of different magnitudes according to equation (2.58).

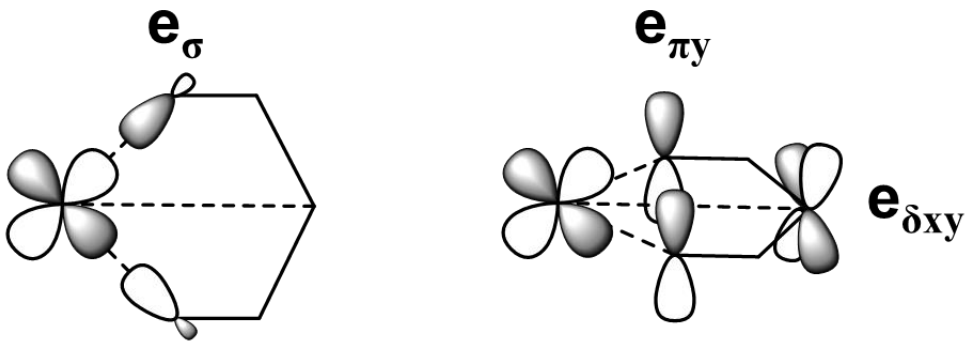

Figure 2.10. The parameterisation scheme of a phase-coupled ligator ligand from the "Orgel effect".

A question arises: how do we parameterise the Orgel effect in the metal-ligand bonding parameterisation scheme? The parameterisation scheme of the Orgel effect for a ligand like $acac^-$ is presented in Figure 2.10. In total, three bonding parameters are required: an e_σ parameter to measure the σ bonding strength; an $e_{\pi y}$ parameter (where the local x direction is directed parallel to the σ bonding plane), which parameterises the ψ-type in-phase π interaction; and an $e_{\delta xy}$ parameter, placed at a coordinate which bisects the X–M–X triad (where X = the coordinating atom and M = the central metal ion) in the plane of the σ bonding framework, representing the χ-type out-of-phase π interaction. Some authors have used specific e_χ and e_ψ parameters, introduced as a rhombic perturbation.[74] The method described above is equivalent and does not require the definition of new parameters.

If one places a simple potential at the coordinating atom positions and parameterises it with e_σ and $e_{\pi y}$, but does not include the non-local $e_{\delta xy}$ perturbation, then a (near) degenerate d_{xz}/d_{yz} pair results. However, the one-electron energetic splitting of the d_{xz}/d_{yz} orbital pair has been determined to be approximately 1500 cm^{-1} in cobalt(II) Schiff base complexes.[75] Other work carried out on the same system, which does not recognise the Orgel effect but instead parameterises the in-plane electron lone pair with an $e_{\sigma\pi x}$ value, manages to provide an

alternative fit of the experimental data.[58] One should note, however, the work that provides an alternative fit of the experimental data reports best fit parameters which are unphysical (a negative Racah B parameter). Hence, their parameterisation scheme should be interpreted cautiously. A more detailed discussion between these two methods can be found by *Bridgeman* and *Gerloch*.[29]

2.3.4.1.5 Cyclopentadienyl ligands.

A common class of organometallic ligand is the cyclopentadienyl ligands. As far as the author is aware, these ligands have never been parameterised with bonding parameters directly. In terms of parameterisation, it depends on the coordination mode. The most common bonding mode is the η^5 bonding mode. If the available bonding interactions are rationalised using a simple frost cycle, we can see that the cyclopentadienyl has five orbitals that could perturb the d orbitals, as shown in Figure 2.8 (F). In this case, it is convenient to place a potential in the centre of the ring. The cyclopentadienyl then has one donor interaction of σ-symmetry and two degenerate donor interactions of π-symmetry. The ligand also has two degenerate acceptor interactions of δ symmetry.

An issue arises with the possibility of three separate σ, π, and δ interactions. It has been established that e_λ are "renormalised" such that $e_\lambda = e_\lambda' - e_\delta'$, where the primes indicate the unnormalized parameters. Given it is often a requirement to set e_δ to 0 cm^{-1} and since it might be non-zero (< 0 cm^{-1}) it might enhance the size of the donation of the e_σ and e_π parameters. However, in a mixed ligand system, it may be unsuitable to set e_δ of the Cp ligand to 0 cm^{-1} because it might take a value < 0 cm^{-1} compared to the e_δ systems of the other ligands in the molecule, which are likely to be of a similar value. More research is required in this area before a conclusion can be reached.

2.3.4.1.6 Olefin ligands

Olefin ligands typically coordinate via the centre of their π bond, as illustrated in Figure 2.8 (G). The π bond acts as a σ donor relative to the central metal ion; the π* anti-bonding orbital acts as a π acceptor interactor with respect to the central metal ion. The $e_{\pi x}$ parameter is orientated along the C=C vector and is assigned a value < 0 cm^{-1}. Little is known about the magnitudes of these parameters and few analyses have been carried out on transition-metal complexes with olefin ligands.[76]

2.3.4.2 Choosing ligands

The first step of a ligand-field analysis is defining the minimal number of ligand types in a molecule. In general, this is as simple as looking at the chemical nature of the coordinating groups within the molecule. If there are multiple phosphines, or amines, etc of a similar bond length then it is an obvious choice to group these together as a single ligand type. Consider, as way of an example, the x-ray structure of a five-coordinate vanadium complex in Figure 2.11.[77] There are three distinct functional groups: the axial ^{t}BuNC, the axial tertiary amine, and the equatorial amides. We would define these three as separate ligands. In doing so, we are assuming that the equatorial amides are similar and engage in similar bonding with the central metal ion.

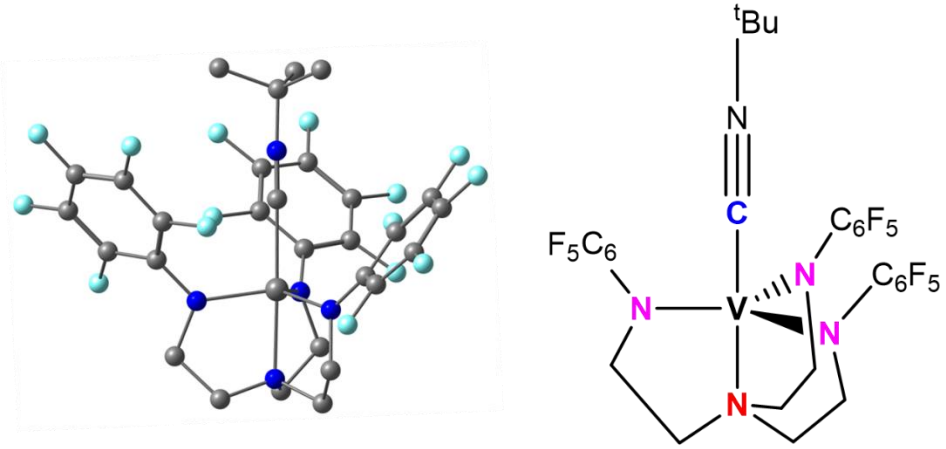

Figure 2.11. The x-ray crystal structure of $(C_6F_5)_3$trenVCN^{t}Bu (left, CSD: WAFGOD) and the representative molecular drawing with the three functional groups coloured in blue, red, and pink (right).[77]

Having defined our three unique ligands in the molecule, one then considers the bonding modes of the ligands. The axial ^{t}BuNC ligand would engage in σ bonding and would likely engage in approximately cylindrical π-bonding as it coordinates linearly. The axial amine would be presumed to engage in σ bonding only. Finally, the equatorial amides are presumed σ donors and likely asymmetric π-donors, π-bonding out of the C–N–C plane. In all, that leaves us with a total of five ligand-field parameters: $e_{\sigma}(^{t}\text{BuNC})$, $e_{\pi}(^{t}\text{BuNC})$, $e_{\sigma}(N_{ax})$, $e_{\sigma}(N_{eq})$, $e_{\pi y}(N_{eq})$, where N_{ax} and N_{eq} are labels for the axial amine and equatorial amides respectively. Where possible, it is desirable to try and reduce the degree of parameterisation further. In the crystal structure, the ^{t}BuNC and N_{ax} coordinating atoms are approximately trans to one another

forming an angle of 177° between the two. As a result, their σ bonding will be correlated (due to holohedral symmetry) and it is possible to set $e_\sigma(^t\text{BuNC}) = e_\sigma(N_{ax})$. In total, we are left with four freely adjustable ligand-field parameters.

2.4 Post-diagonalisation methods

The preceding sections have detailed the construction of an effective Hamiltonian, constructed from ligand-field parameters, which when solved produce a set of eigenfunctions. The solutions produce a set of energy levels (eigenvalues) and their linear combination of angular momentum coupling coefficients (eigenvectors). These eigenfunctions can be used to compute magnetic and spectroscopic properties. This section deals with the linear algebra and equations required to compute these quantities and how one can extract other information such as spin, configurational mixing, and irreducible representation projections.

2.4.1 Projection methods

2.4.1.1 Spin projection

The eigenvectors obtained from the diagonalisation of the full effective Hamiltonian can be characterised by their spin projection. In the absence of spin-orbit coupling, the spin quantum number is a *good* quantum number and can be used to distinguish “spin-allowed” and “spin-forbidden” transitions. For transition metals, even with spin-orbit coupling, the spin quantum number is typically well behaved, especially for 1st row transition metals which have spin-orbit coupling constants < 830 cm^{-1}. However, one can quantify the degree of spin contribution to an electronic state via a projection operator, $\hat{P}(S)$ where S is the spin quantum number. The projection operator acting on a ket with a defined spin is:

$$\hat{P}(S')\left|LSJM_J\right\rangle = \delta_{S'S} \tag{2.63}$$

Applying the projection operator to an eigenvector and taking the scalar product returns the spin-projection,

$$Q^S = \left\langle \Psi \middle| \hat{P}(S)\Psi \right\rangle . \tag{2.64}$$

Where Ψ is the eigenvector. Since the eigenvector is orthonormal, the resulting projection will be between 0 and 1 (inclusive). Although the spin-quantum number is well behaved for 1st row

transition metals, two electronic states close in energy can mix significantly and the assignment as a spin singlet, or triplet, etc, is meaningless.

2.4.1.2 Configuration projection

Implicit in the calculation of the matrix elements between free-ion quantum numbers is the mixing of electronic configurations in the five calculated "mixed" d orbitals. However, projection of these mixing quantities is not trivial and cannot be "back calculated" out of the eigenvectors easily. Those calculations would proceed via the transformation of the eigenvectors from the $\left|L,S,J,M_J\right\rangle$ basis to a linear combination of slater determinants $\left|m_{l1},...,m_{li}\right|$ that are built from the free-ion d-orbitals, not the final mixed d orbitals from the ligand-field diagonalisation. This task is not easy, especially with the construction of the slater determinant couplings using recursion, which becomes increasingly complicated for d^n systems where n > 2. Instead, a different approach was used to construct the configuration projection.

The developed approach produces eigenvectors from the diagonalisation of the many-electron effective Hamiltonian constructed using just the ligand-field potential, where contributions from interelectronic repulsion and spin-orbit coupling are ignored. These eigenfunctions will be labelled as $\Psi(\mathrm{LF})$. Because the ligand-field splitting is a one-electron calculation, there should be a one-to-one mapping between the relative energies of $\Psi(\mathrm{LF})$ and a linear combination of the relative energies of the five d orbitals.

For example, in a spin singlet (S=0) d^2 system, there is a possible configuration where d-orbital 1 is doubly occupied and d-orbital 2 is vacant. Likewise, there is another possible electronic configuration where both d orbitals are singly occupied. Therefore, the eigenfunction of $\Psi(\mathrm{LF})$ associated with the former electronic configuration (the Aufbau ground state) will be the lowest energy spin singlet eigenfunction. Likewise, the eigenfunction of $\Psi(\mathrm{LF})$ which has a corresponding relative energy of $E(orbital\ 2)-E(orbital\ 1)$, representing the one-electron transition from orbital 1 to orbital 2, is assigned to the latter eigenfunction. A list of the possible spatial orbital occupation for each d^n configuration is given in appendix 6.2. Worked examples of this mapping from the d-orbital splitting to the eigenfunctions of $\Psi(\mathrm{LF})$ are given in sections 4.1.3.2 and 4.2.4.3.1. Note that in the event of degeneracies between one-electron orbitals, their separate occupations cannot be distinguished.

It is recognised that the final eigenfunctions [labelled as $\Psi(\text{full})$] obtained by diagonalisation under the effects of the ligand field, interelectronic repulsion, and spin-orbit coupling are just a linear combination of the $\Psi(\text{LF})$ eigenfunctions, such that:

$$\Psi(\text{full}) = \sum_{i}^{N} c_i \Psi(\text{LF}) \tag{2.65}$$

where i spans the size of the number of unique spatial electronic configurations (appendix 6.2) and c_i is the coefficient. Therefore, one can solve for the linear combination of coefficients using linear algebra:

$$\begin{aligned} \mathbf{\Psi}(\text{LF})\mathbf{c} &= \Psi(\text{full}) \\ \mathbf{c} &= \mathbf{\Psi}(\text{LF})^{-1}\Psi(\text{full}) \end{aligned} \tag{2.66}$$

Where $\mathbf{\Psi}(\text{LF})$ are the columns of the $\Psi(\text{LF})$ eigenvectors and $\mathbf{c}$ is the column of linear coefficients.

2.4.2 Magnetism

2.4.2.1 EPR g-factors

Calculation of EPR g-factors can be carried out by the construction of a second-order $\mathbf{g}^2$ tensor over the cartesian basis, an element of which is given by[78]

$$g_{\alpha\beta}^2 = \frac{\sum_i \sum_j \langle i|\mu_\alpha|j\rangle\langle j|\mu_\beta|i\rangle}{\sum_{M_S=-S}^{S} M_S^2} \tag{2.67}$$

where $\alpha,\beta = x,y,z$ and i and j are the indices of the eigenfunctions. The summation in the denominator extends over the effective spin degeneracy of the level. An effective M_s projection of $S=^1/_2$ is used for calculations over a Kramer's doublet, where the calculated g-factors are "effective" g-factors. Otherwise, the sum over S adopts the value of the spin quantum number of the level and the summation over eigenfunctions is extended to the full non-relativistic degeneracy. Solving the tensor gives the three principal g^2 values and their orientations. The principal g-factors extracted from experimental simulations are simply the square roots of the eigenvalues.

2.4.2.2 Paramagnetic susceptibilities

Paramagnetic susceptibilities χ, are a special case of magnetic susceptibility that measure the response of an object to the application of a magnetic field. In other words, paramagnetic susceptibilities measure whether a material is repelled or attracted to an external magnetic field. Paramagnetic materials, which require unpaired electrons, are repelled by an external magnetic field ($\chi > 0$).

The paramagnetic susceptibilities can be computed through the construction of a second rank tensor, which includes a first-order and second-order Zeeman term. The tensor is computed and diagonalised for *each* temperature. An element of the tensor can be computed using the Van Vleck equation[78]

$$\chi_{\alpha\beta} = \sum_i Z_i \left(\frac{\sum_j \langle i|\mu_\alpha|j\rangle\langle j|\mu_\beta|i\rangle}{k_B T} + \frac{\sum_{k\neq i} \langle i|\mu_\alpha|k\rangle\langle k|\mu_\beta|i\rangle + \langle i|\mu_\alpha|k\rangle\langle k|\mu_\beta|i\rangle}{E_k - E_i} \right) \tag{2.68}$$

where $\alpha,\beta = x,y,z$; the i and j indices map over eigenfunctions that are thermally populated; the k indices extend to all other higher lying eigenfunctions, though one can truncate the summation for computational reasons; k_B is the Boltzmann constant; E_i is the i^{th} eigenvalue in the absence of any Zeeman perturbation; and $Z_i = \exp(-E_i/k_B T) \;/\; \sum_k \exp(-E_k/k_B T)$.

2.4.2.3 Mapping eigenvectors on to the magnetic moment operators

Equations (2.67) and (2.68) in this section use matrix elements of the magnetic moment operators acting between two eigenfunctions. No mention has been made thus far of how these quantities are computed. Recall that the matrix elements defined in equation (2.51) are acting between the basis set functions *not* eigenvectors. For our purposes, one may evaluate the required matrix elements using the relationship:

$$\langle i|\mu_\alpha|j\rangle = \sum_a \sum_b c_{ia}^* c_{jb} \left(k_\alpha \langle \Phi_a|L_\alpha|\Phi_b\rangle + g_e \langle \Phi_a|S_\alpha|\Phi_b\rangle \right) \tag{2.69}$$

where i and j are the usual eigenfunctions of the effective Hamiltonian; a and b are indices over the basis set; c_i and c_j are the eigenvector coefficients; Φ are the basis functions defined by the L, S, J, and M_J quantum numbers; L_α and S_α are the orbital and spin angular momentum operators defined by equations (2.50); and $\alpha = x,y,z$.

2.4.3 Spectroscopic intensities

Transition-metal ions give rise to a range of interesting electronic spectra. The phenomenon of optical activity is concerned with the interaction of the external and perpendicular electric and magnetic fields E and H of the radiating light with the electric ($\mathbf{m}$) and magnetic ($\boldsymbol{\mu}$) dipole moments of the molecule. Since the wavelengths that are used in optical spectroscopy are typically much larger than the molecule (or at least the metal ion whose absorptions we are modelling) then we can assume a uniform magnetic and electric field from the radiating light. From Schellman's perturbative approach, three contributions arise that contribute to the total interaction Hamiltonian between the radiating light and the molecule[79]

$$\left(V_{\pm}^{I\to J}\right)^2 = {E_0}^2 \frac{\left(\mathbf{m}^{I\to J}\right)^2}{3} + {H_0}^2 \frac{\left(\boldsymbol{\mu}^{I\to J}\right)^2}{3} \pm \frac{2}{3} E_0 H_0 \left(\mathbf{m}^{I\to J} \bullet \boldsymbol{\mu}^{I\to J}\right) \tag{2.70}$$

where the three components refer to the electric dipole moment strength, the magnetic dipole moment strength, and the rotary strength; V represents the interaction Hamiltonian between the molecule and the radiation; and E_0 term and H_0 terms are the amplitudes of the radiating electric field. These interactions are for a transition between two levels I and J, where the former is lower in energy, comprised of the set of states i and j. The magnetic dipole moment is readily evaluated, and its expression is found in section 2.2.4.5. However, the main contribution to spectroscopic intensity is the electric dipole moment, the matrix element of which are formally forbidden between pure angular d states due to the Laporte selection rule. The computation of spectroscopic intensities is concerned with the evaluation of non-zero values of the electric dipole moment operator acting between formally same parity ligand-field states.

Computing electric dipole moments (and spectroscopic intensities) within LFT for transition metals has not received as much attention as it has for the f block[80]. *Duer et al*. and *Brown et al*. have reviewed the developments in the field and have developed their own methodology for parameterising spectroscopic intensities in a similar fashion to e-values in the ligand-field model.[81,82] They have applied both the static and dynamic (vibronic) contributions of their model to several systems with success. Another method developed by *Whittaker et al*., based on the work of *Gerstman* and *Brill*, involves extending the basis set to include the angular states of the metal p (and f) coupling to the d-orbital manifold.[83,84] The explicit d-p and d-f matrix elements are computed and solved for the extended Hamiltonian. In principle, this latter method is not *truly* a ligand-field method, given the extension of the minimal basis set from just d-states. However, this method has only been applied to the computation of absorption and magnetic circular dichroism spectra of d^9 cupric systems.

This subsection proceeds with an expression for the explicit computation of the magnetic dipole moment transition tensor. Then the origin of the electric dipole moment operator, acting within a same parity basis, is reviewed along with the expression for their evaluation from the eigenfunctions of the effective Hamiltonian. The P_λ and F_λ parameters that are used to compute electric dipole moment operators are then discussed in terms of their properties and physical meaning, Finally, expressions for the absorption, CD and MCD intensities are given. Only a "static" model of intensities is considered; contributions that arise from bending and vibrational modes are ignored.

2.4.3.1 Electric dipole moment operator

The strength of a transition between electronic states requires the evaluation of the electric transition dipole moment operator. The electric dipole moment acting between electronic states of the same parity is formally forbidden according to the Laporte selection rule. Recalling that the electric dipole moment operator can be represented as a rank-1 tensor, the transition dipole moment can be evaluated explicitly for an electric dipole transition between two Russell Saunders states using the Wigner-Eckart theorem (2.34). The matrix element contains the Clebsch-Gordan coefficient $\langle l0k0|l0\rangle = \langle 2010|20\rangle = 0$. It is this Wigner 3j symbol that enforces the Laporte selection rule.

The evaluation of the electric dipole moment operators m_α ($\alpha = x, y, z$) between many electron states can be written as[81]

$$\langle \Psi_I | m_\alpha | \Psi_J \rangle = \sum_n \sum_k \sum_{q,q'} \sum_{i,j} \sum_{\alpha'} c^n_{kq'\alpha'} R^n_{\alpha'\alpha} D^k_{q'q} a^*_{il} a_{jJ} \langle \Phi_i | Y^k_q | \Phi_j \rangle \tag{2.71}$$

where n is the ligand index, $c^n_{kq'\alpha'}$ is the local multipole expansion coefficient (*vide infra*), $D^k_{q'q}$ is the Wigner rotation matrix for the angles α, β, γ, a is the complex eigenvectors from the diagonalisation of the effective Hamiltonian, and the matrix element $\langle \Phi_i | Y^k_q | \Phi_j \rangle$ refers to the spherical harmonic matrix elements that are used for the construction of the ligand-field contribution to the effective Hamiltonian. The Φ are the free-ion basis functions. The rotation matrix $R^n_{\alpha'\alpha}$, relates the local x, y, and z frames of the ligand to the global cartesian frame, given by[34]

$$R^n(\alpha\beta\gamma) = \begin{pmatrix} c_\alpha c_\beta c_\gamma - s_\alpha s_\gamma & s_\alpha c_\beta c_\gamma + c_\alpha s_\gamma & -s_\beta c_\gamma \\ -c_\alpha c_\beta s_\gamma - s_\alpha c_\gamma & -s_\alpha c_\beta s_\gamma + c_\alpha c_\gamma & s_\beta s_\gamma \\ c_\alpha s_\beta & s_\alpha s_\beta & c_\beta \end{pmatrix} \tag{2.72}$$

where c and s here are cosine and sine functions and the subscript refers to the Euler angle

argument. The rotation matrix is equivalent to the direction cosines of the *local* ligand x, y, and z frames with their vectors belonging to the first, second, and third rows respectively.

The $c^{n}_{kq'\alpha'}$ refer to the multipole expansion representation of the local electric dipole moment operator induced within the region of the potential. In general, these are centred on ligands and represent the electric dipole moment as a charge distribution about the metal-ligand axis. In the next chapter, the parameters that are used to evaluate the local multipole expansion of the electric dipole moment are defined and discussed.

2.4.3.2 The transition dipole moment parameters

The multipole expansion coefficient representation of the transition dipole "field" is defined by P_λ and F_λ parameters (referred to as ${}^{L}t_{\lambda}$ in the literature, L = {P, F, R}).[81] These parameters represent the polarisation of the d-orbital basis for a given metal-ligand bond. Since the Laporte selection rule requires that $\Delta l = \pm 1$, only $l = 1$ or $l = 3$ can contribute to d-d transition intensity.

The P and F contributions to the transition dipole moment from a metal-ligand bond does not imply *physical* mixing of explicit P and F orbitals into the basis. Rather it is recognised that the electric dipole moment of a metal-ligand bond is a complicated function; the polarity and charge distribution of the (anti)bonding orbitals are not known *a priori*. In the same way that the symmetry/angular features of a metal-ligand energetic perturbation can be represented by an angular $l = 2$ spherical harmonic basis, so too can the total electric dipole expansion be represented by $l = 1$ and $l = 3$ angular momentum.

It is possible to represent the charge distribution and polarity of a metal-ligand bond via a linear combination of functions. The form of a wavefunction representing a σ bond Ψ_σ, for example, can be constructed using a linear combination of metal-centred functions as given by[81]

$$\Psi_\sigma = c_s Y^{s}_{\sigma} + c_p Y^{p}_{\sigma} + c_d Y^{d}_{\sigma} + c_f Y^{f}_{\sigma} \tag{2.73}$$

where c are the expansion coefficients and Y are the spherical harmonics. Higher order functions are ignored.

Following the rationalisation put forth by *Brown et al*., Figure 2.12 illustrates the effect that the polarisation of a metal-ligand bond has on the d-orbital basis.[81] On the left hand side, the canonical d_{z^2} orbital is shown. It is centrosymmetric. In the middle of Figure 2.12, an

illustrative metal-ligand ligand function with sp character, is shown above the d_{z^2} orbital. The antibonding d_{z^2} orbital is polarised *away* from the metal-ligand bond via the induction of p polarisation into the d_{z^2} orbital. On the right hand side of Figure 2.12, the same metal-ligand bond is shown with added f polarisation, polarising the metal-ligand bond more towards the ligand. This induces f polarisation into the antibonding d_{z^2} orbital, shifting the d electron density further away from the metal-ligand bond.

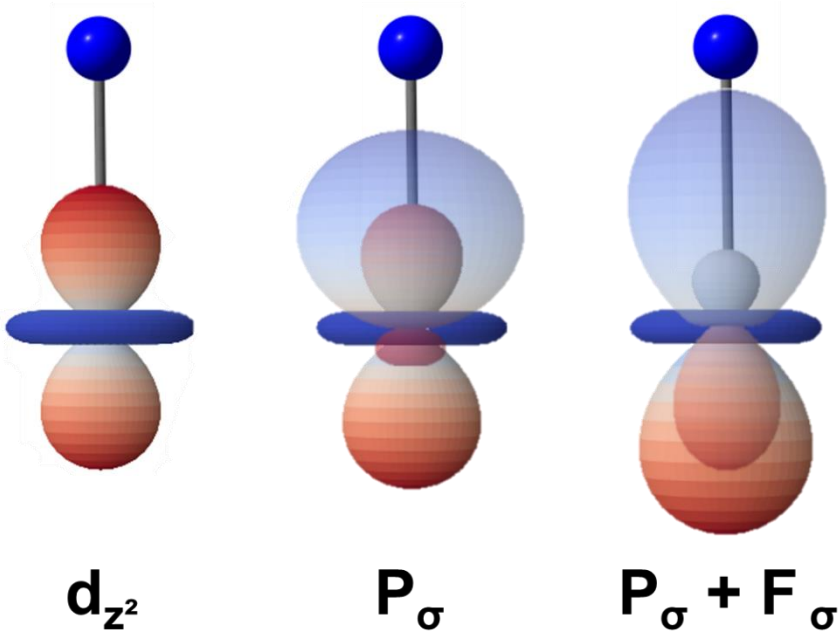

Figure 2.12 The reconstruction of a metal-ligand σ bonding function Ψ_σ using a linear combination of metal-centred spherical harmonics of s, p, and f character and the result polarisation effect on the d_{z^2} orbital.

It is easy to see how variation in the expansion coefficients could effectively recreate both the shape and polarity of the metal-ligand bonding wavefunction.[81] In general, and with all other things being equal, a dipole polarised more towards the ligand than the metal should have a smaller P/F ratio. It is also customary that the signs of P or F parameters should match those of e parameters.[82]

Unless concerned with absolute intensities, the P and F parameters are given relative to one another. It is often useful to set one of these values to some arbitrarily fixed value (e.g. 100) and vary all others. The parameters also differ to conventional e_λ parameters in that two diametrically opposed P (or F) parameters cancel rather than sum. This is because, unlike d orbitals, p and f orbitals are not centrosymmetric. The consequence of this is that highly

symmetric (and homoleptic) systems (a pure octahedral or linear geometry, for example) would generate little to no electric dipole moment intensity. In these systems, it has been shown that electric dipole intensity is gained through vibrational and bending modes, a parametric system which is not considered here.

2.4.3.3 Absorption spectroscopy

The absorbance f of a system between a ground level I and an excited level J, which are comprised of electronic states $\{i\}$ and $\{j\}$ respectively, is given by Piepho and Schatz[85]

$$\frac{f}{E} = \gamma \sum_{i \in I} \sum_{j \in J} \left(\left| \langle i | m_{+1} | j \rangle \right|^2 + \left| \langle i | m_{-1} | j \rangle \right|^2 \right) \tag{2.74}$$

along a given direction, where E is the incident photon energy, γ is a collection of constants, and $m_{\pm 1}$ is the electric transition dipole moment operator in the spherical basis.

For a solution spectrum, which is a collection of randomly orientated molecules, the principal absorbances can be computed by the construction of a second-rank tensor $\mathbf{f}^{I \to J}$ whose elements are given by[81]

$$f_{\alpha\beta}^{I \to J}(\mathbf{m}) = \gamma E \sum_{i \in A} \sum_{j \in B} \langle i | m_\alpha | j \rangle \langle j | m_\beta | i \rangle . \tag{2.75}$$

where α and β belong to the cartesian directions x, y, and z. The subsequent diagonalisation yields the three principal absorbances (oscillator strengths) which are averaged

$$\left(f^{I \to J} \right)_{avg} = E \frac{f_1 + f_2 + f_3}{3} . \tag{2.76}$$

Although equations (2.74) and (2.75) use the electric transition dipole moment operator, the expressions can easily be substituted for the magnetic moment operators in section 2.2.4.5.

2.4.3.4 Circular dichroism

CD is the differential absorption of left and right circularly polarised light and are only observed in chiral molecules. Computing CD spectra requires the computation of the rotary strength, $R^{I \to J}$ which is given by the scalar product of the electric and magnetic dipole moment vectors over the cartesian basis[79,86]

$$R^{I\to J} = \gamma E \sum_{i,j} \mathrm{Im}(\mathbf{m}\bullet\boldsymbol{\mu})$$

$$R^{I\to J} = \gamma E \sum_{i,j}\sum_{\alpha} \mathrm{Im}\left(\langle i|m_\alpha|j\rangle\langle j|\mu_\alpha|i\rangle\right). \tag{2.77}$$

Again, the term is multiplied by the energy of the transition. Being a pseudoscalar, the intensity changes sign under inversion of the molecular frame.

2.4.3.5 Magnetic circular dichroism

The MCD signal is defined as the differential absorption of left and right circularly polarised light in the presence of an external magnetic field.[87,88] For transition metals, the key mechanism for intensity is C-term intensity. C-term intensity dominates at low temperatures due to the differential occupation of the ground state levels, which are energetically split by a magnetic field (Zeeman splitting).

For a transition between a thermally occupied level I and an excited level J, the MCD intensity is given by[85]

$$\frac{\Delta\varepsilon}{E} = \gamma \sum_{i,j} \left(N_i - N_j\right)\left(\left|\langle i|m_{LCP}|j\rangle\right|^2 - \left|\langle i|m_{RCP}|j\rangle\right|^2\right) \tag{2.78}$$

where i labels the initial occupied state and j labels the excited state index. The Boltzmann populations of states i and j are given by N_i and N_j respectively. The operators m_{LCP} and m_{RCP} are the transition dipole moment operators of the left and right circularly polarised light, respectively. E is the transition energy, γ is a collection of constants, and ε is the molar absorption coefficient where $\Delta\varepsilon = \varepsilon_- - \varepsilon_+$.

The perturbative expansion of equation (2.78) reveals three contributing mechanisms in the linear response of a magnetic field[89]

$$\frac{\Delta\varepsilon}{E} = \gamma B\left[-A_1\frac{\partial f(E)}{\partial E} + \left(B_0 + \frac{C_0}{kT}\right)f(E)\right]. \tag{2.79}$$

The A_1, B_0, and C_0 terms describe three different contributions that result from different physical phenomena shown in Figure 2.13.[90] The A_1 term results from the relatively small energetic Zeeman splitting of the excited level J, which causes an incomplete cancellation of MCD intensity resulting in a derivative shaped band. The B_0 term is due to the mixing between a third electronic state, K with either the ground or excited state level, due to the application of the external magnetic field. The B_0 term compounds the “offset” of a band. Finally, the C_0

term is a result of the differential populations of the ground state levels, as given by the Boltzmann distribution.

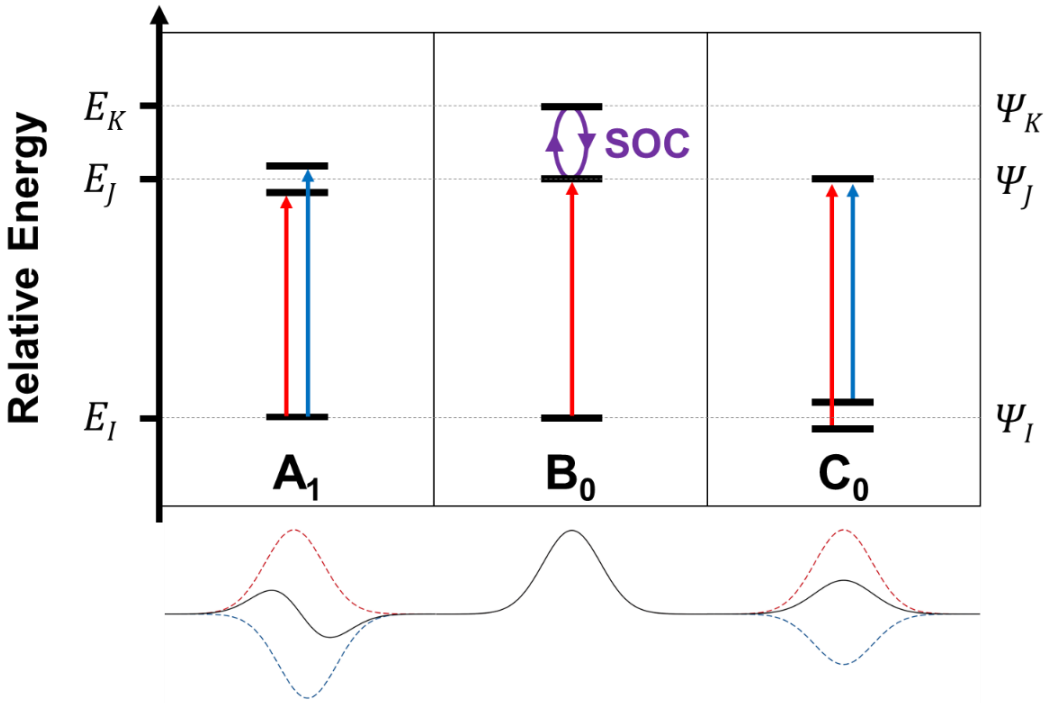

Figure 2.13 The A_1, B_0, and C_0 origins of MCD intensity as given by the perturbative expansion.

Since the transition dipole moment operators of 2.4.3.1 are computed in the coordinate x, y, and z frames, it is convenient to express (2.78) in terms of cartesian operators. Using the conversions $m_{LCP} = m_{-1} = m_x - im_y$ and $m_{RCP} = m_{+1} = m_x + im_y$, the MCD intensity can be expressed as[91]

$$\frac{\Delta\varepsilon}{E} = \gamma \sum_{i,j} \left(N_i - N_j\right) \mathrm{Im}\left(\langle i|m_x|j\rangle\langle j|m_y|i\rangle - \langle i|m_y|j\rangle\langle j|m_x|i\rangle\right) \tag{2.80}$$

where Im is the imaginary part, the real parts of the scalar products are lost upon negation. Equation (2.80) expresses the MCD intensity within the defined cartesian frame. Hence, to get an average spectrum for a series of a randomly orientated molecules the cartesian coordinates of the atoms are rotated about the fixed coordinate frame and the effective Hamiltonian is solved for each iteration over the angular grid. The averaged spectrum is then given by the double integral[91]

$$\left(\frac{\Delta\varepsilon}{E}\right)_{avg} = \int_{\phi=0}^{2\pi} \int_{\theta=0}^{\pi} \left(\frac{\Delta\varepsilon}{E}\right) \sin\theta d\theta d\phi \,. \tag{2.81}$$

3 The Kestrel program

A core aspect of this work is the development of a contemporary ligand-field program aimed at both the specialist and non-specialist alike. A “specialist” refers to someone who is a trained/practicing quantum-chemical researcher or spectroscopist; a “non-specialist” would be a researcher who does not specialise in quantum-chemical methods of spectroscopic analysis. LFT has already proved to be useful to the quantum-chemical community, but its potential is still yet to be exploited by the wider chemical community. A computer program that offers accessible multiconfigurational LFT calculations to the non-specialist, would allow chemists to quickly see how changes in geometry or bonding would alter the physical properties of their molecules. They could perform numerous simulations quickly and receive real time feedback to changes they make to the chemistry of their molecule. For the specialist, the program offers a feature-rich Python module, which can be used as part of custom Python scripts. The computer program developed in this work aims to fulfil this niche.

When designing a computer program that can provide a link between spectroscopy and theory whilst appealing to both the specialist and non-specialist user alike, the design must adhere to some core principles:

1. The program must have a graphical user interface (GUI) and the interface must be intuitive and easy-to-use.
2. The program, where possible, must perform calculations ‘on-the-fly’ in response to a change in its parameters; in doing so, physical properties can be correlated with the electronic structure in real time.
3. The program must be flexible for advanced users who wish to analyse their systems further than the inherent limitations imposed by having a GUI.

Details of the underlying code, algorithms, and application programming interface (API) must be hidden. It cannot be assumed that the user knows how to use command lines, code/script, or make API calls. The role of the GUI is to make the program accessible to anyone. The program that has been designed in accordance with these principles is called Kestrel. Kestrel is formed of two components:

1. **KestrelPy**. The object-orientated module which allows the user to build molecules and run calculations. The module is written in Python (denoted by the suffix “Py”) and accesses Fortran functions and subroutines by fortran-2-python (F2PY).[92–94]

This module allows users to write their own scripts for running ligand-field calculations in a Python environment.

2. **The graphical-user-interface**. The GUI is a stand-alone application that does not require installation and can run out of the box. It is built using the PyQt5 library.[95] This allows the non-specialist to run a range of common calculations and visualise/report their results quickly and easily.

The two components are uncoupled, residing in separate codebases. KestrelPy is a standalone Python library that can be called into any Python script and relies only on a small number of popular scientific libraries. The GUI relies on KestrelPy, but KestrelPy is independent of the GUI.

This chapter is devoted to reviewing the construction of Kestrel, along with a practical guide to ligand-field analysis. The aim is to not to describe the full explicit detail of the program's construction. Doing so is not possible due to the size and complexity of both KestrelPy and the GUI. However, a general overview is provided, and points of interest or importance are discussed. Where necessary snippets of code or scripting are included. First, the Python module KestrelPy is analysed to understand the underlying computational implementation.

3.1 KestrelPy

KestrelPy is a Python module developed in Python and Fortran.[92–94] The package is designed to be the computational core of Kestrel by handling the code that performs the quantum mechanical calculations and data analysis. The module has a minimal number of dependencies. The package requires Python 3.8+ with two common 3rd-party Python packages (NumPy and SciPy) and the compiled Fortran dynamic library housing the computational and linear algebra routines.[92–94,96] The Fortran library can either be compiled locally or pre-built and shared from a similar machine architecture. KestrelPy, being a Python module (which requires knowledge of Python's object-orientated programming) is not targeted at the non-specialist. However, it is designed to be straight forward to run and allows flexibility; all programmatic objects of the molecule and the results of calculations can be accessed, altered, or used. KestrelPy is best suited for the advanced user who wishes to write their own Python scripts to perform ligand-field calculations.

The module bundles aspects of the ligand-field calculations into Python classes. The input to every calculation is the Molecule class, which stores all the information of the molecule being studied including the ligand field, interelectronic repulsion, and spin-orbit coupling parameters etc. The molecule gets passed to a calculations wrapper which can perform many calculations on the electronic structure, magnetism, and intensities. The results of those calculations are returned in a convenient object, which allow for easy access and extraction of those results.

3.1.1 Framework of the package

KestrelPy consists of multiple submodules. Each of these submodules are responsible for housing classes and functions dedicated to a specific task or theme. These submodules are:

- **data**. Contains the classes that store external data that the program can fit to. The program can fit to 5×5 ligand-field matrices, many-electron transition energies, g^2 tensors, and paramagnetic susceptibilities.
- **energy_barrier**. Contains the functions and routines to compute the rate of Quantum-Tunnelling of Magnetisation and the effective barrier of the reversal of magnetisation for single-ion molecular magnets with Kramer's ions.
- **fitting**. Contains the functions and algorithms for carrying out optimisations and parameter-space searches.
- **fortran**. Contains the Fortran90 source code, compiled libraries, and Pythonic interface to the Fortran code.
- **intensities**. Contains the routines to compute spectroscopic intensities of UV-Vis, CD, and MCD.
- **molecules**. Contains all the classes and routines for constructing and interacting with a molecule and its parameters.
- **orca**. Contains the routines for reading ORCA output files. The results extracted from the ORCA output files are then converted to KestrelPy class objects, such as a 5×5 one-electron ligand-field object, which can be used in optimisation calculations.
- **printing**. This submodule handles the input/output of the program.
- **results**. Contains the result objects, which act as a convenient means to interact with the output of the program, rather than interfacing with the Fortran objects directly.

3.1.2 The Molecule class.

The molecule is stored in the Molecule class. The molecule class has a host of attributes and methods that can be called. Each ligand-field parameter associated with either the metal or the ligands and their coordinating atoms are stored in this class. A schematic overview of the Molecule class and its child classes Metal, Ligands, Calculation and Geometry is presented in Figure 3.1. The Molecule class provides a convenient object to store the parameters of the molecule.

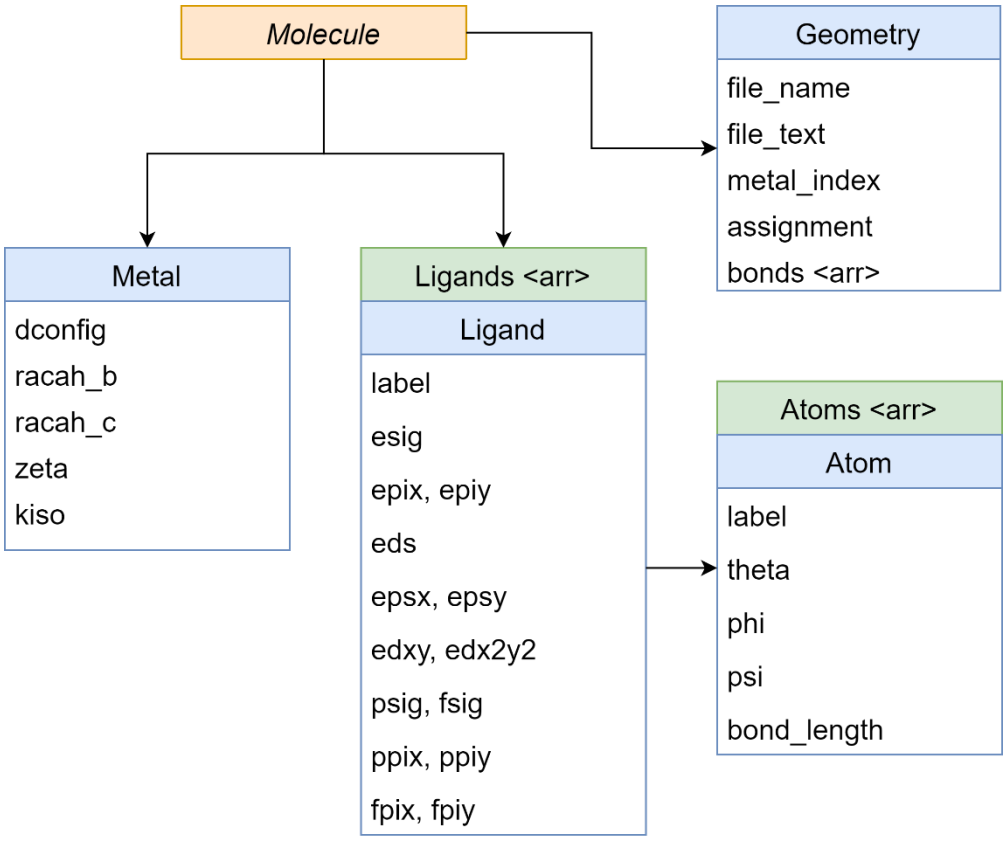

Figure 3.1. Schematic representation of the molecule class object orientated hierarchy and the important class attributes.

3.1.3 Running calculations

KestrelPy contains the code that carries out the actual calculations of the ligand-field model. When the user submits their molecule, either via the GUI or a Python script, KestrelPy handles the parameter extractions and submission of the job. The ligand-field calculations are split into

three steps: 1) construct the ligand-field basis; 2) diagonalise the effective Hamiltonian under contributions from the ligand field, interelectronic repulsion, spin-orbit coupling, and an external magnetic field; and 3) carry out further analysis on the eigenfunctions of the effective Hamiltonian. The third step involves, if desired, computing magnetic properties, spin and configurational projections, and calculating spectroscopic intensities.

Efficient computation is required to make these calculations perform in real-time. Python alone is not quick enough to make use of real-time computation for the evaluation of the relevant integrals and diagonalisation of the effective Hamiltonian matrix. A core part of the KestrelPy module is the use of a custom Fortran 90 library, converted into a Python module using NumPy's Fortran-2-Python (F2PY) package.[93] F2PY provides an interface between Python code and Fortran objects. Fortran is sufficiently fast enough to achieve real-time computation and is supported by a well-established library of linear algebra routines (LAPACK), which are used to optimise the performance of the calculations.[97]

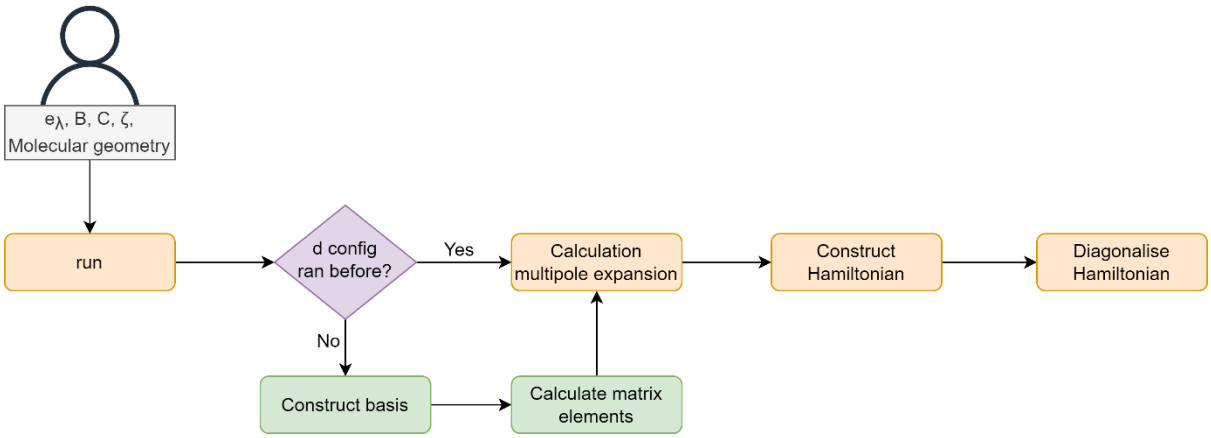

Figure 3.2. The KestrelPy workflow of calculating the eigenfunctions of the effective Hamiltonian

The algorithmic workflow presented in Figure 3.2 shows the steps taken to construct and diagonalise the effective Hamiltonian. When the user passes their molecule (and the relevant parameters: molecular geometry; metal-ligand bonding; interelectronic repulsion; spin-orbit coupling, and the external magnetic field) to the run function, the software first checks if the d^n config has already been run before. If the current d^n config has not been run before, the program constructs the basis set and computes the angular matrix elements under the operators enumerated in chapter 2.2.4. With the basis set specified and the matrix elements computed, the program then calculates the global multipole expansion coefficients.

The program proceeds to construct the final effective Hamiltonian according to equation (2.32) and then diagonalises the Hermitian matrix to get the eigenvalues and eigenvectors of the system.

3.1.3.1 Construction of the basis set

The start of any calculation involves constructing the basis set. If a previous calculation has been run for a given d^n configuration, the basis and matrices are already computed, and this step can be skipped. However, if a new d^n/d^{10-n} configuration is specified then a new basis must be constructed. For the evaluation of the integrals in chapter 2.2.4, the basis must be defined by J, M_J, L, and S quantum numbers. The complete set of Russell-Saunders terms are stored as character arrays, where elements are of the form "2D", for example. The full Russell-Saunders terms, as given by Nielson & Koster, are listed in Table 3.1.[55]

Table 3.1. The list of free-ion Russell-Saunders ^{2S+1}L terms used to specify the basis set. The subscript value is not the conventional J value, but a separate index used to distinguish between sets of terms.

d^n																
1	^2D															
2	^1S	^1D	^1G	^3P	^3F											
3	^2P	$^2D_1$	$^2D_2$	^2F	^2G	^2H	^4P	^4F								
4	$^1S_1$	$^1S_2$	$^1D_1$	$^1D_2$	^1F	$^1G_1$	$^1G_2$	^1I	$^3P_1$	$^3P_2$	^3D	$^3F_1$	$^3F_2$	^3G	^3H	^5D
5	^2S	^2P	$^2D_1$	$^2D_2$	$^2D_3$	$^2F_1$	$^2F_2$	$^2G_1$	$^2G_2$	^2H	^2I	^4P	^4D	^4F	^4G	^6S

From each term one can extrapolate the complete set of J, M_J, L, and S values using the rules for coupling angular momenta detailed in section 2.2.1. The code reads in the Russell-Saunders term as a string, saves a reference to it, and extracts the spin multiplicity and orbital angular momentum. The size of the full basis (accounting for each spin multiplicity) can be calculated from the knowledge of the given d^n configuration. Let n be the number of electrons occupying the five d orbitals, the number of permutations of n electrons occupying 10 sites (spin up and spin down per orbital) is

$$C(10,n) = 10!/n!(10-n)! \tag{3.1}$$

which is the familiar equation for the number of combinations of n objects in r positions.

3.1.3.2 Evaluating matrix elements and solving the effective Hamiltonian

With the basis specified, it is possible to start evaluating the integrals for the various operators appearing in the effective Hamiltonian. The calculation of the integrals requires evaluation of the reduced matrix elements for spherical harmonic, interelectronic repulsion, and spin-orbit coupling operators. These reduced matrix elements are calculatable for the free-ion Russell-Saunders terms as tabulated by Nielson & Koster.[55] There is the opportunity for computational saving here as the reduced matrix elements only depend on the Russell-Saunders term, not the J or M_J quantum numbers. Hence, these values need only be computed once for each possible pair of Russell-Saunders terms. These values are stored in an array called RME of shape (5, NSTATES, NSTATES) where the first index is for specifying the reduced matrix element operator (U^2, U^4, F^2, F^4, and V^{11}) and NSTATES is the number of Russell-Saunders terms appearing in the basis set as given in Table 3.1, e.g. for d^2/d^8, NSTATES=5.

The final effective Hamiltonian matrix to be solved can be as large as 252 x 252 (for d^5, equation (3.1)) involving 63,504 elements alone. These 63,504 elements are each a linear combination of 23 sources (ignoring the spherical Y_0^0 operator), which would result in storing 1,460,592 separate matrix elements before summating. This requires a lot of memory and is inefficient, as not all matrix elements will be non-zero. Due to the power of the Wigner Eckart theorem, it is possible by the application of simple selection rules between angular momentum states to know whether a matrix element is zero or not, as detailed in section 2.2.2. It is therefore efficient to store only non-zero values of the final Hamiltonian matrix rather than storing explicit zero values. An array, called KQMAT, stores the non-zero matrix elements for each operator that appears in the final Hamiltonian along with their corresponding row and column indices. These values are then multiplied by the relevant radial coefficients, for example the multipole expansion coefficients, before being summed together to construct the final Hamiltonian matrix. The final unitary (complex) Hamiltonian matrix is then diagonalised using the ZHEEV function from LAPACK.[97]

3.1.4 Calculation of UV-Vis, CD, and MCD

3.1.4.1 Calculation of electric transition dipole moment integrals

Fast simulations of ligand-field d-d spectra require the efficient evaluation of electron dipole moment integrals between eigenfunctions. As a result, the code which evaluates these integrals is written in Fortran.

When a method requires the electric transition dipole moment integrals, then a get_electric_dipoles method is called, which passes all the required information to the Fortran routines. The program computes the local multipole representations of the transition dipole moments per ligand, which are then rotated using Wigner rotation matrices (as described in section 2.2.3) to construct the global electric transition dipole multipole representation. From there, the program cycles through the valid combinations of k and q values of the spherical harmonic matrix elements used to construct the ligand-field contribution to the effective Hamiltonian (see section 2.2.4.2).

3.1.4.2 Spectrum object

Before discussing the functions that compute the d-d spectra, a quick overview is provided of the Spectrum object which holds the results of these calculations. The Spectrum object is a convenient interface to the results of intensity calculations. The object can be saved and loaded to a file, which means it is unnecessary to carry out the same calculation every time if the user wishes to replot the spectrum. The object also has useful plot_spectrum and plot_bands methods which allow for quickly generating a spectral trace for a given set of x-values and a FWHM value.

3.1.4.3 Calculation of UV-Vis and CD spectra

The calculation of UV-Vis and CD are carried out using KestrelPy functions absorption and circular_dichroism. Spectra at different temperatures can be computed quickly by supplying an array of temperatures. The results are returned as a list of Spectrum objects.

3.1.4.4 Calculations of MCD spectra

MCD calculations are performed using the KestrelPy magnetic_circular_dichroism function. MCD, as given by the name, relies on the application of a magnetic field and hence this must be specified (in units of Tesla).

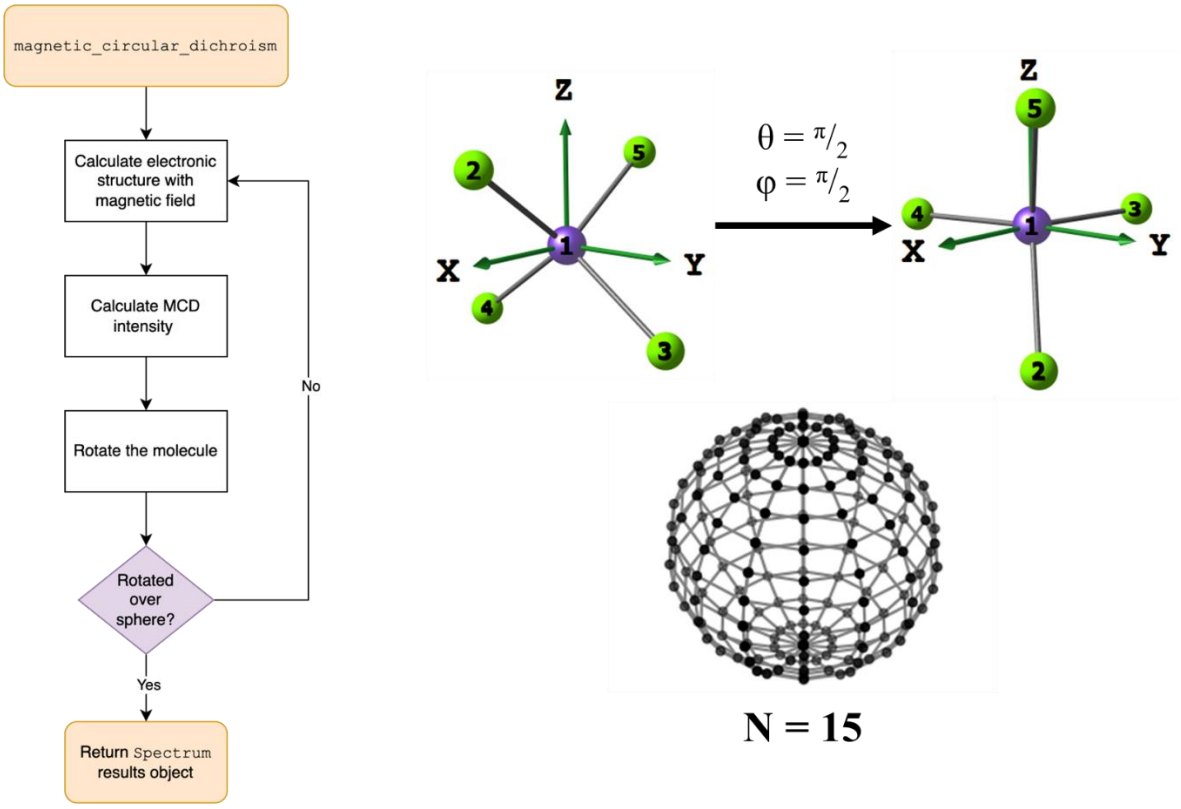

Figure 3.3. The computational workflow for computing the orientationally averaged MCD intensities (left) and an example of a molecular rotation with the full angular grid with a grid size of 15×15 (right) .

Orientationally averaged spectra (in instances with an applied magnetic field) must be computed numerically. This method is the only way to calculate MCD intensity in KestrelPy. This method constructs a spherical angular grid for $0 \leq \theta \leq \pi$ and $0 \leq \varphi \leq 2\pi$ over a defined number of integer steps and rotates the molecule with respect to the global coordinate frame. The angular grid and an example of a molecular rotation are illustrated in Figure 3.3. The rotations of the individual coordinating atoms are performed by using the rotate_atoms method of the molecule class. The spectroscopic intensities are computed for each orientation over the grid and numerically averaged before returning a Spectrum object. The calculations make

use of a computational saving method involving the double integral present in equation (2.81) , which can be approximated using the relationship[89]

$$\int_0^{2\pi}\int_0^{\pi} f(\theta,\varphi)\sin\theta d\theta d\varphi \approx \sum_{\theta,\varphi} f(\theta,\varphi)\sin\theta . \tag{3.2}$$

The calculations are accurate for larger iterations over the angular grid. A grid size of 100 (10 steps over θ and φ each) is typically the minimum grid size to get a good approximation of the MCD spectrum.

Despite best attempts, it was not possible for MCD simulations to be performed quickly enough for real-time applications. This is because the molecule must be rotated over an angular grid and the ligand field evaluated for each orientation. However, the MCD simulation is still quick enough for general use.

3.2 Graphical user interface

The GUI implementation of KestrelPy is constructed using the PyQt5 library and is a fully functional standalone application for Windows 10 and Mac.[95] The program is “frozen” using PyInstaller, which allows for the application to run without any prior set up on the target machine.[98] This makes it portable for sharing and hosting.

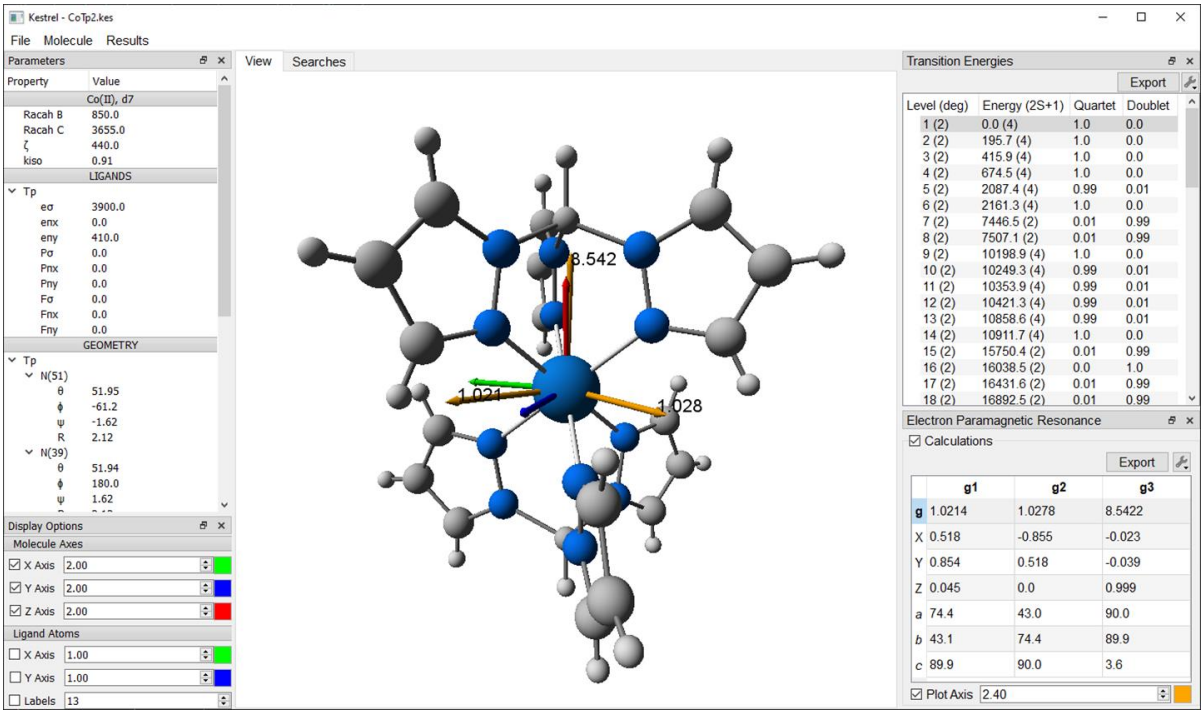

Figure 3.4 An example of the Kestrel window with its molecular visualiser and some of the available dock widgets.

An example of the main window is given in Figure 3.4. In the centre of the window is a tab widget with two tabs. The first tab, labelled as “View”, features a molecular visualiser constructed from PyQtGraph’s fast GlView widget.[99] This molecular visualiser will display the molecular geometry and if requested: the x and y frames of each coordinating atom; the orientations of the g-factor and principal paramagnetic susceptibility frames; the shapes and orientations of the d orbitals; and the ligand-field multipole expansion. The second tab, labelled “Search”, is a host for sub windows which contain the results of parameter scans (section 3.2.4.3) and parameter-space searches (section 3.2.12.5).

The main window also hosts dock windows, which can be docked to the left or the right of the main window. There are four dock widgets shown in Figure 3.4. The two dock windows

on the left-hand side of the window (labelled “Parameters” and “Display Options”) are where the user can alter the input parameters of the ligand-field calculations and display extra information in the molecular visualiser. On the right-hand side of the main window are examples of two dock windows containing some of the results of Kestrel’s ligand-field calculations. The first of these is the “Transition Energies” dock window, which displays the relative energies of spin-allowed and spin-forbidden d-d bands of the molecule. The second dock window contains the calculated g-factors of the ground state KD.

3.2.1 Saving, loading, and starting new files

Kestrel can save and load dedicated save files. These files have a .kes extension and each file hosts a single molecule and a set of ligand-field parameters. The save file also contains GUI specific information. It is also possible to load .mol files, which are the save files of the Molecule object from KestrelPy as mentioned in section 3.1.2.

3.2.2 Setting up a molecule in Kestrel

This section covers the process of importing a molecular geometry and defining the ligands for the ligand-field model. For consistency with the theoretical chapter on identifying ligands in a molecule (section 2.3.4.2) the same molecule $(C_6F_5)_3$trenVCN^{t}Bu will be used here as an example.[77]

3.2.2.1 Import an xyz file

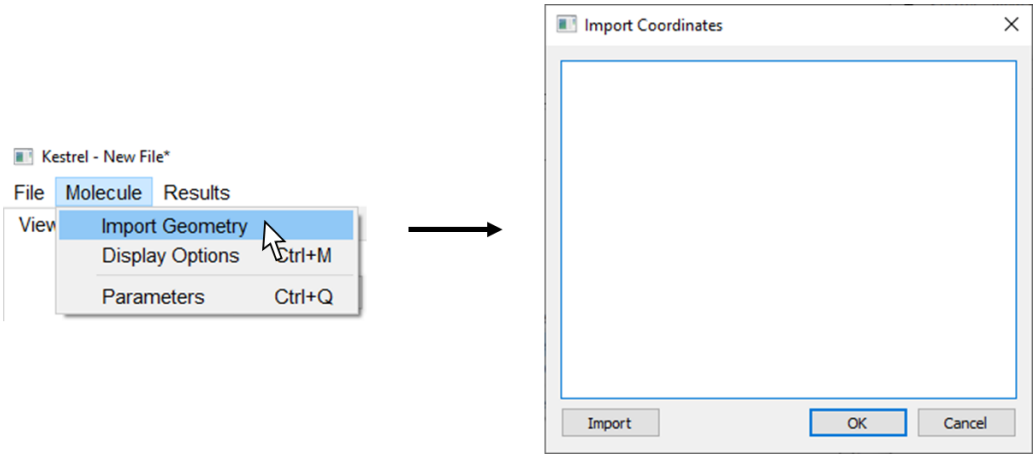

Figure 3.5. The procedure for importing the coordinates of an xyz file.

Every analysis must start with the input of a molecular geometry stored in an xyz file. The user may import a molecular geometry by selecting the “Import Geometry” from the “Molecule” drop down menu, as shown in Figure 3.5. This will open a new window, shown on the right-hand side of Figure 3.5.

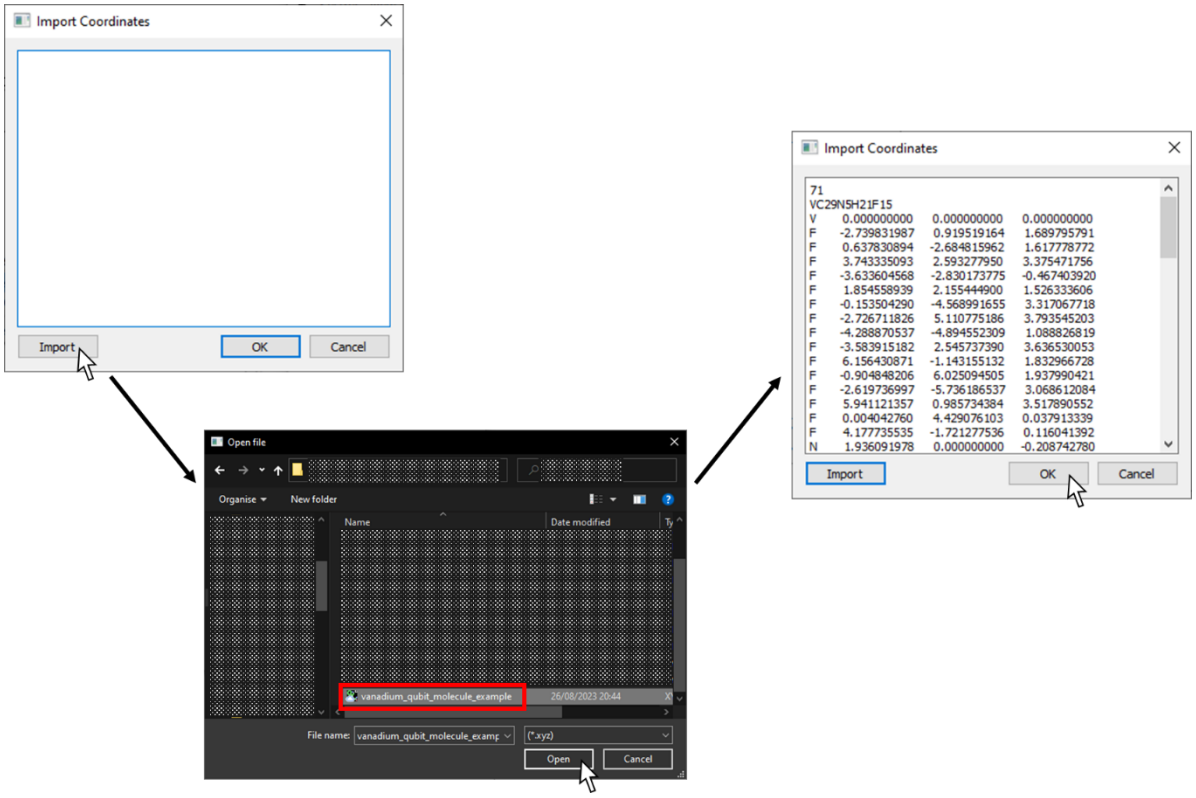

Figure 3.6. The process of importing a molecular geometry stored in an xyz file (CSD: WAFGOD) into Kestrel's GUI.[77]

The user can proceed to import an xyz file by clicking the "Import" button in the bottom left-hand corner, as shown in Figure 3.6. This will prompt the user to select an xyz file. After browsing to the xyz file and selecting it, the contents of the file will be displayed in the window. The user can confirm that the xyz file is the correct one by pressing "OK".

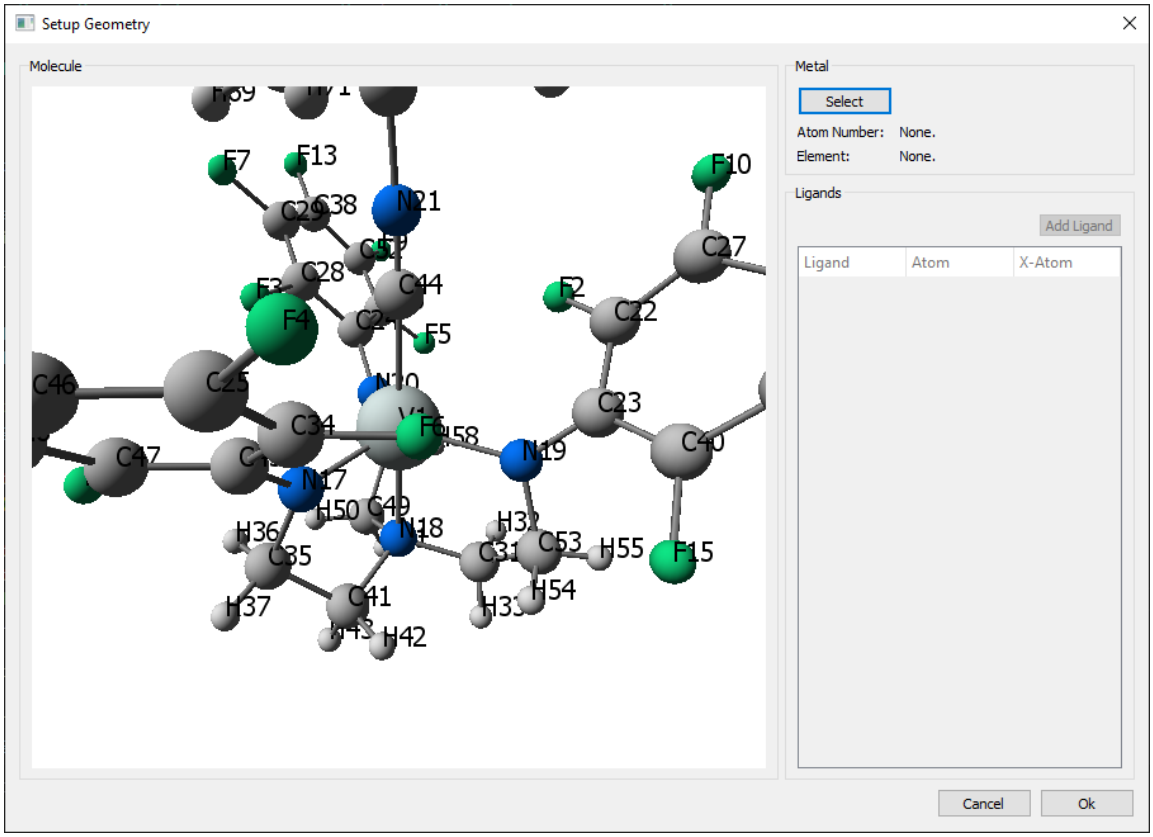

Figure 3.7. The ligand-field parameterisation setup window.

By confirming the xyz file to be read, a new window appears, as shown in Figure 3.7. The window features a rendering of the molecule in the xyz file and labels each atom by its element and index. Note that if one cannot see their molecule, it is likely because the molecule in the xyz file is not located near the origin of the coordinate scheme.

3.2.2.2 Selecting the central metal ion

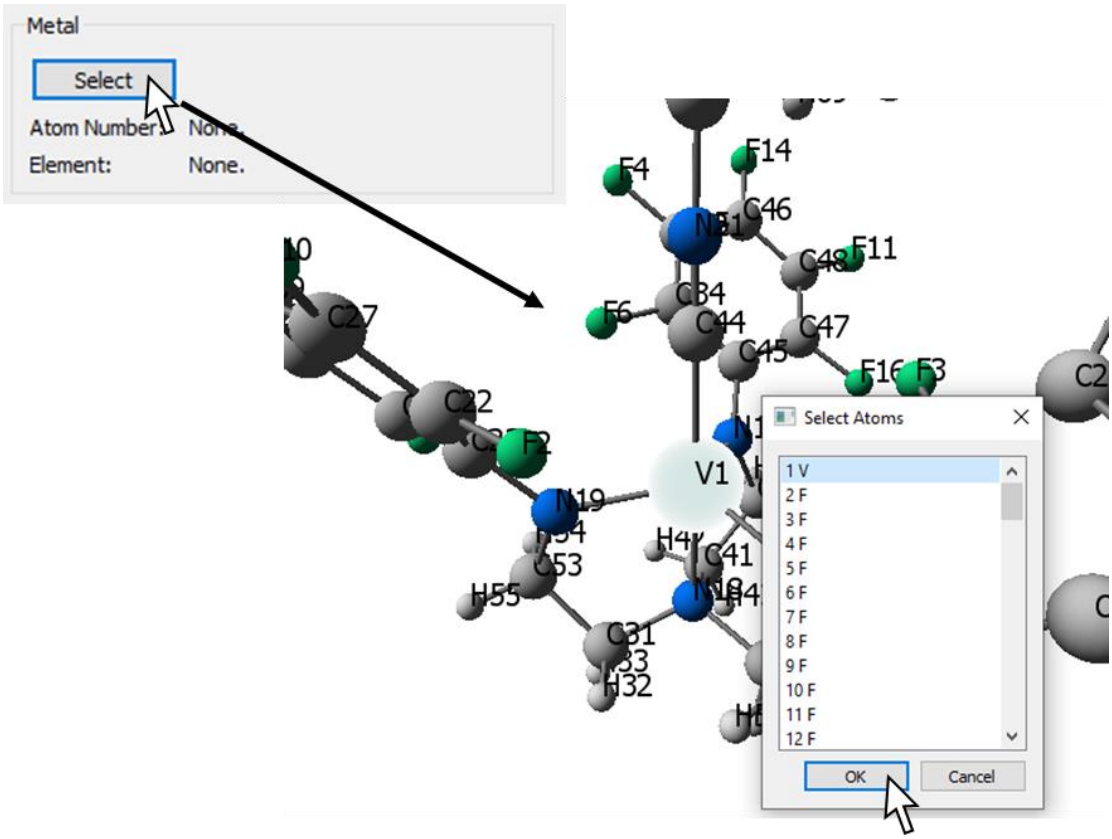

Figure 3.8. Selecting a central metal ion as part of setting up the molecule using Kestrel's GUI.

The first step is to define the central metal ion of the molecule. To do this, the user clicks the "Select" button under the "Metal" section, as shown in Figure 3.8. This will open a new window which allows the user to select the central metal ion from the list of atoms in the xyz file. Selecting an atom will highlight it, as is shown for the vanadium atom in Figure 3.8. Selecting "OK" will assign the central metal ion to the selected atom.

Once the central metal ion is selected, the camera will centre on that atom. The next step is to define the different ligand functional groups in the molecule.

3.2.2.3 Defining the ligands

The final step is to define what ligands exist in the molecule and what coordinating atoms are to be assigned to those ligands. The considerations and methods for choosing a ligand-field

parameterisation scheme are given in chapter 2.3.4 and will not be covered here. However, it is pertinent to remind oneself of the ligand-field parameterisation that was derived for the example vanadium complex (see section 2.3.4.2). Three ligands were identified: the axial *tert*-butyl isocyanide (^{t}BuNC), the axial amine, and the equatorial amides. In the case of the equatorial amides, we will have to orientate the out-of-plane π bonding direction.

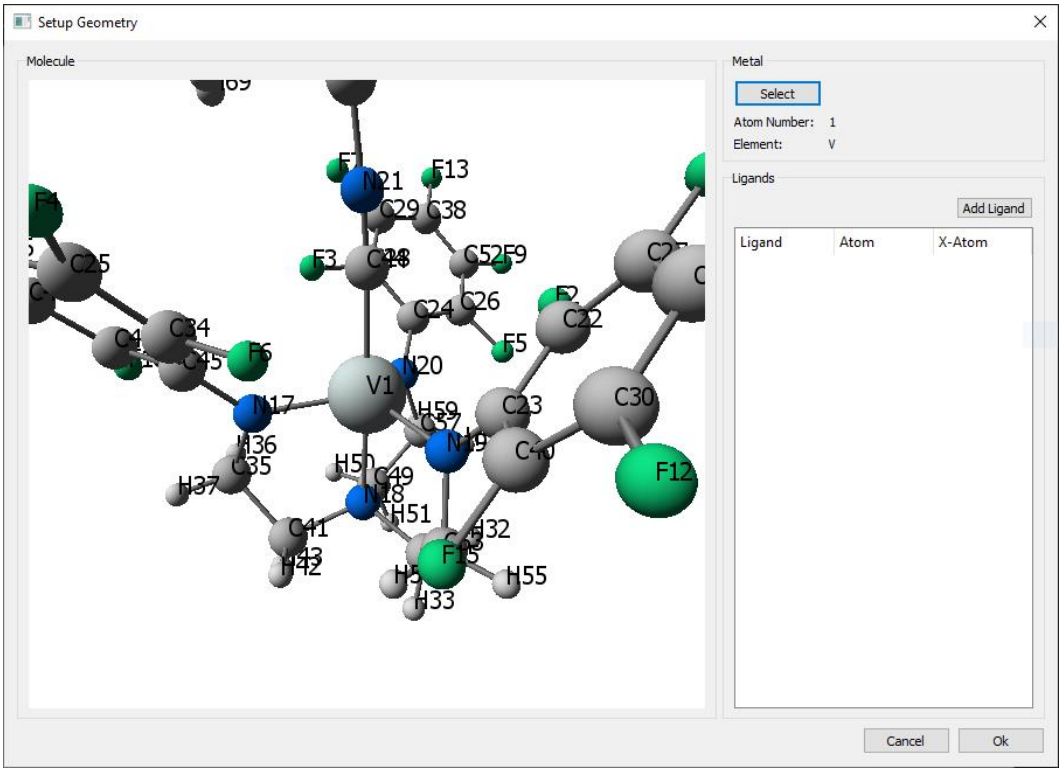

Figure 3.9. The ligand-field parameterisation setup window after successfully selecting a central metal ion in Kestrel's GUI.

Having successfully assigned a central metal ion (for details of which see the previous section, 3.2.2.2) the "Ligands" box will enable, as shown in Figure 3.9. The next step is to add the three ligands which were identified in this molecule (*vide supra*).

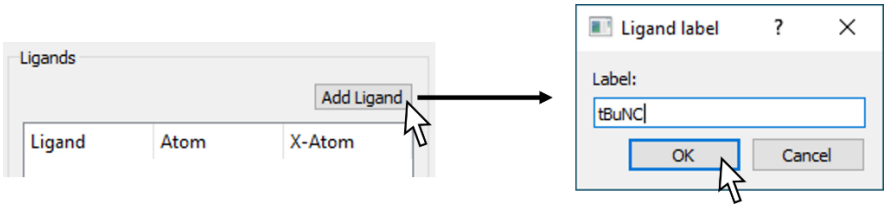

Figure 3.10. The process of adding a ligand by assigning the ligand a label.

To add a ligand, the user selects the “Add Ligand” button. This will prompt the user to select a ligand label, as shown in Figure 3.10. Once the user has chosen a sensible label, they can confirm their choice by selecting “OK”.

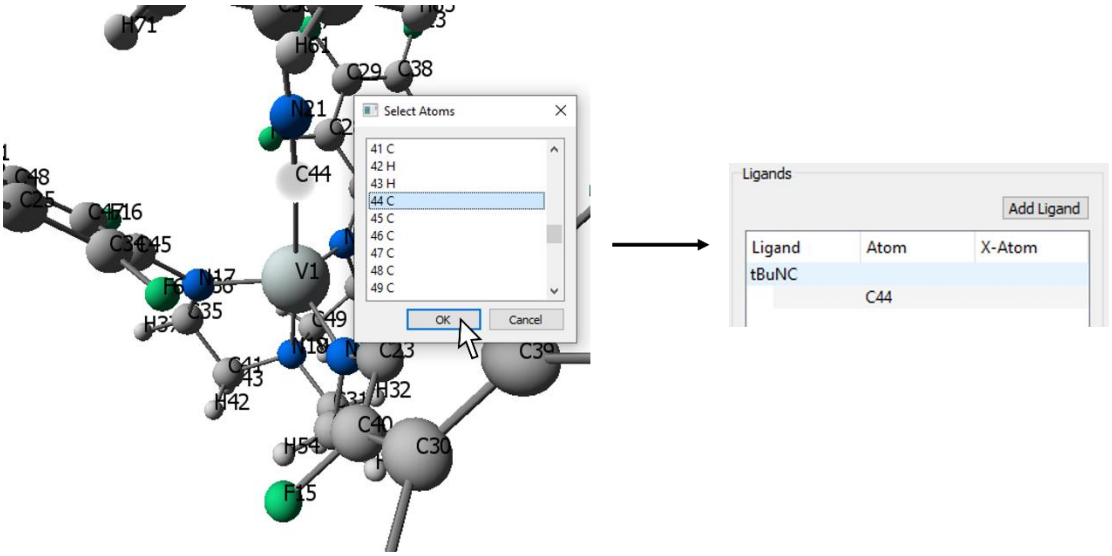

Figure 3.11. The process of assigning a coordinating atom to a ligand.

Once the ligand label is submitted, the user is prompted to select the coordinating atoms which belong to that ligand. In this instance, there is only one coordinating atom we wish to assign to the “tBuNC” ligand, which is carbon atom number 44. Selecting this atom from the list, as shown in Figure 3.11, and selecting “OK” will add that atom to the “tBuNC” ligand. If one wishes to remove a selected atom, the user can right-click on the atom and select “Remove”. Likewise, one can also remove the ligand altogether by right-clicking on the ligand label and selecting “Remove Ligand”. Conversely, there is also an option to assign more

atoms to this ligand. This process of adding a ligand label and assigning atoms to that label is repeated to include the axial amine and the three amide ligands.

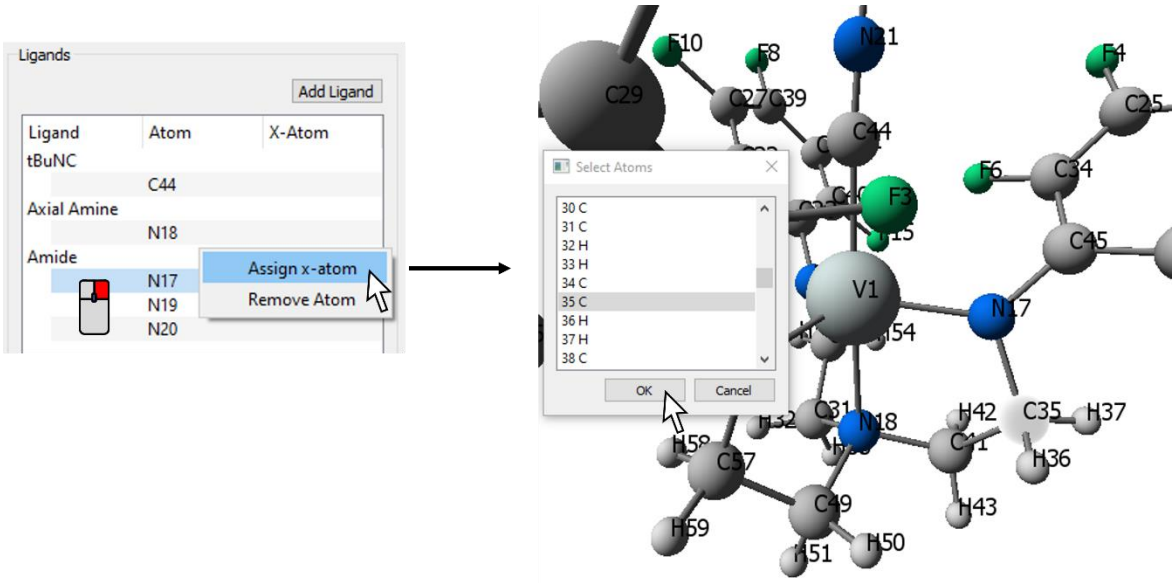

Figure 3.12. Orientating the amide ligand x direction via Kestrel's GUI.

Often, ligands π bond asymmetrically. In the example, the amide ligands π bond perpendicular to the σ bonding framework. To orientate the π bond we can define the local x direction for the amide atoms. The process of orientating the local x direction for the nitrogen atom number 17 is shown in Figure 3.12. By right clicking the atom and selecting "Assign x-atom" we can choose an atom to orientate the local x direction with. In this example, the local x direction is chosen to align with carbon atom 35. This process is repeated for each amide atom.

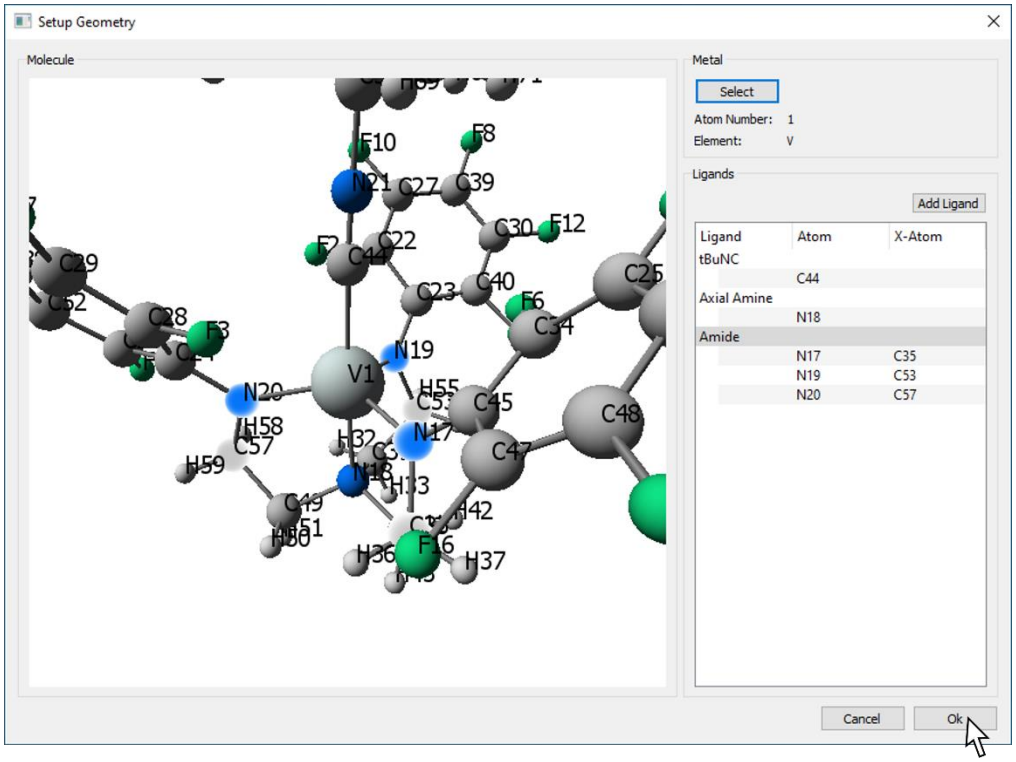

Figure 3.13. The final ligand-field parameterisation setup for the example molecule $(C_6F_5)_3$trenVCN^{t}Bu.

Once the ligand-field parameterisation is setup, as shown in Figure 3.13, the user can select “OK” in the bottom right-hand corner to load the molecular geometry and ligand-field parameterisation into the program.

3.2.3 Molecular visualiser and display options.

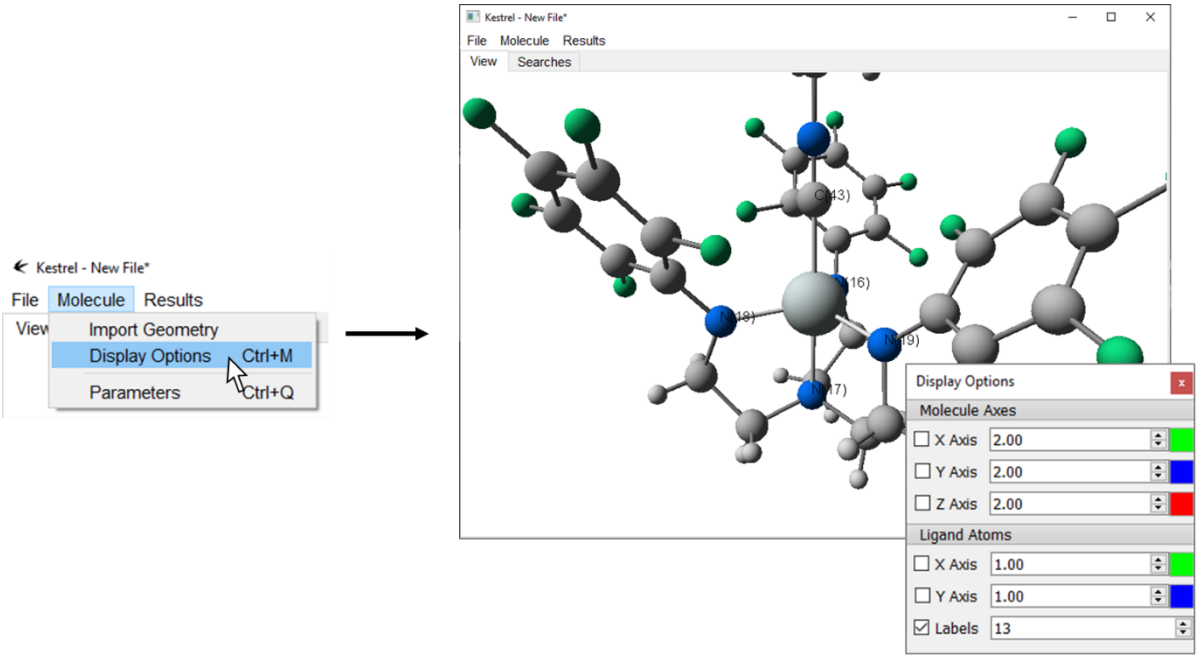

Figure 3.14. The process of opening the display options for the molecular rendering in Kestrel's GUI.

Once the geometry has been imported and the choice of coordinating atoms and ligands has been made, the user is returned to the main window where the imported molecule is rendered, as shown on the right hand side of Figure 3.14. By clicking and dragging around the molecule using the left mouse, the user can rotate freely around the central metal ion. The user can also zoom in and out by scrolling the mouse wheel.

The program also hosts extra display options, as shown in Figure 3.14. These can be opened by selecting "Display Options" from the "Molecule" drop down menu, which will open a new dock window. The dock window contains the options to show/hide, alter the lengths, and change the colours of the molecular coordinate xyz axes and the local ligand x and y directions. The user can show/hide and change the font size of the labels of the coordination atoms.

3.2.4 Parameters

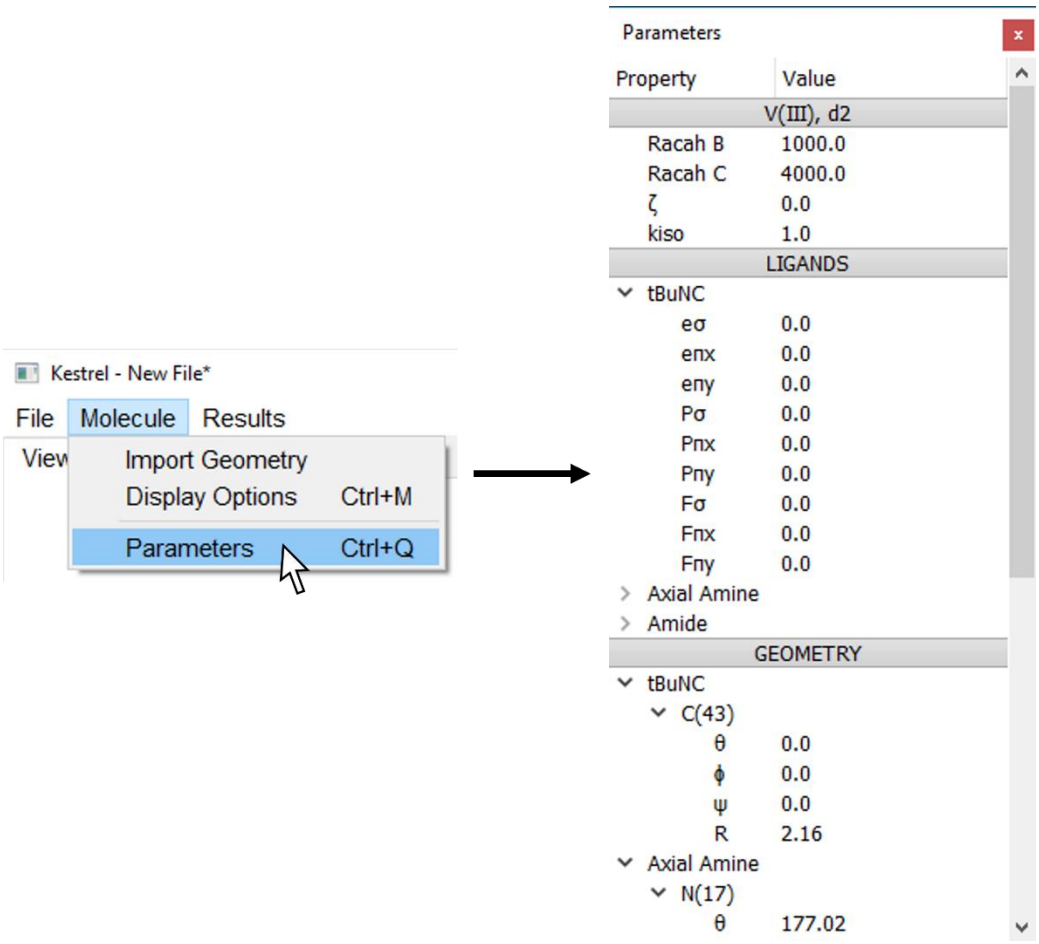

Figure 3.15. The process of opening the parameter dock window in Kestrel's GUI.

The ligand-field parameters can be viewed and changed by selecting "Parameters" from the "Molecule" drop down menu, as shown in Figure 3.15. This will open the parameter dock window. Within the dock window is a tree widget, divided into sections, with the ligand-field parameters and their values. Hovering over a parameter in this widget will provide information about that parameter.

The first of these sections, in Figure 3.15, contains the metal parameters, the header of which displays the element of the central metal ion, its oxidation state, and d^n configuration. In Figure 3.15, the header reads "V(III), d2", despite the program importing the molecular geometry with a "V(II), d3" electronic configuration which is not shown. The d^n electronic configuration can be altered by right clicking on the header and selecting the "Set dconfig" option. The section beneath the header contains all the parameters for defining the interelectronic repulsion, spin-orbit coupling, and angular momentum quenching.

The second section in Figure 3.15 contains the metal-ligand bonding and intensity parameters for each ligand. By right clicking on a ligand label a menu will allow the user to populate the ligand with some illustrative starting e_λ parameters and enable or disable alternative bonding modes (misdirected valence, for example).

The final section in Figure 3.15 holds the geometric θ, φ, ψ, and bond length parameters for each potential. By changing any of these values, the geometry of the potentials are updated in the molecular visualiser. It is possible by right clicking on the header and selecting “Restore Geometry” to reset the spherical polar coordinate angles of the atoms to their original values.

Right clicking on a parameter displays a menu with extra options. One of these options, is the ability to link parameters together by a linear relationship. There is also an option to set a step value so that when you select a parameter you can adjust it by a given amount using the mouse wheel. It is possible to also perform a scan on a parameter between a starting and final value over a number of steps.

3.2.4.1 Initialising starting “guess” parameters

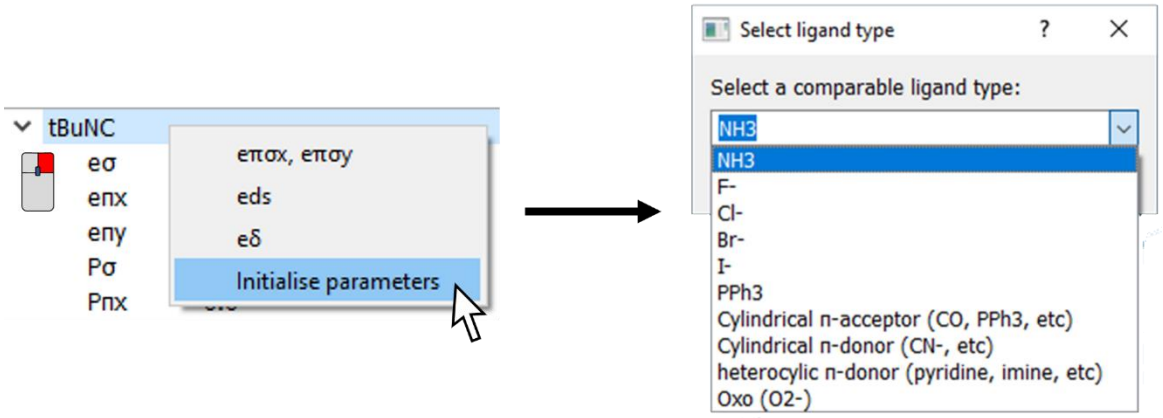

Figure 3.16. The process of generating illustrative starting parameters via Kestrel’s GUI.

Kestrel features the ability to assign illustrative parameter values to a ligand. The process is presented in Figure 3.16. By right clicking on a ligand name and selecting “Initialise parameters”, a window will open with a drop-down widget. From this widget, the user can choose a ligand, or ligand *type*, which best represents their ligand. This will automatically populate the e_λ parameters with fixed *crude* parameter values of a typical magnitude and sign.

Future work could improve this feature by generating starting parameters based on bond length, averaging across values in literature, or utilising machine learning algorithms.

3.2.4.2 Linking parameters together

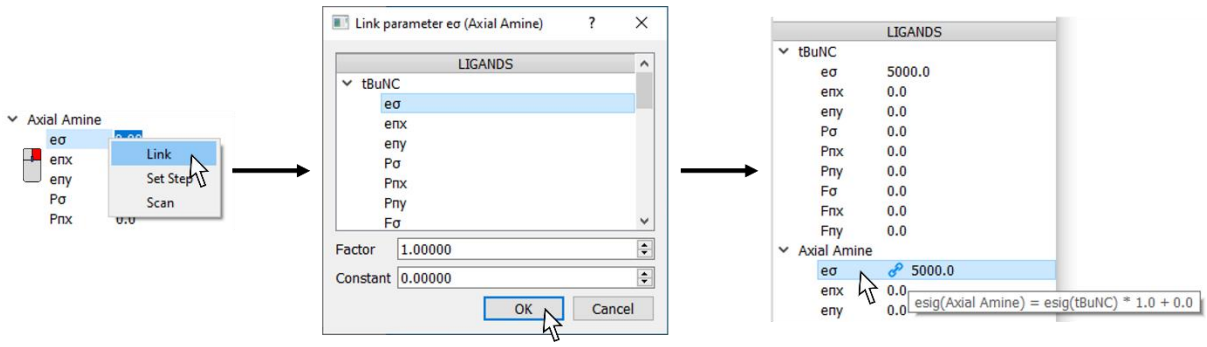

Figure 3.17. The process of linking two ligand e_λ parameters together via Kestrel's GUI.

The GUI is designed to allow the user to easily link the values of any two parameters together. The workflow is presented in Figure 3.17. By right clicking a parameter and selecting the "Link" option, the user is presented with a window of all the parameters which can be linked to. These are parameters of the same type (*vide infra*). Any parameter which would cause a circular link. if linked to, are not included. The user can select a parameter to link to and choose a "factor" and "constant", which define the linking behaviour. The equation used, which links any two parameters together is given by:

$$p_1 = mp_0 + c \tag{3.3}$$

where p_1 is the parameter being linked; p_0 is the parameter which p_1 is linked to; m is the gradient; and c is the constant.

A ligand-field parameter can only be linked to other parameters from the same *type*. To clarify, the parameters associated with ligands (e_λ, P_λ, and F_λ) can only be linked to those parameters either belonging to the same ligand or other ligands. Parameters associated with the metal (Racah B and C, ζ, and k_{iso}) can only be linked together. Likewise, the same rules apply to the parameters controlling the angular geometry about the central metal ion.

3.2.4.3 Scanning parameters

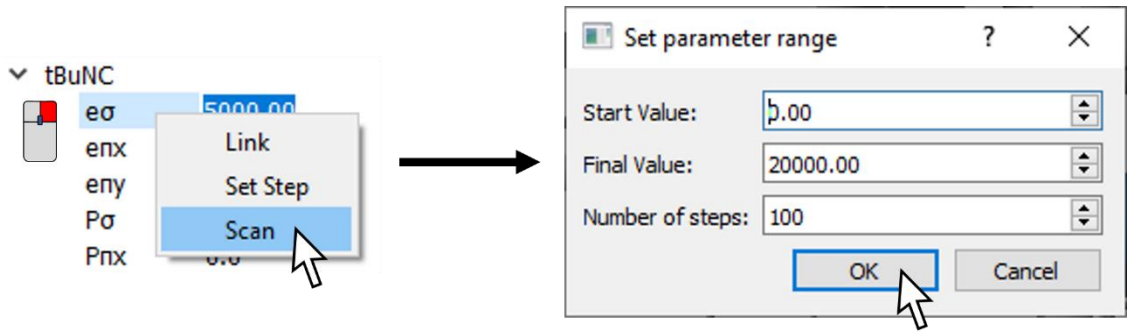

Figure 3.18. The process of scanning a parameter via Kestrel's GUI.

The user can easily perform a parameter "scan", in which a parameter's value is varied from a starting value to a final value. The process for initiating a parameter scan is presented in Figure 3.18. By right clicking a parameter and selecting "Scan", a dialog window will open where the user can submit the starting value and final value of the parameter, and the number of steps taken between the two values.

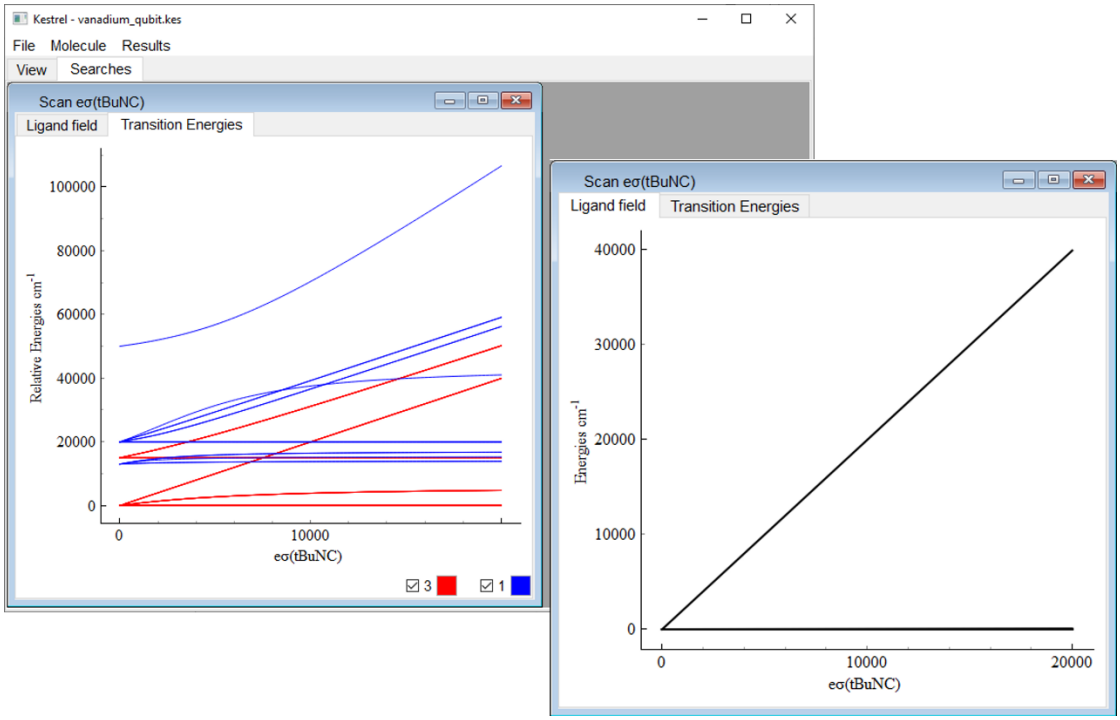

Figure 3.19. The output of a ligand e_σ parameter scan in Kestrel's GUI (left) and the corresponding plot of the d-orbital energies (right).

Once the parameter scan setup in Figure 3.18 has been submitted, the calculation begins. A progress bar will appear showing the user the progress of the scan, which the user can abort. When the parameter scan is completed, the results are displayed in the central window of the GUI, as shown in Figure 3.19. The window features two tabs labelled “Ligand Field” and “Transition Energies”, where each tab contains a plot with the corresponding energy variation of either the d orbitals or the d-d transitions energies respectively.

3.2.5 The ligand-field splitting

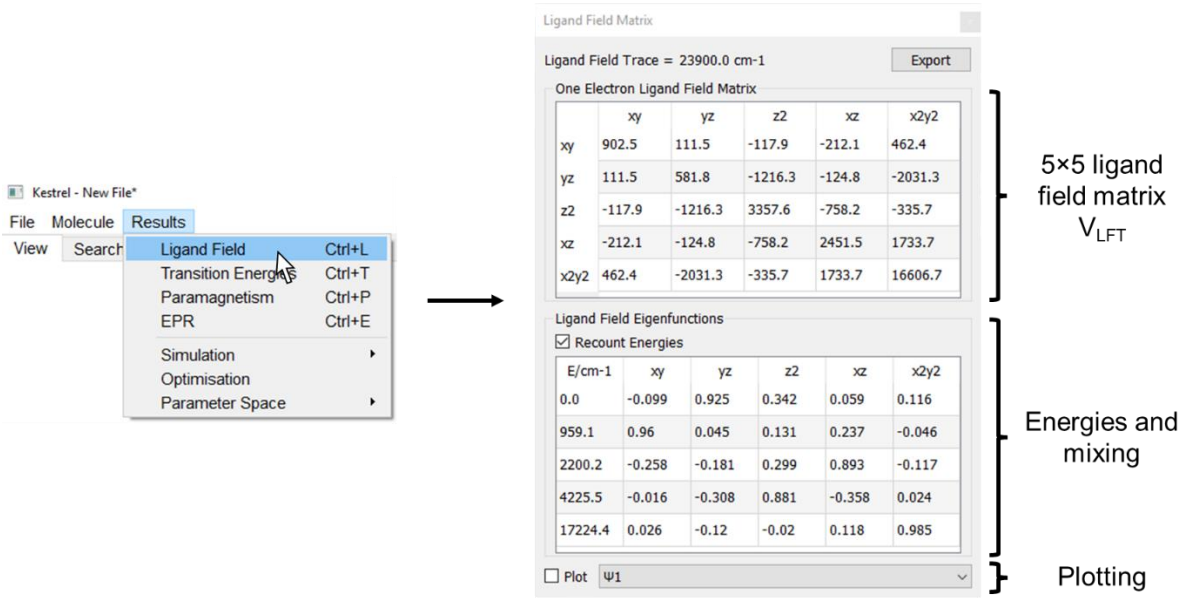

Figure 3.20. The process of opening the ligand-field dock window.

From the “Results” drop down menu at the top of the main window, click “Ligand Field” and a new dock widget appears, as shown in Figure 3.20. This dock widget contains the output of the one-electron ligand-field calculations. The widget contains two tables: the first is the 5×5 one-electron ligand-field matrix; the second is the one-electron ligand-field eigenfunctions.

The one-electron ligand-field eigenfunctions list the energies and linear combination of d orbitals for each final orbital. The first column lists the energies. The remaining columns show the linear combination for the given d orbital in the header. The percentage contribution of a given d orbital to a given final orbital is given by the square of the value multiplied by

100%. As warned in section 2.3.2, this linear combination is a function of the orientation of the molecular xyz frame, as the functions are constructed from the d orbitals orientated in that frame. However, the energies are independent of the choice of frame. Hence the linear combination is only informative if the frame is orientated sensibly.

At the top of the dock window is a value of the ligand-field trace which is simply the sum of the diagonal matrix elements. Finally, at the bottom of the dock widget is the option to render the final mixed d orbitals (and multipole expansion) on top of the molecular rendering. Checking this box will render the object specified in the drop-down combo box.

The final rendered object will appear on top of the rendering of the molecule in the molecular visualiser (see 3.2.3). The objects labelled as “Ψ1”, “Ψ2”, etc are the ligand-field eigenfunctions in order of ascending energy. That is “Ψ1” is the lowest energy d orbital, and so on. The “Multipole Expansion” is the electron charge density of the system. The final shapes and orientation of either the ligand-field eigenfunctions or the multipole expansion do not depend on the orientation of the molecular frame.

3.2.6 Relative energies of many-electron states

The energies of the many-electron states that arise from the different configurational occupations of the final d orbitals under the perturbations of the ligand field, interelectronic repulsion, and spin-orbit coupling can be inspected in the “Transition Energies” dock widget. To open the dock widget, click the “Transition Energies” button from the “Results” drop-down menu at the top of the main window, as shown in Figure 3.21.

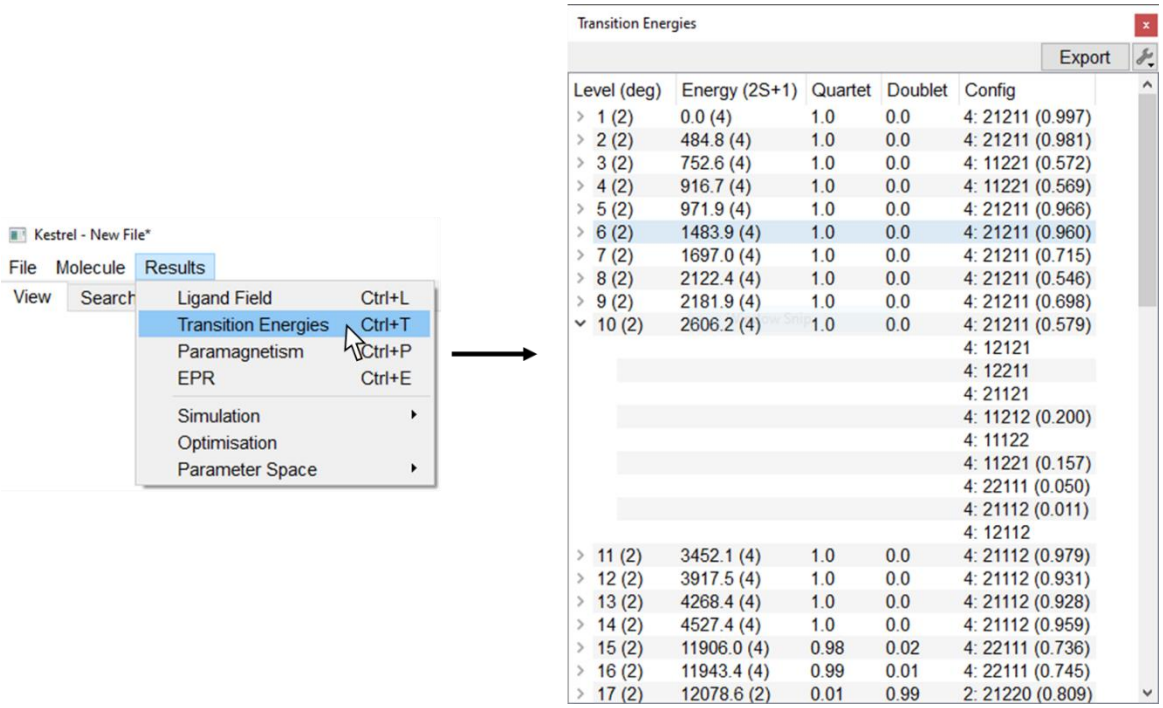

Figure 3.21. The process of opening the transition energies dock widget.

The output window contains a single table of information. The table lists the energies, degeneracies, spin projections, and configurational projections for each level, as shown in Figure 3.21.

The degree of mixing of the spin multiplicities under spin-orbit coupling are show. The spin projections (given by the column labelled “Quartet” and “Doublet”) are to be read as follows: level 1 (at 0 cm^{-1}) is a 100% pure spin quartet; level 15 (at 11906 cm^{-1}) is 98% quartet with 2% doublet spin character mixed in. Using this, one can rationalise the presence or absence of weak spectral features in an experimental UV-Vis spectrum, an example of which is demonstrated in the analysis presented in section 4.1.4.1.

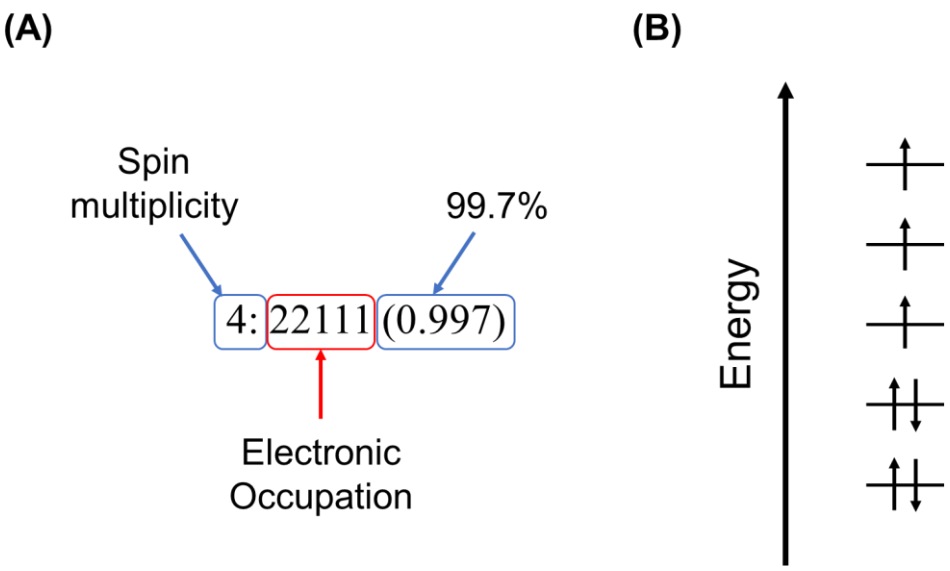

Figure 3.22. The definition of the elements of the configuration projection output (A) and the corresponding 22111 electronic occupation in terms of the five d orbitals in ascending order of energy (B).

The configuration projection shows the electronic occupation of the five d orbitals. The definition of the output is given in Figure 3.22 (A). The first part defines the spin multiplicity of the electronic occupation. The second part is the electronic occupation string, which is to be read in ascending order such that the first occupational number represents the occupation number of the lowest energy d orbital; the second occupation number represents the occupation of the second lowest energy d orbital, and so on. This occupational scheme is shown in Figure 3.22 (B). The third component, contained in brackets, is the ratio contribution of that electronic configuration to that level.

Each row is collapsible. One can see that level 10 in Figure 3.21 is a configurationally mixed level of five configurations (whose ratio parts sum to be > 0.99, this value can be toggled via the spanner button in Figure 3.21). Observation of the expanded row reveals some configurations which do report a ratio in brackets. This is because the electronic configuration is degenerate with the electronic configuration above it and cannot be distinguished. This results from d-orbital degeneracies.

The example output shown in Figure 3.21 is for a d^7 linear complex that is studied in section 4.1.3, with spin-orbit coupling set to 515 cm^{-1}. The complex has a “non-Aufbau” ground state (see section 4.1.3.2 for more detail), where the ground state configuration is not what is expected by filling the d-orbital energies according to the Aufbau principle. For a quartet d^7

complex, the Aufbau ground state would be 22111, but the Kestrel output shows the ground state KD is 99.7% 21211.

3.2.7 EPR g-factors

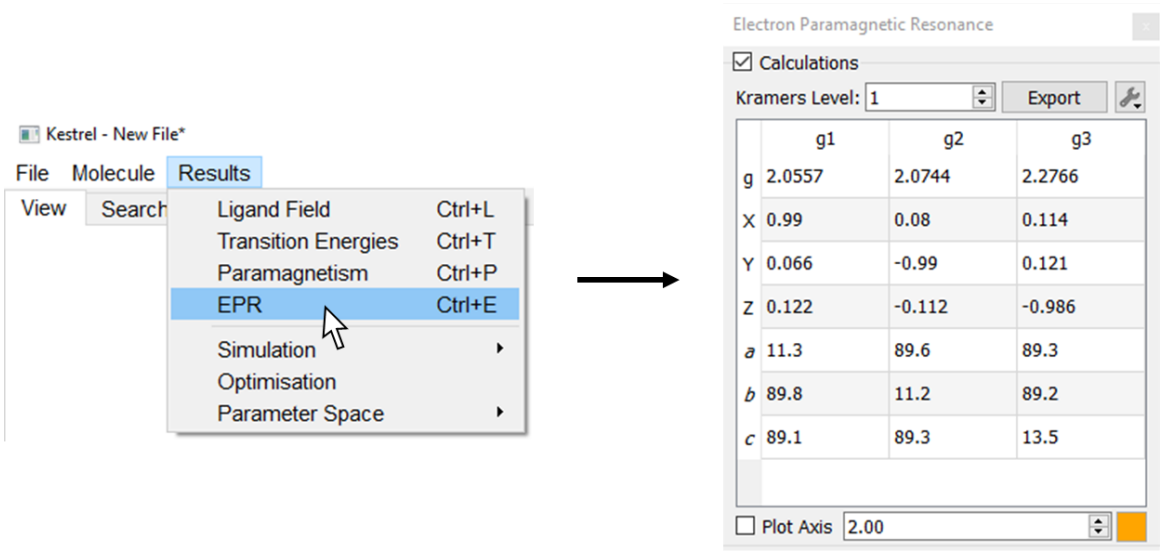

Figure 3.23. The process of opening the EPR results dock window.

Kestrel provides calculations of the EPR g-factors for Kramer's ions. To open the dock window, click the "EPR" button from the "Results" drop-down menu at the top of the main window. A dock window appears containing a check box, as shown in Figure 3.23, which enables/disables the calculation of g-factors for a ground state Kramer's doublet.

By enabling the calculations, a table displays the calculated g-factors. The three columns in Figure 3.23 (right) display the principal g-factors g_1, g_2, and g_3. The first row contains the g-factors. The following three rows display the projection on to the global coordinate frame. The final three rows are the direction cosines from the global coordinate x, y, and z axes. Clicking the spanner button in the top right hand of the dock widget will show options for displaying the value of g_{iso}.

To aid in visualising the orientation of the g-factor frame, the user can overlay the g-factors on the molecular rendering. At the bottom of the dock window is a check box to plot the g-factors. By checking this box, the principal values of g_1, g_2, and g_3 are rendered on top of the molecule. The colour and lengths of the arrows can be varied.

3.2.8 Paramagnetic susceptibilities

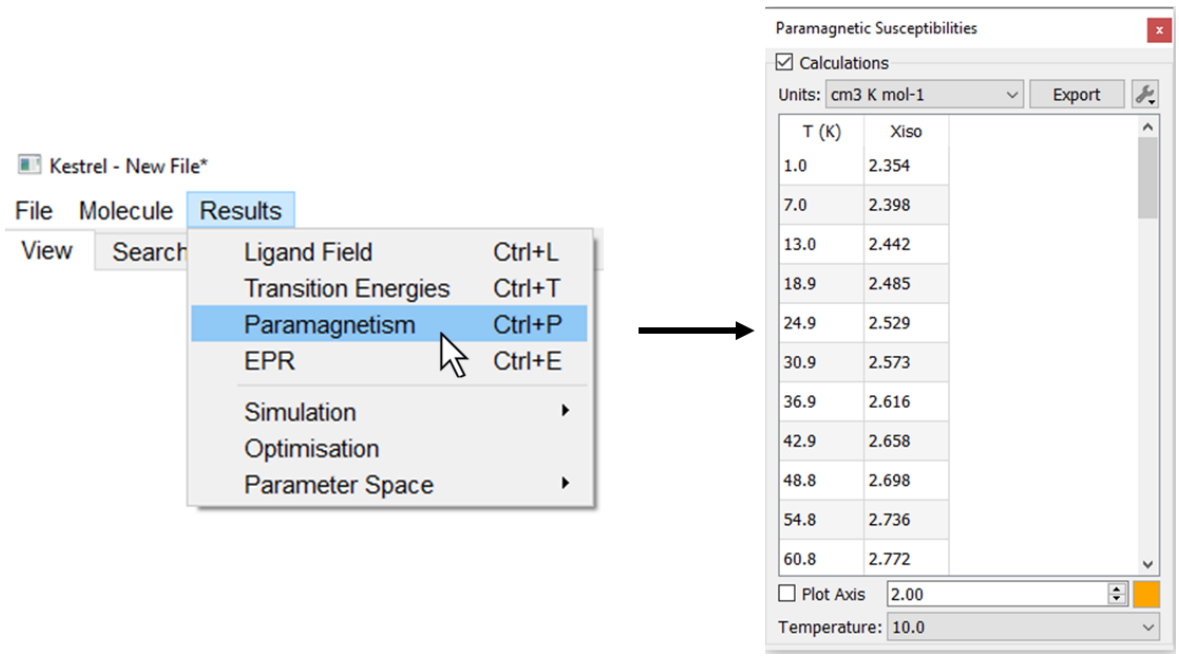

Figure 3.24. The process of opening the paramagnetic susceptibility results window.

To enable the calculation of paramagnetic susceptibilities, open the dock window by clicking the “Paramagnetism” button from the “Results” drop-down menu at the top of the main window, as shown in Figure 3.24. A dock window appears which contains a check box to enable/disable the calculation of paramagnetic susceptibilities.

By enabling the calculations, a table displays the isotropic χT values for different temperatures. The units of the paramagnetic susceptibilities can be changed by selecting a different set of units from the drop-down box in the top left hand corner of the dock window. More options are available by clicking the spanner button in the top right of the dock widget, such as the choice of displaying the principal values and/or the individual elements of the 3x3 tensor. Within that same drop-down menu is the ability to configure the paramagnetic susceptibility calculations by changing the energetic limit of the 1^{st} order and 2^{nd} order Zeeman contribution and the temperatures the susceptibilities are computed for. Note that the user may not request more than 100 temperatures.

To aid in visualising the orientation of the principal paramagnetic susceptibility frame, it is possible to plot the principal values on to the molecule. At the bottom of the dock window is a check box. By enabling this check box, the principal values of χT are rendered on top of the molecule for the temperature displayed in the drop-down box. By changing the

temperature in the drop-down box, it is easy to visualise how the magnetic susceptibility orientation varies. The colour and lengths of the arrows can also be changed.

3.2.9 Plotting the principal and isotropic χT curves

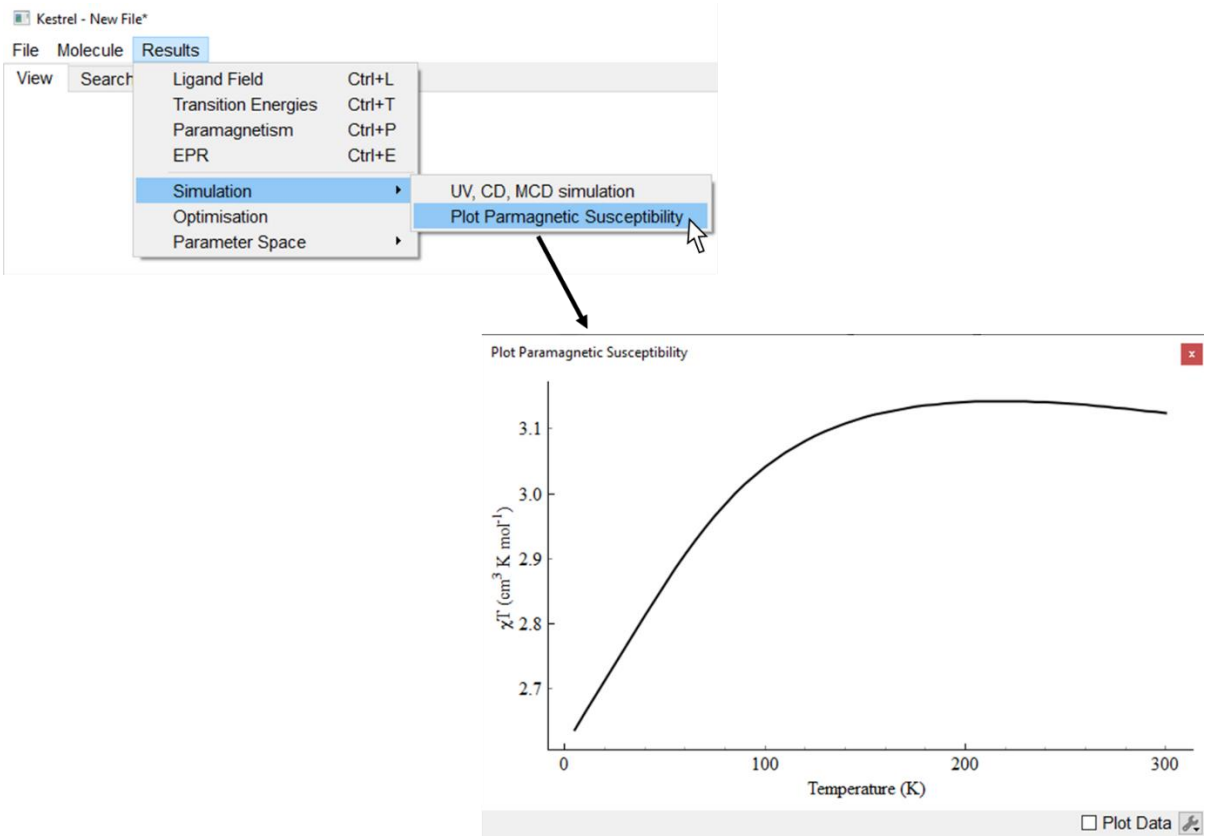

Figure 3.25. The process of opening the principal paramagnetic susceptibilities variation with temperature graph in Kestrel.

It is often easier to interpret changes in the magnetism of a complex with a change in electronic structure by visualising how the values and their dependence on temperature change. To open the plotting window, click on “Results” along the menu bar, hover over “Simulation” and click “Susceptibility Curve” as shown in Figure 3.25. Clicking this opens a floating window on top of the main window.

The new window, shown in Figure 3.25, features a graph. The graph displays data if the paramagnetic susceptibility calculations are enabled (see section 3.2.8). The graphs are plotted in units of χT (cm^3 mol^{-1} K), which is what is typically encountered in the chemical literature.

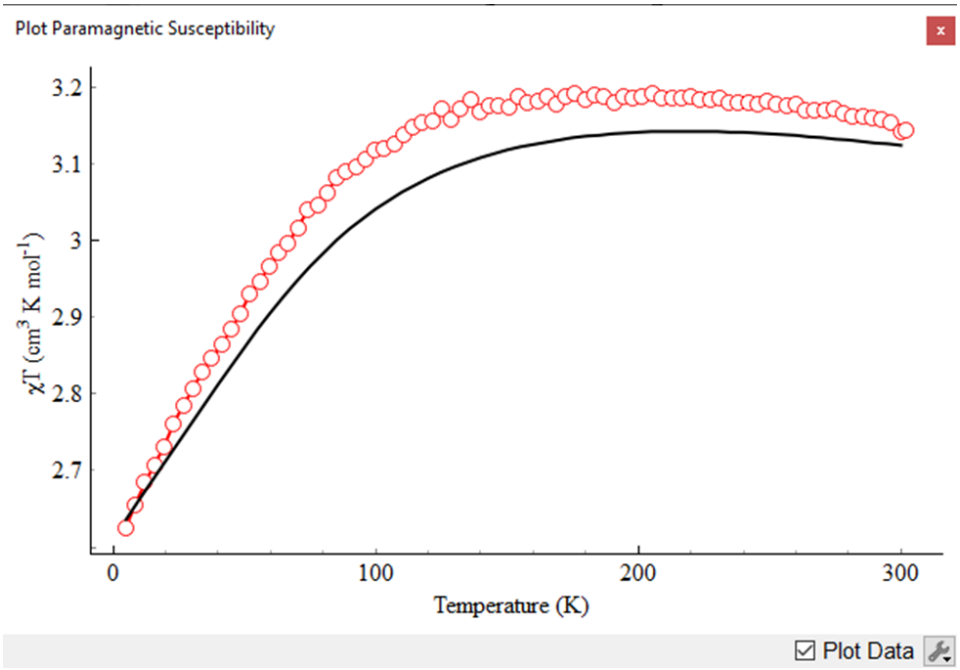

Figure 3.26. The calculated isotropic paramagnetic susceptibility variation with temperature (black) overlaid with comparison data (red).

The graphs can accept external data which can be plotted alongside the calculated values, as shown in Figure 3.26, allowing for a visual comparison. Data is added by clicking on the spanner button in the bottom right corner of the window.

3.2.10 Simulations of UV-Vis, CD, and MCD spectra

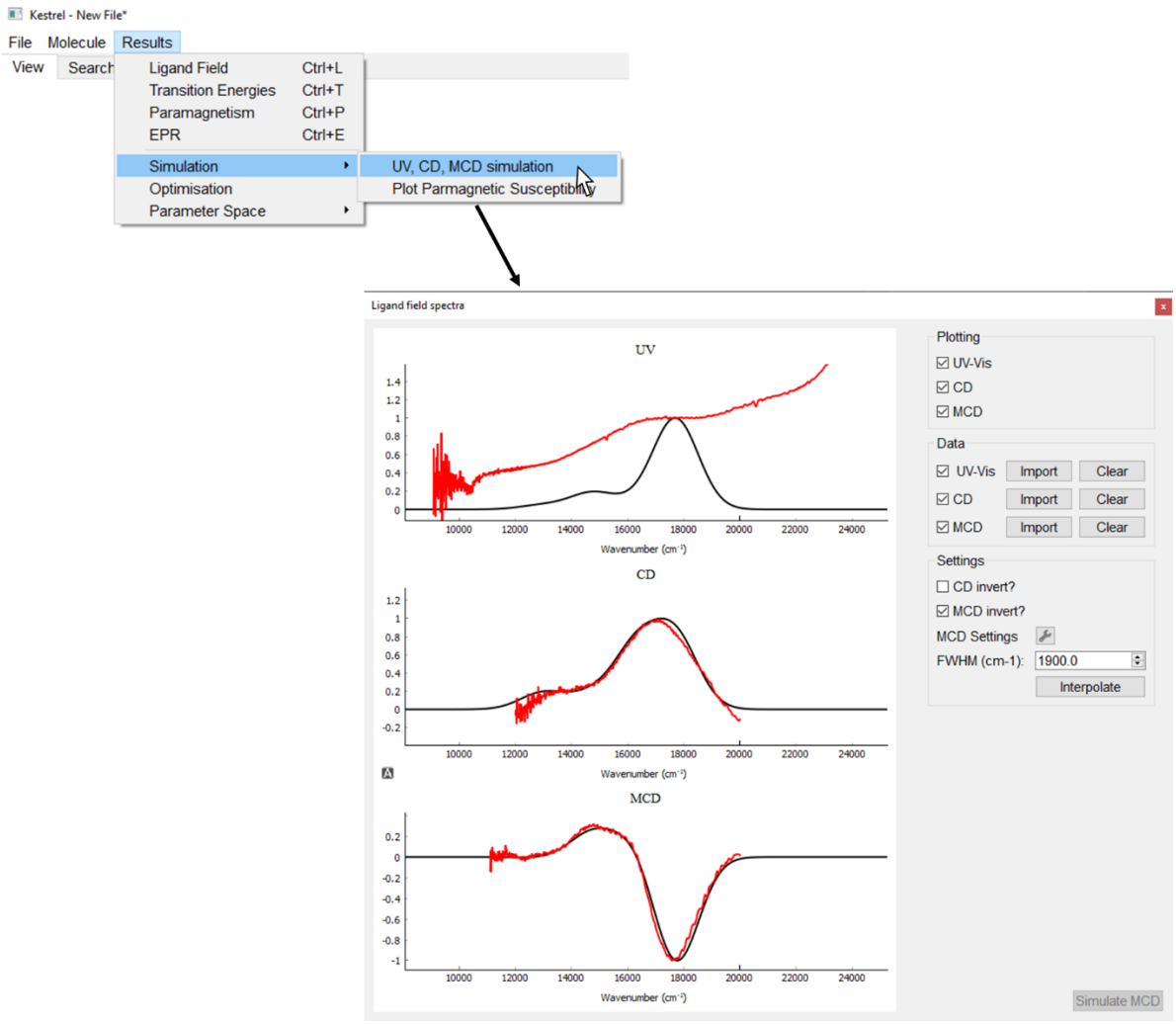

Figure 3.27. The steps to open the ligand-field spectra via Kestrel's GUI.

A unique feature of Kestrel is the ability to simulate UV-Vis and CD spectra in real time. MCD spectra can be (depending on computational factors) simulated quickly, but at present MCD calculations cannot be calculated in real-time. By clicking on the "Results" drop down menu, hovering over "Simulation" and selecting "UV, CD, MCD simulation", as shown in Figure 3.27, the ligand-field spectra window is opened.

The ligand-field spectra window is shown in Figure 3.27. The window features check boxes for the UV-Vis, CD, and MCD spectra, which will enable or disable the calculation of these spectra. While enabled, changes in any ligand-field parameters will recalculate the UV-Vis or CD spectral trace. MCD spectra must be simulated by selecting the "Simulate MCD"

button in the bottom right hand corner. The button will be enabled if there has been a change in the ligand-field parameters since the last simulation.

There are added options to change how the spectra is simulated. Under the “Settings” heading, the user can invert the CD/MCD spectra; via the “MCD Settings” button, choose the magnetic field strength, temperature, or resolution of the angular grid used to simulate the MCD; change the FWHM of each band in the spectrum; and choose the interpolation range for generating the spectral trace.

3.2.11 Optimisation

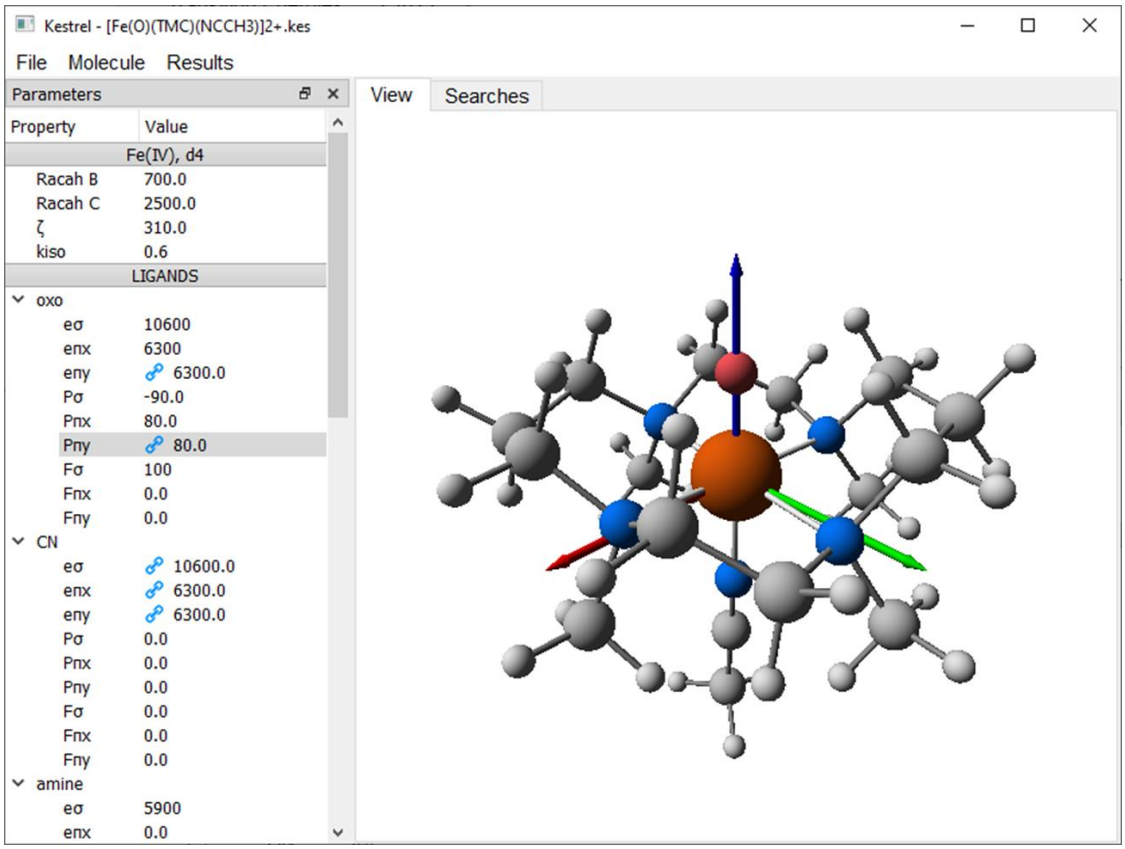

Figure 3.28. The molecular rendering of $[Fe(O)(TMC)(NCCH_3)]^{2+}$ in Kestrel’s GUI.

Kestrel can optimise a set of ligand-field parameters to reproduce supplied data. In this section, we will be using the d^4 iron(IV) oxo complex $[Fe(O)(TMC)(NCCH_3)]^{2+}$ that is studied in section 4.2 to illustrate this feature. Information on the ligand-field parameterisation is given in the methodology (section 4.2.2). The molecular rendering of $[Fe(O)(TMC)(NCCH_3)]^{2+}$ in Kestrel is shown in Figure 3.28. Using $[Fe(O)(TMC)(NCCH_3)]^{2+}$, this section will show how a

user can fit the calculated 5×5 one-electron ligand-field matrix from the results of an ORCA AILFT calculation to extract e_λ parameters.

3.2.11.1 Getting started

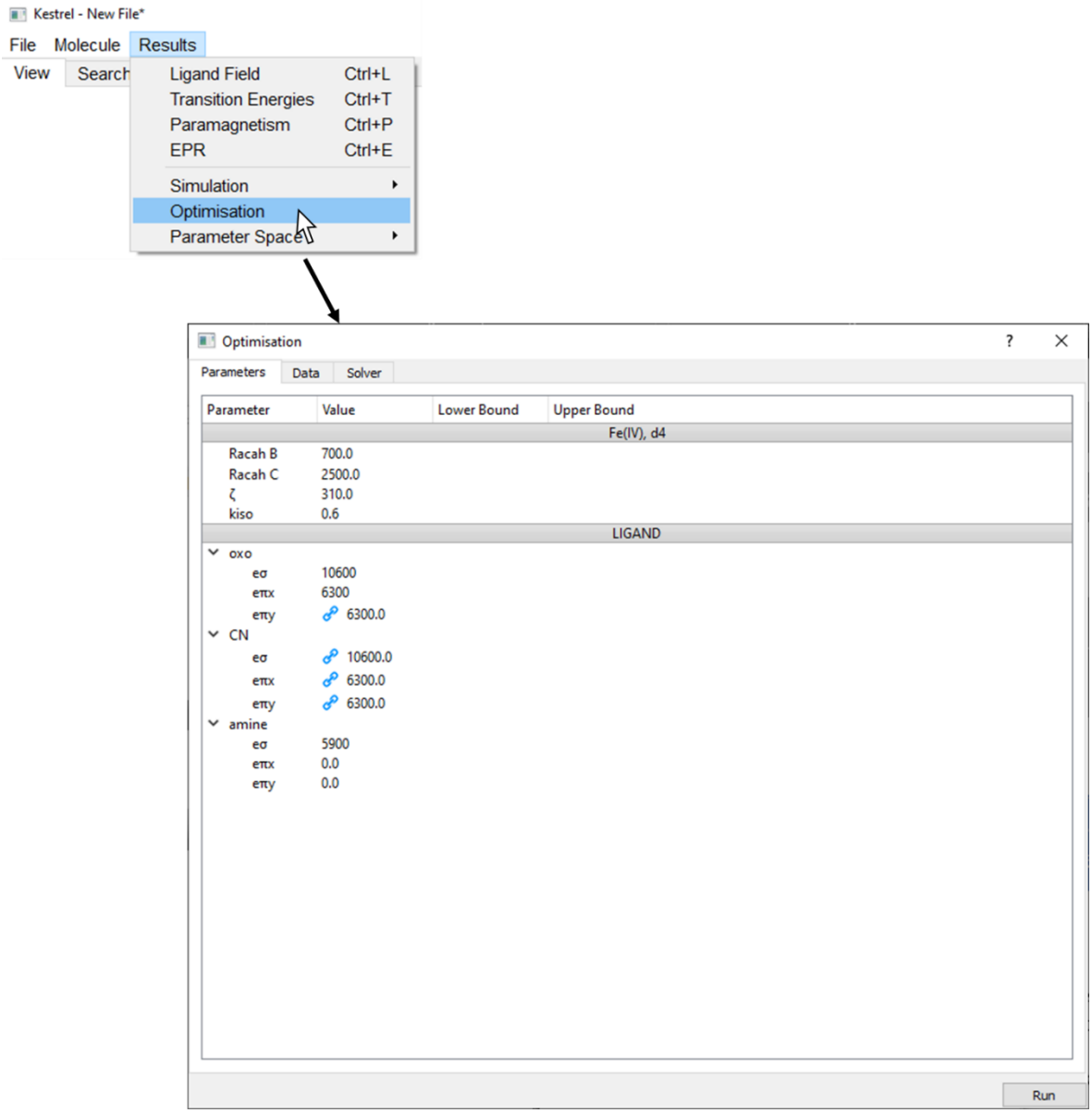

Figure 3.29. The steps to open the optimisation dialog via Kestrel's GUI.

To configure an optimisation, select the "Results" drop-down menu and click the "Optimisation" option, as shown in Figure 3.29. A window will then appear. In this window, the user can configure which ligand-field parameters are to be varied, what data is to be fitted, and the type

of algorithmic solver that will perform the optimisation. An optimisation requires at least two things to run: a minimum of one parameter to be varied; and at least one data set to fit to. If these criteria are not satisfied, Kestrel will warn the user that the calculation is not configured correctly when they try to run the optimisation.

3.2.11.2 Varying the parameters

The 5×5 one-electron ligand-field matrix is a function of the ligand field, which is defined by the e_λ parameters. The matrix elements are not affected by interelectronic repulsion or spin-orbit coupling. Hence, we only need to vary the e_λ parameters. We have three parameters to vary: the σ and π bonding of the oxo, $e_\sigma(O)$ and $e_{\pi x}(O)$ as $e_{\pi y}(O) = e_{\pi x}(O)$, where the axial acetonitrile (CN in Kestrel) is “linked” to the oxo ligand; and the σ bonding strength of the equatorial amines, $e_\sigma(N_{eq})$.

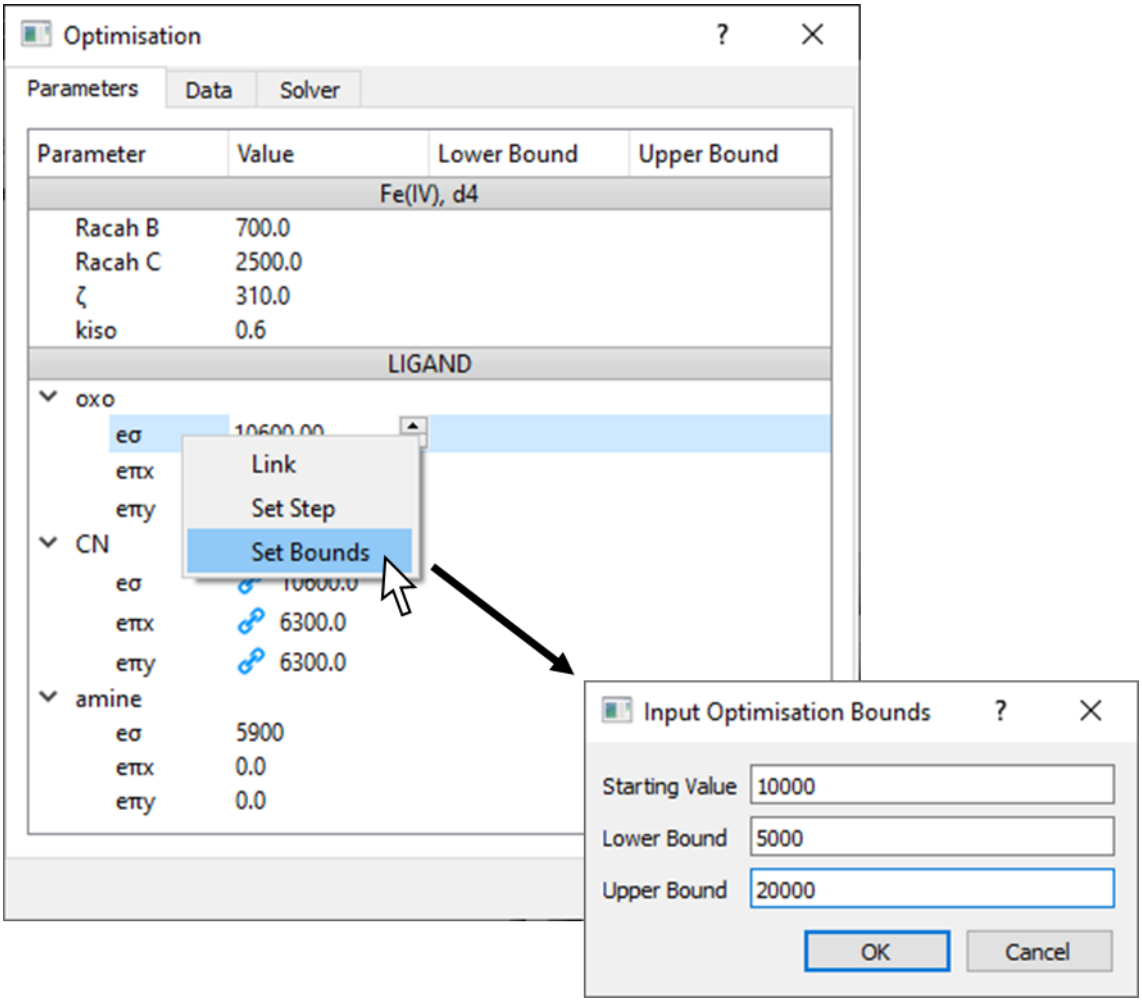

Figure 3.30. Setting the bounds for the e_σ of the oxo ligand in $[Fe(O)(TMC)(NCCH_3)]^{2+}$ using Kestrel's GUI.

To vary a parameter, right click on the parameter label and select "Set Bounds". This will display a small window, which requests the user to input: a "Starting Value", which is the initial value of the parameter; a "Lower Bound", which sets the minimum possible value that the parameter can have; and an "Upper Bound", which sets the maximum possible value that the parameter can be assigned. The starting value must be ≥ lower bound and ≤ the upper bound.

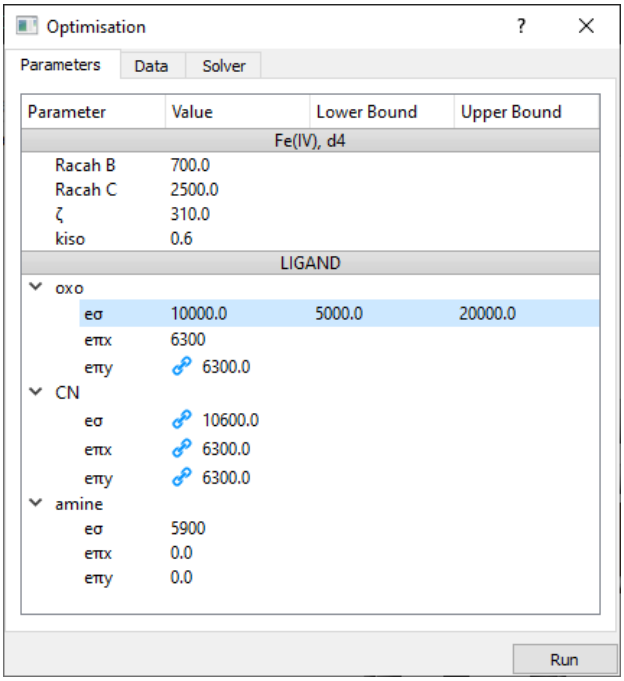

Figure 3.31. The format of setting the optimisation bounds of the oxo's e_σ parameter in $[Fe(O)(TMC)(NCCH_3)]^{2+}$ using Kestrel's GUI.

Selecting "OK" will set those bounds for the ligand-field parameter, which is displayed in the table, as shown in Figure 3.31. The user can specify new bounds by right clicking the parameter and selecting "Set Bounds". The user can also remove the optimisation bounds by right clicking the parameter and selecting "Set Fixed". The user is still able to change the value of the fixed parameters in this window.

3.2.11.3 Choosing to fit a 5×5 ligand-field matrix

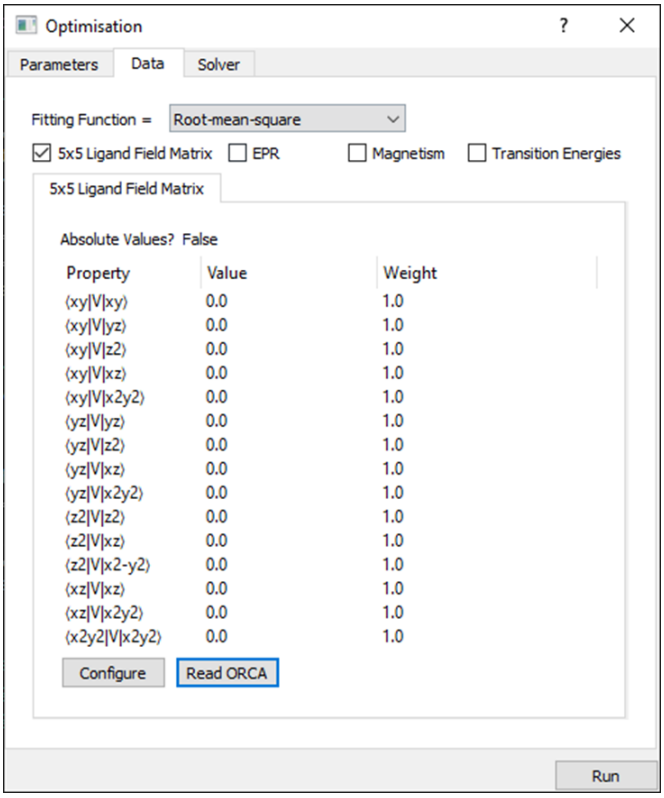

Figure 3.32. Enabling the calculation of a 5×5 ligand-field matrix for use in an optimisation calculation via Kestrel's GUI.

Optimisation of ligand-field parameters require external data to refine against. In this example, we are going to perform a fit to the 5×5 one-electron ligand-field matrix extracted from an AILFT analysis of a minimal active space CASSCF(4, 5) calculation. For details of how the CASSCF(4, 5) was performed, consult section 4.2.2.1. For the analysis of the results, refer to section 4.2.4.1. By navigating to the "Data" tab and checking the "5×5 Ligand Field Matrix" option, the user is shown a table of the 15 unique matrix elements, as presented in Figure 3.32.

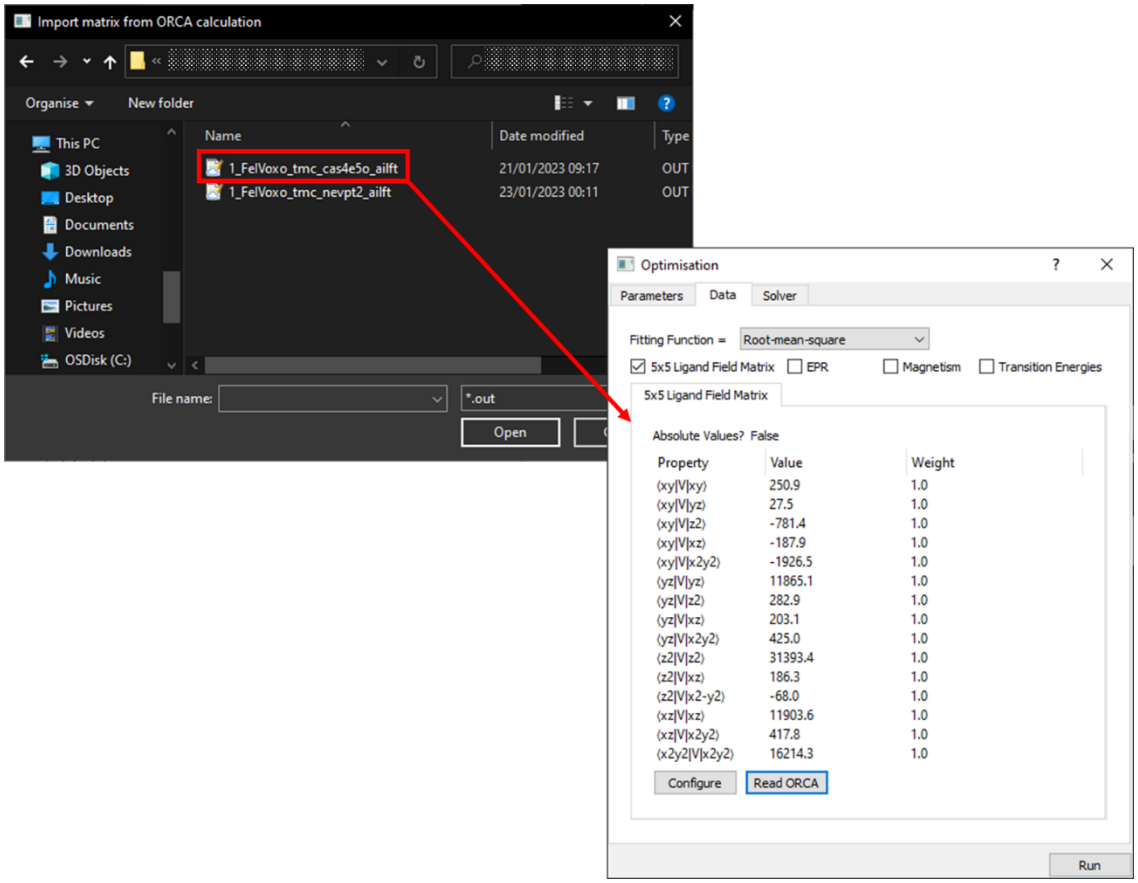

Figure 3.33. Selecting an ORCA output file to extract the 5×5 ligand-field matrix in Kestrel's GUI.

One can manually supply a 5×5 ligand-field matrix by selecting the "Configure" button. However, it is common for the 5×5 ligand-field matrix to originate from the results of an *ab initio* calculation. To read in an ORCA output file, in which an AILFT analysis has taken place, select the "Read ORCA" button and navigate to the file, as shown in Figure 3.33. Selecting that file will automatically extract the matrix and the data window should update to show the 15 unique matrix elements. Note that the current system of reading an ORCA output file was defined for ORCA version 4. Undefined behaviour will occur when trying to read in output files for other versions.

3.2.11.4 Selecting the optimisation method

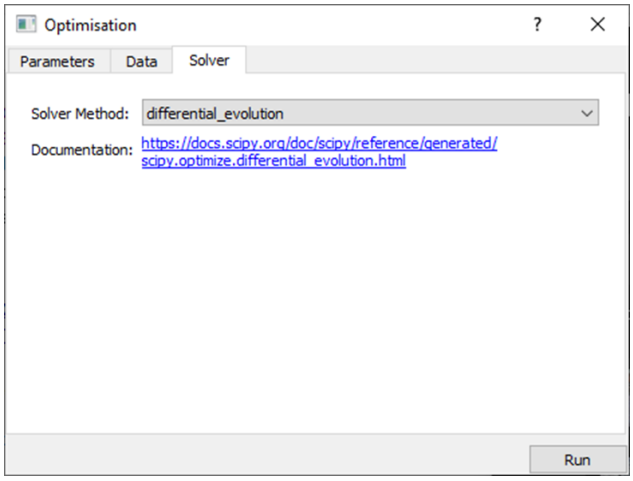

Figure 3.34. The "Solver" tab of the optimisation window.

The optimisation calculations are carried using one of two currently integrated methods from SciPy's optimize library: differential_evolution, a global optimisation method; and minimize, a method for finding local minima, which is sensitive to the choice of starting parameter values.[96] By navigating to the "Solver" tab, as shown in Figure 3.34, the user may choose an optimisation method from the drop down box. Selecting a method will display a link to the documentation.

3.2.11.5 Running the calculation

When the optimisation has been configured, the user can run the calculation by selecting the "Run" button in the bottom right-hand corner of the window. The program will ask for confirmation that the user wishes to run the calculation. By selecting "OK", Kestrel will then ask for a save file name and a folder to store the results of the simulation. After choosing a name and folder location, the optimisation will then perform in the background. When the calculation finishes, an output file will be generated along with a .mol of the molecule with the best fit parameters, the latter of which can be loaded back into the program.

3.2.12 Parameter-space search

Parameter-space searches allow the user to vary a set of ligand-field parameters to create an N-dimensional grid of parameter combinations, iterate over every parameter combination, and compare the results to a data set. Doing so, allows one to explore the quality of fit space visually, discover potential alternative fits, and reveal parameter correlations, if they exist.

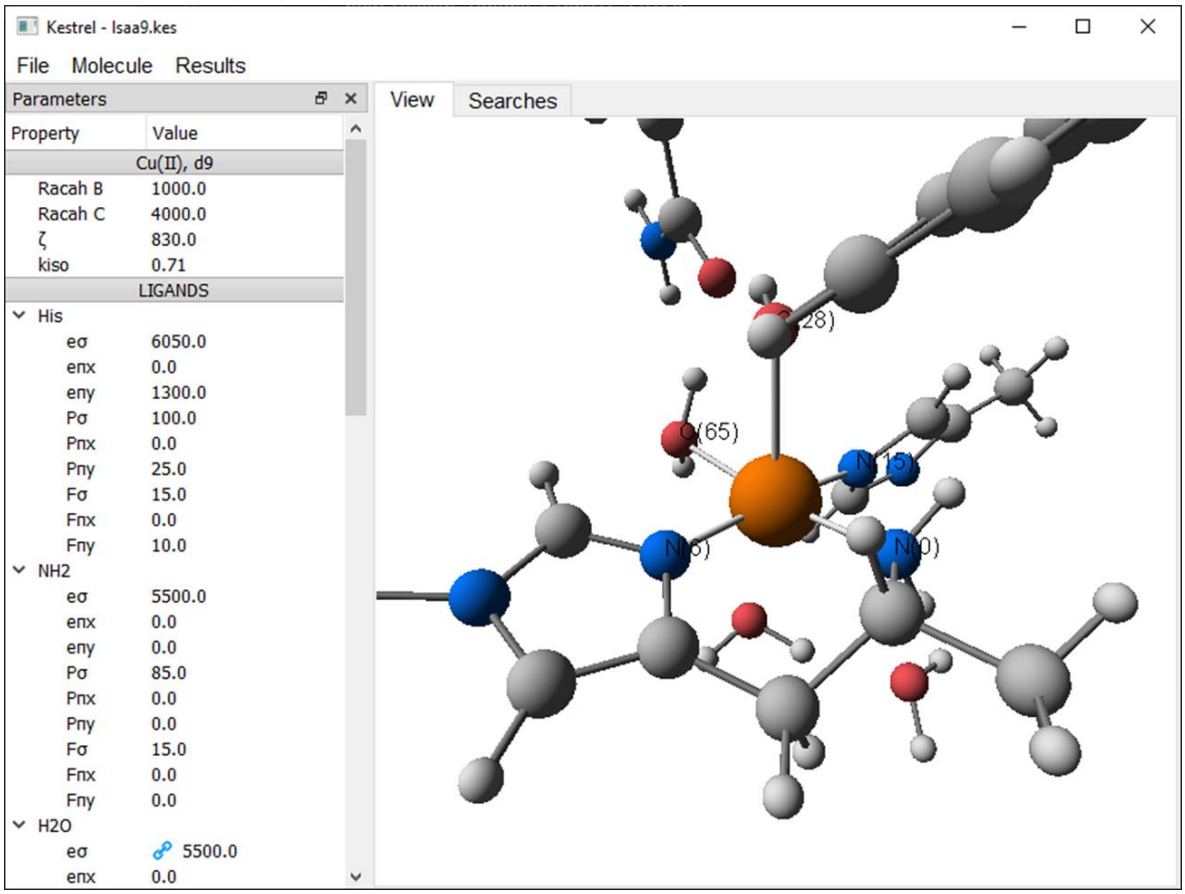

Figure 3.35. The molecular rendering of *Ls*AA9 in Kestrel's GUI.

In this section, we will be using the active site of a copper(II) enzyme, *Ls*AA9, which is analysed in section 4.3 to illustrate this feature. Information on the ligand-field parameterisation is given in the methodology (section 4.3.2) and the molecular rendering of *Ls*AA9 in Kestrel is shown in Figure 3.35. In the ligand-field analysis of this system, the e_λ parameters of the ligands and the orbital angular momentum quenching (k_{iso}) were varied to reproduce the experimental transition energies and EPR g-factors.

3.2.12.1 Getting started

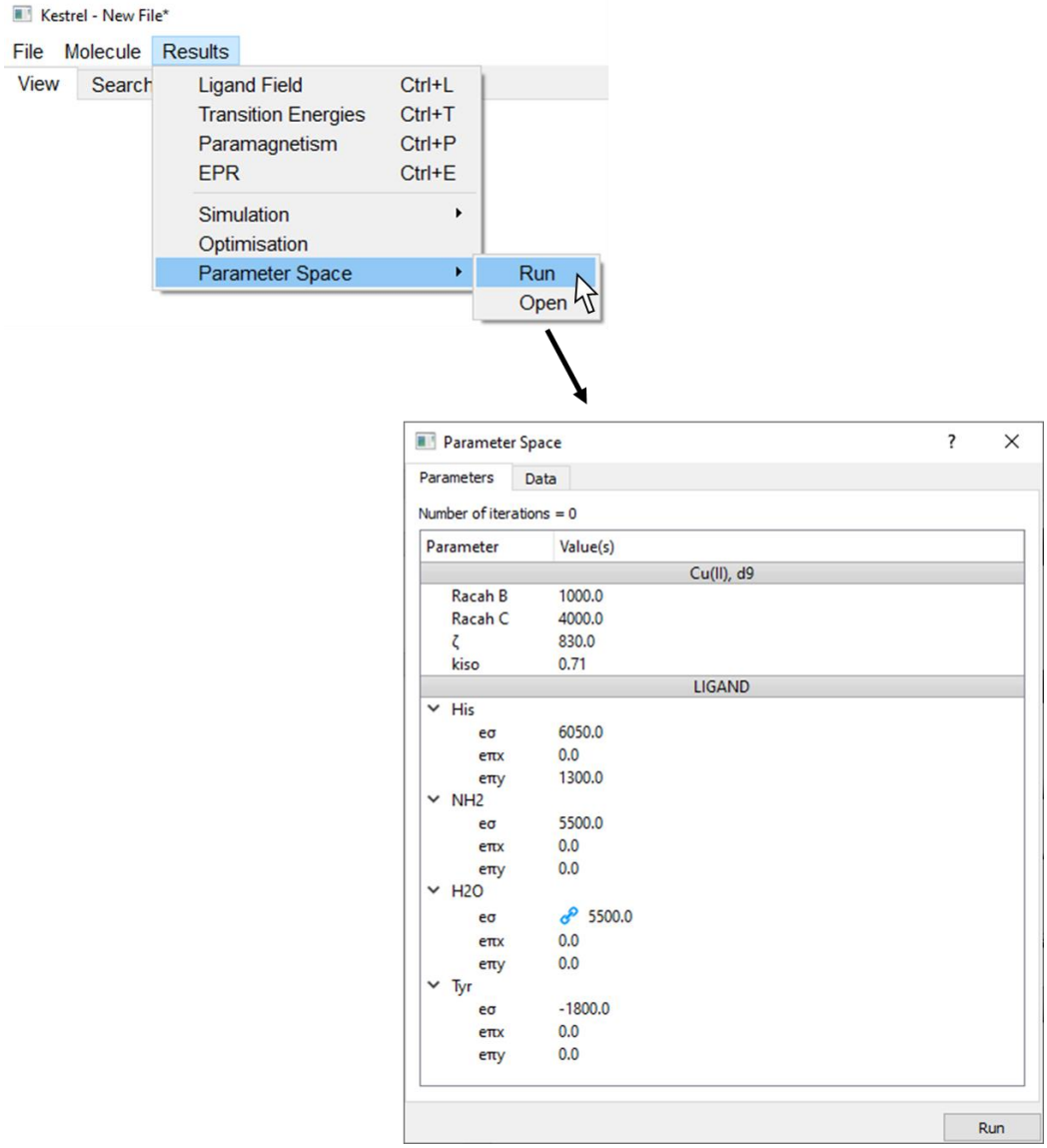

Figure 3.36. The steps to open the parameter-space dialog via Kestrel's GUI.

The user can configure a parameter-space calculation by selecting the "Results" drop-down menu and selecting "Parameter Space", as shown in Figure 3.36. In this window, the user can specify the ligand-field parameters to vary and what data to compare to. A parameter-space search requires at least two things to run: a minimum of two parameters to be varied; and at least one data set to fit to. If either of these criteria are not met, Kestrel will warn the user that the calculation is not configured correctly when they try to run the parameter-space search.

3.2.12.2 Varying parameters

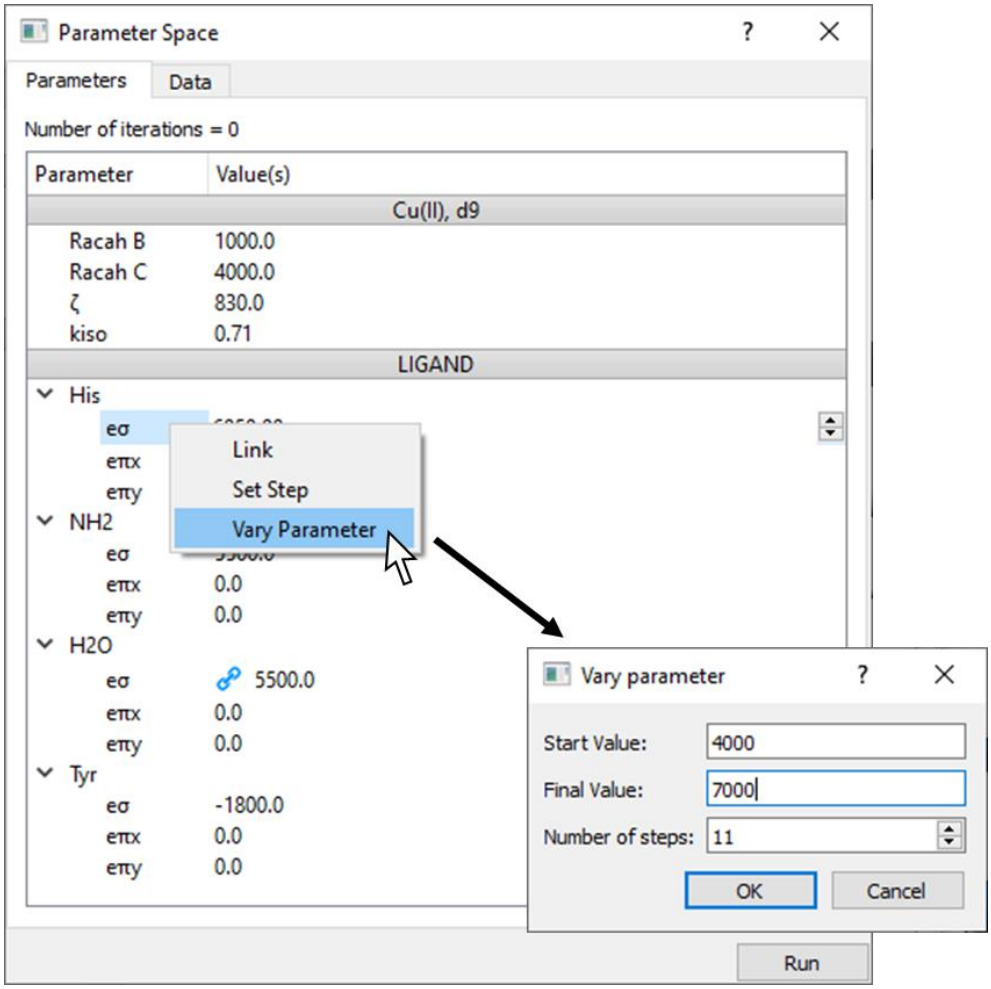

Figure 3.37. Varying the e_σ of the histidine ligands in *Ls*AA9 using Kestrel's GUI.

To vary a ligand-field parameter, right click the parameter label and select the "Vary Parameter" option. Doing so opens a dialog window, as shown in Figure 3.37, which prompts the user to enter: a "Start Value", which is the first value in the sequence; a "Final Value", which is the final value in the sequence; and the "Number of steps" which is the number of values in the sequence. The example given in Figure 3.37 would generate this series of values: 4000, 4300, 4600, 4900, 5200, 5500, 5800, 6100, 6400, 6700, 7000.

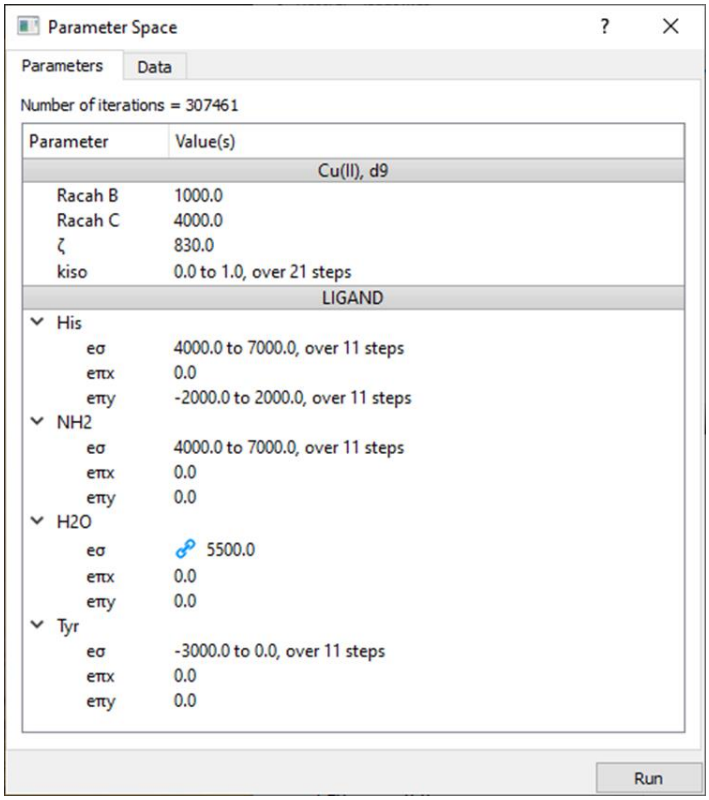

Figure 3.38. The parameter-space range for *Ls*AA9 in Kestrel's GUI.

When a valid parameter range is entered, the parameter value description updates to read "4000.0 to 7000.0, over 11 steps", as shown in Figure 3.38. A counter at the top of the tab labelled "Number of iterations" shows the number of parameter combinations that will be looped over. From Figure 3.38, one can see how varying a reasonable number of parameters can quickly result in a large calculation.

3.2.12.3 Choosing to fit two data sets simultaneously: the EPR g-factors and transition energies

As part of the ligand-field analysis reported in section 4.3.3.1, the ligand-field parameters are varied to find potential fits to the reported experimental EPR g-factors and d-d transition energies. Unlike in section 3.2.11.3, where only one data set was fitted to, it is often convenient to set the "Fitting Function" to the "Normalised root-mean-square" when fitting two or more data sets of different magnitudes, as shown in Figure 3.39. The normalisation divides the calculated root-mean-square by the standard deviation of the data. This places the individual

qualities of fit to the different data on a comparable scale. We will see the advantage of this later.

3.2.12.3.1 EPR g-factors

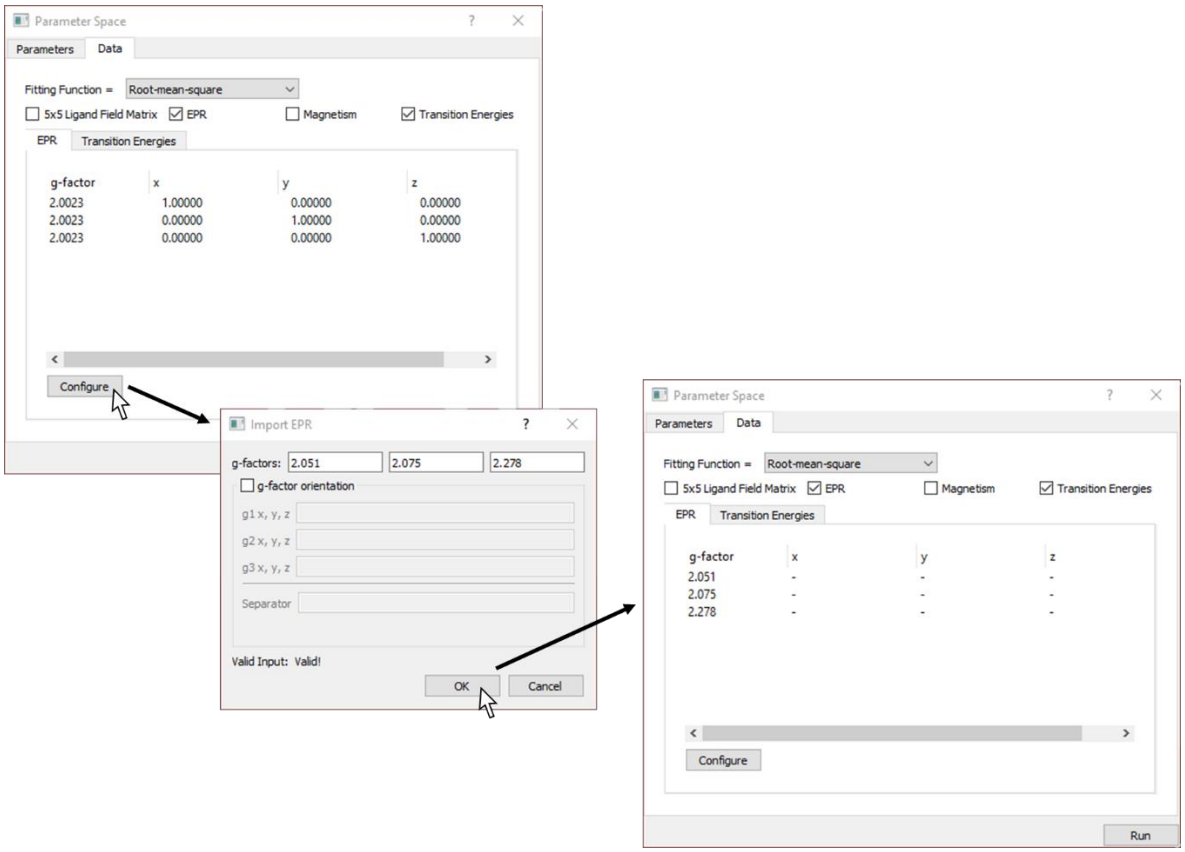

Figure 3.39. Defining the experimental EPR g-factors for *Ls*AA9 to compare to, via Kestrel's GUI.

The process of defining the EPR g-factors to fit to is shown in Figure 3.39. By enabling the "EPR" check box, the EPR data is displayed. By clicking the "Configure" button, the user may define the EPR g-factors and their orientation, if desired. For the present example, defining the g-factors is enough. Entering in the reported g-factors and selecting "OK" correctly imports the values in to the EPR data tab.

3.2.12.3.2 d-d transition energies

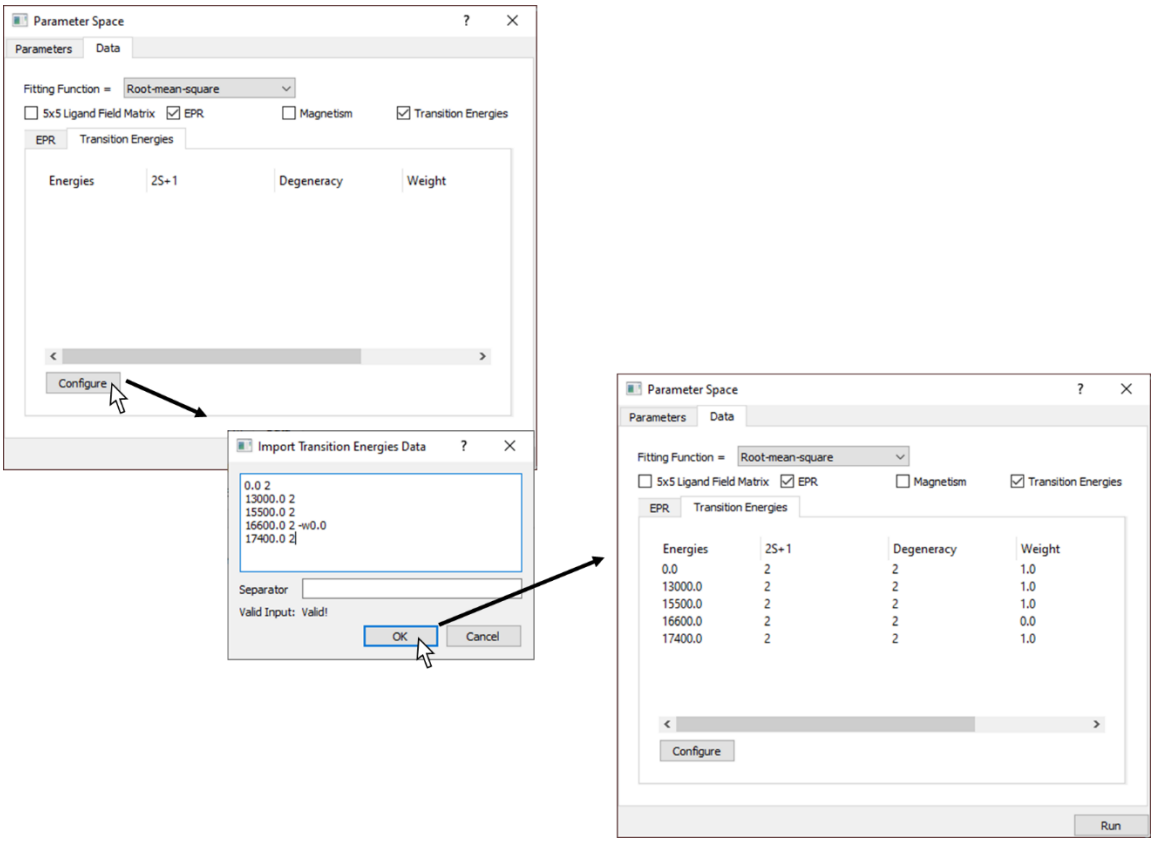

Figure 3.40. Defining the experimental transition energies for *Ls*AA9 to compare to, via Kestrel's GUI.

The process of defining the d-d transition energies to fit is presented in Figure 3.40. The user can configure the d-d transition energies by selecting the "Configure" button in the transition energies data tab. Doing so opens a dialog window, where the user can add the transition energies and spin multiplicities. If the user wishes, they can also define the degeneracies of the level (by adding another integer, e.g. 0.0 2 4 would mean a relative energy of 0 cm^{-1}, with a spin multiplicity of 2 and a degeneracy of 4), or a weighting by using the -w flag as shown in Figure 3.40. This means the transition energy at 16600 cm^{-1} will not be fitted to, but a transition energy must be placed between the transitions at 15500 cm^{-1} and 17400 cm^{-1}. It is also possible to assign a configuration projection assignment to the level using the -c flag followed by an electronic configuration, such as 22221.

3.2.12.4 Running the calculation

Once the calculation is configured, click the “Run” button to submit the calculation. The program will ask for confirmation that the user wishes to run the calculation. By selecting “OK”, the program will ask for a save file name and a folder to store the results of the simulation. After choosing a file name, a progress bar will appear, showing the user how far the calculation has progressed as a percentage of the total number of iterations. This calculation can be cancelled at any time by selecting the “Cancel” button.

3.2.12.5 Visualising the results

When a parameter-space calculation completes, the results are automatically loaded into the program. Alternatively, the user can plot the contour map of any parameter-space calculation by selecting the “Results” drop-down menu and hovering over “Parameter Space” and selecting “Map”. Selecting this option will allow the user to select one or multiple parameter-space output files. The user may open as many of these windows as they wish and can even open multiple instances of the same output file.

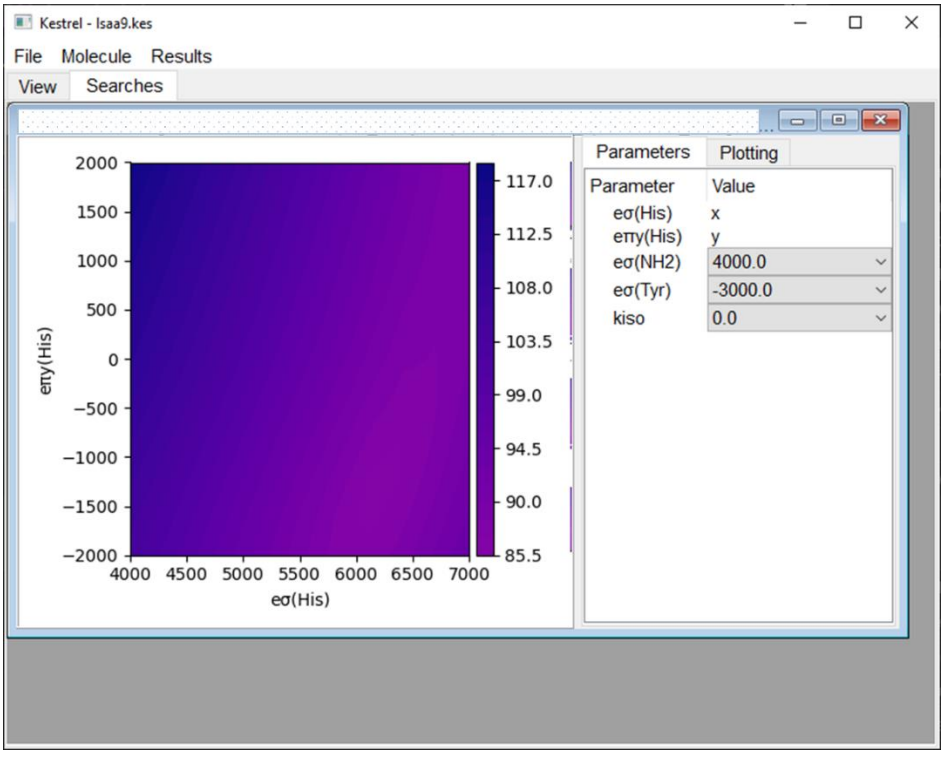

Figure 3.41. The parameter-space “mapping” window in the “Search” tab of the central widget of Kestrel.

The results are displayed in a window located in the central widget of the application window, as shown in Figure 3.41. The left-hand side of the window features a contour plot (rendered using Matplotlib) which plots two separate parameters on its x and y axes.[100] There is a colour bar to the right-hand side of the contour plot, which shows the colour map of the quality of fit values. On the right-hand side of the window is a tab widget with two tabs: the first tab features a list of varied parameters; the second tab is a plotting tab, where the user can configure what data to plot and how it is plotted.

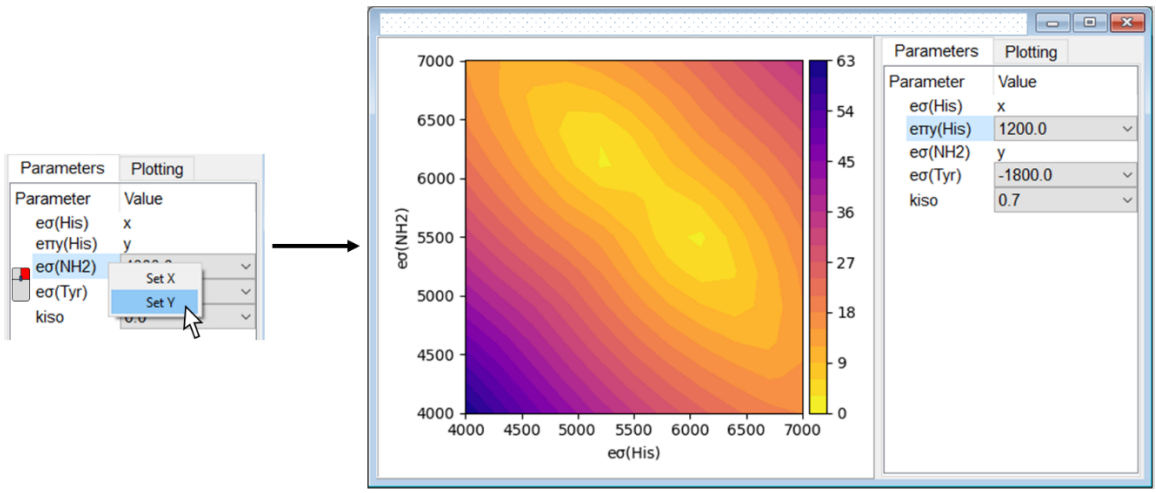

Figure 3.42. The layout and options of the parameter-space "mapping" window.

To explore the relationship between the variation in parameter values and the quality of fit to the data, one can plot any two varied parameters in the list. The user can choose what parameters to vary along the x and y axes by right clicking a parameter and selecting "set x" or "set y", as shown in Figure 3.42. The remaining parameters are assigned the current value displayed in their drop-down widget, which the user can scroll through to see how the best fit parameter space moves.

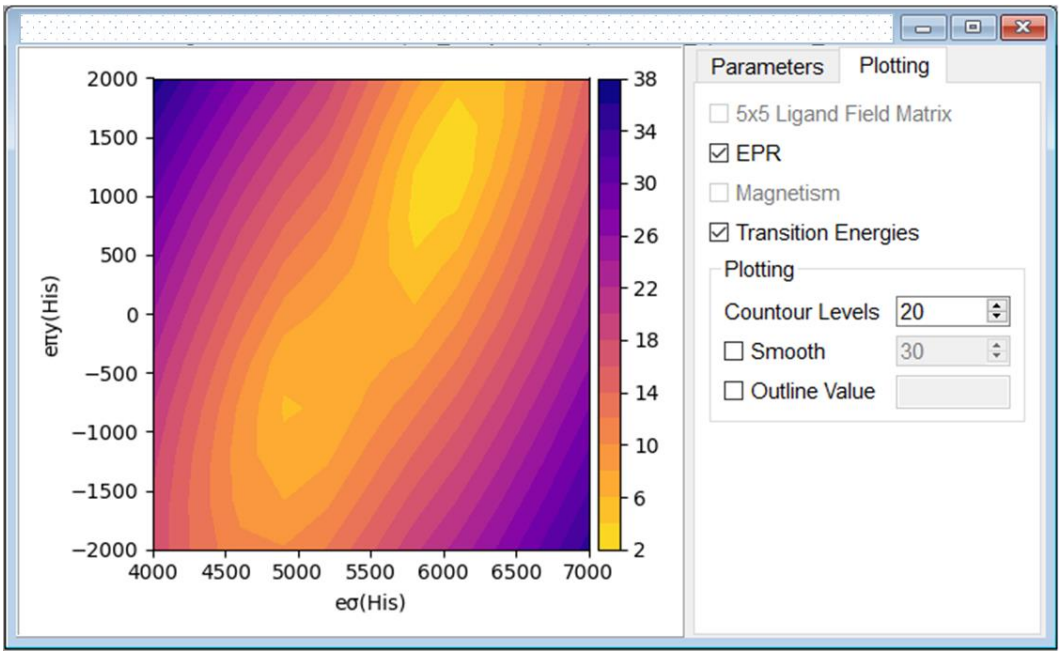

Figure 3.43. The plotting options of the parameter-space output.

If multiple data types were compared to (like in the case for *Ls*AA9) the user may select which data to include in the quality of fit plot. If multiple data types are selected, as shown in Figure 3.43, the sum of their quality of fit metrics are plotted. Here, in this example, both the quality of fit to the transition energies and EPR g-factors are enabled. It is here that using the "Normalised root-mean-square" fitting function is advantageous. From the plot one can see parameter combinations that offer good reproduction of *both* the d-d transition energies and EPR g-factors. If one were to use just the "root-mean-square" metric, a good RMS could be around 100 cm^{-1} and 0.01 for d-d transition energies and EPR g-factors respectively. Plotting their sum only really reports on the quality of fit to the d-d transition energies.

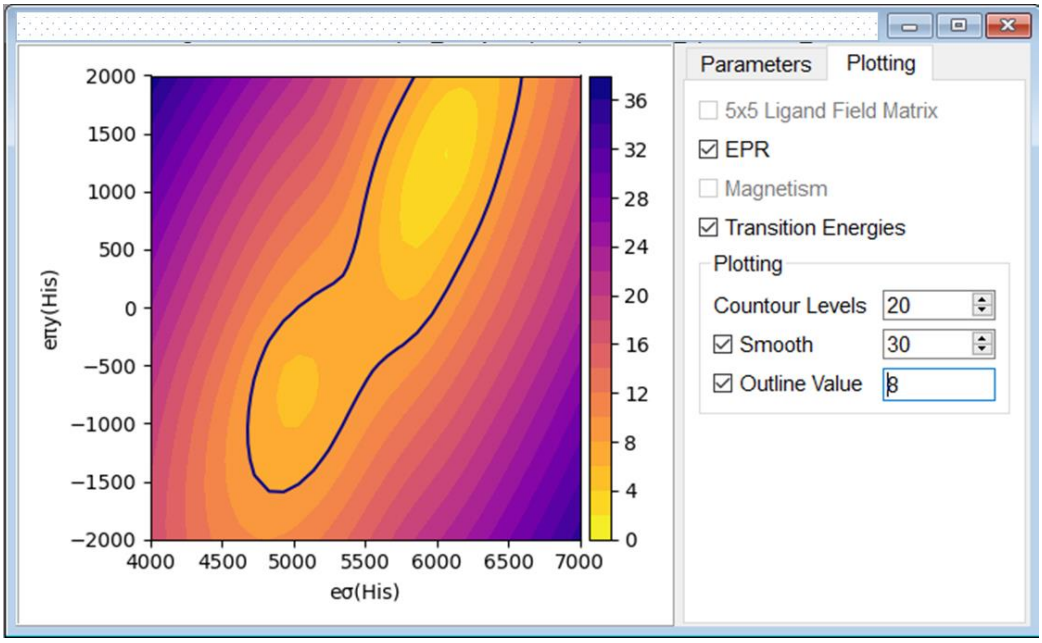

Figure 3.44. Examples of the "smoothing" and "Outline Value" plotting options in the parameter-space output window.

There are also plotting options available. The user can set the number of contour levels to plot and has the option to "smooth" the contour plot, to make the plot more aesthetically pleasing. A useful feature is the ability to outline a certain quality of fit value, which will encircle regions of parameter spaces where the quality of fit is less than or equal to the target value. Examples of these features are shown in Figure 3.44.

4 Ligand-field analysis

4.1 The rational design of single-ion molecular magnets

4.1.1 Introduction

Single molecules can exhibit slow relaxation of their magnetisation.[101] Hence, they can be magnetised in an external magnetic field and retain that magnetisation upon the removal of the external field. Single-molecule magnets that exhibit a single ion are called single-ion molecular magnets (SiMMs). These single-ions are typically either lanthanide or transition-metal ions. These "nanomagnets" have proposed applications in quantum computing as qubits, molecular spintronics, information storage, and magnetic refrigeration.[102–109] However, to be used in such applications, the blocking temperature T_B (the temperature above which the retained magnetisation is lost) must be maximised. Recent advances in lanthanide SiMMs have achieved blocking temperatures up to 80 K.[110] Despite this success, limited access to lanthanide metals make the development of 3d transition-metal complexes more attractive.

SiMM complexes are a bistable system between states with $\pm M_J$ projections. Reversal of the magnetisation of the system involves reversing the sign of the M_J projection. Hence, the barrier to magnetic relaxation U, is given by the depth of the double-well potential surface between the two M_J states (Figure 4.1). A high blocking temperature is associated with slow interconversion between the two states, *ergo* the height/width of the barrier.

However, a molecule has multiple means of relaxation, which can bypass the energetic barrier altogether. These processes are mechanisms of spin-lattice relaxation, where the dipolar spin-spin interactions fluctuate with the vibrations of the molecule.[111] Rationalising the SiMM behaviour of a molecule requires an understanding of these other relaxation mechanisms.

The molecule can relax from one magnetic orientation directly to another (with the same magnitude M_J projection) *through* the energetic barrier. This tunnelling is known as quantum tunnelling of the magnetisation (QTM), depicted by the red dashed arrows in Figure 4.1. At low temperatures, relaxation is dominated by QTM in the ground state Kramer's doublet (KD) (represented by the $+^7/_2$ and $-^7/_2$ states in Figure 4.1). QTM can also occur between states of higher lying excited KDs but requires higher lying excited states are thermally occupied. This is referred to as thermally activated QTM.

Other relaxation mechanisms exist which instead occur via a two-phonon. The first of these is the Raman process which involves the inelastic scattering of a single phonon, exciting the ground state to a "virtual" quantum state before decaying to the reversed magnetised state, changing the kinetic energy of the phonon.[112]

The second two-phonon process is the Orbach process.[113–115] In the Orbach process, the ground state is excited to a higher-lying intermediate state and decays from the intermediate state to the reversed magnetic state. Hence, the system must be able to absorb a phonon of sufficient energy (provided for thermally) and release a phonon when decaying. This effect is dominant at higher temperatures and its contribution is inseparable from thermally activated QTM process.

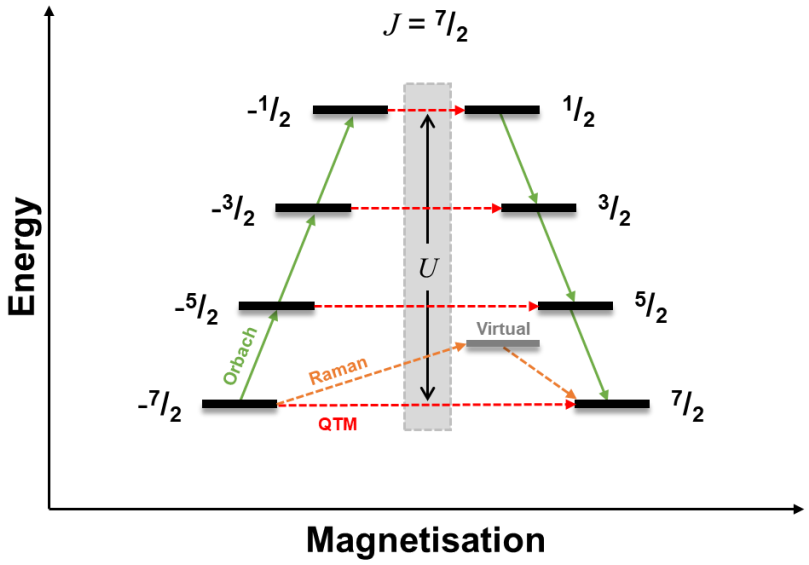

Figure 4.1. The energy barrier (U) to the reversal of magnetisation at zero external magnetic field of a fictitious J = $^7/_2$ system. Black bars represent electronic states with the corresponding M_J projection. Red dotted arrows represent QTM transitions between ±M_J states. Green arrows represent relaxation via a two-step phonon relaxation process known as the Orbach process. Finally, the orange dotted arrow represents the Raman relaxation pathway.

Since these processes bypass the total energetic barrier U, they result in an effective energetic barrier U_{eff}, which is less than U. The parameter U_{eff} is used experimentally as a phenomenological parameter to fit relaxation data of Arrhenius type. Although U_{eff} is associated with the Orbach process, the extracted value does not distinguish between

relaxation sources. Since the Raman and Orbach processes can operate within similar temperature ranges, this can mean extracted values of U_{eff} do not always correspond to the magnitudes of the zero-field splitting of the molecule.[116] To separate these sources of relaxation, some authors have fixed the value of U_{eff} by measuring the zero-field splitting and fitting the relaxation from the Raman process directly.[117] Hence, the prediction of the value of U_{eff} can be important to analyse the SiMM properties of a molecule.

With regards to 3d transition-metal ions, attempts to increase the blocking temperature have focused on maximising their axial magnetic anisotropy, as a means to increasing the height of the barrier between the M_J states and quenching the QTM within the ground state KD.[118] For cobalt(II) Kramer's ions (S=3/2) the value of U_{eff} is attributed to the splitting of the ground and first excited state KD as given by the expression $U_{eff} = |D|(S^2–{}^1/_2)$, where S is the spin quantum number and D is the axial splitting parameter of spin Hamiltonian theory. In addition, developing a complex with SiMM character in the absence of an applied external direct current field requires suppression of QTM in the ground state KD.

Such electronic features of SiMM complexes can be explored by calculations of the various electronic states that contribute to its magnetism. There are methods that use the results of *ab initio* calculations to compute the effective barrier U_{eff} and the time taken for QTM (τ_{QTM}) to occur.[116,119] While theoretical insight into SiMMs can be and have been determined from *ab initio* calculations, the calculation of U_{eff} and τ_{QTM} can equally be calculated from the results of ligand-field calculations with the attendant benefits of speed and chemical intuitiveness that such calculations offer. It is therefore surprising to find that there are no examples of this approach in the literature.

4.1.1.1 Use of ligand-field calculations from Kestrel to calculate U_{eff}.

To investigate whether Kestrel could be used to inform the rational chemical design of SiMMs, three cobalt(II) complexes that could act as SiMMs are shown in Figure 4.2. Complexes **1** ($Co(C(SiMe_2ONaphthyl)_3)_2$), **2** ($CoTp_2$, where Tp = tris(pyrazolyl)borate), and **3** (CoL_2, where H_2L = 1,2-bis(methanesulfonamido)benzene), were selected for a detailed analysis of their electronic structures. Complexes **1** and **2** have been previously been probed geometrically with *ab initio* calculations to gain further insight into improving their SiMM character.[120,121] Complexes **1** and **3** feature magnetic hysteresis in the absence of an applied direct current (dc) field, whereas **2** does not. These systems were chosen to study as they represent varied geometries (2, 6, and 4 coordinate respectively) and are extensively characterised spectroscopically. They are also homoleptic systems so include a minimal number of chemical

variables to both fit and vary. Using Kestrel, investigations were carried out into how changes in metal-ligand bonding and molecular geometry effect the axiality and SiMM properties of these three complexes.

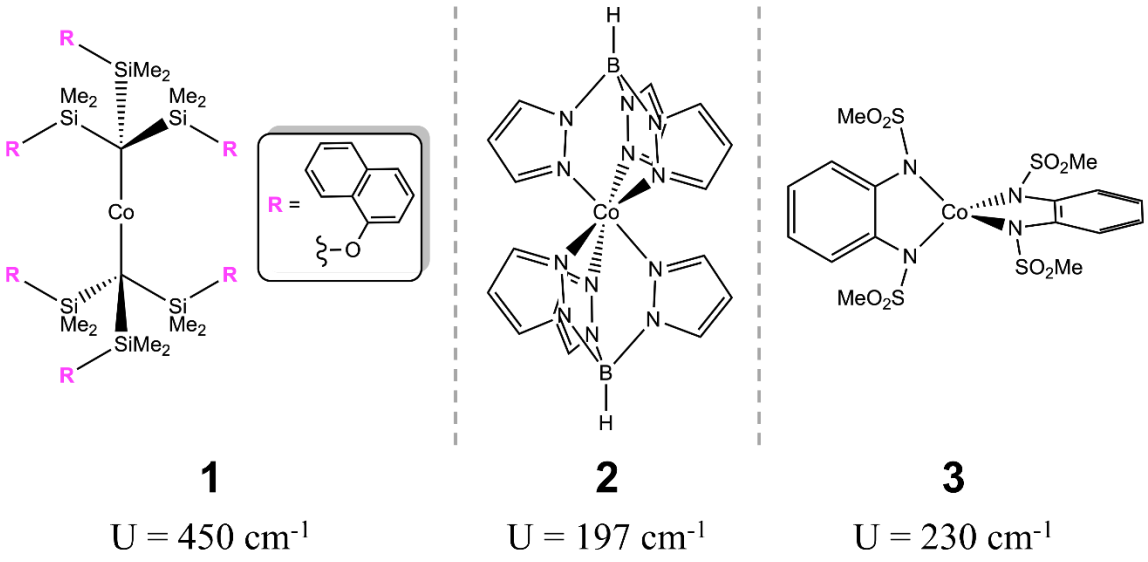

Figure 4.2. Structures of complexes 1, 2, and 3 (see text) with the reported energetic splitting between ground and first excited state Kramer's doublets.[122–124]

4.1.2 Methodology

4.1.2.1 Ligand-field calculations

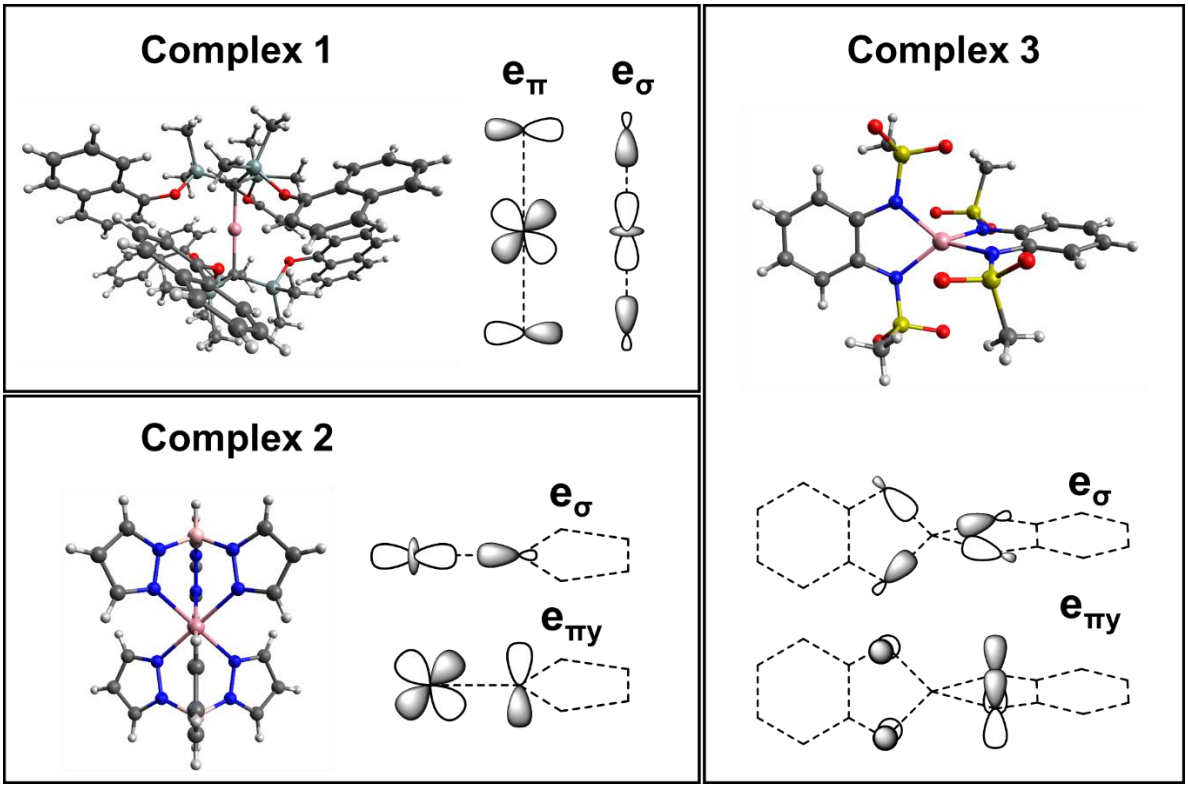

Figure 4.3. The metal-ligand e_λ bonding interactions used to parameterise the ligand field in complexes 1, 2, and 3.

Ligand-field calculations were carried out using Kestrel with the full d^7 configurational basis set (40 quartets and 80 doublet states, which is equivalent to 10 quartet roots and 40 doublet roots). The free-ion cobalt(II) ligand-field parameters are B_0 = 1120 cm^{-1}, C_0 = 4368 cm^{-1}, and ζ_0 = 515 cm^{-1}.[125] The ligand field was parameterised using the metal-ligand bonding parameterisation illustrated in Figure 4.3.

4.1.2.1.1 Complex 1

The molecular geometry was taken from the reported x-ray crystal structure (CSD: FIYMEI).[122] The alkyl ligand e_λ parameters were placed at the coordinating carbon atoms. The alkyl ligand was parameterised using an e_σ and e_π parameter, as illustrated in Figure 4.3. Although an

alkyl ligand would formally be non π-bonding, the possibility of electrostatic contributions to the e_π parameter were investigated. Electrostatic contributions to e_δ were fixed at 0 cm^{-1}.

Parameter-space calculations were used to fit the two reported spin-allowed band in the experimental UV-Vis spectrum, using Kestrel's parameter space feature. Racah B was varied between 0 cm^{-1} and 1000 cm^{-1} in increments of 100 cm^{-1}; e_σ was varied between 0 cm^{-1} and 5000 cm^{-1} in increments of 500 cm^{-1}; and e_π was varied between 0 cm^{-1} and 2500 cm^{-1} in increments of 250 cm^{-1}. Spin-orbit coupling was neglected, and Racah C was fixed at 4000 cm^{-1}.

An optimisation calculation with the same parameters was carried out for each increment of e_π, using the differential evolution function.[96] The best fit parameters from the optimisation calculations were then used to compute the ZFS using the free-ion spin-orbit coupling value as this would represent the maximum possible ZFS for that parameterisation. The ZFS was calculated by subtracting the energy of the first excited state KD from the energy of the ground state KD.

The variation diagrams of the relative energies of the spin-allowed bands in section 4.1.3.2 were calculated using the Kestrel GUI. The ligand-field parameters used were: e_σ = 1950 cm^{-1}, e_π = 375 cm^{-1}, B = 830 cm^{-1}, and C was set arbitrarily large at 10000 cm^{-1}, which placed the spin-forbidden doublet bands very high in energy. Spin-orbit coupling was neglected.

Ligand-field calculations using the low symmetry ligand-field contributions (including off-diagonal elements) were calculated using a custom function which returns a local ligand-field matrix for each alkyl ligand given by:

$$v = \begin{pmatrix} e_{\delta xy} + 0.57 & -24.72 & 0.46 & 33.64 & -0.13 \\ -24.72 & e_{\pi x} - 0.245 & -0.12 & -0.16 & 31.57 \\ 0.46 & -0.12 & e_\sigma & -0.33 & 0.05 \\ 33.64 & -0.16 & -0.33 & e_{\pi x} + 0.245 & 24.77 \\ -0.13 & 31.57 & 0.05 & 24.77 & e_{x^2-y^2} - 0.57 \end{pmatrix} \quad (4.1)$$

where the matrix elements are taken from the results of the CASSCF(7, 5)/NEVPT2 AILFT calculations and supplemented with the ligand e_λ parameters (see section 4.1.2.2 for methodology of *ab initio* calculations and appendix 6.4 for the derivation of the local ligand-field matrix). Twisting the molecule then occurred by rotating the matrix v with the corresponding rotation matrix $\mathbf{R}$. Ligand-field calculations were carried out by calling Kestrel's run_calculation method, which takes the 5×5 ligand-field matrix as an input to define the ligand field.

4.1.2.1.2 Complex 2

The molecular geometry was taken from the reported x-ray crystal structure (CSD: HPYBCO02).[121] Because the pyrazole ligands asymmetrically π bond, the π bonding direction needs to be specified along with the coordinating atom positions. The pyrazole ligands were assigned to the coordinating nitrogen atoms and their local x directions were orientated towards their adjacent nitrogen atoms. The pyrazole ligands were assigned an e_σ and $e_{\pi y}$ parameter, as shown in Figure 4.3. The $e_{\pi x}$ parameter, representing in-plane π bonding, was constrained to 0 cm^{-1}.

Two separate parameter-space calculations were carried out: the first sought to reproduce the reported experimental d-d bands and their assignments; the second sought to reproduce the reported EPR g-factors and isotropic paramagnetic susceptibility variation with temperature.[126–128] The former varied B from 500 cm^{-1} to 1000 cm^{-1}, in increments of 50 cm^{-1}; C from 2000 cm^{-1} to 4000 cm^{-1}, in increment of 200 cm^{-1}; e_σ from 2000 cm^{-1} to 6000 cm^{-1}, in increments of 400 cm^{-1}; and $e_{\pi y}$ from -1000 to 1000 cm^{-1}, in increments of 200 cm^{-1}.

The parameter space that reproduced the magnetic data linked the value of e_σ to $e_{\pi y}$ using the relation:

$$3e_\sigma = 2e_{\pi y} + 10000\ \text{cm}^{-1} \tag{4.2}$$

The parameters B and C were held at 830 cm^{-1} and 3403 cm^{-1} (C/B = 4.1), whilst ζ was varied from 300 cm^{-1} to 500 cm^{-1}, in increments of 20 cm^{-1}; k_{iso} from 0.5 to 1.0, in increments of 0.05; and $e_{\pi y}$ from -1000 cm^{-1} to 1000 cm^{-1}, in increments of 200 cm^{-1}.

The geometric distortions of complex 2 were applied to the x-ray crystal structure geometry. Geometry distortions were applied to the relevant θ and φ parameters of the ligand-field potentials.

4.1.2.1.3 Complex 3

The molecular geometry was taken from the reported x-ray crystal structure (CSD: WAKHOI).[124] Because the amide ligands asymmetrically π bond, the π bonding direction needs to be specified along with the coordinating atom positions. The amide ligands were assigned to the coordinating nitrogen atoms and the local x directions were aligned with the adjacent carbon atoms. The ligand-field parameterisation was taken from the work of *Rechkemmer et al.*[124]

The reported best fit ligand-field parameters of *Rechkemmer et al*. were supplemented with a k_{iso} value. An optimal value of k_{iso} was found by performing an optimisation calculation where k_{iso} was allowed to vary between 0.0 and 1.0 (with a starting value of 0.5). The optimisation was performed on both the reported EPR g-factors and isotropic paramagnetic susceptibility variation with temperature.

The geometric distortions of complex 3 were applied to the x-ray crystal structure geometry. Geometry distortions were applied to the relevant θ, φ, and ψ parameters of the ligand-field potentials.

4.1.2.2 Quantum-chemical calculations

Calculations carried out on **1** were performed using version 4.2.1 of the ORCA software package.[42] The x-ray crystal structure (CSD: FIYMEI) was used for the calculation.[122] In all calculations, the def2-TZVP basis set was applied to all atoms.[129] The /C Auxiliary basis set was used along with the RIJCOSX approximation to accelerate the calculations.[130] Nonrelativistic energy levels and wave functions for **1** were computed using the CASSCF method, averaging over the electron densities of all 40 quartet and 80 doublets roots for seven electrons distributed over five 3d molecular orbitals [CAS(7,5)]. To account for dynamic correlation, N-electron valence perturbation theory to second order (NEVPT2) was used as implemented in the ORCA program.

4.1.2.3 Calculation of τ_{QTM} and U_{eff}

Computation of the effective energetic barrier U_{eff} and the relaxation time was carried out using the same methodology of *Fang et al*. who used the work of *Bing et al*.[119,120] The time of relaxation for QTM within a KD is related to the relaxation rate, ω_{QTM} by

$$\tau_{QTM} = \frac{1}{2\omega_{QTM}} \tag{4.3}$$

$$\omega_{QTM} = \frac{\mu_B \langle B \rangle}{h} \cdot \frac{{g_{xy}}^2}{2\sqrt{{g_{xy}}^2 + {g_z}^2}} \tag{4.4}$$

where μ_B and h are the Bohr magneton and Planck's constant, respectively. $\langle B \rangle$ is the average magnetic field strength (assumed 20 mT) and $g_{xy} = \sqrt{g_x^2 + g_y^2}$. The effective energetic barrier U_{eff} and time for relaxation are then given by

$$U_{eff}(T) = \sum_i \frac{\omega_{QTM,i}^{eff}(T) E_i}{N}, \quad N = \sum_i \omega_{QTM,i}^{eff}(T) \tag{4.5}$$

$$\omega_{QTM,i}^{eff} = \gamma \frac{\exp\left(-E_i / k_B T\right)}{Z} \cdot \frac{{g_{xy}}^2}{2\sqrt{{g_{xy}}^2 + {g_z}^2}}, \quad Z = \sum_i \exp\left(-E_i / k_B T\right) \tag{4.6}$$

where i is the index of the KD (starting from the ground state), k_B is the Boltzmann constant, and T is the temperature.

4.1.3 Complex 1

Detailed experimental ligand-field analyses of linear complexes are limited and analysis of two-coordinate transition-metal complexes often use *ab initio* calculations.[131–135] The *ab initio* calculations, when analysed with a ligand-field model, suggest large e_π interactions (>1000 cm^{-1}) for formally σ-bonding only ligands such as alkyl ligands, or the in-plane direction of an sp^2 hybridised ligand such as an amide. The origins of large e_π effects associated with non-bonding interactions have been attributed to electrostatic contributions and are found in *ab initio* calculations of linear and square planar systems.[20,135,136] These large and anomalous e_π parameters predicted by theoretical calculations are still yet to be verified by a ligand-field analysis of experimental data. Complex **1**, whose detailed spectroscopic characterisation has been reported, provides a useful test case to study the e_π parameter of a formally non π bonding alkyl ligand.[122]

Complex **1** features a formal non-Aufbau electronic configuration ground state characterised by $\delta^3\pi^3\sigma^1$, where δ = (d_{xy}, $d_{x^2-y^2}$), π = (d_{yz}, d_{xz}), and σ = (d_{z^2}).[122] The ligand field has been probed previously by the work of *Bunting et al*. using CASSCF(7, 5)/NEVPT2 calculations, which predicted an orbital splitting of 0, 2913, and 5639 cm^{-1} for the one-electron levels δ, π, and σ respectively.[122] These results imply an e_σ = 2819.5 cm^{-1} and an e_π = 1456.5 cm^{-1}, the latter of which is large for a ligand presumed to not engage in formal π bonding. This system was characterised spectroscopically by *Bunting et al*. using UV-vis diffuse reflectance spectroscopy, far-infrared spectroscopy, and SQUID magnetometry.[122] Although the *ab initio* results are in relative agreement with the experimental magnetic properties and zero-field splitting, the calculated relative energies of the two observed spin-allowed d-d bands (13537 cm^{-1} and 18865 cm^{-1}) are too high when compared to the observed bands (12000 cm^{-1} and 15000 cm^{-1}) in the experimental UV-Vis spectrum, shown in Figure 4.4.

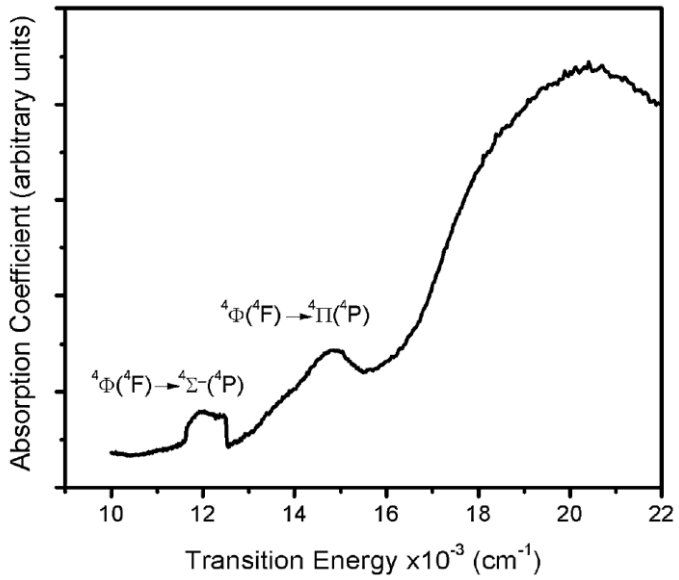

Figure 4.4. The UV-Vis diffuse reflectance spectrum of complex 1 reported by P. C. Bunting, M. Atanasov, E. Damgaard-Møller, M. Perfetti, I. Crassee, M. Orlita, J. Overgaard, J. van Slageren, F. Neese and J. R. Long, *Science*, 2018, 362, eaat7319. Reprinted with permission from AAAS.

The spectroscopic characterisation of **1** offers a deep insight into the electronic structures of linear ligand fields, which are promising candidates for 3d transition-metal SiMMs. The relatively weak ligand field of **1** allows for weaker crystal-field effects to have a greater influence on the electronic structure. An experimentally quantifiable splitting of the δ and π orbitals will allow for an empirical measure of the size of the crystal-field contribution to the e_π parameter.

4.1.3.1 Electronic structure from experiment, Kestrel analysis

The modelling of the electronic structure by *Bunting et al*. using *ab initio* calculations was not able to simultaneously reproduce the experimental d-d transition energies and experimental magnetic properties.[122] In this section, Kestrel is used to reproduce all of the available experimental data reported by *Bunting et al*. In doing so, the aim is to establish a ligand-field splitting and therefore quantify the magnitude of the e_π parameter.

The first step was to determine the ligand-field parameters (e_σ, e_π, and B) in Kestrel that can reproduce the experimental d-d transition energies. It was found that the two d-d bands energies could not be uniquely modelled with three parameters; the problem is

underdetermined. It was possible to set e_π = 0.0 cm^{-1}, reducing the degree of parameterisation in line with chemical intuition and reproduce the d-d band energies. However, it was also possible to assign the ligand a non-negligible and positive e_π parameter.

Since fitting the two spin-allowed d-d bands with three parameters is underdetermined, and *ab initio* calculations predict a substantial e_π value, the strategy was to obtain a reasonable set of best-fit parameters to the d-d band energies. This was achieved by finding the best fit values of e_σ and B for a fixed value of e_π. The e_π parameter was sampled across a range from 0 to 2500 cm^{-1} in increments of 250 cm^{-1}. Negative values of e_π were omitted as there are no formal π-acceptor functions on the alkyl anion and electrostatic contributions would have a destabilising effect (e_π > 0 cm^{-1}). The choice to set the upper bound of the e_π parameter to 2500 cm^{-1} was made on the basis that *ab initio* methods predict an e_π value of 1456.5 cm^{-1} and an e_π value close to, or greater than, 2500 cm^{-1} would be considered unphysical.[122]

Having outlined the strategy for producing a series of best fit parameters for different values of e_π, the values of e_σ and B were varied between values of 0 to 10000 cm^{-1}, and 0 to 1100 cm^{-1} respectively, for a fixed value of e_π. For each value of e_π sampled, there was one minimum within the scanned parameter space, as shown in Figure 4.5. As a general qualitative trend, as the value of e_π increased, the best fit value of e_σ decreased. At an approximate value of e_π = 1500 cm^{-1} (a similar magnitude as to that computed by *ab initio* theory), the best fit e_σ parameter was approximately equivalent. Herein lies the reason for the discrepancy between the *ab initio* computed d-d energies and the energies observed experimentally: the predicted e_σ:e_π ratio is too large for the computed predicted magnitude of e_π. The best fit values for e_π > 1500 cm^{-1} resulted in an alternative electronic structure where the d-orbital ordering is δ < σ < π as e_π > e_σ. The trend between the best fit values of Racah B with increasing e_π is different. When e_σ > e_π, then an increase in e_π resulted in an increase in B. However, when e_σ < e_π, then an increase in e_π resulted in a decrease in B.

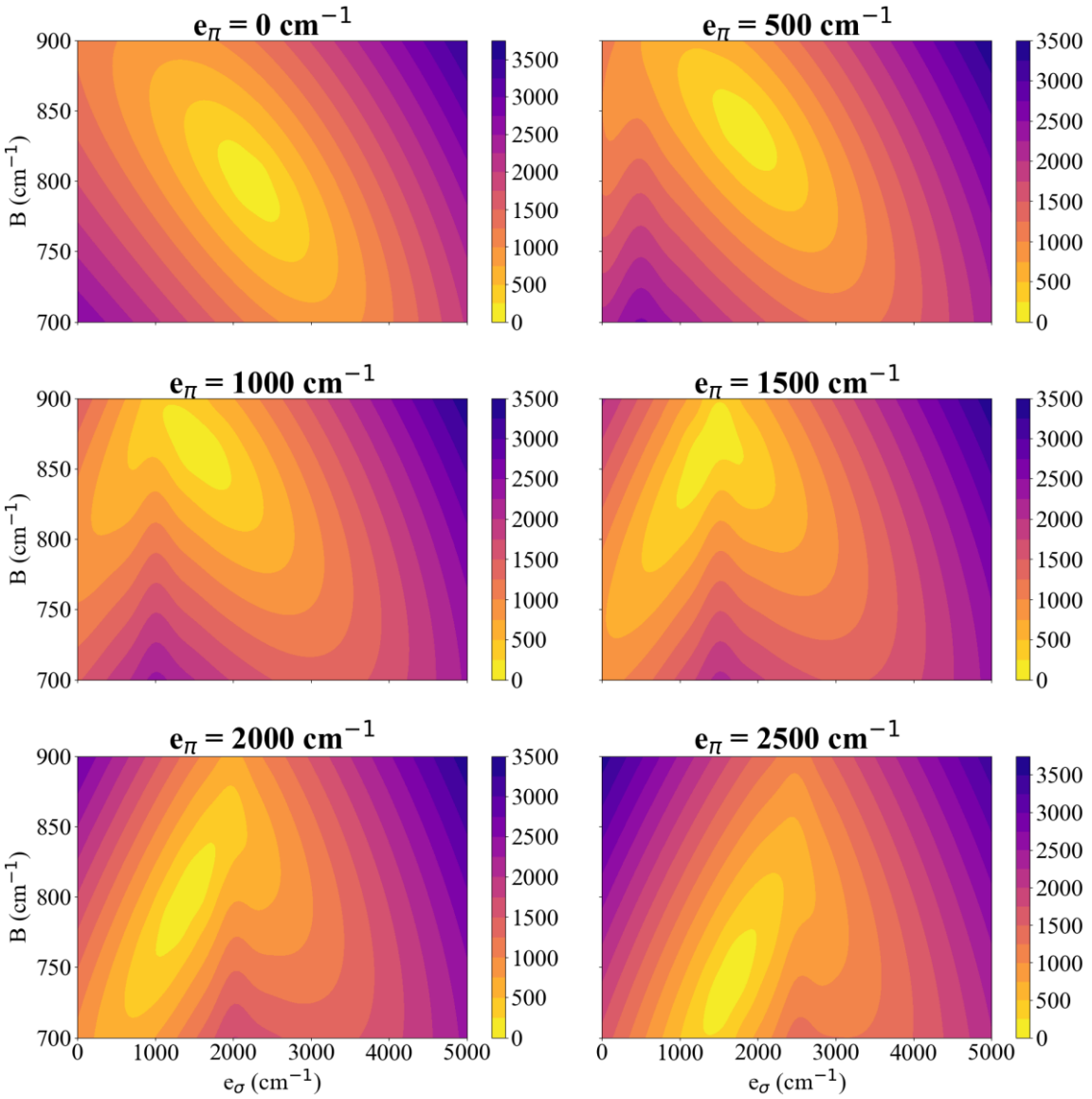

Figure 4.5. Regions of best fit for complex 1 in the reproduction of the two high energy quartet ligand-field transitions at 12000 and 15000 cm^{-1} with fixed values of e_π. Colour bars are the RMS fit (cm^{-1}) values to the two high energy quartet bands.

Reproduction of the high energy d-d bands alone is not sufficient for a unique determination of the electronic structure. The best fit parameters must also reproduce the reported zero-field splitting between the ground and the first excited state KD (450 cm^{-1}) and the reported experimental isotropic χT variation against temperature. Thus, using the free-ion ζ value of 515 cm^{-1}, the magnitude of the ZFS and the isotropic χT against temperature were computed for each value of e_π (along with the corresponding best fit values of e_σ and B).

Figure 4.6 shows the magnitude of the ZFS for each value of e_π and its best fit parameters. The graph clearly shows that for e_π values in the range of 0 cm^{-1} to 750 cm^{-1} the ZFS is greater than or equal to the experimentally observed energy separation. Hence, the fits to the d-d transition energies, where $e_\pi > 750$ cm^{-1}.

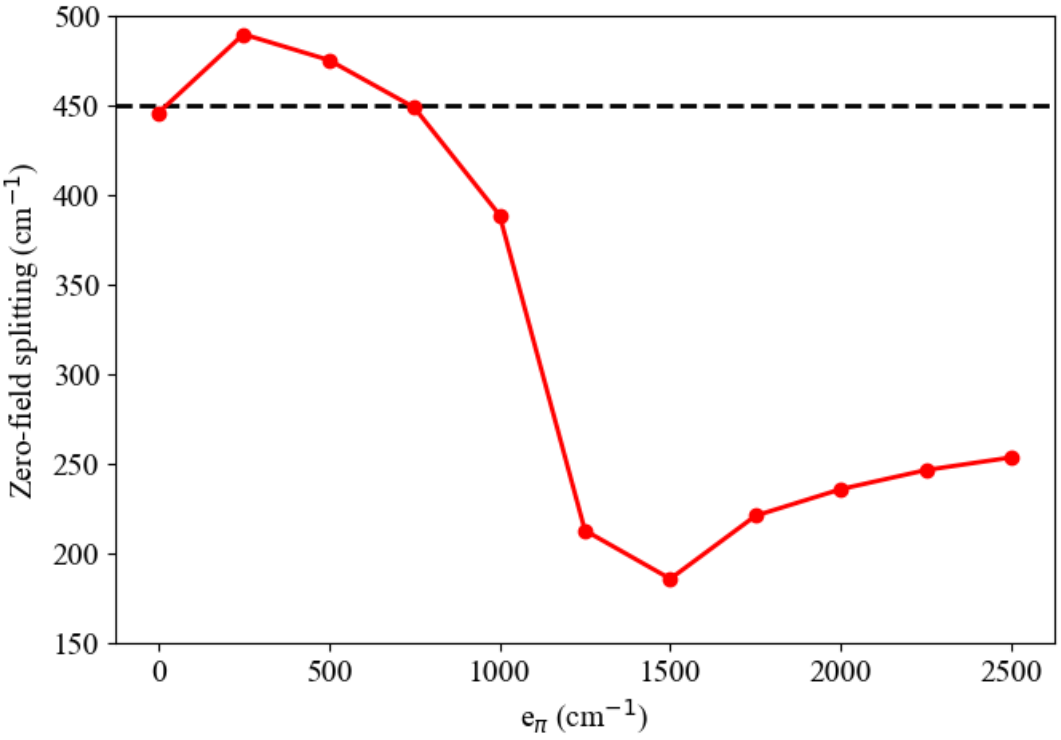

Figure 4.6. The variation in the computed zero-field splitting energy between the ground state and first excited state Kramer's doublet and the five lowest lying Kramer's doublets for the corresponding best fit e_σ and Racah B parameters, as a function of e_π, for complex 1. Zero-field splitting was calculated using a spin-orbit coupling constant of 515 cm^{-1}.

Bunting et al. report a room temperature χT value of 4.89 cm^3 K mol^{-1}.[122] For a low magnetic field (0.1 T) the χT tends to a value of around 4.3 cm^3 K mol^{-1} at low temperatures. The χT values as a function of temperature for the different values of e_π (with corresponding best fit e_σ and Racah B) are presented in Figure 4.7. Each graph offers a reasonable reproduction of the reported experimental data but the graphs for e_π = 250 cm^{-1} and e_π = 500 cm^{-1} closely resemble experiment.[122] Interestingly, the gradient of the graph at higher temperature (150 K to 300 K) is sensitive to the magnitude of the e_π parameter.

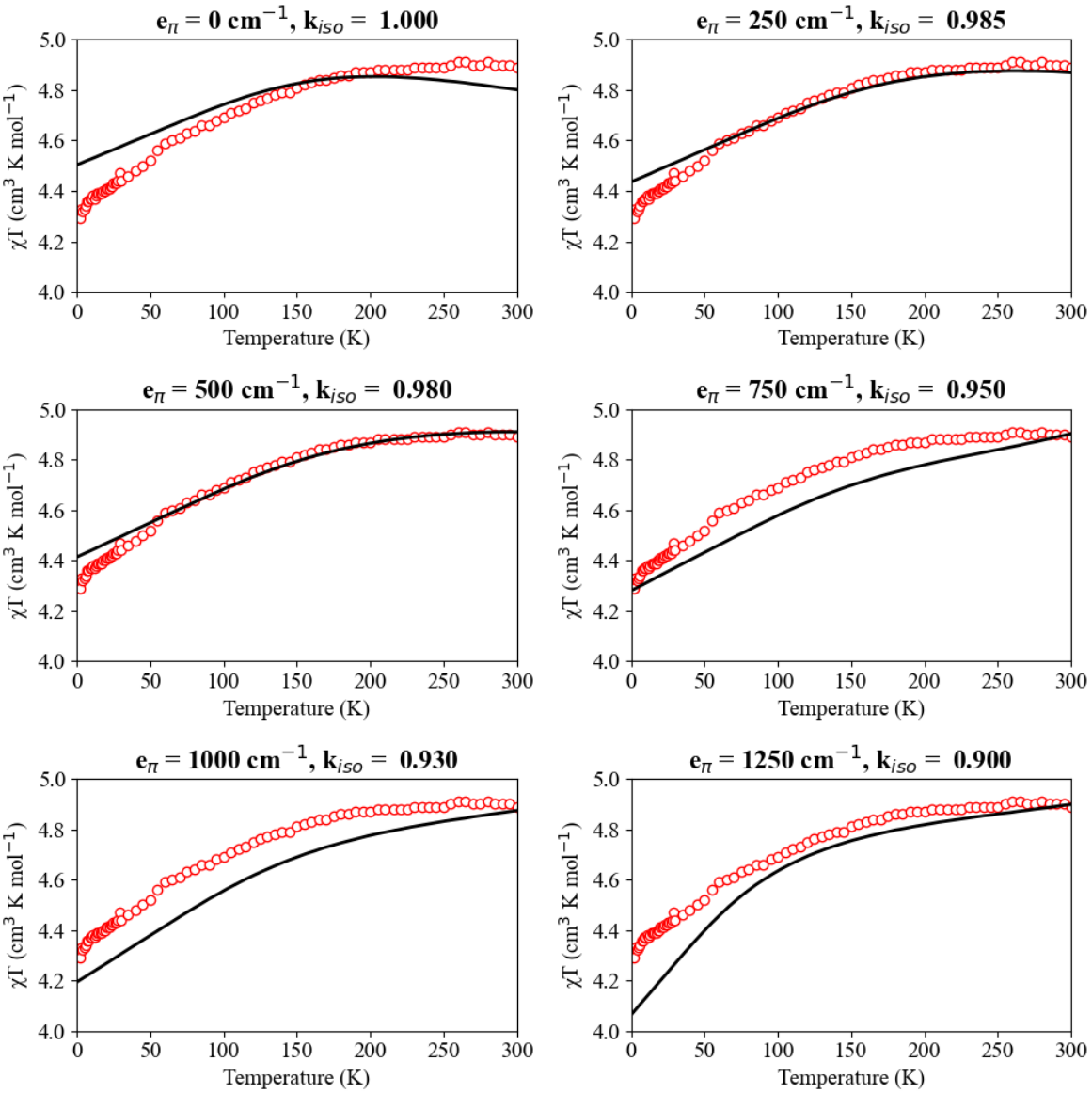

Figure 4.7. The Kestrel calculated (black) χT variation as a function of temperature for the corresponding best fit e_σ and Racah B parameters, as a function of e_π, for complex 1. The simulations were performed using a spin-orbit coupling constant of 515 cm^{-1}. The 0.1 T reported experimental data (red) was supplied by the authors.[122]

Having established a parameter-space range that accounts for the experimental d-d band energies, zero-field splitting, and paramagnetic susceptibilities, the best-fit parameter ranges are: e_σ = 1700 to 2200 cm^{-1}, e_π = 0 to 750 cm^{-1}, B = 800 to 855 cm^{-1}, ζ = 483 to 515 cm^{-1}, k_{iso} = 0.95 to 1.0 cm^{-1}, all of which are chemically reasonable. The average of these ranges gives the final illustrative best fit parameters: e_σ = 1950 cm^{-1}, e_π = 375 cm^{-1}, and B =

830 cm^{-1}. The introduction of spin-orbit coupling does shift the spin-allowed quartet band energies and this is compensated for by dropping Racah B to a value of 775 cm^{-1}. The final illustrative best fit parameters are: e_σ = 1950 cm^{-1}, e_π = 375 cm^{-1}, B = 775 cm^{-1}, C = 3100 cm^{-1}, ζ = 475 cm^{-1}, and k_{iso} = 0.99. This results in a room temperature χT = 4.91 cm^3 K mol^{-1} compared to the experimental value of 4.89 cm^3 K mol^{-1}.

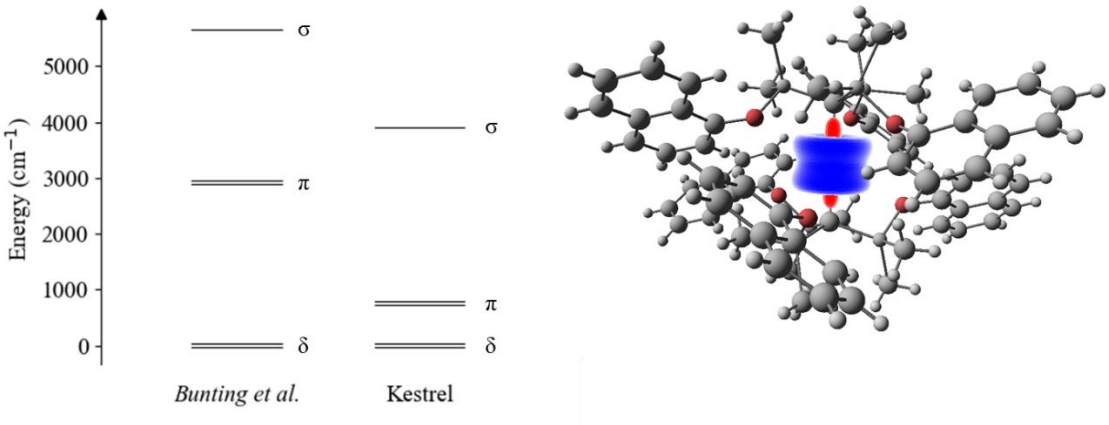

Figure 4.8. The ligand-field splitting as computed by *Bunting et al*. and this work, along with multipole expansion of the x-ray structure (right) for the average best fit parameters in the text.[122]

These best fit ligand-field parameters show a similar electronic structure to that reported by *Bunting et al*.[122] Compared to the one-electron d-orbital splitting found by *Bunting et al*. using *ab initio* calculations, the final illustrative best fit ligand field from Kestrel predicts a smaller energetic gap between the δ orbitals and the σ and π orbitals, shown in Figure 4.8. The smaller energetic gap (resulting from a smaller e_π potential) suggests that this electrostatic contribution is overestimated in *ab initio* theory.

4.1.3.2 Origins of the non-Aufbau ground state

The work of *Bunting et al*. established that the ground state of **1** features a non-Aufbau electronic configuration. Based on the extracted d-orbital splitting pattern of δ < π < σ, the ground state, according to the Aufbau principle for seven electrons, would be $\delta^4\pi^2\sigma^1$. However, the authors showed that the ground state of **1** was the $\delta^3\pi^3\sigma^1$ electronic configuration, where an electron has been promoted from one of the δ(d_{xy}, $d_{x^2-y^2}$) orbitals into one of the π(d_{xz}, d_{yz}) orbitals. Using the illustrative best fit parameters extracted from the previous section, Kestrel

also assigned the ground state as the $\delta^3\pi^3\sigma^1$ electronic configuration, in agreement with *Bunting et al*. The origin of this non-Aufbau ground state was attributed to the relative strength of the interelectronic repulsion with respect to the relatively weak ligand field. To confirm this in Kestrel's ligand-field model, the energies of the quartet electronic states were plotted against the strength of the interelectronic repulsion, shown in Figure 4.9.

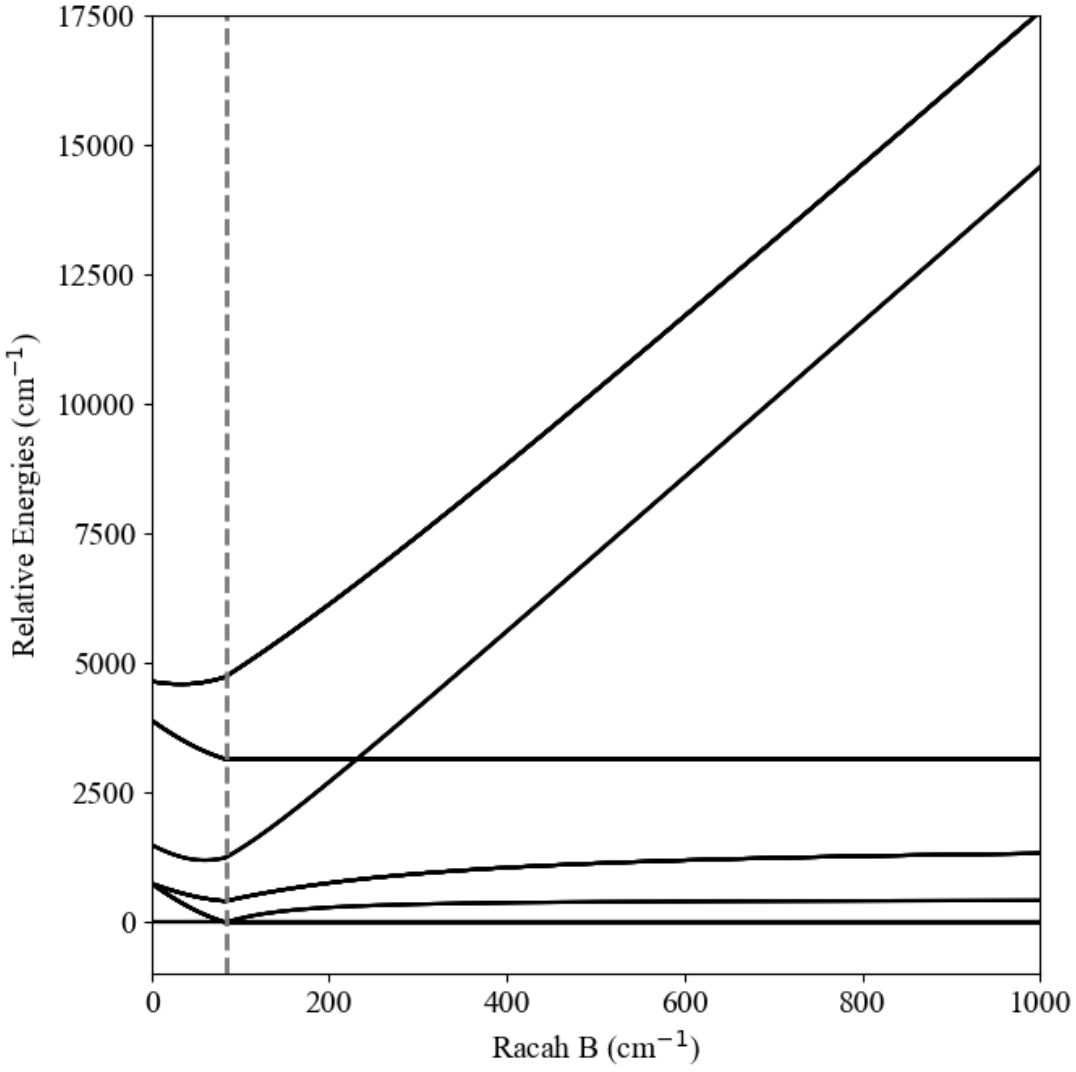

Figure 4.9. The change in relative energies of the complete quartet manifold as a function of the interelectronic repulsion parameter, Racah B. The grey dotted line signifies the interelectronic repulsion strength in which a change in the ground state character occurs.

Figure 4.9 ranges from an absence of interelectronic repulsion (B = 0 cm^{-1}) to near free-ion values using the illustrative best fit parameters (in the absence of spin-orbit coupling). As B is increased from 0 cm^{-1}, the relative energies of the quartet excited states from the ground state decrease. At a value of B around 83 cm^{-1} there is a discontinuity (grey dotted line) in the smooth variation of the energies. After which, increasing B dramatically increases the energy of the two highest excited states and increases the energy of the first two excited states more mildly; the third excited state is invariant to changes in interelectronic repulsion strength. Discontinuities like that observed here are also found in Tanabe-Sugano diagrams for d^4, d^5, d^6, and d^7 electronic configurations, where the discontinuity marks a formal change in the spin quantum number of the ground state (changing from high spin to low spin).[137] However, in the present case there is no change in the spin quantum number of the ground state. Instead, an inspection of the quantum number projections of the eigenfunctions show that this discontinuity marks a formal change in the L (orbital angular momentum) quantum number of the ground state. For B < 83 cm^{-1}, the ground state is predominantly L = 1 (^4P). For B > 83 cm^{-1}, the ground state is characterised by the L = 3 (^4F) quantum number. Care must be taken here to not associate an electronic occupation with an M_L quantum number ($M_L = \sum m_l$) derived from L. The L quantum number is derived from the L^2 operator, whose operation on a ket is a function of recursive permutative operations.[138]

To understand the changes in electronic structures with the variation in Racah B, the relative energies, and electronic configurations, of the ground and excited states at B = 0 and 830 cm^{-1} are given in Table 4.1. In the absence of interelectronic repulsion, each eigenfunction constitutes of a pure electronic configuration. Indeed, these configurations can be derived manually in the absence of interelectronic repulsion (B = 0 cm^{-1}) since one knows the relative energies of the one-electron d orbitals ($\delta < \pi < \sigma$: 0 cm^{-1} < 750 cm^{-1} < 3900 cm^{-1}) and the relative energies of the quartet states will correspond to a linear combination of the one-electron orbital energies. As an example, take the relative energy of the eigenfunction Ψ_2 of 750 cm^{-1}; this is equivalent to the energy $E(\pi) - E(\delta)$ and therefore corresponds to the one-electron jump from the δ orbitals to the π orbitals from the Aufbau ground state. Hence, with an Aufbau ground state of $\delta^4\pi^2\sigma^1$ (at relative energy of 0 cm^{-1}), the first excited state is $\delta^3\pi^3\sigma^1$ and so on.

At the average value of B found in the preceding analysis (B ≈ 830 cm^{-1}), the ground state is a pure $\delta^3\pi^3\sigma^1$ non-Aufbau configuration. The Aufbau configuration is mixed into eigenfunctions Ψ_2 and Ψ_5. The interelectronic repulsion mixes configurations together, redistributing electrons through superposition to minimise the energy of repulsion. The results show that the Aufbau configuration $\delta^4\pi^2\sigma^1$ mixes with the configuration $\delta^2\pi^4\sigma^1$. With increased interelectronic repulsion, the Aufbau configuration that has doubly occupied $d_{x^2-y^2}$ and d_{xy} (δ^4)

orbitals is less stable than having doubly occupied d_{xz} and d_{yz} orbitals (π^4). This is because the δ orbitals occupy the same plane, whereas the π orbitals do not. Hence, the $\delta^4\pi^2\sigma^1$ configuration mixes more into the higher energy Ψ_5 eigenfunction, whereas $\delta^2\pi^4\sigma^1$ mixes more into the lower energy Ψ_2.

Table 4.1. The relative energies (cm^{-1}) and electronic occupations of the d orbitals using the representative best fit ligand-field parameters, e_σ = 1950 cm^{-1}, e_π = 375 cm^{-1}, C/B = 4.0, and ζ = 0.0 cm^{-1}.

Eigenfunctions	Energy (B=0 cm^{-1})	Configuration	Energy (B=830 cm^{-1})	Configuration
Ψ_1	0.0	100% $\delta^4\pi^2\sigma^1$	0.0	100% $\delta^3\pi^3\sigma^1$
Ψ_2	750	100% $\delta^3\pi^3\sigma^1$	419	75.7% $\delta^2\pi^4\sigma^1$ 24.3% $\delta^4\pi^2\sigma^1$
Ψ_3	750	100% $\delta^3\pi^3\sigma^1$	1290	73.2% $\delta^3\pi^3\sigma^1$ 26.8% $\delta^2\pi^3\sigma^2$
Ψ_4	1500	100% $\delta^3\pi^2\sigma^2$	3150	100% $\delta^3\pi^2\sigma^2$
Ψ_5	3900	100% $\delta^2\pi^4\sigma^1$	12031	75.7% $\delta^4\pi^2\sigma^1$ 24.3% $\delta^2\pi^4\sigma^1$
Ψ_6	4650	100% $\delta^2\pi^3\sigma^2$	15060	73.2% $\delta^2\pi^3\sigma^2$ 26.8% $\delta^3\pi^3\sigma^1$

Having established the eigenfunctions and their configurational character, it is possible to rationalise changes in electronic structure due to changes in bonding. Changes in e_λ and the corresponding variation in the quartet state energies are given in Figure 4.10. The variation in e_σ shows a discontinuity at the value of 375 cm^{-1} (equal to e_π), where the ground state changes from σ > π > δ to π > σ > δ. Focusing on the σ > π > δ region, we can see that Ψ_2 and Ψ_5 are invariant to changes in the energy of d_{z^2}. This is because the electronic occupation of σ does not change upon the transition from the ground state to either excited state; both eigenfunctions are mixed $\delta^4\pi^2\sigma^1$ and $\delta^2\pi^4\sigma^1$ configurations. We also observe a differing energetic gradient in the energies of the other excited states, where their sensitivity to e_σ is of the order $\Psi_4 > \Psi_6 > \Psi_3$. These excited states do feature an occupational change of the σ level from the ground state. Their respective sensitivities correlate with the percentage character of a configuration with σ^2 character.

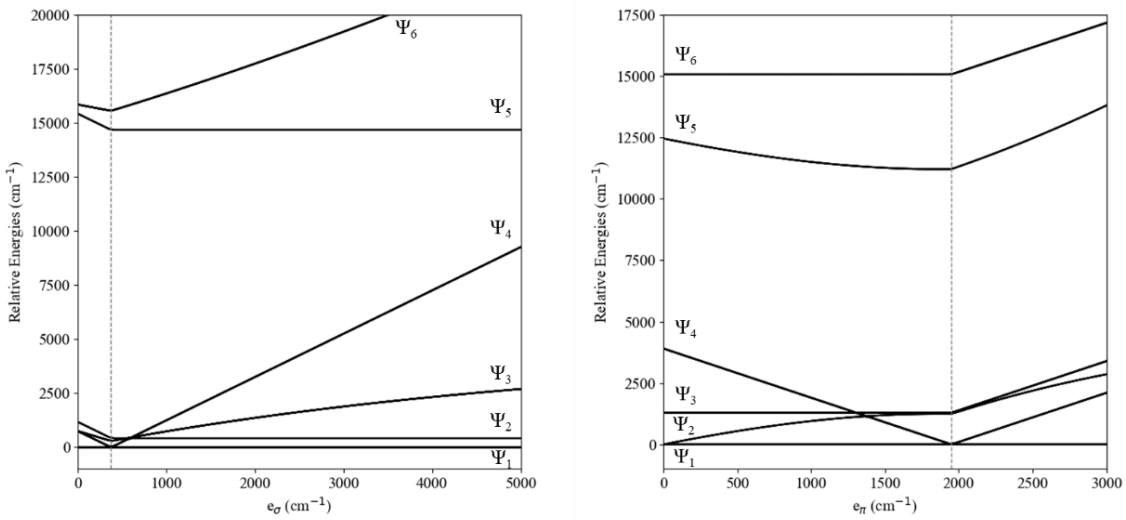

Figure 4.10. The effect that metal-ligand bonding parameters have on the relative energies of the quartet manifold. Variation of e_σ (left) and e_π (right). Grey dotted lines mark a formal change in the ground state electronic configuration.

Similar correlations with electronic occupations are observed in the case of the variation in e_π. The variation in e_σ shows a discontinuity at the value of 1950 cm^{-1} (equal to e_σ), where the ground state changes from σ > π > δ to π > σ > δ. Focusing on the σ > π > δ region, it is Ψ_3 and Ψ_6 that are invariant to changes in e_π. Again, this is due to equal electronic occupation of the π orbitals between ground and excited states. However, Ψ_2, Ψ_4, and Ψ_5 do feature a change in the electronic occupation of the π orbitals and likewise their sensitivity to the energy of those π orbitals correlates with the percentage character of that configurational change in electronic occupation.

4.1.3.3 Low-symmetry components of a linear complex

The model uses a linear ligand field and none of the available experimental data that was analysed in section 4.1.3.1 contains any information on the actual symmetry of the complex. Unfortunately, neither the EPR g-factors nor the paramagnetic susceptibility tensor for **1** have been reported. However, the relaxation time for QTM within the ground state, extracted from experimental relaxation data, has been reported as 16.4 s at 1.8 K.[122]

From equation (4.3), the relaxation time for QTM is a function of the ground state g-factor anisotropy and contains information about the linearity of the electronic structure. The ligand field used thus far is essentially of $D_{\infty h}$ symmetry, where the π(d_{xz}, d_{yz}) and δ(d_{xy}, $d_{x^2-y^2}$)

orbitals are degenerate within their π and δ levels, respectively. As a result, the EPR g-factors within the ground state are calculated as g_z = 11.94 and g_x = g_y = 0.0. The calculated g_x, and g_y values are negligible to machine precision and hence the resulting computed value of τ_{QTM} tends towards infinity. Of course, this is unphysical and in contradiction with the reported time taken (16.4 s); there must be a transverse magnetic moment contribution to give non-zero values of g_x and g_y. Assuming the value of ⟨B⟩ to be 20 mT, the order of magnitude of g_x and g_y (using a g_z of 11.94) in the ground state KD should approximately be 10^{-5}, a value that would otherwise be negligible. However, and as the analysis will reveal, the calculated value of τ_{QTM} is highly sensitive to the magnitudes of g_x and g_y. The question therefore arises: what low symmetry effects cause a non-zero value of g_x and g_y? To generate a transverse magnetic moment there must be a splitting in the π and δ orbitals, which requires separate values of $e_{\pi x}$ and $e_{\pi y}$ and $e_{\delta xy}$ and $e_{\delta x2\text{-}y2}$.

To investigate the source of the anisotropy, a CASSCF(7, 5)/NEVPT2 calculation was carried out on the full x-ray crystal structure of **1**. The calculations agree with the results of *Bunting et al*. and the extracted 5×5 one electron ligand-field matrix unambiguously show off-diagonal matrix elements which originate from the trigonal components of the S_6 symmetry of **1**.[122] Indeed, non-zero off-diagonal elements are found for $\langle d_{xy}|V|d_{yz}\rangle$, $\langle d_{xy}|V|d_{xz}\rangle$, $\langle d_{x^2-y^2}|V|d_{yz}\rangle$ and $\langle d_{x^2-y^2}|V|d_{xz}\rangle$ with an average magnitude of ≈ 57 cm^{-1}. All other off-diagonal matrix element magnitudes are < 1.0 cm^{-1}. The origin of these off-diagonal elements coupling π and δ d orbitals is likely a result of the electrostatic contribution of the second-sphere coordination shell Si and O atoms (appendix 6.3). The 5×5 one-electron ligand-field matrix also revealed a small breaking of the degenerate d_{xz} and d_{yz} (magnitude of ≈ 1.0 cm^{-1}) and d_{xy} and $d_{x^2-y^2}$ (magnitude of ≈ 2.3 cm^{-1}) orbitals.

It would appear from the results of the CASSCF/NEVPT2 calculations that to simulate the low symmetry components of the complex, the ligand-field model must recognise the true local symmetry of the alkyl ligands. To be clear, the e_σ and e_π parameters used to define the ligand field of the alkyl ligands are diagonal perturbations and do not simulate the local trigonal symmetry. To simulate the local trigonal symmetry, off-diagonal perturbative elements must be defined and rotated from the local ligand frame to the global coordinate frame as defined in chapter 2.3.2. The strategy of modelling the low symmetry trigonal crystal/ligand field of the alkyl ligands began by taking the CASSCF computed 5×5 one-electron ligand-field matrix for each ligand and reconstructing them using the best fit e_π and e_δ values. By doing this, the small (presumably) crystal-field effects are extracted from the *ab initio* calculations carried out in this work and supplemented by the best fit e_λ parameters to the experimental values. To do this, the off-diagonal elements are fixed and the asymmetry in $e_{\pi x}$ and $e_{\pi y}$ and in $e_{\delta xy}$ and $e_{\delta x^2-y^2}$ predicted by CASSCF are conserved. The representative best fit diagonal e_σ and e_π (1950

and 375 cm^{-1}, respectively) are added to the relevant diagonal elements to give the local ligand-field frames for both ligands. The local ligand frames computed in this way are given in appendix 6.4. This allows for calculations to be run with Kestrel using the same best fit e_λ parameters but now including a trigonal crystal-field perturbation, predicted by *ab initio* calculations. Using this parameterisation in Kestrel gives a computed τ_{QTM} of ≈ 35 s in good agreement with the experimental value. Note that recreation of the order of magnitude of τ_{QTM} is required here, since the computed value also depends on an average internal magnetic field. The magnitude of the internal magnetic field is not known but is assumed a value of 20 mT in line with the literature.[119] It is important to note that the off-diagonal elements alone do not generate a transverse magnetic moment in the ground state, but lead to breaking of the π and δ level degeneracies are broken by adopting different values of $e_{\pi x}$ and $e_{\pi y}$, and $e_{\delta xy}$ and $e_{\delta x^2-y^2}$, and this generates the transverse magnetic moment.

4.1.3.4 Enhancing the single-ion molecular magnetic properties, using Kestrel in a predictive sense

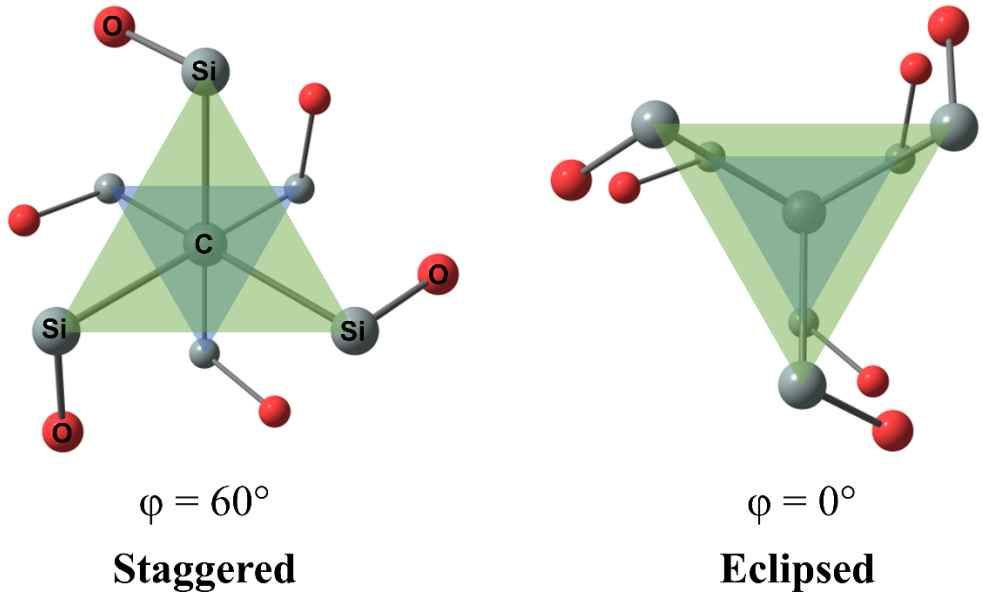

Figure 4.11. The geometric distortion between the two trigonal arms of the ligands in complex 1.

An analysis carried out by *Fang et al.*, showed that by twisting the two alkyl ligands from a staggered to an eclipsed conformation, as shown in Figure 4.11, the τ_{QTM} could be significantly increased.[120] *Fang et al*. used *ab initio* computed g-factors of a truncated molecule to calculate U_{eff} and τ_{QTM}. Here, Kestrel is used to calculate the same properties but using a ligand-field model.

4.1.3.4.1 The single-ion molecular magnetic properties of complex 1

Using the low-symmetry local ligand frames for the staggered conformation (*vide supra*), the relative energies and g-factors of the five lowest lying KDs were calculated in Kestrel and the results are shown in Table 4.2. The calculated ZFS energies are lowered from those calculated in fitting the experimental data because the low symmetry ligand frames reduce the axiality. The experimentally reported ZFS of the first excited KD (KD_2) can be restored by increasing the spin-orbit coupling parameter to 500 cm^{-1}. However, going forward, the best fit ligand-field parameters are used.

One can observe in Table 4.2 that the ground state KD (KD_1) exhibits the slowest rate for QTM and has the smallest g_x and g_y components. Indeed, the relative time taken from QTM to occur is inversely proportional to the magnitude of the g_x and g_y components. KD_3 has the fastest rate for QTM, which is consistent given that the magnetic transition dipole moment is non-zero between states where $\Delta M_J \pm 1$.[138] Since the rate of QTM to occur within KD_2, KD_3, and KD_5 are magnitudes faster than the rate of QTM to occur in KD_1 or KD_4, the Orbach relaxation mechanism is more likely to occur through the former, depending on thermal occupation.

Table 4.2. The Kestrel calculated energies (cm^{-1}) and g-factors of the five lowest lying Kramer's doublets using the low-symmetry parameterisation of 1 with the x-ray structure. Calculations performed using ζ = 475 cm^{-1} and k_{iso} = 0.99.

KD	M_J	Energy	g_x	g_y	g_z	τ_{QTM} (s)
KD_1	±9/2	0.0	0.2226×10^{-4}	0.2706×10^{-4}	11.8647	34.5
KD_2	±7/2	428.7	1.1000	1.0995	7.3423	1.1×10^{-8}
KD_3	±1/2	735.8	3.1010	3.0857	1.1686	8.5×10^{-10}
KD_4	±3/2	896.5	0.0214	0.0023	5.3894	4.2×10^{-5}
KD_5	±5/2	964.5	2.0151	1.9996	2.7079	1.7×10^{-9}

The axiality of the system is influenced by σ and π bonding effects. Using the low symmetry ligand frames, an increase in e_σ and e_π result in further quenching of the QTM within the ground state KD. For values of e_σ = 2500 cm^{-1} and e_π = 750 cm^{-1}, a calculated value of τ_{QTM} = 207 s is predicted. Controlling the magnitude of the electrostatic e_π contribution is difficult. However, if cylindrical π bonding ligands could be used, this could enhance the axiality of the system.

4.1.3.4.2 The single-ion molecular magnetic properties of complex 1 as a function of φ

Next, the ligand frames were rotated to transform the molecule from the staggered conformation to an eclipsed conformation. The g-factors for the ground state KD are given in Table 4.3, as a function of the trigonal twist angle. There is a rapid increase in the time taken for QTM to occur as the molecule is distorted away from the staggered conformation, coinciding with an effective decrease in the magnitudes of g_x and g_y. This results in a four-fold increase in the time taken for QTM to occur in the ground state KD.

Table 4.3. The Kestrel calculated g-factors and time taken for quantum tunnelling of the magnetisation in the ground state Kramer's doublet (KD_1) of complex 1 as a function of φ.

φ (°)	g_x	g_y	g_z	τ_{QTM} (s)
60	0.2226×10^{-4}	0.2706×10^{-4}	11.8647	34.5
50	0.2480×10^{-4}	0.2058×10^{-4}	11.8698	40.8
40	0.1887×10^{-4}	0.1608×10^{-4}	11.8838	69.1
30	0.1142×10^{-4}	0.1019×10^{-4}	11.9030	181.5
20	0.4926×10^{-5}	0.4709×10^{-5}	11.9224	917.1
10	0.9770×10^{-6}	0.1045×10^{-5}	11.9366	20838.0
0	0.4460×10^{-6}	0.4461×10^{-6}	11.9418	107214.0

The energetic barrier to reversal of the magnetisation (U_{eff}) as a function of temperature was computed for three angles of the twist and the results are given in Figure 4.12. Up to a temperature of 25 K, for each angle, the U_{eff} barrier is effectively 0 cm^{-1}. For φ = 60° there is an increase in the U_{eff} at 25 K to the energy of the first excited KD (KD_2) At about 70 K the second excited KD (KD_3) begins to contribute and raises the barrier, but it is unable to saturate

within the temperature range. Comparing this with φ = 30°, the same rise at 25 K is observed but KD_3 begins to contribute at a lower temperature and saturates at around 200 K. Finally, at the eclipsed conformation φ = 0°, the rise at 25 K is associated with the saturation of KD_3, rather than with KD_2. Hence, proceeding from a staggered to an eclipsed geometry also quenches the Orbach relaxation via KD_2 and favours tunnelling through KD_3, which is characterised by an $M_J = \pm 1/2$, effectively raising the barrier of U_{eff} for lower temperatures. Interestingly, the energy of the KD (characterised by $M_J = \pm 1/2$) is a function of the strength of π donation of the axial ligand.

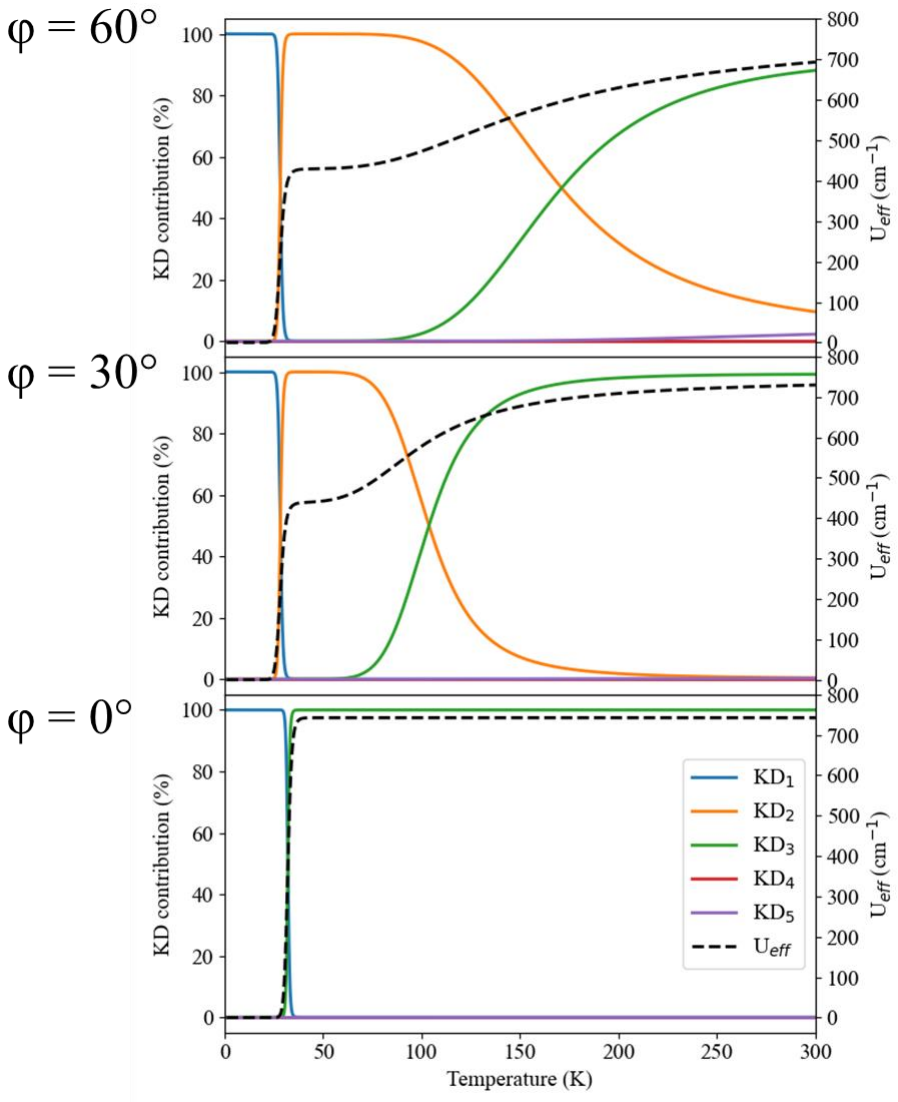

Figure 4.12. The variation of U_{eff} with temperature as a function of the trigonal distortion, φ. The percentage contribution of the five lowest energy $S=^3/_2$ Kramer's Doublets are also plotted. Calculations are performed using the low symmetry parameterisation of 1, ζ = 475 cm^{-1}, and k_{iso} = 0.99.

4.1.3.4.3 Future design considerations for enhancing the single-ion molecular magnetic properties of linear complexes

There are a few design principles to enhance the SiMM properties of linear complexes:

1. **Increase the symmetry.** The low-symmetry components of **1** arise from the crystal field, a perturbation that is hard to alter chemically. However, by twisting the two approximate trigonal ligands so that they eclipse one another removing the off-diagonal matrix elements. It would also be possible to use a ligand with a different local symmetry.
2. **Diminish the crystal field.** It is possible to effectively weaken the crystal field through changing the symmetry of the ligand field, but it is also possible to diminish its strength somewhat by moving the source of the crystal-field perturbations further away. Since the off-diagonal components are a function of the distance of the Si and O atoms, moving them further away would reduce their electrostatic contribution.
3. **Alter the chemistry.** Use a more donating ligand with either greater π or σ donation to increase the axiality of the system. Getting the balance of donating strength against reducing power is key to stabilising a linear cobalt(II) complex.

Kestrel has shown how low symmetry components of the ligand field, precisely the coupling of d_{xz} and d_{yz} to d_{xy} and $d_{x^2-y^2}$, can be reduced by removing the trigonal distortion and moving towards an eclipsed structure. However, the lowering of the symmetry caused by these off-diagonal matrix elements can also be mitigated by separating the energies of d_{z^2}, d_{xz}, and d_{yz} from d_{xy} and $d_{x^2-y^2}$. Hence, stronger π-donation or σ-donation can further quench the QTM in the ground state KD. This is a considerable chemical challenge though, as the synthesis of **1** required the reduction power of the carbanion to be diminished by including electron withdrawing alkoxides.

4.1.4 Complex 2

Complex **2** does not exhibit SiMM behaviour. It has an approximate anti-prismatic structure with a trigonal elongation (θ = 51.9°) and the coordinating pyrazolyl ligands are arranged in a staggered conformation. Trigonal D_3 structures have been of interest due to their large ZFS. However, the anti-prismatic conformation (staggered, φ = 60°) typically only exhibits SiMM behaviour in the presence of an applied static dc field.[121] In prismatic conformations (eclipsed, φ = 0°) the reported U_{eff}, obtained by fitting the kinetic magnetic relaxation time, is substantially smaller than the experimentally determined or predicted ZFS of the ground state energy levels.[139]

Complex **2** was chosen for analysis because it is homoleptic and extensively characterised spectroscopically. Exploring the effect that geometry and metal-ligand bonding of **2** on its potential SiMM behaviour will hopefully aid in the future design of six-coordinate trigonal cobalt(II) complexes to maximise their SiMM behaviour. The analysis establishes an electronic structure derived from the available experimental data and then looks at what effect geometric distortions have on the axiality of the complex. Then the metal-ligand bonding of the asymmetric π-bonding pyrazole ligand is probed to maximise axiality within the ideal geometry.

4.1.4.1 Electronic structure from experiment, Kestrel analysis

4.1.4.1.1 Fitting the reported experimental data

Before any ligand-field analysis of the SiMM behaviour can be carried out, reproduction of the available experimental data must first be accounted for. Complex **2** is characterised experimentally by a d-d spectrum with three spin-allowed bands centred at 11100 cm^{-1} ($^4T_{1g} \rightarrow {}^4T_{2g}$), 19400 cm^{-1} ($^4T_{1g} \rightarrow {}^4A_{2g}$), and 21800 cm^{-1} ($^4T_{1g} \rightarrow {}^4T_{1g}$).[126,127] The spectrum also features two formally spin-forbidden bands at 9100 cm^{-1} ($^4T_{1g} \rightarrow {}^2E_g$), and 15600 cm^{-1} ($^4T_{1g} \rightarrow {}^2T_{2g}$, $^2T_{2g}$). The EPR g-factors are known experimentally with values of $g_\perp$ = 1.02 and $g_\parallel$ = 8.48.[128] Likewise, the energetic splitting of the ground state and first excited state KDs is determined to be 197 cm^{-1}.[123] The isotropic $\chi_M T$ variation with temperature has also been characterised experimentally by SQUID magnetic measurements.[121]

The strategy used to fit the available experimental data was to first gain an estimation of the approximate ligand-field splitting and interelectronic repulsion parameters (B and C) by reproducing the d-d band energies. Keeping the ligand-field splitting and B and C fixed, the

individual metal-ligand bonding e_λ parameters, spin-orbit coupling, and orbital angular moment quenching (k_{iso}) were refined against the available magnetic data. Since **2** is homoleptic, each pyrazole ligand share a common e_σ and out-of-plane $e_{\pi y}$ parameter (see the methodology, section 4.1.2).

The ligand-field analysis of **2** began by considering, as a first approximation, an octahedral crystal field to reproduce the experimental d-d band energies and spin state assignments. In an octahedral crystal field, the experimental d-d spectrum would be characterised by an 10Dq = Δ_o = 11000 cm^{-1} and B = 830 cm^{-1} (C/B = 4.1). On its own, the d-d spectrum does not provide enough detail to fit both e_σ and $e_{\pi y}$ to the Δ_o value as they are linearly related by the relationship $\Delta_o = 3e_\sigma - 2e_{\pi x} - 2e_{\pi y}$, where $e_{\pi x}$ = 0 cm^{-1}. However, this does allow the interelectronic repulsion parameters to be fixed and does provide a useful constraint on the values of e_σ and $e_{\pi y}$.

Having established approximate values of the ligand-field splitting, B, and C, further refinement of the parameter values was carried out by reproducing the magnetic properties of **2**. For the calculation of magnetic properties, it is important to use a realistic structure and as such the x-ray crystal structure was used.[121] The magnetic properties were sensitive to the values of $e_{\pi y}$, ζ, and k_{iso} but insensitive to changes in e_σ. Keeping B and C fixed, e_σ was linearly linked to the value of $e_{\pi y}$ by the relationship $e_\sigma = {}^1/_3 (\Delta_o + 2e_{\pi y})$. The axial EPR g-factors ($g_{||} > g_\perp$) were reproduced using a positive $e_{\pi y}$ parameter value, assigning the pyrazole ligands as a π donor. The ratio of $g_{||} : g_\perp$ was controlled by the magnitude of the $e_{\pi y}$ parameter value. Variation of k_{iso}, ζ, and $e_{\pi y}$ found a fit to the EPR g-factors using the parameter values k_{iso} = 0.91, ζ = 440 cm^{-1}, and $e_{\pi y}$ = 410 cm^{-1}. The experimental d-d spectrum was still well reproduced with an e_σ = 3900 cm^{-1}. This resulted in final EPR g-factors of $g_{||}$ = 8.54 and $g_\perp$ = 1.021, 1.028, in excellent agreement with the reported experimental values. The same parameter set predicted values of χT of 2.36 cm^3 K mol^{-1} and 3.02 cm^3 K mol^{-1} at 1.8 K and 300 K, which agree with the reported experimental values of 2.16 cm^3 K mol^{-1} and 3.08 cm^3 K mol^{-1}, respectively.[121] The lower value observed at 1.8 K is likely a result of saturation effects not modelled with in Kestrel. The simulated variation of the isotropic χT with temperature is given in Figure 4.13. Finally the reported ZFS of 197 cm^{-1} is reproduced with a Kestrel calculated ZFS of 195.7 cm^{-1}.

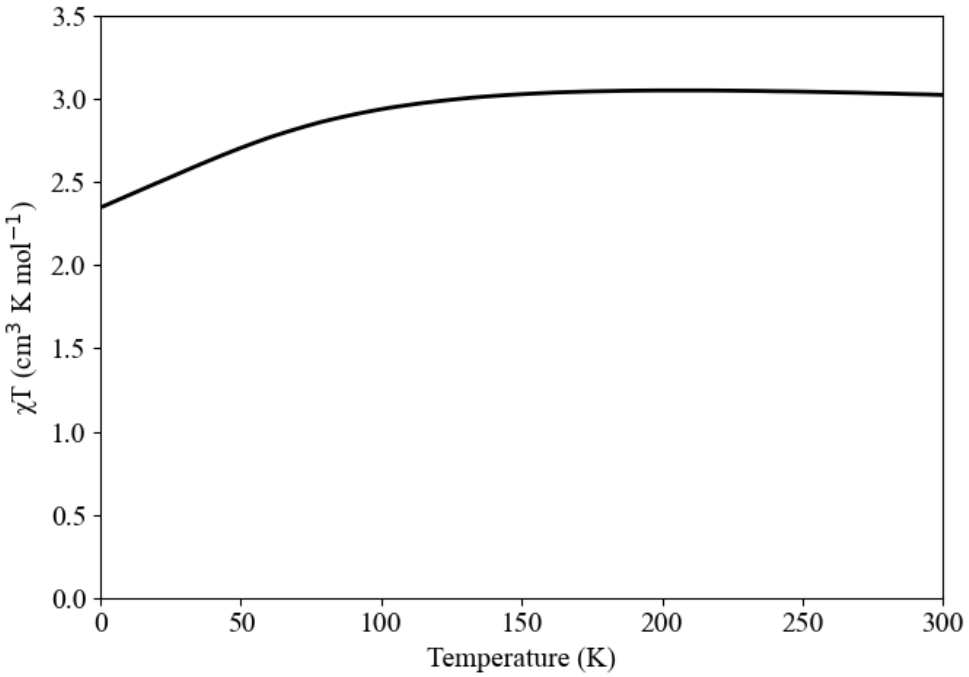

Figure 4.13. The Kestrel calculated isotropic χT variation with temperature for the best fit parameters of complex 2.

4.1.4.1.2 Analysis of the ligand-field splitting

The resulting ligand field from fitting the experimental data is shown in Figure 4.14. The calculated ligand-field splitting has an orbital ordering of d_{z^2} < $d_{x^2-y^2}$, d_{xy} << d_{xz}, d_{yz}. The d_{z^2} orbital is aligned towards the apical BH group of the Tp ligand. The higher energy d_{xz} and d_{yz} orbitals are aligned so that their lobes are directed towards the σ bonding interactions of the coordinating ligands; the lower lying $d_{x^2-y^2}$ and d_{xy} orbitals are aligned so that their lobes are interacting with the π interactions of the pyrazolyl ligands. This rotational feature is due to mixing that occurs between the free-ion d_{xz} and d_{yz} orbitals and the d_{xy} and $d_{x^2-y^2}$

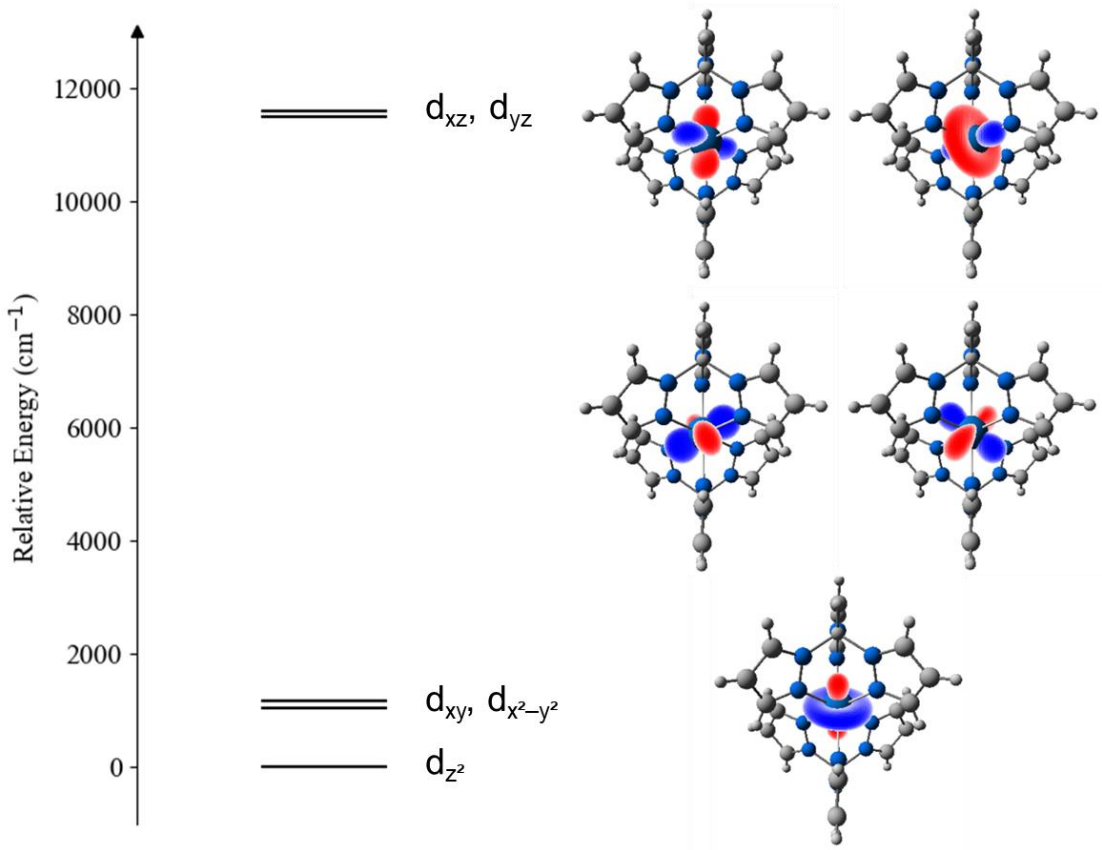

Figure 4.14. The Kestrel calculated ligand-field splitting diagram and Kestrel rendered orbitals for complex 2.

4.1.4.1.3 Analysis of the d-d transition energies

The configurational assignment of the spin-allowed and spin-forbidden bands in Kestrel allow for the relative oscillator strengths to be rationalised. The computed non-relativistic energies (in the absence of spin-orbit coupling) and their configurational composition are presented in Table 4.4.

The ground state $^4T_{1g}$ is split into three separate four-fold degenerate levels of 0.0, 8.0, and 1751.3 cm^{-1}. The principal configurational character is characterised by single electronic occupations of either d_{z^2}, $d_{x^2-y^2}$, or d_{xy}, and single occupation of both the d_{xz} and d_{yz} orbitals. The higher lying component at 1751.3 cm^{-1} is a result of the double occupation of the $d_{x^2-y^2}$ and d_{xy} orbitals. The double occupation of orbitals lying in the same plane will be energetically unstable with respect to the other two components at 0.0 or 8.0 cm^{-1} where the d_{z^2} and either the $d_{x^2-y^2}$ or d_{xy} is doubly occupied. Hence the small energy gap between the $d_{x^2-y^2}$ and d_{xy} orbitals is reflected in the small energy difference (8.0 cm^{-1}) between the ground state and first excited state KDs, where the $d_{x^2-y^2}$ or d_{xy} orbital is singly occupied.

The excited quartet bands at 11000 cm^{-1} and 21800 cm^{-1} (reported with extinction coefficients of ε = 3.4 M^{-1} cm^{-1} and 13.4 M^{-1} cm^{-1}, respectively[112]) are comprised of configurations where an electron has been excited from either the d_{z^2}, $d_{x^2-y^2}$, or d_{xy} into either the d_{xz} or d_{yz} orbitals. The $^4T_{1g} \rightarrow {}^4A_{2g}$ band at 19400 cm^{-1} corresponds to a double electron jump from the doubly occupied orbitals where the final configuration has the d_{z^2}, $d_{x^2-y^2}$, and d_{xy} as all singly occupied, and the d_{xz} and d_{yz} orbitals as both doubly occupied. This configuration has only a single spatial arrangement and the double electron jump explains the relative weakness of the band (ε = 1.3 M^{-1} cm^{-1}). However, the band has substantial admixture from the $(d_{z^2})^1(d_{x^2-y^2})^2(d_{xy})^1(d_{xz})^1(d_{yz})^2$ (15.3%) and $(d_{z^2})^1(d_{x^2-y^2})^1(d_{xy})^2(d_{xz})^2(d_{yz})^1$ (18.3%) configurations, which corresponds to one-electron jumps from the quartet levels at 0.0 and 8.0 cm^{-1} respectively. This configurational mixing contributes to the relative oscillator strength of the band.

Both the spin-forbidden bands $^4T_{1g} \rightarrow {}^2E_g$ and $^4T_{1g} \rightarrow {}^2T_{2g}$, $^2T_{2g}$ are also reproduced. The former is made up of approximately 50:50 $(d_{z^2})^2(d_{x^2-y^2})^2(d_{xy})^2(d_{xz})^1(d_{yz})^0$ and $(d_{z^2})^2(d_{x^2-y^2})^2(d_{xy})^2(d_{xz})^0(d_{yz})^1$. The latter band has a more complicated electronic configurational occupation, which is comprised of configurations where a single unpaired electron occupies the d_{z^2}, $d_{x^2-y^2}$, or d_{xy} set of orbitals. The higher lying d_{xz} and d_{yz} set are either both singly occupied, or one is doubly occupied whilst the other is vacant. Hence, the $^4T_{1g} \rightarrow {}^2T_{2g}$, $^2T_2$ band is preferentially destabilised by greater interelectronic repulsion. The bands are also very weak in the experimental spectrum (ε = 0.4 and 0.1 cm^{-1} M^{-1}, respectively) and this is due a small admixture of quartet spin-allowed character (1%) when spin-orbit coupling is included.

Table 4.4. Reported experimental and Kestrel calculated non-relativistic transition energies (cm^{-1}).[126,127] The largest configurational contributions are included which together account for 99% of the configurational character of the electronic band. The configurational nomenclature 22111 = $(d_{z^2})^2(d_{x^2-y^2})^2(d_{xy})^1(d_{xz})^1(d_{yz})^1$.

Assignment	Energy (experimental)[126]	Energy (Kestrel)	Configuration
$^4T_{1g}$	0.0	0.0	94.8 % 22111 2.8 % 21121 1.4 % 11221
		8.0	95.0 % 21211 3.0 % 21112 1.1 % 12121
		1751.3	91.1 % 12211 4.7 % 12112 4.2 % 11221
$^4T_{1g} \rightarrow {}^2E_g$	9100	7061.1	95.1 % 22210
		7094.9	95.1 % 22201
$^4T_{1g} \rightarrow {}^4T_{2g}$	11000	9913.7	55.4 % 21121 24.0 % 12112 20.5 % 11221
		9998.0	48.7 % 21112 32.4 % 12121 18.8 % 11212
		10517.7	58.0 % 11212 41.7 % 12121
$^4T_{1g} \rightarrow {}^2T_{2g}, {}^2T_{2g}$	15600	15533.3 15564.0 16094.5 16515.8 16522.0 16615.7	(see text)
$^4T_{1g} \rightarrow {}^4A_{2g}$	19400	(4) 20333.7	63.4 % 11122 18.3 % 11221 15.3 % 12112 2.9 % 12211
$^4T_{1g} \rightarrow {}^4T_{1g}$	21800	(4) 21662.6	41.0 % 21121 35.8 % 12112 17.3 % 11221 4.9 % 22111
		(4) 21684.8	48.0 % 21112 24.8 % 12121 22.2 % 11212
		(4) 22214.4	38.1 % 11221 36.0 % 11122 19.2 % 12112 5.6 % 12211

4.1.4.2 Enhancing the single-ion molecular magnetic properties

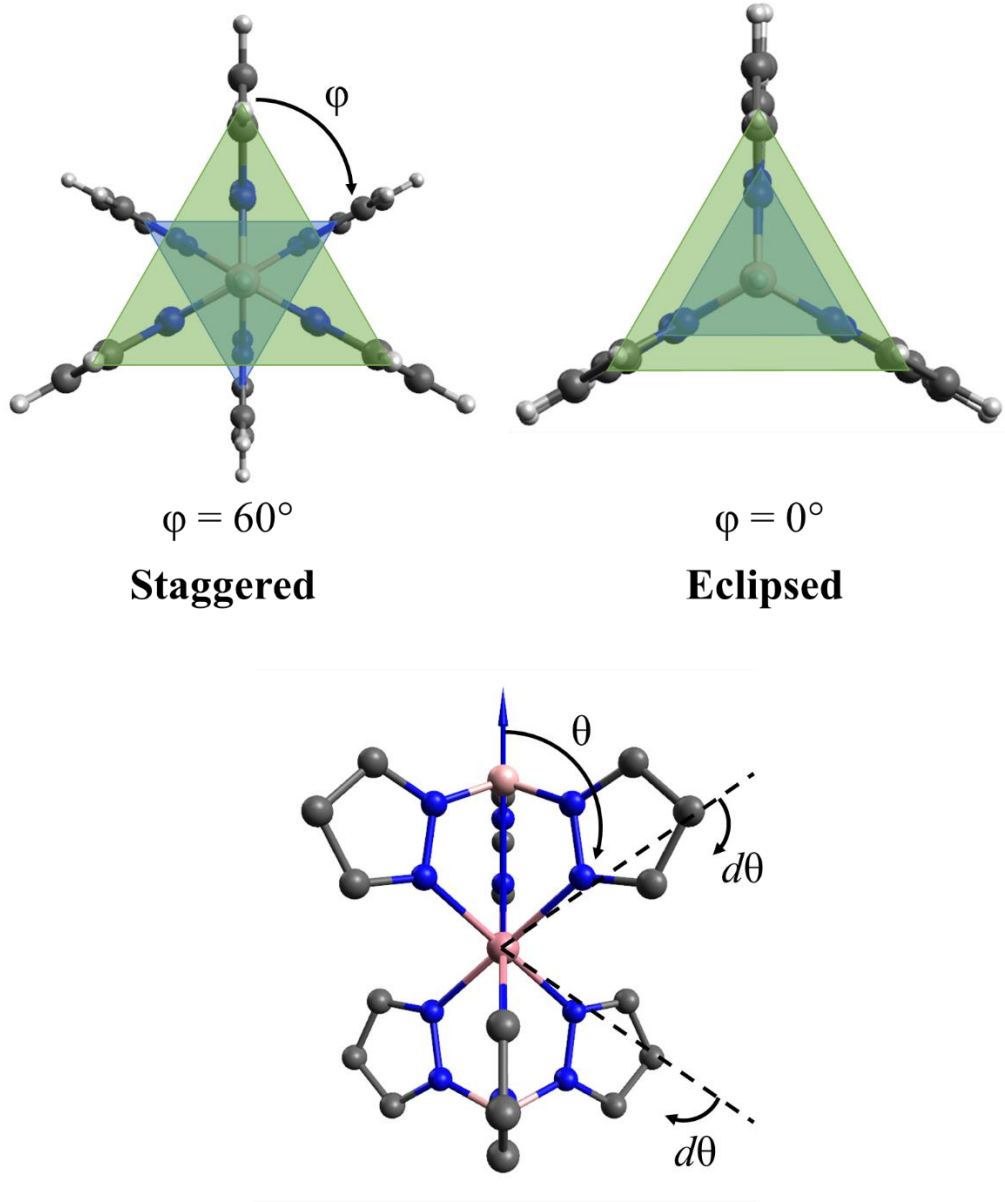

Figure 4.15. The geometric distortions φ, θ, and *d*θ of complex 2.

Theoretical work by *Zhang et al*. showed, using *ab initio* calculations, that if the structure were distorted from a staggered conformation to an eclipsed conformation, then the axial nature of the molecule is enhanced.[121] Inspired by this analysis, Kestrel was used to analyse the effects that geometry and metal-ligand bonding both play in the single-ion molecular magnetic properties of complex 2. Three geometric distortions (Figure 4.15) were investigated. The angle φ describes the "twist" angle made between the two tris(pyrazolyl)borate ligands, where

φ = 60° describes a staggered conformation (D_{3d}) and φ = 0° describes the eclipsed conformation (D_{3h}). The second angle θ describes the trigonal distortion, where θ < 54.74° for trigonal elongation, or θ > 54.74° for trigonal compression. The third angle, *d*θ describes the distortion angle for the tris(pyazolyl)borate ligands about the octahedral angle (θ = 54.74°).

4.1.4.2.1 The single-ion molecular magnetic properties of complex 2

The relative energies and g-factors of the four lowest lying KDs were calculated in Kestrel and the results are shown in Table 4.5. Unlike in complex 1, the ground state KD (KD_1) exhibits the fastest rate for QTM and has the largest g_x and g_y components of the KDs. This fast rate will be responsible for a large source of demagnetistion and hence explains why complex **2** does not exhibit SiMM behaviour in the absence of an external dc field. The time taken for QTM to occur within KD_1, KD_2, and KD_3 are two orders of magnitude faster than the time taken for QTM to occur in KD_4. Therefore, the Orbach relaxation mechanism is likely to occur via either KD_1, KD_2, or KD_3.

Table 4.5. The Kestrel calculated energies (cm^{-1}), g-factors, and time taken for quantum tunnelling of the magnetisation to occur for the four lowest lying Kramer's doublets of complex 2.

KD	M_J	Energy	g_x	g_y	g_z	τ_{QTM} (s)
KD_1	±7/2	0.0	1.0279	1.0214	8.5422	1.5×10^{-8}
KD_2	±5/2	195.7	0.5235	0.7238	4.4610	2.0×10^{-8}
KD_3	±3/2	415.9	0.0347	0.1906	0.6747	6.7×10^{-8}
KD_4	±1/2	674.4	0.0556	0.0829	3.2956	1.2×10^{-6}

4.1.4.2.2 The single-ion molecular magnetic properties of complex 2 as a function of φ

The g-factors and time taken for τ_{QTM} were calculated for KD_1 in Kestrel at different angles of φ and the results are shown in Table 4.6. Like with complex **1**, there is a rapid increase in the time taken for QTM to occur as the molecule is distorted towards the eclipsed conformation. This results in a seven-fold increase in the time taken for QTM to occur in KD_1 of the eclipsed conformation. This explains the observation that eclipsed structures are able to exhibit SiMM behaviour in the absence of an applied external dc field.[140–142] The source of axiality can be rationalised by comparing the symmetries of D_{3h} (eclipsed) to D_{3d} (staggered), where the off-

diagonal ligand-field matrix elements connecting the d_{xz} or d_{yz} to either d_{xy} or $d_{x^2-y^2}$ vanishes in the former.

Table 4.6. The Kestrel calculated g-factors and time taken for quantum tunnelling of the magnetisation to occur in the ground state Kramer's doublet (KD_1) of complex 2 as a function of the angle φ.

φ (°)	g_x	g_y	g_z	τ_{QTM} (s)
60	1.0279	1.0214	8.5422	1.5×10^{-8}
50	0.8930	0.8876	8.6456	2.0×10^{-8}
40	0.6062	0.6030	8.8655	4.4×10^{-8}
30	0.3376	0.3363	9.1038	1.4×10^{-7}
20	0.1479	0.1476	9.3433	7.7×10^{-7}
10	0.0369	0.0369	9.5501	1.3×10^{-5}
0	0.1427×10^{-3}	0.1490×10^{-3}	9.6360	0.81

The effective energy barrier (U_{eff}) was calculated for the select angles of φ: at 60°, 30°, and 0°, and the results are presented in Figure 4.16. Starting with the x-ray crystal structure (φ = 60°), the process of demagnetisation occurs primarily through KD_1, due to the fast rate of QTM calculated in Table 4.5. Even up to a temperature of 300 K, KD_1 contributes approximately 90 % to the value of U_{eff} and KD_2 is a minor contribution, resulting in a U_{eff} of ≈ 50 cm^{-1}. This is consistent with the U_{eff} values extracted using Arrhenius' law by *Zhang et al*. (60.3 cm^{-1} and 51.5 cm^{-1}) under an applied dc field.[121] The authors attributed this lower U_{eff} to Raman processes. The results presented in this work suggest that even if Raman processes were not involved, the Orbach relaxation energy barrier would still be smaller than the zero-field splitting energy.

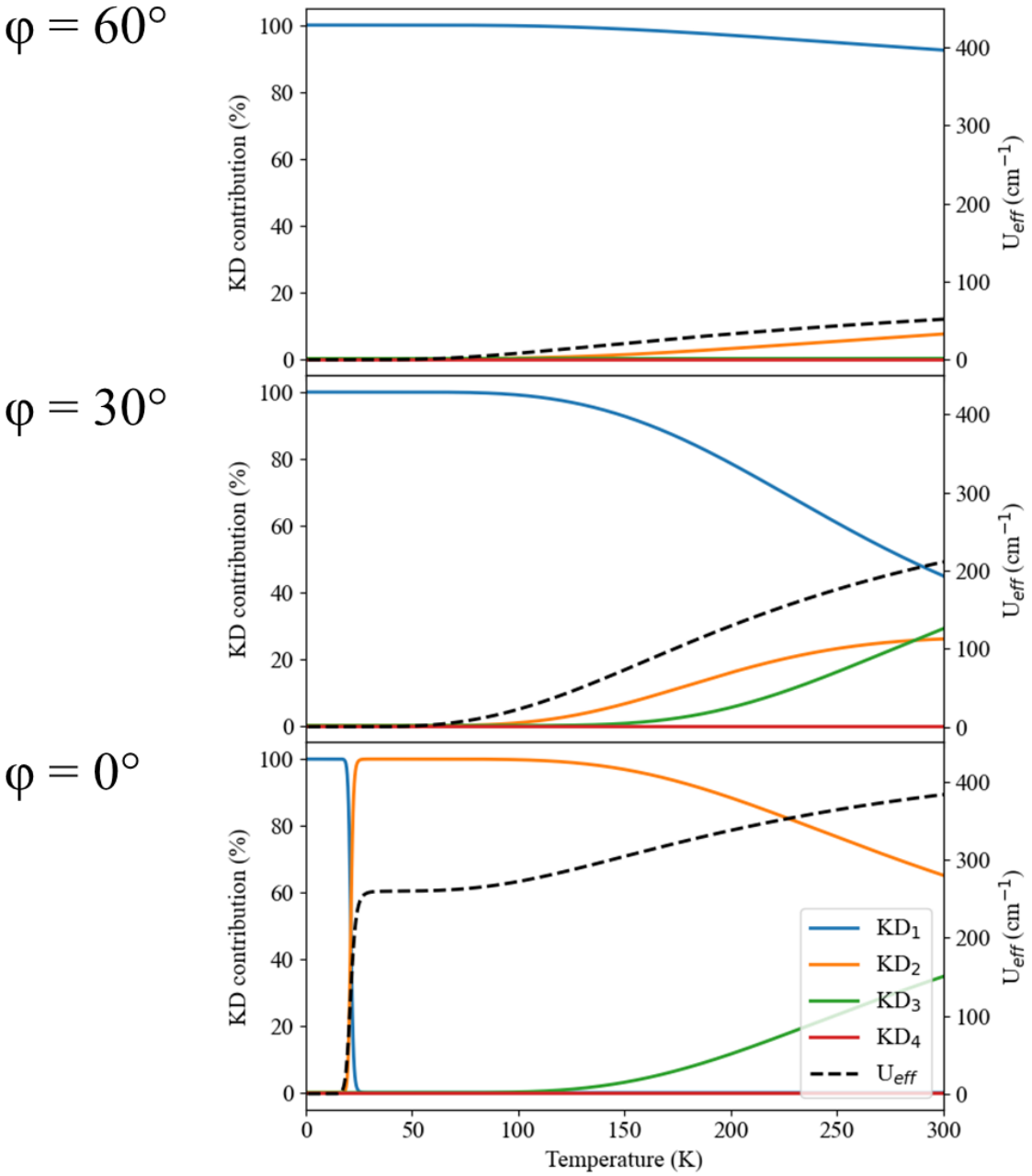

Figure 4.16. The variation the calculated effective barrier of magnetisation against temperature at select angles of φ for complex 2.

However, as the angle of φ decreases, the contribution from KD_2 and KD_3 increase and the U_{eff} energy barrier rises. In the eclipsed structure (φ = 0°), a sharp increase in U_{eff} is predicted at approximately 25 K, where the barrier plateaus. At around 100 K, the Orbach relaxation via KD_3 begins to contribute and slowly raises the energy barrier as the temperature increases.

4.1.4.2.3 The single-ion molecular magnetic properties of the eclipsed structure of complex 2 as a function of θ

Having established that the eclipsed structure (φ = 0°) exhibits potential SiMM behaviour, the value of U_{eff} was calculated at three angles of θ using the eclipsed structure: 35°, 45°, and 55°. The angle of θ in the crystal structure is approximately 51.9°. The results are presented in Figure 4.17.

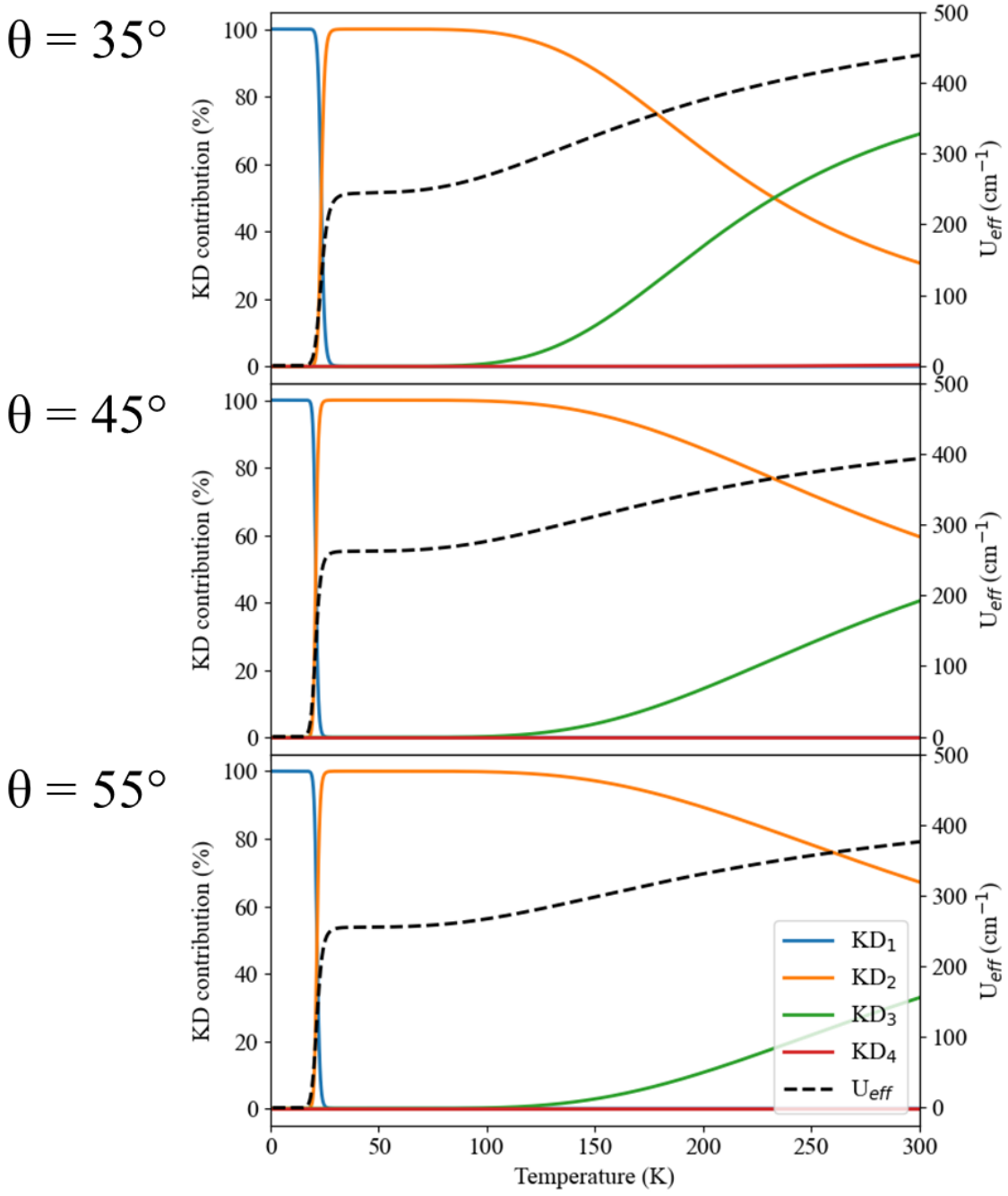

Figure 4.17. The variation the calculated effective barrier of magnetisation against temperature at select angles of θ for the eclipsed structure of complex 2 (φ = 0°).

The calculated properties are less sensitive to changes in θ than they were for changes in φ. In general, the low temperature behaviour does not change substantially as a function of of θ. However, at temperatures of 100 K and above, the contribution from KD_3 to the height of the barrier increases as the angle of θ decreases from 55° to 35°.

4.1.4.2.4 The single-ion molecular magnetic properties of the eclipsed structure of complex 2 as a function of *d*θ

Many eclipsed prismatic structures are heteroleptic, which exhibit deviations away from a symmetrical trigonal compression/elongation. Hence, different angles of θ are common for the different ligand sets. The angle *d*θ was varied in the eclipsed structure of complex **2** to investigate the effect that this distortion has on the time taken for QTM to occur within KD_1. The results are presented in Figure 4.18. Small deviations can have a pronounced effect on the time taken for QTM to occur. For example, a *d*θ of 1.5° results in the time taken for QTM in the ground state KD to occur at an order of magnitude faster. This is an important factor in the design of eclipsed structures.

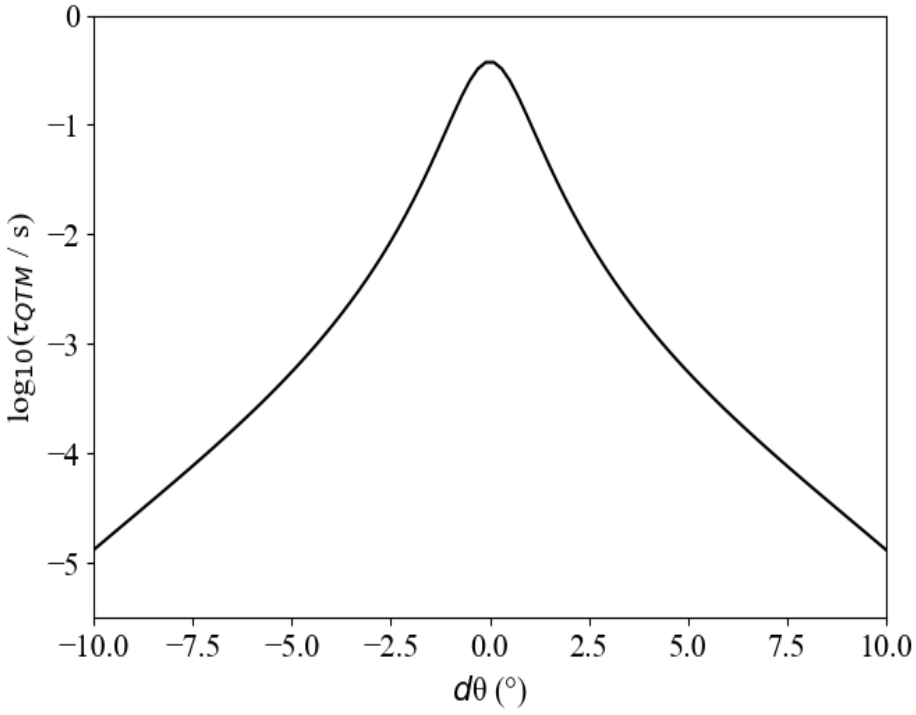

Figure 4.18. The logarithm of the time taken for quantum tunnelling of magnetisation in complex 2 for the eclipsed structure (φ = 0°).

4.1.4.2.5 The effect of metal-ligand bonding on the axiality of the ground state Kramer's doublet

Another aspect of the electronic structure is the metal-ligand bonding, which is not always easy to probe using *ab initio* methods. During the Kestrel fitting to the experimental data, it was found that the calculated EPR g-factors of the ground state KD were very sensitive to the π bonding of the pyrazolyl ligands.

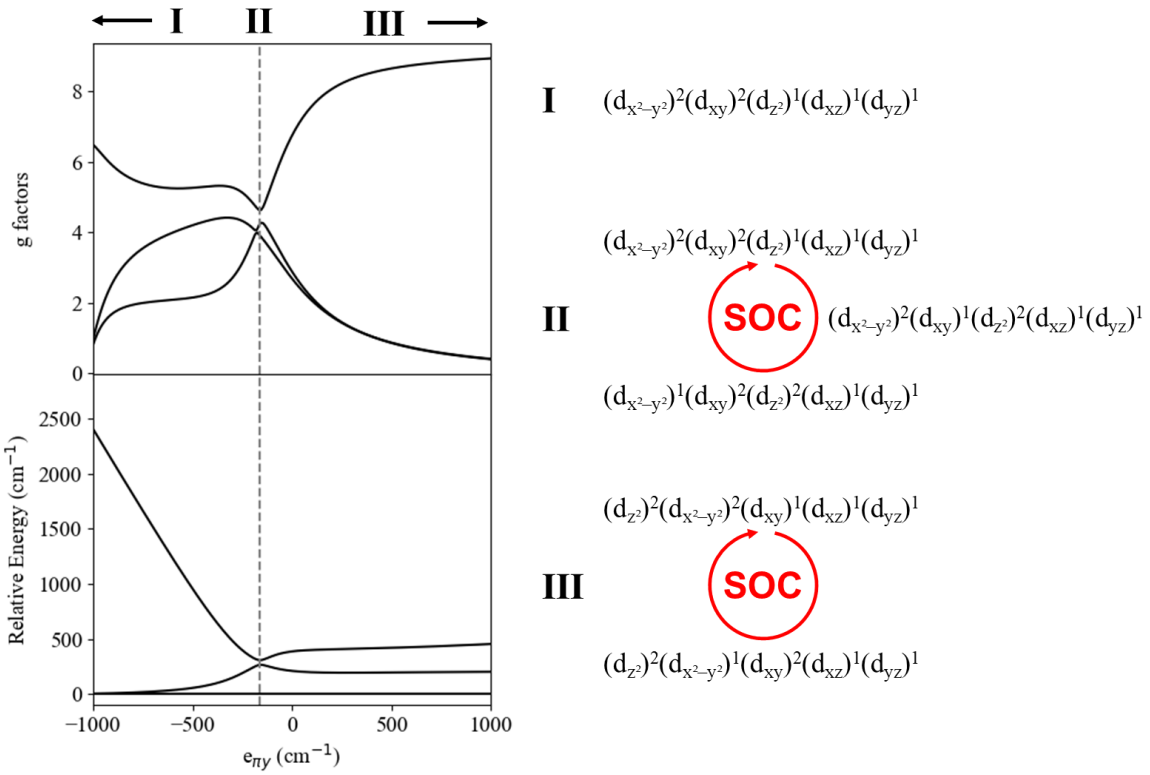

Figure 4.19. The effect that the $e_{\pi y}$ parameter has on the EPR g-factors and the energy of the first three Kramer's doublets calculated using the x-ray crystal structure (anti-prismatic). The dotted line is given for $e_{\pi y}$ = –160 cm^{-1} and corresponds to II. The right of the figure shows the configurational interactions under the effect of spin-orbit coupling (ζ = 440 cm^{-1}) for each region.

The variation of the g-factors and the energies of the low lying KDs in the x-ray structure (φ = 60°) from changes in the $e_{\pi y}$ parameter are shown in Figure 4.19. Three unique electronic structures arise in the variation of $e_{\pi y}$ and are labelled as regions I, II, and III. At the spectroscopically determined $e_{\pi y}$ = 410 cm^{-1}, the EPR g-factors are described by region III.

Due to spin-orbit coupling, the configurations $(d_{z^2})^2(d_{x^2-y^2})^2(d_{xy})^1(d_{xz})^1(d_{yz})^1$ and $(d_{z^2})^2(d_{x^2-y^2})^1(d_{xy})^2(d_{xz})^1(d_{yz})^1$ mix, comprising 47.1 % and 45.8 % configurational character respectively of KD_1. As the π-donation strength increases, the axiality of the ground state KDs also increases. This is because the energy separation of the $d_{x^2-y^2}$ and d_{xy} orbitals is reduced. Hence, the QTM in the ground state can be modified by changing the π-donor capability of the pyrazolyl ligands.

As the π-donation weakens (or π-acceptance increases) in the x-ray structure, the axiality of the ground state is further diminished. At $e_{\pi y} = -160$ cm^{-1} (denoted by the dotted line II in Figure 4.19) an energetic crossing of KD_2 and KD_3 is observed. This crossing is a result of change in the d-orbital splitting, which is now $d_{x^2-y^2}$, $d_{xy} < d_{z^2} << d_{xz}$, d_{yz}. The ground state is represented by a three-way spin-orbit coupled configuration of $(d_{x^2-y^2})^2(d_{xy})^2(d_{z^2})^1(d_{xz})^1(d_{yz})^1$, $(d_{x^2-y^2})^2(d_{xy})^1(d_{z^2})^2(d_{xz})^1(d_{yz})^1$, and $(d_{x^2-y^2})^1(d_{xy})^2(d_{z^2})^2(d_{xz})^1(d_{yz})^1$. This three-way coupled configuration exhibits the largest ZFS and is characterised by rhombic g-values. Hence, a large ZFS does not necessarily always correspond to an axial wavefunction for an S=3/2 system as rhombicity also contributes to the magnitude of the ZFS. Strong π-acceptance (given by region I) resulted in an essentially pure ground state configuration of $(d_{x^2-y^2})^2(d_{xy})^2(d_{z^2})^1(d_{xz})^1(d_{yz})^1$ where both $d_{x^2-y^2}$ and d_{xy} orbitals are doubly occupied. It is evident that the π bonding controls the electronic configuration of the ground state and the resulting axiality. Ideally, increasing the π donation strength results in a greater axiality of the system by energetically separating the $d_{x^2-y^2}$ and d_{xy} orbitals from the d_{z^2} orbital. This results in a ground state spin-orbit coupled configuration where one of the unpaired electrons is in spatial superposition between the $d_{x^2-y^2}$ and d_{xy} orbitals.

The sensitivity of the time taken for QTM to occur in the ground as a function of the pyrazolyl π bonding is also dependent on the geometry. In the x-ray crystal structure, the values of $\log_{10}(\tau_{QTM}) = -7.8$ and -7.0 for $e_{\pi y} = 410$ cm^{-1} and $e_{\pi y} = 1000$ cm^{-1} respectively. Even with a large change in π bonding strength, QTM still dominates the ground state KD. Contrast this with the results from the ideal eclipsed structure where $\log_{10}(\tau_{QTM}) = -0.1$ and 2.5 for $e_{\pi y} = 410$ cm^{-1} and $e_{\pi y} = 1000$ cm^{-1} respectively. Hence, suppression of QTM in the ground state KD is achieved with a combination of an eclipsed geometric structure coupled with an effective increase in π-donation.

4.1.4.2.6 Future design considerations for trigonal D_3 complexes

This analysis provides simple qualitative design principles, which can be utilised to enhance the SiMM character of S=3/2 trigonal D_3 complexes. The findings from Kestrel are summarised as follows:

1. **Enforce a prismatic structure**. This is the most important and dramatic enhancement in both the calculated U_{eff} and τ_{QTM} in the ground state. An eclipsed structure removes off-diagonal low symmetry components of the ligand field.
2. **Maximise π donation and avoid π acceptance**. Choose ligands that are strong asymmetric π donors and do not have access to low lying π accepting orbitals. The π bonding is key to producing the correct electronic configuration mixing in the ground state.
3. **Enforce the d_{xy} and $d_{x^2-y^2}$ orbitals towards degeneracy**. This is coupled with ensuring that the π interaction is perpendicular to the approximate C_2 axis (the Co–B vector) and tweaking the geometry to push the system towards axiality.
4. **Enhance the trigonal elongation**. By enhancing the trigonal elongation, the axiality of the ligand field is also enhanced. The effect of which is not as dramatic however and is suggested to not be the primary focus in these systems. However, what is a major contribution is a symmetrical trigonal elongation (see below).
5. **Use a symmetrical coordination environment**. Kestrel suggests that small deviations in the trigonal elongation/compression between the ligands above and below the equatorial plane have a dramatic effect on the time taken for QTM to occur in the ground state. This is typically a result of using different ligand sets, which coordinate above and below the plane. Ideally, use of the same ligands, or very similar ligands, is required to ensure a more equal trigonal elongation/compression.

4.1.5 Complex 3

Complex **3** is an example of an axially distorted tetrahedral cobalt(II) complex. It features the largest energy barrier (U_{eff} = 230 cm^{-1}) of any high-spin tetrahedral cobalt(II) complex in the literature.[143] These types of complexes make excellent candidates for SiMMs due to their range of geometries and coordinating ligands. Hence, using **3** as a basis, the correlation of axiality with geometry and metal-ligand bonding was explored using Kestrel.

4.1.5.1 Electronic structure from experiment, Kestrel analysis

Complex **3**, unlike complexes **1** and **2**, has already been analysed using a ligand-field model with e_λ parameters. That ligand-field analysis, carried out by *Rechkemmer et al*., reproduced the experimental d-d band energies and the experimental magnitude of the ZFS (2D = 230 cm^{-1}) of complex **3**.[124] The complex has an MCD spectrum (2 T, 1.5 K) with two d-d spin-allowed bands centred at 7000 cm^{-1} ($^4A_2 \rightarrow {}^4T_1(F)$) and 18000 cm^{-1} ($^4A_2 \rightarrow {}^4T_1(P)$), and a further spin-forbidden band centred at approximately 16500 cm^{-1}. The ground state g-factors are reported as $g_\perp$ = 0.0 and $g_{||}$ = 9.1 ± 0.1. The isotropic χT variation with temperature has also been characterised experimentally by static dc magnetic measurements.

Rechkemmer et al. reported best fits to the d-d transition energies and ZFS using parameter values of e_σ = 6410 cm^{-1}, $e_{\pi y}$ = 1841 cm^{-1}, B = 653 cm^{-1}, C = 2942 cm^{-1}, and ζ = 446 cm^{-1}.[124] For calculating the SiMM properties of complex **3** the parameter set requires a realistic value of k_{iso}.

4.1.5.1.1 Fitting of the reported magnetic data

The g-factors for the ground state KD and the reported χT at room temperature (3.14 cm^3 K mol^{-1}) were fitted using the x-ray crystal structure and reported best fit parameters (*vide supra*) in Kestrel. The value of k_{iso} was allowed to vary from 0.0 to 1.0 and an optimised value was found using a value of k_{iso} = 0.82. This gave calculated g-factors of $g_{||}$ = 9.14 and $g_\perp$ = 0.6 × 10^{-2} and a χT of 3.124 cm^3 K mol^{-1} (300 K) in agreement with the reported values. The calculated variation of χT with temperature is presented in Figure 4.20 which faithfully reproduces the reported experimental χT variation.[124] Kestrel predicts that the χT value remains relatively constant until 130 K when the χT value steadily decreases down to a value of 2.621 cm^3 K mol^{-1} at 2 K.

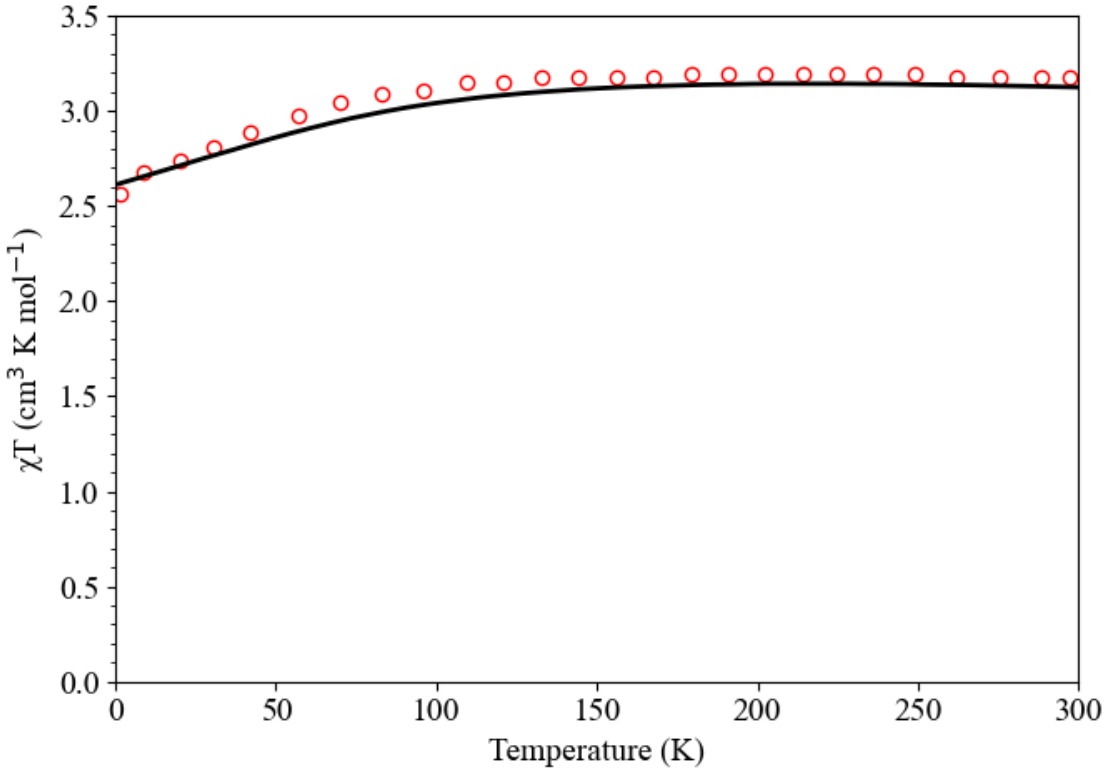

Figure 4.20. The Kestrel calculated isotropic χT variation with temperature for the best fit parameters of complex 3. The reported experimental data (red) supplied by the authors.[124]

4.1.5.1.2 Analysis of the ligand-field splitting

The ligand-field parameters reported by *Rechkemmer et al*. were analysed using Kestrel. Using the x-ray crystal structure, Kestrel calculated a d-orbital splitting of $d_{xy} < d_{x^2-y^2} < d_{z^2} < d_{yz} < d_{xz}$, as shown in Figure 4.21.[124] The d_{xz} and d_{yz} orbitals lobes, in the chosen molecular frame, point towards the coordinating nitrogen atoms and their energy is a measure of the σ bonding strength of the ligands.

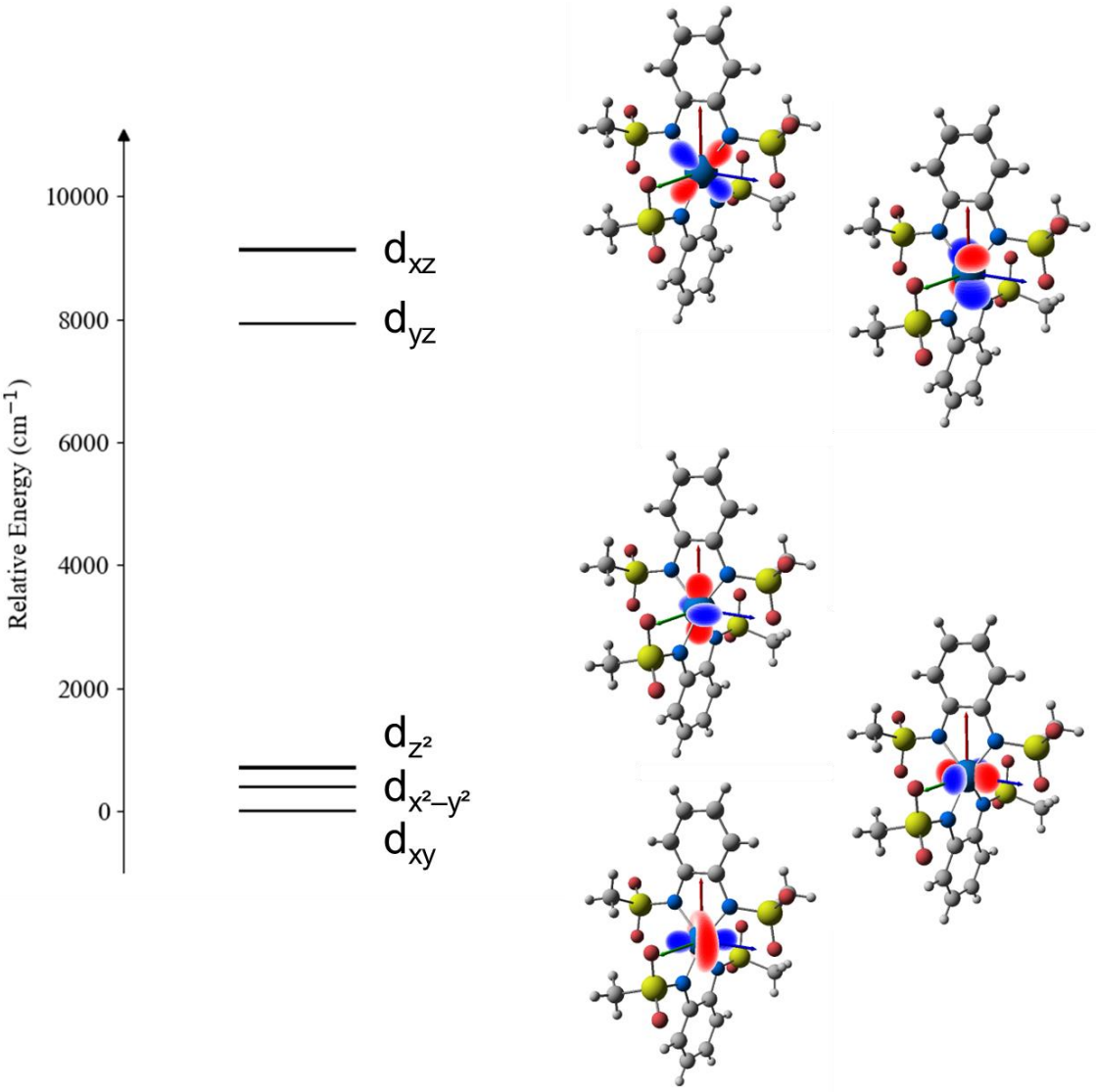

Figure 4.21. The Kestrel calculated ligand-field splitting and orbital projections rendered using Kestrel of complex 3.

4.1.5.1.3 Analysis of the d-d transition energies

Using the ligand-field parameters reported by *Rechkemmer et al*., excellent reproduction of the d-d transition energies was obtained.[124] The final configurational compositions and relevant excitation energies in the absence of spin-orbit coupling are given in Table 4.7.

Upon inspection, the electronic assignments of the excited states differ from those reported by *Rechkemmer et al*.[124] Specifically, the order of the $^4B_1 \rightarrow {}^4A_2$ and $^4B_1 \rightarrow {}^4E$ assignments around 7000 cm^{-1} and 18000 cm^{-1} are reversed. The assignments presented by the authors do not come from their ligand-field analysis, but instead they use the assignments of the electronic states calculated from their *ab initio* calculations (Supplementary Table 3 of

Rechkemmer et al.). Indeed, if the reported ligand-field parameters derived from AILFT by *Rechkemmer et al*. is used (e_σ = 5226 cm^{-1}, $e_{\pi y}$ = 1473 cm^{-1}, B = 1031 cm^{-1}, and C = 4151 cm^{-1}) then Kestrel predicts the same excited state ordering that is presented in their work. Future work to probe the correct excited state ordering by fitting the reported experimental MCD spectrum with Kestrel could provide further insight into the spectroscopy of complex **3**. However, this is beyond the scope of the present analysis. All that is required to probe the SiMM properties of complex **3** is a good representation of the electronic structure of the ground and low-lying excited states. Given the good reproduction of the magnetic data in section 4.1.5.1.1, the current parameterisation is suitable.

Table 4.7. The energies (cm^{-1}) of the many-electron eigenstates using the best fit ligand-field parameters of *Rechkemmer et al*. to the experimental MCD spectrum in the absence of spin-orbit coupling.[124]

Assignment	Energy (experiment)[124]	Energy (Kestrel)	Configuration
$^4B_1$	0	0.0	99.9 % 21211
$^4B_1 \rightarrow {}^4B_2$	Unknown	261.3	80.6 % 12211 19.4 % 22111
$^4B_1 \rightarrow {}^4A_2$	6211	6294.9	70.1 % 22111 17.2 % 12211 9.0 % 11122 2.5 % 12121 1.2 % 21112
$^4B_1 \rightarrow {}^4E$	7236	7229.4 7850.3	99.1 % 21121 79.5 % 12121 14.4 % 21112 2.6 % 11212 2.3 % 22111 6.0 % 11122
$^4B_1 \rightarrow {}^4E$	8217	8621.4 8901.9	76.6 % 12112 23.2% 11221 65.6 % 11212 32.7 % 21112 1.2 % 12121
$^4B_1 \rightarrow {}^4E$	16156	16301.7	42.8 % 22111 33.3 % 21202 12.3 % 12211 8.9 % 21220 1.3 % 01222

Assignment	Energy (experiment)[124]	Energy (Kestrel)	Configuration
	16811	16659.6	66.6 % 12202 23.6 % 22120 6.9 % 22102 1.7 % 10222
$^4B_1 \rightarrow {}^4E$	17952	17900.3 18277.3	76.0 % 11221 23.2 % 12112 51.4 % 21112 31.6 % 11212 16.7 % 12121
$^4B_1 \rightarrow {}^4A_2$	18911	19592.0	90.1 % 11122 8.0 % 22111 1.7 % 12211

In the absence of spin-orbit coupling, the ground state $^4B_1$ multiplet is 99.9% $(d_{xy})^2(d_{x^2-y^2})^1(d_{z^2})^2(d_{yz})^1(d_{xz})^1$. The ground state is therefore a non-Aufbau state. Under the action of spin-orbit coupling (ζ = 446 cm^{-1}), the ground state KD configurational occupation is comprised of 64.1% $(d_{xy})^2(d_{x^2-y^2})^1(d_{z^2})^2(d_{yz})^1(d_{xz})^1$ and 28.8% $(d_{xy})^1(d_{x^2-y^2})^2(d_{z^2})^2(d_{yz})^1(d_{xz})^1$. Spin-orbit coupling mixes configurations where either the d_{xy} or $d_{x^2-y^2}$ is singly occupied together.

Kestrel assigns the Aufbau configuration, $(d_{xy})^2(d_{x^2-y^2})^2(d_{z^2})^1(d_{yz})^1(d_{xz})^1$ as being mixed into the 1st and 2nd excited states (at 261 cm^{-1} and 6294.9 cm^{-1}, respectively). In the presence of spin-orbit coupling, Kestrel also shows a small admixture of quartet character (2%) into the two resolved spin-forbidden bands in the experimental MCD spectrum.

4.1.5.2 Enhancing the single-ion molecular magnetic properties

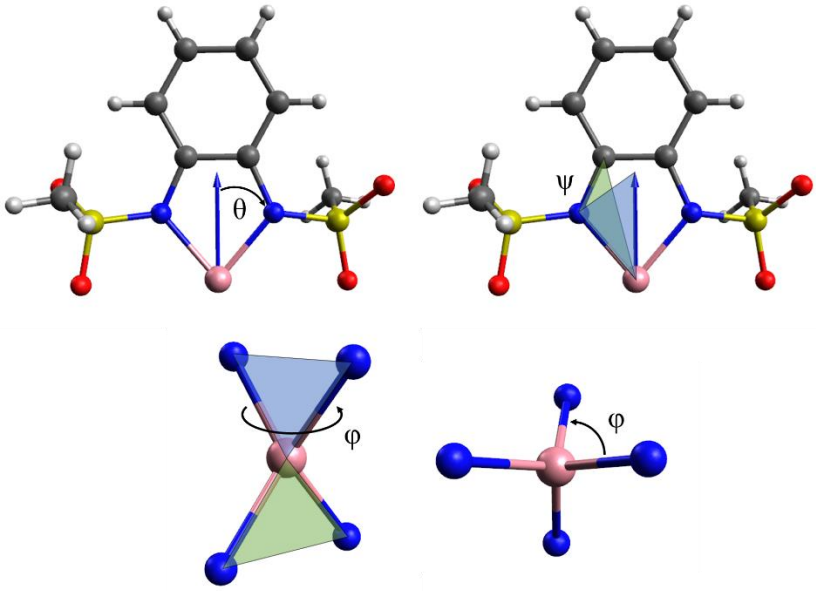

Figure 4.22. The geometric distortions θ, φ, and ψ of complex 3.

Complex **3** features three geometric distortions: the axial distortion θ, the cubic twist φ, and the dihedral angle ψ. The angular geometric parameters are illustrated in Figure 4.22. The angle θ is defined as the angle between the coordinating atom and the coordinate z-axis. This angle is related to the "bite-angle", which is defined as 2θ. A value of θ = 54.75° is the angle found in an ideal tetrahedral system. The cubic twist φ, like that in **1** and **2**, is the dihedral angle that the ligands above the equatorial plane make with the ligands below the equatorial plane. The final angle ψ defines the local π-bonding direction of the ligand. ψ is defined as the projection of the ligand's local x-direction (which is presumed non π-bonding) on to the coordinate z-axis. Hence, the π-bonding occurs perpendicular to this direction. Note, as described in the methodology, the adjacent carbon atom to the coordinating nitrogen in the phenyl ring is used to determine the local x-direction of the ligand.

The average values of θ, φ, and ψ in the x-ray structure are 40.3°, 85.3°, and 2.6°. When compared to the ideal tetrahedral angles (54.8°, 90.0°, and 0.0°), complex **3** is an axially elongated tetrahedron belonging to the approximate D_{2d} point group. The largest deviation from the ideal tetrahedron is observed in the deformation of the θ angle. In this section, the effect that geometric distortions and changes in metal-ligand bonding have on the SiMM behaviour of complex **3** is investigated using Kestrel.

4.1.5.2.1 The single-ion molecular magnetic properties of complex 3

Under spin-orbit coupling, the $^4B_1$ and $^4B_2$ states at 0.0 and 261.3 cm^{-1} (see Table 4.7) split into four KDs. The energies, M_J projection, and g-factors of these four KDs are presented in Table 4.8. The calculated time taken for QTM to occur within the KDs is also tabulated. The ground state (KD_1) exhibits the slowest rate of QTM, whereas KD_3 exhibits the fastest rate of QTM.

Table 4.8. The Kestrel calculated energies (cm^{-1}), g-factors, and τ_{QTM} of the four lowest lying Kramer's doublets of complex 3 using the best fit parameters reported by *Rechkemmer et al*. and a k_{iso} = 0.82.[124]

KD	M_J	Energy	g_x	g_y	g_z	τ_{QTM} (s)
KD_1	±7/2	0.0	0.6275×10^{-2}	0.6378×10^{-2}	9.1396	4.1×10^{-4}
KD_2	±5/2	234.3	2.8242	2.8145	4.4474	1.3×10^{-9}
KD_3	±3/2	626.1	2.7469	2.8919	0.4496	9.0×10^{-10}
KD_4	±1/2	911.0	0.0598	0.0504	2.8563	1.7×10^{-6}

The mechanism of relaxation was investigated by plotting the variation of the calculated U_{eff} against temperature. The variation is presented in Figure 4.23. In region I, T < 20 K, the primary relaxation route is QTM within the ground state KD_1 as no other KDs are thermally occupied. For region II, thermal occupation of the first excited KD_2 raises the U_{eff} barrier to the ZFS value of 234.3 cm^{-1}, where the height of the barrier plateaus. Within III, a small increase of the U_{eff} barrier is observed for increasing temperature. This coincides with thermal occupation of the second excited KD_3. However, the anisotropy is sufficiently larger in KD_2 than in KD_3 such that the Orbach process dominates through the former. Contributions from KD_4 are negligible given the relatively slow rate of QTM in KD_4 compared to KD_2 and KD_3.

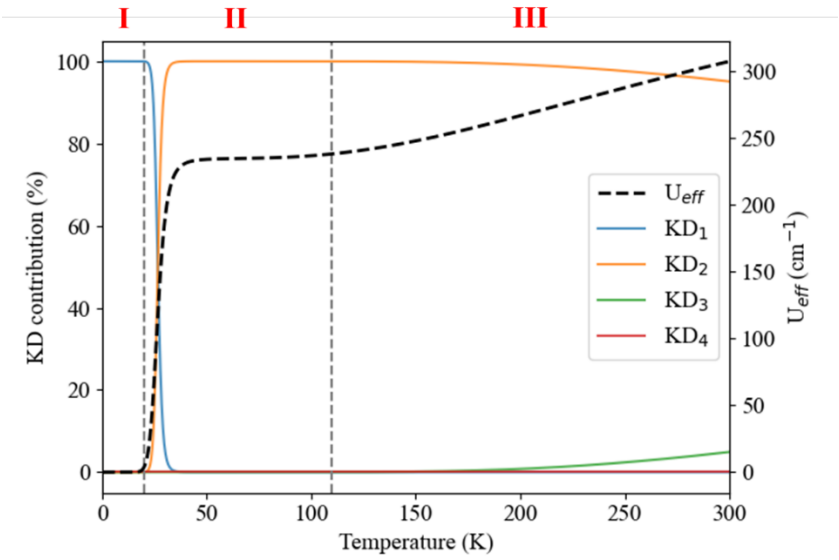

Figure 4.23. Theoretical predictions of U_{eff} and its contributions from the four lowest-lying KDs as a function of temperature for complex 3 calculated using Kestrel.

Having established that Kestrel predicts the effective energetic barrier to occur via the first excited state KD (KD_2), increasing the axiality and energetic height of KD_2 should improve the SiMM characteristics of **3**.

4.1.5.2.2 The single-ion molecular magnetic properties of complex 3 as a function of θ

The axial distortion (θ) is the largest source of geometric distortion in the x-ray crystal structure of complex **3** that this was the first parameter to be investigated. The angle θ was varied over the range of 30° to 60°. Kestrel predicted that the slowest time taken for QTM to occur was at an angle of 38°. At this angle, the magnitude of the ZFS splitting and the predicted value of g_z reach their maximum (≈ 260 cm^{-1} and 1.5 ×10^{-2}, respectively). Hence, the system has reached its most axial electronic structure at the optimum angle of θ = 38°, which is in agreement with the findings of *ab initio* calculations performed by *Legendre et al*.[144] The average bite angle of complex **3** is 40.32°, which is close to the optimum angle. Yet, this small deviation results in a dramatic change in the SiMM behaviour of complex **3**.

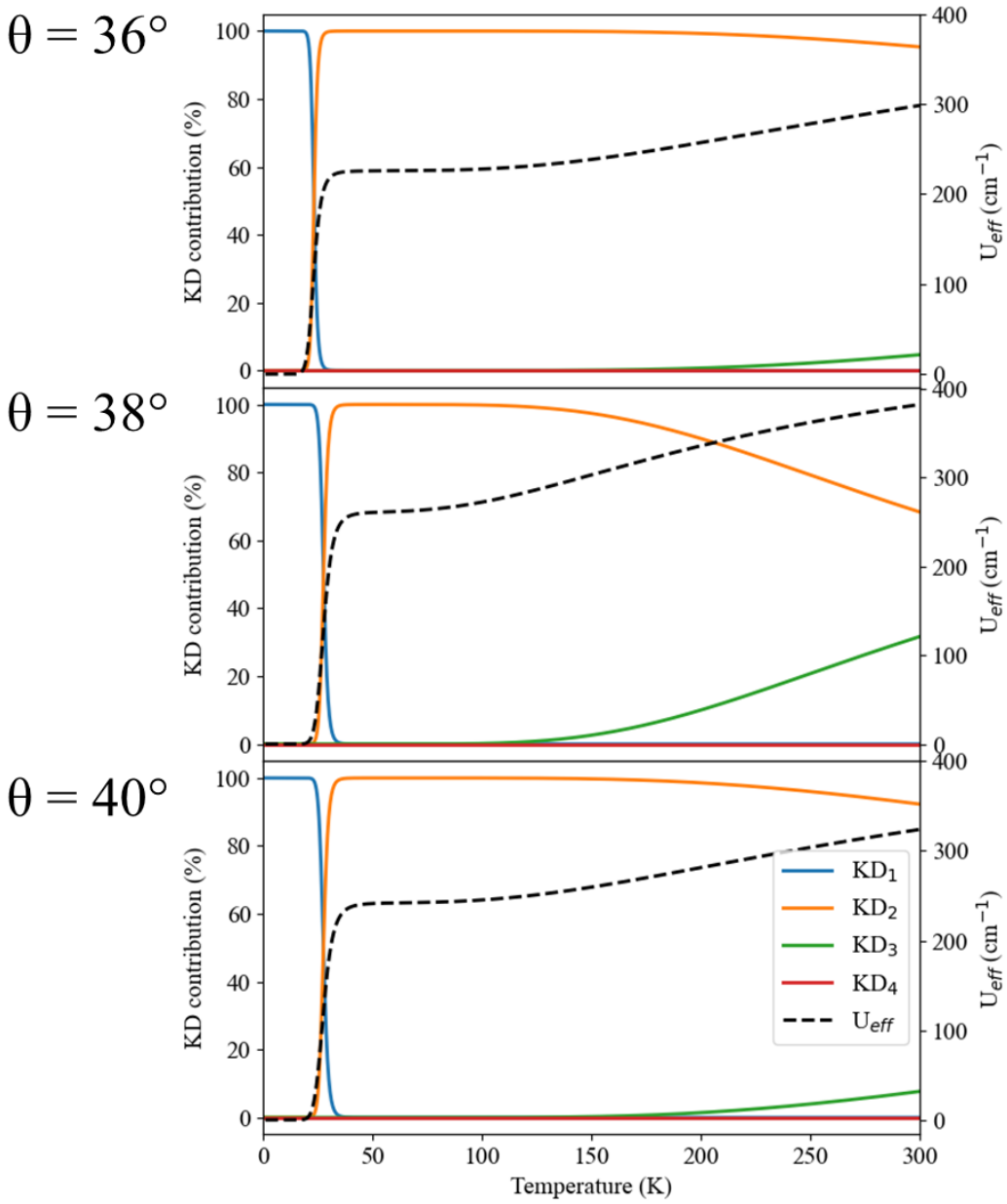

Figure 4.24. The variation in the calculated effective barrier of magnetisation (U_{eff}) of the angle defining the axial elongation in complex 3.

To illustrate the sensitivity of the predicted SiMM behaviour with small changes in θ, the calculated U_{eff} is plotted against temperature for complex **3**, as shown in Figure 4.24, for the angles of 36°, 38°, and 40°. The seemingly small deviation of approximately 2° from the optimum angle has a notable effect on the axiality of the low-lying excited states KD_2 and KD_3, and the magnitude of ZFS. Comparing the calculated U_{eff} dependence on temperature in Figure 4.24 for each angle of θ, the Orbach process is still dominated by the contribution from KD_2, however a larger contribution from KD_3 is observed for T > 100 K, effectively raising U_{eff}

further. However, the energy barrier is still primarily determined by the height of KD_2. By optimising the angle of θ, the relative height of KD_2 can be increased, resulting in a larger U_{eff}.

Like with complex **1** and **2**, the source of the axiality is reflected by the energy gap between the d_{xy} and $d_{x^2-y^2}$ orbitals, where axiality increases as the two orbitals approach degeneracy. This insight has already been demonstrated by *Legendre et al*.[144] Recall that the two lowest energy many-electron quartet states, in the absence of spin-orbit coupling, are comprised primarily of the configurations $(d_{xy})^2(d_{x^2-y^2})^1(d_{z^2})^2(d_{yz})^1(d_{xz})^1$ and $(d_{xy})^1(d_{x^2-y^2})^2(d_{z^2})^2(d_{yz})^1(d_{xz})^1$ respectively. As a result, spin-orbit coupling mixes the occupations $(d_{xy})^2(d_{x^2-y^2})^1(d_{z^2})^2(d_{yz})^1(d_{xz})^1$ and $(d_{xy})^1(d_{x^2-y^2})^2(d_{z^2})^2(d_{yz})^1(d_{xz})^1$ together into the ground state. This maximises the axiality by super-positioning the unpaired electron about the z-axis symmetrically between the d_{xy} and $d_{x^2-y^2}$ orbitals.

4.1.5.2.3 The single-ion molecular magnetic properties of complex 3 as a function of φ

Next, the angle φ was varied between 0° and 90° using the ideal angle of θ = 38° At φ = 0° the molecular geometry is represented by a distorted square planar aligned in the zx plane; at φ = 90° the ligands above and below the equatorial plane are perpendicular to one another.

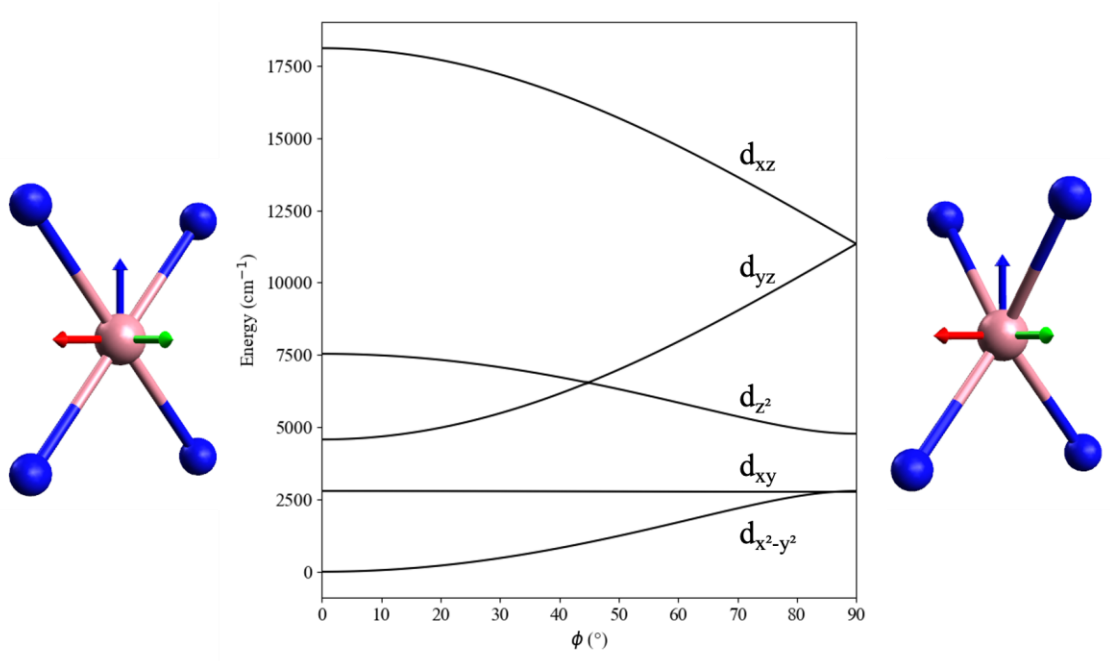

Figure 4.25. The energies of the one-electron orbitals as a function of the torsional distortion φ for complex 3, calculated using Kestrel. The axial distortion was set to the optimal angle of θ = 38°

The results of the angle variation are shown in Figure 4.25. Unlike in complexes **1** and **2** where the axiality of the system benefits from aligning the ligands above and below the equatorial plane, complex **3** instead loses axiality. This is due to an off-diagonal $\langle d_{z^2} | V_{LFT} | d_{x^2-y^2} \rangle$ matrix element, which stabilises the $d_{x^2-y^2}$ orbital and destabilises the d_{z^2} orbital. This matrix element enhances the energy separation gap between the d_{xy} and $d_{x^2-y^2}$ orbitals, which can be seen in Figure 4.25 as the angle of φ deviates from 90°.

At θ = 38° and φ = 0°, representing the largest energy separation of d_{xy} and $d_{x^2-y^2}$, $\tau_{QTM} = 7.1 \times 10^{-10}$ s. However, the calculated time taken for QTM to occur within KD_1 for complex **3** when θ = 38° and φ = 90° is $\tau_{QTM} = 0.40$ s. The optimisation of these two geometric distortions resulted in a τ_{QTM} that is three orders of magnitude larger compared to the τ_{QTM} calculated for the x-ray crystal structure. Indeed, the axiality of the ground state KD is more sensitive to the angle of θ than φ, but if the two distortions can be precisely controlled then QTM in the ground state could be suppressed.

4.1.5.2.4 The single-ion molecular magnetic properties of complex 3 as a function of ψ and $e_{\pi\sigma x}$

Having explored the effect that the angles θ and φ have on the axiality of the system, the local dihedral angle ψ of the coordinating atoms was investigated. The angle ψ dictates the direction that the coordinating nitrogen atoms engage in π-bonding. The local π-bonding directions in **3** are approximately aligned perpendicular to the plane formed by the coordinating nitrogen atom, the cobalt ion, and the coordinate z axis (Figure 4.26 (A)). As well as dictating the alignment of π-bonding, another possibly important effect thus far not discussed is the concept of 'misdirected valency'. The average local angles of C_{α}–N–Co and S–N–Co are 115.1° and 122.4° respectively and this has consequences for the orientation of the σ bond manifesting as projecting away from the direct Co–N bond, as shown in Figure 4.26 (B).

The angle of ψ was varied between the angles of −90° and 90° using the optimised angles of θ = 38° and φ = 90°. The variation in the d-orbital energies with the dihedral angle ψ is shown in Figure 4.26 (C). The figure shows that the degeneracy of the d_{xy} and $d_{x^2-y^2}$ orbitals is achieved for values of ψ = 0°. Infact, Kestrel predicts that under this geometry and parameterisation, the τ_{QTM} = 8354.5 s. Moving to ψ = 1° drops the predicted value of τ_{QTM} = 0.1 s. Whether this level of control over the π bonding angle is realistic or not, these results show how sensitive the SiMM properties to small deviations in the geometric parameters.

The variation in the misdirected valence parameter $e_{\pi\sigma x}$ for the optimal ψ = 0°, as shown in Figure 4.26 (D), increases the energetic gap between d_{xy} and $d_{x^2-y^2}$ regardless of being either a positive or negative quantity. A positive value of $e_{\pi\sigma x}$ destabilises the $d_{x^2-y^2}$, d_{xz}, and d_{yz} orbitals whilst stabilising the d_{z^2}, leaving the d_{xy} orbital unperturbed. Indeed, the SiMM properties of this complex are *very* sensitive to small contributions of misdirected valence. Using the optimised angles of θ, φ, and ψ, small values of $e_{\pi\sigma x}$ = 250 cm^{-1} and $e_{\pi\sigma x}$ = 500 cm^{-1} resulted in τ_{QTM} = 1.5 s and τ_{QTM} = 0.2 s.

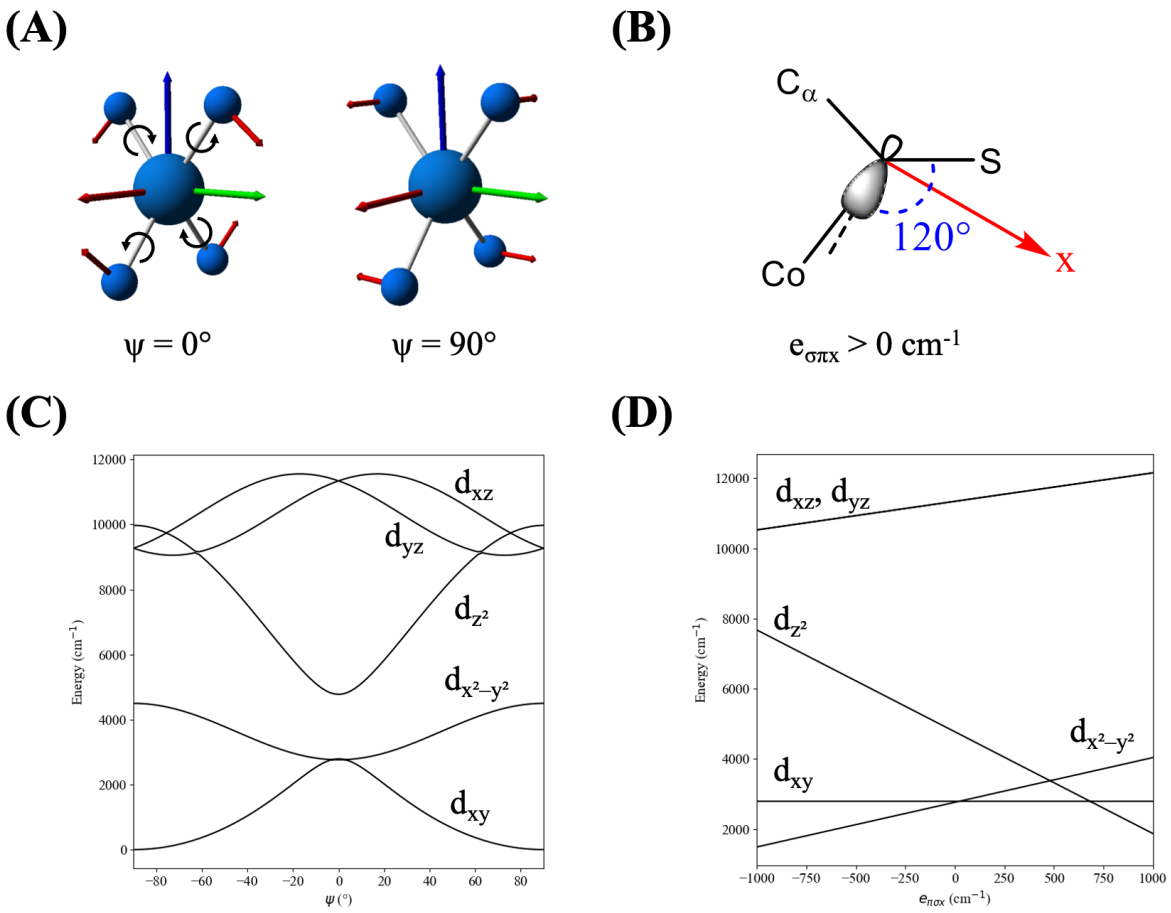

Figure 4.26. The local x-frames superimposed on the coordinating atom for 3 against the coordinate axes (A). A schematic depiction of the misdirected valence arising from the geometric distortion about the coordinating atom (B). The variation in the d-orbital energies with ψ, where $e_{\pi\sigma x}$ = 0 cm^{-1} (C). The variation in the d-orbital energies with values of $e_{\pi\sigma x}$ for ψ = 0° (D). All other ligand-field parameters are their best fit values, and the ideal molecular geometry was used with an angle θ = 38° and φ = 90° (see methodology and text).

The effects of misdirected valence on SiMM properties cannot be ignored. Strategies to quench these contributions involve either controlling the local coordination geometry of the coordinating atom, or by changing the direction of some of the misdirected valence with respect to ligands opposite one another. If, for example, the angle of for ψ the two coordinating atoms within the same plane are orientated in opposite directions (one with ψ = 0°, the other with ψ = 180°), then the contribution from misdirected valence can vanish.

4.1.5.2.5 The relationship between metal-ligand bonding and bite angle θ

Having established optimum angles of θ = 38°, φ = 90°, and ψ = 0° for **3**, the dependence of the optimum angle of θ (which was the most sensitive geometric feature) was investigated with respect to changes in the magnitudes of the σ and π bonding. The angle θ was varied for different values of $e_{\pi y}$. The value of e_{σ} was fixed at 6410 cm^{-1}. The energies of the five d orbitals were then plotted as a function of the bite angle for different magnitudes of π-bonding ranging from 1500 cm^{-1} to 2250 cm^{-1}, as shown in Figure 4.27.

The relative energies and orbital ordering of the d_{xy}, $d_{x^2-y^2}$, and d_{z^2} are sensitive to the angle θ. As the angle θ approaches the tetrahedral limit of θ = 54.75°, the orbitals arrange themselves into the higher and lower lying t_2 and e set. The t_2 and e set degeneracies are lifted due to the out-of-plane π-bonding. From Figure 4.27, the degeneracy of the d_{xy} and $d_{x^2-y^2}$ orbitals (where maximum axiality is achieved) occurs at larger angles of θ for larger values of $e_{\pi y}$. This correlation results from the larger $e_{\pi y}$ value pushing up the energy of the d_{xy}.

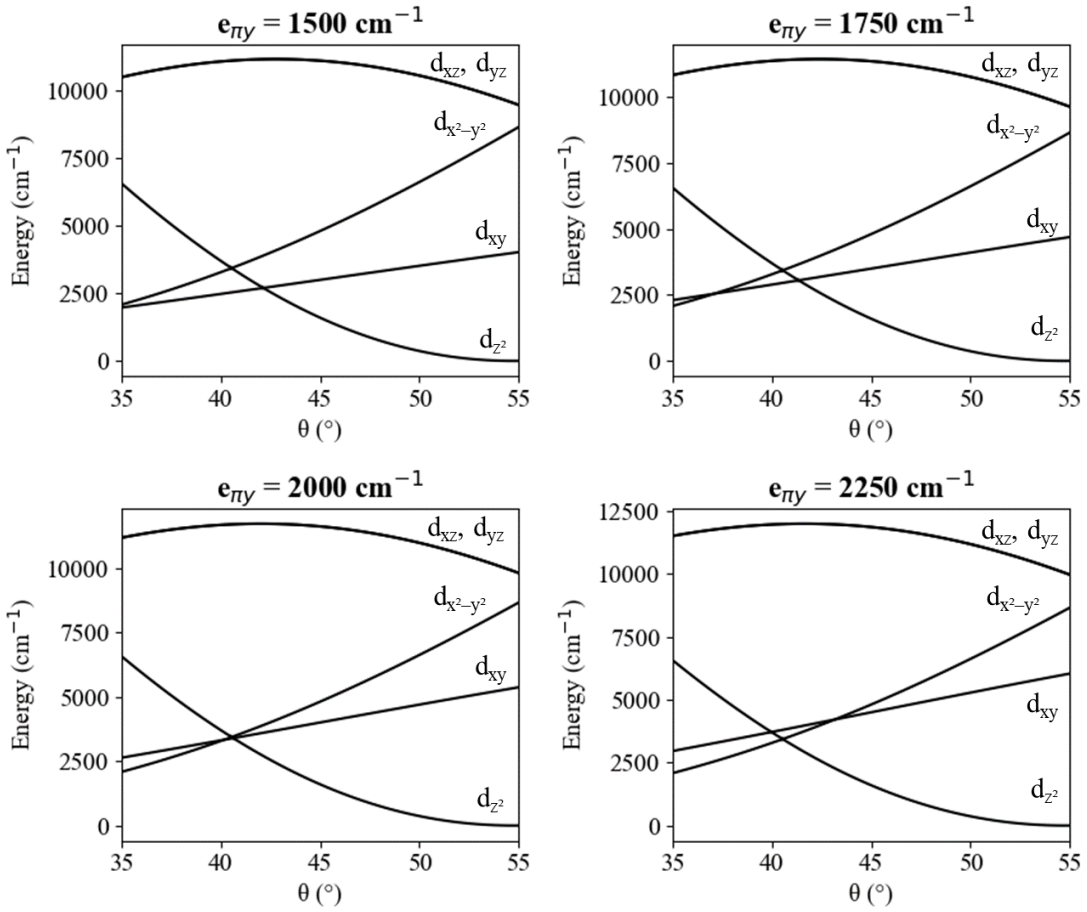

Figure 4.27. The variation in the one-electron d-orbital energies of the 3 as a function of the angle θ. The value of e_σ was held constant at 6410 cm^{-1}. The ideal angles φ = 90° and ψ = 0° were used.

Having established a correlation between the magnitude of $e_{\pi y}$ and the optimum angle of θ, further analysis was carried out to establish what correlation, if any, existed between the ratio of $e_{\pi y}/e_\sigma$ and θ. The ratio $e_{\pi y}/e_\sigma$, and θ were simultaneously varied and the resulting ZFS is presented in Figure 4.28. The optimum angle of θ is linearly correlated with the ratio $e_{\pi y}/e_\sigma$. Hence, the optimum bite angle is a function of the relative π-donor strength. Indeed, for ligands with larger atomic radii (such as sulfur) and hence a larger bite angle, the ZFS is compensated for by increasing the π-donation and lowering the σ-donation. As an example, take the two x-ray structural forms of $[Co(SPh)_4]^{2-}$, $[Co(SPh)_4](PPh_4)_2$ and $[Co(SPh)_4](NEt_4)_2$ with θ = 48.9° and 59.5°, and an experimentally determined ZFS of 110 cm^{-1} and 22 cm^{-1}, respectively.[145,146] The former compound has been analysed using CASSCF/NEVPT2 and a ligand-field fitting of the extracted AILFT one-electron ligand-field matrix found an $e_{\pi y}/e_\sigma \approx 0.33$. Using the angle θ = 48.9°, the ZFS of 110 cm^{-1} is achieved with an $e_{\pi y}/e_\sigma \approx 0.35$ in good agreement with the *ab*

initio derived ratio. Carrying this over to $[Co(SPh)_4](NEt)_4$ gives a calculated ZFS of 11 cm^{-1} from an $e_{\pi y}/e_{\sigma}$ = 0.35, in reasonable agreement with the reported ZFS of 22 cm^{-1}. Of course, ZFS is susceptible to other effects, such as misdirected valence, which was found to be important in $[Co(SPh)_4]^{2-}$. Nonetheless, the optimum bite angle is a function of the $e_{\pi y}/e_{\sigma}$ ratio and approximate knowledge of this ratio will allow for designing molecules with a suitable bite angle to maximise axiality. Analysing Figure 4.28 allows for an empirical linear relationship between the optimum θ angle and the $e_{\pi y}/e_{\sigma}$ bonding ratio to be approximated by the expression

$$\theta_{\text{optimum}} = 80\left(e_{\pi y}/e_{\sigma} + 0.1875\right). \tag{4.7}$$

It is important to note that although **3** exhibits a large ZFS magnitude of 230 cm^{-1}, it is possible to reach a ZFS of up to 280 cm^{-1}.

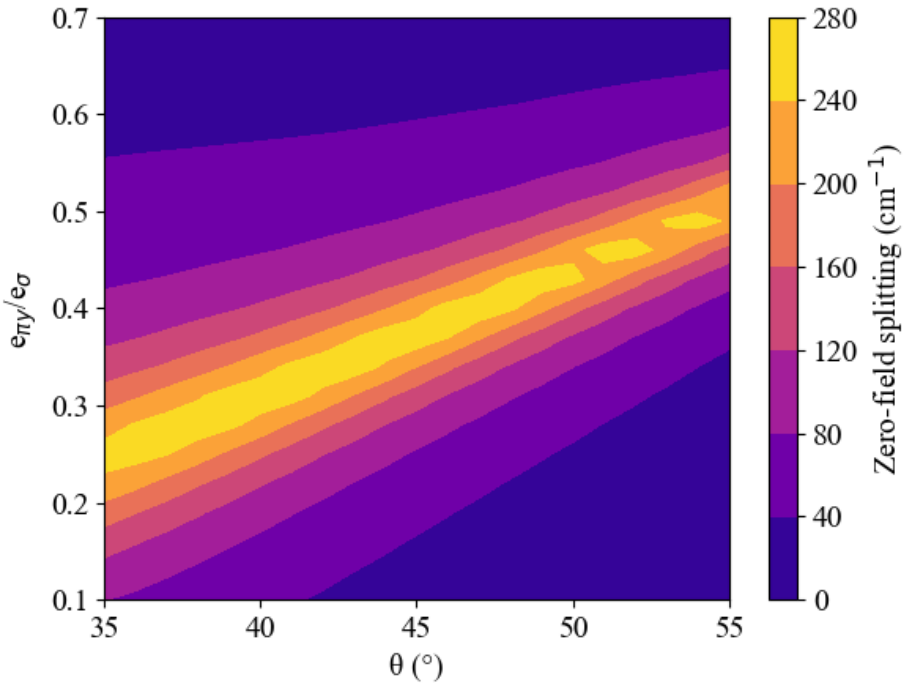

Figure 4.28. The variation in the magnitude of zero-field splitting for changes in the angle θ and $e_{\pi y}/e_{\sigma}$ for 3. Calculations were carried out using the ideal model system.

4.1.5.2.6 Future design considerations for tetrahedral complexes

Analysis of **3** offered an expanded insight into the relationship between metal-ligand bonding and geometry in distorted tetrahedral complexes. The design principles that Kestrel recommends are:

1. **Larger π/σ ratios result in a larger optimal bite angle.** The nature of the bonding between the metal and the ligand will dictate the optimal bite angle. Using the reported $e_{\pi y}$:e_{σ} ratio of Co–S of 0.35 and equation (4.7), the optimum angle is found to be 43°, much larger than the 38° found for complex **3**. In general, ligands with heavier coordinating atoms are likely to be characterised by larger $e_{\pi y}$:e_{σ} ratios.
2. **Minimise misalignment of the out of plane π bonding directions.** Ignoring the effects of misdirected valence, the SiMM properties were acutely sensitive to small deviations away from the ideal angle of ψ = 0°. It will be a challenge to synthesise systems with such accurate control over the local coordination geometry of the ligand.
3. **Minimise in-plane misdirected valence.** The misdirected valence in-plane differentially interacts with the d_{z^2} and $d_{x^2-y^2}$ orbitals, preferentially stabilising one and destabilising the other. The d_{xy} is unperturbed and hence the energy gap between the d_{xy} and $d_{x^2-y^2}$ widens. Removing contributions from misdirected valence is a structural challenge and requires ensuring that the ligand can coordinate in an idealised way. On the other hand, misdirected valence directed in opposite directions can negate their effects.
4. **Prevent alignment of the ligands above and below the equatorial plane.** Unlike in complexes **1** and **2**, aligning the two ligands above and below the equatorial plane destroys the degeneracy of the d_{xy} and $d_{x^2-y^2}$ orbitals.

4.1.6 Conclusion

Kestrel has been used to analyse the SiMM properties of three structurally distinct homoleptic cobalt(II) complexes with large ZFS. In each complex, the ligand-field model was able to reproduce the available experimental data and provide insight into the origins of the axiality that effects the SiMM behaviour. For each system, various geometric and chemical bonding considerations were suggested to enhance the SiMM properties for that class of complex.

Complex **1** is a linear complex that exhibits maximal orbital angular momentum from its unique non-Aufbau ground state. The analysis of the available experimental data was not only able to model the origins of the non-Aufbau ground state, but also allowed an estimation of the strength of the electrostatic contribution to the e_π parameter, which would typically be presumed to be negligible according to chemical intuition. The work established a definite range of the e_π value from 0 cm^{-1} up to 750 cm^{-1}. Although the upper bound is still large for a formally non π bonding ligand, the value was still about half that predicted by *ab initio* calculations performed by *Bunting et al*., implying that the electrostatic effects calculated by CASSCF are perhaps overestimated.[122]

The SiMM properties of **1** were also analysed using the ligand-field model. To the author's knowledge, this was the first time that the experimentally determined time taken for QTM (τ_{QTM}) to occur (reported by *Bunting et al*.) had been modelled using a ligand-field model. The approximation of using just an e_σ and e_π parameter to model the local ligand fields of the alkyl ligands resulted in a linear global ligand field, which gave a perfectly axial system. To be able to model the lower symmetry of the complex, small but significant electrostatic contributions arising from the ligand backbone had to be used and were transferred from a supplementary *ab initio* calculation. By doing this, a reasonable prediction of τ_{QTM} was achieved and the model was able to predict how the axiality depended on the torsional angles of the two ligands with respect to one another in agreement with the *ab initio* results of *Zhang et al*.[120]

Complex **2** is a six coordinate antiprismatic complex that is not conventionally a SiMM but has a large experimentally determined ZFS (197 cm^{-1}). Analysis of the available reported experimental data assigned the pyrazolyl ligands as weak to moderate π donors in this work. Separating the constituent e_σ and $e_{\pi y}$ bonding parameters was made possible by simultaneous reproduction of the optical and magnetic data. The final electronic structure was predicted by the ligand-field model to have very fast rates of QTM in the ground state and, consequently, a value of U_{eff} far smaller than the known ZFS magnitude, which explains the lack of SiMM behaviour observed in **2**. Taking inspiration again from *ab initio* calculations performed by

Zhang et al., the ligand-field model was able to predict that twisting the structure of **2** from an antiprismatic to a prismatic structure would dramatically improve the axiality of the system.[121] The level of agreement between the ligand-field model and the *ab initio* results of *Zhang et al*. were very good. Extending this analysis to look at the effect that the axial distortion and metal-ligand bonding had on the axiality was able to provide clear and straightforward design principles in these types of systems.

Finally, complex **3**, an axially distorted four coordinate complex, was analysed. Complex **3** is an example of a SiMM with a large axial ZFS. The effect that the axial geometric distortion had on the SiMM behaviour was investigated. The ligand-field model predicted that the optimum angle for increasing the ZFS, increasing the U_{eff}, and quenching the QTM within the ground state was with an axial distortion of θ = 38°, which agreed with the *ab initio* results performed elsewhere.[144] Subsequent analysis extended this to investigate the relationship between the optimal angle of θ and the metal-ligand bonding. It was found that stronger π donors (or specifically, a greater $e_{\pi y}/e_{\sigma}$ ratio) require a larger optimum angle of θ and hence it was reasoned that ligands with larger radii for the coordinating atoms (e.g. sulfur) would require a larger optimum angle.

The torsional angles φ and ψ were also investigated for **3**. Unlike with complexes **1** and **2**, aligning the ligands above and below the equatorial plane did not enhance the axiality of the system, but instead diminished it. The angle of the π bonding (associated with ψ) was also found to be important when considering misdirected valence, which can occur under constrained geometric arrangements. Optimising all three geometric distortions would give very large axiality and an effective suppression of QTM within the ground state KD.

This work reproduces the same trends predicted by *ab initio* calculations reported from other authors but within the ligand-field framework and then extends those analyses to consider other geometric distortions and metal-ligand bonding modes. The ease with which changes to metal-ligand bonding or the molecular geometry are made is an advantage of the ligand-field model over *ab initio* methods. This is either because, in *ab initio* models, large changes must be made to the structural backbone of the ligands or the chemical nature of the ligand must be altered. This is readily available and easily achieved with the ligand-field model, which only considers the electronic potential about the central metal ion. This work lays the foundations for future analyses where the SiMM properties are probed, fitted to, and potentially used to inform chemical design to synthesise better SiMMs.

4.2 Ligand fields of nonheme S=1 iron(IV)-oxo complexes

4.2.1 Introduction

Iron(IV)-oxo systems are key reactive intermediates in non-heme iron enzymes. These intermediates oxidise otherwise functionally inert C–H bonds and have been found, or suggested, as part of the catalytic cycle for several non-heme iron enzymes such as TauD, prolyl-4-hydroxylase, halogenase CytC3, SyrB2, TyrH, and PheH.[147–149] In Nature, these Fe^{IV}=O intermediates are found to possess a high-spin (S=2) ground state electronic structure. In addition to the known examples from biology, there are numerous small-molecule biomimetic analogues, the vast majority of which are intermediate S=1 iron(IV) oxo systems.[150] These systems typically feature tetragonally distorted structures. The known high-spin S=2 synthetic analogues are typically five-coordinate trigonal bipyramidal complexes. Illustrative example structures are displayed in Figure 4.29.

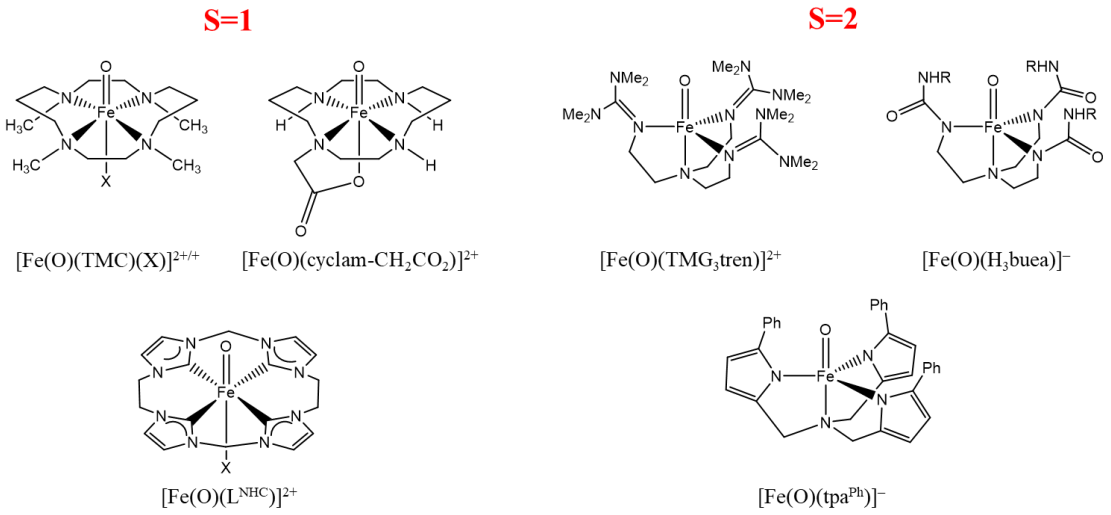

Figure 4.29. Illustrative cubic S=1 and trigonal S=2 Fe=O complexes.[151–156]

These model complexes have been studied both spectroscopically and theoretically. C–H oxidation by them has been suggested to proceed via two primary pathways involving either the $\sigma^*(d_{z^2})$ or $\pi^*(d_{xz}, d_{yz})$ orbitals, as shown in Figure 4.30 (A).[157,158] The reactive pathways are shown to occur on the quintet surface and extensive analysis has shown that the $\sigma^*(d_{z^2})$ channel is likely the most reactive orbital.[159] In this context, intermediate-spin iron(IV)-oxo systems typically access the high-spin quintet surface to generate the catalytically

active species.[158] This is possible because the triplet and quintet spin states entangle under then effects of spin-orbit coupling. Hence, the triplet-quintet energetic separation and mixing under the action of spin-orbit coupling is important for rationalising reactivity.[160] Other factors also have an effect on the reactivity, including the strength of the O–H bond in the corresponding Fe–OH intermediate as well as the sterics of the ligand backbone.[161–163]

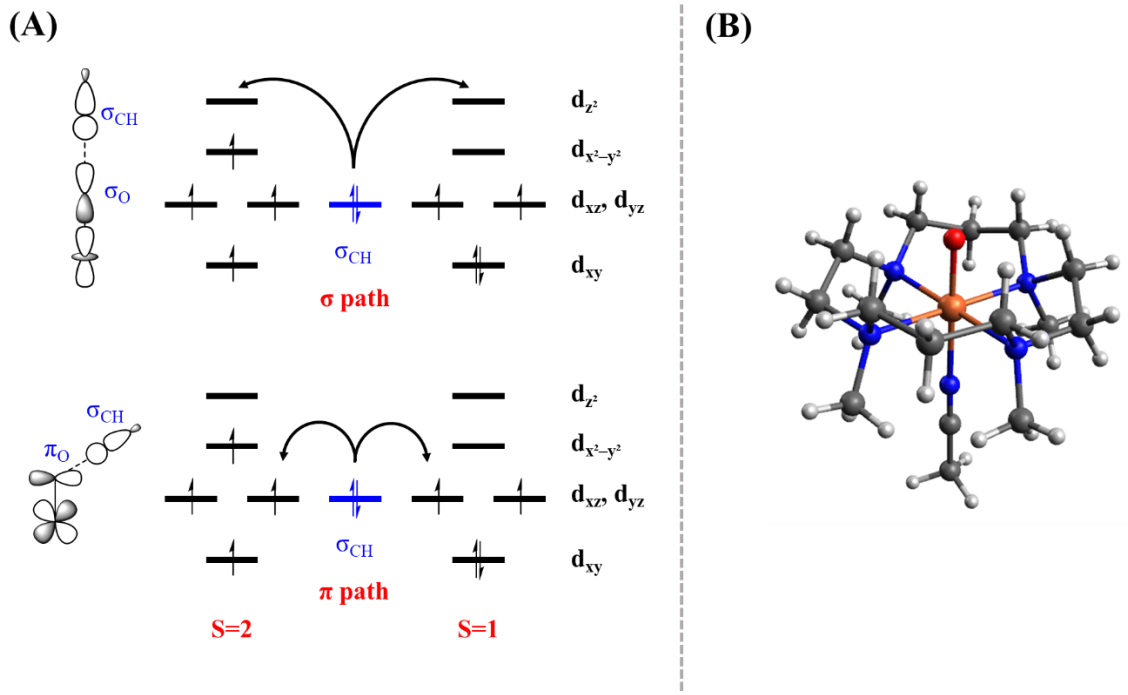

Figure 4.30. (A) The charge transfer processes involved during hydrogen atom abstraction of the CH bond of the $[FeO]^{2+}$ core. (B) the crystal structure (CSDC: WUSJOJ) of $[Fe(O)(TMC)(NCCH_3)]^{2+}$.[151]

In 2003, *Rohde et al*. were the first to structurally characterise a model intermediate spin iron(IV) oxo complex, $[Fe(O)(TMC)(NCCH_3)]^{2+}$ where TMC = 1,4,8,11-tetramethyl-1,4,8,11-tetraazacyclotetradecane, as shown in Figure 4.30 (B).[151] The crystal structure of $[Fe(O)(TMC)(NCCH_3)]^{2+}$ exhibits an approximate tetragonal C_{4v} geometry around the central iron(IV) ion, unlike the trigonal bipyramidal structures found in nature.

This work focussed on the reproduction of the physical properties of $[Fe(O)(TMC)(NCCH_3)]^{2+}$, which had been characterised experimentally by UV-Vis and VT-MCD spectra. The complex was previously subjected to a ligand-field analysis in a publication co-written by the author where a spectroscopic reassignment of the d-d bands was made.[151] The reassignment was controversial because the original assignment made by *Decker et al.*

has served as the primary interpretation of non-heme iron(IV)-oxo ligand-field spectroscopy.[164,165] Further detail of the reported spectroscopy and our reassignment are given in sections 4.2.1.2 and 4.2.1.4.

The analysis of $[Fe(O)(TMC)(NCCH_3)]^{2+}$ reported herein approaches the electronic structure from a different angle. In terms of ligand-field parameterisation, this system represents the simplest spectroscopically characterised S=1 iron(IV)-oxo complex, thus offering a system with a low number of variable parameters. There are a total of three functional groups: the oxo ligand, the acetonitrile ligand, and the equatorial amines. The equatorial amines are presumed σ donor only ligands, which avoids any analysis of any potential equatorial π bonding.

4.2.1.1 Electronic spectroscopy of S=1 Fe(IV) complexes of C_{4v} symmetry

Intermediate spin (S=1) iron(IV)-oxo systems have two unpaired electrons in their ground state. Under approximate C_{4v} symmetry, the d orbitals split into four levels with an orbital ordering of $d_{xy} < d_{xz}/d_{yz} < d_{x^2-y^2} < d_{z^2}$. The dominant electronic configuration for the S=1 ground state is $(d_{xy})^2(d_{xz}, d_{yz})^2(d_{x^2-y^2})^0(d_{z^2})^0$, which has $^3A_2$ symmetry. There are five spin-allowed one-electron transitions: three of ^3E symmetry; and two that give rise to a complicated multiplet structure, as shown in Figure 4.31. The electronic level with ^3E symmetry has an unequal occupation of the d_{xz} and d_{yz} orbitals; either one is doubly occupied whilst the other is singly occupied, or one is singly occupied whilst the other is vacant. These electronic energy levels result from one-electron transitions from the d_{xy} orbital into either the d_{xz} or d_{yz}, or from either of the d_{xz} or d_{yz} orbitals into the $d_{x^2-y^2}$ or d_{z^2} orbitals. Hence, there is a total of three d-d transitions of ^3E symmetry, labelled as ^3E ($d_{xy} \rightarrow d_{xz}, d_{yz}$), ^3E ($d_{xz}, d_{yz} \rightarrow d_{x^2-y^2}$), and ^3E ($d_{xz}, d_{yz} \rightarrow d_{z^2}$).

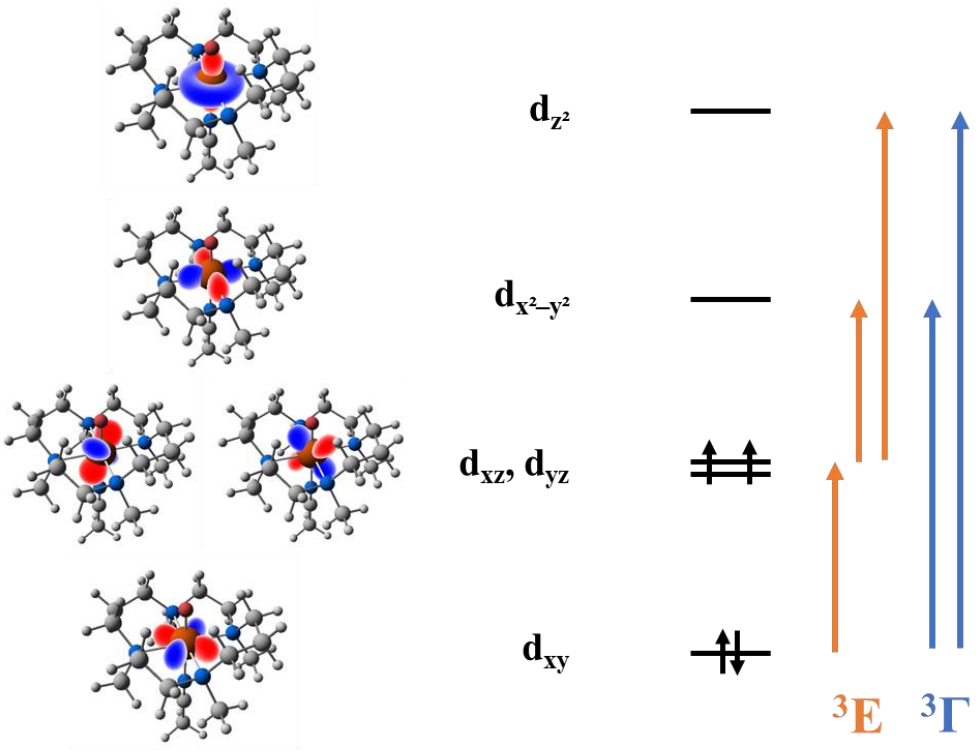

Figure 4.31. The spin-allowed one-electron d-d excitations in an S=1 tetragonal iron(IV) oxo complex. The d orbitals are generated and rendered using Kestrel and serve as illustrative depictions of their shapes and orientation.

There are two further spin-allowed one-electron d-d transitions, arising from electronic transitions from the d_{xy} orbital into either the $d_{x^2-y^2}$ or d_{z^2} orbitals. Each of these transitions has five separate excited states, as explained by *Ye et al.*[166] These transitions have two excited $^3B_1$ ($d_{xy} \rightarrow d_{x^2-y^2}$) and $^3A_1$ ($d_{xy} \rightarrow d_{z^2}$) states, each arising when the two unpaired electrons occupying the d_{xz} and d_{yz} orbitals are parallel. When the two unpaired electrons occupying the d_{xz} and d_{yz} orbitals are anti-parallel, the $d_{xy} \rightarrow d_{x^2-y^2}$ transitions have $^3A_1$, $^3A_2$, and $^3B_1$ symmetries, and the $d_{xy} \rightarrow d_{z^2}$ transition has excited states of $^3A_2$, $^3B_1$, and $^3B_2$ symmetries. From herein, these sets of transitions are labelled as $^3\Gamma$ ($d_{xy} \rightarrow d_{x^2-y^2}$) and $^3\Gamma$ ($d_{xy} \rightarrow d_{z^2}$).

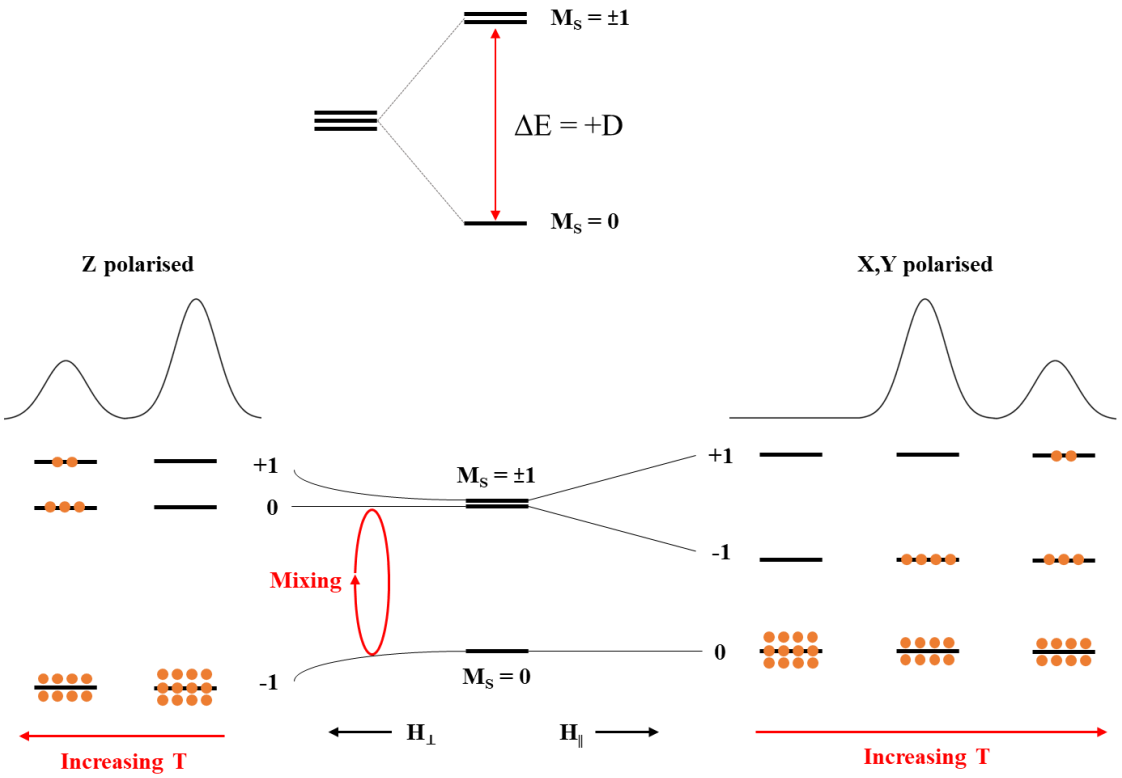

Figure 4.32. The zero-field splitting of the $^3A_2$ ground state under C_{4v} symmetry from spin-orbit coupling (top); and the relative MCD intensity of ligand-field bands from the application of directional magnetic fields as a function of temperature (bottom).

When perturbed by spin-orbit coupling, the $^3A_2$ ground state splits into two sub-levels. For D > 0 cm^{-1}, the $M_S = \pm 1$ levels are destabilised relative to the $M_S = 0$ level by a relative energy of |D|, as shown in Figure 4.32.[167] Under the application of an external magnetic field parallel to the principal C_4 axis, the $M_S = \pm 1$ levels split further.

MCD ligand-field transitions of x,y polarisation show variable temperature dependence when the magnetic field is applied along the C_4 axis.[165] These transitions gain intensity at temperatures when the stabilised $M_S = -1$ state is populated preferentially to the $M_S = +1$ state. As the temperature increases, the higher lying $M_S = +1$ state is populated and the intensity of the MCD signal decreases.

The z polarised transitions gain intensity when the magnetic field is applied in the perpendicular direction to the principal C_4 axis.[165] This direction of the external magnetic field mixes the $M_S = 0$ level into the $M_S = \pm 1$ levels. These transitions are intense in the MCD at low temperatures when the $M_S = -1$ is preferentially populated. As the temperature increases, z polarised transition lose intensity as the higher lying $M_S = -1$ and 0 states are populated.[168]

4.2.1.2 Spectroscopy of $[Fe(O)(TMC)(NCCH_3)]^{2+}$

[Fe(O)(TMC)(NCCH3)]$^{2+}$ was the first example of a spectroscopically characterised S=1 iron(IV)-oxo model complex. The system was characterised by Mössbauer studies, and the electronic structure was characterised by a S=1 ground state with a value of D = +29 cm^{-1}.[151] Subsequent work by *Decker et al*. studied the optical and VT-MCD spectra of this complex (Figure 4.33).[165] Their analysis assigned the presence of five d-d bands in the optical window of 5000 to 28000 cm^{-1}. The relative energies, polarisations, and assignments of these bands are summarised in Table 4.9.

Table 4.9. The experimental d-d transition energies of $[Fe(O)(TMC)(NCCH_3)]^{2+}$ with their irreducible representations, transition assignments, and polarisation behaviour reported by *Decker et al*.[165]

Transition	Energy (cm^{-1})	$^{2S+1}\Gamma$, irrep	Assignment	Polarisation
I	10400	$^3\Gamma$	$d_{xy} \rightarrow d_{x^2-y^2}$	z
II	10600	^3E	$d_{xy} \rightarrow d_{xz}, d_{yz}$	x,y
III	12900	^3E	$d_{xz}, d_{yz} \rightarrow d_{x^2-y^2}$	x,y
IV	17600	^3E	$d_{xz}, d_{yz} \rightarrow d_{z^2}$	x,y
V	24900	$^3\Gamma$	$d_{xy} \rightarrow d_{z^2}$	z

The experimental VT-MCD spectra of *Decker et al*. assigned the polarisation of the individual bands from their variation in intensity with temperature. Bands II, III, and IV reach maximum intensity at 20 K before dropping in intensity for increasing temperatures. Hence, they were assigned to x, y polarised d-d transitions. Bands I and V are at maximum intensity at the lowest temperature probed in the experiment (2 K) and the intensity decreases for higher temperature, assigning them as z-polarised d-d transitions. It should be noted here that the temperature dependence of bands I and II are not exactly known as the bands overlap. Their relative temperature dependence was achieved by assuming that the intensity variation with temperature of band I behaves the same as band V. Band II was assigned as the $d_{xy} \rightarrow d_{xz}$, d_{yz} transition due to the presence of a vibrational progression associated with the weakening of the Fe=O bond via the promotion of an electron from the non-bonding d_{xy} to the anti-bonding d_{xz}/d_{yz} orbitals with π symmetry. Band III is the most intense band in the reported electronic absorption spectrum with an $\varepsilon \approx 400\ M^{-1}\ cm^{-1}$.[165]

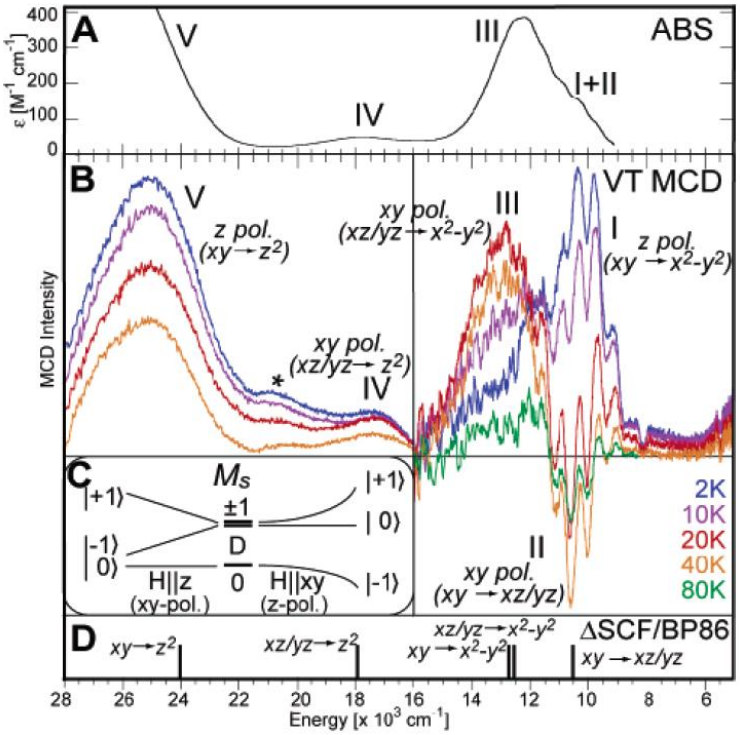

Figure 4.33. The experimental electronic absorption (A) and VT-MCD (B) spectra of $[Fe(O)(TMC)(NCCH_3)]^{2+}$. Selection rules of electronic transition polarisation (C) and ΔSCF/BP86 computed transition energies and assignments (D). Reprinted with permission from A. Decker, J.-U. Rohde, L. Que, and E. I. Solomon, J. Am. Chem. Soc., 2004, 126, 5378–5379. Copyright 2004, American chemical Society.

4.2.1.3 Computational modelling of ligand-field transitions in iron(IV) oxo systems

Due to their complicated multiplet structure and the potential for high covalency in the Fe=O bond, calculations of excited state energies in iron(IV)-oxo systems can be difficult. These difficulties arise from the large number of configuration state functions needed to represent the excited states and the importance of balancing the active space with the ligand orbitals. The following review of previous calculations of S=1 iron (IV)-oxo systems reveals some of these issues.

4.2.1.3.1 Electronic structure analysis of $[Fe(O)(TMC)(NCCH_3)]^{2+}$

The d-d transition energies of $[Fe(O)(TMC)(NCCH_3)]^{2+}$ were computed by *Decker et al*. with both ΔSCF/BP86 and TD-DFT (statistical average of orbital potentials) methods.[169] The former showed good agreement with the relative energies of the ^3E excited states with a difference < 400 cm^{-1} but overpredicted the energies of bands I and V by approximately 2100 and 1000 cm^{-1} respectively. TD-DFT calculations gave a larger deviation in the prediction of the transition energies, except for band I which shifted to within 1100 cm^{-1} of experimental values. While TD-DFT is clearly inferior in this regard, care should be taken when using TD-DFT for iron(IV)-oxo systems, as it does not take into account all constituent roots of the $d_{xy} \rightarrow d_{x^2-y^2}$ and $d_{xy} \rightarrow d_{z^2}$ transitions (see section 4.2.1.1).[170]

The excited state energies of a simpler model system $[Fe(O)(NH_3)_4(H_2O)]^{2+}$ computed by SORCI(4, 5) were compared to the experimental energies of $[Fe(O)(TMC)(NCCH_3)]^{2+}$.[171] The transition energies were in fair agreement with experiment, but the ^3E ($d_{xy} \rightarrow d_{xz}$, d_{yz}) and ^3E (d_{xz}, $d_{yz} \rightarrow d_{x^2-y^2}$) transition energies were underestimated and overestimated respectively, by approximately 2400 cm^{-1}. The calculations predicted that four of the $^3\Gamma$ ($d_{xy} \rightarrow d_{x^2-y^2}$) components are lower in energy than the ^3E (d_{xz}, $d_{yz} \rightarrow d_{x^2-y^2}$) band but still above the ^3E ($d_{xy} \rightarrow d_{xz}$, d_{yz}) band. The relative ordering of excited states, which is not what is expected by a simple molecular orbital analysis, was compared with a computational analysis of a manganese(III) system. Here, the authors concluded that the coulombic and exchange integrals of interelectronic repulsion (as calculated in their models) were anisotropic; some integrals were found to differ by > 1 eV.[172] Note here that in LFT these integrals are constrained to be equal and this explanation, if true, would compromise a core assumption of the ligand-field model that Kestrel employs.

The $[Fe(O)(TMC)(NCCH_3)]^{2+}$ complex was also subjected to a ligand-field density-functional theory (LFDFT) analysis by *Atanasov et al*. as part of an overview and critical evaluation of this method.[173] The LFDFT results were compared with the experimental transition energies (Table 19-13 of *Atanasov et al*.), where only four of the five experimental bands and their polarisation are quoted as 10500 (xy), 13000 (xy), 17000 (z), and 25000 (z) cm^{-1}. The reported overlapping bands of xy and z polarisation at 10400 cm^{-1} and 10600 cm^{-1} are not separately acknowledged. The authors state in Table 19-13 that the band at 17000 cm^{-1} (band IV) is assigned as the $^3\Gamma(d_{xy} \rightarrow d_{x^2-y^2})$, which LFDFT predicts at an energy of 19347 cm^{-1}, as the ^3E (d_{xz}, $d_{yz} \rightarrow d_{z^2}$) is calculated with an energy of 22184 cm^{-1}.[173] The main text does not discuss this reassignment from the assignment made by *Decker et al*. Otherwise, the calculations predict the energies of the other ^3E bands in reasonable agreement with experiment, at 11968 cm^{-1} and 15680 cm^{-1}.

4.2.1.3.2 Electronic structure of other iron(IV) oxo complexes

Ab initio methods have been used to compute the d-d and charge transfer excitation energies for mono and bi nuclear S=1 iron(IV)-oxo systems.[174] One such study focussed on the MCD spectrum of $[Fe(O)(L)(NCMe)]^{2+}$, where L = tris(3,5-dimethyl-4-methoxylpyridyl-2-methyl)amine). The analysis was able to predict VT-MCD spectra from the results of CASSCF(12, 9)/NEVPT2 in good agreement with the experimental VT-MCD data. The analysis afforded good reproduction of the experimental transition energies and placed the $^3A_2$ component of the $^3\Gamma$ ($d_{xy} \rightarrow d_{x^2-y^2}$) transition at 13170 cm^{-1} on top of the ^3E (d_{xz}, $d_{yz} \rightarrow d_{x^2-y^2}$) and ^3E ($d_{xy} \rightarrow d_{xz}$, d_{yz}) excited states calculated at 11950 cm^{-1} and 13360 cm^{-1}, respectively. The electronic structure was found to be like $[Fe(O)(TMC)(NCCH_3)]^{2+}$ and hence this further supported the assignment of the d-d spectrum of $[Fe(O)(TMC)(NCCH_3)]^{2+}$ made by *Decker et al*.

Another *ab initio* analysis of the VT-MCD spectrum of a S=1 iron(IV)-oxo system was carried out for a tetracarbene system with a strong equatorial ligand field.[166] The equatorial ligand field was sufficiently strong that the excited state ordering of the ^3E (d_{xz}, $d_{yz} \rightarrow d_{x^2-y^2}$) and ^3E (d_{xz}, $d_{yz} \rightarrow d_{z^2}$) excitations was reversed in comparison to $[Fe(O)(TMC)(NCCH_3)]^{2+}$, being at 16960 cm^{-1} and 24290 cm^{-1} respectively. The calculations reproduced the MCD assigned energies of the ^3E states to within 3000 cm^{-1} but overpredicted the $^3A_2$ components of the $^3\Gamma$ ($d_{xy} \rightarrow d_{x^2-y^2}$) and $^3\Gamma$ ($d_{xy} \rightarrow d_{z^2}$) excitations by 6000 cm^{-1}. The reason for the poor agreement in the latter electronic levels was attributed to an underestimation of the mixing between the LMCT (O p_x, $p_y \rightarrow d_{xz}$, d_{yz}) and the $^3\Gamma$ states due to the contracted nature of the active space (CASSCF(12, 9)/NEVPT2). Unfortunately, larger active space calculations were not possible due to computational limitation. The computed MCD spectrum did not accurately model the experimental MCD spectra that exhibit all positive intensity at low temperatures for the ^3E (d_{xz}, $d_{yz} \rightarrow d_{z^2}$) band. In fact, the calculated $^3A_2$ components of the $^3\Gamma$ ($d_{xy} \rightarrow d_{x^2-y^2}$) and $^3\Gamma$ ($d_{xy} \rightarrow d_{z^2}$) excitations seemed to show negligible intensity in the simulated spectrum. The authors also carried out a fit of the AOM model to their 5×5 one-electron ligand-field matrix extracted from the AILFT of the CASSCF(4, 5) calculations where the oxo ligand was assigned as a strong σ donor and π donor. Complementary to this, the authors also fitted the energies of the first excited quintet band $^5A_1$ and the three ^3E bands of the CASSCF(12, 9)/NEVPT2 calculations using ligand-field expressions derived from the strong field configurations, parameterised by orbital energies and Racah B and C parameters. These expressions and results were reported in the supporting information. Despite this, no attempt was made by the authors to fit the $^3A_2$ bands ($d_{xy} \rightarrow d_{x^2-y^2}$).

A combination of DFT and *ab initio* calculations (CASSCF(16, 11)) have been used to probe the electronic structure of a quintet trigonal $[Fe(O)(TMG_3tren)]^{2+}$ where TMG_3tren = 1,1,1-tris{2-[N2-(1,1,3,3-tetramethylguanidino)]ethyl}amine.[175] The calculations were able to reproduce the spin-Hamiltonian parameters derived from HFEPR spectroscopy (High-Frequency EPR). LFT calculations were also carried out on the limited spectroscopic data and managed to reproduce the available excited state spectroscopy and the ground state ZFS. The g-factors were calculated from the energies of the ligand-field wavefunctions in the presence of an external magnetic field and compared to the experimentally determined values. The calculated $g_{||}$ [2.0015(5)] was in reasonable agreement with the experimental value extracted by HFEPR, $g_{||}$ = 2.03(2). However, the same LFT calculations predicted a value of $g_{\perp}$ far too low (1.6) compared to the experimentally derived value $g_{\perp}$ = 2.006(2). It should be noted that the ligand-field fitting of $[Fe(O)(TMG_3tren)]^{2+}$ was performed to the d-d transitions and the problem was underdetermined. The authors did not vary the ligand-field parameters to fit the EPR g-factors. It is not clear if there is a set of ligand-field parameters that can reproduce the experimental g-factors.

4.2.1.4 Ligand-field analysis of $[Fe(O)(TMC)(NCCH_3)]^{2+}$

The preceding section outlined the computational methods used to analyse $[Fe(O)(TMC)(NCCH_3)]^{2+}$ and other iron(IV) oxo systems. Ligand-field calculations of iron(IV) oxo complexes in the literature are scarce. There are examples of AOM analyses of the 5×5 one-electron ligand-field matrix extracted from AILFT to provide e_λ parameters. However, the fitting of experimental d-d transitions using an e_λ parameterisation in an intermediate spin (S=1) non-heme iron(IV) oxo complex, to the author's knowledge, has only be carried out using Kestrel by *Comba et al*.[176] That analysis correlated the energetic splitting of the $^3A_2$ ground state with the first excited $^5A_1$ ($d_{xy} \rightarrow d_{x^2-y^2}$) transition and the reported reactivity of a series of S=1 iron(IV)-oxo complexes with different equatorial ligand-field strengths. The calculations showed that weaker σ bonding in the equatorial plane increased the mixing of the $^5A_1$ state into the $^3A_2$ ground state. The analysis accurately reproduced the energies of the three observed ^3E bands in the UV-vis spectra of the analysed complexes.

As part of that work, a ligand-field analysis was carried out on the $[Fe(O)(TMC)(NCCH_3)]^{2+}$ complex to provide an estimate of the e_λ parameters for the Fe=O bond to be used for the other systems of interest. Attempts to fit the experimental d-d bands as assigned by *Decker et al*. were unsuccessful. In particular, the ligand-field analysis was unable to account for the ostensibly low energy of the experimental $^3\Gamma$ ($d_{xy} \rightarrow d_{x^2-y^2}$) transition

at 10400 cm^{-1} and, as such, tentatively reassigned that band as arising from a triplet-to-quintet spin-forbidden $d_{xy} \rightarrow d_{z^2}$ transition, which gains intensity through spin-orbit coupling to the ^3E ($d_{xy} \rightarrow d_{xz}$, d_{yz}) and ^3E (d_{xz}, $d_{yz} \rightarrow d_{x^2-y^2}$) bands. A detailed discussion about the assignment and the electronic structure was beyond the scope of the paper at the time, which aimed to semi-quantitatively show the relationship between the strength of the equatorial ligand field and the triplet-quintet energetic gap. However, Kestrel was able to recreate the energies of all other d-d bands in $[Fe(O)(TMC)(NCCH_3)]^{2+}$, along with the ZFS, and qualitatively reproduce the computed triplet-quintet energy gap predicted by DLPNO-CCSD(T) for the other complexes.[177]

4.2.1.5 This work

At the time of our tentative reassignment of the spin-allowed $d_{xy} \rightarrow d_{x^2-y^2}$ band to the spin-forbidden triplet-to-quintet $d_{xy} \rightarrow d_{z^2}$ transition, Kestrel did not have many of its current features. It did not have, for example, a configuration projection output, nor could it predict d-d transition intensities. The configuration projections were originally carried out by varying Racah B and tracking the energies of the triplet bands. However, given that Kestrel has since developed further and can now predict the UV-Vis and VT-MCD spectral intensities, it is prudent to return to the electronic structure of $[Fe(O)(TMC)(NCCH_3)]^{2+}$.

A further reason for reanalysing $[Fe(O)(TMC)(NCCH_3)]^{2+}$ with Kestrel is that spin-intermediate iron(IV)-oxo systems represent an important class of transition-metal complexes that are characterised as covalent complexes.[161] These types of complexes potentially breach the assumptions of the effective Hamiltonian used by Kestrel, whether it be from charge-transfer mixing, or the spherical treatment of interelectronic repulsion. It is important, therefore, to know whether the ligand-field model can reproduce experiment, what parameters these reproductions involve, and thus establish if the LFT approach is viable for such ostensibly "covalent" complexes.

The approach taken was to perform expanded active space *ab initio* calculations on $[Fe(O)(TMC)(NCCH_3)]^{2+}$ and to then calculate the expected UV-Vis absorption and VT-MCD spectra. The computational work followed the methodologies and processes as outlined before.[166,174] After this, a detailed ligand-field analysis was carried out on the experimental UV-Vis absorption and VT-MCD spectra. The electronic structures from the two methods were compared and their relative merits discussed in terms of reproduction of the experimental data.

4.2.2 Methodology

4.2.2.1 Quantum-chemical calculations

Calculations were performed using ORCA 4.2.1.[42] The basis set used throughout was the ma-def2-TZVP(-f).[129,178] Geometry optimisations were carried out on the x-ray crystal structure (CSD: WUSJOJ)[151] using the BP86 functional along with the van der Waals correction (D3BJ).[179–181] To include the solvation effects of acetonitrile, the CPCM method was used.[182] The density fitting and "chain of spheres" (RIJCOSX) approximations along with the auxiliary basis sets def2-TZV/J were used to improve the speed of calculations.[183,184] *Ab initio* calculations utilised CASSCF and NEVPT2. The minimal active space consisted of four electrons in five orbitals and the expanded active space utilised twelve electrons in nine orbitals. AILFT was carried out using the CASSCF(4, 5) results.[31] MCD calculations were carried out following the relevant protocol.[166,174] The UV-Vis and MCD spectra were plotted using the orca_mapspc command line tool.

4.2.2.2 Ligand-field calculations

Ligand-field calculations were performed using a complete d^4 basis, consisting of 210 basis functions. The DFT optimised geometry given in Table 6.5 (appendix 6.5) was used throughout, except for chapter 4.2.4.3 where an idealised model was used. The idealised geometry used the angular coordinates of a regular octahedron, where θ = 0°, 180°, 90°, 90°, 90°, and 90°, and φ = 0°, 0°, 0°, 90°, 180°, and 270° for the oxo, acetonitrile, and the four amine ligands respectively.

The iron(IV) central metal-ion was parameterised with the interelectronic repulsion parameters B and C, and the spin-orbit coupling operator ζ, with a lower bound of 0 cm^{-1} and upper bounds given by their free-ion values: B_0 = 1144 cm^{-1}, C_0 = 4459 cm^{-1}, and ζ_0 = 520 cm^{-1}.[125]

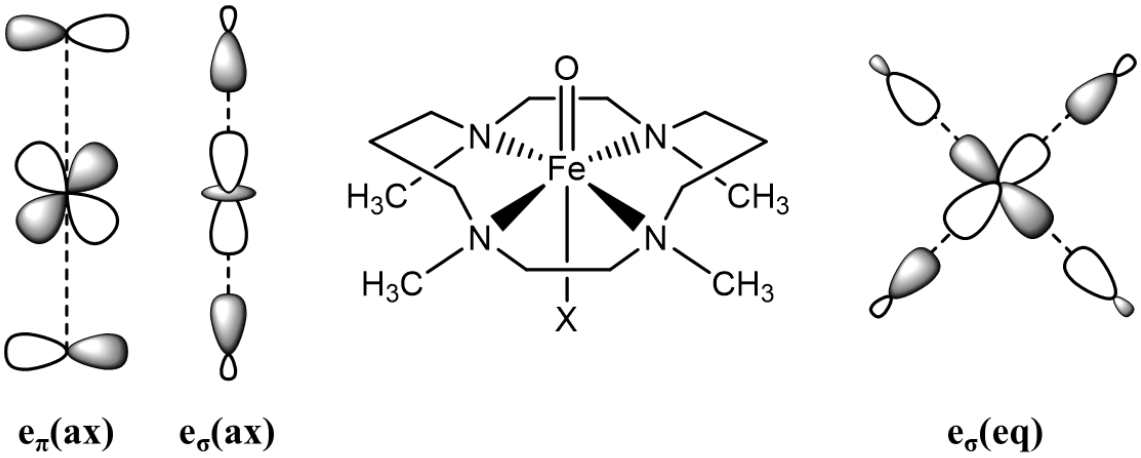

Figure 4.34. The metal-ligand bonding parameterisation for $[Fe(O)(TMC)(X)]^{2+}$, where X = acetonitrile.

The e_λ parameters for the axial oxo and acetonitrile ligands were assigned an overall $e_\sigma(ax)$ and $e_\pi(ax)$ parameter. The equatorial nitrogen ligators of the TMC ligand were each assigned a common $e_\sigma(eq)$ parameter. The metal-ligand bonding pseudo-symmetries are illustrated in Figure 4.34.

For simulating UV-Vis and MCD spectra, intensity parameters P_σ, F_σ, P_π, and F_π were assigned to the oxo ligand, where they represent the difference of the P_λ and F_λ parameters relative to the $NCCH_3$ ligand ($O - NCCH_3$). The equatorial nitrogen atoms were initially simulated using just $P_\sigma(eq)$ and $F_\sigma(eq)$ parameters. However, the geometry is such that the intensity parameters of the equatorial nitrogen atoms approximately cancel out in comparison to the analogous axial values. Therefore, the $P_\sigma(eq)$ and $F_\sigma(eq)$ parameters were fixed to 0 and neglected in the analysis. Predicted UV-Vis and MCD spectra were simulated and plotted with a common FWHM.

4.2.2.3 Fitting results of *ab initio* calculations with the ligand-field model

The 5×5 one-electron ligand-field matrices extracted from the results of CASSCF(4, 5) and NEVPT2 calculations, performed in section 4.2.3.2, were used to extract e_λ parameters. The optimisation was carried out using the differential_evolution method.[96] The $e_\sigma(ax)$ was constrained to a lower bound of 5000 cm^{-1} and an upper bound of 20000 cm^{-1}; the $e_\pi(ax)$ was constrained to a lower bound of 0 cm^{-1} and an upper bound of 10000 cm^{-1}; and the $e_\sigma(eq)$ was constrained to a lower bound of 0 cm^{-1} and an upper bound of 10000 cm^{-1}.

The ligand-field model was used to fit the relevant spin-allowed and spin-forbidden d-d transition energies calculated from a CASSCF(12, 9)/NEVPT2 calculation. The optimisation was also carried out using the differential_evolution method.[96] The Racah B was constrained to a lower bound of 0 cm^{-1} and an upper bound of 1200 cm^{-1}; Racah C was constrained to a lower bound of 0 cm^{-1} and an upper bound of 4500 cm^{-1}; $e_\sigma(ax)$ was constrained to a lower bound of 10000 cm^{-1} and an upper bound of 20000 cm^{-1}; the $e_\pi(ax)$ was constrained to a lower bound of 0 cm^{-1} and an upper bound of 10000 cm^{-1}; and the $e_\sigma(eq)$ was constrained to a lower bound of 0 cm^{-1} and an upper bound of 10000 cm^{-1}.

4.2.2.4 Fitting experimental band energies with the ligand-field model

Variation of the ligand-field parameters (B, C, and e_λ) to determine the parameter value ranges to reproduce the experimental d-d band energies, as presented in chapter 4.2.4.4, were performed using KestrelPy's parameter-space calculations. The Racah B parameter was varied from 0 cm^{-1} to 1000 cm^{-1}, in increments of 100 cm^{-1}; Racah C was varied from 2000 cm^{-1} to 4000 cm^{-1}, in increments of 200 cm^{-1}; $e_\sigma(ax)$ was varied from 9000 cm^{-1} to 13000 cm^{-1}, in increments of 400 cm^{-1}; $e_\pi(ax)$ was varied from 4000 cm^{-1} to 7000 cm^{-1}, in increments of 300 cm^{-1}; and $e_\sigma(eq)$ was varied from 5000 cm^{-1} to 8000 cm^{-1}, in increments of 600 cm^{-1}. The spin-orbit coupling constant ζ was set to 0 cm^{-1}.

The transition energies and their assignments as defined in Table 4.17 were used. The first quintet excited state was weighted (at 0.5) as less important than the *known* spin-allowed band energies.

4.2.2.5 Fitting the experimental UV-Vis and VT-MCD spectra with the ligand-field model

Simulations of the UV-Vis and VT-MCD spectra were calculated as arising from transitions originating within the $^3A_2$ ground state to the complete excited state manifold. The MCD spectra were simulated at 2 K, 10 K, 20 K, 40 K, 80 K with a magnetic field strength of 7 T. MCD simulations were performed over an angular grid of 30 steps spanning $0 \leq \theta \leq \pi$ and $0 \leq \varphi \leq 2\pi$.

Since the calculation of MCD spectra in Kestrel is not sufficiently fast to vary a large number of parameters it was instead chosen to vary the transition dipole moment parameters (excluding equatorial amine parameters, see section 4.2.2.2) and fit the relative intensities of

the experimental UV-Vis and VT-MCD spectra manually. The decision to manually refine the transition dipole moment parameters was made not only because of computational limitations but because at least one chemically sensible fit of the experimental spectrum is required to provide evidence of the d-d band assignment of *Comba et al*.[176]

Saturation of the MCD intensity was performed by calculating the MCD intensities for a temperature range of 2 K to 300 K, in increments of 0.5 K. The intensity value for each temperature was taken by using the Spectrum object's plot_spectrum method with a FWHM = 2500 cm^{-1}.

4.2.3 Quantum-chemical calculations

4.2.3.1 Geometry optimisation

Geometry optimisations of $[Fe(O)(TMC)(NCCH_3)]^{2+}$ were carried out on the x-ray crystal structure coordinates (CSD: WUSJOJ) and the final calculated structure is shown in Figure 4.35.[151] A comparison of the calculated and x-ray structure bond lengths of the first coordination sphere is presented in Table 4.10. The computed structure is in good agreement with the experimental x-ray structure with a RMSD of 0.1511 Å. The main discrepancy found between the calculated and x-ray structures was in the iron-acetonitrile bond length, where the optimised structure has a shorter bond length by 0.057 Å. The remaining iron-nitrogen bond lengths are, on average, 0.018 Å longer than their crystal structure bond lengths. The calculated iron-oxo bond length is close to the experimentally observed bond length. The final optimised coordinates are given in Table 6.5 (appendix 6.5).

Table 4.10. Comparison of the reported experimental (CSD: WUSJOJ) and calculated bond lengths (Å) of $[Fe(O)(TMC)(NCCH_3)]^{2+}$.[151]

Structure	Fe–O	Fe–N3	Fe–N4	Fe–N5	Fe–N6	Fe–N53
WUSJOJ	1.646(6)	2.069(3)	2.109(3)	2.117(3)	2.067(3)	2.058(3)
Calculated	1.65182	2.09567	2.12229	2.12369	2.09289	2.00066

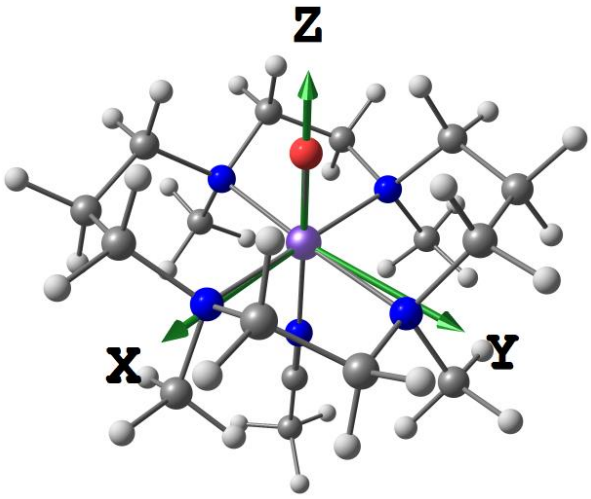

Figure 4.35. The optimised geometric structure of $[Fe(O)(TMC)(NCCH_3)]^{2+}$ in acetonitrile overlaid with the chosen molecular axes used for ligand field and *ab initio* calculations.

4.2.3.2 Minimal active space CASSCF(4, 5)

An *ab initio* calculation was carried out on the minimal active space with four electrons in five orbitals. The calculations were carried out over the full number of configurational roots for the quintet and triplet manifolds (5 and 45 respectively). The calculated relative energies of the relevant d-d transitions are given in Table 4.11.

The CASSCF(4, 5) calculations incorrectly predict a high spin (quintet) ground state. The inclusion of dynamical correlation with NEVPT2 did restore the triplet ground state but erroneously predicted the d-d transition energies in comparison with experiment. As will be shown in section 4.2.3.3, a balanced expanded active space involving ligand orbitals is required to provide quantitatively good reproduction of the experimental ligand-field band energies under NEVPT2 corrections.

Table 4.11. The CASSCF(4, 5) and NEVPT2 calculated non-relativistic d-d transition energies (cm^{-1}) normalised by the energy of the $^3A_2$ state for $[Fe(O)(TMC)(NCCH_3)]^{2+}$

Assignment	CASSCF(4, 5)	NEVPT2	Experiment[165]
$^3A_2$	0.0	0.0	
^3E ($d_{xy} \rightarrow d_{xz}$, d_{yz})	10978.2, 11288.3	17303.1, 17747.1	10400
^3E (d_{xz}, $d_{yz} \rightarrow d_{x^2-y^2}$)	24165.8, 24875.1	12864.0, 14009.1	12900
^3E (d_{xz}, $d_{yz} \rightarrow d_{z^2}$)	19106.3, 19157.6	3971.2, 4997.0	17500
$^3\Gamma$ ($d_{xy} \rightarrow d_{x^2-y^2}$)	10859.4, 12320.1	22807.1, 24004.1	10600
	12576.1, 14714.0	24294.1, 25648.7	
	18099.1	29831.3	
$^3\Gamma$ ($d_{xy} \rightarrow d_{z^2}$)	26534.9, 28307.1	37175.3, 38918.2	24900
	30207.0, 32343.6	39369.6. 40524.4	
	36694.4	41590.3	
$^5A_1$ ($d_{xy} \rightarrow d_{x^2-y^2}$)	–7761.1	7645.7	–
$^5B_1$ ($d_{xy} \rightarrow d_{z^2}$)	7855.0	19854.9	–
^5E ($d_{xy}^1 d_{yz/xz}^1 d_{x^2-y^2}^1 d_{z^2}^1$)	11696.9	21116.7, 25319.4	–
$^5B_2$ ($d_{xz}^1 d_{yz}^1 d_{x^2-y^2}^1 d_{z^2}^1$)	28486.8	54104.4	–

The minimal active space allows for an AILFT analysis to be carried out at the end of the calculation in ORCA using the actorbs_dorbs keyword. The AILFT fit (where ORCA fits the CASSCF/NEVPT2 transition energies using its own ligand-field Hamiltonian) to the CASSCF(4,5) energies was poor with a RMS of 3185.5 cm^{-1} and 5745.2 cm^{-1} for the quintet and triplet manifolds respectively. Hence, the final AILFT fitting from ORCA must be taken with caution. As part of the AILFT analysis, the 5×5 one-electron ligand-field matrix is reported, the diagonalisation of which gives the relative energies of the five mixed d orbitals. These eigenfunctions are presented in Table 4.12. The results give the five relative energies of the d orbitals along with the linear combination of the d orbitals in the molecular frame as shown in Figure 4.35 of section 4.2.3.1. Both the CASSCF(4, 5) and CASSCF(4, 5)/NEVPT2 calculations predicted a d-orbital splitting of $d_{xy} < d_{xz}$, $d_{yz} < d_{x^2-y^2} < d_{z^2}$. As expected, the d_{xz} and d_{yz} orbitals are approximately degenerate. The inclusion of dynamical correlation via NEVPT2 increases the energy gap between the non-bonding d_{xy} and all other d orbitals, implying stronger metal-ligand interactions as a result of dynamic correlation between the ligand field and the d-orbital electrons.

Table 4.12. The energies (cm^{-1}) and eigenvectors of the 5×5 one-electron ligand-field matrices from the AILFT analysis of the CASSCF(4, 5) and NEVPT2 calculations.

Source	Energy	d_{xy}	d_{yz}	d_{z^2}	d_{xz}	$d_{x^2-y^2}$
CASSCF	0.0	0.993	-0.007	0.025	0.011	0.118
	11653.9	-0.014	-0.748	0.004	0.664	0.003
	11972.0	-0.013	-0.657	0.017	-0.741	0.134
	16486.3	-0.117	0.093	-0.005	0.098	0.984
	31344.0	-0.025	0.015	1.000	0.010	-0.001
NEVPT2	0.0	-0.993	0.001	-0.024	-0.006	-0.118
	19226.1	0.004	0.724	0.005	-0.690	0.007
	19570.9	-0.002	-0.689	0.016	-0.723	0.042
	22141.7	-0.118	0.024	-0.001	0.035	0.992
	34991.3	-0.024	0.008	1.000	0.015	-0.002

As part of the AILFT module, the fitted Racah B and C parameters are reported. For the CASSCF(4, 5) calculation, values of B = 1003.1 cm^{-1} and C = 3731.5 cm^{-1} were extracted, representing a 13.3% and 16.3% reduction from the free-ion values respectively. The values extracted for the CASSCF(4, 5)/NEVPT2 energies were B = 836.7 cm^{-1} and C = 1855.6 cm^{-1}, representing a 26.9% and 58.4% reduction from the free-ion values respectively. The inclusion of dynamical correlation severely reduces C with respect to B. The origin of this reduction will be discussed later, but it is evident that the large difference in the reduction of B and C parameters from their free ion values potentially reveals an underlying issue with the AILFT analysis using the CASSCF/NEVPT2 energies. Moreover, caution must be applied to these parameters as the quality of fit of these AILFT analyses from ORCA to the CASSCF(4, 5)/NEVPT2 transition energies are poor (*vide supra*).

4.2.3.3 Expanded active space CASSCF(12, 9)/NEVPT2

Due to the covalency of the Fe=O bond, it is thought that iron(IV)-oxo systems require an expanded active space to achieve quantitative reproduction of ligand-field transition energies.[166,174] Thus, for the studies reported herein, the active space was expanded to include the bonding orbital counterparts of the antibonding d_{xz}, d_{yz}, $d_{x^2-y^2}$, and d_{z^2} orbitals. This choice resulted in an active space involving twelve electrons housed in nine orbitals. Bonding orbitals were chosen from generated quasi-restricted orbitals and the final expanded active CASSCF space orbitals are shown in Figure 4.36.

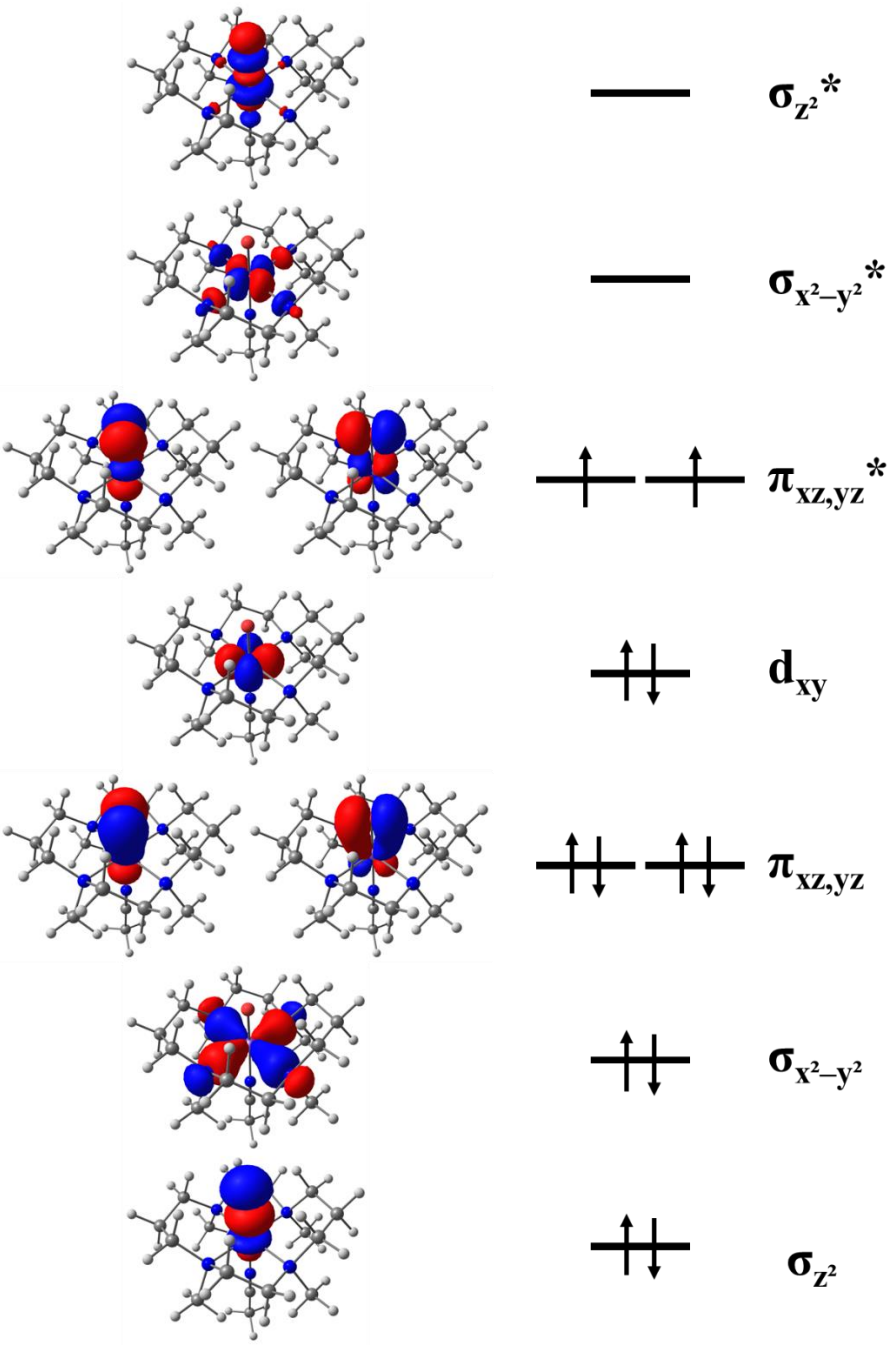

Figure 4.36. The CASSCF(12, 9) optimised active space orbitals plotted with a contour value of 0.05.

The CASSCF(12, 9) calculations, like with the minimal active space, predicted a quintet ground state. The relative triplet CASSCF(12, 9) energies were in poor agreement with the experimentally observed transition energies (Table 4.13). The ^3E (d_{xz}, d_{yz} → $d_{x^2-y^2}$) band was predicted to lie at 5671.5 cm^{-1} and 5960.6 cm^{-1}, under-estimating the calculated transition

energy by approximately 8000 cm^{-1}. However, the ^3E ($d_{xy} \rightarrow d_{xz}$, d_{yz}) transition was predicted at approximately 12199.4 cm^{-1} and 12413.3 cm^{-1}, in reasonable agreement with experiment.

The inclusion of dynamical correlation via NEVPT2 restored the triplet ground state and quantitatively reproduced the observed transition energies. The predicted energies (Table 4.13) of the ^3E ($d_{xy} \rightarrow d_{xz}$, d_{yz}) and ^3E (d_{xz}, $d_{yz} \rightarrow d_{x^2-y^2}$) were very close to one another, resulting in the two bands overlapping and showing good agreement with the experimentally reported energies. The five components of the $^3\Gamma$ ($d_{xy} \rightarrow d_{x^2-y^2}$) transition spanned a range of 12000 cm^{-1} to 17300 cm^{-1}. Indeed, as assigned by *Decker et al*., there are two components of the $^3\Gamma$ ($d_{xy} \rightarrow d_{x^2-y^2}$) transition that lie close to the low energy ^3E ($d_{xy} \rightarrow d_{xz}$, d_{yz}) and ^3E (d_{xz}, $d_{yz} \rightarrow d_{x^2-y^2}$) transitions.[165] Hence, the calculated energies and one-electron transition assignments of the CASSCF(12, 9)/NEVPT2 calculations agree with the assignments of *Decker et al*. Lastly, the computed energy of the first excited quintet state, although not known experimentally, is smaller than predicted by ΔSCF and CASPT2 calculations (6541 cm^{-1} and an average of 3200 cm^{-1}, respectively).[165,177] Analysis of the ZFS (*vide infra*) suggests that the calculated energy of this first excited quintet state is too low.

Table 4.13. The calculated non-relativistic energies (cm^{-1}) normalised by the energy of the $^3A_2$ state, of the CASSCF(12, 9) and dynamical correlation corrections (NEVPT2) calculations with 12 triplet roots and 1 quintet root.

Assignment	CASSCF(12, 9)	NEVPT2	Experiment[165]
$^3A_2$	0	0	0
^3E ($d_{xy} \rightarrow d_{xz}$, d_{yz})	12199.4, 12413.3	11823.1, 11844.4	10400
^3E (d_{xz}, $d_{yz} \rightarrow d_{x^2-y^2}$)	5671.5, 5960.6	11403.8, 11973.3	12900
^3E (d_{xz}, $d_{yz} \rightarrow d_{z^2}$)	17341.7, 17549.3	18010.8, 18279.8	17500
$^3\Gamma$ ($d_{xy} \rightarrow d_{x^2-y^2}$)	6165.0, 6200.6, 7954.9, 9002.6, 13331.9	12105.3, 12272.7, 13197.9, 15211.5, 17309.9	10600
$^5A_1$ ($d_{xy} \rightarrow d_{x^2-y^2}$)	-6693.2	1332.1	–

The ZFS was also qualitatively reproduced with these calculations. The spin Hamiltonian parameter D extracted from an effective Hamiltonian projected on to the QDPT results gave a value of D = +34.8 cm^{-1}, which is in fair agreement with the experimental value of D = +29 cm^{-1} determined from VT-MCD and Mössbauer studies. As expected, the inclusion of the first quintet excited state is very important for reproducing the ZFS. The larger calculated

value of D suggests that the energy of the first excited quintet state is too low with respect to the triplet ground state.

4.2.3.3.1 Excited-state spectroscopy

Having established the calculated electronic structure of $[Fe(O)(TMC)(NCCH_3)]^{2+}$, absorption and MCD spectra were calculated using the wavefunctions of the extended space CASSCF(12, 9)/NEVPT2 calculations. The model was required to simulate both the relative intensities observed in the absorption spectrum and to reproduce the signs, magnitudes, and temperature dependence of the VT-MCD. The absorption spectrum and MCD spectra were simulated using ORCA's orca_mapspc program and the results are shown in Figure 4.37.

The calculated electronic absorption spectrum (Figure 4.37, top) showed two broad d-d bands at 12000 cm^{-1} and 18000 cm^{-1}. The former band is calculated about nine times more intense than the latter, simulated with a FWHM = 2000 cm^{-1}. This qualitatively agrees with the experimental spectrum, but notably the calculated band at 18000 cm^{-1} is too intense with respect to the calculated band at 12000 cm^{-1}. The calculations predict the ^3E (d_{xz}, $d_{yz} \rightarrow d_{x^2-y^2}$) bands to be the most intense, followed by two components of the $^3\Gamma$ ($d_{xy} \rightarrow d_{x^2-y^2}$) bands (predicted at 12105.3 and 12272.7 cm^{-1}). The ^3E ($d_{xy} \rightarrow d_{xz}$, d_{yz}) and ^3E (d_{xz}, $d_{yz} \rightarrow d_{z^2}$) bands are predicted to be equally intense. The remaining bands of the $^3\Gamma$ ($d_{xy} \rightarrow d_{x^2-y^2}$) transitions have a relatively much weaker intensity. The bands of the $^3\Gamma$ ($d_{xy} \rightarrow d_{x^2-y^2}$) should have negligible intensity due to the approximate centrosymmetric structure of the equatorial amines; here the mixing of the more intense ^3E ($d_{xy} \rightarrow d_{xz}$, d_{yz}) band, due to energetic proximity, is responsible for the larger calculated intensity of the two components at 12000 cm^{-1}.

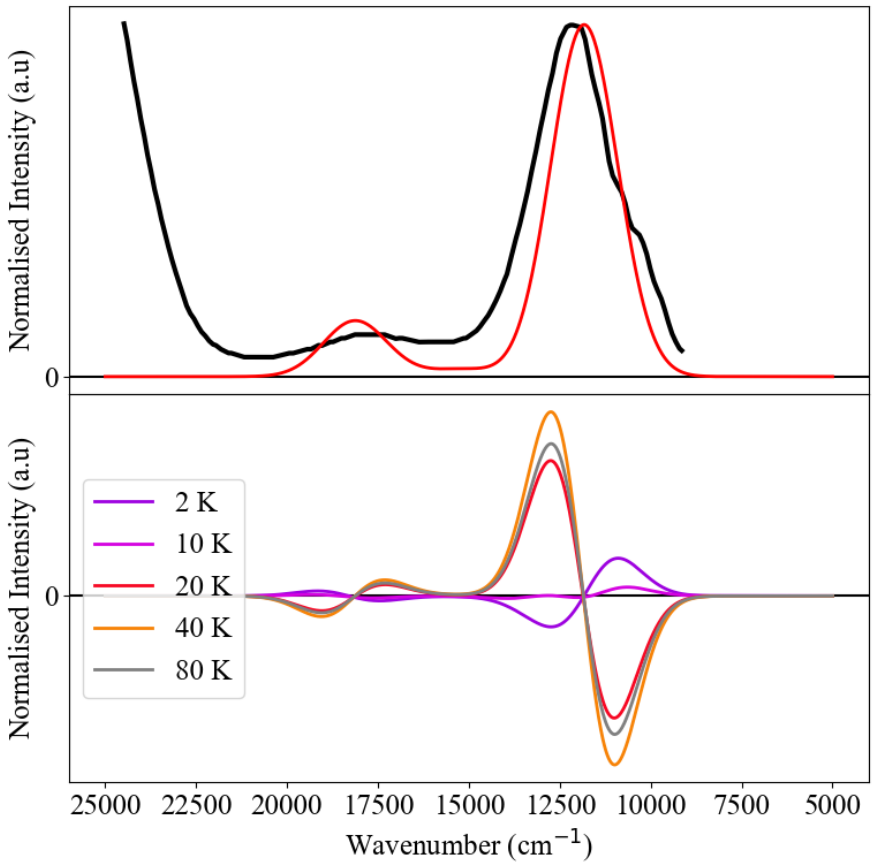

Figure 4.37. The CASSCF(12, 9)/NEVPT2 calculated (red) and reported experimental (black) normalised electronic absorption spectra of $[Fe(O)(TMC)(NCCH_3)]^{2+}$ (top) and the calculated CASSCF(12, 9)/NEVPT2 MCD spectra at 7T (bottom). Spectra are simulated using a FWHM = 2000 cm^{-1}.[165] The experimental UV-Vis is adapted with permission from A. Decker, J.-U. Rohde, L. Que, and E. I. Solomon, J. Am. Chem. Soc., 2004, 126, 5378–5379. Copyright 2004 American Chemical Society.

The calculations predict a pseudo-A-pair feature at 12000 cm^{-1} in the MCD spectrum (Figure 4.37, bottom) that arise from the ^3E ($d_{xy} \rightarrow d_{xz}$, d_{yz}) and ^3E (d_{xz}, $d_{yz} \rightarrow d_{x^2-y^2}$) transitions. Likewise, another pseudo-A-pair features at 18000 cm^{-1}, corresponding to ^3E (d_{xz}, $d_{yz} \rightarrow d_{z^2}$). At 2 K, the relative signs of these pseudo-A-pairs are reversed to what they are at 20 K and above. The overlap of the $^3\Gamma$ ($d_{xy} \rightarrow d_{x^2-y^2}$) bands on the MCD bands at 12000 cm^{-1} does not produce an all-positive feature below 20 K, as observed experimentally. The bands at 2K are also relatively far too weak compared to the bands at 20 K. However, the experimental spectrum does show vibrational fine structure at 12000 cm^{-1}, which could alter the relative intensities of those bands. Another point of discrepancy is the maximum intensity of the two bands at approximately 11000 cm^{-1} and 13000 cm^{-1}. The former is correctly calculated at

maximum intensity at 40 K, but the latter is observed experimentally to reach a maximum intensity at 20 K, which is not reproduced in the calculations. Most notably, what is absent from the calculated 2 K and 10 K MCD spectra is the presence of a positive and intense band at 11000 cm^{-1} and 13000 cm^{-1}.

4.2.3.4 Covalency of the $[Fe–O]^{2+}$ subunit

The covalency of the Fe–O moiety is given by the results of the *ab initio* calculations. Examining the CASSCF(4, 5) and CASSCF(12, 9) optimised orbitals of the active space reveals substantial covalency between the Fe^{IV} and O^{2-} atoms. The percentage contributions to the optimised orbitals from the Fe(IV) d orbitals and oxo orbitals are given in Table 4.14.

Table 4.14. The percentage contributions of the Fe(IV) d orbitals and the oxo p orbitals to the active space anti-bonding d orbitals for CASSCF(4, 5) and CASSCF(12, 9).

Projection	Fe(IV) d CAS(4, 5)	O CAS(4, 5)	Fe(IV) d CAS(12, 9)	O CAS(12, 9)
d_{xy}	97.9%	0.0%	98.3%	0.0%
d_{yz}	68.6%	27.8%	68.9%	28.4%
d_{xz}	68.4%	28.1%	68.8%	28.5%
$d_{x^2-y^2}$	79.6	0.2% (p_x, p_y)	85.7%	0.0%
d_{z^2}	71.3%	14.9%	65.7%	25.1%

In both active spaces, the d_{xy} is effectively non-bonding role, comprising of approximately 98% d_{xy} character. Little change in the overall percentage character is observed by the enlargement of the active space. Likewise, the percentage composition of the Fe–O π bonds remains relatively unchanged between the active spaces. The d_{xz} and d_{yz} orbitals have nearly 30% O p_x, p_y character. Both the $d_{x^2-y^2}$ and d_{z^2} orbitals exhibit a compositional change; the $d_{x^2-y^2}$ is relatively purer in CASSCF(12, 9) than in the CASSCF(4, 5) active space, whereas the opposite trend is found for the d_{z^2} orbital, illustrating how the expansion of the active space strengthens the Fe–O σ bond.

4.2.4 Ligand-field calculations

4.2.4.1 Analysis of the AILFT results

The *ab initio* calculations on the minimal active space produced a 5×5 one-electron ligand-field matrix for both the CASSCF(4, 5) and the NEVPT2 corrected calculations. This matrix is represented by the V^{LFT} matrix in Kestrel, which is constructed from the e_λ parameters of the system and their angular geometry.

By fitting the 5×5 V_{LFT} matrix calculated by ORCA's AILFT module with Kestrel's e_λ parameters, the general metal-ligand bonding situation can be evaluated unambiguously. A fit was carried out on the 5×5 one-electron ligand-field matrix from ORCA's AILFT analysis of the CASSCF(4, 5) results using Kestrel. The resulting fit gave parameters of $e_\sigma(ax)$ = 12996.3 cm^{-1}, $e_\pi(ax)$ = 5979.2 cm^{-1}, $e_\sigma(eq)$ = 5585.9 cm^{-1} with an RMS difference of 222 cm^{-1}. The best fit parameters to the 5×5 one-electron ligand-field matrix for the CASSCF(4, 5)/NEVPT2 calculations gave $e_\sigma(ax)$ = 13883.5 cm^{-1}, $e_\pi(ax)$ = 9775.4 cm^{-1}, $e_\sigma(eq)$ = 7518.8 cm^{-1} with an RMS = 372 cm^{-1}. Hence, the inclusion of dynamical correlation in the restricted active space resulted in a large increase in the $e_\pi(ax)$ and $e_\sigma(eq)$ parameters.

These results lend confidence in the chosen e_λ parameter model. Both of the CASSCF(4, 5) and NEVPT2 one-electron ligand-field matrices were reproduced within the metal-ligand bonding parameterisation of the model. However, the AILFT fit performed by ORCA was not able to fit its ligand-field Hamiltonian on the CASSCF(4, 5) and NEVPT2 corrected transition energies very well (with a total RMS of 3184.5 cm^{-1} and 5784.6 cm^{-1}, respectively), suggesting that the *ab initio* computed energies contain contributions from other sources beyond the limitations of LFT. It is normal for the RMS of the NEVPT2 calculations to be larger than for the CASSCF results. However, CASSCF results usually map very well on to the ligand-field Hamiltonian of AILFT.[31,185]

Although the results of the four electrons in five orbitals active space did not compare well with experiment, the AILFT reflects the same chemical trend as observed in the work of *comba et al.*, and those found in other AILFT analyses of iron(IV) oxo systems.[166,176] The extracted parameters themselves are in good agreement with the ligand-field parameters extracted in our original publication. However, the $e_\sigma(ax)$ parameter was calculated to be some 3000 cm^{-1} lower and $e_\sigma(eq)$ was found to be greater than $e_\pi(ax)$ in contrast to the AILFT analysis.[176]

4.2.4.2 Analysis of the CASSCF(12, 9)/NEVPT2 transition energies

Analysis of the AILFT results highlighted the key chemical trends in the metal-ligand bonding parameters. A direct comparison of the d-d transition energies calculated by Kestrel was made to the CASSCF(12, 9)/NEVPT2 transition energies to analyse the origin of the relatively low energy $^3\Gamma$ ($d_{xy} \rightarrow d_{x^2-y^2}$) transitions and whether the excited state energies and ordering could be reproduced by a parameter set in Kestrel.

The relative energies of the $^3\Gamma$ ($d_{xy} \rightarrow d_{x^2-y^2}$) are primarily sensitive to the e_σ(eq) parameter, whilst some of the components of the $^3\Gamma$ ($d_{xy} \rightarrow d_{x^2-y^2}$) multiplet were also sensitive to Racah B. The energies of the five components could be lowered by dropping the value of e_σ(eq), but this also drops the energy of the ^{3}E (d_{xz}, $d_{yz} \rightarrow d_{x^2-y^2}$) band. The drop in the band energy can be somewhat compensated for by increasing the value of Racah B. However, an increase in Racah B also increases the spitting between the five components of the $^3\Gamma$ ($d_{xy} \rightarrow d_{x^2-y^2}$) band. A reduction in e_σ(eq) and an increase in Racah B also favour the high-spin (S=2) $(d_{xy})^1(d_{yz})^1(d_{xz})^1(d_{x^2-y^2})^1(d_{z^2})^0$ configuration as the ground state, so this must be pushed up in energy relative to the intermediate spin $^3A_2$ ground state by dropping the value of Racah C.

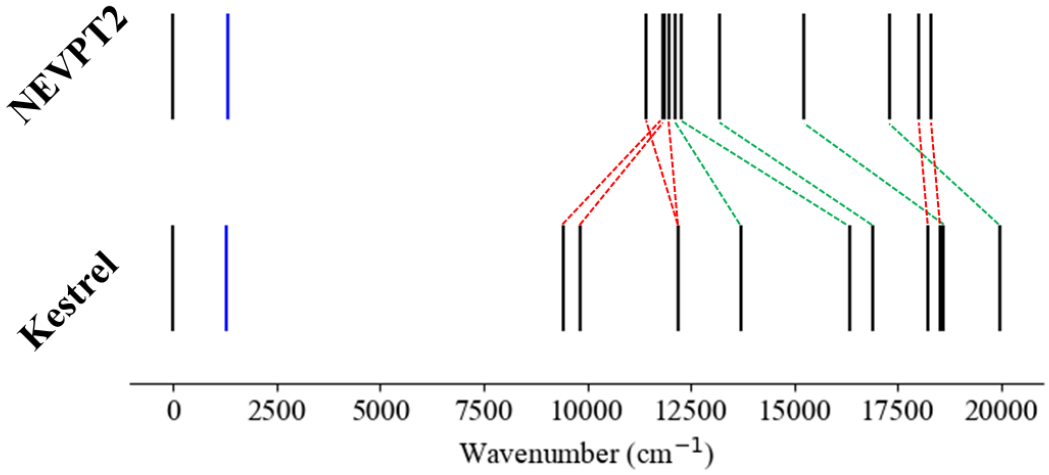

Figure 4.38. Comparison of the CASSCF(12, 9)/NEVPT2 and Kestrel computed transition energies up to 19000 cm^{-1}. Red dotted lines are comparisons between ^{3}E bands and green dotted lines are comparisons between the components of the $^3\Gamma$ ($d_{xy} \rightarrow d_{x^2-y^2}$) bands.

An example of an attempted fit is shown in Figure 4.38. This reproduction of the CASSCF(12, 9)/NEVPT2 transition energies was made using the parameters e_σ(ax) = 11015.0 cm^{-1}, e_π(ax) = 6135.7 cm^{-1}, e_σ(eq) = 5018.5 cm^{-1}, B = 861.2 cm^{-1}, and C = 1878.1 cm^{-1}. Comparing the energies of CASSCF(12, 9)/NEVPT2 and Kestrel (Table 4.15 and Figure 4.38), it is clear that the ligand-field model cannot convincingly reproduce the *ab initio* energies and excited state orderings. A large discrepancy is observed in the energies of the ^{3}E (d_{xz},d_{yz} → $d_{x^2-y^2}$) band, which Kestrel underestimated by 2000 cm^{-1}. The components of the $^3\Gamma$ (d_{xy}→ $d_{x^2-y^2}$) were also predicted to lie too high in energy, but one component could be placed close in energy to the ^{3}E (d_{xz},d_{yz} → $d_{x^2-y^2}$) band. The inability of Kestrel to reproduce quantitatively, in a satisfactory manner, the relative energies of the CASSCF(12, 9)/NEVPT2 likely represents the restricted basis set use in LFT compared to the *ab initio* calculations. However, the restricted basis set does not necessarily imply that LFT is a poorer approach (see below for discussion), and it should be noted in this regard that the UV-Vis and VT-MCD spectra calculated from CASSCF(12, 9)/NEVPT2 calculations do not accurately reproduce the experimental spectra.

Table 4.15. Comparison of the key d-d transition energies (cm^{-1}) computed from the best fit parameters in Kestrel (see text) and CASSCF(12, 9)/NEVPT2 calculations.

Assignment	Kestrel	CASSCF(12, 9)/NEVPT2
$^3A_2$	0	0
^{3}E (d_{xy} → d_{xz}, d_{yz})	12160.2, 12166.2	11823.1, 11844.4
^{3}E (d_{xz}, d_{yz} → $d_{x^2-y^2}$)	9405.2, 9832.1	11403.8, 11973.3
^{3}E (d_{xz}, d_{yz} → d_{z^2})	18216.6, 18522.4	18010.8, 18279.8
$^3\Gamma$ (d_{xy} → $d_{x^2-y^2}$)	13711.6, 16325.9, 16866.5, 18574.3, 19934.5	12105.3, 12272.7, 13197.9, 15211.5, 17309.9
$^5A_1$ (d_{xy} → $d_{x^2-y^2}$)	1263.4	1332.1

Despite the limited quantitative reproduction of *ab initio* predicted transition energies, it is important to examine the best fit ligand-field parameters (*vide supra*). The values of the e_λ parameters are not dissimilar from the values extracted by fitting directly to the 5×5 one-electron ligand-field matrix from CASSCF(4, 5). The e_λ parameters are themselves chemically sensible. The striking feature, however, is the abnormally low C/B ratio (2.18). A low C/B ratio was also observed in the AILFT fit of the CASSCF(4, 5)/NEVPT2 results in section 4.2.3.2. While reductions in B can be expected to be smaller than reductions in C, this does not typically result in a C/B ratio that is as small as 2.175.[186] A review of 25 3d transition-metal

complexes found C/B ratios in the range of 3.60 to 8.36.[186] Accurate Racah B and C parameters for Fe(II) and Fe(III) chloride complexes have been extracted from experimental 2p3d resonant inelastic x-ray scattering experiments and found C/B values of 6.58, 5.26, 3.69, and 3.69 for $[Fe^{III}Cl_4]^{1-}$, $[Fe^{III}Cl_6]^{3-}$, $[Fe^{II}Cl_4]^{2-}$, and $[Fe^{II}Cl_6]^{4-}$ respectively.[187] On this basis, a C/B ratio of 2.175 appears to be unphysically low.

4.2.4.3 Idealised model

Due to the complicated multiplet structure of iron(IV)-oxo systems, it is beneficial to first perform a ligand-field analysis using an idealised C_{4v} structure. The one-electron d-orbital splitting is a simple function of the e_λ parameters and can be evaluated in an idealised structure by the relations

$$\begin{aligned} E\left(z^2\right) &= 2e_\sigma(\text{ax}) + e_\sigma(\text{eq}) \\ E\left(x^2 - y^2\right) &= 3e_\sigma(\text{eq}) \\ E(xz, yz) &= 2e_\pi(\text{ax}) \\ E(xy) &= 0 \end{aligned} \tag{4.8}$$

where the d_{xy} takes a formal non-bonding role. Destabilisation of the π-symmetry d_{xz} and d_{yz} occurs through π donation from the axial oxo and $NCCH_3$ ligands. The energy of d_{z^2} primarily measures the strength of the iron axial ligand σ bonds, but also depends slightly on the energy of the equatorial amine σ bonding strength. The energy of the $d_{x^2-y^2}$ is perturbed by the equatorial nitrogen atoms solely. To ensure that an orbital ordering of $d_{xy} < d_{xz}, d_{yz} < d_{x^2-y^2} < d_{z^2}$ is established, then the metal-ligand bonding parameters must satisfy the following relations: $e_\sigma(\text{eq}) > {}^2/_3 e_\pi(\text{ax})$ and $e_\sigma(\text{ax}) > e_\pi(\text{eq})$.

4.2.4.3.1 Energies of many-electron states

To correlate parameter values with many-electronic configuration energies, it is useful to explore the connection between metal-ligand bonding, d-orbital energies, and interelectronic repulsion parameters. Using arbitrary values for $e_\sigma(\text{ax}) = 10000\ cm^{-1}$, $e_\pi(\text{ax}) = 6000\ cm^{-1}$, and $e_\sigma(\text{eq}) = 5000\ cm^{-1}$, the relative energies and configurational occupations are calculated with and without interelectronic repulsion and listed in Table 4.16. In the absence of interelectronic repulsion, the configurational energy differences are simply the difference in the energies of the one-electron d orbitals. These configurations mix when perturbed by interelectronic repulsion. The configurations of ^3E symmetry mix to a high degree; this is a consequence of the relatively close energies of the d_{xz}, d_{yz}, $d_{x^2-y^2}$, and d_{z^2} orbitals with the arbitrary e_λ parameter

set and reiterates the potential shortcomings in assigning a single electronic configuration to a many-electron excited state in 3d transition-metal complexes.

The four lowest energy components assigned as the $^3\Gamma$ ($d_{xy} \rightarrow d_{x^2-y^2}$) transition have >93% configurational character associated with the $d_{xy} \rightarrow d_{x^2-y^2}$ transition; the highest energy component has a mixed configuration of 66.6% 11110/12010/10210 with 28.8% 11101/12001/10201.

The quintet states, however, do not mix under static correlation because the interelectronic repulsion is treated spherically. The relative energy between the quintet states and the triplet ground state is a factor of both B and C but the relative energies between quintet states is constant, regardless of the values of B and C. An increase in Racah B destabilises the $^3A_2$ ground state and the quintet manifold lowers in energy. This is simply rationalised as a penalty of spin-pairing when going from a quintet to a triplet electronic configuration.

Table 4.16. The Kestrel calculated relative energies of important triplet and quintet excited states and their configuration projection. For the metal-ligand bonding parameters, see the text.

Assignment	Energy (B = 0 cm^{-1}, C = 0 cm^{-1})	Configuration	Energy (B = 500 cm^{-1}, C = 2000 cm^{-1})	Configuration
$^3A_2$	0.0	100% 21100	0.0	98.6% 21100 0.6% 11110
^3E ($d_{xy} \rightarrow d_{\pi}$)	12000.0	100% 12100/11200	11508.3	72.9% 11200/12100 21.0% 20101/21001 2.3% 20110/21010
^3E ($d_{\pi} \rightarrow d_{x^2-y^2}$)	3000.0	100% 20110/21010	8242.2	73.4% 20110/21010 12.2% 20101/21001 10.5% 11200/12100

Assignment	Energy (B = 0 cm^{-1}, C = 0 cm^{-1})	Configuration	Energy (B = 500 cm^{-1}, C = 2000 cm^{-1})	Configuration
^3E ($d_\pi \rightarrow d_{z^2}$)	13000.0	100% 20101/21001	14699.4	63.6% 20101/21001 18.4% 20110/21010 11.3% 11200/12100
$^3\Gamma$ ($d_{xy} \rightarrow d_{x^2-y^2}$)	15000.0	100% 11110/12010 /10210	13475.4, 15398.8, 15674.6, 16368.4, 19411.5	
$^5A_1$ ($d_{xy} \rightarrow d_{x^2-y^2}$)	15000.0	100% 11110	2573.4	100% 11110
$^5B_1$ ($d_{xy} \rightarrow d_{z^2}$)	25000.0	100% 11101	12573.4	100% 11101
^5E ($d_{xy}^1 d_{yz/xz}^1 d_{x^2-y^2}^1 d_{z^2}^1$)	28000.0	100% 10111/11011	15573.4	100% 10111/11011
$^5B_2$ ($d_{xz}^1 d_{yz}^1 d_{x^2-y^2}^1 d_{z^2}^1$)	40000.0	100% 01111	27573.4	100% 01111

4.2.4.3.2 UV-Vis spectroscopy

The correlation of electronic structure with electronic spectroscopy involves understanding the configurational nature of the ground and excited states, and the effects of ligand-induced polarisation into the basis set. Since the equatorial nitrogen ligands are centrosymmetric in this idealised model and presumed to engage in equivalent electronic correlation, their polarisation into the d orbitals effectively cancels and their contribution can be neglected.

The polarisation model requires parameterising the difference of P_σ, F_σ, P_π, and F_π values between the oxo and acetonitrile ligand (labelled O-N_{ax}). First, it is important to analyse the UV-vis and VT-MCD spectra as a function of the transition dipole moment operators. One can begin to rationalise how transition dipole moment operators affect the individual bands of the UV-Vis spectrum. Both P_σ and F_σ induce polarisation into the axial d_{z^2} orbital and so electronic transitions to the d_{z^2} orbital are affected. On the other hand, P_π and F_π affect transitions from (or to) the d_{xz} and d_{yz} orbitals, which means the ^3E bands are affected. The $^3\Gamma$

($d_{xy} \rightarrow d_{x^2-y^2}$) bands should have negligible intensity as the transition dipole moment contributions from the equatorial nitrogen atoms is zero in idealised symmetry. In the absence of spin-orbit coupling, all quintet and singlet bands in the UV-Vis spectrum will thus also have zero intensity.

In Figure 4.39, the relative intensity distributions of the ^3E bands in the simulated absorption spectrum are shown as a function of the axial P and F parameters. The relative intensity distribution of the P_σ and F_σ contributions are identical. The relative intensities of the ^3E bands are largest for the band at 14699 cm^{-1} and lowest for the band at 8242 cm^{-1}. This coincides with the percentage contribution of the d_{xz}, $d_{yz} \rightarrow d_{z^2}$ to a given ^3E band. For P_π and F_π, the relative intensity distributions are different between the two. F_π results in a greater relative intensity of the d_{xz}, $d_{yz} \rightarrow d_{z^2}$ contribution. This is because the f orbitals of π symmetry have a z^2 component to them (f_{xz^2} and f_{yz^2}), which induces intensity into the transition involving d_{z^2}. In both cases of F_π and P_π, the x and y components are the same (p_x, p_y, f_{xz^2} and f_{yz^2}) so that the ^3E (d_{xz}, $d_{yz} \rightarrow d_{x^2-y^2}$) relative intensity changes little between them.

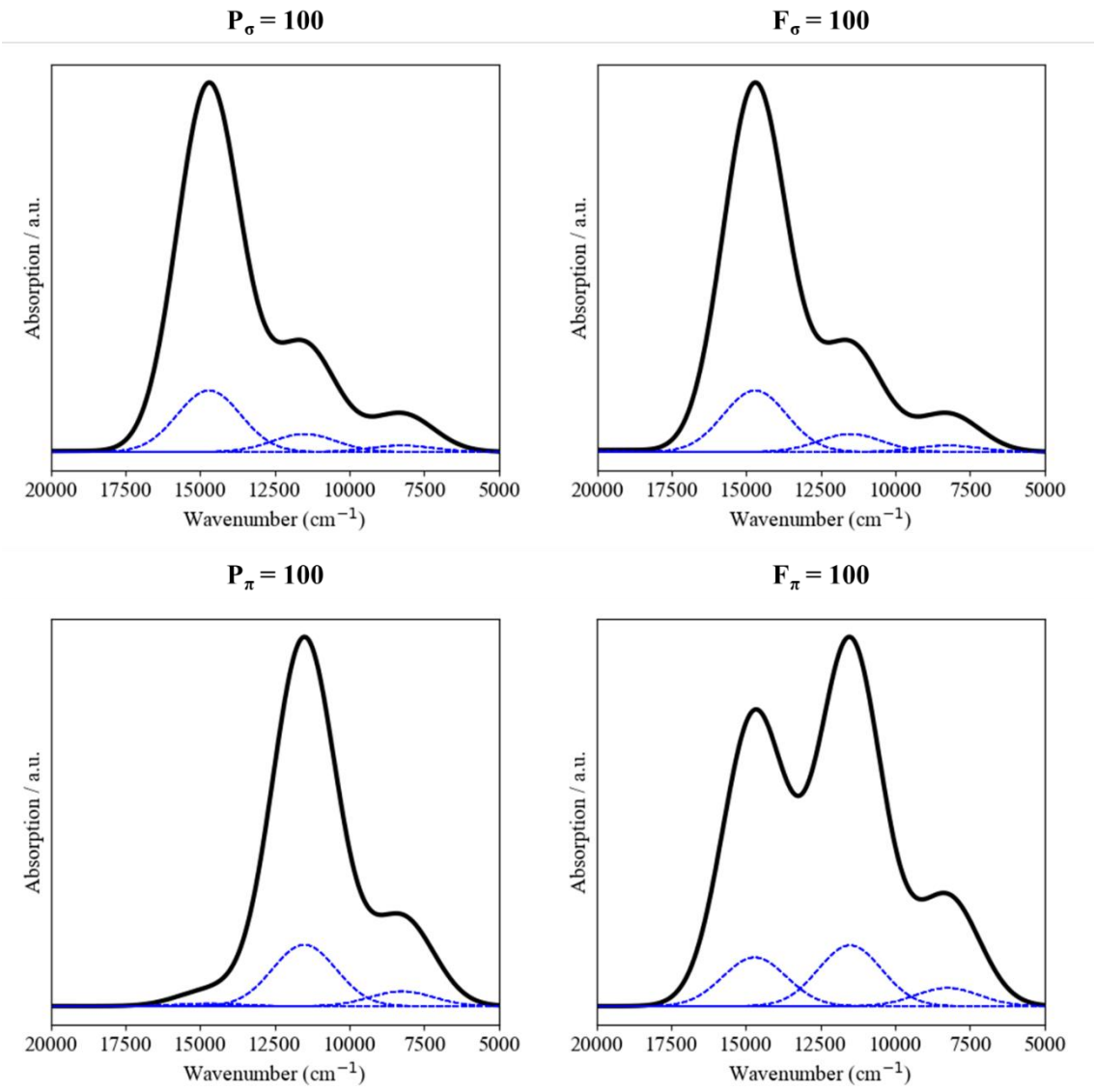

Figure 4.39. The relative absorption bands of the idealised C_{4v} model for $[Fe(O)(TMC)(NCCH_3)]^{2+}$ using only P and F parameters on the oxo ligands. Simulations performed using a FWHM = 2500 cm^{-1}. Calculations performed in the absence of spin-orbit coupling but with B = 500 cm^{-1} and C = 2000 cm^{-1}.

4.2.4.4 Ligand-field analysis of the experiment

The preceding sections examined the results of the *ab initio* calculations and ligand-field analyses of those calculations. The ligand-field calculations could not reproduce the calculated values convincingly. This is perhaps to be expected, given the expanded basis set and the covalent bonding of the Fe–O bond induced within the *ab initio* calculations. This alone does not indicate a failure of LFT, however, since CASSCF(12, 9)/NEVPT2 also did not fully reproduce all aspects of the experimental UV-Vis and MCD spectra.

The goal of LFT is to reproduce experiment and this is possible providing the effective Hamiltonian remains intact. The following section describes the direct ligand-field parameterisation of the reported experimental data. The calculations aim to simulate the magnitude of the ZFS, the d-d band energies in experiment, the relative intensities of the UV-Vis, and the relative intensities and temperature dependence of the bands in the VT-MCD spectrum.

Table 4.17. Possible electronic assignments of the reported experimental band energies (cm^{-1}) of $[Fe(O)(TMC)(NCCH_3)]^{2+}$ to fit in Kestrel. For the electronic assignments, ^3E has labels (1) = $d_{xy} \rightarrow d_{xz}, d_{yz}$, (2) = $d_{xz}, d_{yz} \rightarrow d_{x^2-y^2}$, and (3) = $d_{xz}, d_{yz} \rightarrow d_{z^2}$.

Energy	Comba I	Comba II	General I	General II
0	$^3A_2$	$^3A_2$	$^3A_2$	$^3A_2$
≈3000	$^5A_1$	$^5A_1$	$^5A_1$	$^5A_1$
10400	^3E (1)	^3E (2)	^3E (1)	^3E (2)
10600	$^5B_1$	$^5B_1$	–	–
12900	^3E (2)	^3E (1)	^3E (2)	^3E (1)
17600	^3E (3)	^3E (3)	^3E (3)	^3E (3)

The ligand-field parameterisation has five parameters that dictate the relative energies of the singlet, triplet, and quintet manifolds: $e_\sigma(ax)$, $e_\pi(ax)$, $e_\sigma(eq)$, B, and Racah C. Spin-orbit coupling is a weaker perturbation when compared to the ligand field or interelectronic repulsion and is neglected in these searches but becomes important when reproducing the VT-MCD spectra. By varying these parameters to fit to possible experimental assignments, one can correlate electronic structure with parameterisation. The two assignments analysed are: the assignment of *Comba et al*., in which the band at 10600 cm^{-1} is assigned as a spin-forbidden

triplet to quintet $d_{xy} \rightarrow d_{z^2}$ band; and a further analysis (*General*) which ignores the assignment of the band at 10600 cm^{-1} and fits all other bands. Each of these assignments features two variations, where the order of the ^3E ($d_{xy} \rightarrow d_{xz}$, d_{yz}) and the ^3E (d_{xz}, $d_{yz} \rightarrow d_{x^2-y^2}$) assignments are reversed. The first quintet excited state energy is not known experimentally but is set at 3000 cm^{-1} in line with the predicted DLPNO-CCSD(T) calculations.[177] This band is weighted at 0.5 in the comparison calculations. The electronic assignments, the average best fit values, and the parameter bounds are presented in Table 4.17.

The best fit parameter values for these assignments are presented in Table 4.18. Both assignment sets provide good reproduction of the transition energies (to within a RMS of 500 cm^{-1}). The ordering of the ^3E ($d_{xy} \rightarrow d_{xz}$, d_{yz}) and the ^3E (d_{xz}, $d_{yz} \rightarrow d_{x^2-y^2}$) assignments has a pronounced effect on the e_π(ax) and e_σ(ax) parameters. When the ^3E ($d_{xy} \rightarrow d_{xz}$, d_{yz}) band is placed at 10400 cm^{-1}, e_π(ax) and e_σ(ax) share similar values to those reported by *Comba et al*. of 5584 cm^{-1} and 9288 cm^{-1} respectively.[176] This is consistent with the assumed assignment ordering discussed in that paper. However, when the ^3E (d_{xz}, $d_{yz} \rightarrow d_{x^2-y^2}$) is placed lower in energy than the ^3E ($d_{xy} \rightarrow d_{xz}$, d_{yz}) band then a substantial increase in e_π(ax) and e_σ(ax) was observed. Interestingly, e_σ(eq) did not change by much but instead the ^3E (d_{xz}, $d_{yz} \rightarrow d_{x^2-y^2}$) band was lowered implicitly by increasing e_π(ax) and thereby reducing the energy difference between the d_{xz}/d_{yz}, and $d_{x^2-y^2}$ orbitals.

Table 4.18. The best fit parameters (±) for fitting the different d-d band assignments (see text) for $[Fe(O)(TMC)(NCCH_3)]^{2+}$.

Parameters	Comba I	Comba II	General I	General II
e_σ(ax)	10500 (500)	11200 (600)	10500 (500)	11200 (600)
e_π(ax)	5500 (300)	6550 (450)	5500 (300)	6550 (450)
e_σ(eq)	6800 (600)	7100 (900)	6500 (300)	6500 (300)
B	350 (150)	350 (250)	405 (35)	500 (100)
C	3100 (500)	3400 (600)	2900 (100)	2800 (200)
Σ(avg)	70100	77000	68900	74600

The parameter-space calculations provide a foundation to find fits to the reported experimental UV-Vis and VT-MCD spectra. The chosen best fit parameters (obtained by fitting the UV-Vis and VT-MCD manually) are presented in Table 4.19.

In general, the e_λ parameters reflect the chemical trends extracted from the AILFT analysis in section 4.2.4.1. The average bonding of the axial oxo and acetonitrile is

characterised by strong σ and π donations. The ligand-field trace ($\Sigma = 2e_\sigma^{ax} + 4e_\pi^{ax} + 4e_\sigma^{eq}$) is consistently found at a value around 69000 cm^{-1}, which is in good agreement with the trace found for AILFT analysis of the CASSCF(4, 5)/NEVPT2 active space (Σ = 72253 cm^{-1}). The values of B and C were also sensitively determined and have a dramatic effect on the quality of reproduction of the experimental VT-MCD.

Table 4.19. The best fit ligand-field parameter sets for the reproduction of experimental data. The labels P1 to P5 are alternative fits which offer good reproduction of the available experimental data.

Parameter	Best	P1	P2	P3	P4	P5
$e_\sigma(ax)$	10600	10500	11000	10750	10500	10000
$e_\pi(ax)$	6300	6300	6100	6100	6100	6100
$e_\sigma(eq)$	5900	6100	5900	5800	5900	5900
Σ	70000	70600	70000	69100	69000	68000
B	700	700	570	600	600	700
C	2500	2600	2360	2300	2500	2200
ζ	310	320	360	360	360	320
k_{iso}	0.6	0.6	0.6	0.6	0.6	0.6
$P_\sigma(O-N_{ax})$	-90	-80	-40	-10	0	-80
$P_\pi(O-N_{ax})$	80	70	100	100	100	100
$F_\sigma(O-N_{ax})$	100	100	60	45	45	120
$F_\pi(O-N_{ax})$	0	-15	-20	-20	-20	0

The best fit parameters found that $e_\sigma(eq) \leq e_\pi(ax)$, which corresponds to a ^3E excited state ordering where the formal d_{xz}, $d_{yz} \rightarrow d_{x^2-y^2}$ transition is lower in energy than the $d_{xy} \rightarrow d_{xz}$, d_{yz} transition. This reassignment from that given by *Decker et al*. was also found by *Ye et al*. in their *ab initio* calculations.[174] In general, the best fit values of $e_\sigma(eq)$ in Table 4.19 are typically lower than those found for the corresponding electronic assignment (*Comba II*) in Table 4.17, which is in the range of 6100 to 8000 cm^{-1}, but this was compensated for by an effective increase in the Racah B parameter. As will be discussed later, this parameterisation mixes electronic configurations (4.2.4.6) and is important for the reproduction of the reported experimental UV-Vis and VT-MCD.

These fits assign a consistent polarisation scheme even if the ratios and magnitudes vary. The fits show that $|P_\pi(O-N_{ax})| > |F_\pi(O-N_{ax})|$ and that they are of opposite sign; the same

applies for the σ polarisation, where the magnitudes of $|F_\sigma(O-N_{ax})| > |P_\sigma(O-N_{ax})|$. This means the larger P_π and F_σ polarisations are attributed to the same source, whether it be above or below the equatorial plane. As will be discussed in section 4.2.5.2, the larger P_π and F_σ polarisation are assigned to the oxo, hence the labelling of $(O-N_{ax})$.

4.2.4.5 Comparison with experimental data

The ligand-field analyses presented in section 4.2.4.4 aimed to reproduce three pieces of experimental data: the zero-field splitting, the relative intensities of the UV-Vis, and the temperature dependence behaviour of the VT-MCD. The best fit parameters gave an effective zero-field splitting characterised by spin Hamiltonian parameters of D = +28.7 cm^{-1} and E/D = 7.97 x 10^{-4}, in excellent agreement with values extracted from Mössbauer studies (D = +29 cm^{-1}).[176] The spin-Hamiltonian parameters were calculated by comparison of the zero-field split energies with the solutions of the 3x3 $|S, M_S>$ matrices parameterised by D and E. Calculated UV-Vis and VT-MCD spectra for the best fit and the other fits (Table 4.19) are presented in Figure 4.40. The simulations of the best fit parameter set reproduce the relative intensities of the UV-Vis and the temperature dependence of the VT-MCD spectra.

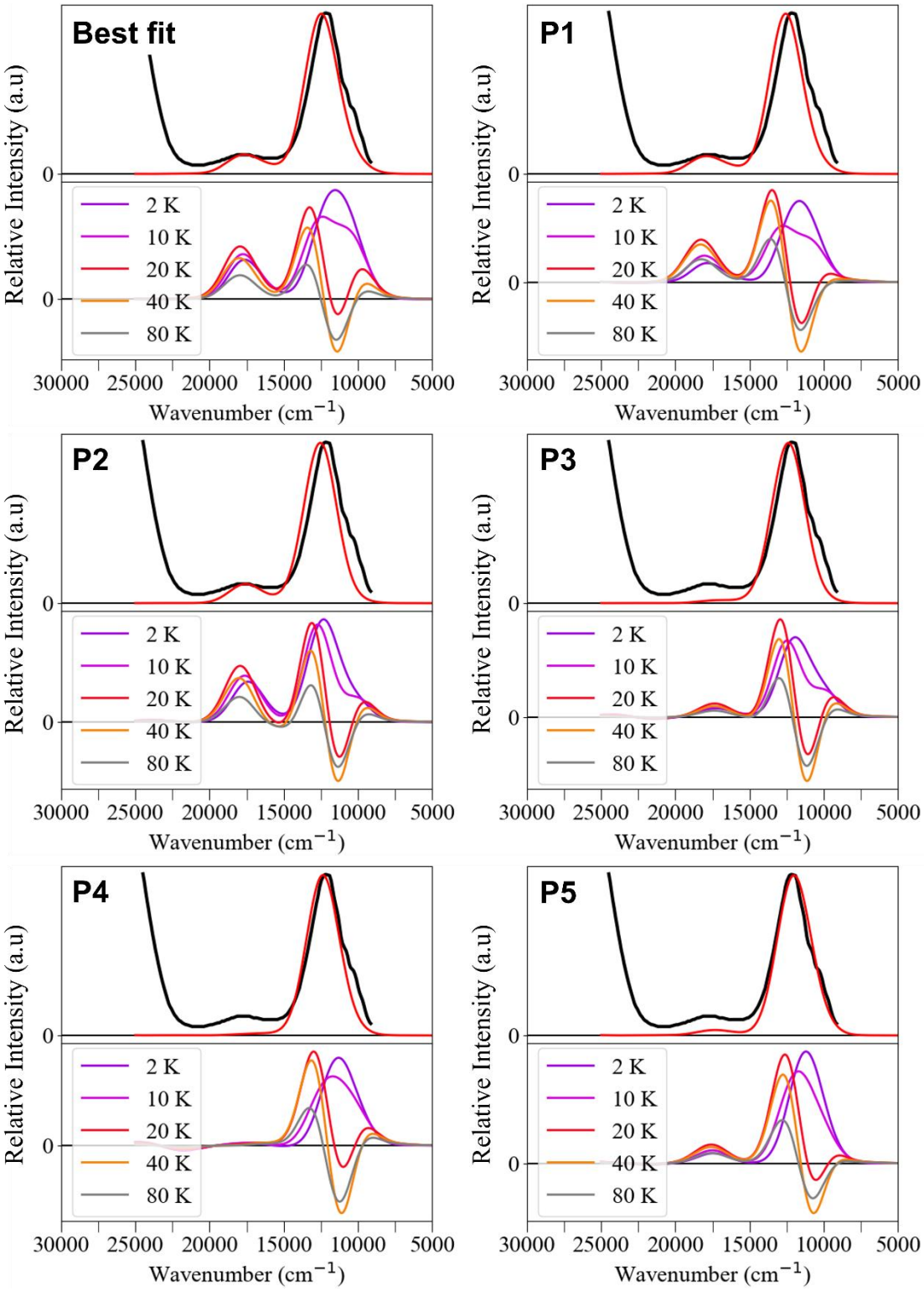

Figure 4.40. The simulated (red) and experimental (black) UV-Vis and 7 T VT-MCD for the parameter sets in Table 4.19. Simulations were performed using a FWHM = 2500 cm^{-1} for each transition. MCD simulations were performed with a 30 × 30 angular grid for θ and φ. The experimental UV-Vis is adapted with permission from A. Decker, J.-U. Rohde, L. Que, and E. I. Solomon, J. Am. Chem. Soc., 2004, 126, 5378–5379. Copyright 2004 American Chemical Society.

The Kestrel simulated UV-Vis spectrum for the best fit ligand-field parameters reproduces the intensity distribution observed in the experimental spectrum. The band at 12000 cm^{-1} is the most intense provided that the magnitude of $|P_\pi| > |F_\pi|$. The shoulder intensity at 10500 cm^{-1} is not reproduced here but this shoulder is likely exaggerated due to the vibronic fine structure, which is not modelled in Kestrel's simulations. An interesting and subtle aspect of the intensity distribution is the relative intensity between the two bands at 12000 cm^{-1} and 17600 cm^{-1}. This intensity arises from formally spin-forbidden quintet bands that mix with nearby spin-allowed triplet bands in that region.

As expected, reproduction of the VT-MCD was found to be a complicated function of the transition dipole moment, ligand field, and interelectronic repulsion parameters. Although the alternative fits presented in Table 4.19 in section 4.2.4.4 do reproduce the general features of the experimental spectra, the best fit parameter set best reproduces details of the low temperature spectra using the most chemically intelligible parameter set. Importantly, the calculated VT-MCD spectrum at 10 K and below has positive intensity in the low energy region (8000 cm^{-1} to 15000 cm^{-1}) as observed experimentally. The positive intensity drops at 10500 cm^{-1} going from 2 K to 10 K but grows at 13000 cm^{-1}, which matches the experimental observation. At 20 K and above, a pseudo-A-pair feature is resolved in this region. Interestingly there appears to be three peaks in this region at 20 K and above at 13000 cm^{-1}, 11000 cm^{-1}, and 9500 cm^{-1}, as is also clearly observed in the experimental 20 K spectrum and to a lesser extent in the 40K and 80K spectra. The positive bands at 13000 cm^{-1} and 9500 cm^{-1} reach their maximum intensity at 20 K before sharply reducing in intensity above 20 K. The negative band at 11000 cm^{-1} reaches its maximum negative intensity at 40 K, in agreement with experiment.

The reproduction of the temperature dependence of the band at 17600 cm^{-1} does not agree perfectly with experiment. Experimentally, this band has maximum intensity at 2 K and has pseudo z-polarised behaviour. However, this band is calculated to reach maximum intensity at approximately 20 K, which is unsurprising for the formally z-polarised ^3E (d_{xz}, d_{yz} $\rightarrow$ d_{z^2}) transition. Despite this discrepancy, the general features of the temperature dependence of the MCD spectra are well reproduced.

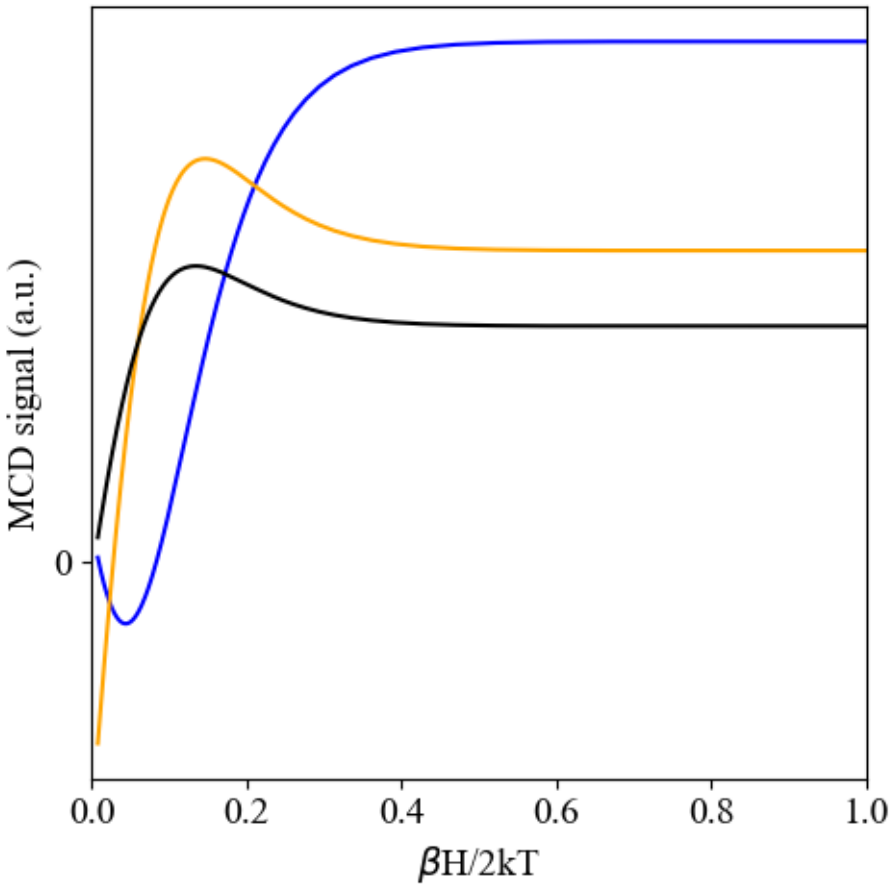

Figure 4.41. The saturation plots generated using Kestrel for the MCD intensity of the bands of $[Fe(O)(TMC)(NCCH_3)]^{2+}$ at 10400 cm^{-1}, 12900 cm^{-1}, and 17600 cm^{-1} at 7 T using the best fit parameters (see text).

The intensities of the MCD bands at the reported experimental energies were calculated (using Kestrel) over a range of temperatures and the resulting saturation plots are presented in Figure 4.41. Both the saturation behaviours at 12900 cm^{-1} and 17600 cm^{-1} exhibit similar saturation behaviours and reach maximum intensity at 17 K. The band at 12900 cm^{-1} becomes negative at temperatures > 85 K, whereas the band at 17600 cm^{-1} does not become negative. The band at 10400 cm^{-1} reaches maximum positive intensity at 2 K and reaches maximal negative intensity at 50 K. This trend agrees with the temperature dependence described by *Decker et al*.[165]

4.2.4.6 Electronic structure

To understand the origins of these electronic/spectroscopic features, an examination is made of the electronic structure. The final ligand-field orbitals have relative energies of 0.0, 12380.1, 12497.3, 17503.2, and 26965.4 cm^{-1} belonging to the primarily d_{xy}, d_{yz}, d_{xz}, $d_{x^2-y^2}$ and d_{z^2} orbital projections respectively, with respect to the principal C_{4v} axis. The shapes and orientations of the ligand-field orbitals are given in Figure 4.42. The d_{xz} and d_{yz} orbitals are orientated to project in between the Fe–N bonds rather than along them. There are no significant deviations from the expected orbital orientations of an approximate C_{4v} complex.

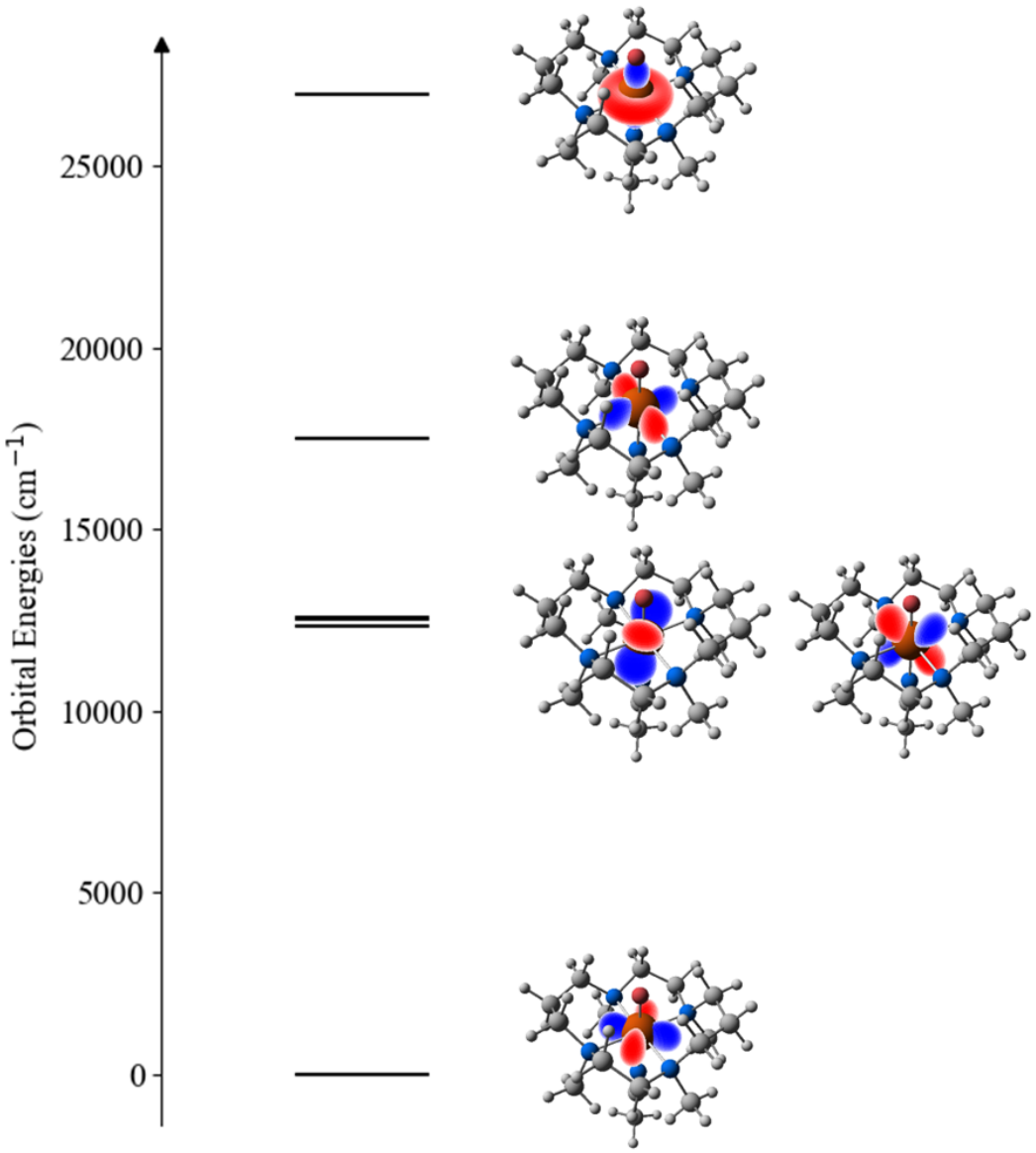

Figure 4.42. The Kestrel rendered ligand-field orbitals for the best fit parameter set (see text) of $[Fe(O)(TMC)(NCCH_3)]^{2+}$.

The final non-relativistic excited-state energies and their configurational projections are given in Table 4.20. The relative energy of the first excited quintet state, the $^5A_1$ ($d_{xy} \rightarrow d_{x^2-y^2}$), is higher in energy than predicted by CASSCF(12, 9)/NEVPT2 but lower than the average energy gap predicted by DLPNO-CCSD(T) of 3600 cm^{-1}.[177]

The ^3E ($d_{xy} \rightarrow d_{xz}$, d_{yz}) experimentally assigned band at 10400 cm^{-1} is modelled as a configurationally mixed $d_{xy} \rightarrow d_{xz}$, d_{yz}, d_{xz}, $d_{yz} \rightarrow d_{x^2-y^2}$, and d_{xz}, $d_{yz} \rightarrow d_{z^2}$ transition, where the first two listed configurations are the dominating contributors. The other ^3E band, assigned as the d_{xz}, $d_{yz} \rightarrow d_{x^2-y^2}$ transition at 12900 cm^{-1} in the experimental spectrum by *Decker et al.*, is a configurational admixture of the ^3E transitions with a larger contribution from the d_{xz}, $d_{yz} \rightarrow d_{z^2}$ band. In between the bands at 12900 cm^{-1} and 10400 cm^{-1} is the spin-forbidden $^5B_1$ ($d_{xy} \rightarrow d_{z^2}$) band, which is integral to the reproduction of the positive feature at 11000 cm^{-1} in the low temperature MCD spectrum. The $^3\Gamma$ ($d_{xy} \rightarrow d_{x^2-y^2}$) multiplet spans an energetic range of 15000 cm^{-1} to 20000 cm^{-1} and is not sufficiently low enough in energy to be involved in the temperature dependent behaviour of the low energy region of the MCD spectrum. The final ^3E band at 17600 cm^{-1} is a configurationally mixed d_{xz},$d_{yz} \rightarrow d_{x^2-y^2}$ / d_{z^2} excited state. The configurationally mixed nature of these excited states means that assignments to simple one-electron d-d transitions is inaccurate.

Table 4.20. The non-relativistic energies (cm^{-1}), assignments, and configurational projection of the key electronic states for the best fit parameter set. Configurational projections of the $^3\Gamma$ bands are omitted for clarity.

$^{2S+1}\Gamma$	Energy (cm^{-1})	2S+1	%	d_{xy}	d_{yz}	d_{xz}	$d_{x^2-y^2}$	d_{z^2}
$^3A_2$	0.0	3	97.2	2	1	1	0	0
$^5A_1$ ($d_{xy} \rightarrow d_{x^2-y^2}$)	1588.9	5	100	1	1	1	1	0
^3E ($d_{xy} \rightarrow d_{xz}, d_{yz}$)	10143	3	43.0	2	1	0	1	0
		3	41.3	1	2	1	0	0
		3	10.1	2	0	1	0	1
	10538.6	3	40.3	2	0	1	1	0
		3	39.6	1	1	2	0	0
		3	14.1	2	1	0	0	1
$^5B_1$ ($d_{xy} \rightarrow d_{z^2}$)	10851.6	5	100	1	1	1	0	1
^3E ($d_{xz}, d_{yz} \rightarrow d_{x^2-y^2}$)	12322.7	3	45.7	1	1	2	0	0
		3	42.4	2	1	0	0	1
		3	8.8	2	0	1	1	0
	12348.2	3	44.5	1	2	1	0	0
		3	39.3	2	0	1	0	1
		3	13.1	2	1	0	1	0
$^3\Gamma$ ($d_{xy} \rightarrow d_{x^2-y^2}$)	15500 to 20000 cm^{-1}							
^3E ($d_{xz}, d_{yz} \rightarrow d_{z^2}$)	17480.1	3	41.9	2	0	1	0	1
		3	31.1	2	1	0	1	0
		3	8.7	1	2	1	0	0
		3	7.1	1	1	1	1	0
		3	5.5	1	1	0	1	1
	17837.4	3	37.5	2	0	1	1	0
		3	37.3	2	1	0	0	1
		3	9.6	1	1	2	0	0
		3	4.8	1	0	1	1	1
		3	4.0	1	2	0	1	0
$^3\Gamma$ ($d_{xy} \rightarrow d_{z^2}$)	21000 to 32000 cm^{-1}							

4.2.5 Discussion

4.2.5.1 The best fit ligand-field, interelectronic repulsion, and spin-orbit coupling parameters

The preceding analysis managed to establish a set of best fit parameters for characterising the $[Fe(O)(TMC)(NCCH_3)]^{2+}$ complex. The ligand-field parameters of the metal-ligand bonding (e_λ), interelectronic repulsion (B, C), and spin-orbit coupling (ζ) were sensitively determined, whereas the isotropic reduction factor k_{iso} was not. Except for k_{iso}, which was not investigated in the previous Kestrel analysis published by *Comba et al*., a similar best-fit parameter set emerged in this analysis.[176] One criterion for assessing the quality of a ligand-field analysis is whether the resulting parameters are chemically and physically sensible.

The best fit e_λ parameter values directly report on individual metal-ligand bonding interactions and hence these are the easiest to evaluate in terms of their chemical intelligibility. The best fit parameters were assigned presuming the equatorial nitrogen donors to be σ donors only. The oxo-acetonitrile pair were assigned as a strong σ and π donor. This concurs with the chemical expectation of metal-ligand bonding for an oxo (as opposed to an oxyl) due to its relatively short bond length. The best fit e_λ parameter signs and magnitudes agree well with the e_λ parameters derived from a direct fit to the AILFT derived CASSCF 5×5 one-electron ligand-field matrix described in section 4.2.4.1. The best fit parameter values predicted a smaller e_σ(ax) parameter than the value extracted from the AILFT analysis because the latter overestimates either the contributing σ donor strength of the acetonitrile or the oxo. Further confidence with the best fit e_λ parameter values is given by comparison of the ligand-field trace (Σ = 70000 cm^{-1}) with the ligand-field traces observed for V(IV)-oxo systems (Σ = 77070 cm^{-1}, 80280 cm^{-1}, and 80460 cm^{-1}, see appendix 6.6), which have traces with a similar order of magnitude.[188] The decrease in the ligand-field trace observed with Fe(IV) compared to V(IV)-oxo systems is likely due to two factors. The first factor is the increased electron density from the increased occupation of the Fe(IV) 3d orbitals compared to the V(IV), which destabilises the metal-ligand bonds due to Pauli repulsions.[26] The second reason is attributed to the chemical difference of the equatorial $acac^-$ ligands in the V(IV)-oxo systems. The $acac^-$ ligands possess a formal negative charge, which can be delocalised onto the vanadium via the ligand π network. This would lead to more electron density donated to the V(IV) ion and result in an increase in the ligand-field trace.

Having established that the metal-ligand bonding parameters are chemically sensible, attention turns to the interelectronic repulsion parameters. The best fit interelectronic repulsion

B and C parameters satisfy the criterion formulated by *Hans-Herbert Schmidtke* for determining physically sensible B and C parameter values.[186] One such criterion for determining if the values of B and C are sensible, is the expectation that B < C and that the reduction in C is greater than the reduction in B from their respective free-ion values. The relative reductions of the best fit values of B and C (ΔB = 444 cm^{-1} and ΔC = 1959 cm^{-1}) fulfil this criterion. The relative nephelauxetic quotients of B and C are reasonable too, where B/B_0 = 0.61 and C/C_0 = 0.56. The reduction of the spin-orbit coupling parameter from the free-ion value adopted a similar magnitude, ζ/ζ_0 = 0.60. Anisotropic 2-electron terms are sequestered into the definition of the e_λ parameters, and the current parameterisation does not require anisotropic interelectronic repulsion parameters, as has been suggested for Mn(IV) complexes.[172] Indeed, there are no large deviations or objectionable parameter values to suggest any breakdown of the effective Hamiltonian. It appears therefore that the spherical approximation of interelectronic repulsion (and spin-orbit coupling) parameters are good approximations.

4.2.5.2 The best fit transition dipole moment parameters

The best fit ligand-field parameters illustrate a consistent polarisation effect from the oxo/acetonitrile. It is not possible to assign unambiguously the polarisation differences to either the oxo or acetonitrile, but chemical intuition would suggest that the oxo (a σ and π donor) is characterised by $P_\pi(O) > P_\pi(NCCH_3)$ and $F_\sigma(O) > F_\sigma(NCCH_3)$. The measure of the difference in the $|P_\lambda|$ and $|F_\lambda|$ values means that it is only possible to compare the polarisation of the Fe–O bond *relative* to the same polarisation effect in the Fe–$NCCH_3$ bond. This polarisation difference is still meaningful, however. A large P_π, associated with a greater P_π contribution from the oxo compared to the acetonitrile, suggests that the π bond of the oxo is polarised more towards the metal. This is corroborated by the small negative values of F_π, suggesting that the π bond of the Fe–$NCCH_3$ is polarised more towards the nitrogen. However, in contrast, the larger F_σ (O) contribution suggests that the electron density in the Fe=O bond is "thinner" and concentrated about the Fe–O axis than in the Fe–N bond, consistent with the formation of a strong Fe=O σ bond. It could also be argued that the electrons in the Fe=O σ bond are polarised more towards the oxo; since the polarisation of the Fe=O π bond is directed towards the metal, this would be the primary delocalisation method of the negative charge on the oxo. Hence, the σ bond electrons, because of the electroneutrality principle, are not delocalised onto the metal to the same extent.

The effects that the signs and ratios of the P and F parameters have on the basis d orbitals are shown in Figure 4.43. Note the effect of the polarisation is exaggerated in Figure 4.43 for clarity. The polarisation of the d_{xz}/d_{yz} orbital results in the reduction of electron density towards the oxo and the density is pushed inwards, away from the Fe=O π bonds; the underside expands and is pushed outwards towards the equatorial plane. The polarisation of the d_{z^2} from the oxo and acetonitrile σ bond results in an elongation of the electron density along the underside and the shortening and rounding of the electron density along the top side, again redirecting electron density away from the stronger Fe=O σ bond.

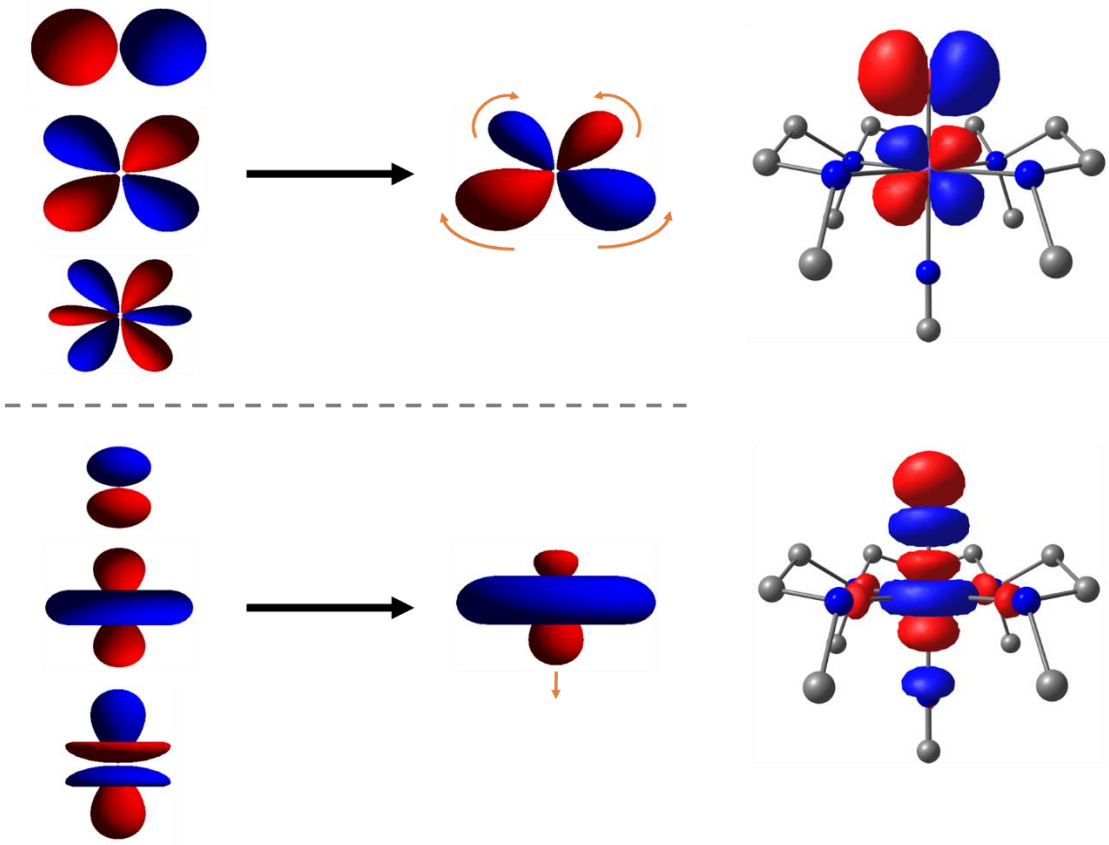

Figure 4.43. The effect of polarisation of P and F functions (left) into the d_{xz}/d_{yz} (top) and d_{z^2} (bottom). The degree of polarisation is exaggerated for clarity. The converged CASSCF(12, 9) anti-bonding active space orbitals (right) for the d_{xz}/d_{yz} and d_{z^2}.

The ligand-field model did not require explicit recognition of P_σ or F_σ parameters of the equatorial amines. There is ground for assigning different parameter values across for the Fe–N_{eq} bonds of different lengths (2.10 Å vs 2.12 Å in the DFT optimised structure) but this wasn't done on the justification of reducing the number of variable parameters and that suitable fits

were obtained without them. To account for the polarisation contributions of the equatorial amines, a dynamic polarisation model would have to be employed.[82]

4.2.5.3 The spin-forbidden triplet to quintet $d_{xy} \rightarrow d_{z^2}$ assignment

This work centred on finding a ligand-field parameter set which could reproduce the experimental UV-Vis and VT-MCD spectra by assigning the low energy z polarised band (at 10600 cm^{-1}) in the VT-MCD spectrum to the spin-forbidden $^5B_1$ ($d_{xy} \rightarrow d_{z^2}$) band. The spin-forbidden $^5B_1$ ($d_{xy} \rightarrow d_{z^2}$) band was found to be a viable alternative assignment of the $^3\Gamma$ ($d_{xy} \rightarrow d_{x^2-y^2}$) band by *Decker et al*. The best fits to the VT-MCD spectra were obtained with values that placed the $^5B_1$ band within the low energy window at 11000 cm^{-1}.

4.2.5.4 Limits of ligand-field theory in Fe(IV)-oxo complexes?

The foregoing analysis was made not only to probe further the electronic structure of these complexes but to attempt to find the limits of the ligand-field model. On the results of this analysis alone, the limits of the ligand-field model have not been conclusively reached. The general features of the UV-Vis and VT-MCD spectra have been reproduced despite the inability to assign the low energy z polarised band as the $^3\Gamma$ ($d_{xy} \rightarrow d_{x^2-y^2}$) band. The models show that the reported experimental spectrum can be reproduced without explicit intensity from the $^3\Gamma$ ($d_{xy} \rightarrow d_{x^2-y^2}$) transitions. Hence, the nature of the positive intensity at 10600 cm^{-1} in the experimental VT-MCD cannot be conclusively assigned as the $^3\Gamma$ ($d_{xy} \rightarrow d_{x^2-y^2}$) transition. On this basis, therefore, the assignments and spectra generated by Kestrel must be considered as a viable alternative to the assignments made by *Decker et al*.

Despite this, both the AILFT fitting and the Kestrel fitting of the ligand-field model to the extended active space CASSCF/NEVPT2 computed transition energies and their assignments was not satisfactorily achieved. The origin of this discrepancy in both the minimal and extended active spaces reflects a breakdown of the effective Hamiltonian from large covalency of the Fe=O functions with the iron(IV) d orbitals. In this regard, the same observation was made by *Ye et al*. in their study of a tetracarbene iron(IV)-oxo system and they concluded that "*Finally, one should point out that more method development is necessary before Fe(IV) high-valent, covalent systems can be treated quantitatively in a satisfactory manner with AILFT*".[166]

Of course, the predicted spectra from Kestrel do not perfectly reproduce the experimental UV-Vis and VT-MCD spectra either. Despite this, the Kestrel generated spectra presented in this work are close theoretical predictions of the reported experimental spectra and all are achieved with a small basis set. Even if it were the case that the assumptions of the ligand-field model have been breached, the remaining predictions of the spectroscopically important features are good. Hence, the ligand-field model appears to be a valid tool for rationalising the electronic structures of intermediate iron(IV) oxo complexes. However, more work must be done to examine the electronic structures of other experimentally characterised iron(IV) oxo complexes before one can make a more general conclusion about the efficacy of the ligand-field model for iron(IV) oxo complexes. If the ligand-field parameterisation is correct, then the covalency between the iron(IV) d orbitals and the oxo π orbitals are overestimated in the *ab initio* calculations.[7] This can be inferred from the values of the interelectronic repulsion parameters (B, C) assigned in the Kestrel calculations, which are larger than expected for a system which is alleged to feature substantial Fe=O covalency.

4.2.6 Conclusion

This study was focused on analysing the reassignment of the spin-allowed $^3\Gamma$ ($d_{xy} \rightarrow d_{x^2-y^2}$) band to a spin-forbidden $^5B_1$ ($d_{xy} \rightarrow d_{z^2}$) band in the VT-MCD spectra of $[Fe(O)(TMC)(NCCH_3]^{2+}$. The ligand-field model as implemented in Kestrel has been able to reproduce the available experimental data in a satisfactory way where the spin-forbidden $^5B_1$ ($d_{xy} \rightarrow d_{z^2}$) band plays an important role in simulating the reported experimental spectra. The analysis shows that d-d transitions in iron(IV) oxo systems cannot be thought of as single one-electron transitions, but rather as configurationally mixed excitations. As a result, the temperature dependence of the experimental VT-MCD is a complicated function of both the underlying electronic structure (from static and dynamic coupling) and the polarisation from the axial oxo and acetonitrile bonding, which cannot (and should not) be understood with simple one-electron descriptions of the constituent orbitals. This work has also characterised a parameter set which shares similar e_λ values to examples found in the literature and to e_λ values extracted from *ab initio* calculations.

The work presented here has shown that LFT can provide a good reproduction of the experimental electronic spectroscopies for $[Fe(O)(TMC)(NCCH_3)]^{2+}$. Extension of this analysis to other characterised intermediate spin iron(IV) oxo complexes is the next stage to see whether a trend in the parameters can be observed and rationalised within the ligand-field model. There are a few other spectroscopically characterised (with VT-MCD) S=1 iron-oxo

complexes that would make good candidates for replication.[166,169,174] These systems include added complications, such as requiring extra parameterisation due to the presence of other π interactions, for example. However, it appears that biologically relevant high-valent iron-oxo systems are parameterizable within the ligand-field model, sufficiently so that insight into these systems can be achieved and correlated with reactivity. Although it was not possible to conclude that the fit is unique, manually fitting the electronic spectroscopy was sensitive to parameter values and an exhaustive search was carried out. For now, there is no systematic way to evaluate a quality of fit algorithmically to the experimental MCD spectra without first speeding up the MCD calculations in Kestrel.

4.3 Electronic structure investigations of lytic polysaccharide monooxygenases

4.3.1 Introduction

Lytic polysaccharide monooxygenases (LPMOs) are a class of copper containing enzymes that can degrade polysaccharides, like cellulose and chitin.[189] These enzymes either perform a monooxygenation or a peroxygenation reaction, which is capable of oxidising strong C–H bonds with a bond dissociation energy (BDE) of around 100 kcal mol^{-1}.[190–192] The precise mechanistic detail of their catalytic activity is currently unknown. Since their discovery in 2010, there has been extensive interest in LPMOs for enhancing the efficiency of biomass conversion to biofuel.[190,193–198] Beyond an interest in their economic and sustainability potential, there has been great interest in understanding the catalytic mechanism and the reactive intermediates responsible for their reactivity.[199–201] Research into LPMOs also extends beyond this. For example, LPMOs have been recently identified as a virulence factor in *Pythophthora infestans* oomycete.[202]

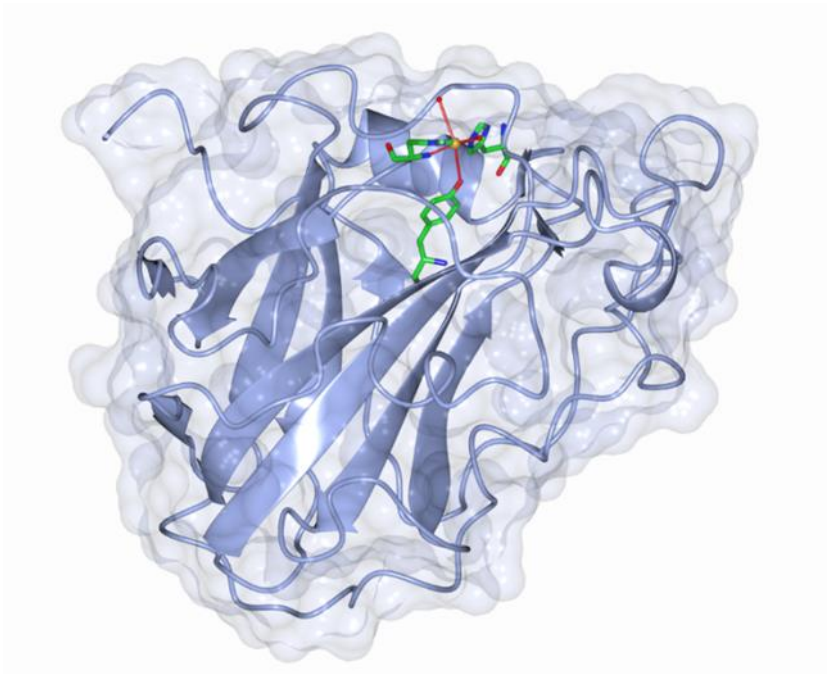

Figure 4.44. The crystallographic structure of the LPMO enzyme, *Ls*AA9 (PDB: 5ACH) rendered using CCP4MG.

Both bacteria and fungi are found to secrete these enzymes and nature has evolved different LPMO families with specific activity. At present, six different families, prefixed with 'auxiliary activities' (AA), are classified in the CAZy database.[203] These families include AA9 (Figure 4.44), AA10, AA11, AA13, AA14, AA15, AA16, and AA17.[204]

4.3.1.1 The histidine brace

The histidine brace is a structural motif common to several proteins, such as LPMOs and particulate methane monooxygenases, which oxidise strong C–H bonds that are otherwise functionally inert.[205–207] The structure of the histidine brace [Figure 4.45 (A)] consists of a N-terminal histidine coordinated at the N_δ of its side chain (His1), *trans* to the N_ε of another histidine (His2), coordinated to a copper ion.[208,209] In the reduced copper(I) state (not shown), this active site is referred to as a so-called "t-shaped" coordination sphere. The oxidised copper(II) state features the same T-shaped coordination sphere but is completed by a fourth ligand, referred to as the exogeneous ligand, to form an approximate square plane. In the resting state, the exogeneous ligand is a water molecule. A second water molecule [not drawn in Figure 4.45 (A)] occupies an axial position *trans* to a tyrosine. This coordination sphere is typical across the LPMO families, except for AA10 LPMOs which instead exhibit a distorted square pyramidal structure.

Curiously in LPMOs, barring those expressed by bacteria, the non-coordinating nitrogen of His1 is methylated [Figure 4.45 (A), blue highlight].[193] The role that this methylation has is unknown. It has been suggested that the methylation might be involved in helping to 'anchor' substrate on to the active site (see section 4.3.1.2).[210] More recent work has also provided evidence that the methylation is involved in a protective mechanism from oxidative damage to the enzyme.[211]

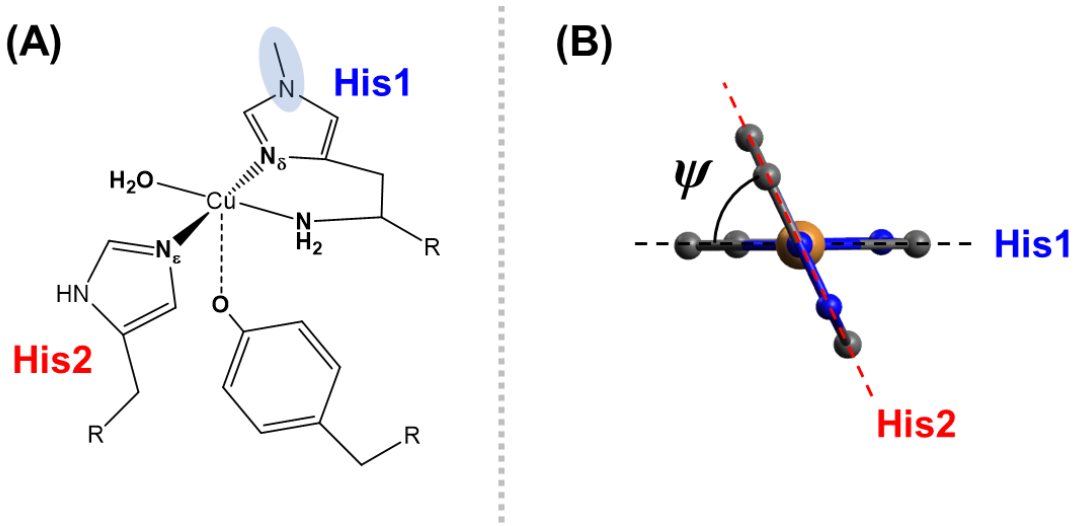

Figure 4.45. A representative drawing of the first coordination sphere of the copper(II) active site in *Ls*AA9 (A); and the definition of the dihedral "twist" ψ, between the two planes of the histidine rings (B).

The two histidine rings coordinate with a characteristic twist, which is defined by the smaller dihedral angle made between the two planes of the histidine rings [Figure 4.45 (B)]. The "twist" has a typical angle in the range of 60° to 65°.[209,212] It is not fully understood what role the histidine brace plays in the catalytic activity of these enzymes. The consequences of the histidine brace "twist" on either the reactivity or the electronic structure remains elusive.

4.3.1.2 The catalytic action of LPMOs

4.3.1.2.1 LPMO activity

LPMOs oxidise recalcitrant polysaccharides. Different families of LPMOs are active on different polysaccharides. For example, the AA9 family is active on a range of polysaccharides including cellulose and xylan. Oxidation of these substrates occur at either the C1 or C4 hydrogen of the glycosidic bond (Figure 4.46).[213] The oxidation results in the cleavage of the glycosidic bond to give two products. The carbon atom (C1 or C4) whose hydrogen atom was abstracted, is converted to the cleaved product C=O. The oxidation proceeds via an external electron donor and molecular oxygen ($R\text{-}H + O_2 + 2e^- + 2H^+ \rightarrow R\text{-}OH + H_2O$) or hydrogen peroxide, where one oxygen atom is incorporated into the oxidised product.[204]

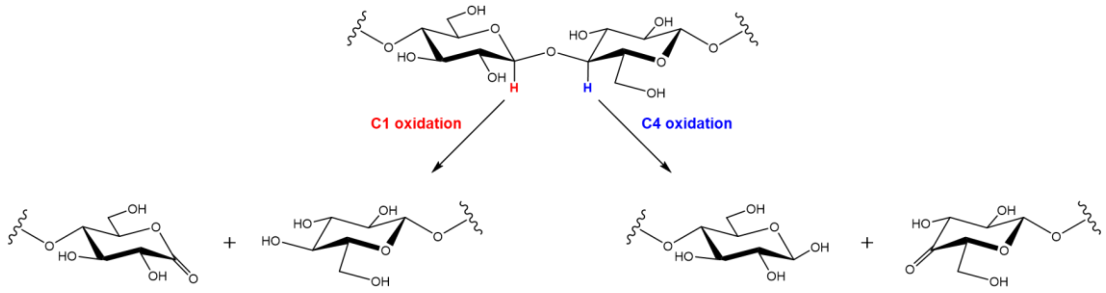

Figure 4.46. C1 or C4 oxidation products of cellulose by the action of an LPMO enzyme.

4.3.1.2.2 Substrate binding

A significant step in understanding the catalytic action of an LPMO enzyme on substrate was published by *Frandsen et al*. in 2016, where the authors reported the first crystal structure of *Ls*AA9 bound to oligosaccharide substrate (Figure 4.47, PDB: 5ACF).[210] The oxidised copper(II) crystal structure showed that the substrate occupies the axial position opposite the tyrosine in the active site and displaces the axial water. This was significant because the blocking of the axial site countered early computational work that suggested that the reactive oxygen species formed in the axial position.[199] The substrate is 'anchored' into position by a hydrogen bonding network and an electrostatic interaction between an oxygen in the substrate and the π network of His1. A chloride ion occupied the exogeneous ligand position, positioning the chloride within range of the C1/C4 hydrogens in the glycosidic bond.

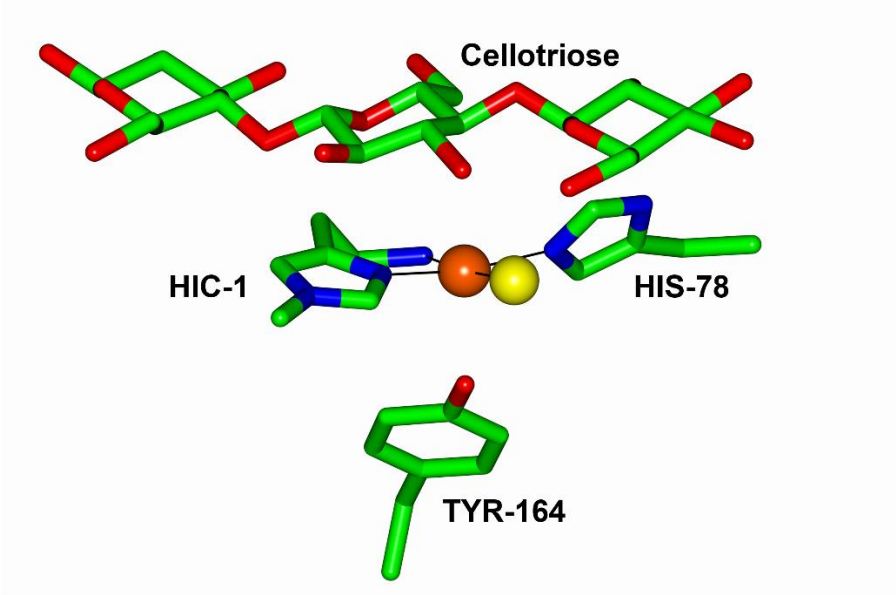

Figure 4.47. The oxidised active site of *Ls*AA9 with cellotriose (PDB: 5ACF) with the chloride anion occupying the exogeneous site. Green, blue, and red cylinders represent carbon, nitrogen, and oxygen atoms, respectively. The copper(II) and chloride ions are represented by the orange and yellow spheres, respectively.

4.3.1.2.3 The suggested reactive intermediate

The details of the catalytic cycle are unknown due to a lack of experimental/spectroscopic data of the reactive intermediates involved. Isotopic labelling shows that an oxygen atom from either molecular O_2 or H_2O_2 is incorporated into the final oxidised product.[190,191] Hence, theoretical/computational work has been focused on elucidating the reactive oxygen species responsible for the oxidation of the strong C–H bond.

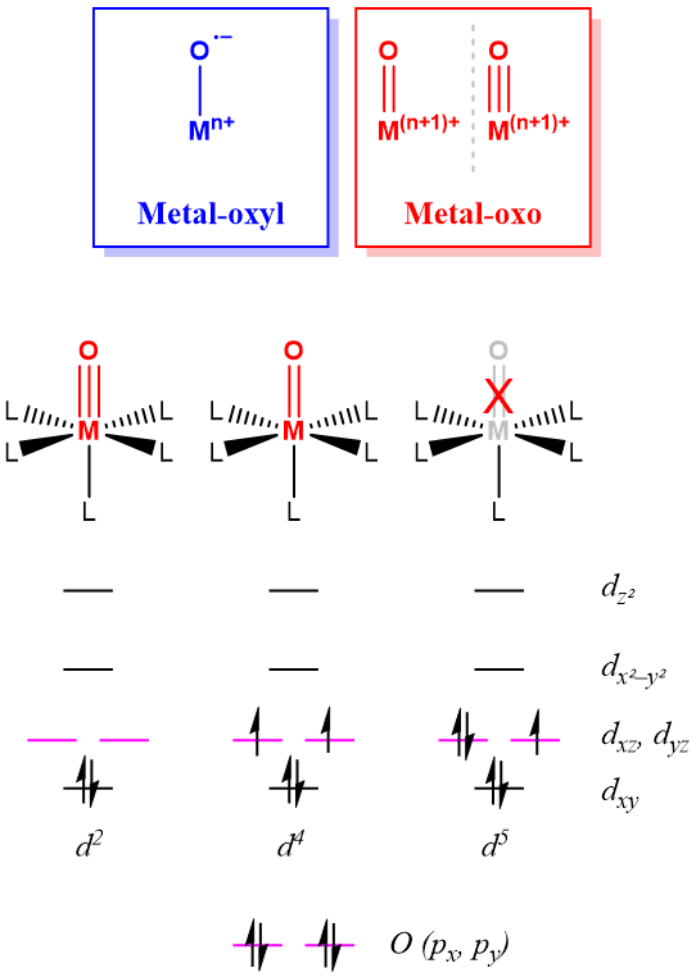

Figure 4.48. A representative Lewis structure for a metal-oxyl and metal-oxo bond (top) and the destabilisation of a formal metal-oxygen π bond resulting in the oxo all (bottom).

A copper(II)-oxyl (Cu-O$^{\bullet}$) has been suggested as one possible reactive species that performs the hydrogen atom abstraction from the substrate. A metal-oxyl has a distinct electronic structure compared to a metal-oxo. The metal-oxyl is drawn as a single bond, whereas the oxo is typically thought of as either a double or triple bond (depending on the occupation of the anti-bonding d orbital) as shown in Figure 4.48 (top). The suggestion of a copper(II)-oxyl, rather than a copper(II)-oxo (like the iron(IV)-oxo in section 4.2), is because the formation of a formal metal-oxo bond in an octahedral geometry is prohibited under the so-called "oxo wall".[4] The oxo wall, illustrated in Figure 4.48 (bottom), shows that the extra electrons that occupy the antibonding d_{xz} and d_{yz} orbitals for d^n configurations with more than four electrons disfavour the formation of strong metal-oxygen π bonds. Since the formation of a copper(II)-oxo is forbidden due to the oxo wall, the potential stabilisation of a copper(II)-oxyl could provide a sufficiently reactive oxygen intermediate to oxidise strong C–H bonds.

4.3.1.2.4 The proposed catalytic cycle

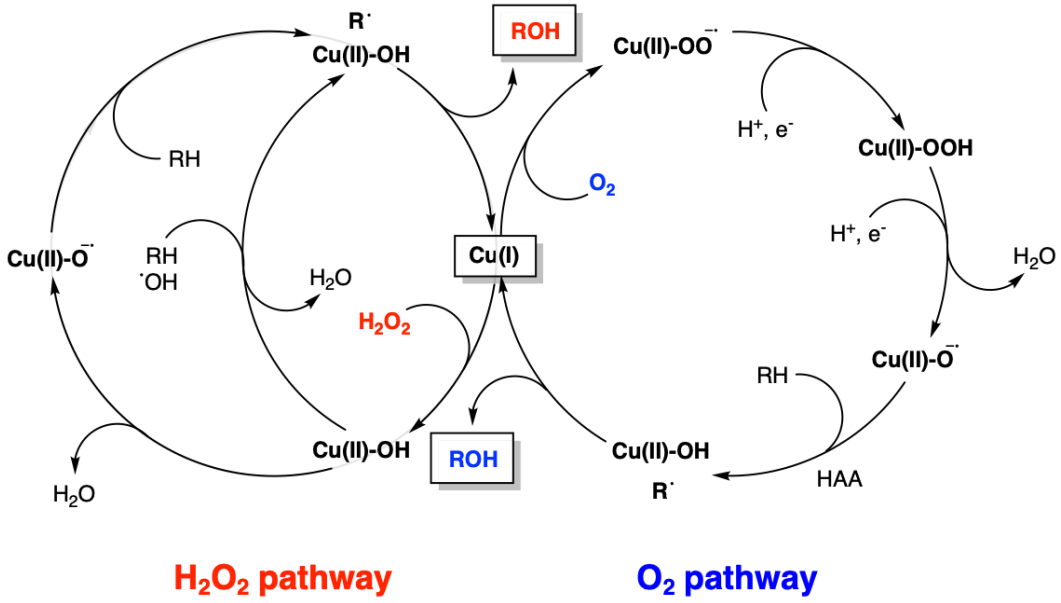

Figure 4.49. The proposed catalytic pathways for peroxygenation (left cycle) and oxidation (right cycle) of substrate (labelled as R).

The O_2 pathway is thought to begin by the reduction of the copper(II) to a copper(I), not shown in Figure 4.49. The first step then involves the binding of molecular oxygen to the copper(I) centre to form a copper(II)-superoxide species. This likely also involves the concurrent binding of substrate. The copper(II)-superoxide species was thought to be the potential reactive oxygen intermediate, but theoretical calculations suggest that it is not sufficiently reactive enough.[214–216] The addition of a proton and an electron, possibly from an external reducing agent, form a copper(II)-hydroperoxyl species that is converted to the putative copper(II)-oxyl reactive intermediate. It has been suggested that the copper(II)-oxyl could be formed by an intermediate step where the copper(II)-OOH converts to a copper(I)-H_2O_2 species before the generation of the copper(II)-oxyl.[217] The putative copper(II)-oxyl is thought to then perform a hydrogen atom abstraction, leaving a radical on the C1 or C4 atom. The copper(II)-hydroxide hydroxylates the substrate to give the final oxidised product and reduces the copper(II) ion back to copper(I).

The H_2O_2 pathway involves the homolytic cleavage of the H_2O_2 molecule and the eventual formation of a copper(II) hydroxide species and an $OH^{\bullet}$ radical. From there, two potential routes have been suggested. The first is that the $OH^{\bullet}$ radical abstracts a hydrogen

from the copper(II) hydroxide to form the putative copper(II)-oxyl, which then performs a hydrogen atom abstraction from the substrate. Alternatively, the $OH^{\bullet}$ radical abstracts a hydrogen from the substrate directly, via a 'caged hydroxyl radical' mechanism.[218] The final stage of the cycle involves the hydrolysis of the substrate, as was seen in the oxygenation mechanism.

4.3.1.3 Spectroscopic characterisation and electronic structure

LPMOs have been extensively studied using EPR spectroscopy. They show that the ground state is a $d_{x^2-y^2}$ SOMO either characterised by a type-2 copper enzyme (axial g-factors $g_3 > g_1 = g_2$) or a rhombic spectrum ($g_3 > g_2 > g_1$). The enzyme *Hj*AA9 (which has an EPR spectrum like other type-2 enzymes) has been probed with a combination of UV-Vis, CD, and MCD in the literature.[219] Only three d-d bands are observed: the $d_{xz} \rightarrow d_{x^2-y^2}$, $d_{xy} \rightarrow d_{x^2-y^2}$, and $d_{yz} \rightarrow d_{x^2-y^2}$ transitions at average energies of 12991 cm^{-1}, 13940 cm^{-1}, and 15705 cm^{-1}. The fourth band, attributed to the $d_{z^2} \rightarrow d_{x^2-y^2}$ transition, is unresolved and presumed to have negligible intensity.

The resting state of the enzyme *Ls*AA9 has been studied extensively by *A. Paradisi* using EPR, UV-Vis, CD, and MCD.[220] *Ls*AA9 shares spectroscopic similarities to *Hj*AA9; both have axial EPR g-factors. In their electronic spectroscopy they both only have three resolved d-d bands, but the *Ls*AA9 bands are blue-shifted by approximately 1500 cm^{-1}. *A. Paradisi* studied *Ls*AA9 in its resting state (*Ls*AA9), in the presence of cellohexaose substrate (*Ls*AA9_C6_H_2O, C6 = cellohexaose), with substrate and chloride (*Ls*AA9_C6_Cl), and with substrate and bromide (*Ls*AA9_C6_Br). As part of that work, *A. Paradisi* calculated the structures of these four models, which were optimised using the BP86 functional, and the calculated structures are used in this work. The truncated structures are presented in Figure 4.50.[220]

The variation of the exogeneous ligand (H_2O, Cl^-, and Br^-) showed notable changes in the EPR g-factors, d-d transition energies, and intensity distributions in their CD and MCD.[220] *A. Paradisi* also carried out TD-DFT and *ab initio* calculations (CASSCF/NEVPT2) with a minimal active space of nine electrons in five orbitals for each system, finding similar d-orbital splitting across the series. The d-orbital splitting as calculated by CASSCF(9, 5)/NEVPT2 calculations was $d_{yz} < d_{xz} < d_{xy} < d_{z^2} < d_{x^2-y^2}$. TD-DFT calculations gave an alternative orbital ordering of $d_{xy} < d_{yz} < d_{xz} < d_{z^2} < d_{x^2-y^2}$. Neither ordering agrees with those derived from the experimental data of *Hj*AA9 or *Ls*AA9.[219,220]

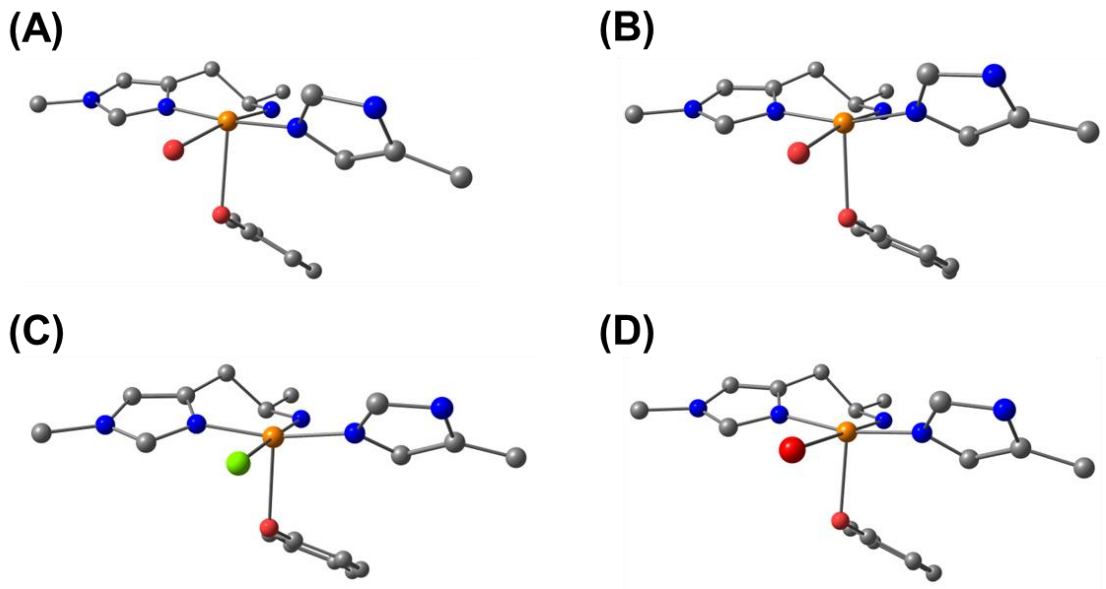

Figure 4.50. The truncated structure of the first coordination sphere of *Ls*AA9 (A), *Ls*AA9_C6_H_2O (B), *Ls*AA9_C6_Cl (C), and *Ls*AA9_C6_Br (D) models with hydrogens and the substrate (for B, C, and D) omitted for clarity. The xyz structures are the DFT optimised structures computed by *A. Paradisi*.[220]

4.3.1.4 The aim of this work

The experimental data reported by *A. Paradisi* has provided a complete spectroscopic characterisation of the copper(II) active site in the resting state and substrate bound structure of *Ls*AA9.[220] This complete spectroscopic characterisation, coupled with the low symmetry of the active site, provides an ideal basis for ligand-field analysis. With this complete spectroscopic data, it is possible that a unique parameter set that characterises LPMO active sites can be found and insight into the unique electronic structure of these complexes can be achieved.

This work aims to reproduce the experimentally observed d-d transition energies, EPR g-factors, UV-Vis, CD, and MCD spectra intensity distributions for *Ls*AA9 in the resting state and the substrate bound structures, within the ligand-field model.

4.3.2 Methodology

4.3.2.1 Ligand-field calculations

A ligand-field analysis was carried out on the DFT optimised geometries computed and reported by *A. Paradisi*.[220] The coordinate scheme, as shown in Figure 4.51, was aligned such that the z axis was oriented along the Cu–Tyr (Tyr = tyrosine) vector and the zx plane was aligned parallel with the Tyr–Cu–His1 plane. The zy plane is automatically aligned perpendicular to the zx plane where the y axis points approximately along the Cu–NH_2 direction.

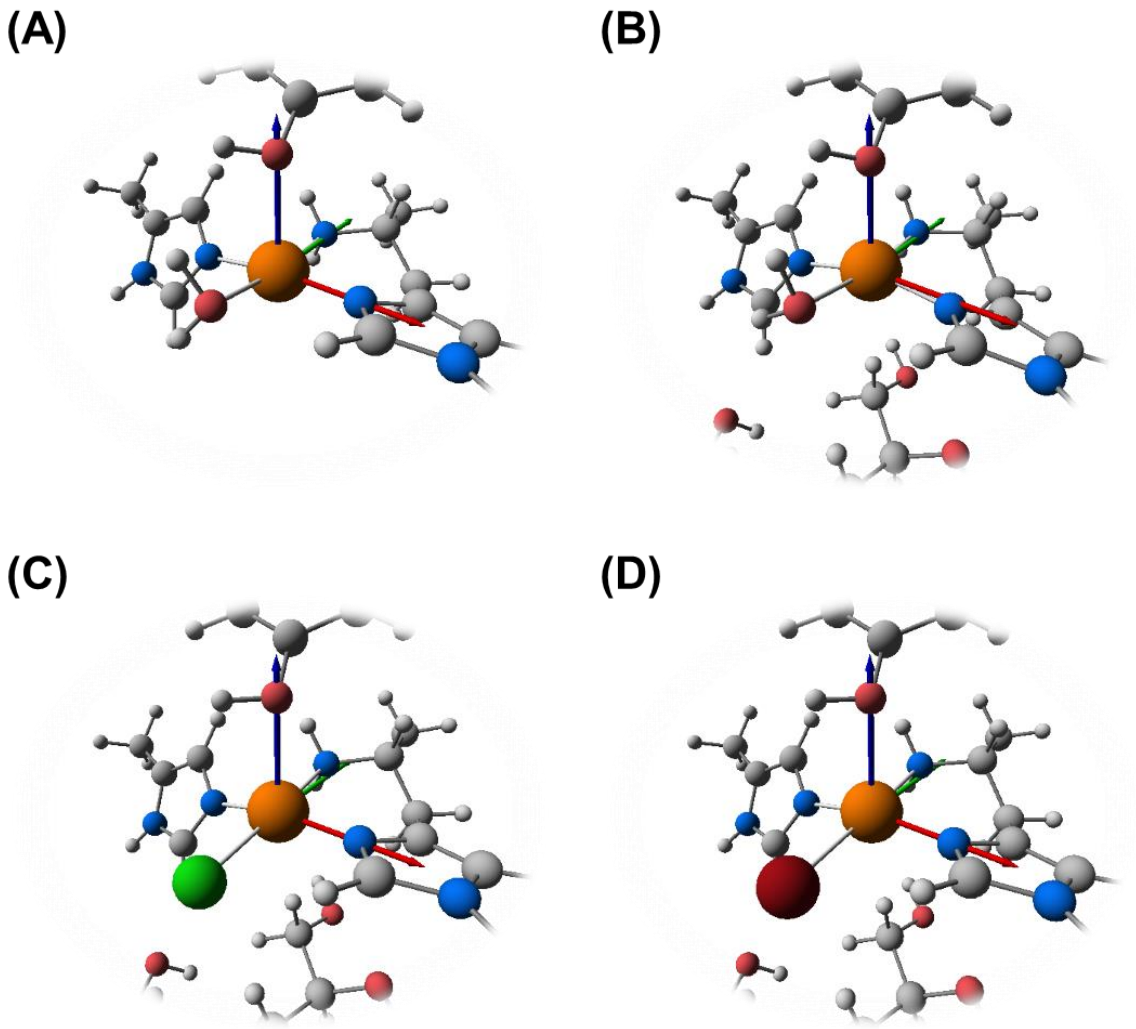

Figure 4.51. The global x (red), y (green), z (blue) coordinate schemes for *Ls*AA9 (A), *Ls*AA9_C6_H_2O (B), *Ls*AA9_C6_Cl (C), and *Ls*AA9_C6_Br (D).

The bonding parameters were chosen such that the histidine brace was assigned common e_σ (His) and $e_{\pi y}$ (His) parameters. The amino terminus and exogeneous ligand (X) were correlated in their σ interactions, so the average σ interaction e_σ (NH_2/X) was used. The exogeneous ligand was assigned a unique e_π for chloride and bromide, and an $e_{\pi x}$ (H_2O) was assigned in *Ls*AA9_C6_H_2O where the local x-direction bisects the H–O–H angle (see section 4.3.3.1). The axial tyrosine was assigned an e_σ (Tyr) interaction. For d^9 Cu^{2+}, there are no interelectronic repulsion parameters. Spin-orbit coupling was parameterised by ζ and was fixed at the free-ion value, ζ_0 = 830 cm^{-1}. The k_{iso} parameter was used to model the orbital angular momentum reduction in the magnetic moment operator.

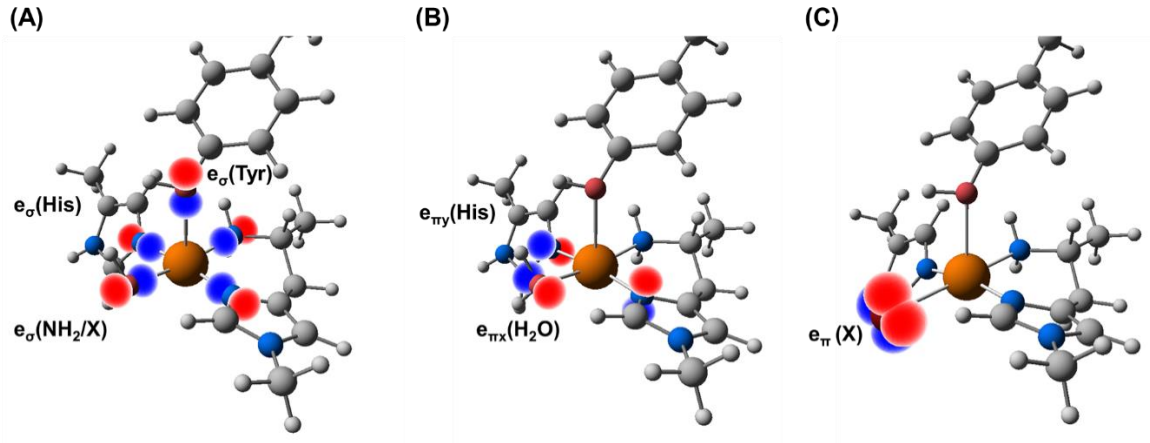

Figure 4.52. The pseudo-symmetries of the local metal-ligand bonding parameters represented by spherical harmonics for the sigma-bonding framework (A); the asymmetric pi-bonding network (B); and the cylindrical pi-bonding network (C); where X = H_2O, Cl, Br. Note the phase information of the spherical harmonics is meaningless in the potential based method.

For the simulation of UV-Vis, CD, and MCD data, transition dipole moment parameters (P_λ and F_λ) are assigned to the ligands. In this work, only relative intensities were reproduced and hence the largest P_λ or F_λ parameter was set to the value of 100 (a.u.). The histidines were set to share a set of transition dipole moment parameters: P_σ (His), F_σ (His), $P_{\pi y}$ (His), and $F_{\pi y}$ (His). In the *Ls*AA9_C6_Cl and *Ls*AA9_C6_Br models the amino terminus and halide are approximately directly *trans* to one another. To reduce the degree of parameterisation, a single P_σ (NH_2 − Cl/Br) and F_σ (NH_2 − Cl/Br) were assigned to the amino terminus position (and measures the relative contribution from the amino terminus compared to the halide) and were allowed to vary between –100 and 100. A positive value is interpreted as a larger

contribution from the amino terminus. The halide ligands were each assigned a P_π (Cl/Br) and F_π (Cl/Br) and were bound to be positive, assuming chloride/bromide are π donors. For the sake of reducing the degree of parameterisation, transition dipole moment parameters from the tyrosine are neglected on the assumption of its non/semi coordinating role (see section 4.3.3.1).

4.3.2.2 Fitting d-d transition energies and EPR g-factors

The analysis began by reproducing the positions of the d-d transition energies and the EPR g-factors. The transition energies were provided by the gaussian deconvolution of the experimental UV-vis, CD, and MCD (Table 4.21) data. Each system featured only three resolved d-d transitions, suggesting the fourth was of negligible intensity. In the water-bound structures (*Ls*AA9 and *Ls*AA9_C6_H_2O), bands I, II and IV are assigned to transitions from the d_{z^2}, d_{xz}, and d_{yz} orbitals respectively. In *Ls*AA9_C6_Cl and *Ls*AA9_C6_Br bands II, III, and IV are assigned as transition from d_{xz}, d_{xy}, and d_{yz}, respectively. The assignment of band II for *Ls*AA9_C6_Cl is different to that of *A. Paradisi* (see section 4.3.3.2).[220]

Table 4.21. The average d-d transition energies (cm^{-1}) and band assignments taken from the Gaussian deconvolution performed by *A. Paradisi* of the experimental UV, CD, and MCD spectra of the *Ls*AA9 structures.[220] Note that the band numbering in *Ls*AA9_C6_Cl is different from the ordering derived from the transition assignments by *A. Paradisi* (see text).

System	Band I	Band II	Band III	Band IV
*Ls*AA9	12810	15443	–	17393
*Ls*AA9_C6_H_2O	13190	15410	–	17517
*Ls*AA9_C6_Cl	–	14510	16263	17547
*Ls*AA9_C6_Br	–	14803	15993	17190

Ligand-field fitting was performed in two stages. First, the d-d transition energies and EPR g-factors were fitted to generate e_λ and k_{iso} parameters. Fitting was performed by varying e_σ(His) from 4000 cm^{-1} to 7000 cm^{-1}; e_π(His) from –2000 cm^{-1} to 2000 cm^{-1}; $e_\sigma(NH_2/X)$ from 4000 cm^{-1} to 7000 cm^{-1}; e_σ(Tyr) from −3000 cm^{-1} to 0 cm^{-1}; and k_{iso} from 0.0 to 1.0. The fitting procedure of the d-d transition energies only fitted the energies of the three resolved bands and the energy of the fourth unresolved band was ignored. Parameter-space searches were

then used to search other regions of fit. The second stage used the optimised e_λ and k_{iso} parameters to generate the eigenvectors and energies for the intensity analysis.

4.3.2.3 Fitting the experimental UV-Vis, CD, and MCD with the ligand-field model

Simulation of the UV-Vis, CD, VT-MCD, and VH-MCD were calculated as arising from transitions originating within the $S=^1/_2$ $d_{x^2-y^2}$ SOMO ground state to the complete excited state manifold. The VT-MCD spectra were simulated at 5 K, 10 K, and 15 K with a magnetic field strength of 7 T. The VH-MCD calculations were simulated at 3 T, 5 T, and 7 T at a temperature of 5 K. MCD simulations were performed by averaging over an angular grid of 30 steps spanning $0 \leq \theta \leq \pi$ and $0 \leq \varphi \leq 2\pi$.

Comparisons were made between the simulated spectra generated by Kestrel and the experimental spectra, where both sets of spectra were normalised by the largest absolute intensity. A common FWHM was applied to each band in the simulated spectra.

4.3.3 Results

The ligand fields were effectively parameterised for each system by reproducing the observed intensity distributions of the UV-Vis, CD and MCD spectra, along with the experimental EPR g-factors. The calculations began by establishing firm e_λ parameters for each of the ligands by reproducing the experimentally observed d-d transition energies and EPR g-factors. The transition dipole moment parameters were then refined against the spectroscopic data separately, holding the other ligand-field parameters fixed. The best fit parameter sets are presented in Table 4.22.

Table 4.22. The best fit ligand-field parameters: bonding parameters (cm^{-1}), isotropic reduction factors, and intensity polarisation parameters (normalised to 100) that provide the best reproduction of the intensity distributions and EPR g-factors. X refers to the nature of the exogeneous ligand (X = H_2O, Cl, Br). The e_π P_π, and F_π values represent πx interactions for *Ls*AA9_C6_H_2O.

Parameters	*Ls*AA9	*Ls*AA9_C6_H_2O	*Ls*AA9_C6_Cl	*Ls*AA9_C6_Br
e_σ (His)	6000	6150	6300	6400
$e_{\pi y}$ (His)	1300	1500	1750	1300
e_σ (NH_2/X)	5500	5800	5425	4900
e_π (X)	0	700	300	300
e_σ (Tyr)	−1800	−2000	−2000	−2000
k_{iso}	0.70	0.67	0.60	0.56
∑	23800	25600	25500	23800
P_σ, F_σ (His)	100, 45	65, 25	27, 19	20, 27
$P_{\pi y}$, $F_{\pi y}$ (His)	35, 10	20, 55	15, 37	17, 35
P_σ, F_σ (NH_2)	90, 0	0, 100	0, 96	0, 80
P_σ, F_σ (X)	20, 10	40, 0	78, 0	99, 0
P_π, F_π (X)	0, 0	85, 5	100, 0	100, 0
FWHM / cm^{-1}	2500	2500	1800	2100

4.3.3.1 Transition energies & EPR

Before proceeding with a fit to the experimentally derived transition energies and EPR g-factors, the underlying metal-ligand interactions were probed for their effect on the d-orbital energies. Naturally, the equatorial e_σ (His), e_σ (NH_2) and e_σ (X) were found to destabilise the

$d_{x^2-y^2}$ and d_{z^2} orbitals. The e_σ (Tyr) primarily effected the d_{z^2} energy. $e_{\pi x}$ and $e_{\pi y}$ for the exogeneous ligand interacted with the d_{xy} and d_{yz} orbitals, respectively.

The $e_{\pi y}$ (His) parameter caused two further perturbations: due to the twist of the histidine brace, d_{xz} is perturbed by His1 and d_{xy} is perturbed by His2. The former interaction is greater than the latter. By assigning the equatorial ligands as σ donors, the exogeneous ligand as a weak π donor (e_π (X) < 500 cm^{-1}), and ignoring the axial tyrosine σ bonding, the resulting d-orbital ordering depends on the π bonding behaviour of the histidines. If the histidines are assigned as π donors ($e_{\pi y}$ (His) > 0 cm^{-1}) then the resulting d-orbital ordering is $d_{yz} < d_{xy} < d_{xz} < d_{z^2} < d_{x^2-y^2}$. If, however, the histidines are assigned as π acceptors ($e_{\pi y}$ (His) < 0 cm^{-1}) then the resulting d-orbital ordering is $d_{xz} < d_{xy} < d_{yz} < d_{z^2} < d_{x^2-y^2}$. The e_π (X) parameter interacts with the d_{xy} and d_{yz} orbitals. If e_π (X) is set 0 cm^{-1}, then d_{yz} remains non-bonding.

Fitting the reported d-d transition energies and their assignments for *Ls*AA9 (Table 4.21) began by constraining all equatorial ligands (the histidines, the amino terminus, and the exogeneous water) to share a common e_σ (equatorial) parameter. The fit began by placing the $d_{yz} \rightarrow d_{x^2-y^2}$ transition as the highest energy band in the spectrum (ca 17300 cm^{-1}). In idealised D_{4h} this energy splitting would be given by $3e_\sigma$ (equatorial), resulting in an approximate value of 5750 cm^{-1}. Hence, it was then possible to fit the band at around 12800 cm^{-1}, assigned to the $d_{z^2} \rightarrow d_{x^2-y^2}$ transition, by setting e_σ (Tyr) = −1500 cm^{-1}. One final band is observed in the spectrum at 15500 cm^{-1}, assigned to the $d_{xz} \rightarrow d_{x^2-y^2}$ transition. This could be reproduced by setting $e_{\pi y}$ (His) = 1300 cm^{-1}, which also placed the final unaccounted for transition, $d_{xy} \rightarrow d_{x^2-y^2}$ around 16600 cm^{-1}. Despite this, the EPR g-factors could not be satisfactorily reproduced with any variation of k_{iso}.

To fit the experimental EPR g-factors (Table 4.23), a further degree of freedom was required. Accordingly, different values of e_σ (His) and e_σ (NH_2/ H_2O) were used. This was found to have no effect on the quality of fit of the transition energies [Figure 4.53 (A)], where the sum was found to be approximately constant: e_σ (His) + e_σ (NH_2/H_2O) = 11600 cm^{-1}. However, when the two parameters were varied to reproduce the EPR g-factors, two separate solutions were found [Figure 4.53 (B)] for a k_{iso} = 0.70. One solution gave parameter values of e_σ (His) = 5100 cm^{-1} and e_σ (NH_2/H_2O) = 6100 cm^{-1} (g_1 = 2.053, g_2 = 2.076, g_3 = 2.283). The other solution gave e_σ (His) = 5900 cm^{-1} and e_σ (NH_2/ H_2O) = 5500cm^{-1} (g_1 = 2.053, g_2 = 2.076, g_3 = 2.279).

These two solutions differ in the orientation of the g-factors [Figure 4.53 (C)]. In the case where e_σ (His) > e_σ (NH_2/H_2O), the smallest g-value was found to align along the histidine directions (g_x). Where e_σ (His) < e_σ (NH_2/H_2O), the smallest g-value was instead orientated

approximately along the H_2O–Cu–NH_2 vector (g_y). The orientation of the g-factors is not known experimentally in *Ls*AA9 but has been determined experimentally in *Ls*AA9_C6_Cl, where g_1 is aligned approximately along the Cu–His direction.[221] Quantum-chemical calculations carried out by *A. Paradisi* orientated g_1 along the Cu–His direction.[220] On this basis, e_σ (His) > e_σ (NH_2/H_2O) was favoured and the alternative fit was disregarded.

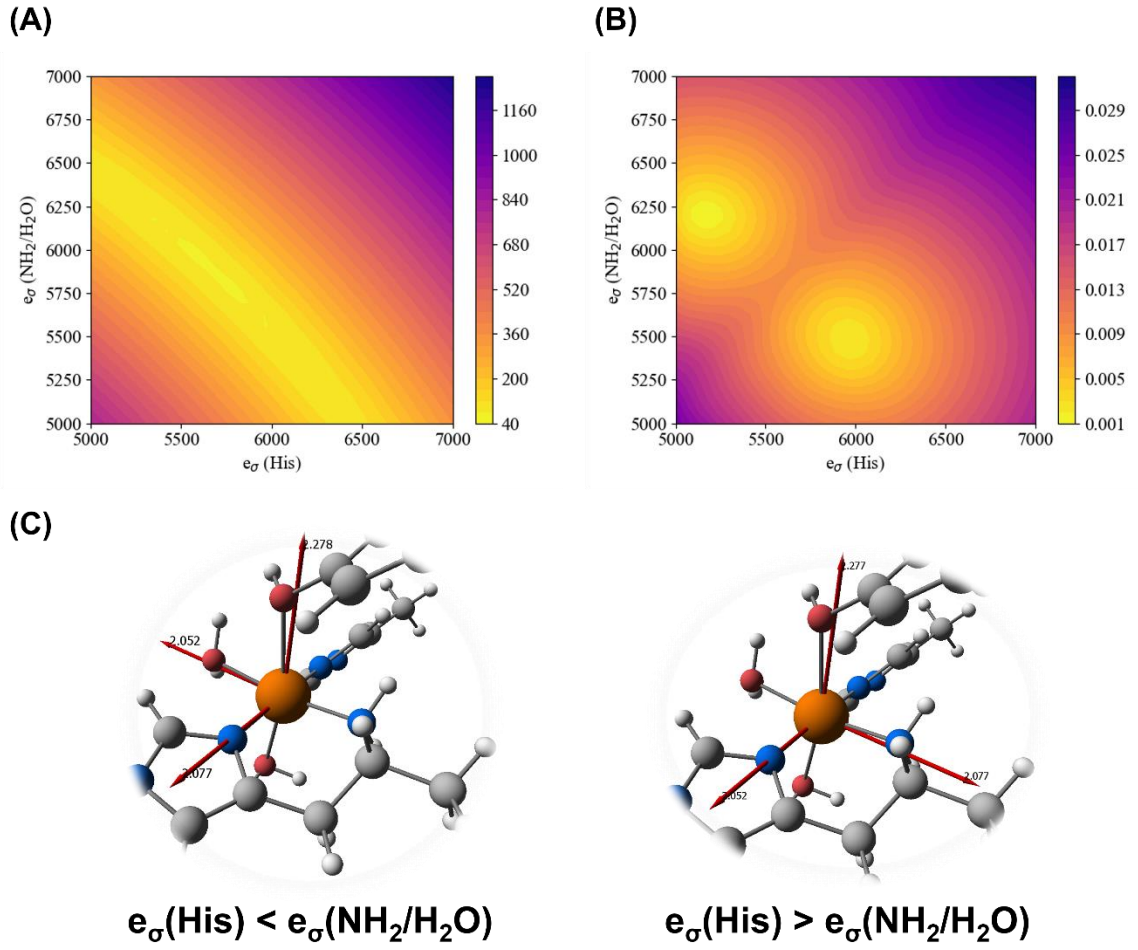

Figure 4.53. The contour maps of best RMS fit (cm^{-1}) values to the transition energies (A) and EPR g-factors (B) of the *Ls*AA9 resting state. The two g-factor orientations given by the two regions of fit to the EPR g-factors (C).

Extending this parameter model to the *Ls*AA9_C6_H_2O system did not satisfactorily reproduce the experimental EPR g-factors. An example of a "best fit" would be e_σ (His) = 6050 cm^{-1}, e_σ (NH_2/H_2O) = 5800 cm^{-1}, $e_{\pi y}$ (His) = 1300 cm^{-1}, e_σ (Tyr) = −2000 cm^{-1}, k_{iso} = 0.69, and ζ = 830 cm^{-1}. This gave g-factors of g_1 = 2.060, g_2 = 2.066, and g_3 = 2.268, where g_1 is too

large compared to the experimental values (Table 4.23). Variations in ζ did not improve the situation.

To reproduce the EPR g-factors in *Ls*AA9_C6_H_2O, the energy of the $d_{xy} \rightarrow d_{x^2-y^2}$ transition (band III, which is not resolved in the experimental spectra) had to be lowered. This could be achieved by increasing the donation strength to the d_{xy} orbital. Hence, an improvement on the quality of fit was found by the inclusion of an $e_{\pi x}$ parameter for the exogeneous H_2O ligand (where the x direction bisects the H–O–H bonds). By adding this interaction, a value of $e_{\pi x}$ (H_2O) = 700 cm^{-1} was assigned to the exogenous water with e_σ (His) = 6150 cm^{-1}, e_σ (NH_2/H_2O) = 5800 cm^{-1}, $e_{\pi y}$ (His) = 1500 cm^{-1}, e_σ (OTyr) = –2000, k_{iso} = 0.67, and ζ = 830 cm^{-1}. This sizeable $e_{\pi x}$ (H_2O) interaction suggests either a change in the coordination mode of the water, or the presence of a different ligand in the exogeneous position (see Discussion, section 4.3.4.2).

*Ls*AA9_C6_Cl has three resolved bands: II, III and IV. The highest energy band IV is at 17547 cm^{-1}, which allowed the assignment of an average e_σ parameter in the equatorial plane of 5850 cm^{-1}. Without a reported energy for band I, the axial tyrosine was presumed to have a similar e_σ parameter to that found in *Ls*AA9_C6_H_2O. The energies of bands II, III and IV were then reproduced via the simultaneous variation of $e_{\pi y}$ (His) and e_π (Cl), resulting in approximate values of 1750 cm^{-1} and 300 cm^{-1} respectively. The value of e_π (Cl) was constrained by the energy of band IV. Then, the EPR g-factors were reproduced by varying e_σ (His), e_σ (NH_2/Cl), and k_{iso}. The orientation of g_2 is known to align along the Cl–Cu–NH_2 vector and, therefore, one can assign e_σ (His) > e_σ (NH_2/Cl).[221] The e_σ (NH_2/Cl) parameter was constrained by the relationship e_σ (Cl) = 2 × 5850 − e_σ (His). This resulted in parameter values of k_{iso} = 0.60, e_σ (His) = 6300 cm^{-1} and e_σ (Cl) = 5425 cm^{-1}. This parameterisation gave calculated g-factors of g_1 = 2.042, g_2 = 2.067, and g_3 = 2.237 in excellent agreement with the experimental values.

*Ls*AA9_C6_Br also has three resolved bands in its spectra: bands II, III, and IV. Like with the analysis of *Ls*AA9_C6_Cl, an average e_σ parameter in the equatorial plane of 5730 cm^{-1} was sufficient for the reproduction of the energy of band IV. Assigning the spin-orbit coupling parameter to its free-ion value, the energies of bands II, III, and IV were all simultaneously reproduced using values of $e_{\pi y}$ (His) = 1200 cm^{-1} and e_π (Br) = 450 cm^{-1}. Next, the EPR g-factors were reproduced and the orientation of g_2 is presumed, like in all systems, to align along the Br–Cu–NH_2 vector. The EPR g-factors were reproduced by varying e_σ (His) and k_{iso} whilst constraining e_σ (Br) by the relationship e_σ (Br) = 2 × 5730 − e_σ (His). This variation resulted in parameter values of k_{iso} = 0.56, e_σ (His) = 6400 cm^{-1} and e_σ (Cl) = 5060

cm^{-1} with a final trace of the ligand-field matrix of 24220 cm^{-1}. The computed g-factors were g_1 = 2.034, g_2 = 2.067, and g_3 = 2.222 in excellent agreement with experiment.

The final calculated EPR g-factors using the best fit parameters (Table 4.22) are given in Table 4.23. The values and their rhombicities are reproduced. The largest deviation between experimental and calculated g-factors is the value of g_2 in *Ls*AA9_C6_H_2O, which differs from the experimental value by 0.004.

Table 4.23. The experimental and Kestrel calculated principal EPR g-factors using the best fit parameters. The experimental EPR g-factors are taken from the simulations of *A. Paradisi*.[220]

System	Experimental[220] g_1, g_2, g_3	Kestrel g_1, g_2, g_3
LsAA9	2.051, 2.075, 2.278	2.052, 2.075, 2.277
LsAA9_C6_H_2O	2.053, 2.062, 2.270	2.056, 2.066, 2.269
LsAA9_C6_Cl	2.042, 2.065, 2.234	2.041, 2.068, 2.237
LsAA9_C6_Br	2.035, 2.071, 2.221	2.032, 2.072, 2.223

4.3.3.2 Ligand field of the histidine brace

Having established e_λ parameters by fitting the d-d transition energies and EPR g-factors, diagonalisation of the 5×5 one-electron ligand-field matrix yields the five ligand-field orbitals and their composition. The calculated one-electron ligand-field splitting is similar across the series (Table 4.24 and Figure 4.54). Because a chemically informed coordinate scheme was chosen (see Methodology, section 4.3.2.1), which was applied consistently to each model and happened to approximately align with the calculated g^2 tensor frame, the d-orbital compositions in Table 4.24 are meaningful. In each system, the final d-orbital ordering (ignoring smaller admixtures) is $d_{yz} < d_{xy} < d_{xz} < d_{z^2} < d_{x^2-y}$. The relative energy of the primarily d_{z^2} and $d_{x^2-y^2}$ orbitals remains stable across the systems. This is a result of the similar e_σ(Tyr) and e_σ(His) + e_σ(NH_2/X) assigned in each system. The relative energies of the d_{xy} and d_{xz} orbitals show greater variation across the systems owing to changes in the histidine and exogeneous ligand π bonding.

Table 4.24. The Kestrel calculated relative energies (cm^{-1}) and eigenvectors of the eigenfunctions of the 5 × 5 one-electron ligand-field matrix for *Ls*AA9 and its substrate bound models.

System	Energy	d_{xy}	d_{yz}	d_{z^2}	d_{xz}	$d_{x^2-y^2}$
*Ls*AA9	0	0.086	-0.98	0.163	-0.015	0.067
	865.9	-0.96	-0.073	0.01	-0.257	0.085
	1486.7	0.251	-0.002	-0.248	-0.935	0.037
	3745.8	-0.063	-0.17	-0.954	0.235	-0.034
	16941.3	-0.065	-0.066	0.036	-0.066	-0.993
*Ls*AA9_C6_H_2O	0.0	0.15	0.981	-0.091	0.023	-0.075
	1304.0	0.946	-0.131	0.247	0.142	-0.086
	2393.0	0.215	-0.035	-0.295	-0.929	0.04
	3559.0	-0.17	0.121	0.919	-0.335	0.027
	17126.3	0.089	0.061	0.002	0.06	0.992
*Ls*AA9_C6_Cl	0.0	-0.090	0.900	0.402	0.068	0.128
	1201.8	0.927	-0.014	0.203	0.312	-0.053
	2557.6	-0.364	-0.242	0.361	0.815	-0.122
	4046.0	-0.024	-0.339	0.816	-0.464	0.054
	17284.0	0.018	-0.129	-0.042	0.135	0.981
*Ls*AA9_C6_Br	0.0	-0.081	0.912	0.378	0.075	0.119
	929.7	0.956	0.009	0.146	0.251	-0.046
	1994.7	-0.282	-0.219	0.329	0.868	-0.105
	3606.3	-0.017	-0.332	0.849	-0.401	0.086
	16652.2	0.026	-0.104	-0.078	0.131	0.982

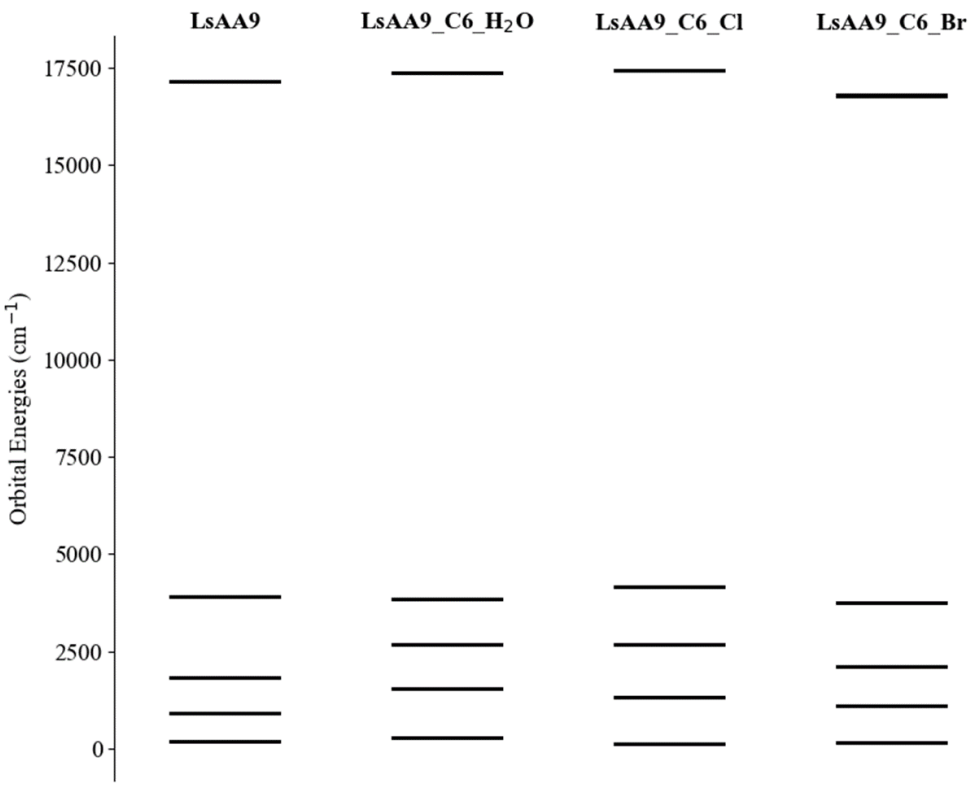

Figure 4.54. The absolute one-electron orbital energies from the diagonalisation of the 5×5 one-electron ligand-field matrix for each of the four LsAA9 systems.

The mixing of d_{z^2} mixing into the $d_{x^2-y^2}$ orbital increases in line with the degree of differential σ bonding in the histidine and amino-terminus/exogeneous directions. This mixing is partly responsible for the rhombicity observed in the values of g_1 and g_2 of the EPR. However, the eigenvector composition is not as useful for visualising the final orbital forms or their orientations. Accordingly, the spherical harmonics are plotted on the central metal copper(II) ion and are shown in Figure 4.55. Careful observation of the d_{xy} and d_{xz} orbitals in *Ls*AA9 reveals them to be rotated about the His2–Cu–His1 axis in a clockwise manner, relative to the other d orbitals. The same rotation of d_{xz} and d_{xy} is observed in *Ls*AA9_C6_Cl/Br but the d_{yz}, d_{z^2} and $d_{x^2-y^2}$ have also rotated about the same axis.

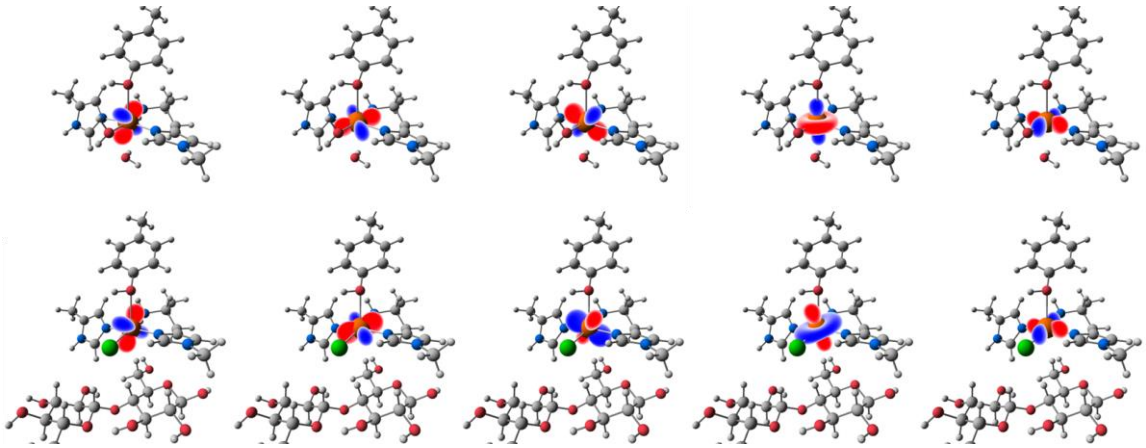

Figure 4.55. The final d-orbital orientations in *Ls*AA9 resting state (top) and in *Ls*AA9_C6_Cl (bottom) generated using Kestrel. The orbitals are ordered left to right from lowest to highest energy, representing the predominantly $d_{yz} < d_{xy} < d_{xz} < d_{z^2} < d_{x^2-y^2}$.

This rotational change can also be seen in the charge densities of the multipole expansion generated by the ligand field (Figure 4.56). The charge density is focused about the equatorial plane in *Ls*AA9 and *Ls*AA9_C6_H_2O. In the halide-bound systems, the charge density is rotated about the His2–Cu–His1 vector to coincide with the X–Cu–NH_2 (X = Cl^-, Br^-) vector. The charge density is also greater in the histidine directions than in the amino terminus and exogeneous ligand directions, reflecting the greater σ donor strength. The lack of any substantive coordination of the tyrosine is evident here by the lack of repulsive charge density in the axial directions.

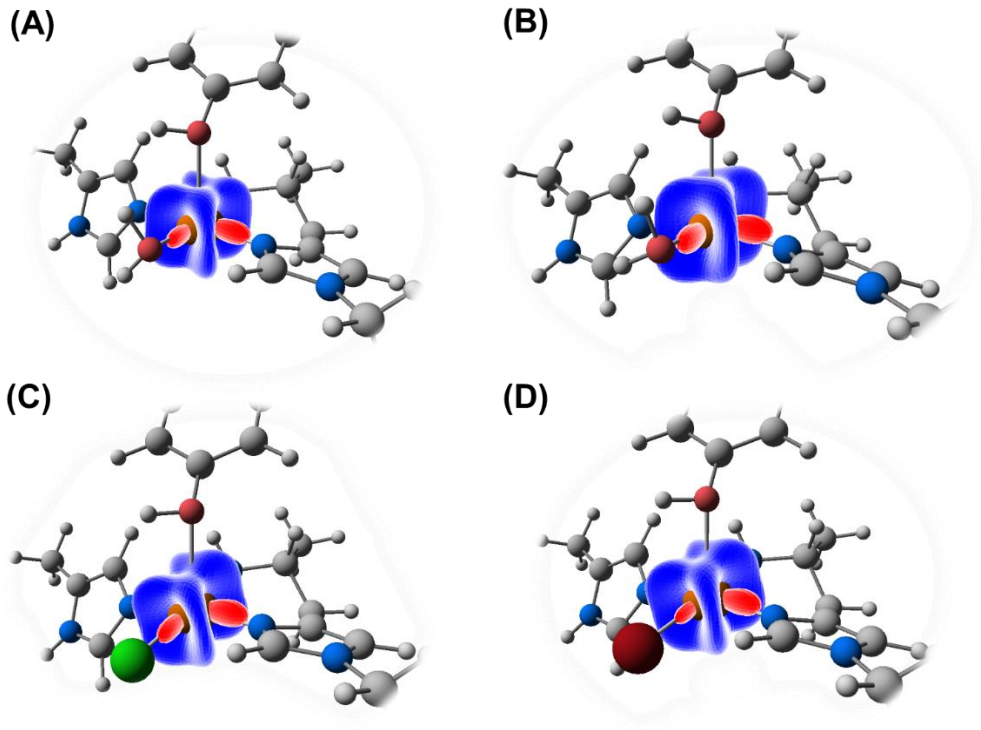

Figure 4.56. The multipole expansions of LsAA9 (A), LsAA9_C6_H_2O (B), LsAA9_C6_Cl (C), and LsAA9_C6_Br (D), rendered using Kestrel.

4.3.3.2.1 The effect of the histidine brace dihedral angle on the d-orbital manifold

The effect of the histidine brace dihedral angle (for a definition of the dihedral angle, see section 4.3.1.1) on the d-orbital orientations was investigated. Figure 4.57 shows the orientation and shape of the second and third lowest energy d orbitals for *Ls*AA9 as a function of the histidine brace dihedral angle. In the optimised structure (dihedral ≈65°), the second and third lowest energy d orbitals are the d_{xy} and d_{xz} orbitals, respectively. Both orbitals are 'rotated' about the coordinate x-axis in a clockwise manner. However, at small angles of ψ of the histidine twist (where His2 is aligned to His1), the formerly predominantly d_{xz} orbital is aligned with the out-of-plane π bonds of the two parallel histidines. The nominally d_{xy} orbital is now essentially non-bonding and is near degenerate with the d_{yz} orbital. The d_{yz} orbital has a small admixture of d_{xy} rotating it anticlockwise about the H_2O–Cu–NH_2. As the dihedral tends to values > 30°, the d_{xz} has rotated clockwise about the x axis again and the second lowest d orbital is nominally d_{xy} again, settling into its canonical orientation when the dihedral angle reaches 40°. Once the angle approaches the angle observed in LPMOs (around 65°), the predominantly d_{xy} and d_{xz} orbitals maximally mix and rotate about the His2–Cu–His1 vector.

When the dihedral angle increases towards 90° a counterclockwise rotation occurs about the His2–Cu–His1 vector.

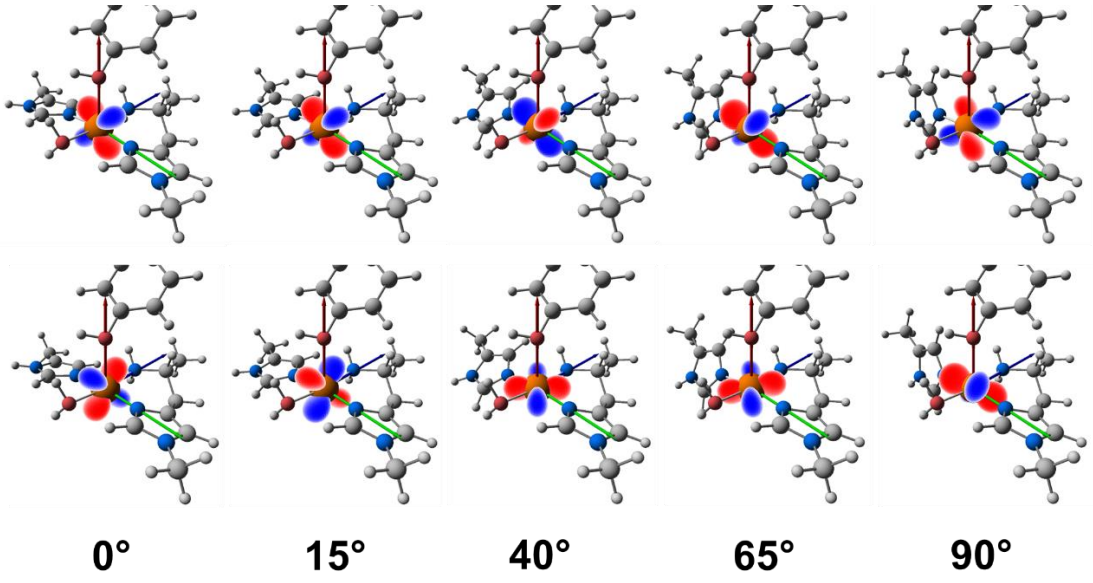

Figure 4.57. The variation in the second (bottom) and third (top) lowest energy d orbitals as a function of the dihedral angle of the histidine brace twist. Green, blue, and red arrows are the x, y, and z axes of the coordinate scheme, respectively.

4.3.3.3 The d-d transitions and configurational mixing

The final d-d transitions are not simple one-electron single slater determinants. The fractional occupation of the one-electron ligand-field orbitals analysed in the preceding section entangle under the action of spin-orbit coupling. In the absence of spin-orbit coupling, the d-d transition energies are simply the difference in the energies of the one-electron ligand-field orbital energies and the $d_{x^2-y^2}$ SOMO. However, under the action of spin-orbit coupling, the d-d transition energies are no longer simple functions of the one-electron energies. The final mixed occupations for the spin-orbit coupled energies are presented in Table 4.25.

There is substantial configurational mixing in each system between the d_{xy} and d_{xz} orbitals for the two bands II and III. The $d_{x^2-y^2}$ SOMO ground state remains relatively pure, as expected from the large energetic separation from the $d_{x^2-y^2}$ and all other orbitals. This is supported, even in the substrate bound structures, by the analysis of the hyperfine coupling constants in their EPR spectra.[210]

Table 4.25. The Kestrel calculated relative energies (cm^{-1}) of the five many-electron energy levels and the mixing of the d^9 configurations (a label 12222 would represent a configuration of $(d_{yz})^1(d_{xy})^2(d_{xz})^2(d_{z^2})^2(d_{x^2-y^2})^2$), where the labelled d orbital denotes the singly occupied d-orbital character of that configuration.

System	Energy	12222 "d_{yz}"	21222 "d_{xy}"	22122 "d_{xz}"	22212 "d_{z^2}"	22221 "$d_{x^2-y^2}$"
*Ls*AA9	0.0	0.000	0.000	0.001	0.002	0.996
	12971.2	0.021	0.005	0.052	0.921	0.000
	15194.6	0.124	0.239	0.615	0.021	0.000
	16418.9	0.014	0.684	0.282	0.017	0.003
	17395.3	0.839	0.070	0.049	0.041	0.001
*Ls*AA9_C6_H_2O	0.0	0.001	0.002	0.001	0.000	0.996
	13235.8	0.013	0.011	0.143	0.833	0.000
	14717.7	0.085	0.152	0.666	0.096	0.000
	16087.3	0.022	0.782	0.160	0.033	0.003
	17526.6	0.880	0.052	0.030	0.037	0.001
*Ls*AA9_C6_Cl	0.0	0.000	0.002	0.001	0.000	0.996
	12964.1	0.015	0.005	0.105	0.875	0.000
	14725.1	0.070	0.107	0.745	0.077	0.000
	16281.8	0.033	0.824	0.126	0.015	0.003
	17675.9	0.882	0.061	0.023	0.033	0.001
*Ls*AA9_C6_Br	0.0	0.000	0.003	0.001	0.000	0.996
	12778.1	0.020	0.004	0.090	0.885	0.000
	14564.6	0.100	0.146	0.698	0.056	0.000
	15961.0	0.029	0.773	0.178	0.017	0.003
	17097.2	0.850	0.074	0.033	0.042	0.001

4.3.3.4 UV-Vis, CD, and MCD spectra

4.3.3.4.1 Spectra simulation

The eigenvectors and transition energies established by the fits to the transition energies and EPR g-factors have been used to compute relative intensities of bands in the UV-Vis, CD, and MCD spectra of the *Ls*AA9 models. The experimental spectra are reported by *A. Paradisi*.[220]

The reported experimental UV-Vis and CD were recorded at room temperature and the reported experimental MCD were recorded at temperatures of 5 K ,10 K, and 15 K, and at field strengths of 7 T, 5 T, and 3 T. The best fit transition dipole moment parameters reported in Table 4.22 offer the best simultaneous reproduction of the UV-Vis, CD, VT-MCD, and VH-MCD.

Despite the approximately centrosymmetric arrangement of the ligands about the copper(II) ion, the effective lower symmetry of the histidine brace twist and the differing chemical nature of the ligands placed *trans* to one another allowed for the static transition dipole moment parameters to be used. Using the chemically sensible choice of transition dipole moment model parameters, the key spectroscopic features of the experimental UV-Vis, CD, and MCD were reproduced in the ligand-field model, except for *Ls*AA9_C6_H_2O. Each *Ls*AA9 model was assigned a FWHM that was applied to each of the d-d bands across all the calculated spectra.

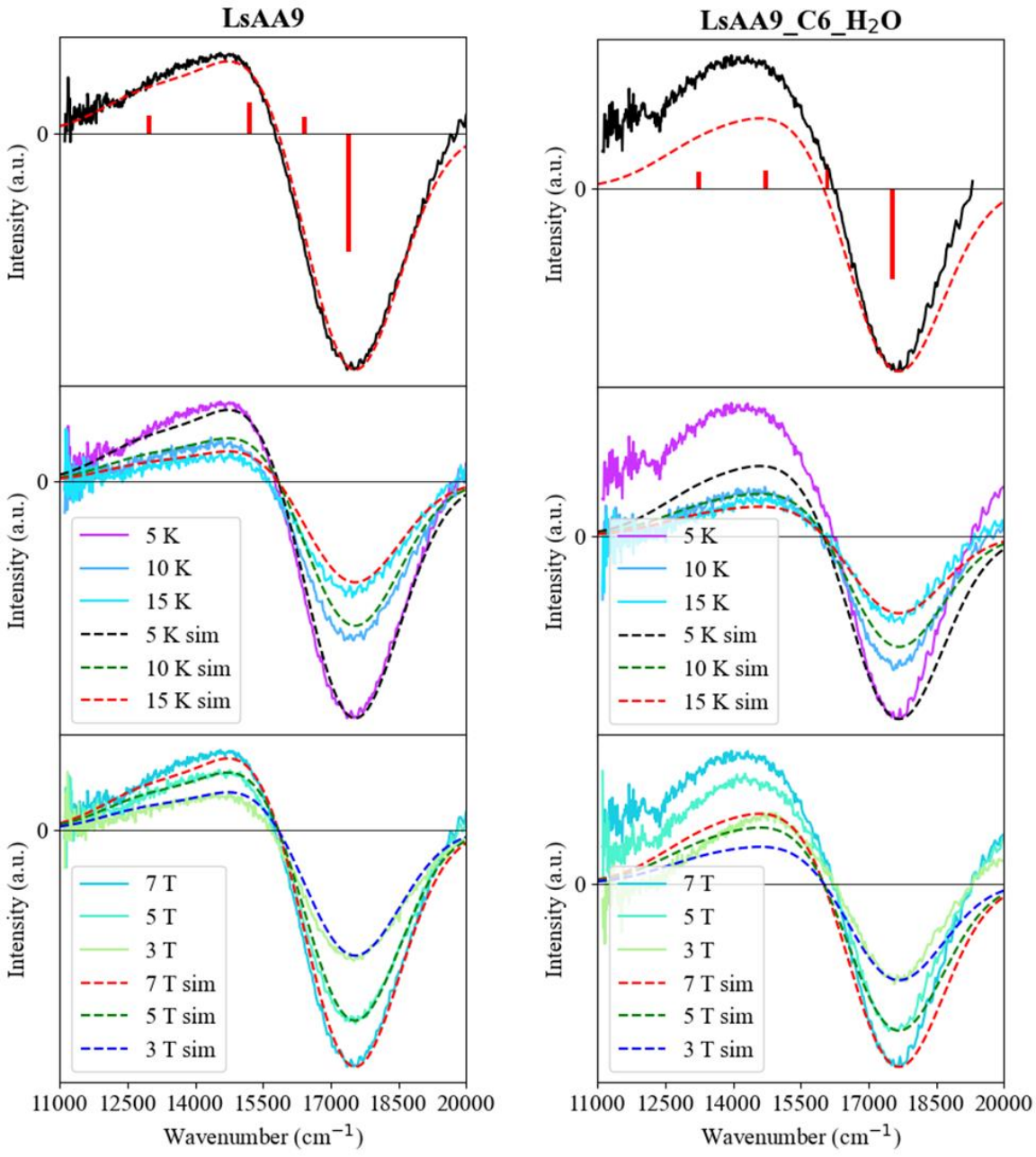
LsAA9
LsAA9_C6_H2O
Intensity (a.u.)
0
5 K
10 K
15 K
5 K sim
10 K sim
15 K sim
7 T
5 T
3 T
7 T sim
5 T sim
3 T sim
11000 12500 14000 15500 17000 18500 20000
Wavenumber (cm−1)

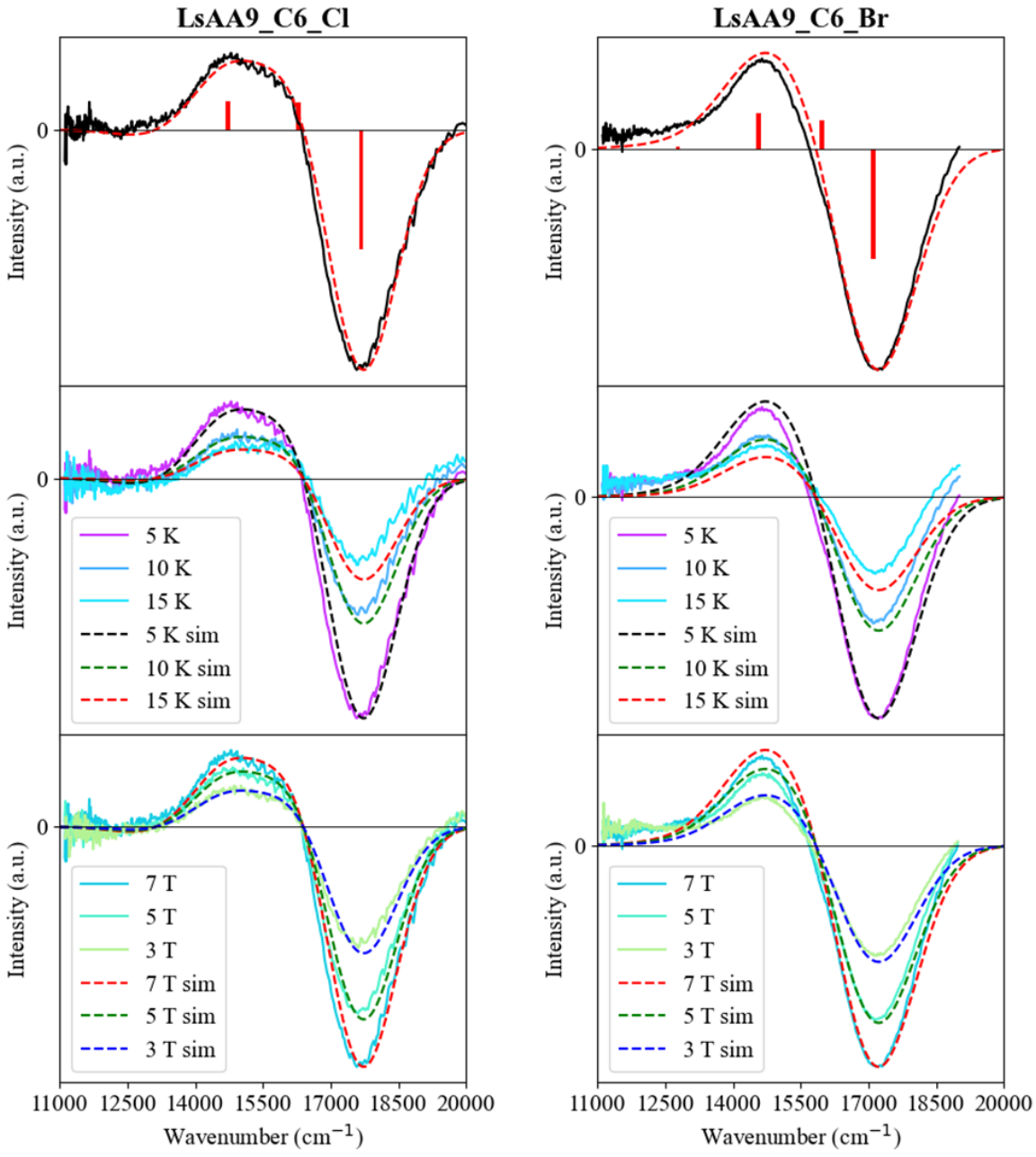

Figure 4.58. The experimental (black) and Kestrel simulated (red) MCD spectra at 7T and 5K (top); Kestrel calculated variable-temperature MCD at 7T (middle); and variation-field MCD at 5K (bottom), for the *Ls*AA9 models. The spectra were simulated using the parameters in Table 4.22. The spectra were simulated using an angular resolution of 30 steps per θ and φ angles. The experimental MCD spectra were recorded and reported by *A. Paradisi*.[220]

Comparisons of the reported experimental and Kestrel simulated MCD spectra for the LsAA9 models are presented in Figure 4.58. The MCD, VT-MCD, and VH-MCD spectra of

*Ls*AA9, *Ls*AA9_C6_Cl, and *Ls*AA9_C6_Br are reproduced well within the ligand-field model. On the other hand, it was not possible to reproduce the intensity distribution of *Ls*AA9_C6_H_2O. The cause of this discrepancy is not known, for the CD and UV-Vis spectra are reproduced (*vide infra*). It is possible that there is an issue with the experimental base-line and this prevents a satisfactory fit to the experimental MCD to be found. This line of enquiry requires further study.

The calculated MCD spectra feature a positive band (II) at around 15500 cm^{-1} and an intense negative band (IV) at 17500 cm^{-1}. Kestrel assigns these opposite signed bands as a pseudo-A-pair formed by the spin-orbit coupling between the d_{xz} and d_{yz} orbitals, which were assigned to these transitions in section 4.3.3.2. The band (III) at 16000 cm^{-1} is relatively weak compared to the intense band at 17500 cm^{-1} and this explains its absence in the gaussian deconvolution performed by *A. Paradisi*.[220]

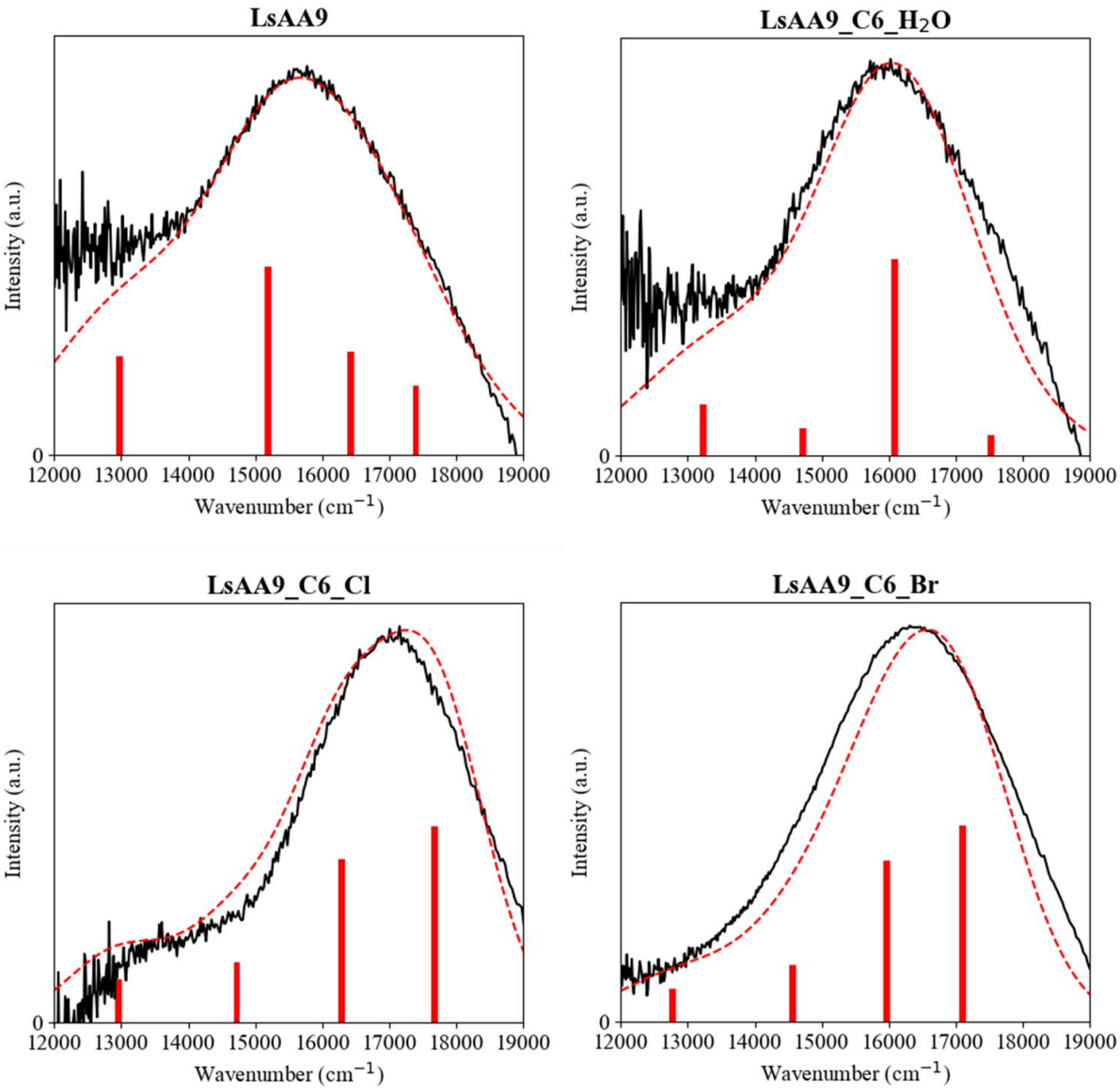

Figure 4.59. The experimental (black) and Kestrel simulated (red) CD spectra at 300 K for the *Ls*AA9 models. The experimental CD spectra were recorded by *A. Paradisi* at room temperature.[220]

The CD spectra were simultaneously fitted along with the MCD spectra and were satisfactorily reproduced for each of the *Ls*AA9 models. The CD simulations were very sensitive to the parameter values and hence the experimental CD spectra provided a constraint on the transition dipole moment parameters. The substrate bound models showed large contributions from band III (and IV for *Ls*AA9_C6_Cl and *Ls*AA9_C6_Br). This is a result of the π transition dipole moment contributions from the exogeneous ligand. Hence, the large contribution from band III in *Ls*AA9_C6_H_2O is from the $P_{\pi x}(H_2O)$ and $F_{\pi x}(H_2O)$, which mostly

interacts with d_{xy}; the larger contributions from band III and IV in *Ls*AA9_C6_Cl and *Ls*AA9_C6_Br arise from the P_{π}(Cl/Br) value.

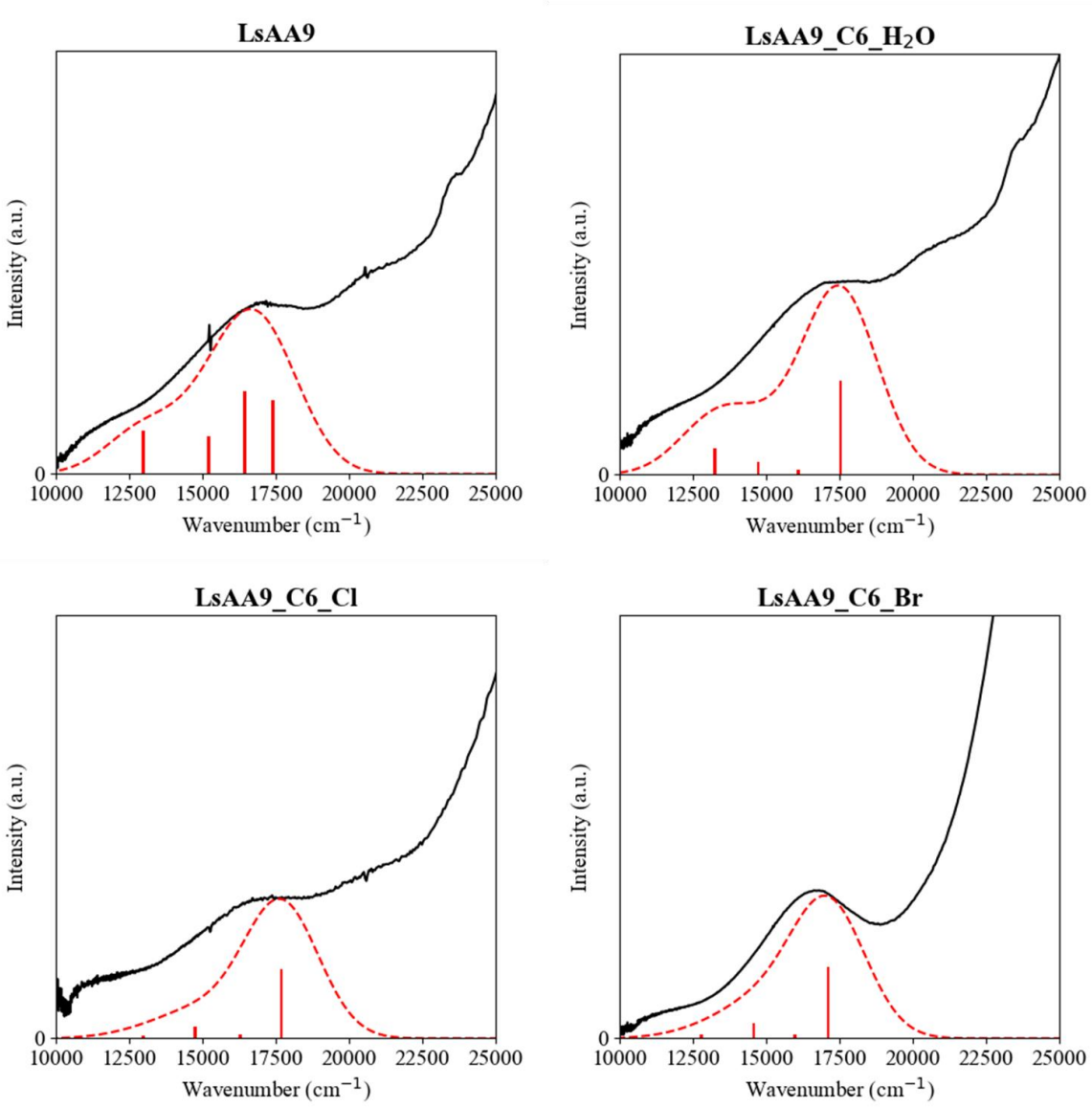

Figure 4.60. The experimental (black) and simulated (red) UV-Vis spectrum at 300 K for *Ls*AA9 models, scaled to experiment using a FWHM of 3000 cm^{-1}. The experimental UV-Vis spectra were recorded by *A. Paradisi* at room temperature.[220]

The calculated UV-Vis spectra (Figure 4.60) reproduce the general experimental spectroscopic features of a broad and relatively intense band at 17500 cm^{-1}, with a weaker band around 13000 cm^{-1}. In the *Ls*AA9 and *Ls*AA9_c6_H_2O models, the low energy band (I) at 13000 cm^{-1} is relatively more intense than predicted in the other models. Unlike with the CD

and MCD spectra, it was not possible to precisely reproduce the experimental spectral trace of the UV-Vis and attempts to do so required values of FWHM > 3000 cm^{-1}. Despite this, the Kestrel simulations did reproduce the general features of the intensity distributions and constrained the possible values of the transition dipole moment parameters further.

4.3.3.4.2 The transition dipole moment parameters

The preceding section has demonstrated that the best fit ligand-field parameters in Table 4.22 reproduces the reported experimental d-d spectroscopy. In this section, a rationalisation of the best fit transition dipole moment parameters are provided.

It is interesting to compare the transition dipole moment contributions from the histidines in the resting state *Ls*AA9 model compared to the substrate bound models. In the substrate bound models, the F_{σ}(His) / P_{σ}(His) and $F_{\pi y}$(His) / $P_{\pi y}$(His) ratios increase relative to the resting state, reflecting the shorter Cu–His bond length and the formation of a stronger bond.

The NH_2/H_2O pair in the *Ls*AA9 model has a larger transition dipole moment contribution from the amino terminus compared to the water. The distorted molecular geometry and the lack of any π bonding from the exogeneous ligands means that determination of separate P_{σ} and F_{σ} parameters for the amino terminus and water were possible in *Ls*AA9. Unlike in *Ls*AA9, separate P_{σ} and F_{σ} parameters could not be simultaneously determined for the amino terminus and exogeneous ligand in the substrate bound models. Instead, the difference in P_{σ} and F_{σ} between the amino terminus and exogeneous ligand was parameterised. In each of the substrate bound structures, the larger F_{σ} contribution is assigned to the amino-terminus, whereas the larger P_{σ} contribution is attributed to the exogeneous ligand. This suggests that the bonding electron density formed between he copper(II) and the amino terminus is polarised more towards the amino terminus, which is consistent with the relatively shorter and presumably stronger copper-amino terminus bond.[81]

The analysis found that the P_{σ}(X) contribution increases in the order H_2O < Cl < Br. This trend can be easily rationalised by considering the valence orbitals of the exogeneous ligands: the 2p, 3p, and 4p orbitals for the water, chloride, and bromide respectively. The increase in the principal quantum number of the valence p orbital results in a metal-ligand bond where the p orbital can extend closer towards the metal, resulting in a stronger p orbital polarisation into the d-orbital basis and hence a larger P_{σ} contribution.

The transition dipole moment parameters extracted from the intensity analysis precluded the use of P_λ or F_λ parameters for the axial tyrosine. Variation in P_σ and F_σ of the axial tyrosine had little effect on the calculated spectra. The contribution to the d-d spectroscopic intensities from the axial tyrosine is expected to be negligible given its semi-coordination role. A semi-coordination role is typically assigned to the axial ligands in tetragonally elongated Cu(II) complexes, where the bond between the copper and the axial ligands are typically weak.[62] Hence, we would not expect a transition dipole moment contribution from the axial directions since the primary stabilisation mechanism (for $e_\sigma < 0$ cm^{-1}) is from d-s coupling with a 4s orbital, which would not contribute to the transition dipole moment intensity ($\Delta l = \pm 1$).

4.3.4 Discussion

4.3.4.1 The ligand field of *Ls*AA9.

This work presents the first ligand-field analysis of all the experimental properties of an LPMO enzyme. The final best fit parameter sets, presented in Table 4.22, faithfully reproduce all the available experimental data, except for the MCD spectra of *Ls*AA9_C6_H_2O. In this section, the chemical interpretation of the ligand-field parameters is discussed.

The histidines themselves are assigned as reasonably strong σ and π donors. The final e_σ (His) and $e_{\pi y}$ (His) are similar to values extracted for pyridine (py) and pyrazole (pz) in $[Cu((pz)_2(py)CH)_2][NO_3]_2$, where e_σ(py) = 6590 cm^{-1}, $e_{\pi y}$(py) = 1300 cm^{-1}, e_σ(pz) = 5540 cm^{-1}, and $e_{\pi y}$(pz) = 740 cm^{-1}.[222] The amino terminus and exogeneous water pair (NH_2/X) were found to be, on average due to holohedral symmetry, weaker σ donors than the histidines. This assignment was made based on the EPR g-factor orientation, where the orientation of the g_1 and g_2 values were dictated by the relative σ bonding strengths of the histidines versus the NH_2/X pair. The decrease in e_σ (NH_2/X) across the group H_2O > Cl > Br primarily reflects the weakening of the σ bonding strength of the exogeneous ligand, in line with the spectrochemical series. Concurrent with this effective weakening of the average σ donor strength of NH_2/X is the effective increase in σ donation of the histidine, attributed to the *cis* influence as illustrated in Figure 4.61. This occurs without a substantial change in the ligand-field trace, suggesting that the *cis* influence acts in accordance with the electroneutrality principle.

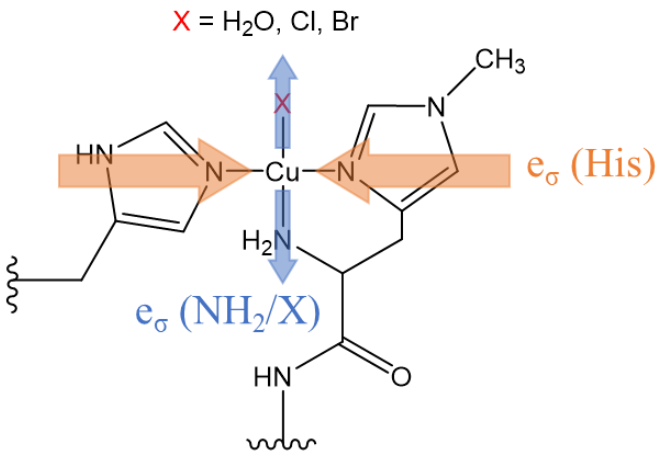

Figure 4.61. Schematic representation of the *cis* influence operating through the e_σ parameter in the *Ls*AA9 active site equatorial coordination sphere.

The ligand-field analysis was also able to establish the π bonding interaction of the exogeneous ligand. In *Ls*AA9, the exogeneous water was assigned as a σ donor only but an extra π interaction was required for the exogeneous water in *Ls*AA9_C6_H_2O. A focused discussion on the origin of this extra π interaction is given in section 4.3.4.2. The chloride and bromide exogeneous ligands were both assigned a small e_π donation value (350 cm^{-1}). This value is smaller than the sensitively determined e_π = 925 cm^{-1} reported for chloride in square planar $[CuCl_4]^{2-}$.[223] This reduction in the e_π parameter can be rationalised through the longer Cu–X (X = Cl, Br) bond lengths calculated in the model complexes compared to the crystal structure $[CuX_4]$ bond lengths (2.41 Å vs 2.27 Å for *Ls*AA9_C6_Cl and $[CuCl_4]^{2-}$ respectively, and 2.56 Å vs 2.43 Å, for *Ls*AA9_C6_Br and $[CuBr_4]^{2-}$, respectively).[224,225] The longer Cu–X bond length is likely a result of the aforementioned *cis* influence (*vide supra*) from the strong σ and π donor histidines. Another possible cause of the smaller e_π parameter for the halides is the potential formation of a halogen hydrogen bond. In each model, the halide approaches the C4 hydrogen (Cl–H 2.50 Å, Br–H 2.55 Å), making an effective Cu–X–H (X = Cl or Br) angle of 98.2° and 95.9° for chloride and bromide, respectively. It has been shown that a Cu–X–H angle < 100° is required for an effective halogen hydrogen bond.[226] If there is any appreciable halogen hydrogen bonding, this will diminish the e_π parameter of the halide, as the halide p_π orbital is partly engaged in hydrogen bonding. However, the existence of a halogen hydrogen bond is speculative and further work would be required to establish its existence.

The axial tyrosine was assigned a negative e_σ parameter which represents an overall stabilisation of the d_{z^2} orbital. This stabilisation effect, typically attributed to the exchange integral *K* of the d_{z^2} electron with the higher-lying 4s orbital, is typical in Jahn-Teller elongated copper(II) complexes.[29] For copper(II) systems with negligible axial interactions, the total d_{z^2}

stabilisation is found to be about 6000 cm^{-1}.[62] Taking the difference of this stabilisation value (as an estimation of the total stabilisation from d-s mixing) with the stabilisation assigned in these systems (1800 cm^{-1} for *Ls*AA9 and 2000 cm^{-1} for all others), the axial copper(II)-tyrosine bond destabilises the d_{z^2} by 4000 cm^{-1}. This value is smaller than the e_σ parameter found for the equatorial ligands, which is expected given the longer copper(II)-tyrosine bond length. Interestingly, the value of e_σ (Tyr) remains constant throughout, even though the calculated copper(II)-tyrosine bond length decreases from 2.55 Å in the resting state model to 2.42 Å, 2.50 Å, and 2.49 Å, in the substrate bound water, chloride, and bromide models respectively.

Lending further support to the assigned ligand-field e_λ parameters, the final ligand-field traces lie in the range of 23800 cm^{-1} to 25900 cm^{-1}, which is sensible given that a typical ligand-field trace for a copper(II) complex can typically range from 20000 cm^{-1} up to 30000 cm^{-1}.[29,227] This same reasoning favours the assignment of the histidines as π donors rather than π acceptors. Care must be taken to not take the values of the ligand-field trace literally, but instead to use them as a useful check/guide on the magnitudes of the e_λ parameters.

The orbital angular momentum was found to be quenched in the order of *Ls*AA9_C6_Br > *Ls*AA9_C6_Cl > *Ls*AA9_C6_H_2O > *Ls*AA9, where *Ls*AA9_C6_Br had the smallest value of k_{iso}. The value of k_{iso} was sensitively determined both because ζ was fixed at the free-ion value and that the final values of k_{iso} offered excellent reproduction of both the EPR g-factors and CD spectra. There was some correlation between ζ and k_{iso}, so fixing the former allowed for unique values of k_{iso} to be obtained. The magnitudes of the assigned k_{iso} (in the range of 0.56 to 0.70) are on the same scale as those obtained for $CuCl_4$ (0.68) and for CuN_4 systems (0.7).[223,228] The orbital angular momentum quenching is rationalised by considering two separate effects: 1) the increased electron density on the copper(II) accompanying the addition of substrate, and 2) the increased spin-orbit coupling constant of bromide versus chloride. The former effect can be observed by the increased ligand-field trace in both *Ls*AA9_C6_H_2O and *Ls*AA9_C6_Cl compared to the resting state and represents how a stronger ligand-field quenches the orbital angular momentum contribution. The latter effect, which has been shown to reduce the effective value of the spin-orbit coupling constant of the metal (and because ζ is fixed in this case, k_{iso} will be reduced). This effect will be larger with bromide than chloride due to bromide having a much larger spin orbit coupling constant (2460 cm^{-1} vs 590 cm^{-1} for bromine and chlorine respectively).[229]

4.3.4.2 The nature of the exogenous ligand in *Ls*AA9_C6_H_2O

The ligand-field parameterisation of the resting state and substrate bound models with a halide anion as the exogeneous ligand were straightforward and did not require the use of any unexpected or extra e_λ parameters. However, when fitting the EPR g-factors of *Ls*AA9_C6_H_2O, it was not possible to satisfactorily reproduce the magnitudes of the g-factors without invoking a non-zero $e_{\pi x}$ value. Without invoking an $e_{\pi x}$ interaction, the degree of separation of g_3 from g_1 and g_2 was too small compared to the g-factors determined experimentally. To aid in rationalising the magnitudes of the EPR g-factors, LFT provides approximate expression for the EPR g-factors in an effective D_{4h} symmetry[6]

$$
\begin{aligned}
g_z &\approx g_e + \frac{8\zeta\alpha^2_{x^2-y^2}\alpha^2_{xy}}{E_{xy}} \\
g_x &\approx g_e + \frac{2\zeta\alpha^2_{x^2-y^2}\alpha^2_{yz}}{E_{yz}} \\
g_y &\approx g_e + \frac{2\zeta\alpha^2_{x^2-y^2}\alpha^2_{xz}}{E_{xz}}
\end{aligned}
\tag{4.9}
$$

Where g_e is the electron g-factor, ζ is the spin-orbit coupling constant, α is the fractional orbital character and E is the energy of the many electron transition energy from the subscript orbital to the $d_{x^2-y^2}$ SOMO.

The π interaction that was assigned to the water interacted with the d_{xy} orbital. From equation (4.9), the energy of the transition originating from the d_{xy} (band III) affects the g_z value. By destabilising the d_{xy} orbital, the many electron transition energy E_{xy} decreases. In turn, this increases the value of g_z and by simultaneously reducing k_{iso}, the experimental EPR g-factors were reasonably reproduced.

Not only was an $e_{\pi x}$ value assigned to the exogeneous water ligand, but a $P_{\pi x}$ and $F_{\pi x}$ were required to satisfactorily reproduce the UV-Vis and CD. However, the inability to accurately reproduce the MCD spectra of *Ls*AA9_C6_H_2O results in conclusions about the nature of the $P_{\pi x}$ and $F_{\pi x}$ parameters as unreliable. The assignment of an $e_{\pi x}$ (and $P_{\pi x}$ and $F_{\pi x}$) value is not expected, given that the π lone pair of the water molecule is assumed to interact weakly and an $e_{\pi x}$ value is not required in the analysis of *Ls*AA9. If the exogeneous ligand is indeed a water molecule (*vide infra*), does a rationalisation for the requirement of an $e_{\pi x}$ parameter exist?

An examination of the DFT optimised geometries of *Ls*AA9, compared to *Ls*AA9_C6_H_2O, reveals a change in the coordination angle that the water makes with respect

to the copper, as illustrated in Figure 4.62. In the *Ls*AA9 resting state, the plane containing the oxygen and hydrogen atoms of the water makes an angle of 122°, whereas the water molecule coordinates at a smaller angle of 111° in *Ls*AA9_C6_H_2O. This change would direct the σ bond partially *away* from the Cu–O vector and the bond would be described as a misdirected bond. This would be represented by both an $e_{\pi x}$ and an $e_{\sigma \pi x}$ parameter, the latter of which was neglected in the analysis.

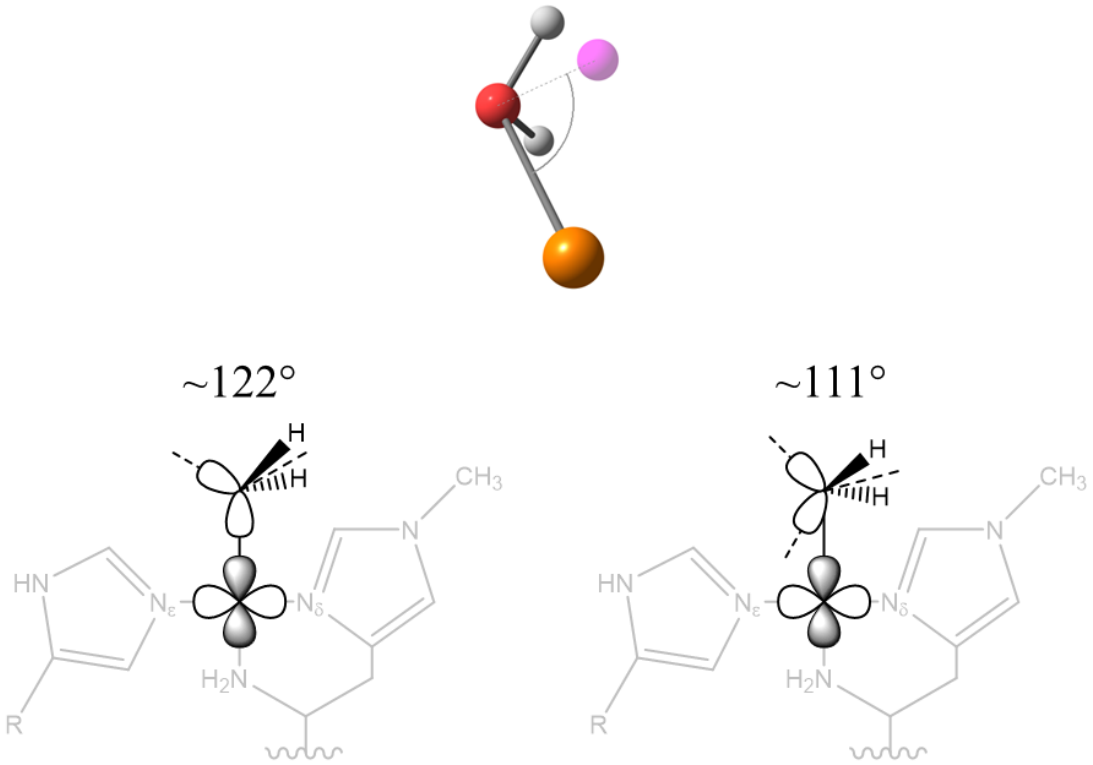

Figure 4.62. The definition of the angle of coordination of a water molecule to the copper ion (top) and an illustration of the resulting orbital orientations from the coordination angles in *Ls*AA9 and *Ls*AA9_C6_H_2O (bottom).

An unpublished analysis of the EPR spectrum of *Ls*AA9 in the presence of substrate as a function of pH finds no change in the spectrum as the pH changes; this is not the case in the absence of substrate.[230] A possible explanation of these results is the suggestion that the exogeneous water is not a water molecule but rather a hydroxide ligand. This analysis provides some evidence of this by the assignment of a relatively large e_{π} interaction from the exogeneous ligand which would be explained by the presence of a hydroxide.

4.3.4.3 The d-orbital ordering

The best fit parameters assign a d-orbital ordering of $d_{yz} < d_{xy} < d_{xz} < d_{z^2} < d_{x^2-y^2}$. If the histidines were instead modelled as π acceptors (rather than assigned as π donors) then the resulting orbital ordering would be $d_{xz} < d_{xy} < d_{yz} < d_{z^2} < d_{x^2-y^2}$. The orbital ordering in both cases is a consequence of the orientation of the histidine π bonding network. The orbital ordering as predicted by LFT agrees with the analysis of *Hansson et al*. who derived the same d-orbital ordering by a qualitative analysis of the CD and MCD spectra of the similar *Hj*AA9 enzyme.[219]

In contrast with these results is the d-orbital ordering predicted by CASSCF(9, 5)/NEVPT2 calculations, carried out by *A. Paradisi*.[220] Those calculations predicted an ordering of $d_{yz} < d_{xz} < d_{xy} < d_{z^2} < d_{x^2-y^2}$. This alternative orbital ordering, which places the d_{xy} orbital higher in energy than the d_{xz} and d_{yz} orbitals, is similar to the d-orbital ordering that *ab initio* calculations predict for square planar copper(II) complexes, such as $[Cu(NH_3)_4]^{2+}$, which (ignoring the d_{z^2} and $d_{x^2-y^2}$ energies) predicts a d-orbital splitting of $d_{yz} \approx d_{xz} < d_{xy}$.[6] This is only possible if an e_π parameter is used, as shown in Figure 4.63, which should be negligible given that ammonia is a σ donor only ligand. This D_{4h} splitting is attributed to the crystal-field (electrostatic) potential.

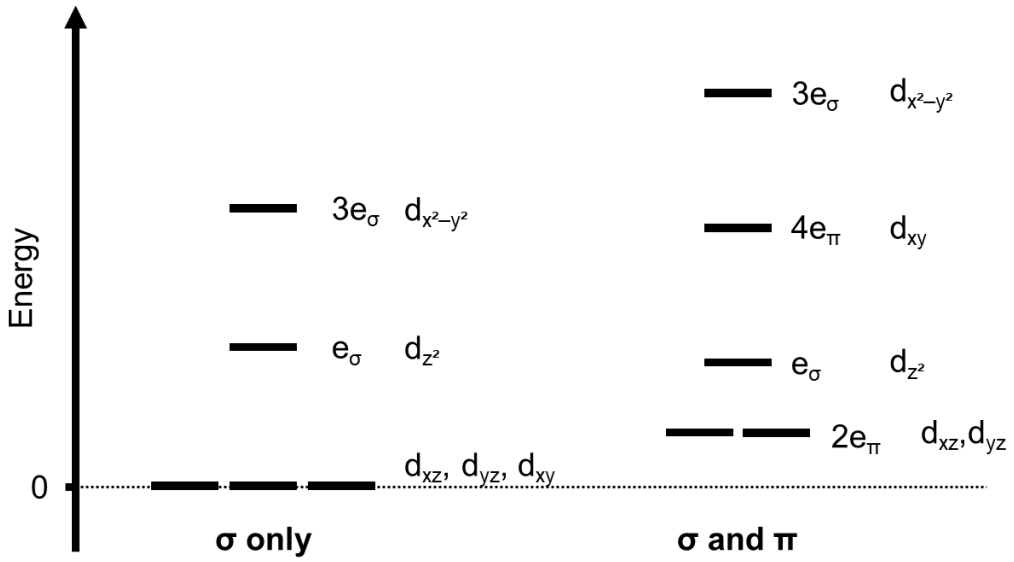

Figure 4.63. The d-orbital splitting from a D_{4h} square planar system using e_σ only (left) and a combination of e_σ and e_π (right).

Of course, the model used in this analysis does not explicitly consider any kind of electrostatic contribution to the e_λ parameters. To place the d_{xy} orbital above the d_{xz} orbital using the electrodynamic ligand-field model in this work, a combination of these effects must occur: 1) There is a large π donor effect that interacts with the d_{xy} orbital, presumably from the exogeneous ligand; and 2) the His2 must be a much stronger π donor than His1. Neither circumstance appears likely, it is more likely that the electrostatic contribution (the crystal field) is overestimated and preferentially destabilises the d_{xy} orbital relative to the d_{xz} and d_{yz} orbitals.

Despite the fact that recent suggestions that aliphatic amines are good π donors (via an electrostatic contribution) on the basis of *ab initio* analyses, it appears that *ab initio* calculations overpredict the electrostatic contribution, as found in the Kestrel analysis of the linear dialkyl cobalt(II) system, described in section 4.1.3.[66] The model that Kestrel employs here, assumes that the contribution to the aspherical ligand-field potential (the multipole expansion potential responsible for d-orbital splitting) is primarily from electrodynamic coupling.

4.3.4.4 Electrodynamic “torque”

The analysis established that the dihedral angle of the histidine brace twist was responsible for orientating the d_{xz} and d_{xy} orbitals via an “electrodynamic torque”. This torque results from the electronic strain of physically rotating the d_{xz} and d_{xy} orbitals about the His2–Cu–His1 axis.

This torque can have consequences for metal-ligand bonding and geometry. Examining the DFT optimised geometries of the equatorial coordination plane reveals different coordination geometries adopted by the water bound and halide bound structures. The calculated water bound structures (with and without substrate) feature an equatorial plane where the amino terminus, exogeneous water, and the two histidines form an approximate 90° angle to the axial tyrosine (Figure 4.64). Contrast this with the halide bound structure where the Cl–Cu–NH_2 axis is rotated about the His2–Cu–His1 axis, placing the chloride below the plane (and closer to the substrate) and the amino terminus above the plane. A similar geometry is exhibited in the calculated structure of *Ls*AA9_C6_Br. The glutamine in the outer coordination sphere acts as a hydrogen bond donor to the equatorial water, pulling it up above the equatorial plane. The lack of such interaction allows the halide to move towards the substrate.

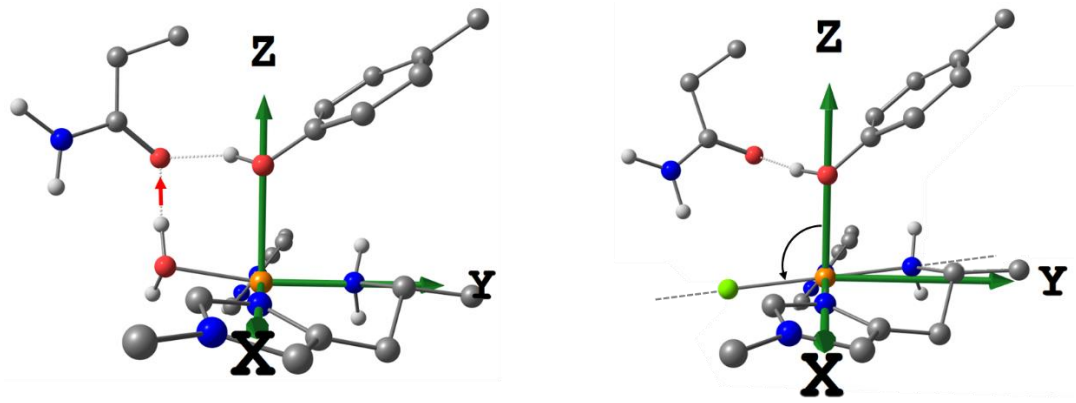

Figure 4.64. The difference in the equatorial coordination sphere in *Ls*AA9 resting state and *Ls*AA9_C6_Cl where the Cl-Cu-NH_2 vector has rotated about the cartesian x-axis. Truncated forms of the DFT optimised geometries are taken from the work of *A. Paradisi*.[220] Hydrogens attached to carbon atoms have been omitted for clarity.

An analysis of the ligand fields under different dihedral angles of histidine brace twist (section 4.3.3.2) shows that in the water bound structures, the d_{xz} and d_{xy} orbitals are rotated about the His2–Cu–His1 axis in the same direction as observed for the X–Cu–NH_2 triad in the halide bound structures. However, in the water bound structures, the d_{yz}, d_{z^2} and $d_{x^2-y^2}$ orbitals remain primarily in their canonical orientations. The strain is generated because the d_{yz}, d_{z^2} and $d_{x^2-y^2}$ orbitals are constrained by the molecular geometry and prevented from twisting.

Careful examination of the multipole expansions and the final d-orbital orientations of *Ls*AA9 and *Ls*AA9_C6_Cl (Figure 4.65) reveals a strain in the charge density of the resting state compared to the halide bound structure. The histidine brace produces a torque by the histidine π bonding network, which is counteracted by the σ bonding network of the amino terminus and water, the latter of which is held in place by the glutamate hydrogen bond. The charge density in *Ls*AA9_C6_Cl has rotated about the x axis in line with the π-induced rotation of the histidines, in turn rotating the d_{yz}, d_{z^2}, and $d_{x^2-y^2}$ orbitals about the same axis.

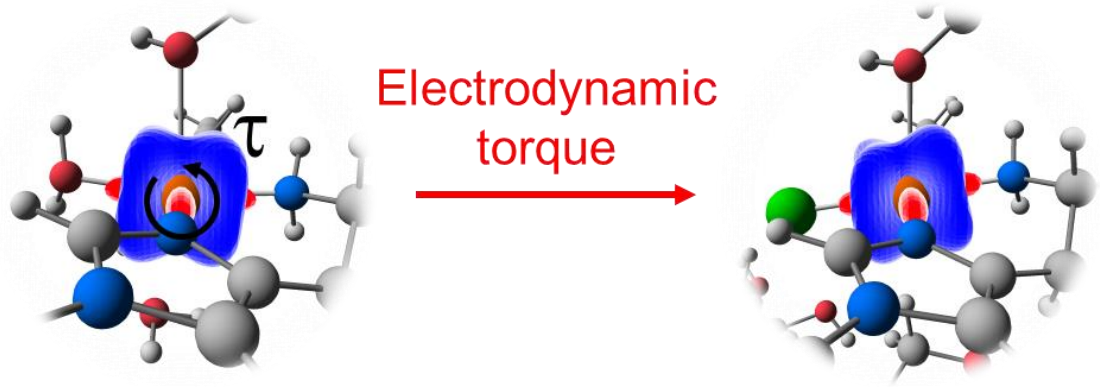

Figure 4.65. Kestrel rendering of the ligand field. The strain results in an electrodynamic torque generated by the twist in the dihedral angle between the two histidine π bonding networks, which drives a rotation about the His2–Cu–His1 axis of the copper d electrons.

The typical dihedral angle in the range of 60° to 65° for the histidine brace twist generates the greatest strain in the direction shown in Figure 4.65. A larger dihedral angle, in the range of 70° to 90°, generates a strain in the opposite direction, which would tilt the exogeneous ligand away from the substrate. A smaller dihedral angle mixes the d_{xy} and d_{yz} orbitals, rotating them about the X–Cu–NH_2 direction instead. The removal of the hydrogen bonding induced strain by the substitution of water with a halide releases the tension and allows the X–Cu–NH_2 group to relax and rotate out of plane. This rotation has consequences for reactivity: the redox active SOMO ($d_{x^2-y^2}$) and the exogeneous ligand are orientated more towards the substrate.

Although the present discussion has speculated about some of the potential consequences of an electrodynamic torque, there is spectroscopic evidence that a rotation of the equatorial plane along the His1–Cu–His2 axis is part of a protective mechanism for LPMOs against oxidative damage. Work by *Paradisi et al*. reported that *Ls*AA9 forms a purple-coloured copper(II)-tyrosyl radical bond when the protein is exposed to H_2O_2 in the absence of substrate.[231] The formation of this species coincides with the rotation of the $d_{x^2-y^2}$ SOMO out of the equatorial plane to be directed along the histidine and tyrosine directions. The tyrosine is thought to act as a “charge-transfer” pathway for the excess charge. Although this process is not likely solely driven by the electrodynamic torque of the histidine, it is possible that the rotation is facilitated by the electrodynamic torque generated by the histidine brace twist.

4.3.4.5 Catalytic activity

The histidine brace 'twist' results in the mixing of the d_{xz} and d_{xy} orbitals under the effect of spin-orbit coupling (see section 4.3.3.2). This is noteworthy as the d_{xy} orbital can interact with the π system of the exogeneous ligand, and this allows therefore for the π networks of the histidines and exogeneous ligands to interact with one another. Given that the histidines are assigned as strong π donors, their π donation would presumably diminish the π donating strength of the exogeneous ligand. Indeed, this is observed in the diminished e_{π} strengths of the halide anions. To compensate for the diminished π bonding strength, the σ bonding strength of the exogeneous ligand increases.[20] Increased σ bonding (which will form a stronger bond than any potential π bonding) might explain the increased preferential binding for chloride in the presence of substrate.[210]

The histidine twist and its relatively strong π donor strength have potential consequences for the reactivity/formation of a copper(II)-oxyl intermediate as part of its catalytic cycle. Theoretical investigations by *Huber et al.* predict that a stronger ligand donor set preferentially stabilises a Cu(III)–OH/Cu(II)–O•.[232] The authors also predict that a stronger ligand donor set results in longer Cu–O bonds and increased spin localisation on the copper. Research into small biomimetic complexes of the LPMO active site has shown that Cu(III)–OH species are capable of oxidising C–H bonds with large BDE of > 100 kcal mol^{-1}.[233,234]

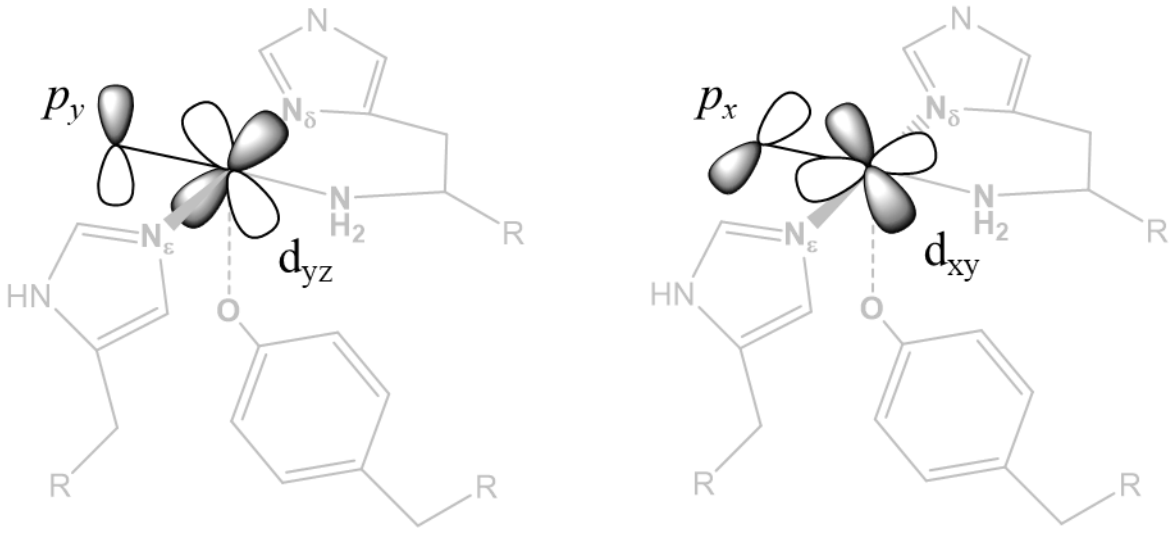

Figure 4.66. The putative copper-oxygen reactive intermediate *p* orbital alignment with the d_{yz} and d_{xy} orbitals on the copper.

As had been discussed at length, the histidine brace twist destabilises the d_{xy} relative to the d_{yz} and orientates these two lowest lying orbitals towards the exogeneous ligand. The orientation and relative energies of the d_{yz} and d_{xy} orbitals could play a role in the orientation of the oxygen p_x and p_y orbitals of the putative copper(II)-O•/copper(III)–OH species, as shown in Figure 4.66. The oxygen of the putative oxyl contains one p orbital of with a single unpaired electron and another p orbital with a pair of electrons. The p orbital with the single unpaired electron, when bonded to the copper(II) ion, will be higher in energy than the p orbital with the lone pair. In this regard the relative energies of the d_{xy} and d_{yz} orbitals might play a role in orienting these p orbitals with respect to the notional equatorial coordination plane of the copper.

Given that the electron pair will experience greater electronic repulsion with charge density on the copper(II), it can be hypothesised that the lone pair would align with the d_{yz} orbital. This is based on two factors: first, the electron density in the plane occupied by the d_{yz} orbital will be smaller (given its non-bonding role) than in the plane occupied by the d_{xy} orbital, which is enhanced by the π donation of His2; and secondly, the electronic correlation will be maximised between electrons of similar energy. Since the lone pair p orbital will be at a lower energy than the unpaired electron p orbital, the former will correlate more strongly with the electrons in the lower energy d_{yz} orbital. On this basis then, the lone pair on the putative oxyl will be directed along the axial direction and, importantly, orientated towards the C–H bond of the substrate. Such an arrangement can facilitate the oxidation of the substrate C–H bond via a concerted proton-coupled electron transfer as has been suggested by *Bertini et al*.[235] Future computational work that investigates the action of a putative copper(II)-oxyl on substrate as a function of the histidine twist angle would provide further insight into the potential role of the histidine brace twist on the catalytic activity of LPMOs.

4.3.5 Conclusion

The LPMO enzyme *Ls*AA9 has been analysed for the first time using a ligand-field model. The model was applied successfully to the reproduction of the experimental spectroscopic and magnetic data. The ligand-field parameterisation provided a better reproduction of the total experimental data than the results of DFT and *ab initio* calculations carried out by *A Paradisi*.[220] The simultaneous reproduction of d-d band energies, EPR g-factors (and their approximate orientations), UV-Vis, CD, and MCD intensity distributions enabled an unambiguous ligand-field parameter set to emerge. The resulting best fit ligand-field parameters serve as a reliable set of starting parameters for the future analysis of other LPMO enzymes. Future work

focusing on the reproduction of experimental data within the ligand-field model will enable the rationalisation in the difference/similarity of reactivity through the electronic structure.

As part of this analysis, it was found that all parameters emerged naturally from the chemical metal-ligand bonding picture for the system, except for *Ls*AA9_C6_H_2O which required an $e_{\pi x}(H_2O)$, $P_{\pi x}(H_2O)$, and $F_{\pi x}(H_2O)$ parameter assigned to the exogeneous ligand. This apparent π interaction was particularly important for the recreation of the experimental EPR g-factors and intensity distributions. This work provides some quantitative evidence for the possibility that the exogeneous ligand is a hydroxide rather than a water molecule. Further work is required to elucidate the true nature of the exogeneous ligand.

An important question in LPMO research pertains to the role, if any, that the histidine brace twist plays in the electronic structure of the copper(II) ion.[209] This work identified a consequence of the histidine brace twist angle on the underlying d-orbital manifold. The twist causes an “electrodynamic torque” that is applied to the d-orbital manifold. It has been argued in this work that this torque, generated by the mixing of d_{xz} and d_{xy}, applies some electronic strain to the d-orbital manifold. In turn, this favours the rotation of the $d_{x^2-y^2}$ and the exogeneous ligand is lifted towards the substrate, making the C1/C4 hydrogen more accessible to the reactive intermediate. This same torque might play some role in the rotation of the $d_{x^2-y^2}$ observed in the formation of a copper(II)-tyrosyl.[231] This would imply the twist is an essential feature of a self-oxidative prevention mechanism and would explain the near constant twist value. Further work would be required to explore the effect that this twist might have on LPMO reactivity pathways.

For now, it would be interesting to compare the ligand-field parameters extracted for *Ls*AA9 in this work and the resting state of *Hj*AA9. The experimental characterisation of *Hj*AA9 is reported by *Hansson et al*. and includes UV-Vis, CD, MCD, and EPR g-factors.[219] The ligand field appears to be weaker in *Hj*AA9, compared to *Ls*AA9, where the highest energy d-d band in *Hj*AA9 is about 16000 cm^{-1}, compared to 17500 cm^{-1} in *Ls*AA9. Importantly, the CD spectrum of *Hj*AA9 features a negative band assigned as the transition from $d_{xy} \rightarrow d_{x^2-y^2}$. This band is positive in the CD spectrum of *Ls*AA9 and its substrate bound systems. Are these differences due to a difference in the molecular geometry around the copper(II) ion, or of the metal-ligand bonding? The x-ray crystal structure of *Hj*AA9 (PDB: 5O2W) shows a similar geometry to that observed in *Ls*AA9 (CSD: 5ACH), however this work has revealed how sensitive the CD and MCD spectra are to small changes in geometry.

5 Conclusion and future work

Although LFT is an old model, the origins of which date back near to the founding of quantum mechanics, the model continues to remerge into the chemical literature. Currently, LFT has found renewed interest in the chemical literature and is a common tool used to analyse the electronic structure of 3d transition-metal complexes, primarily to fit the results of *ab initio* calculations. This work aimed to create a new contemporary ligand-field program and to determine if a ligand-field model could be used to provide chemical insight into contemporary topics of (bio)-inorganic chemistry. To this end, a standalone computer program and Python package, called Kestrel, was constructed to provide a feature-rich ligand-field model that can compute a range of optical, spectroscopic, and magnetic properties, all whilst being easy-to-use. Kestrel is not just another ligand-field program; the user focused design and the real time computation of transition energies, spectroscopic intensities, magnetic, and SIMM behaviour sets Kestrel apart from the other available ligand-field programs. Kestrel was successfully applied to three case studies, which serve as worked examples and sources of inspiration for future applications.

Kestrel provides promise for ligand-field analyses beyond that of just analysing the results of experimental or *in silico* data. Ligand-field analyses have not historically been used in a predictive sense; the analyses of the SiMM behaviour in chapter 4.1 demonstrate Kestrel's ability to be used to optimise a physical property for a change in geometry or metal-ligand bonding. This is an area where Kestrel can be used to great effect. The predictions from Kestrel had closely mirrored the predictions reported by *ab initio* calculations. The ligand-field calculations are not only much faster but allow one to change the metal-ligand bonding more easily. This can be very useful for optimising the desired properties of a transition-metal complex, such as controlling the energetic separation of spin states – an effect which is important in the reactivity of iron(IV)-oxo complexes – or tuning the magnetic properties to design optimal SiMMs or molecular qubits. Even in the absence of transferable or well-defined e_λ parameters, the general qualitative trends of a change in metal-ligand bonding or geometry can still be analysed and that trend is useful.

The application of Kestrel in this work also demonstrates the importance of explicitly treating the effects of multiconfigurational mixing in 3d transition-metal complexes.[10,31,236] In each study, the mixing of electronic configurations has explained many of the optical and magnetic properties of the studied complexes. The results suggest that we should think of the electronic structure not as a single well defined electronic configurations, but rather as the

spatial superposition of the possible electronic configurations within the five d orbitals. The strength of that mixing is a result of the interelectronic repulsion and spin-orbit coupling magnitudes. Even small configurational mixing can have a dramatic effect on optical or magnetic properties of a transition-metal complex. The use of single-slater determinant DFT calculations for electronic structure calculations of 3d transition-metal complexes miss this important contribution. This is likely why there has been a shift towards using multiconfigurational methods, such as CASSCF/NEVPT2, for electronic structure calculations. This important effect, coupled with the connection between first principles physics and the origin of the ligand-field parameters, is the reason LFT consistently remains relevant. The origins of multiconfigurational mixing due to changes in geometry or bonding become obvious in the parametric ligand-field model, where the change in configurational mixing and the resulting physical property is calculated instantly in response to a change in electronic structure. Kestrel can offer this insight in a chemically intuitive and user-friendly way. Sophisticated CASSCF/NEVPT2 calculations offer objectivity but do not lend themselves to making such direct connections between chemical language and electronic structure like LFT does.

Despite this, there is a view that regards sophisticated *ab initio* calculations as the standard by which semi-empirical methods are evaluated against. This is in no small part due to Ernest R. Davidson, who prioritised obtaining "*the right answer for the right reasons*" as the primary goal of quantum chemistry.[237] Although this goal was pursued in the adoption of *ab initio* calculations over calibrated methods (DFT, for example), this viewpoint is important in the context of this work because, at times, the electronic structure predicted by LFT differs from the predictions of *ab initio* theory. This is the primary contention in the electronic structure analysis of the iron(IV)-oxo complex in chapter 4.2. The excited state ordering predicted by ligand-field calculations and expanded active space CASSCF/NEVPT2 are different. However, LFT was able to reproduce the available experimental data, whereas the CASSCF/NEVPT2 calculations performed in this work could not. Which is correct? One could argue that trying different basis sets and active space sizes could improve the quality of the *ab initio* calculation and a better reproduction of the experimental VT-MCD could be achieved. Even so, this would not falsify the ligand-field parameterisation, which would continue to reproduce the experimental data. All of this, therefore, leads to a question: how can the ligand-field approach be falsified? One way would be the failure of LFT to reproduce the VT-MCD of a wider range of iron(IV) oxo systems. However, if both LFT and *ab initio* can account for experiment, this still does not falsify the ligand-field electronic structure. Dismissing the ligand-field parameterisation because it does not align with the expectations of *ab initio* calculations is not an objective assessment of the model.

Despite the apparent success of LFT, the suggestion that it can provide "*a right answer for the right reasons*", where *ab initio* might not, does require further scrutiny. The ligand-field model is limited first and foremost by a lack of knowledge about the magnitudes of ligand-field parameters *a priori*. Chemical bias must be introduced to reduce the number of variable parameters or to bias one potential fit from another. For example, the metal-ligand bonding parameters (e_λ) are assumed to arise from electrodynamic coupling of the d electrons with the bonding/anti-bonding electrons between the ligand and metal. This assumption is at the core of LFT; it underpins ubiquitous concepts like the qualitative ordering of the spectrochemical series and the Dewar-Chatt Duncanson model.[238]

Apparently anomalous e_π parameters have been encountered in ligand-field analysis for canonically non π interacting ligands, such as amines. These non-zero e_π parameters have been attributed to electrostatic effects, which obfuscate the chemical meaning of the e_λ parameters, diminishing their predictability and insight. The experimental evidence for large non-zero e_π parameters is limited but *ab initio* calculations predict large non-zero values. Two systems provided good experimental evidence that the electrostatic contributions to non-bonding e_π parameters were small. The clearer and more convincing case was the parameterisation of the ligand field of the alkyl anions of the linear $Co(C(SiMe_2ONaphthyl)_3)_2$ system in section 4.1.3. The parameterisation managed to reproduce all the available experimental data. The resulting d-orbital splitting arising from a non-zero (positive) e_π interaction was found to be in the range of 0 cm^{-1} to 750 cm^{-1}, at least half of that predicted by *ab initio* calculations reported by *Bunting et al*.[122] Added to this, the d-orbital splitting extracted from reproduction of all the available experimental data by Kestrel, when compared to *ab initio* calculations reported by *A. Paradisi* on the *Ls*AA9 enzyme, suggests that *ab initio* calculations overpredict the contribution from the electrostatic crystal field as well.[220] The Kestrel ligand-field analyses reported in section 4 support the assertion that metal-ligand perturbations arise from primarily electrodynamic effects and that electrostatic contributions are possibly over predicted by CASSCF calculations.

After several years of continual development, Kestrel is a fully fledged ligand-field program. Future development of the program could involve incorporating ligand-field molecular mechanics, which can predict both a transition-metal complexes' geometry and electronic structure simultaneously.[239] This not only would provide another set of experimental data to reproduce (which is nearly always available) but would also provide greater insight into the structure-function correlation. Another obvious expansion of the software is to include the f^n and p^n configurations.[55] The modular design of KestrelPy should make extensions to the Python library easy (and independent of any Fortran code, if desired).

LFT continues to be a useful model for the chemical community. The ligand-field model, as implemented in Kestrel, has been shown to provide physically and chemically sensible results, is easy to understand, and moreover has predictive capability. Importantly, Kestrel makes the essential connection between the rigorous quantum mechanical treatment of d electron energetics and the ‘chemistry’ of a ligand field, all essentially in real time. It is perhaps here where Kestrel and LFT find their greatest utility.

6 Appendices

6.1 Tables of metal-ligand bonding parameters reported for ligand-field analyses of experimental and computational data

Table 6.1. Metal-ligand bonding parameters for transition-metal complexes with a coordination number of 2.

MX_2	Oxidation	eσ	eπ	Void	Σ	Program	Data	Source
Fe(CH3)2	II	1799	1757		10626	ORCA	AILFT	https://doi.org/10.1039/C2SC21394J
Fe(NH2)2	II	2478	5354, 1454		26372	ORCA	AILFT	https://doi.org/10.1039/C2SC21394J
Fe(OH)2	II	3560	4478, 2921		25032	ORCA	AILFT	https://doi.org/10.1039/C2SC21394J
Fe[N(SiMe3)(Dipp)]2	II	3351	5137, 1828		27250	ORCA	AILFT	https://doi.org/10.1039/C2SC21394J
Fe[C(SiMe3)3]2	II	2513	2364		14482	ORCA	AILFT	https://doi.org/10.1039/C2SC21394J
Fe[N(H)Ar′]2	II	4418	3973, 932		24728	ORCA	AILFT	https://doi.org/10.1039/C2SC21394J
Fe[N(H)Ar*]2	II	4512	3860, 1018		24464	ORCA	AILFT	https://doi.org/10.1039/C2SC21394J
Fe[O(Ar′)]2	II	5255	3397, 2439		24098	ORCA	AILFT	https://doi.org/10.1039/C2SC21394J
Fe[N(H)Ar#]2	II	5291	3414, 884		24238	ORCA	AILFT	https://doi.org/10.1039/C2SC21394J
Fe[N(t-Bu)2]2	II	3977	4530, 2321		26074	ORCA	AILFT	https://doi.org/10.1039/C2SC21394J
[Fe(C(SiMe3)3)2]−	II	-1139	843.75		1097	ORCA	AILFT	https://doi.org/10.1038/nchem.1630
CoCSi3R6	II	2819.5	1456.5		11465	ORCA	AILFT	https://doi.org/10.1038/nchem.1630
CoCSi3R6	II	2100	375		5700	Kestrel	experiment	This work
CuCl2	II	3750	4500		25500	None	experiment	https://doi.org/10.1039/DT9930001061
CuCl2 - void	II	3600	4050	-300	21000	None	experiment	https://doi.org/10.1039/DT9930001061

MX_2	Oxidation	eσ	eπ	Void	Σ	Program	Data	Source
CuCl2	II	5000	9500		48000	None	experiment	https://doi.org/10.1039/DT9930001061
CuCl2 - void	II	4250	7250	-1500	25500	None	experiment	https://doi.org/10.1039/DT9930001061
CuCl2	II	3535	2786		18214	ORCA	AILFT	https://doi.org/10.1002/ejic.202100936
Cu(NH3)2 - void	II	4553	0	-5587	3519	ORCA	AILFT	https://doi.org/10.1002/ejic.202100936
CuH2	II	2583	0	-3109	2057	ORCA	AILFT	https://doi.org/10.1002/ejic.202100936
ScH2	II	-4861.5	0	-1009	-10732	ORCA	AILFT	https://doi.org/10.1002/ejic.202100936

Table 6.2. Metal-ligand bonding parameters for transition-metal complexes with a coordination number of 4.

MXY	Oxidation	$e_\sigma(X)$	$e_\pi(X)$	$e_\sigma(Y)$	$e_\pi(Y)$	Σ	Program	Data Type	Source
CoCl(PPh3)3	I	5430	1380	3340	-310	16350	Ligfield/DNS	experiment	https://doi.org/10.1021/ic202185x
CoCl(PPh3)3	I	5310	1350	3470	-322	16488	Ligfield/DNS	experiment	https://doi.org/10.1021/ic202185x
CoCl(PPh3)3	I	5190	1320	3435	-319	16221	Ligfield/DNS	experiment	https://doi.org/10.1021/ic202185x
NiBr3(PPh3)	II	3000	700	5000	-1500	15200	CAMMAG	experiment	https://doi.org/10.1021/ic50218a019
NiI3(PPh3)	II	2000	600	6000	-1500	12600	CAMMAG	experiment	https://doi.org/10.1021/ic50218a020
NiCl2(PPh3)2	II	5227	2421	5509	-1235	26216	CAMMAG/AOMX	experiment	https://doi.org/10.1021/ic020198j

MXY	Oxidation	$e_\sigma(X)$	$e_\pi(X)$	$e_\sigma(Y)$	$e_\pi(Y)$	Σ	Program	Data Type	Source
NiCl2(PPh3)2	II	5689	1138	4192	-1674	17618	CAMMAG/AOMX	experiment	https://doi.org/10.1021/ic020198j
NiCl2(PPh3)2	II	4500	2000	4500	-2500	16000	CAMMAG	experiment	https://doi.org/10.1039/DT9790001836
NiBr2(PPh3)2	II	3184	517	4292	-501	15016	CAMMAG/AOMX	experiment	https://doi.org/10.1021/ic020198j
NiBr2(PPh3)2	II	4000	1500	4000	-1500	16000	CAMMAG	experiment	https://doi.org/10.1039/DT9790001836
NiI2(PPh3)2	II	2000	600	5509	-1235	12478	CAMMAG/AOMX	experiment	https://doi.org/10.1021/ic020198j

Table 6.3. Metal-ligand bonding parameters for transition-metal complexes with a coordination number of 6.

MXYZ	Oxidation	$e_\sigma(X)$	$e_\pi(X)$	$e_\sigma(Y)$	$e_\pi(Y)$	$e_\sigma(Z)$	$e_\pi(Z)$	Σ	Program	Data Type	Source
CrF6	III	6868	1755					62268	ORCA	AILFT	https://doi.org/10.1007/430_2011_57
CrF6	III	8272	2375					78132	ORCA	AILFT	https://doi.org/10.1007/430_2011_57
CrF6	III	7400	1700					64800	?	experiment	https://doi.org/10.1007/3-540-08887-3_3
CrCl6	III	4730	715					36960	ORCA	AILFT	https://doi.org/10.1007/430_2011_57
CrCl6	III	6430	1270					53820	ORCA	AILFT	https://doi.org/10.1007/430_2011_57
CrCl6	III	5900	900					46200	?	experiment	https://doi.org/10.1007/3-540-08887-3_3
CrBr6	III	4223	596					32490	ORCA	AILFT	https://doi.org/10.1007/430_2011_57

MXYZ	Oxidation	$e_\sigma(X)$	$e_\pi(X)$	$e_\sigma(Y)$	$e_\pi(Y)$	$e_\sigma(Z)$	$e_\pi(Z)$	Σ	Program	Data Type	Source
CrBr6	III	6114	1142					50388	ORCA	AILFT	https://doi.org/10.1007/430_2011_57
CrBr6	III	4900	600					36600	?	experiment	https://doi.org/10.1007/3-540-08887-3_3
CrI6	III	3855	469					28758	ORCA	AILFT	https://doi.org/10.1007/430_2011_57
CrI6	III	5976	1023					48132	ORCA	AILFT	https://doi.org/10.1007/430_2011_57
CrI6	III	4300	600					33000	?	experiment	https://doi.org/10.1007/3-540-08887-3_3
Cr(en)2F2	III	7233	0	8033	2000			34532	None	experiment	https://doi.org/10.1039/dt9750000650
Cr(en)2Cl2	III	7500	0	5857	1040			28794	None	experiment	https://doi.org/10.1039/dt9750000650
Cr(en)2Br2	III	7500	0	5120	750			26740	None	experiment	https://doi.org/10.1039/dt9750000650
Cr(en)2I2	III	6987	0	4292	594			23746	None	experiment	https://doi.org/ 10.1039/dt9750000650
Cr(en)2(H2O)2	III	7833	0	7497	1410			33480	None	experiment	https://doi.org/10.1039/dt9750000650
Cr(en)2(OH)2	III	6640	0	7473	1405			31036	None	experiment	https://doi.org/10.1039/dt9750000650
Cr(en)2(dmso)2	III	7534	0	6769	1653			31912	None	experiment	https://doi.org/10.1039/dt9750000650
Cr(pd)2F2	III	7343	0	9093	2450			37772	None	experiment	https://doi.org/10.1039/dt9750000650
Fe(L1)(O)(MeCN)	IV	6893	0	9288	5584	9288	5584	57316	Kestrel	experiment	https://doi.org/10.1039/D1FD00073J
Fe(L1)(O)(Cl)	IV	6201	0	9288	5584	9288	5584	54548	Kestrel	experiment	https://doi.org/10.1039/D1FD00073J

MXYZ	Oxidation	$e_\sigma(X)$	$e_\pi(X)$	$e_\sigma(Y)$	$e_\pi(Y)$	$e_\sigma(Z)$	$e_\pi(Z)$	Σ	Program	Data Type	Source
Fe(L1)(O)(Br)	IV	5782	0	9288	5584	9288	5584	52872	Kestrel	experiment	https://doi.org/10.1039/D1FD00073J
Fe(L2)(O)(MeCN)	IV	6770	0	9288	5584	9288	5584	56824	Kestrel	experiment	https://doi.org/10.1039/D1FD00073J

6.2 Tabulation of all unique orbital occupations for each d^n electronic configuration

Tabulated here are the unique orbital occupations for each electron belonging to a d^n configuration. The final d orbitals are labelled 1 to 5. Orbital 1 is the lowest energy ligand-field orbital and orbital 5 is the highest energy ligand-field orbital. There are *n* columns, for *n* electrons. In each row, the n^{th} column will display the orbital (1 to 5) that the n^{th} electron occupies. No spin projection (M_S) character is contained in these lists because they cannot be extracted in a J, M_J, L, S basis set without first transforming to the uncoupled L, S, M_L, M_S basis. Also note that a permutation of the orbital labels between the *n* electrons is ignored. E.g., 1 3 1 is the same as 1 1 3 etc.

Note that the spatial orbital occupations for configurations belonging to higher spin-multiplicities also belong to lower spin-multiplicities. Hence, these occupations are not repeated in the lists of the lower spin-multiplicities. Finally, the d^1 to d^5 configurations are explicitly listed. The occupation patterns are the exact same for d^6 to $d^{9,}$ but the occupations are for holes, rather than electrons.

Table 6.4.The unique orbital occupations of the *n* electrons for d^n configurations (n = 1 through to 5)

d^n	Spin Multiplicity	Electron 1	Electron 2	Electron 3	Electron 4	Electron 5
1	Doublet (5 roots)	1				
		2				
		3				
		4				
		5				
2	Triplets (10 roots)	1	2			
		1	3			
		1	4			
		1	5			
		2	3			
		2	4			
		2	5			
		3	4			
		3	5			
		4	5			

d^n	Spin Multiplicity	Electron 1	Electron 2	Electron 3	Electron 4	Electron 5
	Singlets (5 + 10 = 15 roots)	1	1			
		2	2			
		3	3			
		4	4			
		5	5			
3	Quartets (10 roots)	1	2	3		
		1	2	4		
		1	2	5		
		1	3	4		
		1	3	5		
		1	4	5		
		2	3	4		
		2	3	5		
		2	4	5		
		3	4	5		
	Doublets (20 + 10 = 30 roots)	1	1	2		
		1	1	3		
		1	1	4		
		1	1	5		
		2	2	1		
		2	2	3		
		2	2	4		
		2	2	5		
		3	3	1		
		3	3	2		
		3	3	4		
		3	3	5		
		4	4	1		
		4	4	2		
		4	4	3		
		4	4	5		
		5	5	1		
		5	5	2		
		5	5	3		
		5	5	4		
4	Quintets (5 roots)	1	2	3	4	
		1	2	3	5	
		1	2	4	5	
		1	3	4	5	
		2	3	4	5	
	Triplets (30 + 5 = 35 roots)	1	1	2	3	
		1	1	2	4	
		1	1	2	5	
		1	1	3	4	

d^n	Spin Multiplicity	Electron 1	Electron 2	Electron 3	Electron 4	Electron 5
		1	1	3	5	
		1	1	4	5	
		2	2	1	3	
		2	2	1	4	
		2	2	1	5	
		2	2	3	4	
		2	2	3	5	
		2	2	4	5	
		3	3	1	2	
		3	3	1	4	
		3	3	1	5	
		3	3	2	4	
		3	3	2	5	
		3	3	4	5	
		4	4	1	2	
		4	4	1	3	
		4	4	1	5	
		4	4	2	3	
		4	4	2	5	
		4	4	3	5	
		5	5	1	2	
		5	5	1	3	
		5	5	1	4	
		5	5	2	3	
		5	5	2	4	
		5	5	3	4	
	Singlets	1	1	2	2	
	(10 + 30 + 5 = 45 roots)	1	1	3	3	
		1	1	4	4	
		1	1	5	5	
		2	2	3	3	
		2	2	4	4	
		2	2	5	5	
		3	3	4	4	
		3	3	5	5	
		4	4	5	5	
5	Sextets (1 root)	1	2	3	4	5
	Quartets (20 + 1 = 21 roots)	1	1	2	3	4
		1	1	2	3	5
		1	1	2	4	5
		1	1	3	4	5
		2	2	1	3	4
		2	2	1	3	5
		2	2	1	4	5

d^n	Spin Multiplicity	Electron 1	Electron 2	Electron 3	Electron 4	Electron 5
		2	2	3	4	5
		3	3	1	2	4
		3	3	1	2	5
		3	3	1	4	5
		3	3	2	4	5
		4	4	1	2	3
		4	4	1	2	5
		4	4	1	3	5
		4	4	2	3	5
		5	5	1	2	3
		5	5	1	2	4
		5	5	1	3	4
		5	5	2	3	4
	Doublets (30 + 20 + 1 = 51 roots)	1	1	2	2	3
		1	1	2	2	4
		1	1	2	2	5
		1	1	3	3	2
		1	1	3	3	4
		1	1	3	3	5
		1	1	4	4	2
		1	1	4	4	3
		1	1	4	4	5
		1	1	5	5	2
		1	1	5	5	3
		1	1	5	5	4
		2	2	3	3	1
		2	2	3	3	4
		2	2	3	3	5
		2	2	4	4	1
		2	2	4	4	3
		2	2	4	4	5
		2	2	5	5	1
		2	2	5	5	3
		2	2	5	5	4
		3	3	4	4	1
		3	3	4	4	2
		3	3	4	4	5
		3	3	5	5	1
		3	3	5	5	2
		3	3	5	5	4
		4	4	5	5	1
		4	4	5	5	2
		4	4	5	5	3

6.3 Electrostatic origin of the low-symmetry components of $Co(C(SiMe_2ONaph)_3)_2$

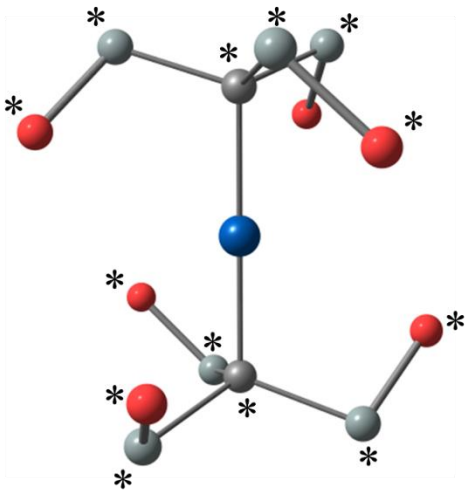

Figure 6.1. The truncated xyz structure of the coordinating alkyl ligand and closest second-sphere coordination shell. Asterisks indicate atoms where a point charge is placed. O = red, Si = turquoise, C = grey, and Co = blue.

To investigate potential crystal-field contributions to the low symmetry components of the ligand field, a crystal field is generated for the second coordination sphere, shown in Figure 6.1. A point charge with magnitude Q was placed at each of the silicon and oxygen atoms indicated with an asterisk (with Co–X lengths of 3.139 Å and 3.104 Å respectively). For the sake of reducing the number of parameters to a minimum, the same point charge magnitude is assigned to all six silicon, six oxygen, and two carbon atoms. A value of Q = 0.65 produces a V_{LFT} matrix in reasonable agreement with the *ab initio* predicted values:

$$v(CASSCF\ /\ NEVPT2) = \begin{pmatrix} 4.55 & -49.43 & 0.92 & 67.28 & -0.26 \\ -49.43 & 2902.00 & -0.23 & -0.32 & 63.13 \\ 0.92 & -0.23 & 5723.90 & -0.66 & 0.10 \\ 67.28 & -0.32 & -0.66 & 2902.98 & 49.54 \\ -0.26 & 63.13 & 0.10 & 49.54 & 2.27 \end{pmatrix}$$

$$v(Kestrel) = \begin{pmatrix} 2.24 & -56.34 & 0.01 & 64.11 & 0.00 \\ -56.34 & 3252.47 & 0.01 & -0.01 & 64.09 \\ 0.01 & 0.01 & 4936.26 & -0.01 & -0.03 \\ 64.11 & -0.01 & -0.01 & 3252.55 & 56.33 \\ 0.00 & 64.09 & -0.03 & 56.33 & 2.24 \end{pmatrix}$$

6.4 The 5×5 one-electron ligand-field matrix from a converged CASSCF(7, 5)/NEVPT2 calculation on $Co(C(SiMe_2ONaph)_3)_2$.

The 5×5 one-electron ligand-field matrix is computed as:

$$V = \begin{pmatrix} 4.55 & -49.43 & 0.92 & 67.28 & -0.26 \\ -49.43 & 2902.00 & -0.23 & -0.32 & 63.13 \\ 0.92 & -0.23 & 5723.90 & -0.66 & 0.10 \\ 67.28 & -0.32 & -0.66 & 2902.98 & 49.54 \\ -0.26 & 63.13 & 0.10 & 49.54 & 2.27 \end{pmatrix}$$

For two ligands linear to one another, with geometric angles θ = 0°, 180°, φ = 0°, 0°, and ψ = 0°, 0°, the *local* one-electron ligand-field matrices for ligands 1 and 2 are:

$$v(1) = \begin{pmatrix} 2.28 & -24.72 & 0.46 & 33.64 & -0.13 \\ -24.72 & 1451.00 & -0.12 & -0.16 & 31.57 \\ 0.46 & -0.12 & 2861.95 & -0.33 & 0.05 \\ 33.64 & -0.16 & -0.33 & 1451.49 & 24.77 \\ -0.13 & 31.57 & 0.05 & 24.77 & 1.14 \end{pmatrix}$$

$$v(2) = \begin{pmatrix} 2.28 & -24.72 & -0.46 & -33.64 & 0.13 \\ -24.72 & 1451.00 & 0.12 & 0.16 & -31.57 \\ -0.46 & 0.12 & 2861.95 & -0.33 & 0.05 \\ -33.64 & 0.16 & -0.33 & 1451.49 & 24.77 \\ 0.13 & -31.57 & 0.05 & 24.77 & 1.14 \end{pmatrix}.$$

Note that the difference between the potential matrices is given by the signs of the matrix elements connecting the orbitals d_{xy} and d_{yz} to d_{z^2}, d_{xz}, and $d_{x^2-y^2}$. This is a consequence of the different trigonal geometries of the two ligands in the same frame. Keeping the off-diagonal matrix elements fixed but correcting the magnitudes of the diagonal $\langle d_i | v | d_i \rangle \left(d_i = d_{yz}, d_{z^2}, d_{xz} \right)$ elements give the final parameterisation:

$$\Delta_{\pi} = \left\langle d_{xy} \left| v \right| d_{xy} \right\rangle - \left\langle d_{x^2-y^2} \left| v \right| d_{x^2-y^2} \right\rangle$$

$$\Delta_{\delta} = \left\langle d_{xz} \left| v \right| d_{xz} \right\rangle - \left\langle d_{yz} \left| v \right| d_{yz} \right\rangle$$

$$\left\langle d_{z^2} \left| v \right| d_{z^2} \right\rangle = e_{\sigma}$$

$$\left\langle d_{yz} \left| v \right| d_{yz} \right\rangle = e_{\pi} - \Delta_{\pi}/4$$

$$\left\langle d_{xz} \left| v \right| d_{xz} \right\rangle = e_{\pi} + \Delta_{\pi}/4$$

$$\left\langle d_{x^2-y^2} \left| v \right| d_{x^2-y^2} \right\rangle = -\Delta_{\delta}/4$$

$$\left\langle d_{xy} \left| v \right| d_{xy} \right\rangle = +\Delta_{\delta}/4$$

6.5 The S=1 BP86, ma-def2-tzvp(-f) geometry optimised coordinates of $[Fe(O)(TMC)(NCCH_3)]^{2+}$ in acetonitrile.

Table 6.5. The xyz cartesian coordinates of the DFT optimised structure of $[Fe(O)(TMC)(NCCH_3)]^{2+}$

Element	X	Y	Z
Fe	0.0000	0.0000	0.0000
O	0.0000	0.0000	1.6518
N	2.0927	0.0000	0.1114
N	0.1911	2.1130	-0.0528
N	-2.1220	0.0728	-0.0436
N	-0.2583	-2.0736	0.1163
C	2.3731	1.2881	0.8220
H	3.4584	1.4757	0.8281
H	2.0292	1.1659	1.8548
C	1.6546	2.4188	0.1397
H	2.0845	2.6026	-0.8510
H	1.7584	3.3475	0.7187
C	-0.5902	2.6451	1.1147
H	-0.4303	3.7360	1.1383
H	-0.1503	2.2089	2.0183
C	-2.0911	2.3704	1.0639
H	-2.5199	2.8612	1.9508
H	-2.5468	2.8841	0.2066
C	-2.5512	0.9158	1.1234
H	-2.1726	0.4321	2.0301
H	-3.6535	0.8965	1.1475
C	-2.6053	-1.3421	0.1407
H	-3.5437	-1.3361	0.7129
H	-2.8342	-1.7410	-0.8538
C	-1.5738	-2.1981	0.8224
H	-1.8930	-3.2522	0.8217

Element	X	Y	Z
H	-1.4145	-1.8792	1.8576
C	0.7608	-2.7556	0.9738
H	0.5391	-3.8341	0.9402
H	0.5994	-2.4027	1.9999
C	2.2023	-2.4933	0.5774
H	2.3847	-2.7124	-0.4843
H	2.8271	-3.2018	1.1392
C	2.6551	-1.0966	0.9609
H	2.3473	-0.8902	1.9933
H	3.7529	-1.0152	0.9064
C	2.7928	-0.0184	-1.2024
H	3.8751	0.0829	-1.0308
H	2.4532	0.8050	-1.8353
H	2.5973	-0.9628	-1.7189
C	-0.2070	2.8544	-1.2841
H	0.0085	3.9233	-1.1353
H	-1.2688	2.7419	-1.5000
H	0.3715	2.4889	-2.1363
C	-2.8109	0.5702	-1.2681
H	-3.8972	0.4662	-1.1264
H	-2.5021	-0.0213	-2.1331
H	-2.5895	1.6209	-1.4493
C	-0.3172	-2.7751	-1.1963
H	-0.5260	-3.8414	-1.0230
H	0.6408	-2.6733	-1.7133
H	-1.1053	-2.3531	-1.8239
N	0.0232	-0.0333	-2.0003
C	0.0497	-0.0829	-3.1574
C	0.0832	-0.1469	-4.5953
H	-0.9365	-0.0420	-4.9909
H	0.5002	-1.1151	-4.9061
H	0.7135	0.6650	-4.9841

6.6 Calculation of the ligand-field traces for V(IV)-oxo systems

The ligand-field parameters (e_λ) of three V(IV)-oxo systems are reported by *Stappen et al*.[188] The complexes **1** ($VO(acac)_2$), **2** ($VO(acac)_2$nPrCN), and **3** ($VO(acac)_2$Py) are presented in Figure 6.2. The ligand-field traces were calculated using the following relationships:

$$\sum(\mathbf{1}) = e_\sigma(O) + 2e_\pi(O) + 4e_\sigma(acac) + 4\Delta e_{\pi s}(acac)$$
$$= 26730 + 2\times 11690 + 4\times 6000 + 4\times 740 = 77070\ \text{cm}^{-1}$$
$$\sum(\mathbf{2}) = 2e_\sigma(O,N) + 4e_\pi(O,N) + 4e_\sigma(acac) + 4\Delta e_{\pi s}(acac)$$
$$= 2\times 15740 + 4\times 4870 + 4\times 6210 + 4\times 1120 = 80280\ \text{cm}^{-1}$$
$$\sum(\mathbf{3}) = 2e_\sigma(O,N) + 2e_\pi(O) + 4e_\sigma(acac) + 4\Delta e_{\pi s}(acac) + e_{\pi s}(N)$$
$$= 2\times 15720 + 2\times 8830 + 4\times 6200 + 4\times 1410 + 460 = 80460\ \text{cm}^{-1}$$

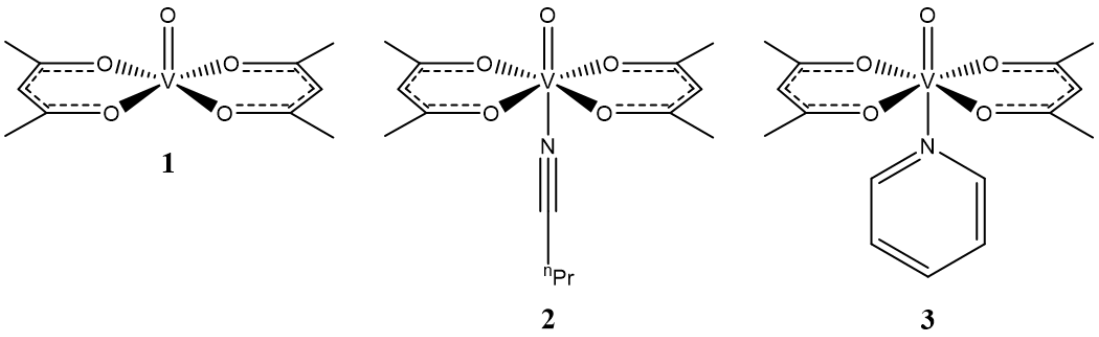

Figure 6.2. The V(IV)-oxo systems (1-3) analysed using a ligand-field model by *Stappen et al*.[188]

7 List of abbreviations

AILFT	*Ab Initio* Ligand-Field Theory
AOM	Angular Overlap Model
BDE	Bond Dissociation Energy
CASSCF	Complete Active Space Self-Consistent Field
CD	Circular Dichroism
dc	Direct Current
DFT	Density-Functional Theory
EPR	Electron Paramagnetic Resonance
FWHM	Full-Width Half Maximum
GUI	Graphical User Interface
KD	Kramer's Doublet
LFT	Ligand Field Theory
LMCT	Ligand to Metal Charge Transfer
LPMO	Lytic Polysaccharide Monooxygenase
MCD	Magnetic Circular Dichroism
NEVPT2	N-Electron Valence Perturbation Theory
QTM	Quantum Tunnelling of the Magnetisation
RMS	Root Mean Square
SCF	Self-Consistent Field
SiMM	Single-ion Molecular Magnet
SOMO	Singly Occupied Molecular Orbital
TD-DFT	Time-Dependent Density-Functional Theory
VH-MCD	Variable Field Magnetic Circular Dichroism
VT-MCD	Variable Temperature Magnetic Circular Dichroism
UV-Vis	Ultraviolet-visible
ZFS	Zero-Field Splitting

8 References

1 F. Neese, M. Atanasov, G. Bistoni, D. Maganas and S. Ye, *J. Am. Chem. Soc.*, 2019, **141**, 2814–2824.

2 B. Kirchner, F. Wennmohs, S. Ye and F. Neese, *Curr. Opin. Chem. Biol.*, 2007, **11**, 134–141.

3 M. Atanasov, D. Aravena, E. Suturina, E. Bill, D. Maganas and F. Neese, *Coord. Chem. Rev.*, 2015, **289**–**290**, 177–214.

4 V. A. Larson, B. Battistella, K. Ray, N. Lehnert and W. Nam, *Nat. Rev. Chem.*, 2020, **4**, 404–419.

5 A.-M. Ariciu, D. H. Woen, D. N. Huh, L. E. Nodaraki, A. K. Kostopoulos, C. A. P. Goodwin, N. F. Chilton, E. J. L. McInnes, R. E. P. Winpenny, W. J. Evans and F. Tuna, *Nat. Commun.*, 2019, **10**, 3330.

6 F. Neese, *Magn. Reson. Chem.*, 2004, **42**, S187–S198.

7 B. Pritchard and J. Autschbach, *Inorg. Chem.*, 2012, **51**, 8340–8351.

8 F. Neese, *JBIC J. Biol. Inorg. Chem.*, 2006, **11**, 702–711.

9 K. R. Bryenton, A. A. Adeleke, S. G. Dale and E. R. Johnson, *WIREs Comput. Mol. Sci.*, 2023, **13**, e1631.

10 S. K. Singh, J. Eng, M. Atanasov and F. Neese, *Coord. Chem. Rev.*, 2017, **344**, 2–25.

11 F. Neese, T. Petrenko, D. Ganyushin and G. Olbrich, *Coord. Chem. Rev.*, 2007, **251**, 288–327.

12 R. Finkelstein and J. H. Van Vleck, *J. Chem. Phys.*, 1940, **8**, 790–797.

13 M. Gerloch, J. H. Harding and R. G. Woolley, in *Structure and Bonding*, Springer, Berlin, 1981, pp. 1–46.

14 H. Bethe, *Ann. Phys.*, 1929, **395**, 133–208.

15 J. H. Van Vleck, *Phys. Rev.*, 1932, **41**, 208–215.

16 R. Schlapp and W. G. Penney, *Phys. Rev.*, 1932, **42**, 666–686.

17 J. H. Van Vleck, *J. Chem. Phys.*, 1935, **3**, 807–813.

18 J. S. Griffith and L. E. Orgel, *Q. Rev. Chem. Soc.*, 1957, **11**, 381–393.

19 C. J. Ballhausen, *Int. J. Quantum Chem.*, 1971, **5**, 373–377.

20 R. J. Deeth, *Eur. J. Inorg. Chem.*, 2022, **2022**, e202100936.

21 C. J. Ballhausen, *J. Chem. Educ.*, 1979, **56**, 357.

22 E. Larsen and G. N. La Mar, *J. Chem. Educ.*, 1974, **51**, 633.

23 A. D. Liehr, *J. Chem. Educ.*, 1962, **39**, 135.

24 M. Gerloch and R. G. Woolley, *J. Chem. Soc. Dalt. Trans.*, 1981, 1714.

25 C.-S. Cao, H.-S. Hu, J. Li and W. H. E. Schwarz, *Pure Appl. Chem.*, 2019, **91**, 1969–1999.

26 M. Kaupp, *J. Comput. Chem.*, 2007, **28**, 320–325.

27 J. K. McCusker, *Science*, 2019, **363**, 484–488.

28 R. G. Woolley, *Mol. Phys.*, 1981, **42**, 703–720.

29 A. J. Bridgeman and M. Gerloch, in *Progress in Inorganic Chemistry*, ed. K. D. Karlin, Wiley, New York, 1996, pp. 179–281.

30 M. Wolfsberg and L. Helmholz, *J. Chem. Phys.*, 1952, **20**, 837–843.

31 M. Atanasov, D. Ganyushin, K. Sivalingam and F. Neese, in *Molecular electronic structures of transition metal complexes II*, eds. D. M. P. Mingos, P. Day and J. P. Dahl, Springer, Berlin, 2011, vol. 143, pp. 149–220.

32 L. Lang, M. Atanasov and F. Neese, *J. Phys. Chem. A*, 2020, **124**, 1025–1037.

33 M. Gerloch and R. F. McMeeking, *J. Chem. Soc. Dalt. Trans.*, 1975, 2443.

34 M. Gerloch, *Magnetism and ligand-field analysis*, Cambridge University Press, Cambridge, 1st edn., 1983.

35 A. Bronova, T. Bredow, R. Glaum, M. J. Riley and W. Urland, *J. Comput. Chem.*, 2018, **39**, 176–186.

36 H. Adamsky, T. Schönherr and M. Atanasov, in *Comprehensive Coordination Chemistry II*, eds. C. Edwin, J. A. McCleverty and T. J. Meyer, Elsevier, 2003, pp. 661–664.

37 J. Bendix, in *Comprehensive Coordination Chemistry II*, eds. C. Edwin, J. A. McCleverty and T. J. Meyer, 2003, pp. 672–669.

38 J. Krzystek, G. J. Yeagle, J.-H. Park, R. D. Britt, M. W. Meisel, L.-C. Brunel and J. Telser, *Inorg. Chem.*, 2003, **42**, 4610–4618.

39 B. R. McGarvey and J. Telser, *Inorg. Chem.*, 2012, **51**, 6000–6010.

40 J. Telser, *J. Braz. Chem. Soc.*, 2006, **17**, 1501–1515.

41 F. Neese, *WIREs Comput. Mol. Sci.*, 2022, **12**, e1606.

42 F. Neese, *WIREs Comput. Mol. Sci.*, 2012, **2**, 73–78.

43 F. Neese, L. Lang and V. G. Chilkuri, in *Topology, Entanglement, and Strong Correlations. Modeling and Simulation*, eds. E. Pavarini and E. Koch, Forschungszentrum Jülich, Jülich, 2020, p. 34.

44 P.-O. Löwdin, *J. Mol. Spectrosc.*, 1963, **10**, 12–33.

45 P. O. Löwdin, in *Perturbation Theory and its Application in Quantum Mechanics*, ed. C. H. Wilcox, Wiley, New York, 1966, pp. 255–294.

46 B. L. Silver, *Irreducible tensor methods: an introduction for chemists*, Academic Press, New York, 1976.

47 H. N. Russell and F. A. Saunders, *Astrophys. J.*, 1925, **61**, 38.

48 G. Racah, *Phys. Rev.*, 1942, **62**, 438–462.

49 E. P. Wigner, in *The Collected Works of Eugene Paul Wigner*, Springer, Berlin, 1993, pp. 608–654.

50 E. Wigner, *Group theory and its application to the quantum mechanics of atomic spectra*, Academic Press, New York, 1959.

51 C. E. Schäffer, in *Structure and Bonding*, Springer, Berlin, 1968, vol. 5, pp. 68–95.

52 E. Wigner, *Zeitschrift für Phys.*, 1927, **43**, 624–652.

53 C. Eckart, *Rev. Mod. Phys.*, 1930, **2**, 305.

54 J. Hunt, *Stud. Hist. Philos. Sci. Part A*, 2021, **87**, 28–43.

55 C. W. Neilson and G. F. Koster, *Spectroscopic Coefficients for pn, dn and fn Configurations*, MIT Press, Cambridge, Massachusetts, 1963.

56 E. U. Condon and G. H. Shortley, *The theory of atomic spectra*, Cambridge University Press, Cambridge, 1951.

57 C. E. Schäffer, *Pure Appl. Chem.*, 1970, **24**, 361–392.

58 R. J. Deeth, M. J. Duer and M. Gerloch, *Inorg. Chem.*, 1987, **26**, 2573–2578.

59 A. Rockenbauer, É. Budó-Záhonyi and L. I. Simándi, *J. Chem. Soc. Dalt. Trans.*, 1975, 1729–1737.

60 B. R. McGarvey, *Can. J. Chem.*, 1975, **53**, 2498–2511.

61 M. A. Hitchman and P. J. Cassidy, *Inorg. Chem.*, 1979, **18**, 1745–1754.

62 R. J. Deeth and M. Gerloch, *Inorg. Chem.*, 1984, **23**, 3846–3853.

63 R. J. Deeth, *Dalt. Trans.*, 2020, **49**, 9641–9650.

64 M. J. Riley, *Inorganica Chim. Acta*, 1998, **268**, 55–62.

65 M. T. Ashby, *Comments Inorg. Chem.*, 1990, **10**, 297–313.

66 M. Buchhorn and V. Krewald, *Dalt. Trans.*, 2023, **52**, 6685–6692.

67 M. A. Atanasov, T. Schönherr and H.-H. Schmidtke, *Theor. Chim. Acta*, 1987, **71**, 59–73.

68 R. J. Deeth, M. J. Duer and M. Gerloch, *Inorg. Chem.*, 1987, **26**, 2578–2582.

69 R. J. Deeth and M. Gerloch, *Inorg. Chem.*, 1987, **26**, 2582–2585.

70 N. D. Fenton and M. Gerloch, *Inorg. Chem.*, 1987, **26**, 3273–3277.

71 M. J. Duer and M. Gerloch, *Inorg. Chem.*, 1989, **28**, 4260–4264.

72 P. E. Hoggard, in *Optical Spectra and Chemical Bonding in Inorganic Compounds. Structure and Bonding*, eds. D. M. P. Mingos and T. Schönherr, Springer, Berlin, 2004, pp. 37–57.

73 L. E. Orgel, *J. Chem. Soc.*, 1961, 3683–3686.

74 M. A. Atanasov and M. A. Hitchman, *Inorg. Chem.*, 1993, **32**, 3973–3975.

75 M. A. Hitchman, *Inorg. Chem.*, 1977, **16**, 1985–1993.

76 H. R. C. Jaw, T. H. Chang and J. I. Zink, *Inorg. Chem.*, 1987, **26**, 4204–4208.

77 M. S. Fataftah, S. L. Bayliss, D. W. Laorenza, X. Wang, B. T. Phelan, C. B. Wilson, P. J. Mintun, B. D. Kovos, M. R. Wasielewski, S. Han, M. S. Sherwin, D. D. Awschalom and D. E. Freedman, *J. Am. Chem. Soc.*, 2020, **142**, 20400–20408.

78 A. Bencini, C. Benelli and D. Gatteschi, *Coord. Chem. Rev.*, 1984, **60**, 131–169.

79 J. A. Schellman, *Chem. Rev.*, 1975, **75**, 323–331.

80 B. M. Walsh, in *Advances in Spectroscopy for Lasers and Sensing*, Springer Netherlands, Dordrecht, 2006, pp. 403–433.

81 C. A. Brown, M. J. Duer, M. Gerloch and R. F. McMeeking, *Mol. Phys.*, 1988, **64**, 825–841.

82 M. J. Duer, S. J. Essex, M. Gerloch and K. M. Jupp, *Mol. Phys.*, 1993, **79**, 1147–1165.

83 B. S. Gerstman and A. S. Brill, *J. Chem. Phys.*, 1985, **82**, 1212–1230.

84 G. A. Landrum, C. A. Ekberg and J. W. Whittaker, *Biophys. J.*, 1995, **69**, 674–689.

85 S. B. Piepho and P. N. Schatz, *Group theory in spectroscopy: with applications to magnetic circular dichroism*, Wiley, New York, 1983.

86 I. Warnke and F. Furche, *WIREs Comput. Mol. Sci.*, 2012, **2**, 150–166.

87 A. D. Buckingham and P. J. Stephens, *Annu. Rev. Phys. Chem.*, 1966, **17**, 399–432.

88 P. N. Schatz and A. J. McCaffery, *Q. Rev. Chem. Soc.*, 1969, **23**, 552.

89 D. Ganyushin and F. Neese, *J. Chem. Phys.*, 2008, **128**, 114117.

90 W. R. Mason, *A Practical Guide to Magnetic Circular Dichroism Spectroscopy*, Wiley, 2007.

91 F. Neese and E. I. Solomon, *Inorg. Chem.*, 1999, **38**, 1847–1865.

92 G. Van Rossum and F. L. Drake, *Python 3 Reference Manual*, CreateSpace, Scotts Valley, CA, 2009.

93 C. R. Harris, K. J. Millman, S. J. van der Walt, R. Gommers, P. Virtanen, D. Cournapeau, E. Wieser, J. Taylor, S. Berg, N. J. Smith, R. Kern, M. Picus, S. Hoyer, M. H. van Kerkwijk, M. Brett, A. Haldane, J. F. del Río, M. Wiebe, P. Peterson, P. Gérard-Marchant, K. Sheppard, T. Reddy, W. Weckesser, H. Abbasi, C. Gohlke and T. E. Oliphant, *Nature*, 2020, **585**, 357–362.

94 J. M. Ortega, *An introduction to Fortran 90 for scientific computing*, Saunders College Pub., Fort Worth, 1994.

95 PyQt5 PyPI, https://pypi.org/project/PyQt5, (accessed 13 August 2020).

96 P. Virtanen, R. Gommers, T. E. Oliphant, M. Haberland, T. Reddy, D. Cournapeau, E. Burovski, P. Peterson, W. Weckesser, J. Bright, S. J. van der Walt, M. Brett, J. Wilson, K. J. Millman, N. Mayorov, A. R. J. Nelson, E. Jones, R. Kern, E. Larson, C. J. Carey, İ. Polat, Y. Feng, E. W. Moore, J. VanderPlas, D. Laxalde, J. Perktold, R. Cimrman, I.

Henriksen, E. A. Quintero, C. R. Harris, A. M. Archibald, A. H. Ribeiro, F. Pedregosa, P. van Mulbregt, A. Vijaykumar, A. Pietro Bardelli, A. Rothberg, A. Hilboll, A. Kloeckner, A. Scopatz, A. Lee, A. Rokem, C. N. Woods, C. Fulton, C. Masson, C. Häggström, C. Fitzgerald, D. A. Nicholson, D. R. Hagen, D. V. Pasechnik, E. Olivetti, E. Martin, E. Wieser, F. Silva, F. Lenders, F. Wilhelm, G. Young, G. A. Price, G.-L. Ingold, G. E. Allen, G. R. Lee, H. Audren, I. Probst, J. P. Dietrich, J. Silterra, J. T. Webber, J. Slavič, J. Nothman, J. Buchner, J. Kulick, J. L. Schönberger, J. V. de Miranda Cardoso, J. Reimer, J. Harrington, J. L. C. Rodríguez, J. Nunez-Iglesias, J. Kuczynski, K. Tritz, M. Thoma, M. Newville, M. Kümmerer, M. Bolingbroke, M. Tartre, M. Pak, N. J. Smith, N. Nowaczyk, N. Shebanov, O. Pavlyk, P. A. Brodtkorb, P. Lee, R. T. McGibbon, R. Feldbauer, S. Lewis, S. Tygier, S. Sievert, S. Vigna, S. Peterson, S. More, T. Pudlik, T. Oshima, T. J. Pingel, T. P. Robitaille, T. Spura, T. R. Jones, T. Cera, T. Leslie, T. Zito, T. Krauss, U. Upadhyay, Y. O. Halchenko and Y. Vázquez-Baeza, *Nat. Methods*, 2020, **17**, 261–272.

97 E. Anderson, Z. Bai, C. Bischof, S. Blackford, J. Demmel, J. Dongarra, J. Du Croz, A. Greenbaum, S. Hammarling, A. McKenney and D. Sorensen, *LAPACK Users' Guide*, Society for Industrial and Applied Mathematics, Philadelphia, PA, Third., 1999.

98 pyinstaller PyPI, https://pypi.org/project/pyinstaller, (accessed 13 August 2020).

99 pyqtgraph, https://github.com/pyqtgraph/pyqtgraph, (accessed 30 January 2023).

100 J. D. Hunter, *Comput. Sci. Eng.*, 2007, **9**, 90–95.

101 G. A. Craig and M. Murrie, *Chem. Soc. Rev.*, 2015, **44**, 2135–2147.

102 A. Gaita-Ariño, F. Luis, S. Hill and E. Coronado, *Nat. Chem.*, 2019, **11**, 301–309.

103 G. Aromí, D. Aguilà, P. Gamez, F. Luis and O. Roubeau, *Chem. Soc. Rev.*, 2012, **41**, 537–546.

104 S. G. McAdams, A.-M. Ariciu, A. K. Kostopoulos, J. P. S. Walsh and F. Tuna, *Coord. Chem. Rev.*, 2017, **346**, 216–239.

105 Y.-Z. Zheng, G.-J. Zhou, Z. Zheng and R. E. P. Winpenny, *Chem. Soc. Rev.*, 2014, **43**, 1462–1475.

106 W.-M. Wang, T.-L. Han, Y.-L. Shao, X.-Y. Qiao, Z.-L. Wu, Q.-L. Wang, P. F. Shi, H.-L. Gao and J.-Z. Cui, *New J. Chem.*, 2018, **42**, 14949–14955.

107 L. Bogani and W. Wernsdorfer, *Nat. Mater.*, 2008, **7**, 179–186.

108 J. M. Frost, K. L. M. Harriman and M. Murugesu, *Chem. Sci.*, 2016, **7**, 2470–2491.

109 M. Affronte, *J. Mater. Chem.*, 2009, **19**, 1731–1737.

110 C. A. P. Goodwin, F. Ortu, D. Reta, N. F. Chilton and D. P. Mills, *Nature*, 2017, **548**, 439–442.

111 F. Luis and M. Evangelisti, in *Molecular Nanomagnets and Related Phenomena. Structure and Bonding*, ed. S. Gao, Springer, Berlin, 2014, pp. 431–460.

112 J. H. Van Vleck, *Phys. Rev.*, 1940, **57**, 426–447.

113 R. Orbach, *Proc. R. Soc. London. Ser. A. Math. Phys. Sci.*, 1961, **264**, 485–495.

114 R. Orbach, *Proc. R. Soc. London. Ser. A. Math. Phys. Sci.*, 1961, **264**, 458–484.

115 C. B. P. Finn, R. Orbach and W. P. Wolf, *Proc. Phys. Soc.*, 1961, **77**, 261–268.

116 D. Aravena, *J. Phys. Chem. Lett.*, 2018, **9**, 5327–5333.

117 M. L. Baker, S. J. Blundell, N. Domingo and S. Hill, in *Molecular Nanomagnets and Related Phenomena. Structure and Bonding*, ed. S. Gao, Springer, Berlin, 2014, pp. 231–291.

118 A. Sarkar, S. Dey and G. Rajaraman, *Chem. – A Eur. J.*, 2020, **26**, 14036–14058.

119 B. Yin and C.-C. Li, *Phys. Chem. Chem. Phys.*, 2020, **22**, 9923–9933.

120 F. Lu, W.-X. Guo and Y.-Q. Zhang, *Inorg. Chem.*, 2022, **61**, 295–301.

121 J. Zhang, J. Li, L. Yang, C. Yuan, Y.-Q. Zhang and Y. Song, *Inorg. Chem.*, 2018, **57**, 3903–3912.

122 P. C. Bunting, M. Atanasov, E. Damgaard-Møller, M. Perfetti, I. Crassee, M. Orlita, J. Overgaard, J. van Slageren, F. Neese and J. R. Long, *Science*, 2018, **362**, eaat7319.

123 A. A. Pavlov, J. Nehrkorn, Y. A. Pankratova, M. Ozerov, E. A. Mikhalyova, A. V. Polezhaev, Y. V. Nelyubina and V. V. Novikov, *Phys. Chem. Chem. Phys.*, 2019, **21**, 8201–8204.

124 Y. Rechkemmer, F. D. Breitgoff, M. Van Der Meer, M. Atanasov, M. Hakl, M. Orlita, P. Neugebauer, F. Neese, B. Sarkar and J. Van Slageren, *Nat. Commun.*, 2016, **7**, 1–8.

125 B. Figgis, *Introduction to ligand fields*, Interscience Publishers, New York, 1966.

126 J. P. Jesson, *J. Chem. Phys.*, 1966, **45**, 1049–1056.

127 J. P. Jesson, S. Trofimenko and D. R. Eaton, *J. Am. Chem. Soc.*, 1967, **89**, 3148–3158.

128 A. R. Marts, J. C. Kaine, R. R. Baum, V. L. Clayton, J. R. Bennett, L. J. Cordonnier, R.

McCarrick, A. Hasheminasab, L. A. Crandall, C. J. Ziegler and D. L. Tierney, *Inorg. Chem.*, 2017, **56**, 618–626.

129 F. Weigend and R. Ahlrichs, *Phys. Chem. Chem. Phys.*, 2005, **7**, 3297–3305.

130 A. Hellweg, C. Hättig, S. Höfener and W. Klopper, *Theor. Chem. Acc.*, 2007, **117**, 587–597.

131 R. Khurana and M. E. Ali, *Inorg. Chem.*, 2022, **61**, 15335–15345.

132 W. J. M. Blackaby, K. L. M. Harriman, S. M. Greer, A. Folli, S. Hill, V. Krewald, M. F. Mahon, D. M. Murphy, M. Murugesu, E. Richards, E. Suturina and M. K. Whittlesey, *Inorg. Chem.*, 2022, **61**, 1308–1315.

133 C. G. Werncke, E. Suturina, P. C. Bunting, L. Vendier, J. R. Long, M. Atanasov, F. Neese, S. Sabo-Etienne and S. Bontemps, *Chem. - A Eur. J.*, 2016, **22**, 1668–1674.

134 J. M. Zadrozny, D. J. Xiao, M. Atanasov, G. J. Long, F. Grandjean, F. Neese and J. R. Long, *Nat. Chem.*, 2013, **5**, 577–581.

135 M. Atanasov, J. M. Zadrozny, J. R. Long and F. Neese, *Chem. Sci.*, 2013, **4**, 139–156.

136 R. J. Deeth, *Eur. J. Inorg. Chem.*, 2020, **2020**, 1960–1963.

137 Y. Tanabe and S. Sugano, *J. Phys. Soc. Japan*, 1954, **9**, 766–779.

138 C. J. Ballhausen, *Introduction to ligand field theory*, McGraw-Hill, New York, 1962.

139 A. A. Pavlov, D. Y. Aleshin, S. A. Savkina, A. S. Belov, N. N. Efimov, J. Nehrkorn, M. Ozerov, Y. Z. Voloshin, Y. V. Nelyubina and V. V. Novikov, *ChemPhysChem*, 2019, **20**, 1001–1005.

140 V. V. Novikov, A. A. Pavlov, Y. V. Nelyubina, M.-E. Boulon, O. A. Varzatskii, Y. Z. Voloshin and R. E. P. Winpenny, *J. Am. Chem. Soc.*, 2015, **137**, 9792–9795.

141 Y. Peng, T. Bodenstein, K. Fink, V. Mereacre, C. E. Anson and A. K. Powell, *Phys. Chem. Chem. Phys.*, 2016, **18**, 30135–30143.

142 A. A. Pavlov, Y. V. Nelyubina, S. V. Kats, L. V. Penkova, N. N. Efimov, A. O. Dmitrienko, A. V. Vologzhanina, A. S. Belov, Y. Z. Voloshin and V. V. Novikov, *J. Phys. Chem. Lett.*, 2016, **7**, 4111–4116.

143 P. Kumar Sahu, R. Kharel, S. Shome, S. Goswami and S. Konar, *Coord. Chem. Rev.*, 2023, **475**, 214871.

144 C. M. Legendre, E. Damgaard-Møller, J. Overgaard and D. Stalke, *Eur. J. Inorg. Chem.*,

2021, **2021**, 3108–3114.

145 E. A. Suturina, J. Nehrkorn, J. M. Zadrozny, J. Liu, M. Atanasov, T. Weyhermüller, D. Maganas, S. Hill, A. Schnegg, E. Bill, J. R. Long and F. Neese, *Inorg. Chem.*, 2017, **56**, 3102–3118.

146 E. A. Suturina, D. Maganas, E. Bill, M. Atanasov and F. Neese, *Inorg. Chem.*, 2015, **54**, 9948–9961.

147 C. Krebs, D. Galonić Fujimori, C. T. Walsh and J. M. Bollinger, *Acc. Chem. Res.*, 2007, **40**, 484–492.

148 W. Nam, *Acc. Chem. Res.*, 2007, **40**, 522–531.

149 X. Shan and L. Que, *J. Inorg. Biochem.*, 2006, **100**, 421–433.

150 L. J. Que, *Acc. Chem. Res.*, 2007, **40**, 493–500.

151 J.-U. Rohde, J.-H. In, M. H. Lim, W. W. Brennessel, M. R. Bukowski, A. Stubna, E. Münck, W. Nam and L. Que, *Science*, 2003, **299**, 1037–1039.

152 C. A. Grapperhaus, B. Mienert, E. Bill, T. Weyhermüller and K. Wieghardt, *Inorg. Chem.*, 2000, **39**, 5306–5317.

153 S. Meyer, I. Klawitter, S. Demeshko, E. Bill and F. Meyer, *Angew. Chemie Int. Ed.*, 2013, **52**, 901–905.

154 J. England, M. Martinho, E. R. Farquhar, J. R. Frisch, E. L. Bominaar, E. Münck and L. Que Jr., *Angew. Chemie Int. Ed.*, 2009, **48**, 3622–3626.

155 D. C. Lacy, R. Gupta, K. L. Stone, J. Greaves, J. W. Ziller, M. P. Hendrich and A. S. Borovik, *J. Am. Chem. Soc.*, 2010, **132**, 12188–12190.

156 J. P. Bigi, W. H. Harman, B. Lassalle-Kaiser, D. M. Robles, T. A. Stich, J. Yano, R. D. Britt and C. J. Chang, *J. Am. Chem. Soc.*, 2012, **134**, 1536–1542.

157 D. Janardanan, Y. Wang, P. Schyman, L. Que and S. Shaik, *Angew. Chemie*, 2010, **122**, 3414–3417.

158 D. Mandal, D. Mallick and S. Shaik, *Acc. Chem. Res.*, 2018, **51**, 107–117.

159 S. Ye and F. Neese, *Curr. Opin. Chem. Biol.*, 2009, **13**, 89–98.

160 H. Hirao, D. Kumar, L. Que and S. Shaik, *J. Am. Chem. Soc.*, 2006, **128**, 8590–8606.

161 B. Mondal, L. Roy, F. Neese and S. Ye, *Isr. J. Chem.*, 2016, **56**, 763–772.

162 A. R. McDonald and L. Que, *Coord. Chem. Rev.*, 2013, **257**, 414–428.

163 T. K. Roy, A. Suresh, A. Sinha, J. P. Biswas and D. Maiti, 2023, pp. 185–204.

164 A. Anilkumar, P. Ash, A. R. Chakravarty, P. Comba, S. DeBeer, A. Dey, A. Draksharapu, D. Goswami, S. Itoh, K. Karlin, K. V. Lakshmi, S. Mazumdar, D. Pantazis, D. Parker, L. Que, G. Rajaraman, S. P. Rath, C. Sastri, S. Sen Gupta and E. I. Solomon, *Faraday Discuss.*, 2022, **234**, 245–263.

165 A. Decker, J.-U. Rohde, L. Que, and E. I. Solomon, *J. Am. Chem. Soc.*, 2004, **126**, 5378–5379.

166 S. Ye, C. Kupper, S. Meyer, E. Andris, R. Navrátil, O. Krahe, B. Mondal, M. Atanasov, E. Bill, J. Roithová, F. Meyer and F. Neese, *J. Am. Chem. Soc.*, 2016, **138**, 14312–14325.

167 R. Boča, *Coord. Chem. Rev.*, 2004, **248**, 757–815.

168 E. I. Solomon, S. D. Wong, L. V Liu, A. Decker and M. S. Chow, *Curr. Opin. Chem. Biol.*, 2009, **13**, 99–113.

169 A. Decker, J.-U. Rohde, E. J. Klinker, S. D. Wong, L. Que, and E. I. Solomon, *J. Am. Chem. Soc.*, 2007, **129**, 15983–15996.

170 F. Neese, *J. Inorg. Biochem.*, 2006, **100**, 716–726.

171 J. C. Schöneboom, F. Neese and W. Thiel, *J. Am. Chem. Soc.*, 2005, **127**, 5840–5853.

172 C. A. Grapperhaus, E. Bill, T. Weyhermüller, F. Neese and K. Wieghardt, *Inorg. Chem.*, 2001, **40**, 4191–4198.

173 M. Atanasov, P. Comba, C. A. Daul and F. Neese, *Model. Myster. Magic Mol.*, 2008, 411–445.

174 S. Ye, G. Xue, I. Krivokapic, T. Petrenko, E. Bill, L. Que Jr and F. Neese, *Chem. Sci.*, 2015, **6**, 2909–2921.

175 L. Bucinsky, G. T. Rohde, L. Que, A. Ozarowski, J. Krzystek, M. Breza and J. Telser, *Inorg. Chem.*, 2016, **55**, 3933–3945.

176 P. Comba, G. Nunn, F. Scherz and P. H. Walton, *Faraday Discuss.*, 2021, **234**, 232–244.

177 P. Comba, D. Faltermeier, S. Krieg, B. Martin and G. Rajaraman, *Dalt. Trans.*, 2020, **49**, 2888–2894.

178 J. Zheng, X. Xu and D. G. Truhlar, *Theor. Chem. Acc.*, 2011, **128**, 295–305.

179 A. D. Becke, *Phys. Rev. A*, 1988, **38**, 3098–3100.

180 S. Grimme, J. Antony, S. Ehrlich and H. Krieg, *J. Chem. Phys.*, 2010, **132**, 154104.

181 S. Grimme, S. Ehrlich and L. Goerigk, *J. Comput. Chem.*, 2011, **32**, 1456–1465.

182 D. M. York and M. Karplus, *J. Phys. Chem. A*, 1999, **103**, 11060–11079.

183 F. Weigend, *Phys. Chem. Chem. Phys.*, 2006, **8**, 1057.

184 F. Neese, F. Wennmohs, A. Hansen and U. Becker, *Chem. Phys.*, 2009, **356**, 98–109.

185 L. Lang, M. Atanasov and F. Neese, *J. Phys. Chem*, 2020, **2020**, 1025–1037.

186 H.-H. Schmidtke, in *Optical Spectra and Chemical Bonding in Inorganic Compounds. Structure and Bonding*, eds. D. M. P. Mingos and T. Schönherr, 2004, vol. 106, pp. 19–35.

187 A. W. Hahn, B. E. Van Kuiken, M. Al Samarai, M. Atanasov, T. Weyhermüller, Y. T. Cui, J. Miyawaki, Y. Harada, A. Nicolaou and S. DeBeer, *Inorg. Chem.*, 2017, **56**, 8203–8211.

188 C. Van Stappen, D. Maganas, S. Debeer, E. Bill and F. Neese, *Inorg. Chem.*, 2018, **57**, 6421–6438.

189 S. J. Horn, G. Vaaje-Kolstad, B. Westereng and V. Eijsink, *Biotechnol. Biofuels*, 2012, **5**, 45.

190 G. Vaaje-Kolstad, B. Westereng, S. J. Horn, Z. Liu, H. Zhai, M. Sørlie and V. G. H. Eijsink, *Science*, 2010, **330**, 219–222.

191 B. Bissaro, Å. K. Røhr, G. Müller, P. Chylenski, M. Skaugen, Z. Forsberg, S. J. Horn, G. Vaaje-Kolstad and V. G. H. Eijsink, *Nat. Chem. Biol.*, 2017, **13**, 1123–1128.

192 J. Gao, D. A. Thomas, C. H. Sohn and J. L. Beauchamp, *J. Am. Chem. Soc.*, 2013, **135**, 10684–10692.

193 G. R. Hemsworth, E. M. Johnston, G. J. Davies and P. H. Walton, *Trends Biotechnol.*, 2015, **33**, 747–761.

194 B. S. Donohoe and M. G. Resch, *Curr. Opin. Chem. Biol.*, 2015, **29**, 100–107.

195 R. A. Sheldon, *J. Mol. Catal. A Chem.*, 2016, **422**, 3–12.

196 C. P. Kubicek and E. M. Kubicek, *Curr. Opin. Chem. Biol.*, 2016, **35**, 51–57.

197 J. Hu, R. Chandra, V. Arantes, K. Gourlay, J. Susan van Dyk and J. N. Saddler, *Bioresour. Technol.*, 2015, **186**, 149–153.

198 G. Müller, A. Várnai, K. S. Johansen, V. G. H. Eijsink and S. J. Horn, *Biotechnol. Biofuels*, 2015, **8**, 187.

199 S. Kim, J. Ståhlberg, M. Sandgren, R. S. Paton and G. T. Beckham, *Proc. Natl. Acad. Sci.*, 2014, **111**, 149–154.

200 B. Wang, P. H. Walton and C. Rovira, *ACS Catal.*, 2019, **9**, 4958–4969.

201 B. Bissaro, B. Streit, I. Isaksen, V. G. H. Eijsink, G. T. Beckham, J. L. DuBois and Å. K. Røhr, *Proc. Natl. Acad. Sci.*, 2020, **117**, 1504–1513.

202 F. Sabbadin, S. Urresti, B. Henrissat, A. O. Avrova, L. R. J. Welsh, P. J. Lindley, M. Csukai, J. N. Squires, P. H. Walton, G. J. Davies, N. C. Bruce, S. C. Whisson and S. J. McQueen-Mason, *Science*, 2021, **373**, 774–779.

203 A. Levasseur, E. Drula, V. Lombard, P. M. Coutinho and B. Henrissat, *Biotechnol. Biofuels*, 2013, **6**, 41.

204 Z. Forsberg, M. Sørlie, D. Petrović, G. Courtade, F. L. Aachmann, G. Vaaje-Kolstad, B. Bissaro, Å. K. Røhr and V. G. Eijsink, *Curr. Opin. Struct. Biol.*, 2019, **59**, 54–64.

205 R. L. Lieberman and A. C. Rosenzweig, *Nature*, 2005, **434**, 177–182.

206 R. Balasubramanian and A. C. Rosenzweig, *Acc. Chem. Res.*, 2007, **40**, 573–580.

207 M. O. Ross and A. C. Rosenzweig, *J. Biol. Inorg. Chem.*, 2017, **22**, 307–319.

208 R. J. Quinlan, M. D. Sweeney, L. Lo Leggio, H. Otten, J.-C. N. Poulsen, K. S. Johansen, K. B. R. M. Krogh, C. I. Jørgensen, M. Tovborg, A. Anthonsen, T. Tryfona, C. P. Walter, P. Dupree, F. Xu, G. J. Davies and P. H. Walton, *Proc. Natl. Acad. Sci.*, 2011, **108**, 15079–15084.

209 L. Ciano, G. J. Davies, W. B. Tolman and P. H. Walton, *Nat. Catal.*, 2018, **1**, 571–577.

210 K. E. H. H. Frandsen, T. J. Simmons, P. Dupree, J.-C. N. Poulsen, G. R. Hemsworth, L. Ciano, E. M. Johnston, M. Tovborg, K. S. Johansen, P. von Freiesleben, L. Marmuse, S. Fort, S. Cottaz, H. Driguez, B. Henrissat, N. Lenfant, F. Tuna, A. Baldansuren, G. J. Davies, L. Lo Leggio and P. H. Walton, *Nat. Chem. Biol.*, 2016, **12**, 298–303.

211 D. M. Petrović, B. Bissaro, P. Chylenski, M. Skaugen, M. Sørlie, M. S. Jensen, F. L. Aachmann, G. Courtade, A. Várnai and V. G. H. Eijsink, *Protein Sci.*, 2018, **27**, 1636–1650.

212 T. Tandrup, S. J. Muderspach, S. Banerjee, G. Santoni, J. Ø. Ipsen, C. Hernández-Rollán, M. H. H. Nørholm, K. S. Johansen, F. Meilleur and L. Lo Leggio, *IUCrJ*, 2022, **9**, 666–681.

213 P. H. Walton and G. J. Davies, *Curr. Opin. Chem. Biol.*, 2016, **31**, 195–207.

214 C. M. Phillips, W. T. Beeson, J. H. Cate and M. A. Marletta, *ACS Chem. Biol.*, 2011, **6**, 1399–1406.

215 X. Li, W. T. Beeson, C. M. Phillips, M. A. Marletta and J. H. D. Cate, *Structure*, 2012, **20**, 1051–1061.

216 W. T. Beeson, V. V. Vu, E. A. Span, C. M. Phillips and M. A. Marletta, *Annu. Rev. Biochem.*, 2015, **84**, 923–946.

217 B. Wang, Z. Wang, G. J. Davies, P. H. Walton and C. Rovira, *ACS Catal.*, 2020, **10**, 12760–12769.

218 B. Wang, E. M. Johnston, P. Li, S. Shaik, G. J. Davies, P. H. Walton and C. Rovira, *ACS Catal.*, 2018, **8**, 1346–1351.

219 H. Hansson, S. Karkehabadi, N. Mikkelsen, N. R. Douglas, S. Kim, A. Lam, T. Kaper, B. Kelemen, K. K. Meier, S. M. Jones, E. I. Solomon and M. Sandgren, *J. Biol. Chem.*, 2017, **292**, 19099–19109.

220 A. Paradisi, PhD thesis, University of York, 2020.

221 L. Ciano, A. Paradisi, G. R. Hemsworth, M. Tovborg, G. J. Davies and P. H. Walton, *Dalt. Trans.*, 2020, **49**, 3413–3422.

222 T. Astley, A. J. Canty, M. A. Hitchman, G. L. Rowbottom, B. W. Skelton and A. H. White, *J. Chem. Soc. Dalt. Trans.*, 1991, 1981–1990.

223 A. Dick, H. Rahemi, E. R. Krausz, G. R. Hanson and M. J. Riley, *J. Chem. Phys.*, 2008, **129**, 214505.

224 R. K. Szilagyi, M. Metz and E. I. Solomon, *J. Phys. Chem. A*, 2002, **106**, 2994–3007.

225 L. V. Stepakova, M. Y. Skripkin, L. V. Chernykh, G. L. Starova, L. Hajba, J. Mink and M. Sandström, *J. Raman Spectrosc.*, 2008, **39**, 16–31.

226 F.-Y. Lin and A. D. MacKerell, *J. Phys. Chem. B*, 2017, **121**, 6813–6821.

227 A. J. Bridgeman, S. J. Essex and M. Gerloch, *Inorg. Chem.*, 1994, **33**, 5411–5423.

228 P. Comba, T. W. Hambley, M. A. Hitchman and H. Stratemeier, *Inorg. Chem.*, 1995,

34, 3903–3911.

229 J. C. Rivoal and B. Briat, *Mol. Phys.*, 1974, **27**, 1081–1108.

230 P. H. Walton and L. Ciano, unpublished work.

231 A. Paradisi, E. M. Johnston, M. Tovborg, C. R. Nicoll, L. Ciano, A. Dowle, J. McMaster, Y. Hancock, G. J. Davies and P. H. Walton, *J. Am. Chem. Soc.*, 2019, **141**, 18585–18599.

232 S. M. Huber, M. Z. Ertem, F. Aquilante, L. Gagliardi, W. B. Tolman and C. J. Cramer, *Chem. - A Eur. J.*, 2009, **15**, 4886–4895.

233 P. J. Donoghue, J. Tehranchi, C. J. Cramer, R. Sarangi, E. I. Solomon and W. B. Tolman, *J. Am. Chem. Soc.*, 2011, **133**, 17602–17605.

234 D. Dhar, G. M. Yee, A. D. Spaeth, D. W. Boyce, H. Zhang, B. Dereli, C. J. Cramer and W. B. Tolman, *J. Am. Chem. Soc.*, 2016, **138**, 356–368.

235 L. Bertini, R. Breglia, M. Lambrughi, P. Fantucci, L. De Gioia, M. Borsari, M. Sola, C. A. Bortolotti and M. Bruschi, *Inorg. Chem.*, 2018, **57**, 86–97.

236 K. Pierloot, *Int. J. Quantum Chem.*, 2011, **111**, 3291–3301.

237 E. R. Davidson, *Annu. Rev. Phys. Chem.*, 2019, **70**, 1–20.

238 J. Chatt, *Nature*, 1950, **165**, 637–638.

239 R. Deeth, *Coord. Chem. Rev.*, 2001, **212**, 11–34.